

# nature

## THE PATH TO FLIGHT

Meet the closest relatives to early flying vertebrates

Randy Moore/13

### Coronavirus

Why have so many rich nations struggled with contact-tracing?

### Dams busted

The 1.2 million barriers fragmenting Europe's rivers

### Tipping the balance

Human-made mass set to exceed global biomass

# Nature.2020.12.19

[Sat, 19 Dec 2020]

- [Donation](#)
- [This Week](#)
- [News in Focus](#)
- [Books & Arts](#)
- [Work](#)
- [Research](#)
- [Amendments & Corrections](#)

# Donation

- -> [\*\*打赏 - Donation\*\*](#)

## 打赏 - JUST FOR FUN

支持分享! 一杯咖啡钱, 打赏金额随意, 感谢大家~ :)

支付宝

微信



支付就用支付宝



打开支付宝[扫一扫]

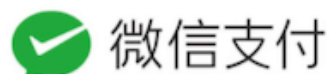
免费寄送收钱码: 拨打95188-6

<https://blog.csdn.net/bboyfelyu>

推荐使用微信支付



Mr.SIMPLE (\*\*辉)



本书来自: [www.github.com/hehonghui](http://www.github.com/hehonghui)

---

This article was downloaded by **calibre** from <http://economist.cool/donate.html>

# This Week

- **[How to rebuild the US Environmental Protection Agency](#)** [16 December 2020]  
Editorial • Joe Biden must take charge of repairing the EPA — and safeguard it in perpetuity.
- **[The EU must learn from the anti-expert narrative that drove Brexit](#)** [16 December 2020]  
Editorial • The sentiment that underpinned the Brexit referendum's success is not limited to the United Kingdom.
- **[Farewell to Europe's Horizon 2020](#)** [16 December 2020]  
World View • Although imperfect, the world's biggest funding scheme got a lot right.
- **[How bits of 'glass' take shape inside a cell](#)** [14 December 2020]  
Research Highlight • Odd protein droplets that behave like liquids make a smooth shift to having the properties of a solid.
- **[An 'aerosol factory' churns high in the Himalayas](#)** [07 December 2020]  
Research Highlight • Tiny particles forming on the roof of the world can affect global climate.
- **[Why pandas like to roll in piles of poo](#)** [08 December 2020]  
Research Highlight • A steaming pile holds allure for giant pandas, especially at one time of year.
- **[Sourdough starters give rise to a new line of yeast](#)** [09 December 2020]  
Research Highlight • Artisanal baking practices nourished a strain of yeast that is distinct from industrial microbes.

EDITORIAL

16 December 2020

# How to rebuild the US Environmental Protection Agency

Joe Biden must take charge of repairing the EPA — and safeguard it in perpetuity.



Biden needs to oversee efforts to strengthen the EPA. The durability of his commitments to protect public health and the environment depend on it. Credit: Carolyn Kaster/AP/Shutterstock

When former US president Richard Nixon proposed establishing the Environmental Protection Agency (EPA) in 1970, he spoke of the need to preserve Earth as a place that is both habitable by — and hospitable to —

people. Nixon, a Republican, acknowledged his own fear of creating a new federal bureaucracy. But the task of rescuing the natural environment, he argued, required a strong, independent agency that would be able to marshal “a coordinated attack on the pollutants which debase the air we breathe, the water we drink, and the land that grows our food”.

The EPA’s successes are undeniable. Over the past 4 decades, US emissions of the most common pollutants, as measured by weight, have fallen by 71%, even as the country’s population grew by some 105 million people and the size of its economy nearly tripled. Most emissions from the average automobile have fallen by 98–99% over the same period, to take just one industrial sector. Petrol is cleaner — and free of toxic lead. City sewage and industrial waste no longer flow unchecked into waterways, and rivers no longer catch fire as a result of discharged oil waste. And, internationally, the EPA’s science and regulatory standards have helped other countries to protect their environments, too.

But on President Donald Trump’s watch, regulatory standards have been weakened, research teams slashed and independent scientific advice relentlessly assaulted. Four years on, the outgoing administration has not just dismantled environmental and public-health protections, but also systematically undermined the EPA’s scientific and regulatory foundations — invariably in favour of the industries that the agency regulates. Incoming president Joe Biden and his vice-president, Kamala Harris, have a considerable restoration task ahead of them.



# Can Joe Biden rebuild the ravaged US Environmental Protection Agency?

Although Trump swung the axe, the EPA's destruction was a long time in the making. Its fiercest critics have sought to cut the agency back for years, arguing that the nation's air and water are already cleaner than they have been in decades and that stronger regulations come at the expense of jobs and economic growth.

Biden's campaign pledges suggest that he and his team have every intention of working to restore and strengthen rules and regulations, and to rebuild the EPA's in-house science teams. But the incoming administration must think seriously about structural reforms. In addition to the need for past damage to be repaired, the agency must be strengthened in a way that makes it harder for any future administration to even think about strangling the structures of evidence that are essential to good policy. This will not be easy, but the following actions will help.

An EPA administrator will soon be nominated. Once in the post, they must make it an urgent priority to nominate an assistant administrator for the EPA's research division, the Office of Research and Development (ORD). This position has not been filled for eight years. Senate Republicans refused to confirm former president Barack Obama's last nominee, and the EPA leadership appointed by Trump never nominated anybody.



## **The sustained undermining of science by the EPA's leaders is a travesty.**

Scientists at ORD conduct the core scientific assessments and research that feed into the agency's regulatory decisions. It's important that the ORD chief sits at the top table so that the division — and science more broadly — has a voice alongside the regulatory and political interests that the EPA administrator has to work with. The new EPA administrator should also consider bringing in a separate chief scientist who can represent science across the entire agency.

Another notable EPA role is that of the scientific-integrity official, whose job is to ensure that the agency's career scientists and political appointees alike abide by the agency's scientific code of conduct. This role needs to be upgraded to a more senior position that reports directly to the administrator and is situated alongside the EPA's inspector-general, who has broad authority to investigate malfeasance, such as allegations of corruption or conflicts of interest, at the agency.

Staff incentive structures should also be reviewed. The aim of such structures must always be to prioritize independence and honesty over efficiency or obedience. At an agency whose primary purpose is to protect human life, the leadership must be told the truth, not what it wants to hear.



## **Five ways that Trump is undermining environmental protections under the cover of coronavirus**

Under the incoming administration, the White House Office of Science and Technology Policy is expected to reprise its former role as coordinator and connector of science across federal agencies. As part of that mission, it should explore the idea of appointing someone to oversee scientific-integrity rules across federal agencies, and to provide relevant support when needed.

There are also things that Congress can do to better insulate the EPA from political interference, including codifying scientific-integrity policies at the EPA and other agencies through legislation. Democrats have already introduced a bill with this aim. Giving scientific-integrity policies the force of law would raise the stakes for future administrations, and make it illegal for leaders to disobey such policies.

But Biden's first step must be to appoint an EPA administrator who understands how government works and has the vision and steel to carry out his aggressive environmental agenda. They must lead with the purpose of securing the EPA's mission and independence in perpetuity, not just over the next four years.

Success here will also require a role for the incoming president. One of the greatest challenges all presidents face is choosing which actions to delegate, to whom, and to what extent. Biden will need to take personal charge of the pandemic response, but he must also make strengthening the EPA a priority, not least because the viability — and durability — of his commitments to protect public health and the environment depend on it.

The need to take these steps, aimed at strengthening science and scientific integrity at the EPA, was brought into sharp focus by the actions of the Trump administration, which exposed a deep flaw in the agency's current system: policies relating to integrity were designed with the assumption that the EPA leadership would guard and enforce them. Under Trump, leaders used the power of their offices to turn the clock back on important environmental and public-health regulations. The EPA has lived through the most dangerous period of its 50-year history — Biden's administration has the chance to ensure that the agency is never put in the same position again.

doi: <https://doi.org/10.1038/d41586-020-03539-z>

## Jobs from Nature Careers

- - - [All jobs](#)
    - - [Study Nurse \(m/w/d\)](#)

[German Cancer Research Center in the Helmholtz Association \(DKFZ\)](#)

[Heidelberg, Mannheim, Germany](#)

[JOB POST](#)

- [Two Research Software Engineers](#)

[Jülich Research Centre \(FZJ\)](#)

[Garching, Germany](#)

[JOB POST](#)

- [Softwareentwickler/in \(w/m/d\) für Experimentsysteme](#)

[Helmholtz-Zentrum Berlin for Materials and Energy \(HZB\)](#)

[Berlin, Germany](#)

[JOB POST](#)

- [Software Developer \(f/m/d\) for Experiment Systems](#)

Helmholtz-Zentrum Berlin for Materials and Energy (HZB)

Berlin, Germany

JOB POST

---

This article was downloaded by **calibre** from <https://www.nature.com/articles/d41586-020-03539-z>

| [Section menu](#) | [Main menu](#) |

## EDITORIAL

16 December 2020

# The EU must learn from the anti-expert narrative that drove Brexit

The sentiment that underpinned the Brexit referendum's success is not limited to the United Kingdom.



In the run-up to the Brexit referendum in 2016, then UK justice secretary Michael Gove (left) famously told Faisal Islam at Sky News that people had had enough of experts. Credit: Dan Kitwood/Getty

The United Kingdom's departure from the European Union is not only a tragedy for its people, but also an existential shock for the EU. The EU is as much an idea as an economic and political union. It has been a global

symbol of how enemies can become friends and partners in prosperity. It is also remarkable for the value it places on science and expertise, which are at the heart of its commitment to the rule of law, representative democracy, free trade and free movement of people.

Researchers are integrated into EU decision-making to help to ensure that policy is informed by a consensus of evidence, a system sometimes called technocratic governance. The EU itself also supports the world's largest regional research fund — the 85-billion (US\$100-billion) Horizon Europe programme. That the United Kingdom, formerly one of the EU's biggest economies, has chosen to reject an institution that values evidence and science so highly is of huge significance.

As the clock ticks towards 31 December, after which the United Kingdom will no longer be required to align itself with EU rules, the EU's researchers must study the anti-expert narrative that contributed to Brexit, and its potential to be used in the union's 27 remaining member countries to undermine evidence and the rule of law.



**UK and EU: Cherish what you have achieved and stay close**

EU policymakers contend that the United Kingdom is an outlier, and that Brexit will not affect the remaining 27 member states. The United Kingdom, according to this view, was never a fully aligned EU country. It was not among the founding nations. It chose to stay out of the Eurozone. Had UK governments been more committed to the EU, why would they have chosen to give citizens the option of leaving — first in 1975, and again in 2016? Such arguments are not incorrect, but, at the same time, some of the forces that shaped Brexit do not apply only to the United Kingdom.

For example, Johan Schot, a historian of science and technology policy at Utrecht University in the Netherlands and co-author of *Writing the Rules for Europe* (2018), a history of how expert knowledge helped to create the EU, says some EU citizens have become dissatisfied with technocratic governance. There's also a perception that when decisions are made only on the basis of expert evidence, people aren't in control of their own choices, adds Kalypso Nicolaidis, an international-relations researcher at the University of Oxford, UK. Both Nicolaidis — author of *Exodus, Reckoning, Sacrifice* (2019), a book on the lessons that the United Kingdom and the EU can learn from Brexit — and Schot say that EU leaders must find more participatory methods of governance, so that citizens are reassured that they have more of a voice in the decisions made on their behalf.

This advice should be heeded. Brexit's architects implicitly targeted the research community when they categorized researchers as 'experts' and separate from 'the people'. So, whereas in 2016 the United Kingdom's researchers — who were among the leaders and supporters of the Remain campaign — argued, among other things, that Brexit's uncertainty would harm the country, the Leave campaign responded by seeking to divide researchers from the rest of society. Pro-Brexit minister Michael Gove famously remarked that the British people "have had enough of experts", which included research organizations. It was an extraordinary thing to say, but it spoke to the campaign's overall narrative that 'the people' would be better off if the United Kingdom left the EU — in contrast to those who benefit from the free movement of people and from EU funding.



## **Brexit's back: the five issues that will shape science**

As populist parties prepare for elections in Germany next year and in France in 2022, they might decide to adopt this narrative, given its apparent success in the United Kingdom. Even in countries where such parties do not fare well, they have been able to influence mainstream parties to adopt some of their ideas and policies. And it will not be lost on some mainstream parties that dividing experts from the broader population could be a part of a winning formula.

Researchers will always be essential to the EU. Horizon Europe, too, will be central to the global challenges that the world faces — from COVID-19 to climate change. And the projects it funds might yet benefit from the involvement of UK researchers, albeit as associate members.

But although Brexit itself is likely to be an isolated event, the tactics used to achieve it aren't. There are lessons here not only for the EU's leaders, but also for researchers, who should seek to understand how their work was used in an anti-expert narrative. And the EU must beware the risks of such

narratives spreading, because, should they do so, that could have far-reaching consequences.

Nature 588, 370 (2020)

doi: <https://doi.org/10.1038/d41586-020-03540-6>

## Jobs from Nature Careers

- - - [All jobs](#)
    - - [Study Nurse \(m/w/d\)](#)

[German Cancer Research Center in the Helmholtz Association \(DKFZ\)](#)

[Heidelberg, Mannheim, Germany](#)

[JOB POST](#)

- [Two Research Software Engineers](#)

[Jülich Research Centre \(FZJ\)](#)

[Garching, Germany](#)

[JOB POST](#)

- [Softwareentwickler/in \(w/m/d\) für Experimentsysteme](#)

[Helmholtz-Zentrum Berlin for Materials and Energy \(HZB\)](#)

[Berlin, Germany](#)

JOB POST

- **Software Developer (f/m/d) for Experiment Systems**

Helmholtz-Zentrum Berlin for Materials and Energy (HZB)

Berlin, Germany

JOB POST

---

This article was downloaded by **calibre** from <https://www.nature.com/articles/d41586-020-03540-6>

| [Section menu](#) | [Main menu](#) |

WORLD VIEW  
16 December 2020

# Farewell to Europe's Horizon 2020



Although imperfect, the world's biggest funding scheme got a lot right.

## **Alison Abbott**

Alison Abbott is a science writer in Munich, Germany, and a former senior European correspondent for *Nature*.

[Contact](#)

### Search for this author in:

- [Pub Med](#)
- [Nature.com](#)
- [Google Scholar](#)

Like national presidencies, European Union framework research programmes have a fixed term in which they can execute their agenda —

bolstering the economy, improving sustainability and so on. How well they do is best assessed in retrospect.

The current scheme, Horizon 2020, is the world's biggest multinational research programme, having distributed €74 billion (US\$90 billion) to more than 150,000 scientists participating in 31,000 projects or grants. When it ends this year, how will it be judged?

I think history will look kindly on it. Stripped of much of the legendary bureaucracy that has plagued these framework programmes in the past, it has become fit for purpose.

As a journalist, I have followed successive EU framework research programmes since the early 1990s. The scientific community had a love–hate relationship with them. But the mood changed for the better with the launch of Horizon 2020, the eighth in the series. Outrage became the exception, and my stories less colourful.

How did these programmes evolve into something scientists no longer loved to hate? One key was the expansion in Horizon 2020 of the European Research Council (ERC), which gives large grants to individual researchers. That was an instant, rocketing success. But there is more to it.



## Europe the rule-maker

The programmes are executed by the European Commission, whose job is to serve the political agendas of the EU member states and the European Parliament. The programmes differ from their national counterparts in that they mostly require scientists from different countries to collaborate in projects that fit into economic and social policies.

A central, unchanging aspiration is for borderless research so that scientists across the continent can work in any country without disadvantage and can freely exchange research materials and data. But the commission is often pressed by its political masters to address issues that are indirectly related to research — for example, supporting gender equality, raising the economic prospects of poorer countries or recreating the innovative spirit of California's Silicon Valley.

Those aims produced application procedures of bewildering complexity. What's more, with politicians keen to stamp out fraudulent use of any funds, the commission added requirements for burdensome progress reports on research projects. It also added some of its own unforced, and unnecessary, complications.

Serious efforts to reduce complexity became visible during Framework Programme 7 (FP7, 2007–13) and paid off in Horizon 2020, with simplified application and reporting procedures. This resulted in the average time from application to contract shrinking from around 18 to 6 months.

Critical to the turnaround, Horizon 2020 created a dedicated funding stream for excellence-driven fundamental research. Brussels had long ignored calls for such a stream because basic research was considered a matter of culture, like art, for which the commission had no competence. Such concerns were eventually trumped by arguments that basic research is fuel for economic innovation and is a bulwark against brain drain. Politicians were appeased by another dedicated funding stream to promote innovation.



## Where is the brain in the Human Brain Project?

The ERC is the major component of the fundamental research stream. After a limited test run in FP7, it was embedded in Horizon 2020. An independent evaluation earlier this year concluded that around 80% of ERC-funded projects make scientific breakthroughs or major advances.

The funding stream also included the flamboyant Flagship competitions — billion-euro, ten-year projects exploiting digital technologies. Their pilot phase in FP7 was rocky, but they blossomed amid intense competition in Horizon 2020 to spawn some splendid ideas, such as digitizing health data or the history of European cities. To my regret, they will not be continued in Horizon 2020's successor. Horizon Europe, which launches next month, will instead support smaller, safer versions called missions.

In parallel with Horizon 2020, the EU made a political decision to allow research facilities to be eligible for EU infrastructure subsidies. This raises the potential of research communities in poorer regions to become more competitive for research funds. Happily, this concept is, like the ERC, now

embedded in the commission's psyche; it will continue in Horizon Europe and probably beyond.

Despite the massive simplification and rule relaxations, application procedures for Horizon 2020 were still heavy, and applicants had low success rates. Just 13% of ERC applications are approved, and rates are even worse for thematic collaborations such as health (10%) and climate (11%). This may be somewhat improved in Horizon Europe, with its higher budget of €95 billion.

Still, there is no research programme in the world like Horizon 2020. Twenty years ago, I would not have predicted that an EU framework research programme would become an object of envy. It achieved this because the political mood was accommodating. That can shift. Already, early commission hopes that Horizon Europe would open more widely to the world have been dashed as the global political mood becomes more nationalistic.

But mostly, the spirit of Horizon 2020 will live on in its successor.

Nature **588**, 371 (2020)

doi: <https://doi.org/10.1038/d41586-020-03516-6>

## **Jobs from Nature Careers**

- - - [All jobs](#)
    - - [Study Nurse \(m/w/d\)](#)

[German Cancer Research Center in the Helmholtz Association \(DKFZ\)](#)

[Heidelberg, Mannheim, Germany](#)

JOB POST

- **Two Research Software Engineers**

Jülich Research Centre (FZJ)

Garching, Germany

JOB POST

- **Softwareentwickler/in (w/m/d) für Experimentsysteme**

Helmholtz-Zentrum Berlin for Materials and Energy (HZB)

Berlin, Germany

JOB POST

- **Software Developer (f/m/d) for Experiment Systems**

Helmholtz-Zentrum Berlin for Materials and Energy (HZB)

Berlin, Germany

JOB POST

---

This article was downloaded by **calibre** from <https://www.nature.com/articles/d41586-020-03516-6>



Living cells can harbour protein aggregates with the properties of soft glasses. Credit: EYE OF SCIENCE/SPL

Biophysics

14 December 2020

## How bits of ‘glass’ take shape inside a cell

Odd protein droplets that behave like liquids make a smooth shift to having the properties of a solid.

Some living cells contain protein clusters that behave like liquid droplets. But these droplets gradually stiffen with age, and new experiments have revealed that they turn into a curious material: a soft ‘glass’.

Previous research showed that cellular protein droplets can solidify, but how they do so has puzzled researchers. To understand the shift, Anthony Hyman at the Max Planck Institute of Molecular Cell Biology and Genetics in Dresden, Germany, Frank Jülicher at the Max Planck Institute for the Physics of Complex Systems, also in Dresden, and their colleagues prepared droplets of protein isolated from cells and compared newly formed droplets with aged droplets.

The researchers used laser beams to squeeze and stretch the droplets, which became more elastic with age. In separate experiments, droplets became smaller and denser as they grew older, and the movement of tracer beads in the droplets became restricted.

The observations suggest that, over time, the interactions between the proteins making up the droplets grew stronger, restraining the proteins. As the proteins froze into place, the liquid droplets gradually solidified — a process typically seen when glassy materials form.

[Science \(2020\)](#)

- [Biophysics](#)

---

This article was downloaded by **calibre** from <https://www.nature.com/articles/d41586-020-03546-0>



Data from the Pyramid International Laboratory/Observatory at the base of Mount Everest show that local winds help to generate atmospheric particles that affect cloud formation. Credit: Alamy

Atmospheric science

07 December 2020

## An ‘aerosol factory’ churns high in the Himalayas

Tiny particles forming on the roof of the world can affect global climate.

An observatory on the flanks of Mount Everest has revealed that even the clean air of the Himalayas can generate atmospheric particles that play an important part in shaping Earth's climate.

Aerosols are microscopic airborne particles that form from both natural sources, such as gases released by plants, and pollutants emitted by human activities. Aerosols can affect cloud formation and sunlight's passage through the air, but not all of their effects on climate are clear.

Aiming to study aerosols in near-pristine air, Federico Bianchi at the University of Helsinki and his colleagues set up atmospheric monitoring instruments just a few kilometres below Everest's summit. The team took observations during months when pollution from India and nearby countries rarely drifts to the site.

Despite this, many aerosol particles formed on days when the wind blew up a valley towards the observatory. The winds probably carried gases that were emitted by vegetation and were then transformed into particles at higher altitudes.

The Himalayas thus act as an aerosol factory, pumping naturally sourced particles into the atmosphere. Knowing about this natural source of aerosols could help scientists to untangle the effects of human-made aerosols.

[Nature Geosci. \(2020\)](#)

- [Atmospheric science](#)

---

This article was downloaded by **calibre** from <https://www.nature.com/articles/d41586-020-03478-9>



Giant pandas have thick coats but sometimes don an extra outer layer against the winter's chill. Credit: Fuwen Wei

Animal behaviour

08 December 2020

# Why pandas like to roll in piles of poo

A steaming pile holds allure for giant pandas, especially at one time of year.

Wild giant pandas sometimes mess up their neat black and white outfits by rolling in horse manure — and now scientists have an explanation for why the animals engage in this odd activity.

Fuwen Wei at the Chinese Academy of Sciences in Beijing, Ren Lai at the Chinese Academy of Sciences in Kunming and their colleagues studied 38 instances of the behaviour in giant pandas (*Ailuropoda melanoleuca*) in the Qinling Mountains, where, for millennia, animals have been exposed to horses travelling ancient trade routes. The pandas usually chose manure less than ten days old, prompting the team to wonder whether they were seeking volatile compounds that are present only in fresh dung. Sure enough, experiments with zoo pandas showed that the animals enjoyed rolling in hay dosed with volatile beta-caryophyllene and caryophyllene oxide.

But why? The authors only observed horse-manure rolling from November to April, and 95% of rolling events were recorded when the temperature was a chilly  $-5^{\circ}\text{C}$  to  $15^{\circ}\text{C}$ . Mice treated with the chemicals could better withstand cold temperatures. The researchers conclude that pandas use chemicals in horse dung to block cold receptors in their skin, making them feel more comfortable — even if they look less tidy — in the winter.

[Proc. Natl Acad. Sci. USA \(2020\)](#)

- [Animal behaviour](#)

---

This article was downloaded by **calibre** from <https://www.nature.com/articles/d41586-020-03477-w>



Staff of life: artisanal baker's yeast has genetic ties to strains found in fruit and other natural sources. Credit: Getty

Genomics

09 December 2020

## Sourdough starters give rise to a new line of yeast

Artisanal baking practices nourished a strain of yeast that is distinct from industrial microbes.

Humans used yeast to make bread well before the coronavirus pandemic, when stay-at-home orders unleashed a bread-baking frenzy. Now, a survey of yeasts (*Saccharomyces cerevisiae*) from around the world shows that, over the course of centuries, industrial and artisanal bread making have each led to the evolution of a distinct lineage of baker's yeast.

Bakers can ferment their dough with industrial cultures of *S. cerevisiae* or with sourdough, a mix of water and flour fermented by *S. cerevisiae* and other microbes. To characterize these leavening agents, Delphine Sicard at the University of Montpellier in France and her colleagues analysed 229 *S. cerevisiae* strains — 31 mass-produced strains sold in stores and used in industrial bakeries and 198 strains from sourdough starters.

Compared with *S. cerevisiae* used to produce beer and wine, both types of baking yeast produce more CO<sub>2</sub>, which helps the dough to rise. Industrial strains tend to be more genetically similar to beer-making yeasts, whereas most sourdough strains resemble yeasts found in natural environments, including water and fruit.

Preserving a range of bread-making practices will help to maintain this genetic diversity, the researchers say.

[Curr. Biol. \(2020\)](#)

- [Genomics](#)

---

This article was downloaded by **calibre** from <https://www.nature.com/articles/d41586-020-03487-8>

# News in Focus

- **[Excitement over Biden's pick to lead US health agency](#)** [16 December 2020]  
News Round-Up • The latest science news, in brief.
- **[US authorization of first COVID vaccine marks new phase in safety monitoring](#)** [11 December 2020]  
News • The FDA has issued an emergency-use authorization for the Pfizer–BioNTech vaccine. Regulators are gearing up to look for side effects.
- **[Oxford COVID-vaccine paper highlights lingering unknowns about results](#)** [08 December 2020]  
News • The Oxford–AstraZeneca partnership is the first major developer to publish detailed data from phase III trials.
- **[Physicists in China challenge Google's 'quantum advantage'](#)** [03 December 2020]  
News • Photon-based quantum computer does a calculation that ordinary computers might never be able to do.
- **[Scientists fear that 'covidization' is distorting research](#)** [02 December 2020]  
News • Some researchers worry that shifting priorities towards pandemic-focused science comes at the expense of other disciplines.
- **[How kids' immune systems can evade COVID](#)** [10 December 2020]  
News • Childrens' untrained immune response seems to be key to eliminating SARS-CoV-2.
- **[CRISPR gene therapy shows promise against blood diseases](#)** [08 December 2020]  
News • Researchers report early successes using genetic approaches to treat sickle-cell anaemia and β-thalassaemia.
- **[Why many countries failed at COVID contact-tracing — but some got it right](#)** [14 December 2020]  
News Feature • Rich nations have struggled with one of the most basic and important methods for controlling infectious diseases.

- **How COVID-19 is changing the cold and flu season** [15

December 2020]

News Feature • Measures meant to tame the coronavirus pandemic are quashing influenza and most other respiratory diseases, which could have wide-ranging implications.

---

| [Next section](#) | [Main menu](#) | [Previous section](#) |

NEWS ROUND-UP

16 December 2020

# Excitement over Biden's pick to lead US health agency

The latest science news, in brief.



Walensky is a prominent HIV/AIDS researcher, with expertise in virus testing and prevention.

## Excitement over Biden's pick to lead US health agency

A renowned HIV/AIDS researcher, Rochelle Walensky, will become the head of the US Centers for Disease Control and Prevention (CDC) after Joe Biden takes over as president — and [scientists are thrilled](#).

“Collectively, it feels like the entire infectious-disease and public-health community is excited to have her in the position, and to help lead the CDC during such a pivotal time,” wrote Saskia Popescu, an epidemiologist at George Mason University who is based in Phoenix, Arizona, in an e-mail to *Nature*.

The CDC’s reputation as a world-leading health agency has suffered during the pandemic. President Donald Trump’s administration has been widely criticized for sidelining the agency and its science.

Throughout the pandemic, Walensky (pictured), currently chief of infectious diseases at Massachusetts General Hospital in Boston and a researcher at Harvard Medical School, has been outspoken about the importance of science-based decision-making in the pandemic response. “I’m honored to be called to lead the brilliant team at the CDC,” she tweeted after the announcement. “We are ready to combat this virus with science and facts.”

## Researchers' mixed feelings on 'pay to publish' system

A [survey of nearly 1,000 academic researchers in South Africa](#) suggests that the majority are in favour of keeping a government scheme that offers cash rewards for publishing research papers, even though they agree that this can promote unethical practices.

The publication-incentive programme — which awards payments when researchers publish journal articles, conference proceedings and book chapters — is the country's largest single pool of research funding. But it has attracted criticism. Some researchers say that it promotes publishing in predatory journals, which charge fees but typically do not provide peer review, and encourages 'salami slicing' of studies to produce multiple papers rather than one high-quality article.

In a survey of 967 South African academics, more than two-thirds of respondents agreed that incentives enticed researchers to salami-slice their research, and more than a half agreed that they led to inappropriate author attribution. But 68% of respondents thought that the country should keep its incentive system.

An ongoing shortage of research funds could be one reason for this apparent contradiction. South Africa's Department of Science and Innovation, a major research funder, saw its budget slashed by 16% this year following a pandemic-related economic downturn.

# PAPER MONEY

A survey of South African academics found that the majority did not want to see the end of publication rewards even though they think the system is flawed.

■ Agree ■ Neither agree or disagree ■ Disagree

**Incentives directly linked to number of publications promote the practice of publication of 'smallest publishable units'** (935 respondents)



**Incentives may lead to the inappropriate allocation of authorship** (298)



**Incentives that are paid directly to individual authors may lead to unethical publication behaviour** (934)



**Incentives should be abolished** (930)



**Incentives should not be abolished** (935)



©nature

Source: Elsie Breet, Jan Botha, Lyn Horn, Leslie Swartz

## **Snakebite's toll on life in India**

Every year, snakebites cost India's citizens the equivalent of 3 million years of health and productivity. That figure comes from the [first analysis of the toll of snakebites on survivors](#), who can be left with disabling conditions such as amputation, kidney disease and severe scarring.

Snakebite “is just still really not very well studied or understood at the same level as a lot of these other [tropical] diseases”, says Nick Roberts, who was part of the team at the Seattle-based University of Washington’s Institute for Health Metrics and Evaluation that calculated the figure. Now a first-year medical student at Weill Cornell Medicine in New York, Roberts presented the results during November’s virtual meeting of the American Society of Tropical Medicine and Hygiene.

The World Health Organization designated poisoning by snakebite a neglected tropical disease in 2017. And last year, it launched a global initiative to halve the number of deaths and disabilities it causes by 2030.

The initiative highlights the need for better data, says Prabhat Jha, director of the Centre for Global Health Research in Toronto, Canada. If you’re going to achieve that goal, “then you need to know where the problems are”.



Farmers who work in fields in India are especially at risk of getting bitten by snakes such as the Russell's viper (*Daboia russelii*) shown here. Credit: John Benjamin Owens, MEFGL Bangor University/Captive & Field Herpetology

Nature 588, 375 (2020)

doi: <https://doi.org/10.1038/d41586-020-03517-5>

## Jobs from Nature Careers

- - - [All jobs](#)
    - - [Mitarbeiter/in \(w/m/d\) im Verwaltungsdienst \(Sekretär/in\) Teilzeit \(75%\)](#)

Karlsruhe Institute of Technology (KIT)

Karlsruhe, Germany

JOB POST

- Foreign Language Assistant/ -Correspondent (f/m/x)

Helmholtz Centre Potsdam - German Research Centre for Geosciences (GFZ)

Potsdam, Germany

JOB POST

- Technischer Mitarbeiter (w/m/d) im Bereich Facilitymanagement

Helmholtz Centre Potsdam - German Research Centre for Geosciences (GFZ)

Potsdam, Germany

JOB POST

- Study Nurse (m/w/d)

German Cancer Research Center in the Helmholtz Association (DKFZ)

Heidelberg, Mannheim, Germany

JOB POST

| [Section menu](#) | [Main menu](#) |

NEWS

11 December 2020

- Update [12 December 2020](#)

# US authorization of first COVID vaccine marks new phase in safety monitoring

The FDA has issued an emergency-use authorization for the Pfizer–BioNTech vaccine. Regulators are gearing up to look for side effects.

**Heidi Ledford**

**Search for this author in:**

- [Pub Med](#)
- [Nature.com](#)
- [Google Scholar](#)

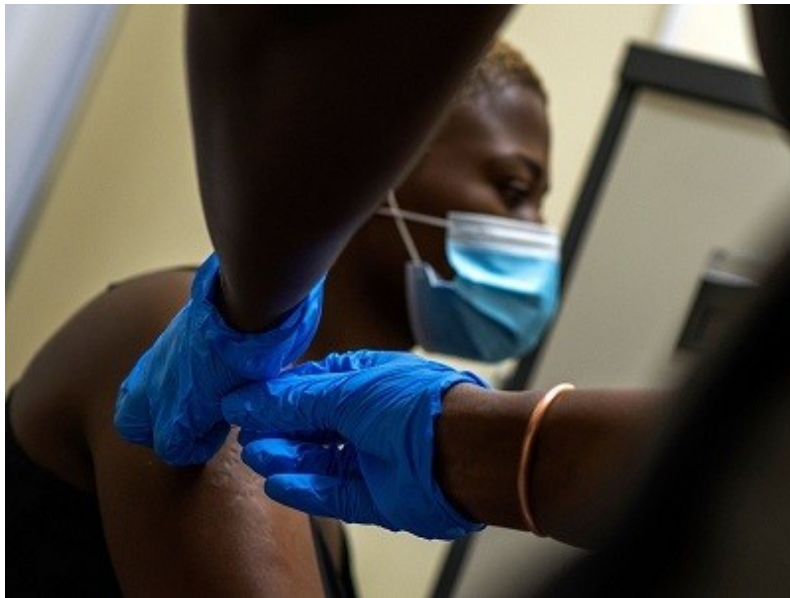


The US Food and Drug Administration is expected to authorize an emergency rollout of the Pfizer–BioNTech COVID-19 vaccine. Credit: Hugh Hastings/Getty

The US Food and Drug Administration (FDA) has granted an emergency-use authorization for the country's first COVID-19 vaccine. The vaccine, made by Pfizer of New York City and BioNTech of Mainz, Germany, can now be administered in the United States outside a clinical trial.

The decision, announced on 11 December, trails behind emergency authorization of the same vaccine in the United Kingdom and Canada, and news that the United Arab Emirates has approved another COVID-19 vaccine, produced by Sinopharm of Beijing.

The FDA decision follows a vote by its advisory committee on 10 December: the committee voted 17 to 4, with one abstention, to recommend the vaccine.



## The UK has approved a COVID vaccine — here's what scientists now want to know

Taken together, these developments mean that the world is entering a new phase in its fight against the coronavirus pandemic: sifting through reports from the hundreds of thousands of people who get the first jabs, in search of potential — and probably rare — side effects, and then working out whether those events are likely to have been caused by the vaccine.

“It is very difficult to prove causation,” says Peter Todd, a partner at Hodge Jones & Allen Solicitors in London, who has handled vaccine-injury cases for about 20 years. “Vaccine effects are so rare, you need a massive and very powerful epidemiological study to show that there actually is an association with the vaccine.”

The FDA advisory committee based its recommendation on data from more than 43,000 people — most of whom were followed for a median of 2 months after their second shot of the vaccine. An analysis of the first 170 cases of COVID-19 in the group indicated that the vaccine is 95% effective

at preventing symptomatic SARS-CoV-2 infections. The results from the trial were published on 10 December in *The New England Journal of Medicine*<sup>1</sup>.

## Reported side effects

The vaccine also seems to be safe, the trial found: the most common side effects included fatigue, headache and fever. There were four cases of Bell's palsy — a condition that temporarily weakens some muscles in the face — among those who received the vaccine, compared with none among those who received the placebo. But the FDA could not definitively link the condition to the vaccine, agency medical officer Susan Wollersheim told the committee: this frequency of Bell's palsy is not unusual in the general population, and one of the study participants affected by it had a history of the condition.

Nevertheless, on the first day of administering Pfizer's vaccine to older adults in care homes and to front-line health-care workers, the United Kingdom uncovered another possible safety concern: two recipients with a history of severe allergic reactions, called anaphylaxis, experienced an episode after getting the vaccine.

That serves as a good example of the side effects that can emerge when a vaccine is moved out of carefully controlled clinical trials, says Todd.



## COVID vaccination logistics: five steps to take now

Still, the FDA advisers were not dissuaded by the reports: “The vaccinator should be able to handle anaphylactic reaction,” said Cody Meissner, a paediatrician at the Tufts University School of Medicine in Boston, Massachusetts. “That’s recommended for any vaccine.”

But paediatrician Paul Offit of the Children’s Hospital of Philadelphia in Pennsylvania expressed concerns that anyone with a history of strong allergies could be deterred from receiving the vaccine. He recommended that a small study be done of people with common allergies, for example to eggs or peanuts, to confirm safety in that population. “This issue is not going to die until we have better data,” he told the committee. “I think we need to offer people some solace that this is not going to be a problem for them.”

### **Long-term monitoring**

Most reactions to vaccines become apparent within six weeks of receiving the jab, but longer tracking is useful for picking up any adverse events that might appear later, and could also help rule out connections to medical

events that are falsely attributed to vaccines, FDA vaccinologist Philip Krause said. “Safety follow-up can play a big role in helping us determine what the vaccine doesn’t cause,” he said.

At the advisory meeting, the US Centers for Disease Control and Prevention (CDC) laid out complex plans for monitoring Pfizer’s vaccine if it is approved for rollout across the country. The plans included pre-existing programmes, such as the FDA and CDC Vaccine Adverse Event Reporting System, which collects reports of safety concerns. The CDC also intends to roll out a new programme called v-Safe, which will send text messages to health-care workers who receive the vaccine, to ask about any possible adverse events. Meanwhile, researchers at Brown University in Providence, Rhode Island, are designing a system to monitor residents of long-term care homes.



## **Anti-vaccine movement could undermine efforts to end coronavirus pandemic, researchers warn**

Researchers will trawl through reports of adverse events in search of those that might have some connection to vaccination. That link is usually

established through a combination of factors: the number of people who experienced the event, the length of time that elapsed between vaccination and the potential side effect, and a possible biological link.

The more time elapses between the jab and the event, the more cases are needed to suggest causality, says Robert Heyderman, an infectious-disease researcher at University College London who chairs the data and safety monitoring boards for a COVID-19 vaccine developed by the University of Oxford, UK, and AstraZeneca of Cambridge, UK. “It is not until you see these vaccines implemented at scale that you’ll start to see unusual events and try to work out whether there’s a link to the vaccine,” says Heyderman.

As the vaccine rollout continues, it will be important to communicate information about any potential vaccine side effects to the public — while conveying the relative size of those risks. A person would probably be more at risk from crossing a road than from receiving a vaccine, says Heyderman.

Clear communication is particularly important in the era of social media and vaccine hesitancy, when anecdotal reports of a medical event after vaccination can be amplified on the Internet and can feed into pre-existing fears about vaccines. “As soon as you get mistrust around a vaccine, you won’t get the vaccine uptake that you need in order to control the pandemic,” says Heyderman.

Nature 588, 377-378 (2020)

doi: <https://doi.org/10.1038/d41586-020-03542-4>

## Updates & Corrections

- **Update 12 December 2020:** On 12 December, the story was updated with the US FDA's decision to issue an emergency use authorization for the Pfizer–BioNTech vaccine.

## References

1. 1.

Polack, F. P. *et al.* *N. Engl. J. Med.*  
<https://doi.org/10.1056/NEJMoa2034577> (2020).

## Jobs from Nature Careers

- - - [All jobs](#)
    - - [Study Nurse \(m/w/d\)](#)  
  
[German Cancer Research Center in the Helmholtz Association \(DKFZ\)](#)  
  
[Heidelberg, Mannheim, Germany](#)  
  
[JOB POST](#)
      - [Two Research Software Engineers](#)  
  
[Jülich Research Centre \(FZJ\)](#)  
  
[Garching, Germany](#)  
  
[JOB POST](#)
      - [Softwareentwickler/in \(w/m/d\) für Experimentsysteme](#)  
  
[Helmholtz-Zentrum Berlin for Materials and Energy \(HZB\)](#)  
  
[Berlin, Germany](#)  
  
[JOB POST](#)
      - [Software Developer \(f/m/d\) for Experiment Systems](#)

Helmholtz-Zentrum Berlin for Materials and Energy (HZB)

Berlin, Germany

JOB POST

---

This article was downloaded by **calibre** from <https://www.nature.com/articles/d41586-020-03542-4>

| [Section menu](#) | [Main menu](#) |

NEWS

08 December 2020

# Oxford COVID-vaccine paper highlights lingering unknowns about results

The Oxford–AstraZeneca partnership is the first major developer to publish detailed data from phase III trials.

**Heidi Ledford**

Search for this author in:

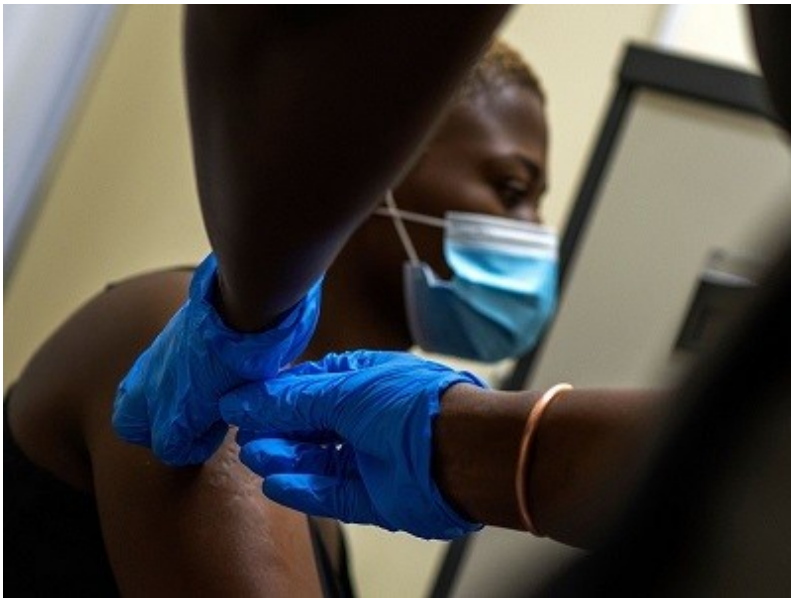
- [Pub Med](#)
- [Nature.com](#)
- [Google Scholar](#)



The results suggest that the Oxford–AstraZeneca vaccine is safe and effective. Credit: Juan Mabromata/AFP/Getty

The first formally [published results](#) from a large clinical trial of a COVID-19 vaccine — which scientists hope could be among the cheapest and easiest to distribute around the world — suggest that the vaccine is safe and effective. But the data also highlight a number of lingering unknowns, including questions about the most effective dosing regimen and how well it works in older adults.

The vaccine, developed by the University of Oxford, UK, and the pharmaceutical firm AstraZeneca in Cambridge, UK, has been closely watched, in part because it is likely to be simpler to distribute than the two RNA-based vaccines from companies [Pfizer](#) and [Moderna](#), which need to be stored at low temperatures. The Oxford team is also now the first of these three leading COVID-vaccine developers to publish results from its phase III trials in a peer-reviewed journal — so far, the findings have been disseminated only through press releases.



## The UK has approved a COVID vaccine — here's what scientists now want to know

Researchers have been eager to delve into the details of Oxford's results, which were published in *The Lancet*<sup>1</sup> on 8 December, after [preliminary results released last month](#) showed an unexpected increase in efficacy among a subset of study participants who, owing to a measurement error, received less of the vaccine in the first of their two doses. Some statisticians also raised concerns that the results pool data from different trials, rather than drawing from a single study.

### Dosing puzzle

When data from the various dosing regimens were combined, the study found that the vaccine was 70% effective at preventing symptomatic coronavirus infections. The standard regimen — two doses of the same strength administered a month apart — had an efficacy of 62%, whereas the regimen with a lower initial dose yielded an efficacy of 90%. “The efficacy

and the safety are fine,” says virologist Stephen Griffin at the University of Leeds, UK. “Overall, what you can say is that it does work.”

At a press briefing on 8 December, study investigators said that the data were pooled in agreement with guidance from regulators. However, researchers have struggled to explain how a higher efficacy could be achieved from a lower initial dose, and trial investigators have said that a separate trial is needed to follow up on the finding. Furthermore, the low-dose arm of the trial did not include anyone over the age of 55, raising concerns that the higher efficacy was merely a by-product of excluding an age group that is particularly vulnerable to COVID-19.

But reviewers of the *Lancet* paper asked the team to break down its data by age, which revealed that even in adults under the age of 55, efficacy was still higher in the low-dose group than among those who received the standard dose, says Andrew Pollard, director of the Oxford Vaccine Group at the University of Oxford and a co-author of the paper.

Overall, it remains unclear how much the over-55 age group will benefit from even the standard dose of the vaccine: only 12% of those in the group evaluated for vaccine efficacy were over 55. Earlier studies<sup>2</sup> of the vaccine showed that immune responses in people over 55 were comparable to those in younger study participants, suggesting that the vaccine will work well in older adults. But the larger clinical trial has few data from older adults so far, because they were recruited to the study later, says Pollard. The published results are interim data from more than 11,000 of the roughly 24,000 participants enrolled, and researchers might learn more about the vaccine in older adults as more data come in.

## Symptomless infections

Another lingering question is whether the vaccine is capable of fighting asymptomatic infections; an immunization that could do that could be key to shaping the course of the pandemic. The Oxford–AstraZeneca team is the only one of the three leading vaccine developers that monitored for asymptomatic infections, by collecting weekly swabs from some participants to determine whether they had the coronavirus but did not become ill. The

data show that the low-dose vaccine regimen was about 60% effective at reducing asymptomatic infections, but it is unclear whether the standard dose significantly reduced them at all.

Researchers are concerned about asymptomatic infections because people who have them might unknowingly continue to transmit the virus to others, despite being vaccinated. Although asymptomatic infections are not a direct measure of disease transmission, researchers have looked to this data as an indication of how much vaccines might affect the spread of COVID-19. “For now, this is the only study that’s given us data on that,” says Griffin. “And it’s a bit troubling.”

Trials of the two leading RNA vaccines have not gathered data on asymptomatic infections, but the vaccines have been more than 90% effective in preventing symptoms of COVID-19. And even if the efficacy of the Oxford vaccine proves to be lower than those of the other two, it is still likely to be beneficial, says Griffin. The lower efficacy has to be balanced against the practicalities of vaccinating everyone who needs it, he adds. “It’s going to come down to a cost–benefit analysis.”

Oxford and AstraZeneca have agreed to provide the vaccine to buyers for US\$2–3 per dose. And the vaccine is made of DNA encoding a coronavirus protein that is shuttled into cells in a harmless virus, a product that will be cheaper and easier to make in bulk than the RNA vaccines from Pfizer and Moderna, says Griffin. It also does not need to be stored at temperatures as low as the RNA vaccines, one of which must be kept at  $-70^{\circ}\text{C}$  until shortly before it is administered.

## More than one

And the scale of the pandemic means that it will be crucial to have more than one COVID-19 vaccine, said AstraZeneca chief executive Pascal Soriot at a press briefing. Even combined, the planned number of doses from Moderna, Pfizer and AstraZeneca would still not be enough to vaccinate everyone in the world. “It is really important to have several vaccines,” he said.

Oxford's data come on the day that the United Kingdom began administering the Pfizer and BioNTech vaccine outside trials, less than a week after UK regulators [became the first to grant an emergency-use authorization to one of the major vaccines.](#)

The Oxford data have now been submitted to regulators around the world, said Mene Pangalos, AstraZeneca's executive vice-president of biopharmaceuticals research and development at a press briefing.

In the United States, a panel of advisers to the Food and Drug Administration (FDA) will meet on 10 December to discuss the Pfizer–BioNTech vaccine, and an emergency-use authorization is expected to follow shortly afterwards. Moderna, which is based in Cambridge, Massachusetts, also [announced positive clinical-trial results](#) last month for its vaccine, which FDA advisers will discuss on 17 December.

Nature **588**, 378-379 (2020)

doi: <https://doi.org/10.1038/d41586-020-03504-w>

## References

1. 1.

Voysey, M. *et al.* *Lancet* [https://doi.org/10.1016/S0140-6736\(20\)32661-1](https://doi.org/10.1016/S0140-6736(20)32661-1) (2020).

2. 2.

Ramasamy, M. N. *et al.* *Lancet* [https://doi.org/10.1016/S0140-6736\(20\)32466-1](https://doi.org/10.1016/S0140-6736(20)32466-1) (2020).

## [Jobs from Nature Careers](#)

- - - [All jobs](#)
    -

- **Study Nurse (m/w/d)**

German Cancer Research Center in the Helmholtz Association (DKFZ)

Heidelberg, Mannheim, Germany

JOB POST

- **Two Research Software Engineers**

Jülich Research Centre (FZJ)

Garching, Germany

JOB POST

- **Softwareentwickler/in (w/m/d) für Experimentsysteme**

Helmholtz-Zentrum Berlin for Materials and Energy (HZB)

Berlin, Germany

JOB POST

- **Software Developer (f/m/d) for Experiment Systems**

Helmholtz-Zentrum Berlin for Materials and Energy (HZB)

Berlin, Germany

JOB POST

NEWS

03 December 2020

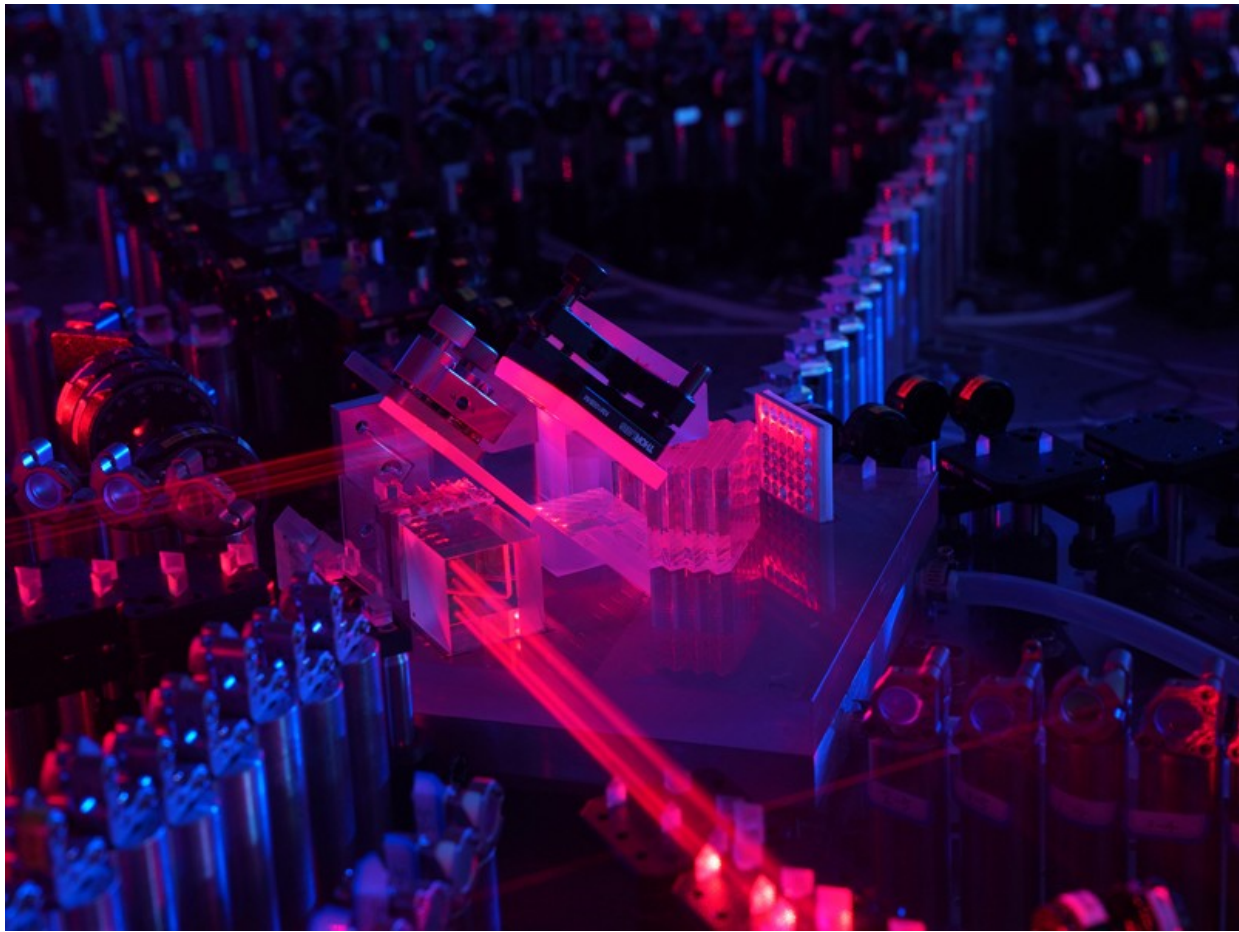
# Physicists in China challenge Google's 'quantum advantage'

Photon-based quantum computer does a calculation that ordinary computers might never be able to do.

**Philip Ball**

Search for this author in:

- [Pub Med](#)
- [Nature.com](#)
- [Google Scholar](#)



This photonic computer performed in 200 seconds a calculation that on an ordinary supercomputer would take 2.5 billion years to complete.Credit: Hansen Zhong

A team in China claims to have made the first definitive demonstration of ‘quantum advantage’ — exploiting the counter-intuitive workings of quantum mechanics to perform computations that would be prohibitively slow on classical computers.

They have used beams of laser light to perform a computation which had been mathematically proven to be practically impossible on normal computers. The team achieved within a few minutes what would take half the age of Earth on the best existing supercomputers. Contrary to [Google’s first demonstration of a quantum advantage](#), performed last year, their version is virtually unassailable by any classical computer. The results appeared in *Science* on 3 December<sup>1</sup>.

“We have shown that we can use photons, the fundamental unit of light, to demonstrate quantum computational power well beyond the classical counterpart,” says Jian-Wei Pan at the University of Science and Technology of China in Hefei. He adds that the calculation that they carried out — called the boson-sampling problem — is not just a convenient vehicle for demonstrating quantum advantage, but has potential practical applications in graph theory, quantum chemistry and machine learning.

“This is certainly a tour de force experiment, and an important milestone,” says physicist Ian Walmsley at Imperial College London.

## Quantum advantage challenged

Teams at both academic and corporate laboratories have been vying to demonstrate quantum advantage (a term that has now largely replaced the earlier ‘quantum supremacy’).

Last year, researchers at Google’s quantum-computing laboratory in Santa Barbara, California, announced the first-ever demonstration of quantum advantage. They used their state-of-the-art Sycamore device, which has 53 quantum bits (qubits) made from superconducting circuits that are kept at ultracold temperatures<sup>2</sup>.

But some quantum researchers contested the claim, on the grounds that a better classical algorithm that would outperform the quantum one could exist<sup>3</sup>. And researchers at IBM claimed that its classical supercomputers could in principle already run existing algorithms to do the same calculations in 2.5 days.

To convincingly demonstrate quantum advantage, it should be unlikely that a significantly faster classical method could ever be found for the task being tested.

The Hefei team, led by Pan and [Chao-Yang Lu](#), chose a different problem for its demonstration, called boson sampling. It was devised in 2011 by two computer scientists, Scott Aaronson and Alex Arkhipov<sup>4</sup>, then at the Massachusetts Institute of Technology in Cambridge. It entails calculating

the probability distribution of many bosons — a category of fundamental particle that includes photons — whose quantum waves interfere with one another in a way that essentially randomizes the position of the particles. The probability of detecting a boson at a given position can be calculated from an equation in many unknowns.

## 200 seconds

But the calculation in this case is a ‘#P-hard problem’, which is even harder than notoriously tricky NP-hard problems, for which the number of solutions increases exponentially with the number of variables. For many tens of bosons, Aaronson and Arkhipov showed that there’s no classical shortcut for the impossibly long calculation.

A quantum computer, however, can sidestep the brute-force calculation by simulating the quantum process directly — allowing bosons to interfere and sampling the resulting distribution. To do this, Pan and colleagues chose to use photons as their qubits. They carried out the task on a photonic quantum computer working at room temperature.

Starting from laser pulses, the researchers encoded the information in the spatial position and the polarization of particular photon states — the orientation of the photons’ electromagnetic fields. These states were then brought together to interfere with one another and generate the photon distribution that represents the output. The team used photodetectors capable of registering single photons to measure that distribution, which in effect encodes the calculations that are so hard to perform classically.

In this way, Pan and colleagues could find solutions to the boson-sampling problem in 200 seconds. They estimate these would take 2.5 billion years to calculate on China’s TaihuLight supercomputer — a quantum advantage of around  $10^{14}$ .

## Practical problems

“This is the first time that quantum advantage has been demonstrated using light or photonics,” says Christian Weedbrook, chief executive of quantum-

computing startup Xanadu in Toronto, Canada, which is seeking to build practical quantum computers based on photonics.

Walmsley says this claim of quantum advantage is convincing. “Because [the experiment] hews very closely to the original Aaronson–Arkhipov scheme, it is unlikely that a better classical algorithm can be found,” he says.

However, Weedbrook points out that as yet, and in contrast to Google’s Sycamore, the Chinese team’s photonic circuit is not programmable, so at this point “it cannot be used for solving practical problems”.

But he adds that if the team is able to build an efficient enough programmable chip, several important computational problems could be solved. Among those are predicting how proteins dock to one another and how molecules vibrate, says Lu.

Weedbrook notes that photonic quantum computing started later than the other approaches, but it could now “potentially leap-frog the rest”. At any rate, he adds, “It is only a matter of time before quantum computers will leave classical computers in the dust.”

Nature **588**, 380 (2020)

doi: <https://doi.org/10.1038/d41586-020-03434-7>

## References

1. 1.

Zhong, H.-S. *et al. Science* <https://doi.org/10.1126/science.abe8770> (2020).

2. 2.

Arute, F. *et al. Nature* **574**, 505–510 (2019).

3. 3.

Pednault, E., Gunnels, J. A., Nannicini, G., Horesh, L. & Wisnieff, R. Preprint at <https://www.arxiv.org/abs/1910.09534> (2019).

#### 4. 4.

Aaronson, S. & Arkhipov, A. *Proc. 43rd Annual Symposium on Theory of Computing* 333–342 (2011).

### Jobs from Nature Careers

- - - [All jobs](#)
    - - [Study Nurse \(m/w/d\)](#)  
[German Cancer Research Center in the Helmholtz Association \(DKFZ\)](#)  
[Heidelberg, Mannheim, Germany](#)  
[JOB POST](#)
      - [Two Research Software Engineers](#)  
[Jülich Research Centre \(FZJ\)](#)  
[Garching, Germany](#)  
[JOB POST](#)
      - [Softwareentwickler/in \(w/m/d\) für Experimentsysteme](#)  
[Helmholtz-Zentrum Berlin for Materials and Energy \(HZB\)](#)  
[Berlin, Germany](#)

JOB POST

- **Software Developer (f/m/d) for Experiment Systems**

Helmholtz-Zentrum Berlin for Materials and Energy (HZB)

Berlin, Germany

JOB POST

---

This article was downloaded by **calibre** from <https://www.nature.com/articles/d41586-020-03434-7>

| [Section menu](#) | [Main menu](#) |

NEWS

02 December 2020

# Scientists fear that ‘covidization’ is distorting research

Some researchers worry that shifting priorities towards pandemic-focused science comes at the expense of other disciplines.

**David Adam**

Search for this author in:

- [Pub Med](#)
- [Nature.com](#)
- [Google Scholar](#)



Some scholars are concerned that intense focus on pandemic-related research will affect other work. Credit: David Mareuil/Anadolu Agency via Getty

Like millions of others, neuroscientist Lis Evered felt her career threatened by the COVID-19 pandemic. But her concern was not over security and funding. It went deeper — to her motivation and purpose as a scientist.

“I was carrying around this burden of thinking that I’m a complete failure because I’m not leading the charge on curing COVID. It felt like my work was not important anymore,” she says.

Evered, who is at Weill Cornell Medicine in New York City, studies peri-operative cognitive disorders in older people — such as delirium after surgery — and she felt sidelined as colleagues and journals pivoted towards research with more obvious relevance to fighting COVID-19. But then she came across a word that changed her perspective: ‘covidization’. “I felt a weight lift off me,” she says.

[Coined in April](#) by Madhukar Pai, a tuberculosis researcher at McGill University in Montreal, Canada, covidization describes the distorting impact of the pandemic on the way science is funded, produced, published and reported on. Pai was worried that the pandemic would force countries, funders, health agencies and researchers to focus too much on infectious threats of pandemic significance. Research into other factors vital for public health, from non-infectious diseases to climate change, could lose out.

For Evered, who came across the word in [an article Pai wrote](#) in July, it gave her the confidence that non-COVID-19 science was still a worthy pursuit.

## Funding priorities

Covidization of research does have benefits: extra funds are one. By April, the European Commission alone had committed €137.5 million (US\$165 million) to scientists working on the pandemic, which is more than it spent on research into HIV/AIDS, tuberculosis and malaria in 2018. The money is speeding vaccine development, and funding research into topics such as mental health and the effect of social inequality on the pandemic. But Pai argues that this sudden shift in priorities and surge of activity is also harming the research enterprise. “There is a fear of missing out,” he says. “And it’s turned into a feeding frenzy.”

Pai identifies three problem areas within covidization. The first is funders diverting or delaying money from curiosity-driven research and handing it to pandemic-related proposals. The Canadian Institutes of Health Research cancelled its annual spring grant competition in April because of the pandemic, and soon afterwards announced a new Can\$108-million (US\$83-million) scheme to fund projects “responding to the current phase of COVID-19 pandemic”. (The agency did subsequently review and fund the original spring grants.)

Covidization of research is even distorting efforts to protect global health, says Colin Carlson, a biologist at Georgetown University in Washington DC. “I don’t think a model in which folks who work in that field, like myself, try to ride the funding wave necessarily helps,” Carlson says.

Conservation and wildlife organizations are using COVID to reframe basic research on deforestation, biodiversity loss and the wildlife trade as pandemic-preparedness, he adds. “Everyone is trying to sell what they’re doing as COVID and that dilutes the work that people are doing,” he says.

## COVID trespassers

The second problem is scientists from different fields now researching and publishing on epidemiology, infectious diseases and immunology — areas in which they might be poorly qualified.

And the third is that, given the deluge of research done under the umbrella of COVID-19 often published as unreviewed preprints, it’s increasingly hard for the public, media and policymakers to distinguish reliable evidence from the rest.

[A study on the “carnage of substandard research”](#) by Katrina Bramstedt, a bioethicist at the Luxembourg Agency for Research Integrity and Bond University in Gold Coast, Australia, found that 19 published articles and 14 preprints about COVID-19 had been retracted, withdrawn, or had an expression of concern issued by the end of July.

When people divert from their primary field — say, nuclear physics — to work on COVID, they are prone to making mistakes because they lack the expert-level insight, Pai says. Blogs and preprint servers mean that half-baked ideas and poor-quality research do not have to pass peer review, he says. For instance, studies from non-experts have appeared on how eating cucumber and cabbage can protect against the coronavirus. “They get quoted, they get into the media and then it’s mayhem,” Pai says. “So an average policymaker or journalist is really struggling to know who to believe.”

## Off-piste study

Scientists straying from their field of expertise in this way is an example of what Nathan Ballantyne, a philosopher at Fordham University in New York City, calls “epistemic trespassing”. Although scientists might romanticize the

role and occasional genuine insight of an outsider — such as the writings of physicist Erwin Shrödinger on biology — in most cases, he says, such academic off-piste manoeuvrings dump non-experts head-first in deep snow.

Many trespassers have good intentions, Ballantyne says, and crossing disciplinary lines can be positive for research. Many researchers [have found productive new directions for their own work](#). But he says that outsiders should collaborate with a genuine expert — and that studies that do not list such an expert as a co-author should raise a red flag to other researchers and the media.

Some research funders have recognized the threat of covidization. Matthias Egger, president of the National Research Council of the Swiss National Science Foundation warned earlier this year of the “instant experts” thrown up by the pandemic. “Colleagues who had spent their academic careers far removed from viruses and lung inflammation have now miraculously revealed themselves as experts,” he wrote [in an opinion piece](#). Throwing money at COVID-19 at the expense of other science could be a mistake, he said, and researchers should concentrate on the questions they decided to pursue. “There will be no covidization of research here,” he said.

“Whether your chosen field is the coelacanth, exoplanets, social inequality or global warming, please keep doing what you do.”

Nature 588, 381-382 (2020)

doi: <https://doi.org/10.1038/d41586-020-03388-w>

## Jobs from Nature Careers

- - - [All jobs](#)
    - - [Study Nurse \(m/w/d\)](#)

German Cancer Research Center in the Helmholtz Association (DKFZ)

Heidelberg, Mannheim, Germany

JOB POST

- **Two Research Software Engineers**

Jülich Research Centre (FZJ)

Garching, Germany

JOB POST

- **Softwareentwickler/in (w/m/d) für Experimentsysteme**

Helmholtz-Zentrum Berlin for Materials and Energy (HZB)

Berlin, Germany

JOB POST

- **Software Developer (f/m/d) for Experiment Systems**

Helmholtz-Zentrum Berlin for Materials and Energy (HZB)

Berlin, Germany

JOB POST

NEWS

10 December 2020

# How kids' immune systems can evade COVID

Childrens' untrained immune response seems to be key to eliminating SARS-CoV-2.

**Bianca Nogradiy**

Search for this author in:

- [Pub Med](#)
- [Nature.com](#)
- [Google Scholar](#)



Children rarely show symptoms of COVID-19, even if they are infected. Credit: Thomas Lohnes/Getty

Young children account for only a small percentage of COVID-19 infections<sup>1</sup> — a trend that has puzzled scientists. Now, a growing body of evidence suggests why: kids' immune systems seem better equipped to eliminate SARS-CoV-2 than are adults'.

“Children are very much adapted to respond — and very well equipped to respond — to new viruses,” says Donna Farber, an immunologist at Columbia University in New York City. Even when they are infected with SARS-CoV-2, children are most likely to experience mild or asymptomatic illness<sup>2</sup>.

Another clue that children’s response to the virus differs from that of adults is that some children develop COVID-19 symptoms and antibodies specific to SARS-CoV-2 but never test positive for the virus on a standard RT-PCR test. In one study, three children under ten from the same family developed SARS-CoV-2 antibodies<sup>3</sup> — and two of them even experienced mild

symptoms — but none tested positive on RT-PCR, despite being tested 11 times over 28 days while in close contact with their parents, who had tested positive.

## Quick response

Their immune system sees the virus “and it just mounts this really quick and effective immune response that shuts it down, before it has a chance to replicate to the point that it comes up positive on the swab diagnostic test”, says Melanie Neeland, an immunologist who studied the family, at the Murdoch Children’s Research Institute in Melbourne, Australia.

Even in children who experienced the severe but rare complication called multisystem inflammatory syndrome in response to SARS-CoV-2 infection, studies report that the rate of positive results on RT-PCR range from just 29% to 50%<sup>4,5,6</sup>.

Farber says the types of antibody children develop offer clues about what is going on. In a study<sup>7</sup> of 32 adults and 47 children aged 18 or younger, she and colleagues found that children mostly produced antibodies aimed at the SARS-CoV-2 spike protein, which the virus uses to enter cells. Adults generated similar antibodies, but also developed antibodies against the nucleocapsid protein, which is essential for viral replication. Farber says the nucleocapsid protein is typically released in significant quantities only when a virus is widespread in the body.

The kids lacked nucleocapsid-specific antibodies, which suggests that they aren’t experiencing widespread infection, says Farber. Children’s immune responses seem to be able to eliminate the virus before it replicates in large numbers, she says.

## Adaptive vs innate immune system

Farber suggests that the reason children can neutralize the virus is that their T cells are relatively naive. T cells are part of the body’s adaptive immune system, which learns to recognize pathogens it encounters over a lifetime. Farber says that because children’s T cells are mostly untrained, they might

have a greater capacity to respond to new viruses — a phenomenon she is studying in more detail.

But other evidence suggests the situation is not so straightforward: a study<sup>8</sup> of people with COVID-19 that included 65 children and young people under the age of 24, along with 60 adults, found that the adults had a stronger T-cell response to the virus spike protein than did the children and young people. But Farber says the study measured memory T-cell responses, which are much less developed in children, rather than naive T-cell activity.

Children's ability to neutralize the virus might also be linked to the fact that they have a strong innate immune response from birth, says Alasdair Munro, who studies paediatric infectious diseases at University Hospital Southampton, UK. "There's been some suggestion that the rapidity and scale of their innate immune response might be protective against the initiation of infection," he says. But this effect is difficult to study, and raises the question of why it isn't seen with other viruses that can cause severe disease in children, he says.

## Other factors

Children are also the main reservoir for seasonal coronaviruses that cause the common cold. Some researchers have suggested that antibodies for these coronaviruses might confer some protection against SARS-CoV-2, but the evidence is mixed<sup>9,10</sup>, says Munro.

Meanwhile, there is evidence that when children are exposed to the virus, they receive a smaller dose than adults, because their noses contain fewer ACE2 receptors<sup>11</sup>, which the virus uses to gain access to cells. This might also explain why COVID-19 is less prevalent in children than in adults, say researchers.

Munro says it is unlikely that there is a single explanation for why COVID-19 seems to affect children less than adults. "Biology is rarely so straightforward."

doi: <https://doi.org/10.1038/d41586-020-03496-7>

## References

1. 1.  
Wu, Z., McGoogan, J. M. *J. Am. Med. Assoc.* **323**, 1239–1242 (2020).
2. 2.  
Dong, Y. *et al. Pediatrics* **145**, e20200702 (2020).
3. 3.  
Tosif, S. *et al. Nature Commun.* **11**, 5703 (2020).
4. 4.  
Dufort, E. M. *et al. N. Engl. J. Med.* **383**, 347–358 (2020).
5. 5.  
Feldstein, L. R. *et al. N. Engl. J. Med.* **383**, 334–346 (2020).
6. 6.  
Whittaker, E. D. *et al. J. Am. Med. Assoc.* **324**, 259-269 (2020).
7. 7.  
Weisberg, S. P. *et al. Nature Immunol.* <https://doi.org/10.1038/s41590-020-00826-9> (2020).
8. 8.  
Pierce, C. A. *et al. Sci. Transl. Med.* **564**, eabd5487 (2020).
9. 9.

Ng, K. W. *et al.* *Science* <https://doi.org/10.1126/science.abe1107> (2020).

10. 10.

Huang, A. T. *et al.* *Nature Commun.* **11**, 4704 (2020).

11. 11.

Bunyavanich, S., Do, A. & Vicencio, A. *J. Am. Med. Assoc.* **323**, 2427-2429 (2020).

## **Jobs from Nature Careers**

- - - [All jobs](#)
    - - [Study Nurse \(m/w/d\)](#)

[German Cancer Research Center in the Helmholtz Association \(DKFZ\)](#)

[Heidelberg, Mannheim, Germany](#)

[JOB POST](#)

- [Two Research Software Engineers](#)

[Jülich Research Centre \(FZJ\)](#)

[Garching, Germany](#)

[JOB POST](#)

- [Softwareentwickler/in \(w/m/d\) für Experimentsysteme](#)

[Helmholtz-Zentrum Berlin for Materials and Energy \(HZB\)](#)

[Berlin, Germany](#)

[JOB POST](#)

▪ [Software Developer \(f/m/d\) for Experiment Systems](#)

[Helmholtz-Zentrum Berlin for Materials and Energy \(HZB\)](#)

[Berlin, Germany](#)

[JOB POST](#)

---

This article was downloaded by **calibre** from <https://www.nature.com/articles/d41586-020-03496-7>

| [Section menu](#) | [Main menu](#) |

NEWS

08 December 2020

- Correction [09 December 2020](#)

# CRISPR gene therapy shows promise against blood diseases

Researchers report early successes using genetic approaches to treat sickle-cell anaemia and β-thalassaemia.

**Heidi Ledford**

Search for this author in:

- [Pub Med](#)
- [Nature.com](#)
- [Google Scholar](#)



Credit: Arshad Arbab/EPA/Shutterstock

In 1949, biochemist Linus Pauling declared<sup>1</sup> [sickle-cell anaemia the first “molecular disease”](#) after discovering that the condition is caused by a flaw in the body’s oxygen-carrying protein, haemoglobin. Now, more than 70 years later, cutting-edge genetic techniques could provide a molecular treatment.

In *The New England Journal of Medicine*<sup>2,3</sup>, separate research teams report promising results from trials of two pioneering gene therapies that target the root cause of sickle-cell anaemia. Both aim to boost the production of an alternative form of haemoglobin, called fetal haemoglobin. One study does so using [CRISPR–Cas9 genome editing](#). And, because it is the first published account of using the gene-editing system to treat a heritable disease, it provides an important proof of concept for that technology.

The other approach shuttles in the code for an RNA that alters expression of the fetal haemoglobin gene. Both treatments relieved participants of the debilitating episodes known as pain crises that come with sickle-cell disease.

“To have something like these two techniques is a great opportunity,” says Renee Garner, a paediatrician at the Louisiana State University School of Medicine in New Orleans. “It would just open the doors of hope for these patients.”

Both clinical trials have enrolled only a handful of participants, and it is too soon to say how long the effects will last — the first participant in the RNA study was treated nearly two-and-a-half years ago. The CRISPR–Cas9 approach is also being used to treat people with severe forms of a related genetic disorder called  $\beta$ -thalassaemia, and those participants have not required the blood transfusions usually needed to manage the disease.

“It is very promising,” says Marina Cavazzana, a gene therapy researcher at Necker Children’s Hospital in Paris. “We need new technologies and more than one product in the market to face the huge problem of sickle cell.”

Sickle-cell disease and  $\beta$ -thalassaemia are two of the most common genetic disorders attributable to mutations in a single gene. Both conditions affect the production of  $\beta$ -globin, a component of haemoglobin. People with severe  $\beta$ -thalassaemia have anaemia; in sickle-cell anaemia, the blood cells become deformed, clump together and can clog blood vessels, sometimes starving tissues of oxygen and causing pain episodes. Each year, 60,000 people are diagnosed worldwide with a severe form of  $\beta$ -thalassaemia, and 300,000 are diagnosed with sickle-cell disease.

Both diseases can be cured by a bone-marrow transplant, although most people with the conditions cannot find a suitably matched donor. But in recent years, a variety of experimental gene-therapy approaches have burst onto the scene. Last year, the European Union approved a gene therapy called Zynteglo to treat  $\beta$ -thalassaemia. That approach uses a virus to shuttle a functioning copy of the  $\beta$ -globin gene into blood-producing stem cells. Bluebird Bio, a biotechnology company in Cambridge, Massachusetts, is conducting clinical trials of a similar approach in people with sickle-cell disease as well.

The CRISPR and RNA approaches take a different tack. They seek to boost expression of a form of haemoglobin that is normally produced in the fetus and then switched off shortly after birth. Researchers had hypothesized that

turning this fetal haemoglobin back on could compensate for the disabled  $\beta$ -globin produced by people with sickle cell anaemia or  $\beta$ -thalassaemia.

Both studies suggest that this is the case. In one, a team that includes researchers from two Massachusetts companies — Vertex Pharmaceuticals in Boston and CRISPR Therapeutics in Cambridge — used CRISPR–Cas9 to alter a region of a gene called *BCL11A*, which is required to switch off production of fetal haemoglobin. By disabling this gene, the team hoped to turn fetal-haemoglobin production back on in adult red blood cells.

The other study's team — led by haematologist David Williams at Boston Children's Hospital and researchers from Bluebird Bio — used a snippet of RNA that switches off expression of the *BCL11A* gene in red blood cells.

The CRISPR–Cas9 publication reports data from two participants, one with  $\beta$ -thalassaemia and one with sickle-cell disease, but the trial has now treated a total of 19 people, says David Altshuler, chief scientific officer at Vertex. Williams' publication, meanwhile, reports data from six participants with sickle-cell disease, and his trial has since treated three more.

So far, the participants with  $\beta$ -thalassaemia have not needed blood transfusions, and participants with sickle-cell disease have not reported pain crises since the treatment. Side effects from the therapies — which included infection and abdominal pain — were temporary and linked to the treatments needed to prepare the bone marrow for the procedure.

In both cases, blood stem cells are removed from the marrow, then modified and reinfused into the patients. But before the cells are reintroduced, the participant is treated with drugs to ablate the remaining blood stem cells. This treatment can be difficult and risky, and leaves the participant at risk of infection until the marrow recuperates; it can also damage fertility. Researchers are now hunting for gentler ways to [prepare the bone marrow for such infusions](#).

Until the therapies are made safer, such approaches will probably be restricted only to people with severe disease that does not respond to treatment using other drugs, says haematologist David Rees at King's College Hospital, London. "Scientifically, these studies are quite exciting,"

he says. “But it’s hard to see this being a mainstream treatment in the long term.”

Nature **588**, 383 (2020)

doi: <https://doi.org/10.1038/d41586-020-03476-x>

## Updates & Corrections

- **Correction 09 December 2020:** An earlier version of this story mistakenly said that 10 people had been treated in the CRISPR trial. The correct number is 19.

## References

1. 1.

Pauling, L., Itano, H. A., Singer, S. J. & Wells, I. C. *Science* **110**, 543–548 (1949).

2. 2.

Frangoul, H. *et al.* *N. Engl J. Med.*  
<https://doi.org/10.1056/NEJMoa2031054> (2020).

3. 3.

Esrick, E. B. *et al.* *N. Engl J. Med.*  
<https://doi.org/10.1056/NEJMoa2029392> (2020).

## Jobs from Nature Careers

- - - [All jobs](#)
  - 
  -

## **Study Nurse (m/w/d)**

German Cancer Research Center in the Helmholtz Association (DKFZ)

Heidelberg, Mannheim, Germany

JOB POST

- **Two Research Software Engineers**

Jülich Research Centre (FZJ)

Garching, Germany

JOB POST

- **Softwareentwickler/in (w/m/d) für Experimentsysteme**

Helmholtz-Zentrum Berlin for Materials and Energy (HZB)

Berlin, Germany

JOB POST

- **Software Developer (f/m/d) for Experiment Systems**

Helmholtz-Zentrum Berlin for Materials and Energy (HZB)

Berlin, Germany

JOB POST

## NEWS FEATURE

14 December 2020

- Correction [17 December 2020](#)

# Why many countries failed at COVID contact-tracing — but some got it right

Rich nations have struggled with one of the most basic and important methods for controlling infectious diseases.

**Dyani Lewis**

Dyani Lewis is a freelance science journalist in Melbourne, Australia.

**Search for this author in:**

- [Pub Med](#)
- [Nature.com](#)
- [Google Scholar](#)



Health-care workers conduct contact-tracing amid the COVID-19 pandemic in Soyapango, El Salvador, in July. Credit: Jose Cabezas/Reuters

When Ebola ripped through communities in West Africa between 2014 and 2016, Tolbert Nyenswah saw at first hand how health workers extinguished the epidemic by finding and quarantining contacts of those who caught the disease. The former director of Liberia's public-health institute thought contact-tracers would again rise to the challenge this year, keeping COVID-

19 in check as it swept the globe. “Contact-tracing is one of the greatest tools that countries should deploy and use effectively to contain the outbreak,” he says.

But nine months after the World Health Organization (WHO) labelled COVID-19 as a pandemic, few countries are wielding contact-tracing effectively. “By now, what I was expecting is that 100% of people coming in contact with COVID-19 would have been traced,” says Nyenswah, now an infectious-diseases researcher at Johns Hopkins Bloomberg School of Public Health in Baltimore, Maryland.

Across the Western world, countries have floundered with this most basic public-health procedure. In England, tracers fail to get in touch with one in eight people who test positive for COVID-19; 18% of those who are reached provide no details for close contacts. In some regions of the United States, more than half of people who test positive provide no details of contacts when asked. These statistics come not from the first wave of COVID-19, but from November, long after initial lockdowns gave countries time to develop better contact-tracing systems.

The reasons for the failures are complex and systemic. Antiquated technology and underfunded health-care systems have proved ill-equipped to respond. Wealthy nations have struggled to hire enough contact-tracers, marshal them efficiently or make sure that people do self-isolate when infected or that they quarantine when a close contact has the disease. And overstretched contact-tracers have been met with distrust by people wary both of health authorities and of the technologies being deployed to fight the pandemic. Meanwhile, researchers who are keen to draw lessons from contact-tracing operations are stymied by a dearth of data.

A handful of places stand out as exemplars of successful contact-tracing — including South Korea, Vietnam, Japan and Taiwan. Many of these have cracked down on COVID-19 early, isolated infected people and their contacts and used personal data such as mobile-phone signals to track obedience. Not all of those techniques are transferable to countries now struggling to contain massive outbreaks. But they still provide some lessons.

Measures that work include tracing multiple layers of contacts, investigating outbreak clusters and providing people who are advised to quarantine with safe places to do so and with financial compensation. Technology might help, too: from software that streamlines conventional contact-tracing efforts, to smartphone apps that alert people that they might have been exposed to SARS-CoV-2.

## A string of failures

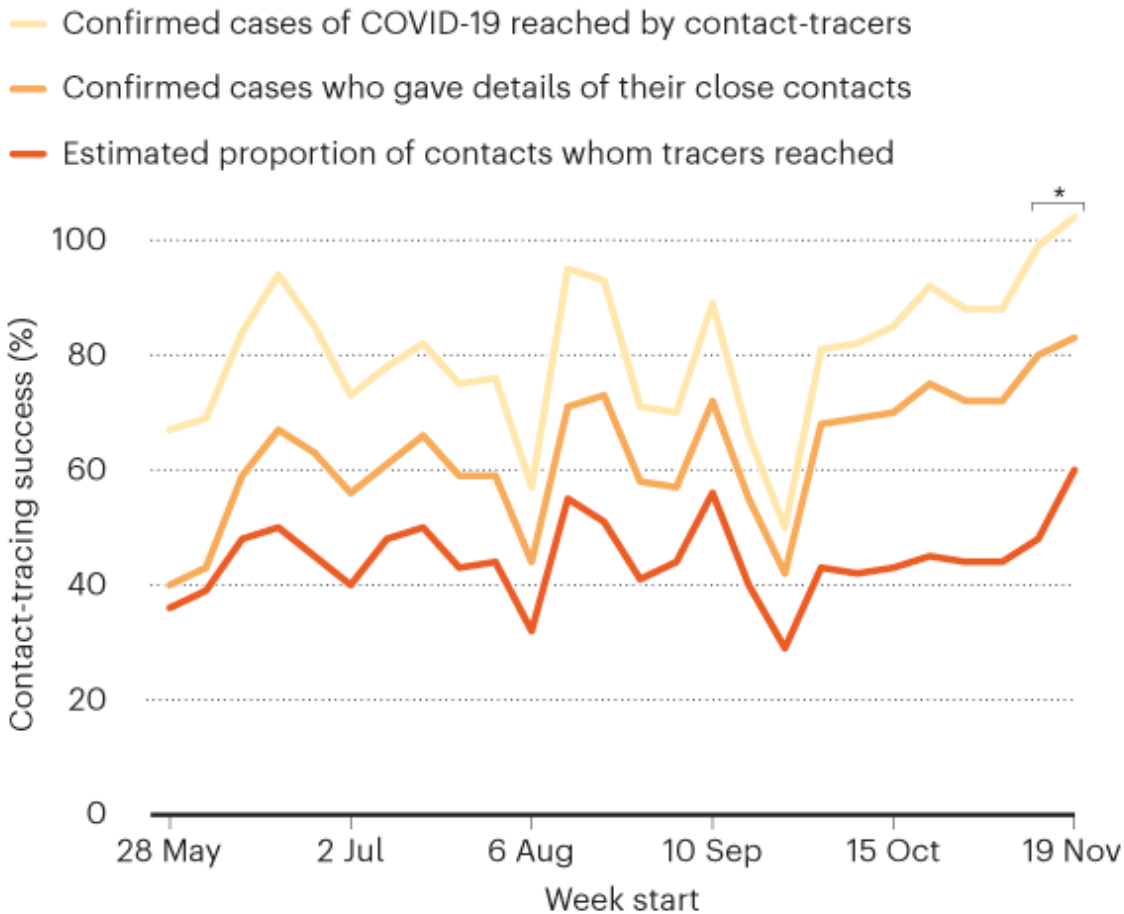
The textbook version of contact-tracing starts with someone testing positive for COVID-19 and isolating themselves. A contact-tracer interviews this person to find out who they might have exposed while infected, usually from 48 hours before the positive test, or before symptoms appeared (if there were any). Close contacts — those who've spent more than 15 minutes close to the infected person — are of special interest, but anyone who shared public transport or an office space might qualify. Tracers then call or visit those contacts to tell them they need to quarantine, so that they don't pass the virus on to more people. The chain of transmission is broken.

In reality, failures occur at every stage of this test–trace–isolate sequence. People get COVID-19 and don't know it, or delay getting tested. Positive results can take days to be confirmed. Not everyone who tests positive isolates when requested; one survey in May found that in the United Kingdom, 61% of people who were self-isolating said they'd left their house in the past day<sup>1</sup>. People can't always be reached for an interview or don't provide details of their close contacts. And not all contacts are reached, or are willing to comply with quarantine orders.

Because of this series of problems, researchers estimate that in England this year, tracers typically reached less than half of the close contacts of people who'd had a positive COVID-19 test (see ‘Missed contacts’). There are no data on how many of these contacts actually quarantined in turn.

## MISSED CONTACTS

Between late May and November, contact-tracers in England generally reached less than half of the close contacts of people who tested positive for COVID-19.



\*Number rises over 100% because some positive cases were carried over from the previous week.

©nature

Source: <https://covid.i-sense.org.uk>

The United States is in a particularly dire situation. “Public-health authorities are struggling to reach cases and contacts” despite aggressive efforts, says John Oeltmann, head of contact-tracing assessment at the US Centers for Disease Control and Prevention (CDC) in Atlanta, Georgia. He and his team evaluated two counties in North Carolina. In June and July, 48% of cases in one county and 35% in the other reported no contacts. Of the contacts whose details were provided, one-quarter in one county and almost half in the other couldn’t be reached on the phone after three attempts

over consecutive days<sup>2</sup>. In New Jersey, just 49% of cases between July and November were contacted; only 31% of those provided any contact details. “These results are not rare,” says Oeltmann.

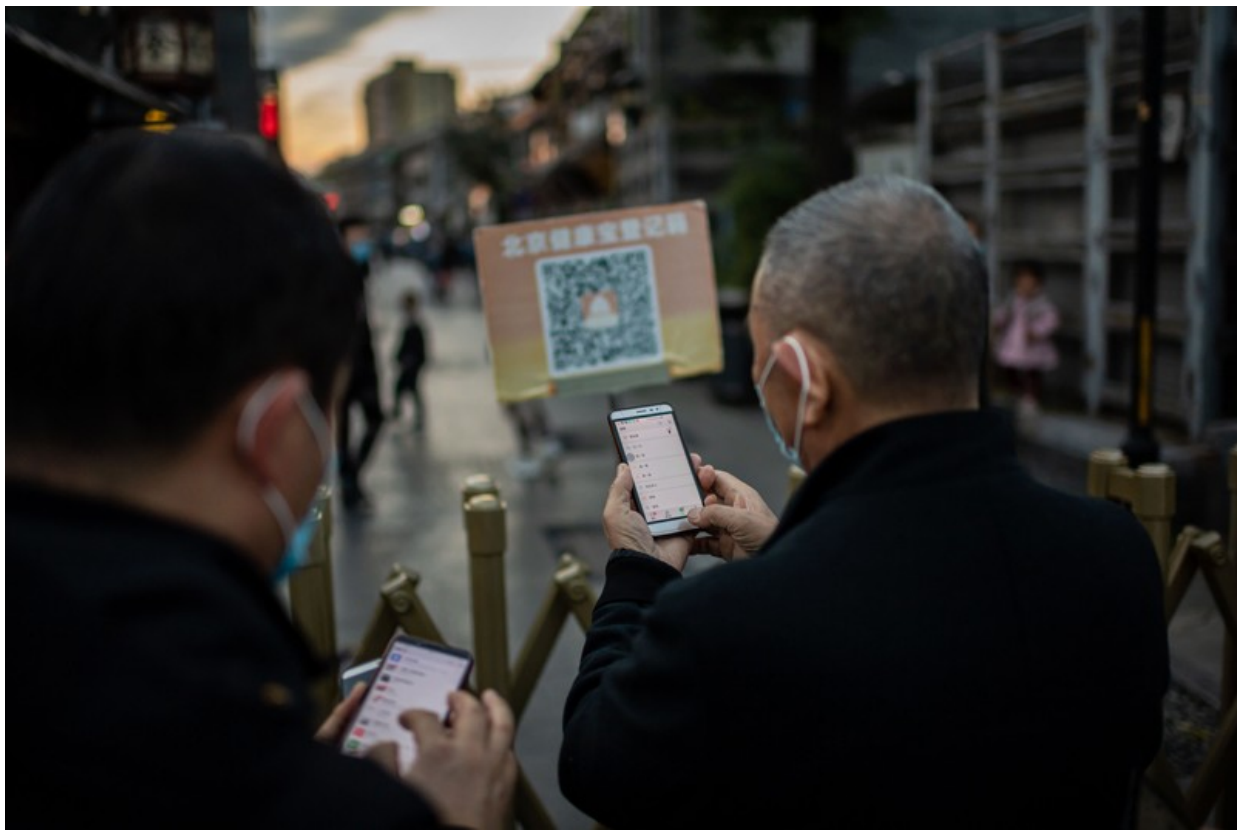
Such data, which demonstrate how poorly contact-tracing is working, are scarce. Only a handful of US states openly report contact-tracing metrics. And although the European Centre for Disease Prevention and Control (ECDC) lists the types of data that countries should gather to monitor contact-tracing efforts, none is reported back to the ECDC or is readily available for comparison. This makes it difficult to compare failures in contact-tracing between countries.

## Finding contacts

In South Korea, [authorities use data-surveillance techniques](#) to get around the problem of people being unwilling to disclose — or unable to recall — close contacts<sup>3</sup>. “We need to double-check,” says Daejoong Lee at the South Korean Ministry of Economy and Finance. A law passed in response to an outbreak of Middle East respiratory syndrome (MERS) in 2015 allows authorities to use data from credit cards, mobile phones and closed-circuit television to trace a person’s movements and identify others they might have exposed to the virus. Information about cases is published online, an approach that allowed the country to avoid broad lockdowns and “worked very well”, says Lee. Still, in March, the Korea Centers for Disease Control issued guidelines limiting the release of ‘excessive’ information, after regional governments published maps of infected people’s routes in too much detail. In one case, a person was wrongly accused of having an affair with his sister-in-law because their overlapping maps revealed they dined together at a restaurant.

Tracers in Vietnam also use extra data — such as Facebook or Instagram posts and mobile-phone location data — to check a person’s movements against those reported to contact-tracers. But the country’s success was down to “the boots on the ground”, says Todd Pollack, an infectious-disease specialist at the Partnership for Health Advancement in Vietnam, a collaboration that provides training and support for the nation’s health system. Contact-tracers interview people face-to-face and use the extra

surveillance data to prod for more details. Other places, including Israel, Armenia, Russia, Ecuador and Taiwan, gather mobile-phone location data to aid contact-tracing efforts. But in Slovakia, a constitutional court suspended the government's attempt to permit this practice.



Beijing controls residents' movements with smartphone scanners to quell outbreaks. Credit: Nicolas Asfouri/AFP/Getty

Once tracers in Vietnam identify close contacts, they send them to designated quarantine facilities. It's a practice that has worked elsewhere — including in Taiwan. Since February, the WHO has recommended this approach for suspected and confirmed cases, as well as for close contacts of cases, particularly if an infected person is unable to isolate themselves from others in their household<sup>4</sup>. Hong Kong and South Africa have non-mandatory quarantine facilities for close contacts, and others have facilities for travellers from abroad, but most countries lack out-of-home quarantine. In the United States, it's estimated that one in five households lacks the space required to keep others in the house safe<sup>5</sup>.

## Against the clock

The WHO's benchmark for a successful COVID-19 contact-tracing operation is to trace and quarantine 80% of close contacts within 3 days of a case being confirmed — a goal few countries achieve.

But even that's not quick enough, says Christophe Fraser, a mathematical biologist at the University of Oxford, UK. Transmission is too rapid and the virus can spread before symptoms emerge, he points out. Modelling by Fraser and his team suggests that even if all cases isolate and all contacts are found and quarantined within three days, the epidemic will continue to grow. He says that in a single day, 70% of cases need to isolate and 70% of contacts need to be traced and quarantined for the outbreak to slow (defined as each infected person passing the virus to fewer than one other, on average)<sup>6</sup>.

But there are ways that contact-tracers can get ahead of a rapidly spreading outbreak. One is to cast a wider net around each case, so that second-order contacts — ‘contacts of contacts’ — are traced and quarantined; in Vietnam, tracers sometimes reached out to third-order contacts if a case was identified late in its infectious cycle. As many as 200 contacts for each case are found and tested, says Pham Quang Thai, an epidemiologist at the National Institute of Hygiene and Epidemiology in Hanoi, who leads the national contact-tracing taskforce. “If we want to run as fast as the virus, we have to chase not only the first round,” he says.

“Tracing the contacts of contacts is a great strategy,” says Nyenswah. But in many places, he says, even tracing the first ring of contacts is proving tough.

The number of contacts identified for each COVID-19 case varies wildly, from an average of 17 per case in Taiwan, to 2 in the United Kingdom, 1.4 in France and less than one in parts of the United States. During the outbreak of severe acute respiratory syndrome (SARS) in Toronto in 2003, around 23,000 contacts for an estimated 251 cases — nearly 100 contacts per case — were told to quarantine. But it’s difficult to interpret these numbers. A country with no restrictions on movement will inevitably need to trace more contacts than one that is in some form of lockdown, for instance.



Paul Persaud, a health official in Paterson, New Jersey, holds a weekly meeting with contact-tracers. Credit: Bryan Anselm/NYT/Redux/eyevine

Another useful strategy is to trace a new case's contacts as far back as a fortnight before they caught the virus, to identify who infected them. This 'backwards contact tracing' is extremely effective for the coronavirus because of its propensity to be passed on in superspreading events, says Adam Kucharski, an infectious-diseases modeller at the London School of Hygiene & Tropical Medicine. One study in Hong Kong found that 19% of cases of COVID-19 were responsible for 80% of transmission, and 69% of cases didn't transmit the virus to anyone<sup>7</sup>. (The SARS outbreak in 2003 had similar transmission dynamics.) Any new case is more likely to have emerged from a cluster of infections than from one individual, so there's value in going backwards to find out who else was linked to that cluster. Japan recognized this feature early and adopted cluster-focused contact-tracing in February; it traces contacts up to 14 days before symptom onset, rather than the usual 48 hours.

In Australia, contact-tracing lessons have been learnt the hard way. A second wave of COVID-19 cases sent the country's second-largest city of Melbourne into a marathon lockdown in August that lasted for 112 days. By the time restrictions eased at the end of October, contact-tracers had adopted the Japanese practice of backwards-tracing contacts for the previous 14 days, and the Vietnamese practice of quarantining first- and second-order contacts. The overhauled system is yet to be tested, because the lockdown eliminated community transmission.

## An army of tracers

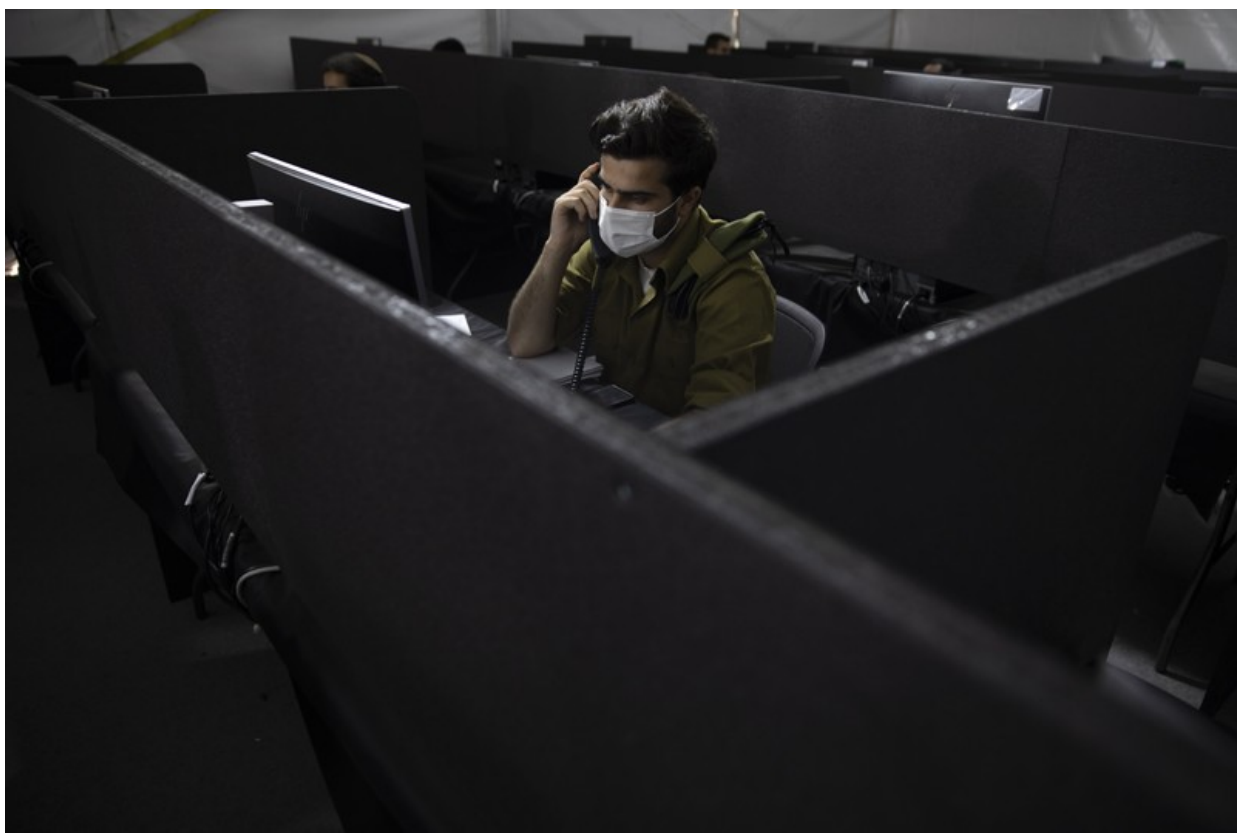
All of these approaches require an army of contact-tracers, but few affluent Western countries had such people in reserve when COVID-19 hit, perhaps because outbreaks of infectious diseases are less common in those regions. In April, a US report (see [go.nature.com/348knvz](https://go.nature.com/348knvz)) estimated that around 30 contact-tracers per 100,000 people are needed during surges in case numbers — a nationwide workforce of nearly 100,000. At the time, the United States had only 2,200 contact-tracers. It now has around 50,000, but this ranges from 60 per 100,000 in Washington DC to 2 per 100,000 in Montana and Iowa. Vietnam had more than 12,000 trained contact-tracers at the outset.

Many regions have bolstered tracing efforts using students, off-work airline staff and volunteers, but have still struggled as case numbers rise. Germany planned to recruit to the level of 25 per 100,000, but imposed a second lockdown. So, too, did England, which has a tracing workforce close to 32 per 100,000. In countries that got on top of their outbreaks quickly, that level of workforce expansion was never required. Taiwan's population of 24 million was served by 600 contact-tracers at the peak of its outbreak — just 2.5 contact-tracers per 100,000<sup>8</sup>.

Edward Salsberg, a health-workforce economist at George Washington University in Washington DC, says that a national or regional workforce could service different communities as hotspots occur. Private call-centre contractors are another workaround, but this strategy has mixed results. Outsourcing worked well in Massachusetts, says Marcus Plescia, the chief medical officer at the US non-profit Association of State and Territorial Health Officials, in Charlotte, North Carolina. But in England, poor

coordination between contractors and health authorities left call-centre staff underused despite huge demand, according to media reports. Selina Rajan, a public-health specialist at the London School of Hygiene & Tropical Medicine, says that the quality of information also suffered. “It’s focused very much on the supply of people to make calls and not necessarily on the outcome,” she says. “I don’t actually think those people are really qualified enough.”

In the United States, public-health officials are faced with tough choices as tracers struggle to keep up. Some are prioritizing at-risk groups, or are ceasing to check on people asked to quarantine. The CDC now recommends that tracers focus on cases infected in the past six days, and encourages cases to notify their own household contacts. In California and New Mexico, lockdowns have returned.



An Israeli soldier in a call centre in Ramla talks to a person infected with coronavirus to try to identify their contacts. Credit: Sebastian Scheiner/AP/Shutterstock

Large swathes of the world now have widespread community transmission, meaning that numerous cases can't be linked to identified ones — a sign that contact-tracing is failing to keep pace. In Vietnam, by contrast, "less than 1%" of cases during the latest outbreak had an unknown source, says Thai. These cases prompted a swift response, usually in the form of a hyper-local lockdown — of a single street, village or suburb — to contain the outbreak. Vietnam "just did everything you're supposed to do", says Pollack. Responders acted more quickly and maybe more comprehensively, he adds, "but it's not like they did something magical".

Still, high case numbers aren't an excuse to give up on contact-tracing, Rajan says. UK government science advisers have been criticized for saying in February that the practice "should be discontinued" when cases got too high — advice the government followed in March — rather than urging the country to build up its tracing capacity. Abandoning contact-tracing left epidemiologists blind to details about where and why new cases were cropping up, Rajan says.

## Technology tricks — and troubles

Smart data-management systems can ease the workload of contact-tracers and help countries get by with fewer disease detectives. Many nations, including South Korea, Vietnam and Germany, developed their own; state governments in Australia and the United States are adopting a commercial system. These are useful because they can record who has been contacted and avoid repeated phoning of people who are contacts of multiple cases, says Karin Verspoor, a computational linguistics researcher at the University of Melbourne — a situation that has been a problem in the United Kingdom and Australia.

Other tasks typically managed by contact-tracers can also be delegated to technology. In Vietnam, contacts log their health status through a symptom-tracking app, freeing up contact-tracers to interview newly infected individuals. People can also report the movements or symptoms of relatives who might not own a smartphone. In South Korea, Kenya and South Africa, authorities use phone location data to identify quarantine breaches.

At the beginning of the pandemic, overstretched contact-tracers in the United States, Australia and the United Kingdom faced the extra burden of antiquated health-care systems. In Australia, as well as in US states such as Hawaii and Washington, health departments are often notified of new cases by fax or phone. “It’s somewhat embarrassing,” says Plescia, but “we never invested in the systems to allow them to do it differently”. Entering names and other details into a database from faxed notifications causes big delays, he says, so that the window during which contact-tracing might make a difference vanishes.

“If there’s a single lesson that every country needs to learn, it’s invest in your public-health system,” says Rajan.

## Assistance from apps

One idea touted early on was to do contact-tracing with smartphone apps. These emit Bluetooth signals to other phones; when a person tests positive for coronavirus, their phone app notifies others who were in close proximity for 15 minutes or more (if they have installed the app). In theory, such technology could notify contacts almost instantaneously. Apps can also help shop owners and restaurants to log who has visited their premises.



# South Korea is reporting intimate details of COVID-19 cases: has it helped?

Contact-tracing apps have met with concerns over privacy, and although they are becoming common — at least 46 countries have developed some form of app — uptake rates remain low. “Adoption is not phenomenal anywhere,” says Effy Vayena, a bioethicist at the Swiss Federal Institute of Technology in Zurich, who is involved in the development of the Swiss contact-tracing app. “The trust question is crucial,” she says. It is exacerbated by a history of large-scale data breaches and privacy scandals in digital technologies.

Despite the low uptake, Fraser says, apps are a worthwhile adjunct to manual efforts, because small effects can accumulate over time. “This isn’t a silver bullet,” he says, but “it’s not just a gimmick”, either.

## **Trust deficit**

For contact-tracing to work, people with COVID-19 must be prepared to answer questions about their whereabouts, and they must isolate themselves from others while unwell. In many places, that’s not happening.

A survey of attitudes to contact-tracing across 19 countries in August found that nearly three-quarters of respondents would be willing to provide contact information<sup>9</sup>. But rates varied. In Vietnam, only 4% of participants said that they wouldn’t provide this information. In the United States and Germany, the proportion was 21%, and in France, it was 25%. Concerns around data privacy and tracking are partly to blame, says researcher Sarah Jones at Imperial College London, who co-led the survey. “Many health authorities and governments, especially in North America and Western Europe, may need to urgently improve public-health messaging to mitigate concerns about contact-tracing,” she says.

“Public trust in all sorts of institutions is declining,” says sociologist Robert Groves, former director of the US Census Bureau, who notes that this is especially the case in large urban areas where social cohesion has also declined. But the low numbers of people providing details of contacts or responding to calls from contact-tracers, while disappointing, are not surprising, says Mary Bassett, a public-health researcher at Harvard University in Cambridge, Massachusetts. Some communities that have been hardest hit by COVID-19 have a long-standing distrust of public-health authorities, she says. “For the African American community, there’s a history of malfeasance on the part of the public-health system,” she says, “and for the Latino community, there’s a problem of members of the community who are undocumented” — and fear deportation.

Systems are often hampered by a lack of support for people who fall ill or need to quarantine, too. Providing adequate financial compensation for personal hardship as a result of quarantine could shift people’s reluctance to comply. The prospect of being without income for two weeks — or losing a job entirely — is a big burden, says Plescia, and might explain people’s reluctance to provide details for their close contacts.

If Western countries are not prepared to enforce case isolation (as Singapore does), quarantine contacts separately (as happens in Vietnam) or adopt digital measures to identify people (as in South Korea), some might ask whether contact-tracing is up to the task of suppressing the spread of COVID-19 in these locations — even if nations get better at recursive and backwards tracing .

But Nyenswah isn’t writing it off. Even in the United States, he says, the practice could yet work to bring case numbers down. It will be difficult, but it’s essential for regional and national leaders to clearly communicate the importance of contact-tracing, he says. “There is no substitute for political leadership in an outbreak response.”

Nature 588, 384-387 (2020)

doi: <https://doi.org/10.1038/d41586-020-03518-4>

## Updates & Corrections

- **Correction 17 December 2020:** An earlier version of this feature referred to the wrong guidance from the WHO on quarantining contacts in designated facilities. It should have referred to guidance issued in February, not August. The text and reference 4 have been updated accordingly. Furthermore, it erred in stating that the WHO declared COVID-19 a pandemic.

## References

1. 1.  
Smith, L. E. *et al. Public Health* **187**, 41–52 (2020).
2. 2.  
Lash, R. R. *et al. Morb. Mortal. Wkly Rep.* **69**, 1360–1363 (2020).
3. 3.  
COVID-19 National Emergency Response Center. *Osong Public Health Res. Perspect.* **11**, 60–63 (2020).
4. 4.  
World Health Organization. *Considerations for Quarantine of Individuals in the Context of Containment for Coronavirus Disease: Interim Guidance*, 29 February 2020 (WHO, 2020).
5. 5.  
Sehgal, A. R., Himmelstein, D. U. & Woolhandler, S. *Ann. Intern. Med.* <https://doi.org/10.7326/M20-4331> (2020).
6. 6.  
Ferretti, L. *et al. Science* **368**, eabb6936 (2020).
7. 7.

Adam, D. C. *et al.* *Nature Med.* **26**, 1714–1719 (2020).

8. 8.

Jian, S.-W., Cheng, H.-Y., Huang, X.-T. & Liu, D.-P. *Int. J. Infect. Dis.* **101**, 348–352 (2020).

9. 9.

Institute of Global Health Innovation. *COVID-19: Perceptions of Contact Tracing. Global Report* (IGHI, 2020).

## **Jobs from Nature Careers**

- - - [All jobs](#)
    - - [Study Nurse \(m/w/d\)](#)

[German Cancer Research Center in the Helmholtz Association \(DKFZ\)](#)

[Heidelberg, Mannheim, Germany](#)

[JOB POST](#)

- [Two Research Software Engineers](#)

[Jülich Research Centre \(FZJ\)](#)

[Garching, Germany](#)

[JOB POST](#)

- [Softwareentwickler/in \(w/m/d\) für Experimentsysteme](#)

[Helmholtz-Zentrum Berlin for Materials and Energy \(HZB\)](#)

[Berlin, Germany](#)

[JOB POST](#)

▪ [Software Developer \(f/m/d\) for Experiment Systems](#)

[Helmholtz-Zentrum Berlin for Materials and Energy \(HZB\)](#)

[Berlin, Germany](#)

[JOB POST](#)

---

This article was downloaded by **calibre** from <https://www.nature.com/articles/d41586-020-03518-4>

| [Section menu](#) | [Main menu](#) |

NEWS FEATURE  
15 December 2020

# How COVID-19 is changing the cold and flu season

Measures meant to tame the coronavirus pandemic are quashing influenza and most other respiratory diseases, which could have wide-ranging implications.

**Nicola Jones**

Nicola Jones is a science journalist based in Pemberton, British Columbia

**Search for this author in:**

- [Pub Med](#)
- [Nature.com](#)
- [Google Scholar](#)



Despite signs of reduced influenza transmission, people in the United States are being encouraged to get the vaccine. Credit: Jeffrey Greenberg/Universal Images Group via Getty

By mid-December, the Northern Hemisphere is usually well into the start of its annual cold and flu season — but so far this year, even as the COVID-19 pandemic surges in dozens of countries, the levels of many common seasonal infections remain extremely low.

The pandemic caused by the SARS-CoV-2 coronavirus has infected at least 67 million people and killed 1.5 million worldwide. The patchwork of responses intended to fight the pandemic — from temporary lockdowns to mask wearing, social distancing, enhanced personal hygiene and reduced travel — has had a huge impact on other common respiratory illnesses, too.

In the Southern Hemisphere — now past its winter — seasonal influenza hardly struck at all. That looks as though it might happen in the north, too. Conversely, some common-cold viruses have thrived, and tantalizing evidence suggests that they might, in some cases, protect against COVID-19.

Despite humanity's long history with colds and flu, the viruses that cause them still hold many mysteries. Scientists hope this year's disrupted seasons could reveal new information about the transmission and behaviour of these unwelcome annual guests: how these viruses respond to health measures, how they interact and what that might mean for long-term disease burdens. "This is a natural experiment for so many respiratory viruses," says Sonja Olsen, an epidemiologist at the National Center for Immunization and Respiratory Diseases, part of the US Centers for Disease Control and Prevention (CDC) in Atlanta, Georgia.

## The influenza fizzle

In May, at the tail end of the first wave of COVID-19 deaths in many nations, and when some of the strictest lockdowns were in place, health workers noted an [abrupt and early halt to the 2019–20 flu season](#) in the Northern Hemisphere.



## How coronavirus lockdowns stopped flu in its tracks

That might partly have been an artefact caused by fewer people coming to a clinic for testing, experts say, but it was also attributable to the effectiveness

of policies such as social distancing. After the pandemic started, positive tests for the flu virus plummeted by 98% in the United States, for example, whereas the number of samples submitted for testing dropped by only 61%<sup>1</sup>. In the end, the US 2019–20 flu season was rated as ‘moderate’ by the CDC, which estimates that 38 million people fell ill with influenza, and 22,000 people died. That’s fewer than in recent years, but not unprecedented.

After the flu season in the north ended early, it hardly got going at all in the Southern Hemisphere. There were astonishingly few cases of seasonal flu there from April to July 2020 — even as global COVID-19 cases continued to climb. In Australia, Chile and South Africa, a grand total of just 51 cases of flu were spotted in more than 83,000 tests<sup>1</sup>. “We know it’s less transmissible than coronavirus, so it makes sense,” says Olsen, but the decline was still “greater than expected”. Influenza’s absence has been attributed to pandemic-response measures, but they don’t tell the whole story.

“Some South American countries haven’t done such a good job controlling COVID, but even there flu is low,” says virologist Richard Webby at St Jude’s hospital in Memphis, Tennessee. “I don’t think we can put it all down to mask wearing and social distancing.” He suspects that the dearth of international travel played a part. Flu typically travels around the world from one winter to another, while maintaining a lower year-round presence in the tropics. Although the mechanisms underlying this behaviour aren’t entirely clear, the movement of people clearly contributes.



Enhanced school cleaning might have reduced the spread of some viruses, but others persist. Credit: Oli Scarff/AFP via Getty

Increased influenza vaccination might have contributed to the disappearance, too. Australia, for example, saw more than 7.3 million flu jabs administered by 20 May 2020, compared with 4.5 million by that date in 2019, and 3.5 million in 2018. It's unclear if that trend will hold in the north.

Vaccination rates in the United States for seasonal flu have been trending upwards for years: slightly more than half of the US population over six months of age was vaccinated in 2019–20, up 2.6 percentage points from the previous year. But it is unclear whether Americans will be more or less inclined towards flu vaccinations this year, particularly given the tumultuous backdrop of the pandemic and the change in president.

## Viral unknowns

Most experts are cautiously betting on a very mild flu season for the Northern Hemisphere this year. That would be good news on many fronts — in particular, it would help to alleviate the potential burden on the health system, from hospitals to testing centres, caused by simultaneous waves of flu and COVID-19. But surprises could be in store.

No one really knows, for example, why one nation, such as Australia, can be hit hard by influenza for several years while a neighbouring country, such as New Zealand, sees very low rates, says Webby. Even influenza's seasonality isn't entirely understood, nor exactly how it travels around the globe. "We don't have a real good handle on why it's a winter disease," he says. Untangling lessons about flu from this year's data will be interesting but difficult, Olsen says, because pandemic policies and compliance vary on the national, state and even neighbourhood level.



## How Iceland hammered COVID with science

And the changing trends could have consequences. If this year's flu season does fizzle out in the Northern Hemisphere, that could make it harder to predict the right strains to put in 2021's flu vaccine. It could also have

intriguing, longer-term consequences. Webby speculates that a low-flu season might kill off less-common variants of influenza. “A lot of different flus have been circulating in recent years. Are they all going to make it out of this or not?” he asks. “It’s possible that what this season will do is actually make the virological picture a lot simpler. That may be permanent, potentially.”

At the same time, Webby adds, the lack of viral competition in human hosts could conceivably open a door for new swine-flu variants in the future. “We get a handful of those every year, in the agricultural-fair season,” Webby says. “One of the things holding those viruses back a lot is natural immunity. If flu is low for a few seasons, that might leave a gap for swine viruses to have more impact.”

“I am sure that flu will come back with a vengeance at some stage in the future,” says Robert Ware, a clinical epidemiologist at Griffith University in Queensland, Australia, “but it might take a few years.”

## Bucking the trend

Influenza viruses aren’t the only ones affected by pandemic-response measures. There are hundreds of viruses that cause respiratory symptoms similar to those of a common cold, from parainfluenza to metapneumovirus. And most of these viruses, too, seem to have been held at bay in the Southern Hemisphere’s winter.

In particular, researchers saw some abrupt declines in respiratory syncytial virus (RSV), a common virus that typically infects young children and can sometimes cause serious conditions such as pneumonia. There is no vaccine for RSV, and the virus causes about 5% of deaths in children under five around the world. In Western Australia, RSV in children declined by 98% (and flu by 99.4%) through their winter 2020, even though schools were open<sup>2</sup>.

The RSV reprieve might be only temporary, though. Data from Australia’s most populous region, New South Wales (NSW), for example, show RSV detections climbing back up in October (see “Shifting patterns of cold and

flu”). And a build-up of susceptible, uninfected children might result in bigger waves of infection in future, some researchers warn<sup>3</sup>.

## SHIFTING PATTERNS OF COLDS AND FLU

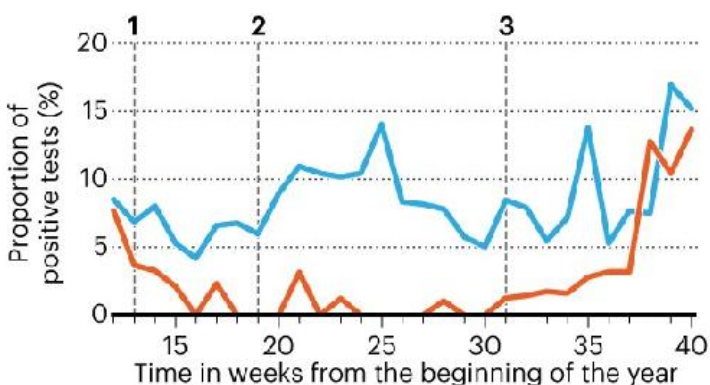
Following the United Kingdom's national lockdown in March 2020, there was a drop in detection of most common respiratory viruses, including rhinovirus. Infections didn't rise when lockdown eased, but they did rise rapidly after schools started again in September.

— Rhinovirus-positive 2019 (of 1,898 adults tested)

— Rhinovirus-positive 2020 (of 3,898 adults tested)

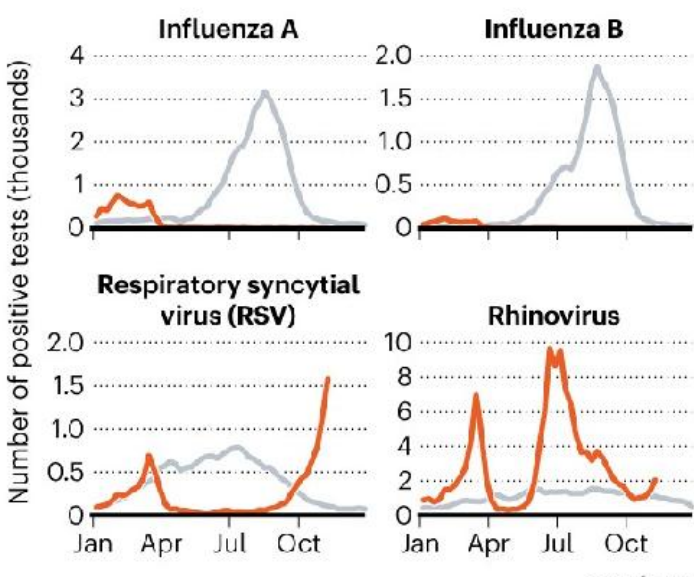
1. Nationwide lockdown 2. Lockdown easing

3. Return to schools



Data from New South Wales in Australia show large declines in influenza detection this year relative to previous ones. Respiratory syncytial virus (RSV) also decreased to lower levels than usual but bounced back rapidly in October. There were large spikes of rhinovirus detection however, compared with previous years, although this might have been due to increased testing.

— 2020 — Average 2015–2019



©nature

Sources: UK: ref. 4; NSW: NSW ministry of Health

There is one major exception to the downward viral trend. “The one virus that’s not being halted is the rhinovirus,” says Janet Englund, a paediatric infectious disease researcher at Seattle Children’s Hospital in Washington. Rhinoviruses are the major cause of the common cold, especially in children. More than a hundred strains exist, and about a dozen typically circulate in any given community. In one study in Southampton, UK, rhinovirus detection in adults admitted to hospital remained lower over the summer of 2020 than in summer 2019, but shot up as usual once schools reopened in September<sup>4</sup>. Data from NSW likewise show an apparent surge in rhinoviruses over the southern winter. Although some of these peaks are probably due to an increase in testing in people with mild cold symptoms, these viruses certainly did not decline as others did.

“No one really knows why” rhinoviruses are proving so persistent, says Englund. Some viruses that cause cold-like symptoms are very different from each other in structure; in particular, rhinoviruses, unlike influenza and coronaviruses, don’t have an outer lipid coat, or envelope, which is vulnerable to soaps and sanitizers. In NSW, detection of the non-enveloped adenoviruses, which also cause cold-like symptoms, held relatively steady throughout the southern winter, rather than crashing like flu or surging like rhinovirus. “The expectation is that rhinovirus is perhaps more stable on surfaces,” Englund says, allowing greater transmission between children on hands, desks and doorknobs. There is also thought to be greater asymptomatic transmission of rhinoviruses, which would allow them to circulate more freely in schools, even when sick children are staying at home.

The good news is that the common cold might help to protect people against COVID-19. One study<sup>5</sup> of more than 800,000 people, for example, showed that adults who had had cold symptoms within the previous year were less likely to test positive for SARS-CoV-2 — although why this is so remains a mystery.

## Cross-protection?

One possible explanation is that previous infection with a coronavirus (another cause of the common cold) could confer some immunity to SARS-CoV-2 — although it's notable that people can get the same coronavirus colds over and over again, and multiple cold viruses at once<sup>6</sup>. Previous coronavirus infections do seem to generate T cells and B cells — immune-system cells that help to attack and remember pathogens — that can recognize SARS-CoV-2. These pre-existing cells might provide some partial cross-protection against the new coronavirus<sup>7</sup>.

A few studies have shown that, because of other coronavirus infections, about one-quarter of people have antibodies that can bind to the SARS-CoV-2 virus, says Scott Hensley, a viral immunologist at the University of Pennsylvania in Philadelphia. One study<sup>8</sup> showed that these antibodies can actually neutralize SARS-CoV-2 infections, stopping the virus from invading cells. Strong cross-neutralization of SARS-CoV-2 by antibodies against other coronaviruses would be “really spectacular”, says Qiuwei Abdullah Pan at Erasmus University Medical Center in Rotterdam, the Netherlands, because it would open the door to universal coronavirus vaccines that protect across the board. But other studies<sup>9</sup>, including Hensley’s<sup>10</sup>, found that these antibodies cannot neutralize SARS-CoV-2 or protect against COVID-19. “Cross-neutralization has not been proven,” says Pan. Even if it is, he says, “I would expect the activity would probably be very moderate.”



## Meet the scientists investigating the origins of the COVID pandemic

Another way that seasonal colds might be contributing to COVID-19 immunity is that a current rhinovirus infection might interfere directly with SARS-CoV-2 — perhaps by kicking off interferon responses, part of the immune system that inhibits viral reproduction. A study<sup>6</sup> by Ware and his colleagues, for example, shows that someone with a rhinovirus infection is 70% less likely to also get a common coronavirus infection, compared with someone who doesn't have the sniffles. Clinical microbiologist Alberto Paniz Mondolfi at the Icahn School of Medicine at Mount Sinai, New York, and colleagues have shown markedly few rhinovirus co-infections in people with SARS-CoV-2 in New York City<sup>11</sup>. "Rhinovirus is one tough virus," says Paniz Mondolfi. Its fast growth stops other viruses from taking off, and it could conceivably be outcompeting SARS-CoV-2, he says.

This viral interference might be a powerful effect. Ellen Foxman, an immunologist at the Yale School of Medicine in New Haven, Connecticut, and colleagues have found evidence that rhinoviruses might have derailed the influenza H1N1 pandemic that occurred in 2009, for example<sup>12</sup>. Hospitalized adults had fewer-than-expected instances of co-infection with both viruses. And, in cell cultures, rhinovirus infection stopped that strain of H1N1 from infecting cells. Foxman is now looking to see whether rhinovirus infection can block SARS-CoV-2; she expects results soon.

Overall, it's a "very likely scenario" that rhinoviruses and other coronaviruses will help to stem the spread of COVID-19, says Paniz Mondolfi. "I think many virologists, like me, have been waiting for this season to look at how this will evolve."

But with so many unknowns surrounding all these viruses, most researchers say that people should be ready for a worst-case scenario — from a bad flu season compounding the challenges of COVID-19, to future outbreaks of RSV. "It's best to be prepared," says Olsen. "We don't know what's going to happen."

Nature **588**, 388–390 (2020)

doi: <https://doi.org/10.1038/d41586-020-03519-3>

## References

1. 1.

Olsen, S. J. *et al.* *MMWR Morb. Mortal. Wkly Rep.* **69**, 1305–1309 (2020).

2. 2.

Yeoh, D. K. *et al.* *Clin. Infect. Dis.* <https://doi.org/10.1093/cid/ciaa1475> (2020).

3. 3.

Baker, R. E. *et al.* *Proc. Natl Acad. Sci. USA* <https://doi.org/10.1073/pnas.2013182117> (2020).

4. 4.

Poole, S., Brendish, N. J., Tanner, A. R. & Clark, T. W. *Lancet Respir. Med.* **8**, e92–e93 (2020).

5. 5.

Aran, D., Beachler, D. C., Lanes, S. & Overhage, J. M. *J. Infect.* <https://doi.org/10.1016/j.jinf.2020.10.023> (2020).

6. 6.

Grimwood, K., Lambert, S. B. & Ware, R. S. *Pediatrics* **146**, e2020009316 (2020).

7. 7.

Grifoni, A. *et al.* *Cell* **181**, 1489–1501.e15 (2020).

8. 8.

Ng, K. W. *et al.* *Science* <https://doi.org/10.1126/science.abe1107> (2020).

9. 9.

Poston, D. *et al.* Preprint at medRxiv  
<https://doi.org/10.1101/2020.10.08.20209650> (2020).

10. 10.

Anderson, E. M. *et al.* Preprint at medRxiv  
<https://doi.org/10.1101/2020.11.06.20227215> (2020).

11. 11.

Nowak, M. D., Sordillo, E. M., Gitman, M. R. & Paniz Mondolfi, A. E. *J. Med. Virol.* **92**, 1699–1700 (2020).

12. 12.

Wu, A., Mihaylova, V. T., Landry, M. L. & Foxman, E. F. *Lancet Microbe* **1**, e254–e262 (2020).

## **Jobs from Nature Careers**

- - - [All jobs](#)
    - - [Study Nurse \(m/w/d\)](#)

[German Cancer Research Center in the Helmholtz Association \(DKFZ\)](#)

[Heidelberg, Mannheim, Germany](#)

JOB POST

- **Two Research Software Engineers**

Jülich Research Centre (FZJ)

Garching, Germany

JOB POST

- **Softwareentwickler/in (w/m/d) für Experimentsysteme**

Helmholtz-Zentrum Berlin for Materials and Energy (HZB)

Berlin, Germany

JOB POST

- **Software Developer (f/m/d) for Experiment Systems**

Helmholtz-Zentrum Berlin for Materials and Energy (HZB)

Berlin, Germany

JOB POST

---

This article was downloaded by **calibre** from <https://www.nature.com/articles/d41586-020-03519-3>

## Books & Arts

- **[Women of the Nobel factory share their stories](#)** [15

December 2020]

Book Review • From sequencing to stardom — alumnae of the Laboratory of Molecular Biology reflect on how they succeeded in science.

BOOK REVIEW  
15 December 2020

- Correction [18 December 2020](#)

# Women of the Nobel factory share their stories

From sequencing to stardom — alumnae of the Laboratory of Molecular Biology reflect on how they succeeded in science.

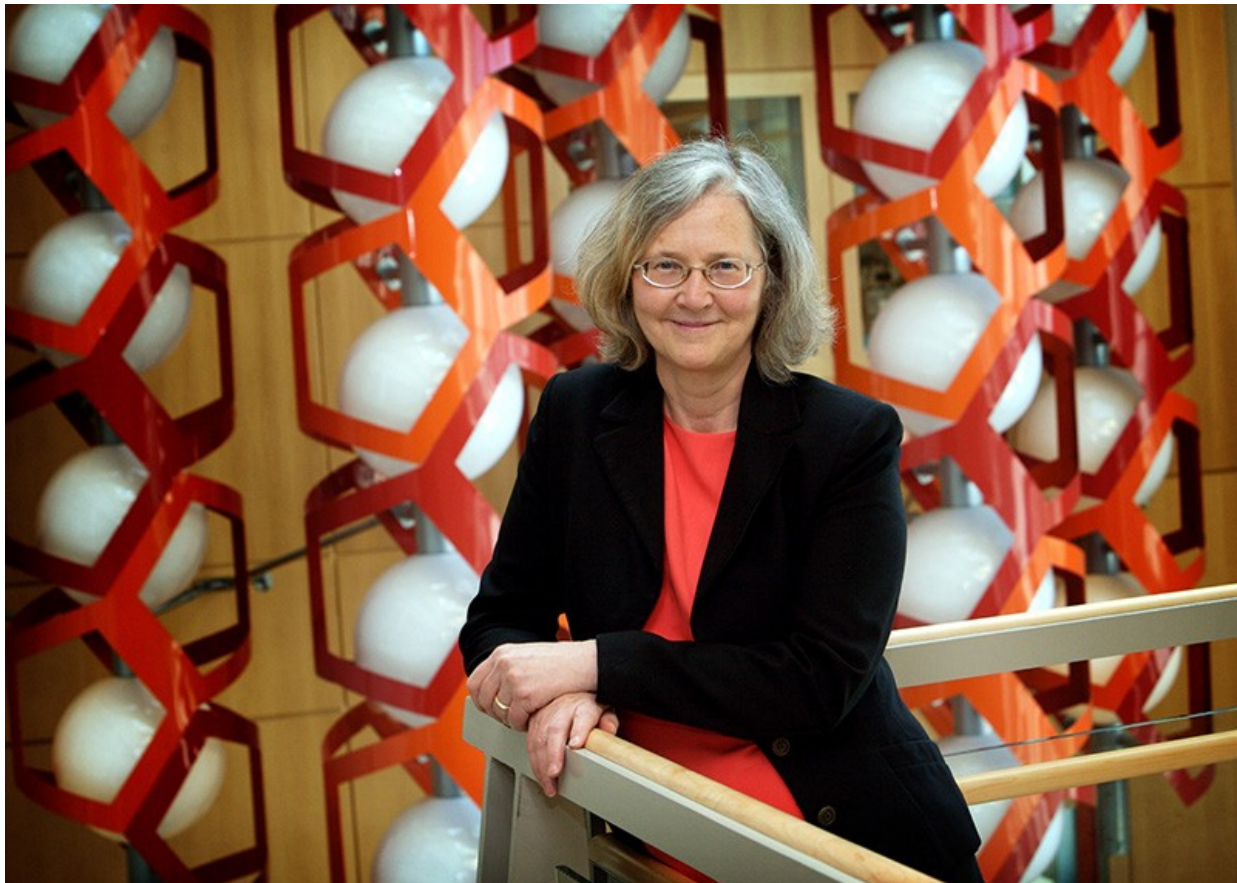
## Georgina Ferry

Georgina Ferry is a science writer based in Oxford, UK. Her books include biographies of Max Perutz and Dorothy Hodgkin.

[Contact](#)

**Search for this author in:**

- [Pub Med](#)
- [Nature.com](#)
- [Google Scholar](#)



Elizabeth Blackburn won a Nobel prize in 2009 for discoveries about telomeres. Credit: Thor Swift/New York Times/Redux/eyevine

### **Ahead of the Curve: Women scientists at the MRC Laboratory of Molecular Biology** Kathleen Weston MRC LMB (2020)

In May 1986, PhD student Kathleen Weston headed the author list on a correspondence to *Nature* titled ‘Sexist ads’. The 46 signatories, half of them women, worked at the Medical Research Council’s Laboratory of Molecular Biology (LMB) in Cambridge, UK. They upbraided the journal for a series of adverts that portrayed “men (and in some cases animals) as serious-minded scientists, and women as dumb decorative objects” ([K. Weston et al. Nature 321, 106; 1986](#)).

Female researchers in many nations are now less likely to encounter assumptions that their profession is exclusively male. This is in part thanks to women such as the 635 who have passed through the LMB since it opened

in 1962. In *Ahead of the Curve*, Weston spotlights some to ask: what are their recipes for success?

They are necessarily a select bunch. The LMB, a research institute with a headcount of more than 800 scientists and support personnel, claims 27 Nobel prizewinners among its staff and alumni. It has been a magnet for researchers looking to work at the forefront of structural biology, protein chemistry and cell biology. Weston found it “frightening” when she arrived in 1983, not because of sexism but because it “discriminated against mediocrity”. Her book is based on interviews with women who thrived in this high-pressure environment and went on to become global leaders in their fields.



## Three extraordinary women run the gauntlet of science — a documentary

Nobel-prizewinning molecular biologist Elizabeth Blackburn puts her finger on the obvious question: “Was there some preselection going on, so that the women who went there would have succeeded one way or another anyway?”

Probably, yes. They won their places on the basis of exceptional ability, showed determination in the face of setbacks and worked 15-hour days, 6 or 7 days a week. Cellular geneticist Sarah Teichmann remembers working “all the time, even on Christmas Eve and Christmas day” as an undergraduate because she “had nothing to calibrate myself against”.

Their passion for science trumped everything. “There was a freewheeling approach at the LMB that you could just tackle anything fearlessly, and that was fantastic and very helpful,” says immunologist Philippa Marrack, a PhD student there from 1968 to 1971.

## Credit where it's due

Molecular biophysicist Joan Steitz faced overt obstacles early in her career in the United States, such as being turned down for a PhD because she was a woman, so starting her postdoc at the LMB in 1967 was a revelation. “There was constant discussion about science,” she says, and “everyone was expected to interact on a par with people like Max” (Perutz, Nobel-prizewinning chair of the LMB). Learning RNA sequencing from a pioneer of the technique, divisional head Frederick Sanger, Steitz made key discoveries in gene expression and in 1969 became the first woman to speak at the annual week of lab talks. “In some places you wouldn’t get acknowledged for what you’d done but that was never the case at the LMB,” she says.



Mariann Bienz, the only woman to head a division at the LMB, works on signalling cascades.Credit: MRC Laboratory of Molecular Biology

She is one of several women featured in the book who made career choices to fit in with their partners' movements, yet flourished. Molecular biologist Daniela Rhodes took a technician job at the LMB with biophysicist Aaron Klug while her husband completed his studies; she stayed on to do a PhD and, in 1987, became a tenured group leaders. Blackburn followed her husband to Yale University in New Haven, Connecticut, where she started her Nobel-prizewinning work on telomeres, repeating sequences that protect the ends of chromosomes from deterioration.

Cell biologists Mariann Bienz and Hugh Pelham bonded over heat-shock proteins when she was an LMB postdoc and he a newly minted group leader. She later took a 40% salary cut to return from an assistant professorship in Zurich, Switzerland, to a group-leader position at the LMB, partly so that she, Pelham and their children could live together. Her output “took a dip”

when her children were small, she says, but she became head of the cell-biology division in 2007 and is now deputy director of the LMB.

These women's scientific questions range widely. Molecular biologist Melina Schuh's group was the first to capture developing human eggs with high-resolution microscopy, working in partnership with a Cambridgeshire *in vitro* fertilization clinic. Teichmann went for big-picture bioinformatics, spending her PhD at the LMB "hunched over a computer", classifying protein structures.



Scientists of the Laboratory of Molecular Biology in Cambridge, UK, past and present.Credit: MRC Laboratory of Molecular Biology

But their anecdotes point to similarities in the ways they run labs. For instance, Teichmann's experience of the "open-minded, pleasant and democratic management style" of structural biologist Janet Thornton's lab at University College London, where she was a postdoc, influenced how she does things.

## Equalize the pipeline

Weston gave up research to become a science writer a decade ago. Her account is lively, but embedded as it is in the history of molecular biology as practised at the LMB and beyond, it occasionally loses sight of the human stories in enthusiasm for the technical details. Only a subset of readers will stay with blow-by-blow accounts of clathrin-coated vesicles or the role of hypermutation in antibody diversity.



## Women in crystallography

At the LMB today, women comprise half the PhD students and postdocs, but only around one-quarter of group leaders. Bienz is the only woman in nearly 60 years to have headed one of the four divisions. Women's lack of progression is a universal problem, so focusing on the success stories might seem to dodge the issue. Yet Weston shows that the LMB high-flyers faced

many of the setbacks that make academia a ‘leaky pipeline’ for women: a lack of role models, the need to balance work and family, unconscious bias in appointments, impostor syndrome and salary disparities. Weston does not comment, however, on the fact that most of her interviewees came from well-educated and economically advantaged backgrounds, and all of them are white.

What is clear is that science is richer because these women kept going. They now mentor female colleagues and lobby their institutions for more family-friendly practices. Weston wryly suggests that rather than fretting when women find a rewarding alternative career, as she did, academia should present it as a positive option for men, too. “Perhaps what is required is more support for excellent women, combined with a leakier pipeline for less good men,” she concludes.

Nature **588**, 392-393 (2020)

doi: <https://doi.org/10.1038/d41586-020-03520-w>

## Updates & Corrections

- **Correction 18 December 2020:** An earlier version of this article incorrectly stated that Daniela Rhodes’s husband was studying at Cambridge, and that Rhodes was one of the first tenured female group leaders at the LMB. The text has now been corrected.

## Jobs from Nature Careers

- - - [All jobs](#)
    - 
    - [\*\*Study Nurse \(m/w/d\)\*\*](#)

[German Cancer Research Center in the Helmholtz Association \(DKFZ\)](#)

Heidelberg, Mannheim, Germany

JOB POST

- **Two Research Software Engineers**

Jülich Research Centre (FZJ)

Garching, Germany

JOB POST

- **Softwareentwickler/in (w/m/d) für Experimentsysteme**

Helmholtz-Zentrum Berlin for Materials and Energy (HZB)

Berlin, Germany

JOB POST

- **Software Developer (f/m/d) for Experiment Systems**

Helmholtz-Zentrum Berlin for Materials and Energy (HZB)

Berlin, Germany

JOB POST

# Work

- **[2020: the year of hard-won lessons](#)** [15 December 2020]  
Career Feature • Researchers reflect on a challenging pandemic year and on how lockdowns changed their approach to work and their perceptions of the scientific enterprise.
- **[The zoologist tracking an island's rebirth](#)** [14 December 2020]  
Where I Work • How horses and cows are enticing skylarks and starlings back to an island meadow.

## CAREER FEATURE

15 December 2020

- Correction [18 December 2020](#)

# 2020: the year of hard-won lessons

Researchers reflect on a challenging pandemic year and on how lockdowns changed their approach to work and their perceptions of the scientific enterprise.

## Virginia Gewin

Virginia Gewin is a freelance writer in Portland, Oregon.

### Search for this author in:

- [Pub Med](#)
- [Nature.com](#)
- [Google Scholar](#)

[Find a new job](#)



Sanam Mustafa demonstrates her laboratory's work in biophotonics. Credit: Dr Erik Schartner

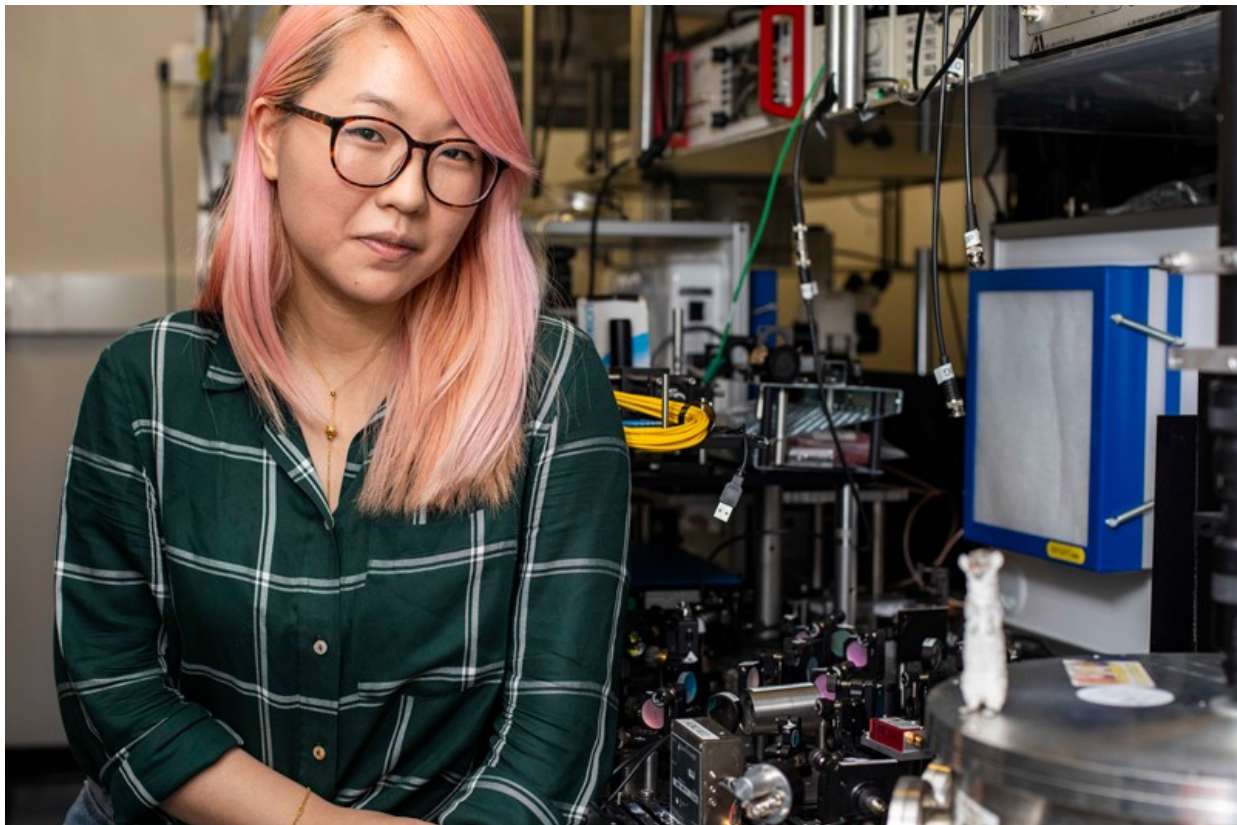
At the best of times, science is a complex juggling act of research, teaching, mentoring, grant writing and publishing. The COVID-19 pandemic has brought nationwide lockdowns, rising racial tensions and virtual scientific life. For many, 2020 has been a year in which doing well has meant simply muddling through. The darkest moments, however, can often help to reveal a clear purpose.

Female researchers are [disproportionately affected by the pandemic](#). *Nature* spoke to seven about what they have taken away from this year of upheaval, and how, despite challenges, they forged new career directions and launched new initiatives.

## Frustration into action

Not long after Lia Li's University College London laboratory shut down in March, the physicist was put on furlough until July. Since then, a 25% occupancy limit on campus has prompted her to forgo lab time so that PhD students can finish crucial data collection. "I'm an experimentalist who hasn't been able to do experiments, so I've had to reimagine my academic identity," says Li, who since 2016 has supported her independent research with grants.

Unable to conduct her university experiments, she says, she was able to focus on writing the business plan for the start-up she has been developing since 2016. Her fledgling company, Zero Point Motion, which she hopes to launch in the next few years, will design and produce optical sensors that track the position of an object in 3D space.



Lia Li next to her experiment at University College London.Credit: Agnese Abrusci

Li says that she was also motivated to focus on her business by her struggles with the fact that the academic system works well only for some. When her

start-up is under way, she will codify equal pay and anti-racism into workplace codes of conduct, and make the workspace welcoming for scientists from under-represented groups. “It’s scary to consider starting a company in the middle of a pandemic, but carving out my own anti-racist work environment has been driving me during the lockdown,” she says. “This was the year that kicked my bum into gear.”

## **Embrace virtual meetings**

Like many academics, Sonia Seneviratne, a climate scientist at the Institute for Atmospheric and Climate Science at the Swiss Federal Institute of Technology in Zurich, Switzerland, went from travelling every month to no trips at all this year. “This was a good change. I’m quite happy to have less travel,” she says. Her initial concern about having fewer interactions with colleagues has been assuaged by attending virtual conferences. She advocates a continuation of the online-conference model where possible, which, she says, had long been a topic of discussion, particularly among climate-change researchers. “The thought was, ‘We’ll do this eventually’,” says Seneviratne. The pandemic not only forced mass adoption of virtual meetings but proved that they work well.



Sonia Seneviratne advocates a continuation of the online-conference model. Credit: Markus Bertschi/ETH Zurich

Nadya Mason, a physicist at the University of Illinois at Urbana-Champaign, where she is director of the Materials Research Science and Engineering Center, says that everyone travelling less can make international collaborations easier. “Since we are not spending time travelling, we can ‘see’ collaborators around the world much more readily than we used to,” she says.



## Collection: Coronavirus and scientific careers

The virtual meetings have allowed Mason, an experimentalist, to maintain intellectual momentum working with a European theorist to better understand a data set. Mason also joins another female physicist for virtual ‘happy hours’, which, she says, helps to nurture a sense of connection.

### **Find strength in numbers**

Jenea Adams, a second-year PhD student in genomics and computational biology at the University of Pennsylvania in Philadelphia, says that her lowest point this year was around 4 July, a US public holiday that celebrates the nation’s independence from the United Kingdom. Racial unrest in Philadelphia made it difficult for her to focus on her PhD programme or to pretend that nothing was happening. The tensions around the killing of George Floyd and the associated Black Lives Matter protests felt like “another pandemic on top of a pandemic”, says Adams.

With more time at home because of the lockdown, Adams felt prompted to focus more on a networking project that she’d started in January, triggered

by the realization that she knew only three other Black women in computational biology. A Google spreadsheet of names, e-mail addresses, research interests and academic institutions mushroomed into the Black Women in Computational Biology Network (see [go.nature.com/33w1lg9](http://go.nature.com/33w1lg9)). The group has some 120 members around the world and more than 160 allies, who contribute mentorship or collaboration, including a few venerated computational biologists, she says.



Jenea Adams expanded a fledgling network into The Black Women in Computational Biology Network. Credit: University of Dayton Communications

As Twitter hashtags proliferated to highlight Black scientists in different disciplines, Adams found colleagues in #BlackInData, #BlackInCancer, #BlackInBio. Her network's Twitter feed @blkwomencompbio, now has nearly 2,500 followers. "The hashtags offered an avenue of communication for us to connect and build community," she says. In addition to creating a chat channel for the new network on the messaging platform Slack, the collective is now promoting ways into the field as well as producing career-

development workshops and seminars to engage with the rest of the field on its [YouTube page](#). “We used virtual communication to build community, so that people could feel seen and heard over the last year — which helped us to define our mission and ourselves during a difficult time,” Adams says. “Collective action is more important than I had appreciated.”

## Bend, don’t break

Lydia Jennings, a PhD student in soil science at the University of Arizona in Tucson, says that, above all, she has learnt resilience this year. Jennings had expected to graduate in May 2020 and defend her doctoral dissertation in August. But the pandemic upended those plans and brought other disruptions, from a burgled flat and lockdown-related research delays that left her scrambling for funding, to the fact that some of the state’s first deaths from COVID-19 were within her Indigenous Huichol and Pascua Yaqui communities. “Hearing how many friends were losing family members when I was already trying to maintain my mental strength was tough,” she says.

Lockdowns also prevented Jennings from re-running about 40 samples that she needed to analyse her data fully. She’s thankful that her adviser was able to cobble together funding support for her to complete her PhD. But her relief was tempered when her flat was robbed in late November, a few days before her rescheduled dissertation defence. And she sees the cancellation of the graduation ceremony as robbing her of the opportunity to graduate with 12 other Indigenous women receiving PhDs — a notable achievement when less than 1% of US PhD holders are Indigenous. “It was going to be such a special moment for us — being able to amplify our communities,” Jennings says.



Nadya Mason has found that travelling less can make international collaborations easier.Credit: L. Brian Stauffer

The group is trying to find a way to celebrate this achievement virtually. To that end, Jennings is also planning to run 80 kilometres of the Arizona Trail, which traverses the state, in honour of 50 living and late Indigenous scientists. She plans to signify different scientists' names, areas of study and Indigenous affiliation with placards or other visual information when a friend films her run, planned for February or March, as a short documentary. "I want to honour those Indigenous scientists who came before me," she says.

Jennings says that her new-found resilience will help as she turns to studying severe impacts of climate change.

## **Ask for what you need**

Molecular pharmacologist Sanam Mustafa, at the University of Adelaide in Australia, decided to be assertive and seek a grant application extension, despite the low odds that she'd get one. With a 4-year-old and a new baby, and with the university locked down for eight weeks from April, Mustafa struggled to meet the application deadline of 30 April, for which the funder had specified no extensions. "I was writing this grant at three or four in the morning while the baby was sleeping," she says. Mustafa decided that a pandemic was reason enough to bend the rules. "I put my case in writing," she says. "I wanted only two more days — a weekend — to wrap it up." Her new-found assertiveness paid off. The extension was granted within hours, and the application was submitted. "COVID life is similar to being a new parent — everything is very up in the air," she says.

Mustafa does not yet know if she won the grant, but she says that her second takeaway message from the experience is that academia — and funders — need to incorporate flexibility.

## Do meaningful science

Halley Froehlich, an aquaculture and fisheries scientist at the University of California, Santa Barbara, has been establishing her first lab and teaching her first classes this year. She learnt to focus on research that will have a significant societal impact. "What I do now will dictate what my lab looks like in ten years," she says.

For example, instead of joining several working groups on aquacultural stewardship, she is focusing only on the one that is most related to climate. She had always been enthusiastic about research related to climate policy and has now made that one of her priorities. "I want to feel like I'm contributing to energy policy and food production," she says.

California's state government has asked her and colleagues to help develop a science-based framework for the development of marine aquaculture in the state, she says. As a new US administration takes shape, she's heartened that it looks as if expertise matters again, and science has a role in society.

doi: <https://doi.org/10.1038/d41586-020-03521-9>

## Updates & Corrections

- **Correction 18 December 2020:** An earlier version of this Career feature misstated the age of Sanam Mustafa's child and the month that her university went into lockdown.

## Jobs from Nature Careers

- - - [All jobs](#)
    - - [Study Nurse \(m/w/d\)](#)  
  
[German Cancer Research Center in the Helmholtz Association \(DKFZ\)](#)  
  
[Heidelberg, Mannheim, Germany](#)  
  
[JOB POST](#)
      - [Two Research Software Engineers](#)  
  
[Jülich Research Centre \(FZJ\)](#)  
  
[Garching, Germany](#)  
  
[JOB POST](#)
      - [Softwareentwickler/in \(w/m/d\) für Experimentsysteme](#)  
  
[Helmholtz-Zentrum Berlin for Materials and Energy \(HZB\)](#)

Berlin, Germany

JOB POST

▪ **Software Developer (f/m/d) for Experiment Systems**

Helmholtz-Zentrum Berlin for Materials and Energy (HZB)

Berlin, Germany

JOB POST

---

This article was downloaded by **calibre** from <https://www.nature.com/articles/d41586-020-03521-9>

| [Section menu](#) | [Main menu](#) |

WHERE I WORK

14 December 2020

# The zoologist tracking an island's rebirth

How horses and cows are enticing skylarks and starlings back to an island meadow.

**Virginia Gewin**

Virginia Gewin is a freelance writer in Portland, Oregon.

**Search for this author in:**

- [Pub Med](#)
- [Nature.com](#)
- [Google Scholar](#)



Lilla Lovász studying large grazers in nature reserves in France, just north of Basel, Switzerland

Lilla Lovász is a PhD student in zoology at the University of Basel, Switzerland. Credit: Clara Tuma for *Nature*

Just inside France's border with Germany, enclosed between the Rhine River and the Grand Canal of Alsace, lies an island that is becoming a haven for biodiversity. The site, to the north of Basel, Switzerland, is being made into a conservation area in a joint project between the National Nature Reserve of the Petite Camargue and the French energy company EDF. The aim is to create a self-sustaining mosaic of forest and meadows that can host many species of flora and fauna.

As part of my PhD programme in zoology, I study how the landscape of a 32-hectare test area of the island changes over time. I and my colleagues are documenting the diversity of birds, amphibians, butterflies and plants.

Meadows are a rare and precious habitat in central Europe. Without floods, fires or large grazing animals, meadows typically have to be maintained through mowing or grazing. The reserve's managers use cows and horses as grazers to prevent forests from taking over the island.

In 2018, we introduced Konik horses, which might be direct descendants of wild horses, followed by Highland cows. Currently, we have seven of each.

I conduct vegetation surveys between June and September and do bird surveys year round. In this picture, I'm carrying on with one of my responsibilities — attending to the horses' GPS collars and replacing batteries. I have to be in a calm state to take a horse's collar off and put it back on, because they are so sensitive to human moods. They have to be in the right mood, too, or I'll get a warning kick.

It's been fascinating to watch the changes here over the past three years. Nature is returning, and more species are coming back. In particular, the common starling (*Sturnus vulgaris*) and Eurasian skylarks (*Alauda arvensis*), whose populations are declining in Europe, are benefiting here from the horses and cows. We think that the grazers help starlings — for example, by flushing out the insects that they feed on.

Nature **588**, 530 (2020)

doi: <https://doi.org/10.1038/d41586-020-03522-8>

## Jobs from Nature Careers

- - - [All jobs](#)
    - - [Study Nurse \(m/w/d\)](#)

German Cancer Research Center in the Helmholtz Association (DKFZ)

Heidelberg, Mannheim, Germany

JOB POST

▪ **Two Research Software Engineers**

Jülich Research Centre (FZJ)

Garching, Germany

JOB POST

▪ **Softwareentwickler/in (w/m/d) für Experimentsysteme**

Helmholtz-Zentrum Berlin for Materials and Energy (HZB)

Berlin, Germany

JOB POST

▪ **Software Developer (f/m/d) for Experiment Systems**

Helmholtz-Zentrum Berlin for Materials and Energy (HZB)

Berlin, Germany

JOB POST

# Research

- **European rivers are fragmented by many more barriers than had been recorded** [16 December 2020]  
News & Views • An atlas of European river barriers has been made, by curating and correcting existing records, and by surveying 2,700 kilometres of waterways. It reveals that rivers are fragmented by an amazing number of obstructions.
- **Quantum engineering for optical clocks** [16 December 2020]  
News & Views • Atomic clocks known as optical clocks are more accurate and stable than current timekeepers. Two quantum-engineering approaches could improve the performance of optical clocks even further and extend their applications.
- **Engineered antibodies to combat viral threats** [18 November 2020]  
News & Views • As the COVID-19 pandemic rages globally, interest in antiviral treatments has never been higher. Antibodies are key defence components, and engineering them to better exploit their natural functions might boost therapeutic options.
- **Closest relatives found for pterosaurs, the first flying vertebrates** [09 December 2020]  
News & Views • Dinosaur relatives called pterosaurs are the earliest known flying vertebrates. The branch of the evolutionary tree from which pterosaurs evolved has been unclear, but new fossil discoveries offer a solution to the mystery.
- **Spin transport in a tunable Heisenberg model realized with ultracold atoms** [16 December 2020]  
Article • Spin transport far from equilibrium is studied in a Heisenberg model with adjustable anisotropy realized with coupled ultracold  $^7\text{Li}$  atoms, and different dynamical regimes are found for positive and negative anisotropies.
- **Half-minute-scale atomic coherence and high relative stability in a tweezer clock** [16 December 2020]  
Article • A tweezer clock containing about 150  $^{88}\text{Sr}$  atoms achieves trapping and optical excited-state lifetimes exceeding 40 seconds, and shows relative fractional frequency stability similar to that of leading atomic clocks.
- **Entanglement on an optical atomic-clock transition** [16 December 2020]  
Article • A many-atom state of trapped  $^{171}\text{Yb}$  atoms that are entangled on an optical atomic-clock transition overcomes the standard quantum limit, providing a proof-of-principle

demonstration towards entanglement-based optical atomic clocks.

- **Tuning the Chern number in quantum anomalous Hall insulators** [16 December 2020]

Article • The number of edge channels in quantum anomalous Hall insulators is controlled by varying either the magnetic dopant concentration or the interior spacer layer thickness, yielding Chern numbers up to 5.

- **Topological superconductivity in a van der Waals heterostructure** [16 December 2020]

Article • A van der Waals structure based on a two-dimensional magnet and layered superconductor offers a potential system in which topological superconductivity could be easily tuned and integrated into devices.

- **Self-assembly of a layered two-dimensional molecularly woven fabric** [16 December 2020]

Article • An anion and metal ion template is used to form woven polymer patches that are joined together by polymerization into a fully woven, two-dimensional, molecular patchwork.

- **More than one million barriers fragment Europe's rivers** [16 December 2020]

Article • Validated barrier inventories and modelling indicate that Europe's rivers are fragmented by more than one million barriers, such as dams, weirs and fords, causing major impacts on biodiversity.

- **Global human-made mass exceeds all living biomass** [09 December 2020]

Article • Estimates of global total biomass (the mass of all living things) and anthropogenic mass (the mass embedded in inanimate objects made by humans) over time show that we are roughly at the timepoint when anthropogenic mass exceeds total biomass.

- **Enigmatic dinosaur precursors bridge the gap to the origin of Pterosauria** [09 December 2020]

Article • Lagerpetids, bipedal archosaurs that are thought to be related to dinosaurs, are instead a sister group to pterosaurs, and although they have no obvious flight adaptations they share numerous synapomorphies with pterosaurs across the entire skeleton.

- **Values encoded in orbitofrontal cortex are causally related to economic choices** [02 November 2020]

Article • Direct electrical stimulation of the brain in rhesus monkeys (*Macaca mulatta*) predictably varied subjective valuation and choices, linking valuation and economic decision making to the orbitofrontal cortex.

- **Assembly of synaptic active zones requires phase separation of scaffold molecules** [18 November 2020]

Article • The components of active zones at neuronal synapses are well known, but the processes underlying the assembly of these structures are less so; here, a role for liquid–liquid phase separation of scaffold proteins is identified.

- **Neurotoxic microglia promote TDP-43 proteinopathy in progranulin deficiency** [31 August 2020]

Article • In the absence of progranulin, microglia enter a disease-specific state that causes endolysosomal dysfunction and neurodegeneration, and these microglia promote TDP-43 granule formation, nuclear pore defects and cell death specifically in excitatory neurons via the complement activation pathway.

- **Cells of the adult human heart** [24 September 2020]

Article • Single-cell and single-nucleus RNA sequencing are used to construct a cellular atlas of the human heart that will aid further research into cardiac physiology and disease.

- **The functional proteome landscape of Escherichia coli** [09 December 2020]

Article • Thermal proteome profiling combined with a reverse genetics approach provides insights into the abundance and thermal stability of the global proteome of Escherichia coli.

- **Feeding induces cholesterol biosynthesis via the mTORC1-USP20–HMGCR axis** [11 November 2020]

Article • mTORC1 stabilizes HMG-CoA reductase, a rate-limiting enzyme in the cholesterol biosynthesis pathway, via the deubiquitylase USP20 in response to feeding.

- **Fc-optimized antibodies elicit CD8 immunity to viral respiratory infection** [08 October 2020]

Article • An antibody Fc domain variant with enhanced binding to an activating Fc receptor on dendritic cells promotes the induction of a protective CD8 T cell response.

- **IFITM3 functions as a PIP3 scaffold to amplify PI3K signalling in B cells** [04 November 2020]

Article • IFITM3 shifts upon phosphorylation from acting as an antiviral effector to being a scaffold for PIP3 and thereby amplifies PI3K signalling, which can be co-opted for malignant transformation in B cell leukaemia and lymphoma.

- **Structures and distributions of SARS-CoV-2 spike proteins on intact virions** [17 August 2020]

Article • Cryo-electron microscopy and tomography studies reveal the structures, conformations and distributions of spike protein trimers on intact severe acute respiratory syndrome coronavirus 2 (SARS-CoV-2) virions and provide a basis for understanding the interactions of the spike protein with neutralizing antibodies.

- **A hydrophobic ratchet entrenches molecular complexes** [09 December 2020]

Article • Accumulation of hydrophobic residues at the interface between monomers may favour the maintenance of multimeric protein states during evolution, even if multimerization confers no functional advantage.

- **Structural basis for the action of the drug trametinib at KSR-bound MEK** [14 September 2020]

Article • Crystal structures of the MEK kinase bound to the scaffold protein KSR and various MEK inhibitors, including the anti-cancer drug trametinib, reveal the molecular and functional mechanisms behind MEK inhibition.

- **Structure of the shutdown state of myosin-2** [02 December 2020]

Article • The structure of myosin-2 in the shutdown state reveals how the shutdown state is stabilized and how phosphorylation of light chains allows myosin to be activated.

- **Cryo-EM structure of the inhibited (10S) form of myosin II** [02 December 2020]

Article • High-resolution cryo-electron microscopy structure of smooth muscle myosin II in the inhibited state enables increased understanding of the functions of the head and tail regions in regulation of myosin activity and the pathological mechanisms of disease mutations.

- **Beta human papillomaviruses and skin cancer** [16 December 2020]

Matters Arising •

- **Reply to: Beta human papillomaviruses and skin cancer** [16 December 2020]

Matters Arising •

NEWS AND VIEWS

16 December 2020

# European rivers are fragmented by many more barriers than had been recorded

An atlas of European river barriers has been made, by curating and correcting existing records, and by surveying 2,700 kilometres of waterways. It reveals that rivers are fragmented by an amazing number of obstructions.

**Christiane Zarfl &**

Christiane Zarfl is at the Centre for Applied Geoscience, Eberhard Karls University of Tübingen, D-72076 Tübingen, Germany.

[Contact](#)

**Search for this author in:**

- [Pub Med](#)
- [Nature.com](#)
- [Google Scholar](#)

**Bernhard Lehner**

Bernhard Lehner is in the Department of Geography, McGill University, Montreal, Quebec H3A 0B9, Canada.

[Contact](#)

**Search for this author in:**

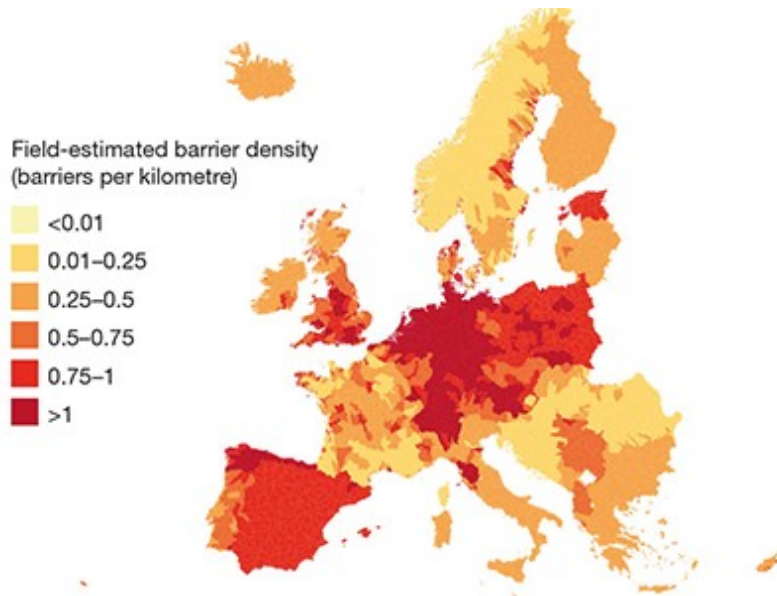
- [Pub Med](#)

- [Nature.com](#)
- [Google Scholar](#)



**Figure 1 | The weir at Pulteney Bridge, Bath, UK.** Belletti *et al.*<sup>1</sup> estimate that more than 1.2 million artificial constructions, such as weirs, dams and locks, alter the flow of Europe's rivers and streams. Credit: Getty

If you asked a child in Europe to draw a river, what would this picture look like? Would it resemble a natural, wild and scenic river, with braided and meandering flow paths in a vast floodplain, fringed by riverine vegetation? Or would it show a modern, well-managed river with houses lined up along the banks and boats passing by on a confined channel? [Writing in Nature](#), Belletti *et al.*<sup>1</sup> report a remarkably detailed survey of river barriers in Europe, which suggests that the second picture would be much more likely.



## Read the paper: More than one million barriers fragment Europe's rivers

Free-flowing rivers have become increasingly rare, because centuries of human activities have altered their passage and channels: dams and levees have been built to protect us from floods; weirs have been added (Fig. 1) to abstract water for irrigation or human use; locks and canals have been used to ensure and expand navigable waters; and river flows have been trapped or diverted for power-generating applications ranging from ancient waterwheels to modern hydroelectricity plants. Diverse in-stream structures have been constructed for these purposes, such as large concrete dams, wooden locks, small weirs and partially submerged fords. All of these interventions fragment the rivers and disturb the flow in various ways across different spatial and temporal scales, affecting the transport and delivery of sediments and nutrients<sup>2,3</sup>, and the migration and dispersal of aquatic organisms<sup>4</sup>.

Researchers and water managers who want to investigate the consequences — both beneficial and harmful — of these modifications must first ask some

fundamental questions. How many barriers have been installed, and what types? And, most importantly, where have they been built?

Perhaps surprisingly, the answers are largely unknown. No comprehensive inventory of barriers has been available on a continental scale that includes structures less than 10 metres high, uses consistent, clearly defined terminology and does not under-represent certain barrier sizes and types or geographical regions. This is not least because of the long history of barrier construction and the general lack of documentation. Recent research<sup>5</sup> has compiled global data for the locations of dams, but mostly only those that are larger than 10–15 m in height or visible in space-satellite imagery.

The degree of connectivity of rivers worldwide has also been quantified<sup>6</sup> using records for about 20,000 of the largest dams. The study not only accounted for longitudinal connectivity along the river, but also considered lateral interactions with the floodplain, temporal flow alterations, and vertical exchanges of water with the atmosphere and groundwater; such exchanges are often lost in cities if rivers are lined with concrete or forced into underground channels. According to that study, the main causes of the decline in the number and condition of free-flowing rivers are dam-related effects, such as river fragmentation, flow regulation and sediment entrapment. However, because the data underpinning this research did not take smaller barriers into account, the estimated 63% global loss of very long free-flowing rivers (greater than 1,000 km in length) probably represents only the tip of the iceberg.



## A river that flows free connects up in 4D

This type of knowledge gap motivated Belletti *et al.* to compile a pan-European atlas of river barriers for 36 countries. The primary aim was to quantify the density of artificial barriers (defined as any built structure that can cause longitudinal discontinuity) across the rivers of these countries. The results are a prerequisite for various approaches<sup>7</sup> that analyse the level of river fragmentation.

The authors took on the tedious and challenging task of compiling records from 120 local, regional and national databases. They curated the data, for example to remove duplicates and ensure consistency in the size categories and terminology, and then mapped out all the barriers to the European river network — a system that contains 1.65 million km of rivers.

However, Belletti and co-workers recognized that there will be inherent biases in the source data, such as the omission of small or unusual barriers. They therefore made an impressive effort to test the quality of their data: they surveyed about 2,700 km of the river network in 26 countries by walking along selected river stretches during low-flow conditions. The

researchers recorded the characteristics of each barrier observed, such as its location, size and whether it was abandoned or still in use. None of the 147 surveyed rivers was found to be free of obstructions, a concerning observation in itself. The findings from this monumental field trip were used to improve the precision of the calculated barrier density, correcting errors and biases in the existing records.

Finally, Belletti and colleagues extrapolated their data to estimate the barrier density in countries and regions with missing data records, taking into account anthropogenic and environmental factors, such as the degree of urbanization and the amount of agriculture. Although each step of the study has its own shortcomings, as the authors discuss, the combination of approaches strengthens the overall quality of results and reduces uncertainties caused by the variability of the available data across large regions and across several scales in barrier size.

Belletti *et al.* identified almost 630,000 unique barrier records, the majority of which were for ramps and bed sills, weirs and culverts. This is the most comprehensive inventory of river barriers ever created. Nevertheless, it still substantially under-represents reality: the number of barriers observed in the field study was, on average, 2.5 times that reported in the existing inventory. In fact, the authors estimate that there are more than 1.2 million artificial barriers obstructing Europe's rivers and streams, possibly making it the most fragmented river network in the world.



## Mississippi rising

The authors estimate that barrier densities range from 5 barriers per 1,000 km in Montenegro to almost 20 barriers per km in the Netherlands. Their statistical model suggests that the average barrier density across Europe is 0.6 per km, which is similar to the value obtained from the field observations (0.74 per km), confirming the robustness of the modelling results. Central Europe has the highest abundance and density of barriers, whereas rivers in the Balkans in southeastern Europe, in parts of northern Scandinavia and in some remote areas in southern Europe remain relatively free-flowing. The authors point out, however, that these unfragmented rivers face new threats from a boom in hydropower development, which could put the biodiversity and ecosystem health of the rivers at risk<sup>8</sup>.

Given the challenges of global environmental change, finding sustainable solutions to protect fluvial ecosystems and their associated services to humans will need a combination of actions — for example, measuring the ecological impacts of barriers; developing models of regional hydropower installations to find ways of minimizing the environmental toll on the river system while maximizing electricity production; and examining past and future trends in barrier construction and their effects. All of these require a large knowledge base and data that fit the scale, complexity and resolution of the questions to be asked. For example, some barrier types might interrupt sediment transport but pose no problem for a specific aquatic organism, whereas others might be detrimental to that organism despite not interrupting sediment movement.

Belletti and colleagues' river-barrier atlas for Europe is an excellent accomplishment, but more efforts like this are now needed. After all, river barriers and their effects are not confined to Europe, and data availability tends to be even more restricted in many other parts of the world. A large global network of scientists and stakeholders will need to join forces to compile data and develop tools (such as the Global Dam Watch initiative at <http://globaldamwatch.org>) before a complete assessment of the impacts of barriers — both large and small — on river ecosystems can be achieved.

doi: <https://doi.org/10.1038/d41586-020-03440-9>

## References

1. 1.  
Belletti, B. *et al.* *Nature* **588**, 436–441 (2020).
2. 2.  
Dunn, F. E. *et al.* *Sci. Total Environ.* **642**, 105–116 (2018).
3. 3.  
Van Cappellen, P. & Maavara, T. *Ecohydrol. Hydrobiol.* **16**, 106–111 (2016).
4. 4.  
Reid, A. J. *et al.* *Biol. Rev.* **94**, 849–873 (2018).
5. 5.  
Mulligan, M., van Soesbergen, A. & Sáenz, L. *Sci. Data* **7**, 31 (2020).
6. 6.  
Grill, G. *et al.* *Nature* **569**, 215–221 (2019).
7. 7.  
Jumani, S. *et al.* *Environ. Res. Lett.* <https://doi.org/10.1088/1748-9326/abcb37> (2020).
8. 8.  
Schiemer, F. *et al.* *Landscape Ecol.* **35**, 953–968 (2020).

[\*\*Jobs from Nature Careers\*\*](#)

- - - [All jobs](#)
    - - [\*\*Study Nurse \(m/w/d\)\*\*](#)

[German Cancer Research Center in the Helmholtz Association \(DKFZ\)](#)

[Heidelberg, Mannheim, Germany](#)

[JOB POST](#)

■ [\*\*Two Research Software Engineers\*\*](#)

[Jülich Research Centre \(FZJ\)](#)

[Garching, Germany](#)

[JOB POST](#)

■ [\*\*Softwareentwickler/in \(w/m/d\) für Experimentsysteme\*\*](#)

[Helmholtz-Zentrum Berlin for Materials and Energy \(HZB\)](#)

[Berlin, Germany](#)

[JOB POST](#)

■ [\*\*Software Developer \(f/m/d\) for Experiment Systems\*\*](#)

[Helmholtz-Zentrum Berlin for Materials and Energy \(HZB\)](#)

[Berlin, Germany](#)

[JOB POST](#)

---

This article was downloaded by **calibre** from <https://www.nature.com/articles/d41586-020-03440-9>

| [Section menu](#) | [Main menu](#) |

NEWS AND VIEWS  
16 December 2020

# Quantum engineering for optical clocks

Atomic clocks known as optical clocks are more accurate and stable than current timekeepers. Two quantum-engineering approaches could improve the performance of optical clocks even further and extend their applications.

**Christian Lisdat &**

Christian Lisdat is in the Optical Lattice Clocks Working Group, National Metrology Institute (PTB), 38116 Braunschweig, Germany.

[Contact](#)

**Search for this author in:**

- [Pub Med](#)
- [Nature.com](#)
- [Google Scholar](#)

**Carsten Klemp**

Carsten Klemp is at the Institute for Satellite Geodesy and Inertial Sensing, German Aerospace Center (DLR), 30167 Hannover, Germany.

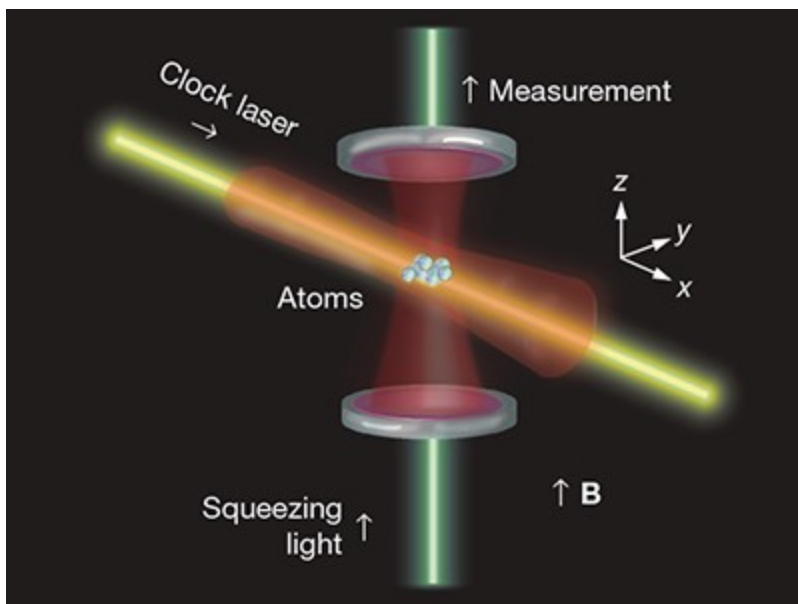
[Contact](#)

**Search for this author in:**

- [Pub Med](#)
- [Nature.com](#)

- [Google Scholar](#)

Today's most accurate clocks mark the passage of time using transitions of electrons between two energy states in an atom. Such clock transitions are typically induced by the oscillating light wave of a laser that has long-term and ultrahigh frequency stability. In the case of atomic clocks called optical-lattice clocks, ensembles of atoms that have two outer electrons are trapped in a lattice-like pattern of superimposed optical waves, known as a standing wave. The frequency of the optical-lattice light is chosen to be 'magic', which means that the light has minimal impact on the frequency of the electronic transitions used for timekeeping. In two papers in *Nature*, Pedrozo-Peñaflor *et al.*<sup>1</sup> and Young *et al.*<sup>2</sup> demonstrate how concepts in modern quantum technology could aid the development of next-generation optical-lattice clocks.



## [Read the paper: Entanglement on an optical atomic-clock transition](#)

In the past decade, optical-lattice clocks have undergone improvement at a tremendous rate. However, at least three challenges remain. First, the magic-frequency trap still has a slight effect on the electronic-transition

frequency. Second, the clock stability is degraded by clock dead times — periods in which the atoms are being prepared for use, rather than used for timekeeping. And third, quantum fluctuations pose a limit to clock stability. This limit can be surpassed only by the production of a quantum phenomenon called squeezing.

Pedrozo-Peñaflor and colleagues [transferred squeezing in an ensemble of ytterbium-171 atoms](#) from a transition between two sublevels of the lowest-energy electronic state of the atoms to the clock transition (Fig. 1a). How does this squeezing help the clock's performance? Typically, atomic clocks use atoms that are simultaneously in the lower and upper electronic states of the clock transition — a situation known as a quantum superposition. For optical-lattice clocks, many such atoms are prepared in parallel.

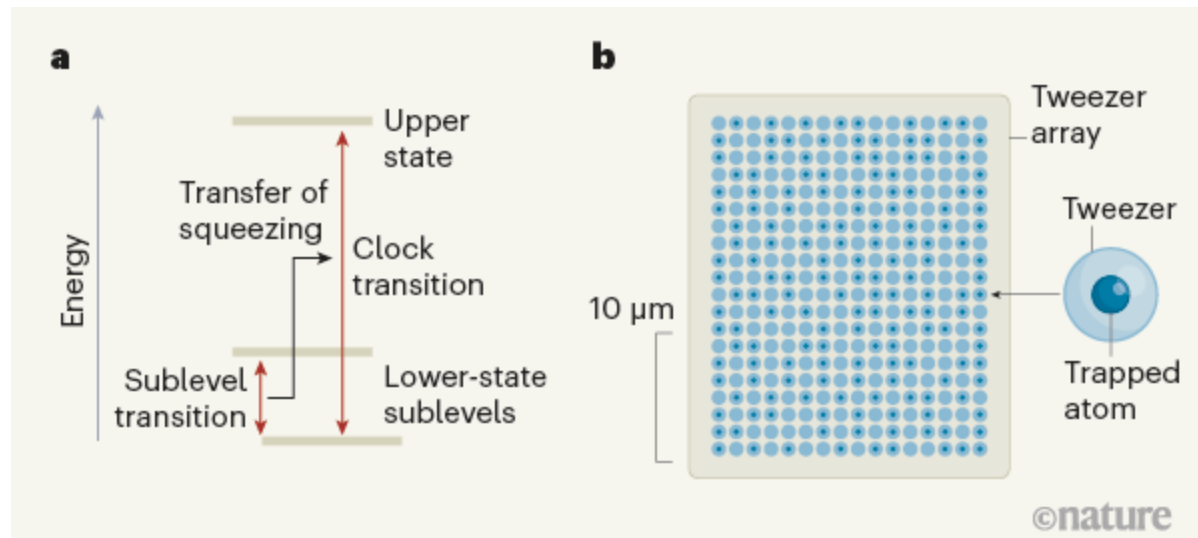
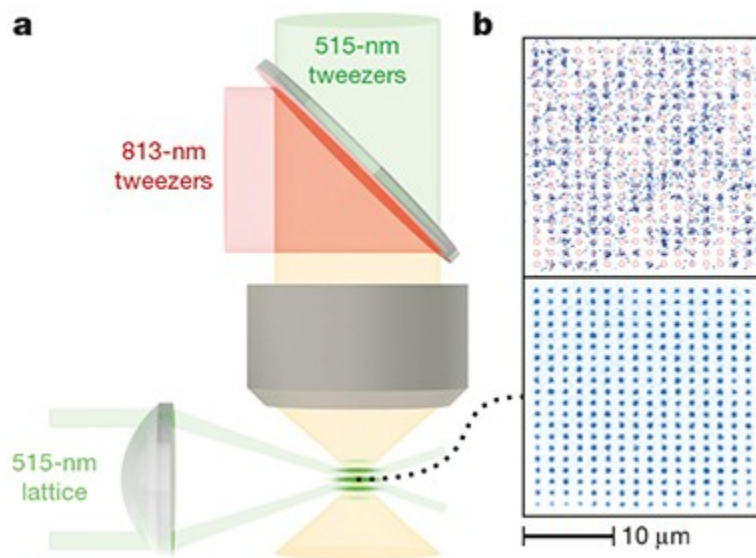


**Figure 1 | Improvements to optical-lattice clocks.** **a**, Precise timekeepers called optical-lattice clocks fine-tune the frequency of laser light so that it can drive transitions of electrons between a lower energy state and an upper energy state in an atom (the clock transition); the fine-tuned light waves thus act as a precise ‘pendulum’ for the clock. Pedrozo-Peñaflor *et al.*<sup>1</sup> demonstrated that a quantum phenomenon known as squeezing can be transferred from a transition between two sublevels of the lower state to the clock transition. Such squeezing can improve the stability of optical-lattice clocks. **b**, Young *et al.*<sup>2</sup> made a  $16 \times 20$  array of laser traps called tweezers, and trapped about 150 neutral atoms for clock measurements. They found that this set-up enables a highly stable clock operation.

If the lower and upper states contribute equally to each superposition, the atomic clock ticks at the correct rate. In a clock measurement, each superposition is randomly and individually reduced to either the lower or upper state. These random outcomes add up to the quantum fluctuations mentioned earlier, and degrade the clock stability. But if a squeezed state is used in the clock, the atoms no longer act individually, and the quantum fluctuations are suppressed.

Pedrozo-Peñaflor *et al.* achieved such suppression in a realistic clock measurement sequence, albeit with a short, millisecond-long probe time for the squeezed state. For high-performance clock operation, this interrogation time would need to be extended by a factor of 1,000, to about one second — a long time for such a fragile system to exist. However, the authors found that their squeezed state could persist for nearly that long.

These measurements indicate that quantum correlations can be combined with the second-long interrogation times that are accessible in optical clocks. But before these clocks can benefit from the demonstrated squeezing, a further technical challenge must be overcome. Often, clock stability is limited by the combination of tiny frequency fluctuations in the ultrastable laser that excites the superposition state and of the dead times for atom preparation.



# Read the paper: Half-minute-scale atomic coherence and high relative stability in a tweezer clock

Young *et al.* devised [an approach to mitigate this challenge](#). They added an ensemble of about 150 neutral clock atoms to a  $16 \times 20$  array of magic-frequency laser traps known as tweezers (Fig. 1b). The array was loaded with the atoms extremely quickly by an optical potential (potential-energy profile) that was much stronger than that of the tweezer array. The main achievement of the work presented here is the engineering of the array, which enables a high-performance clock operation.

The authors minimized dead time by combining such high performance with long interrogation times of more than 20 seconds. They then made use of the fact that the tweezers in the system can be read out individually to carry out simultaneous clock measurements on two sub-ensembles in the array. They observed a relative stability of the clocks operating on the sub-ensembles that is close to the current record for optical-lattice clocks<sup>3–5</sup>.

The geometry of the tweezer array can be chosen at will. For instance, increased distances between tweezers suppress undesirable hopping of atoms between the tweezers and frequency shifts called Doppler shifts. Furthermore, the clock can be operated with much lower intensities of the trapping lasers than when the distances are not increased. Therefore, Young and colleagues' approach provides an alternative to the use of traps that have high potential-energy barriers between tweezers to prevent hopping, or of gravity-assisted hopping inhibition in optical-lattice clocks<sup>6</sup>. Moreover, the concept opens a path for a new type of neutral-atom clock based on individually controlled atoms.

Although Young *et al.* have achieved excellent clock stability, the characterization of the frequency uncertainty in the clock transition is the next step to realizing a fully operational optical-tweezer clock. For

example, the method used to form the tweezer array causes frequency shifts across the array that must be controlled.

These two studies impressively demonstrate how quantum-technology developments and precision metrology benefit each other. For optical clocks, sophisticated tools and platforms are now at hand. And in turn, squeezed ensembles of individually detectable clock atoms constitute exciting systems for further applications in the fields of quantum simulation and quantum information.

Nature **588**, 397-398 (2020)

doi: <https://doi.org/10.1038/d41586-020-03510-y>

## References

1. 1.

Pedrozo-Peñafield, E. *et al.* Nature **588**, 414–418 (2020).

2. 2.

Young, A. W. *et al.* Nature **588**, 408–413 (2020).

3. 3.

Oelker, E. *et al.* Nature Photon. **13**, 714–719 (2019).

4. 4.

Schioppo, M. *et al.* Nature Photon. **11**, 48–52 (2017).

5. 5.

Schwarz, R. *et al.* Phys. Rev. Res. **2**, 033242 (2020).

6. 6.

Lemonde, P. & Wolf, P. *Phys. Rev. A* **72**, 033409 (2005).

## Jobs from Nature Careers

- - - [All jobs](#)
    - - [Mitarbeiter/in \(w/m/d\) im Verwaltungsdienst \(Sekretär/in\) Teilzeit \(75%\)](#)  
  
[Karlsruhe Institute of Technology \(KIT\)](#)  
  
[Karlsruhe, Germany](#)  
  
[JOB POST](#)
      - [Foreign Language Assistant/ -Correspondent \(f/m/x\)](#)  
  
[Helmholtz Centre Potsdam - German Research Centre for Geosciences \(GFZ\)](#)  
  
[Potsdam, Germany](#)  
  
[JOB POST](#)
      - [Technischer Mitarbeiter \(w/m/d\) im Bereich Facilitymanagement](#)  
  
[Helmholtz Centre Potsdam - German Research Centre for Geosciences \(GFZ\)](#)  
  
[Potsdam, Germany](#)  
  
[JOB POST](#)

▪ **Study Nurse (m/w/d)**

German Cancer Research Center in the Helmholtz  
Association (DKFZ)

Heidelberg, Mannheim, Germany.

**JOB POST**

---

This article was downloaded by **calibre** from <https://www.nature.com/articles/d41586-020-03510-y>.

| [Section menu](#) | [Main menu](#) |

## NEWS AND VIEWS

18 November 2020

# Engineered antibodies to combat viral threats

As the COVID-19 pandemic rages globally, interest in antiviral treatments has never been higher. Antibodies are key defence components, and engineering them to better exploit their natural functions might boost therapeutic options.

**Xiaojie Yu &**

Xiaojie Yu is in the Centre for Cancer Immunology, School of Cancer Sciences, University of Southampton Faculty of Medicine, Southampton SO16 6YD, UK.

[Contact](#)

**Search for this author in:**

- [Pub Med](#)
- [Nature.com](#)
- [Google Scholar](#)

**Mark S. Cragg**

Mark S. Cragg is in the Centre for Cancer Immunology, School of Cancer Sciences, University of Southampton Faculty of Medicine, Southampton SO16 6YD, UK, and at the Institute for Life Sciences, University of Southampton.

[Contact](#)

**Search for this author in:**

- [Pub Med](#)
- [Nature.com](#)
- [Google Scholar](#)

The use of antibodies to combat human disease dates back to the 1890s. At that time, the physiologist Emil von Behring used blood extracts from rabbits infected with the bacterium that causes diphtheria to tackle that infection. It was discovered only later that antibodies targeting the bacterium were the active ingredient. Amazingly, such serum therapy is still practised today. For example, blood (described as convalescent plasma) donated by people who have recovered from COVID-19, which contains antibodies targeting the SARS-CoV-2 virus, is used as a treatment for people with coronavirus infection. Writing in *Nature*, Bournazos *et al.*<sup>1</sup> report progress in efforts to aid antiviral responses by engineering human antibodies to enhance their antiviral activity.

Antibodies are a key component of what is called the adaptive branch of the immune system. They can recognize a part of a foreign molecule called an antigen and mobilize various immune processes to neutralize the threat posed by the disease-causing agent. From the work in this area since von Behring's discovery, punctuated by multiple Nobel prizes, we have learnt much about the regulation, structure and function of antibodies, and their use in the clinic has grown exponentially (see [go.nature.com/3kltoqZ](https://go.nature.com/3kltoqZ)) . Nevertheless, efforts to manipulate, engineer and improve antibodies remain highly topical.

The Fab domain and the Fc domain (Fig. 1) are the two evolutionarily conserved structural components of antibodies. The Fab domain has a variable antigen-binding region, which is different in every antibody, whereas the Fc domain is a constant structure that is largely similar in different antibodies. The Fc domain engages with other elements of the immune system, including a family of what are called Fc receptors, found on a range of immune and non-immune cells<sup>2</sup>. A type of antibody known as IgG engages a subfamily of Fc receptors called the FcγRs. The FcγRs fall into two main classes: activating FcγRs (including the proteins FcγRI, FcγRIIa and FcγRIIIa) and the sole inhibitory FcγR, FcγRIIb. FcγR engagement stimulates or inhibits immune cells, respectively, and the

balance of activating to inhibitory engagement determines the responses of cell types that have both activating and inhibitory Fc $\gamma$ Rs<sup>2</sup>.

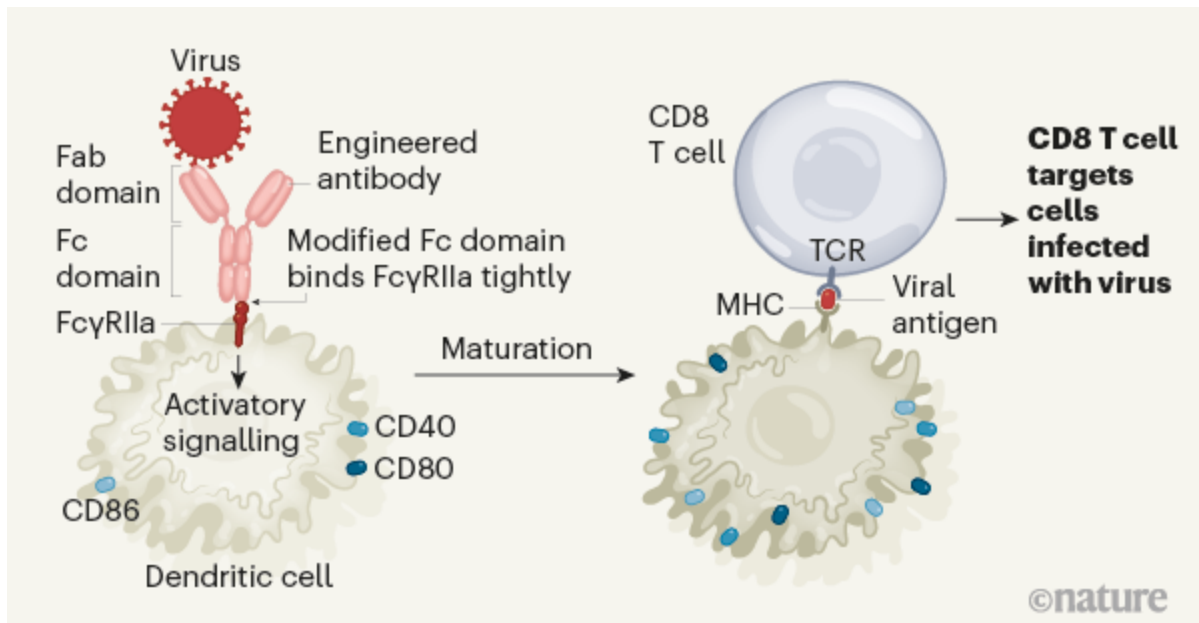


**Figure 1 | Boosting antibody-mediated antiviral responses.** Antibodies consist of Fab domains, which bind to disease-causing agents such as viruses, and an Fc domain, which enlists other defence components.

Bournazos *et al.*<sup>1</sup> engineered an antiviral antibody to have an Fc domain that had an enhanced ability to bind to the receptor protein Fc $\gamma$ RIIa. This receptor is found on immune cells such as dendritic cells (which express the defence-boosting proteins CD40, CD80 and CD86). Antibody binding to Fc $\gamma$ RIIa triggers signalling that drives dendritic-cell maturation, as indicated by a rise in the expression of CD40, CD80 and CD86. The MHC receptor on dendritic cells can present a viral fragment called an antigen. When the TCR protein of an immune cell called a CD8 T cell recognizes viral antigen, it causes the T cell to kill cells infected with the virus. Consistent with this model, the authors report that mice exposed to influenza virus were better protected from disease if they received the engineered anti-flu antibody than were animals that received a version of the antibody that did not have enhanced binding to Fc $\gamma$ RIIa.

Although antibodies first entered the clinic for use against infection, so far, it has been mainly in combating cancer and autoimmunity that monoclonal antibodies (those with specificity for a single antigen) have had their

greatest medical impact. Blockbuster drugs such as trastuzumab (Herceptin; for the treatment of breast cancer), rituximab (for auto-immune diseases and blood cancers) and adalimumab (Humira; for rheumatoid arthritis) have transformed patient outcomes. These advances have been followed by the use of antibodies called immune-checkpoint blockers, which help to unleash immune responses against tumour cells. Such successes have resulted in seven of the top ten global bestselling drugs in 2019 being antibodies<sup>3</sup>.

These clinical achievements have fuelled efforts to learn more about the mechanisms underlying antibody action. This led to the rapid realization that FcγRs have pivotal roles in many IgG-mediated functions. Yet it soon became clear that not all patients respond optimally, and there is a need to develop more-effective antibodies for therapeutic purposes. This ushered in the era of Fc engineering, in which key amino-acid residues and sugars in the Fc domain were identified and modified to selectively enhance or reduce their interaction with different FcγRs<sup>4,5</sup>.

As the use of monoclonal antibodies has grown, it has been found that different classes of monoclonal antibody require engagement with different FcγRs for optimal activity. For example, antibodies that target tumour cells directly for deletion require activating FcγRs on tumour-killing immune cells, whereas immunostimulatory antibodies that are often directed to receptors of the TNF receptor family on immune cells require inhibitory FcγRs<sup>6</sup>. Yet other types of antibody work optimally without FcγR interaction. In the realm of cancer, this knowledge has guided the development of next-generation antibodies that carry modified Fc domains, such as the antibody drugs atezolizumab and durvalumab, which are engineered for minimal engagement with FcγRs, and the drugs mogamulizumab and obinutuzumab, in which the Fc domain is engineered to increase its binding affinity for FcγRIIIa (ref. 4)<sup>4</sup>.

By contrast, the role of FcγRs in affecting antiviral antibody therapies remains relatively under-examined<sup>7</sup>. Indeed, for many researchers, the drive has been to optimize the Fab domain — developing it to serve as a way to tag the virus and prevent its entry into the cell, thus halting transmission and viral replication. However, studies using different viral models have

shown that the Fc domain is needed for optimal antiviral therapy<sup>7</sup>.

Bournazos *et al.* used mice in which the mouse Fc $\gamma$ R was replaced with human Fc $\gamma$ R. They found that anti-influenza antibodies directed to bind to various antigens on the viral surface provide an enhanced antiviral therapy if the Fc domain can bind to Fc $\gamma$ Rs, and, in particular, if they are engineered to engage with Fc $\gamma$ RIIa more tightly than normal.

Fc $\gamma$ RIIa is expressed on a type of immune-cell lineage that can present antigens to other immune cells during the process that triggers further adaptive defence responses, including those by immune cells called T cells. Interestingly, if Bournazos and colleagues' anti-flu antibody was engineered so that its Fc domain selectively engaged another activating receptor, Fc $\gamma$ RIIIa, which is thought to mediate the activity of many tumour-targeting monoclonal antibodies (although all activating Fc $\gamma$ Rs probably contribute to tumour-cell deletion *in vivo*<sup>8</sup>), it failed to exhibit increased therapeutic activity compared with wild-type anti-flu IgG that had a non-engineered Fc domain. This suggests that antitumour and antiviral antibodies use distinct mechanisms to mediate their activity, and thus that distinct Fc-engineering approaches are needed to optimize the use of such antibodies.

The authors found that, compared with wild-type anti-flu IgG that had a non-engineered Fc domain, the antibody engineered to have enhanced Fc $\gamma$ RIIa binding induced greater maturation of antigen-presenting cells called dendritic cells, and a greater response *in vivo* by immune cells called CD8 T cells, which can kill unwanted cells such as those harbouring virus (Fig. 1). This implies that the engagement of activating Fc $\gamma$ Rs on antigen-presenting cells enhances their antigen-presenting capability, and therefore puts Fc $\gamma$ RIIa in the spotlight as a key receptor for antibody-mediated antiviral defences.

It is possible that such Fc $\gamma$ RIIa-optimized antibodies would also augment other antiviral immune responses. However, the mice that received the engineered antibodies showed no modulation of the natural antibody response to the virus that is mediated by immune cells called B cells. This indicates that the T-cell and B-cell responses are probably regulated independently in this infection model. In the absence of an augmented natural-antibody response, adding other monoclonal-antibody therapeutics,

such as immunostimulatory antibodies (themselves targeting alter-native Fc $\gamma$ Rs), might further boost antiviral responses compared with using this engineered antibody alone.

There are concerns about augmenting antibody activity because it might trigger unwanted consequences; after all, evolution has fine-tuned antibody activity over eons. One phenomenon observed with viral infections such as dengue is antibody-dependent enhancement, whereby antibody-coated viruses gain entry to cells through IgG–Fc $\gamma$ R interactions, which can exacerbate the disease in some people<sup>9</sup>. Bournazos *et al.* found that, in their influenza model, which, like SARS-CoV-2, targets the lung, the Fc $\gamma$ RIIa-enhanced antibody did not result in higher than normal inflammation (indicative of potential toxicity) or other evidence of antibody-dependent enhancement, such as an increase in viral infectivity. This suggests that such an approach is safe in this context.

The possibility of such a problem remains for other viruses. For example, it is unclear whether antibody-dependent enhancement occurs in people who have COVID-19, in which excessive inflammation has been a feature of severe disease. If so, Fc-enhanced antibodies that drive inflammation could make their use counter-productive as a treatment for COVID-19. However, the success of convalescent plasma in treating COVID-19 indicates that this is probably not the case.

We should be cautious about drawing conclusions regarding human disease on the basis of mouse studies. Although these animals were engineered to express human rather than mouse Fc $\gamma$ R, they do not recapitulate the full spectrum of human Fc $\gamma$ R expression patterns and genetic variation<sup>10</sup>. Of note, there are multiple human variants of Fc $\gamma$ R that have different binding affinities for IgG, and whether Fc $\gamma$ RIIa-optimized monoclonal antibodies would be equally effective in treating people who have these variants is unclear.

Nevertheless, Fc-domain engineering for antiviral therapy is a promising avenue to pursue, and Bournazos and colleagues' results support the continued development of such reagents for testing in the clinic. As the Northern Hemisphere moves into winter, with the dual hazards of seasonal

influenza and the ongoing COVID-19 pandemic, the need for better treatments for both of these viral threats will become increasingly clear.

Nature **588**, 398–399 (2020)

doi: <https://doi.org/10.1038/d41586-020-03196-2>

## References

1. 1.

Bournazos, S., Corti, D., Virgin, H. W. & Ravetch, J. V. *Nature* **588**, 485–490 (2020).

2. 2.

Nimmerjahn, F. & Ravetch, J. V. *Nature Rev. Immunol.* **8**, 34–47 (2008).

3. 3.

Urquhart, L. *Nature Rev. Drug Discov.* **19**, 228 (2020).

4. 4.

Liu, R., Oldham, R. J., Teal, E., Beers, S. A. & Cragg, M. S. *Antibodies* **9**, 64 (2020).

5. 5.

Shields, R. L. *et al.* *J. Biol. Chem.* **276**, 6591–6604 (2001).

6. 6.

Beers, S. A., Glennie, M. J. & White, A. L. *Blood* **127**, 1097–1101 (2016).

7. 7.

Chan, K. R., Ong, E. Z., Mok, D. Z. & Ooi, E. E. *Expert Rev. Anti-Infect. Ther.* **13**, 1351–1360 (2015).

8. 8.

Minard-Colin, V. *et al.* *Blood* **112**, 1205–1213 (2008).

9. 9.

Goncalvez, A. P., Engle, R. E., St. Claire, M., Purcell, R. H. & Lai, C.-J. *Proc. Natl Acad. Sci. USA* **104**, 9422–9427 (2007).

10. 10.

Kerntke, C., Nimmerjahn, F. & Biburger, M. *Front. Immunol.* **11**, 118 (2020).

## Competing Financial Interests

M.S.C. acts as a consultant for a number of biotech companies, being retained as a consultant for BioInvent, and has received research funding from BioInvent, GSK, UCB, iTeos and Roche. None of these associations relate to antiviral therapy.

## Jobs from Nature Careers

- - - [All jobs](#)
    - - [Study Nurse \(m/w/d\)](#)

[German Cancer Research Center in the Helmholtz Association \(DKFZ\)](#)

[Heidelberg, Mannheim, Germany](#)

JOB POST

- **Two Research Software Engineers**

Jülich Research Centre (FZJ)

Garching, Germany

JOB POST

- **Softwareentwickler/in (w/m/d) für Experimentsysteme**

Helmholtz-Zentrum Berlin for Materials and Energy (HZB)

Berlin, Germany

JOB POST

- **Software Developer (f/m/d) for Experiment Systems**

Helmholtz-Zentrum Berlin for Materials and Energy (HZB)

Berlin, Germany

JOB POST

---

This article was downloaded by **calibre** from <https://www.nature.com/articles/d41586-020-03196-2>

NEWS AND VIEWS

09 December 2020

# Closest relatives found for pterosaurs, the first flying vertebrates

Dinosaur relatives called pterosaurs are the earliest known flying vertebrates. The branch of the evolutionary tree from which pterosaurs evolved has been unclear, but new fossil discoveries offer a solution to the mystery.

**Kevin Padian**

Kevin Padian is in the Department of Integrative Biology and the Museum of Paleontology, University of California, Berkeley, California 94720, USA.  
[Contact](#)

**Search for this author in:**

- [Pub Med](#)
- [Nature.com](#)
- [Google Scholar](#)

In 1812, Georges Cuvier, the incomparable anatomist at the Museum of Natural History in Paris, produced the first comprehensive book to be published on the history of fossil tetrapods (animals with backbones, excluding fishes)<sup>1</sup>. Cuvier surveyed all that was known of the palaeontology of these animals, exploring the wonders of their great variation and strange fossil forms. Some were clear relatives of familiar living animals; others were strange and difficult to classify. But none was quite as odd as a small, long-beaked, long-limbed creature from the Jurassic period (around 150

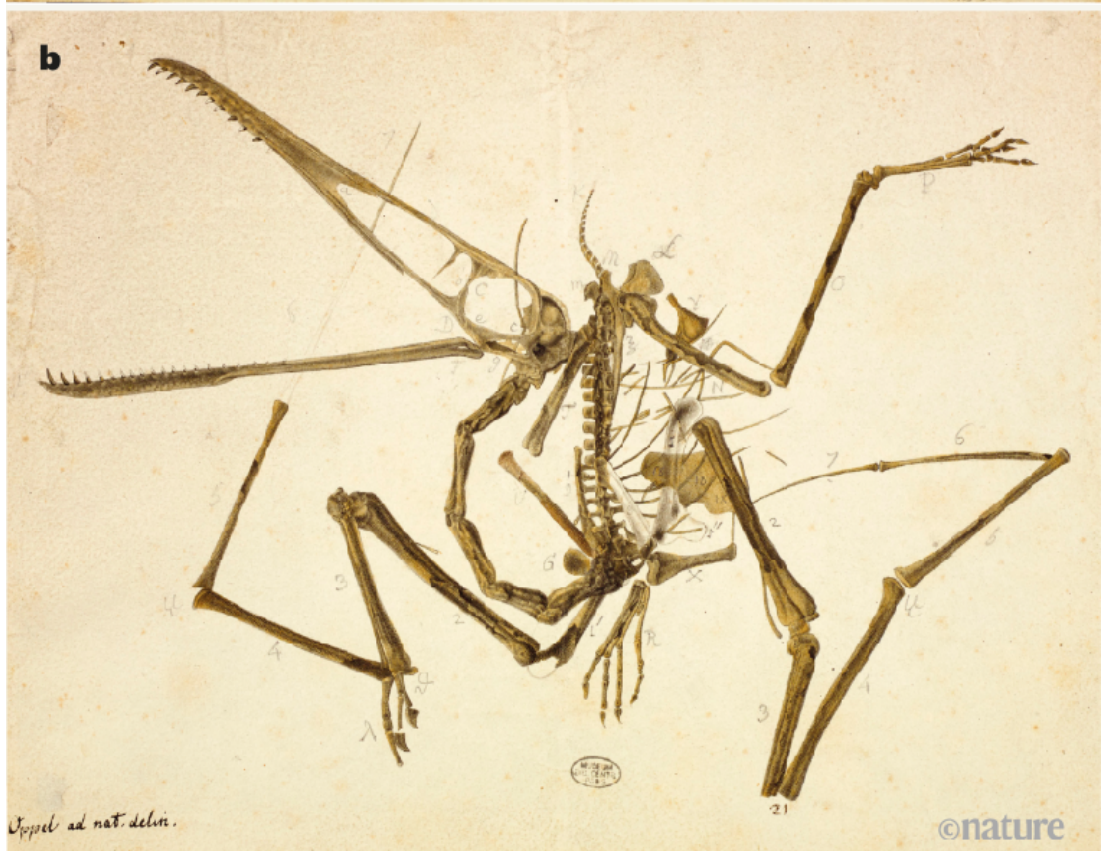
million years ago) that was excavated in Bavaria, Germany. [Writing in Nature](#), Ezcurra *et al.*<sup>2</sup> shed first light on the origin of this striking group.



## [Read the paper: Enigmatic dinosaur precursors bridge the gap to the origin of Pterosauria](#)

In 1800, Cuvier had received a letter from his friend Jean Hermann, professor and curator of natural history at Strasbourg in France<sup>3</sup>. Hermann told Cuvier of a fossil he had read about, in the collections in Mannheim, Germany, that was unlike anything he had ever encountered. On the basis of the original<sup>3</sup> and classically philosophical description by Cosimo Collini in 1784, Hermann described some of its features and enclosed sketches he had made (Fig. 1a). He realized that the animal had a very long finger that he correctly thought would support a wing membrane. This could not be a bird, but bats have wings supported by finger bones, so maybe the animal was something like that. Hermann drew the creature as a kind of mammal, complete with soft ear pinnae, fur (also prescient) and genitalia.

\* Je ne vois pas pourquoi j'ai eu l'idée de courber en dedans cette espèce, 150  
a pourquoi elle ne peut pas être droite, plus étendue par conséquent, de sorte la  
peau tendue par l'espèce postérieure, ce qui doit augmenter beaucoup la faculté  
de voler de l'animal.



Upoel ad nat. delin.

©nature

**Figure 1 | Ptéro-dactyle sketches.** **a**, A sketch made by Jean Hermann based on a fossil description that he sent in a letter to Georges Cuvier at the Museum of Natural History in Paris, who was preparing a book about fossils of tetrapods (animals with backbones, not including fishes). **b**, A drawing by Michael Oppel of the original fossil specimen corresponding to the creature shown in **a**. Cuvier named the creature a ptéro-dactyle, and it was the earliest known member of the group called pterosaurs, the first vertebrates to evolve the ability to fly. Credit: Muséum national d'Histoire naturelle

Cuvier was fascinated and frustrated. He wanted a cast of the fossil, but Hermann died before he could help. In the following years, naturalists who saw the specimen sent drawings to Cuvier (Fig. 1b), but he could not get his hands on a fossil cast until 1818, after his book had been published. Worse still, all the drawings were notably different. Yet, thanks to his anatomical expertise, Cuvier could reconcile the discrepancies, and he realized that the animal's features made it a reptile, not a mammal.

But it was no ordinary reptile. Cuvier inferred that it flew, was warm-blooded, had a hairy covering, walked on its back legs and folded its wings. He wrote<sup>4</sup>: “of all the organisms whose ancient existence is revealed in this book, these are incontestably the most extraordinary, and if we saw them alive, would seem the strangest as compared to all living beings.” And he concluded: “[it] would seem, to those who have not followed this entire discussion, the product of a sick imagination rather than the ordinary forces of nature.”

Welcome to the world of pterosaurs, or, as Cuvier named the first ones, ptéro-dactyles, which means wing-fingers (a typo in his original title rendered them pétro-dactyles, or rock-fingers). More than two centuries later, pterosaurs remain among the most controversial animals in the fossil record. In the 1980s, it was established that pterosaurs actively flapped their wings (instead of merely gliding), and walked on hindlimbs organized like those of birds and other dinosaurs<sup>5</sup>, and that they were much more bird-like than bat-like.

Well over 100 probably valid kinds of pterosaur are currently known from all over the world, from the Triassic through to the Cretaceous periods (approximately 235 million to 66 million years ago). Some (Fig. 2) are

extremely bizarre<sup>6</sup>; but their origins and relationships to other archosaurs (crocodiles and birds, including dinosaurs) have not been well established.

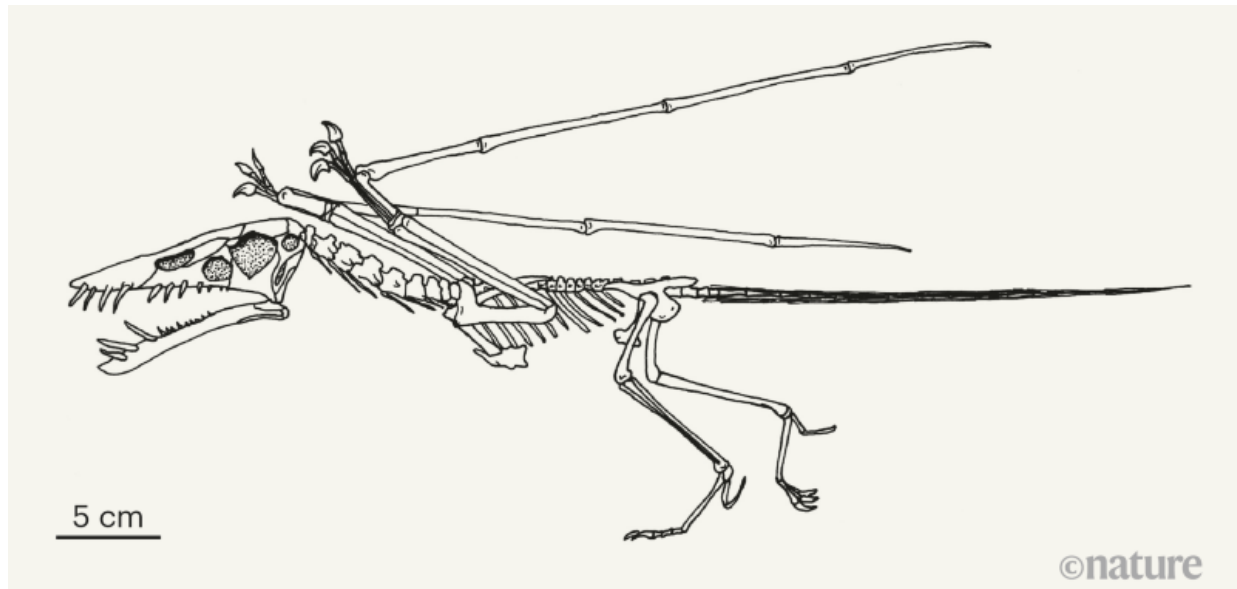


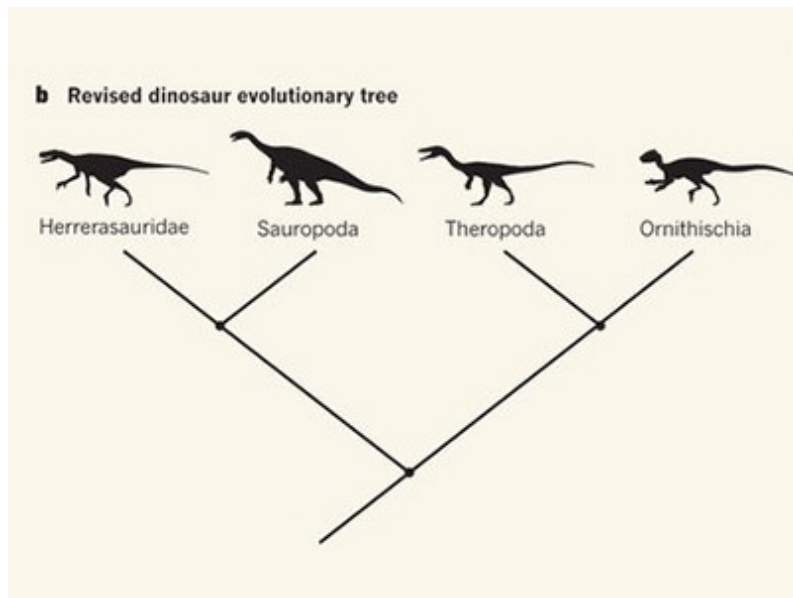
**Figure 2 | *Dorygnathus*.** Reconstruction of an early pterosaur. Ezcurra *et al.*<sup>2</sup> have identified dinosaur relatives called lagerpetids as being the long-sought probable closest relatives of pterosaurs. Credit: Kevin Padian

In the 1980s, it was suggested that the closest relatives of pterosaurs were small bipedal reptiles closely aligned with dinosaurs<sup>7</sup>, and this theory was supported by even the earliest phylogenetic analyses of how these groups fit on the evolutionary tree<sup>8</sup>. But the fossil evidence that was needed to confirm this was elusive: pterosaurs are so strangely constructed that their extreme adaptations for flight actually mask many of the features that might otherwise reveal their relationships to other animals.

Ezcurra and colleagues provide this long-sought evidence, which points to a specific group of dinosaur-line archosaurs. The authors examined all the remains of the likely candidate groups known worldwide, some of which were specimens they had collected themselves. These small animals are called lagerpetids, a name that means rabbit-reptiles. They had long legs, a bipedal stance and the ability to run fast. Lagerpetids lived in the Middle and Late Triassic (some 235 million to 205 million years ago) and are known mostly from the Americas; however, deposits of this age are not well distributed worldwide. Lagerpetids form a constellation of bird-line

archosaurs that would include creatures such as lagosuchids, silesaurids, *Scleromochlus* and the first pterosaurs and dinosaurs.

So what makes lagerpetids the best candidates for pterosaur kinfolk? It has been clear for several decades that pterosaurs evolved from small bipedal archosaurs whose hindlimbs were organized like those of birds and other dinosaurs, rather than like the more sprawling hindlimbs of crocodiles<sup>5,9</sup>. The proportions of their slender limbs, as well as the shape of their back, are fully consistent with a bird-like body plan<sup>9</sup>.



## Dividing the dinosaurs

Lagerpetids fit this profile, and, unlike other candidate relatives, they share some features with pterosaurs that other archosaurs do not. The authors made this finding through the use of an approach called phylogenetic systematics, which has been applied to uncover relationships between every group of organisms, including dinosaurs<sup>10</sup>. It searches out newly evolved features that link different organisms, the reasoning for this being that the most recently evolved traits must have appeared in forms most recently diverged from each other, and hence must be the closest genetically. These features, which often seem trivial even to experienced observers, provide the key to relationships, and sometimes to the evolution of adaptations, because

one divergent group, the flying pterosaurs in this case, might have unusual features that reflect functions its sister divergent group lacks.

Ezcurra *et al.* realized that, although lagerpetids didn't fly, they share specific features with pterosaurs, such as complex characteristics of their braincase and inner ear, that might relate to the increased agility they had evolved. Their elongated hand (palm) bones (hyperelongated in pterosaurs, along with the fourth finger) suggest a good starting point for animals to evolve flight. Other shared features of the skull, jaws, pelvis, fore- and hindlimbs and vertebrae make a compelling case for the relationship.

The results presented by Ezcurra *et al.* don't lay out the complete evolutionary path from a small, Earth-bound reptile to the first flying vertebrates. But one day a pterosaurian ancestor might emerge from Triassic rocks to fill in some of the blanks, in much the same way that the discovery of *Archaeopteryx* provided key clues to the early stages of bird flight.

Meanwhile, Ezcurra and colleagues' study underscores the view that pterosaurs are the closest major group to dinosaurs, that another group (lagerpetids) formerly thought close to dinosaurs are now shown to be even closer to pterosaurs than previously thought, and that the common ancestor of all of these groups was probably a small, long-limbed, short-bodied, slender biped with a large head, peg-like teeth, considerable agility and an acute awareness of its surroundings. So, ground-dwelling pterosaur precursors already had forelimbs that were free to evolve flapping flight. Cuvier, although he did not accept evolutionary transmutation to explain the transitions between major forms of life, would otherwise have felt vindicated regarding his original inferences about the anatomy and ecology of pterosaurs.

Nature 588, 400-401 (2020)

doi: <https://doi.org/10.1038/d41586-020-03420-z>

## References

1. 1.

Cuvier, G. *Recherches sur les Ossemens Fossiles des Quadrupèdes* (Deterville, 1812).

2. 2.

Ezcurra, M. *et al. Nature* **588**, 445–449 (2020).

3. 3.

Taquet, P. & Padian, K. *C. R. Palevol* **3**, 157–175 (2004).

4. 4.

Cuvier, G. *Ann. Mus. d'Hist. Nat.* **13**, 424–437 (1809).

5. 5.

Padian, K. *Paleobiology* **9**, 218–239 (1983).

6. 6.

Paul, G. S. *The Princeton Field Guide to Pterosaurs* (Princeton Univ. Press, in the press).

7. 7.

Padian, K. in *3rd Symp. Mesozoic Terrestrial Ecosystems: Short Papers* (eds Reif, W.-E. & Westphal, F.) 163–168 (Attempto, 1984).

8. 8.

Gauthier, J. A. PhD thesis, Univ. California, Berkeley (1984).

9. 9.

Padian, K. *Zitteliana* **28B**, 21–28 (2008).

10. 10.

Padian, K. *Nature* **543**, 494–495 (2017).

## Jobs from Nature Careers

- - - [All jobs](#)
    - - [Mitarbeiter/in \(w/m/d\) im Verwaltungsdienst \(Sekretär/in\) Teilzeit \(75%\)](#)

[Karlsruhe Institute of Technology \(KIT\)](#)

[Karlsruhe, Germany](#)

[JOB POST](#)

- [Foreign Language Assistant/ -Correspondent \(f/m/x\)](#)

[Helmholtz Centre Potsdam - German Research Centre for Geosciences \(GFZ\)](#)

[Potsdam, Germany](#)

[JOB POST](#)

- [Technischer Mitarbeiter \(w/m/d\) im Bereich Facilitymanagement](#)

[Helmholtz Centre Potsdam - German Research Centre for Geosciences \(GFZ\)](#)

[Potsdam, Germany](#)

[JOB POST](#)

- [Study Nurse \(m/w/d\)](#)

German Cancer Research Center in the Helmholtz  
Association (DKFZ)

Heidelberg, Mannheim, Germany

JOB POST

---

This article was downloaded by **calibre** from <https://www.nature.com/articles/d41586-020-03420-z>

| [Section menu](#) | [Main menu](#) |

- Article
- [Published: 16 December 2020](#)

# Spin transport in a tunable Heisenberg model realized with ultracold atoms

- [Paul Niklas Jepsen](#) [ORCID: orcid.org/0000-0003-0763-4420](#)<sup>1,2,3</sup>,
- [Jesse Amato-Grill](#)<sup>1,2,3</sup>,
- [Ivana Dimitrova](#)<sup>1,2,3</sup>,
- [Wen Wei Ho](#)<sup>3,4</sup>,
- [Eugene Demler](#) [ORCID: orcid.org/0000-0002-2499-632X](#)<sup>3,4</sup> &
- [Wolfgang Ketterle](#) [ORCID: orcid.org/0000-0002-9528-3044](#)<sup>1,2,3</sup>

[Nature](#) volume 588, pages403–407(2020) [Cite this article](#)

- 1084 Accesses
- 71 Altmetric
- [Metrics details](#)

## Subjects

- [Quantum simulation](#)
- [Ultracold gases](#)

## Abstract

Simple models of interacting spins have an important role in physics. They capture the properties of many magnetic materials, but also extend to other

systems, such as bosons and fermions in a lattice, gauge theories, high-temperature superconductors, quantum spin liquids, and systems with exotic particles such as anyons and Majorana fermions<sup>1,2</sup>. To study and compare these models, a versatile platform is needed. Realizing such systems has been a long-standing goal in the field of ultracold atoms. So far, spin transport has only been studied in systems with isotropic spin–spin interactions<sup>3,4,5,6,7,8,9,10,11,12</sup>. Here we realize the Heisenberg model describing spins on a lattice, with fully adjustable anisotropy of the nearest-neighbour spin–spin couplings (called the XXZ model). In this model we study spin transport far from equilibrium after quantum quenches from imprinted spin-helix patterns. When spins are coupled only along two of three possible orientations (the XX model), we find ballistic behaviour of spin dynamics, whereas for isotropic interactions (the XXX model), we find diffusive behaviour. More generally, for positive anisotropies, the dynamics ranges from anomalous superdiffusion to subdiffusion, whereas for negative anisotropies, we observe a crossover in the time domain from ballistic to diffusive transport. This behaviour is in contrast with expectations from the linear-response regime and raises new questions in understanding quantum many-body dynamics far away from equilibrium.

[Access through your institution](#)

[Change institution](#)

[Buy or subscribe](#)

## Access options

Subscribe to Journal

Get full journal access for 1 year

185,98 €

only 3,58 € per issue

[Subscribe](#)

All prices are NET prices.  
VAT will be added later in the checkout.

Rent or Buy article

Get time limited or full article access on ReadCube.

from \$8.99

[Rent or Buy](#)

All prices are NET prices.

### **Additional access options:**

- [Log in](#)
- [Access through your institution](#)
- [Learn about institutional subscriptions](#)

**Fig. 1: Tunability of the XXZ model with  ${}^7\text{Li}$  and implementation of a spin helix.**

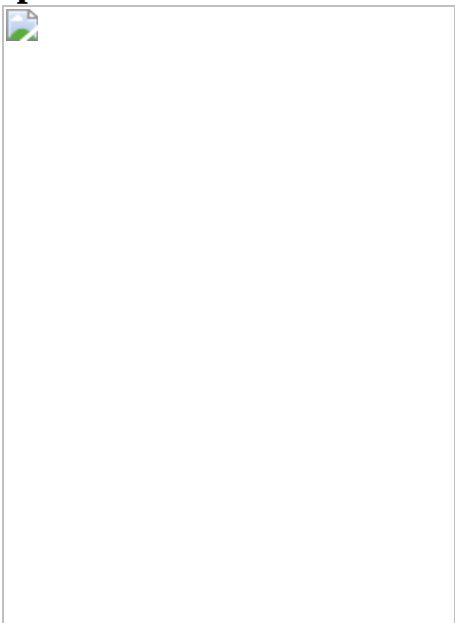


**Fig. 2: Ballistic and diffusive spin transport.**



**Fig. 3: Power-law scalings.**



**Fig. 4: Temporal crossover from ballistic to diffusive transport for negative anisotropies  $\Delta < 0$ .**



## Data availability

The data that support the findings of this study are available from the corresponding author upon reasonable request.

## References

1. 1.

Lee, P. A. From high temperature superconductivity to quantum spin liquid: progress in strong correlation physics. *Rep. Prog. Phys.* **71**, 012501 (2007).

[ADS](#) [Google Scholar](#)

2. 2.

Broholm, C. et al. Quantum spin liquids. *Science* **367**, eaay0668 (2020).

[CAS](#) [PubMed](#) [PubMed Central](#) [Google Scholar](#)

3. 3.

Nichols, M. A. et al. Spin transport in a Mott insulator of ultracold fermions. *Science* **363**, 383–387 (2019).

[ADS](#) [CAS](#) [PubMed](#) [PubMed Central](#) [Google Scholar](#)

4. 4.

Brown, R. C. et al. Two-dimensional superexchange-mediated magnetization dynamics in an optical lattice. *Science* **348**, 540–544 (2015).

[ADS](#) [MathSciNet](#) [CAS](#) [PubMed](#) [PubMed Central](#) [MATH](#) [Google Scholar](#)

5. 5.

Fukuhara, T. et al. Quantum dynamics of a mobile spin impurity. *Nat. Phys.* **9**, 235–241 (2013).

[CAS](#) [Google Scholar](#)

6. 6.

Fukuhara, T. et al. Microscopic observation of magnon bound states and their dynamics. *Nature* **502**, 76–79 (2013).

[ADS](#) [CAS](#) [PubMed](#) [PubMed Central](#) [Google Scholar](#)

7. 7.

Hild, S. et al. Far-from-equilibrium spin transport in Heisenberg quantum magnets. *Phys. Rev. Lett.* **113**, 147205 (2014).

[ADS](#) [PubMed](#) [PubMed Central](#) [Google Scholar](#)

8. 8.

Koschorreck, M., Pertot, D., Vogt, E. & Köhl, M. Universal spin dynamics in two-dimensional Fermi gases. *Nat. Phys.* **9**, 405–409 (2013); corrigendum **10**, 170 (2014).

[CAS](#) [Google Scholar](#)

9. 9.

Trotzky, S. et al. Observation of the Leggett–Rice effect in a unitary Fermi gas. *Phys. Rev. Lett.* **114**, 015301 (2015).

[ADS](#) [CAS](#) [PubMed](#) [PubMed Central](#) [Google Scholar](#)

10. 10.

Palzer, S., Zipkes, C., Sias, C. & Köhl, M. Quantum transport through a Tonks–Girardeau gas. *Phys. Rev. Lett.* **103**, 150601 (2009).

[ADS](#) [PubMed](#) [PubMed Central](#) [Google Scholar](#)

11. 11.

Sommer, A., Ku, M., Roati, G. & Zwierlein, M. W. Universal spin transport in a strongly interacting Fermi gas. *Nature* **472**, 201–204 (2011).

[ADS](#) [CAS](#) [PubMed](#) [PubMed Central](#) [Google Scholar](#)

12. 12.

Krinner, S. et al. Mapping out spin and particle conductances in a quantum point contact. *Proc. Natl. Acad. Sci. USA* **113**, 8144–8149 (2016).

[ADS](#) [CAS](#) [PubMed](#) [PubMed Central](#) [Google Scholar](#)

13. 13.

Vasseur, R. & Moore, J. E. Nonequilibrium quantum dynamics and transport: from integrability to many-body localization. *J. Stat. Mech.* **2016**, 064010 (2016).

[MathSciNet](#) [MATH](#) [Google Scholar](#)

14. 14.

Bertini, B. et al. Finite-temperature transport in one-dimensional quantum lattice models. Preprint at <https://arxiv.org/abs/2003.03334> (2020).

15. 15.

Ljubotina, M., Žnidarič, M. & Prosen, T. Spin diffusion from an inhomogeneous quench in an integrable system. *Nat. Commun.* **8**, 16117 (2017).

[ADS](#) [CAS](#) [PubMed](#) [PubMed Central](#) [Google Scholar](#)

16. 16.

Gopalakrishnan, S. & Vasseur, R. Kinetic theory of spin diffusion and superdiffusion in XXZ spin chains. *Phys. Rev. Lett.* **122**, 127202 (2019).

[ADS](#) [CAS](#) [PubMed](#) [PubMed Central](#) [Google Scholar](#)

17. 17.

Ilievski, E., De Nardis, J., Medenjak, M. & Prosen, T. Superdiffusion in one-dimensional quantum lattice models. *Phys. Rev. Lett.* **121**, 230602 (2018).

[ADS](#) [PubMed](#) [PubMed Central](#) [Google Scholar](#)

18. 18.

Else, D. V., Monroe, C., Nayak, C. & Yao, N. Y. Discrete time crystals. *Annu. Rev. Condens. Matter Phys.* **11**, 467–499 (2020).

[Google Scholar](#)

19. 19.

Basov, D. N., Averitt, R. D. & Hsieh, D. Towards properties on demand in quantum materials. *Nat. Mater.* **16**, 1077–1088 (2017).

[ADS](#) [CAS](#) [PubMed](#) [PubMed Central](#) [Google Scholar](#)

20. 20.

Langen, T., Gasenzer, T. & Schmiedmayer, J. Prethermalization and universal dynamics in near-integrable quantum systems. *J. Stat. Mech.* **2016**, 064009 (2016).

[MathSciNet](#) [MATH](#) [Google Scholar](#)

21. 21.

Zhang, J. et al. Observation of a many-body dynamical phase transition with a 53-qubit quantum simulator. *Nature* **551**, 601–604 (2017).

[ADS](#) [CAS](#) [PubMed](#) [PubMed Central](#) [Google Scholar](#)

22. 22.

Bernien, H. et al. Probing many-body dynamics on a 51-atom quantum simulator. *Nature* **551**, 579–584 (2017).

[ADS](#) [CAS](#) [PubMed](#) [PubMed Central](#) [Google Scholar](#)

23. 23.

Barends, R. et al. Digital quantum simulation of fermionic models with a superconducting circuit. *Nat. Commun.* **6**, 7654 (2015).

[ADS](#) [CAS](#) [PubMed](#) [PubMed Central](#) [Google Scholar](#)

24. 24.

Davis, E. J. et al. Protecting spin coherence in a tunable Heisenberg model. *Phys. Rev. Lett.* **125**, 060402 (2020).

[ADS](#) [CAS](#) [PubMed](#) [PubMed Central](#) [Google Scholar](#)

25. 25.

Signoles, A. et al. Glassy dynamics in a disordered Heisenberg quantum spin system. Preprint at <https://arxiv.org/abs/1909.11959> (2019).

26. 26.

Trotzky, S. et al. Time-resolved observation and control of superexchange interactions with ultracold atoms in optical lattices. *Science* **319**, 295–299 (2008).

[ADS](#) [CAS](#) [PubMed](#) [PubMed Central](#) [Google Scholar](#)

27. 27.

Gross, C. & Bloch, I. Quantum simulations with ultracold atoms in optical lattices. *Science* **357**, 995–1001 (2017).

[ADS](#) [CAS](#) [PubMed](#) [PubMed Central](#) [Google Scholar](#)

28. 28.

Jaksch, D., Bruder, C., Cirac, J. I., Gardiner, C. W. & Zoller, P. Cold bosonic atoms in optical lattices. *Phys. Rev. Lett.* **81**, 3108–3111 (1998).

[ADS](#) [CAS](#) [Google Scholar](#)

29. 29.

Kuklov, A. B. & Svistunov, B. V. Counterflow superfluidity of two-species ultracold atoms in a commensurate optical lattice. *Phys. Rev. Lett.* **90**, 100401 (2003).

[ADS](#) [CAS](#) [PubMed](#) [PubMed Central](#) [Google Scholar](#)

30. 30.

Duan, L.-M., Demler, E. & Lukin, M. D. Controlling spin exchange interactions of ultracold atoms in optical lattices. *Phys. Rev. Lett.* **91**, 090402 (2003).

[ADS](#) [PubMed](#) [PubMed Central](#) [Google Scholar](#)

31. 31.

García-Ripoll, J. J. & Cirac, J. I. Spin dynamics for bosons in an optical lattice. *New J. Phys.* **5**, 76 (2003).

[Google Scholar](#)

32. 32.

Altman, E., Hofstetter, W., Demler, E. & Lukin, M. D. Phase diagram of two-component bosons on an optical lattice. *New J. Phys.* **5**, 113 (2003).

[ADS](#) [Google Scholar](#)

33. 33.

Amato-Grill, J., Jepsen, N., Dimitrova, I., Lunden, W. & Ketterle, W. Interaction spectroscopy of a two-component Mott insulator. *Phys. Rev. A* **99**, 033612 (2019).

[ADS](#) [Google Scholar](#)

34. 34.

Jordan, P. & Wigner, E. Über das Paulische Äquivalenzverbot. *Z. Phys.* **47**, 631–651 (1928).

[ADS](#) [CAS](#) [MATH](#) [Google Scholar](#)

35. 35.

Ioffe, A. F. & Regel, A. R. Non-crystalline, amorphous and liquid electronic semiconductors. *Prog. Semiconduct.* **4**, 237–291 (1960).

[Google Scholar](#)

36. 36.

Mott, N. F. Conduction in non-crystalline systems IX. the minimum metallic conductivity. *Philos. Mag. A* **26**, 1015–1026 (1972).

[ADS](#) [CAS](#) [Google Scholar](#)

37. 37.

Brown, P. T. et al. Bad metallic transport in a cold atom Fermi–Hubbard system. *Science* **363**, 379–382 (2019).

[ADS](#) [CAS](#) [PubMed](#) [PubMed Central](#) [Google Scholar](#)

38. 38.

Dubkov, A. A., Spagnolo, B. & Uchaikin, V. V. Lévy flight superdiffusion: an introduction. *Int. J. Bifurc. Chaos* **18**, 2649–2672 (2008).

[MATH](#) [Google Scholar](#)

39. 39.

Andreev, A. È. et al. Correlation theory of processes with stationary random increments of order  $n$ . *Am. Math. Soc. Transl.* **8**, 87 (1958).

[Google Scholar](#)

40. 40.

Agarwal, K., Gopalakrishnan, S., Knap, M., Müller, M. & Demler, E. Anomalous diffusion and Griffiths effects near the many-body localization transition. *Phys. Rev. Lett.* **114**, 160401 (2015).

[ADS](#) [PubMed](#) [PubMed Central](#) [Google Scholar](#)

41. 41.

Vosk, R., Huse, D. A. & Altman, E. Theory of the many-body localization transition in one-dimensional systems. *Phys. Rev. X* **5**, 031032 (2015).

[Google Scholar](#)

42. 42.

Guardado-Sánchez, E. et al. Subdiffusion and heat transport in a tilted two-dimensional Fermi–Hubbard system. *Phys. Rev. X* **10**, 011042 (2020).

[CAS](#) [Google Scholar](#)

43. 43.

Antal, T., Rácz, Z., Rákos, A. & Schütz, G. M. Transport in the XX chain at zero temperature: emergence of flat magnetization profiles. *Phys. Rev. E* **59**, 4912–4918 (1999).

[ADS](#) [CAS](#) [Google Scholar](#)

44. 44.

Gobert, D., Kollath, C., Schollwöck, U. & Schütz, G. Real-time dynamics in spin- $\frac{1}{2}$  chains with adaptive time-dependent density matrix renormalization group. *Phys. Rev. E* **71**, 036102 (2005).

[ADS](#) [MathSciNet](#) [Google Scholar](#)

45. 45.

Misguich, G., Pavloff, N. & Pasquier, V. Domain wall problem in the quantum XXZ chain and semiclassical behavior close to the isotropic point. *SciPost Phys.* **7**, 025 (2019).

[ADS](#) [MathSciNet](#) [CAS](#) [Google Scholar](#)

46. 46.

Ljubotina, M., Žnidarič, M. & Prosen, T. A class of states supporting diffusive spin dynamics in the isotropic Heisenberg model. *J. Phys. A Math. Theor.* **50**, 475002 (2017).

[ADS](#) [MathSciNet](#) [MATH](#) [Google Scholar](#)

47. 47.

Castro-Alvaredo, O. A., Doyon, B. & Yoshimura, T. Emergent hydrodynamics in integrable quantum systems out of equilibrium. *Phys. Rev. X* **6**, 041065 (2016).

[Google Scholar](#)

48. 48.

Bertini, B., Collura, M., De Nardis, J. & Fagotti, M. Transport in out-of-equilibrium XXZ chains: exact profiles of charges and currents. *Phys. Rev. Lett.* **117**, 207201 (2016).

[ADS](#) [PubMed](#) [PubMed Central](#) [Google Scholar](#)

49. 49.

Caux, J.-S. & Mossel, J. Remarks on the notion of quantum integrability. *J. Stat. Mech.* **2011**, P02023 (2011).

[MATH](#) [Google Scholar](#)

50. 50.

Dimitrova, I. et al. Enhanced superexchange in a tilted Mott insulator. *Phys. Rev. Lett.* **124**, 043204 (2020).

[ADS](#) [CAS](#) [PubMed](#) [PubMed Central](#) [Google Scholar](#)

51. 51.

Greiner, M. *Ultracold Quantum Gases in Three-dimensional Optical Lattice Potentials*. PhD thesis, Ludwig-Maximilians-Universität München (2003).

52. 52.

Łącki, M., Delande, D. & Zakrzewski, J. Dynamics of cold bosons in optical lattices: effects of higher Bloch bands. *New J. Phys.* **15**, 013062 (2013).

[Google Scholar](#)

53. 53.

Will, S. et al. Time-resolved observation of coherent multi-body interactions in quantum phase revivals. *Nature* **465**, 197–201 (2010).

[ADS](#) [CAS](#) [PubMed](#) [PubMed Central](#) [Google Scholar](#)

54. 54.

Lühmann, D.-S., Jürgensen, O. & Sengstock, K. Multi-orbital and density-induced tunneling of bosons in optical lattices. *New J. Phys.* **14**, 033021 (2012).

[ADS](#) [Google Scholar](#)

55. 55.

Stöferle, T., Moritz, H., Schori, C., Köhl, M. & Esslinger, T. Transition from a strongly interacting 1D superfluid to a Mott insulator. *Phys. Rev. Lett.* **92**, 130403 (2004).

[ADS](#) [PubMed](#) [PubMed Central](#) [Google Scholar](#)

56. 56.

Secker, T., Amato-Grill, J., Ketterle, W. & Kokkelmans, S. High-precision analysis of Feshbach resonances in a Mott insulator. *Phys. Rev. A* **101**, 042703 (2020).

[ADS](#) [MathSciNet](#) [CAS](#) [Google Scholar](#)

57. 57.

Bradley, C. C., Sackett, C. A. & Hulet, R. G. Bose–Einstein condensation of lithium: observation of limited condensate number. *Phys. Rev. Lett.* **78**, 985–989 (1997).

[ADS](#) [CAS](#) [Google Scholar](#)

58. 58.

Ketterle, W., Durfee, D. S. & Stamper-Kurn, D. M. Making, probing and understanding Bose–Einstein condensates. In *Bose–Einstein*

*Condensation in Atomic Gases* (eds Inguscio, M. et al.) 67–176 (IOS Press, 1999).

[Download references](#)

## Acknowledgements

We thank M. D. Lukin, N. Y. Yao and M. Knap for discussions, Y. K. Lee for experimental assistance, as well as C. M. E. Paus for sharing computing resources, and J. de Hond for comments on the manuscript. We acknowledge support from the NSF through the Center for Ultracold Atoms and grant number 1506369, NSF (grant number OAC-193471), ARO-MURI Non-Equilibrium Many-Body Dynamics (grant number W911NF-14-1-0003), AFOSR-MURI Photonic Quantum Matter (grant number FA9550-16-1-0323), AFOSR-MURI Quantum Phases of Matter (grant number FA9550-14-1-0035), ONR (grant number N00014-17-1-2253), ARO (grant number W911NF-20-1-0163), the Vannevar Bush Faculty Fellowship, and the Gordon and Betty Moore Foundation EPiQS Initiative (grant number GBMF4306).

## Author information

### Affiliations

1. Department of Physics, Massachusetts Institute of Technology, Cambridge, MA, USA

Paul Niklas Jepsen, Jesse Amato-Grill, Ivana Dimitrova & Wolfgang Ketterle

2. Research Laboratory of Electronics, Massachusetts Institute of Technology, Cambridge, MA, USA

Paul Niklas Jepsen, Jesse Amato-Grill, Ivana Dimitrova & Wolfgang Ketterle

3. MIT-Harvard Center for Ultracold Atoms, Cambridge, MA, USA

Paul Niklas Jepsen, Jesse Amato-Grill, Ivana Dimitrova, Wen Wei Ho, Eugene Demler & Wolfgang Ketterle

4. Department of Physics, Harvard University, Cambridge, MA, USA

Wen Wei Ho & Eugene Demler

## Authors

1. Paul Niklas Jepsen

[View author publications](#)

You can also search for this author in [PubMed](#) [Google Scholar](#)

2. Jesse Amato-Grill

[View author publications](#)

You can also search for this author in [PubMed](#) [Google Scholar](#)

3. Ivana Dimitrova

[View author publications](#)

You can also search for this author in [PubMed](#) [Google Scholar](#)

4. Wen Wei Ho

[View author publications](#)

You can also search for this author in [PubMed](#) [Google Scholar](#)

5. Eugene Demler

[View author publications](#)

You can also search for this author in [PubMed](#) [Google Scholar](#)

6. Wolfgang Ketterle

[View author publications](#)

You can also search for this author in [PubMed](#) [Google Scholar](#)

## Contributions

P.N.J., J.A.-G., I.D. and W.K. conceived the experiment. P.N.J., J.A.-G. and I.D. developed the experimental setup and took the data. P.N.J. led the data analysis. W.W.H. and E.D. developed the theoretical analysis. W.W.H. performed the numerical simulations. All authors discussed the results and contributed to the writing of the manuscript.

## Corresponding author

Correspondence to [Paul Niklas Jepsen](#).

## Ethics declarations

## Competing interests

The authors declare no competing interests.

## Additional information

**Peer review information** *Nature* thanks Jean-Philippe Brantut, Tomaž Prosen and the other, anonymous, reviewer(s) for their contribution to the peer review of this work.

**Publisher's note** Springer Nature remains neutral with regard to jurisdictional claims in published maps and institutional affiliations.

## Extended data figures and tables

### [Extended Data Fig. 1 Determination of the Heisenberg parameters.](#)

**a**, Corrections for tunnelling  $\langle(\tilde{t}-\tilde{t}^0)^2\rangle^{1/2}$  (green), on-site interactions  $(U-U^0)/U^0$  (blue), superexchange  $(J-J^0)/J^0$  (purple) and off-site interactions  $-2V/J^0$  (orange), where  $\tilde{t}$

$(\tilde{t})^{(0)}$ ,  $U^{(0)}$  and  $\langle J \rangle^{(0)} = 4 \{(\tilde{t})^2\}^{(0)} / \{U\}^{(0)}$  are the uncorrected values and  $(\tilde{t}), U$  and  $\langle J \rangle = 4 \{\tilde{t}\}^2 / U$  include corrections, at a lattice depth of  $13E_R$  (solid line) and  $9E_R$  (dotted line). **b**, As a function of magnetic field  $B$  we show the scattering lengths  $a_{\uparrow\uparrow}$  (blue),  $a_{\uparrow\downarrow}$  (purple) and  $a_{\downarrow\downarrow}$  (orange) measured in our previous work (points<sup>33</sup>). Here  $a_0$  is the Bohr radius. **c, d**, We interpolate the data in **b** using hyperbolic fits (solid lines) and calculate values for the transverse coupling constant  $J_{xy}$  (purple), the longitudinal coupling constant  $J_z$  (yellow) and the anisotropy  $\Delta = J_z/J_{xy}$  (black), without corrections (dashed line) and including corrections (solid line) for a lattice depth of  $11E_R$ . The excluded region ( $|a_{\uparrow\uparrow}| > 700a_0$ ) is around a Feshbach resonance in the  $|\uparrow\rangle$  state near 845.4 G.

## Extended Data Fig. 2 Contrast measurement.

**a–d**, The distribution of atoms in the  $|\uparrow\rangle$  state. Every pixel is a local measurement of the column density (number of atoms per unit area). The  $y$  and  $z$  axes are displayed in units of the lattice spacing  $a = 0.532 \mu\text{m}$ . The images are projected (integrated) along the  $y$  direction from  $y = -30a$  to  $+30a$  to obtain the linear density (number of atoms per unit length). The resulting 1D distributions are fitted with  $f(z) = g(z)[1 + \{\mathcal{C}\}\cos(Qz + \theta)]/2$  (solid line), where  $g(z)$  is a Gaussian envelope (dashed line), between  $z = \pm 54a$ . The data in **a–d** were measured at different evolution times  $t = 0$  (**a**),  $2.3\hbar/J_{xy}$  (**b**),  $6.3\hbar/J_{xy}$  (**c**) and  $12.0\hbar/J_{xy}$  (**d**), for anisotropy  $\Delta \approx 0$  and wavelength  $\lambda = 10.4a$ . The obtained contrast  $\langle C(t) \rangle$  is shown in Fig. 2a. In general, we also normalize by the initial contrast  $\langle C(0) \rangle$  to correct for finite optical imaging resolution. This is important for shorter wavelengths  $\lambda$  close to the optical resolution of  $3 \mu\text{m}$ , where the measured contrast  $\langle C(t) \rangle$  is reduced compared to the real contrast  $C(t) = \langle C(t) \rangle / \langle C(0) \rangle$ .

## Extended Data Fig. 3 Dispersion relations.

For all positive anisotropies  $\Delta \geq 0$ , the time evolution of the contrast  $c(t)$  shows a damped oscillatory component, in addition to the overall exponential decay. For larger  $\Delta$ , the oscillations become smaller. **a–c**, Decay and weak oscillation at the isotropic point  $\Delta \approx 1$  measured for different wavelengths  $\lambda$ , at three different lattice depths  $9E_R$  (orange),  $11E_R$  (blue) and  $13E_R$  (yellow). Solid lines are fits  $c(t) = [a_0 + b_0\cos(\omega t)]e^{-t/\tau} + c_0$  and dashed lines show the overall decay  $a_0e^{-t/\tau} + c_0$ , around which the oscillations take place. The oscillations become more pronounced for short wavelengths  $\lambda$ , because the decay time ( $\tau \propto \lambda^2$ ) decreases with smaller wavelength more strongly than the oscillation period ( $T \propto \lambda$ ). **d**, The oscillation frequencies follow linear dispersion relations  $\omega(Q) = vQ$  shown for  $\Delta = -0.12$  (red),  $0.35$  (orange),  $0.78$  (yellow),  $1.01$  (blue) and  $1.27$  (light blue). **e**, The obtained velocities  $v$  decrease with increasing anisotropy  $\Delta$ . For  $\Delta = 1.58$  (open symbol), oscillations are small and the measurement was limited to large values of  $Q$ , which precluded recording a full dispersion relation. We note that although the oscillations are difficult to discern by eye (for example, in **a**), especially for large anisotropies  $\Delta$  and small wavevectors  $Q$ , the fitted oscillation frequencies  $\omega$  all fall very well on linear dispersion relations, which demonstrates that those barely visible oscillations are real. The linear scaling  $\omega(Q) = vQ$  persists even in the superdiffusive, diffusive and subdiffusive regimes, where the power-law scaling of the decay time constant  $\tau \propto Q^{-\alpha}$  is strongly nonlinear. This small ballistic (oscillatory) component may be related to our initial condition of a spin helix, which in the mapping to lattice fermions is a 100% density modulation, which reduces scattering at early times.

### Extended Data Fig. 4 Effect of finite hole concentration.

By varying the thermal fraction  $N_{\text{th}}/N$  of the Bose–Einstein condensate before it is loaded into the optical lattice, we vary the energy and entropy of the atoms in the spin chain, and therefore the concentration of holes. (For our conditions, doubly occupied sites have higher energies than holes). Measurements are shown here for  $\Delta \approx 0$  and  $\lambda = 10.4a$ , at a lattice depth of  $11E_R$ . **a**, Decay curves  $c(t)$  for varying hole concentrations ranging from low (blue) to high (orange) thermal fraction. Solid lines are fits  $c(t) =$

$[a_0 + b_0 \cos(\omega t)] e^{-t/\tau} + c_0$ . **b**, The background contrast  $c_0$  increases monotonously with thermal fraction  $N_{\text{th}}/N$ . A linear fit (solid line) extrapolates to  $c_0 = 0.01(2)$ , consistent with zero, for  $N_{\text{th}}/N = 0$ . This suggests that all of the background contrast is due to hole excitations. **c**, Higher hole concentrations suppress the oscillating fraction  $b_0/(a_0 + b_0)$ . **d**, Holes do not affect the oscillation period  $T = 2\pi/\omega$ . **e**, Holes decrease the decay time  $\tau$ , albeit slightly. **b–e** show that almost all of our measurements are not sensitive to a small thermal fraction, which is usually  $N_{\text{th}}/N \leq 0.05$  throughout this work. The behaviour shown in **c** and **e** is most probably caused by mobile holes in the central part of the Mott insulator. Indeed, numerical simulations of the  $\langle \tilde{t} \rangle - J$  model reproduce such effects (Fig. 2a). Note though that for the isotropic case  $\Delta \approx 1$ , a previous work<sup>7</sup> found a  $\sim 50\%$  change in decay time when the hole concentration changed from 0 to 5%. Our numerical simulations (Extended Data Fig. 8b) do not show such strong sensitivity (for any anisotropy, even at  $\Delta = 1$ ), possibly owing to asymmetry in the on-site interactions ( $U_{\uparrow\uparrow} \neq U_{\uparrow\downarrow} \neq U_{\downarrow\downarrow}$ ) in our system. On the other hand, a finite background contrast (**b**) is probably caused by immobile holes located in the outer parts of the atom distribution where first-order tunnelling is suppressed by the gradient of the (harmonic) trapping potential<sup>50</sup>. Immobile holes disrupt spin transport, and so we expect that the imprinted spin modulation in these regions will not (or only very slowly) decay. **f**, **g**, The region with immobile holes is visible as a shell of low atomic density surrounding the Mott insulator in the in situ images for large hole concentration (**f**) and is absent for low hole concentration (**g**). The three curves in both **f** and **g** show the local contrast as a function of distance  $r$  from the centre of the atom cloud for the evolution times  $t = 0$  (top),  $2.7\hbar/J_{xy}$  (middle) and  $21.7\hbar/J_{xy}$  (bottom). The two in situ images in both **f** and **g** are for  $t = 0$  (top) and  $21.7\hbar/J_x$  (bottom). The dashed lines indicate contours of constant radius,  $r = 30a$  (**f**) and  $r = 20a$  (**g**).

## Extended Data Fig. 5 Decay behaviour as a function of anisotropy.

**a, b**, Decay behaviour ranging from negative (**a**) to positive (**b**) anisotropy, for a fixed wavelength  $\lambda = 10.4a$ . Using  $\Delta \approx 0$  as a reference point, we show

how the temporal profile of the decay curve  $c(t)$  changes when we introduce positive or negative interactions. Every data point is an average of two measurements at lattice depths  $11E_R$  and  $13E_R$ . In **a**, from bottom to top:  $\Delta = -0.12$  (red),  $-0.59$  (pink),  $-0.81$  (yellow),  $-1.02$  (blue),  $-1.43$  (green) and  $-1.79$  (purple). In **b**, from bottom to top:  $\Delta = -0.13$  (red),  $0.08$  (purple),  $0.35$  (pink),  $0.55$  (orange),  $0.78$  (yellow),  $1.01$  (blue),  $1.27$  (light blue) and  $1.58$  (green). Regardless of sign, for increasing  $|\Delta|$  the decay always slows down and the revivals damp more quickly. However, there is a big difference in how this slowdown happens: for increasing positive interactions  $\Delta > 0$ , the initial rate of decay decreases continuously (**b**); by contrast, for all negative interactions  $\Delta < 0$ , the initial rate of decay stays constant (and is ballistic), coinciding with the  $\Delta \approx 0$  case (**a**). It is only after a critical time  $t_0$  that the decay suddenly starts slowing down (and becomes diffusive) for times  $t > t_0$ . This critical time  $t_0$  decreases with increasing negative interaction strength  $|\Delta|$ .

### Extended Data Fig. 6 Collapse of decay curves for positive anisotropies.

All decay curves  $c(t)$  for wavelengths  $\lambda = 15.7a, 13.4a, 11.7a, 10.4a, 9.4a, 8.5a, 7.8a, 7.2a$  and  $6.7a$  collapse very well into a single curve for all evolution times  $t$ , when time units are rescaled by  $\lambda^\alpha$ , where the exponent  $\alpha$  is a function of anisotropy  $\Delta$ , both for experiment (points) and theory (solid lines). Experimental points were measured for lattice depths  $9E_R$  (red),  $11E_R$  (blue) and  $13E_R$  (yellow). **a, b**, Ballistic regime ( $\alpha = 1$ ). **c**, Superdiffusion ( $\alpha = 1.5$ ). **d**, Diffusion ( $\alpha = 2$ ). **e, f**, Subdiffusion ( $\alpha = 2.5, 3$  for experiment and  $\alpha = 3.5, 4.5$  for numerical simulations; in **f**, experiments covered a reduced range  $\lambda \leq 10.4a$ ). For all anisotropies  $\Delta \geq 0$  (**a–f**) the experimentally measured oscillation frequencies  $\omega$  follow linear dispersion relations (Extended Data Fig. 3) and have a scaling behaviour different from the decay rates. However, such oscillations are small outside the ballistic regime  $\alpha \approx 1$ , and therefore only lead to a small deviation from the collapse behaviour. Note also the different timescales in experiments and simulations for  $\Delta > 1$ .

## Extended Data Fig. 7 Collapse at short times for negative anisotropies.

All decay curves  $c(t)$  for different wavelengths  $\lambda$  collapse into a single curve at early times, when time units are rescaled by  $\lambda$  (indicating ballistic behaviour). For later times the decay is diffusive with different scaling. **a–c**, Theory (from top to bottom:  $\lambda = 31.3a, 23.5a, 18.8a, 15.7a, 13.4a, 11.7a, 10.4a, 9.4a, 8.5a, 7.8a, 7.2a, 6.7a$  and  $6.3a$ ). The dotted lines are exponential fits  $\langle \{ \{ \text{rm} \{ e \} \} \rangle^{\{-t/\{\tau_{\text{II}}\}_{\{ \{ \text{rm} \{ II \} \} \}}\}}$  to the diffusive regime and the time constants  $\tau_{\text{II}}$  are shown in Extended Data Fig. 8a. **d–f**, Experiment (from top to bottom:  $\lambda = 18.8a, 13.4a, 10.4a, 8.5a, 7.2a$  and  $6.3a$ ). Every data point is an average of two measurements at lattice depths  $11E_R$  and  $13E_R$ . The black dashed line indicates the ballistic case  $\Delta \approx 0$  (see Fig. 2c).

## Extended Data Fig. 8 Power-law scalings (theory) and diffusion coefficients.

**a, b**, Decay time constants  $\tau$  for different anisotropies  $\Delta$  ranging from negative (**a**) to positive (**b**). Numerical results are shown in **a** for  $\Delta = -1$  (blue),  $-1.5$  (green) and  $-2$  (purple) and in **b** for  $\Delta = 0$  (red),  $0.5$  (orange),  $0.85$  (yellow),  $1$  (blue) and  $1.5$  (green). Solid lines are power-law fits (to the filled symbols). Open symbols are excluded from the fit owing to finite-size effects. Crossed symbols are results from  $\langle \tilde{t} \rangle - J$  model simulations including 5% hole fraction. Fitted power-law exponents are shown in Fig. 3c. For positive anisotropies  $\Delta \geq 0$  the decay time  $\tau$  is defined as  $\tau = \tau'/\ln(1/0.60)$  with  $c(\tau') = 0.60$ . For negative anisotropies  $\Delta < 0$ , the decay time  $\tau_I$  for short times (I) is defined as  $\langle \{ \tau \}_{\{ \{ \text{rm} \{ I \} \} \}} \rangle = 10 \langle \{ \tau \}_{\{ \{ \text{rm} \{ I \} \} \}} \rangle^{\{ \{ \prime \} \}}$  with  $\langle c(\{ \tau \}_{\{ \{ \text{rm} \{ I \} \} \}}^{\{ \{ \prime \} \}}) \rangle = 0.90$ . For longer times (II), the decay time  $\tau_{\text{II}}$  is obtained from exponential fits  $\langle \{ \{ \text{rm} \{ e \} \} \rangle^{\{-t/\{\tau_{\text{II}}\}_{\{ \{ \text{rm} \{ II \} \} \}}\}}$  to the diffusive long-time tail (see dotted curves in Extended Data Fig. 7a–c). **c**, Diffusion coefficients for the diffusive long-time regime (II) obtained from theory (open symbols) and experiment (filled symbols). For negative anisotropies  $\Delta < 0$ , values were determined from quadratic power-law fits  $1/\tau = DQ^2$  to the data points in **a** (theory) and Fig. 3a (experiment) for the

diffusive regime (II). Note that for  $\Delta \geq 0$  the system is only diffusive for  $\Delta = +1$ , as shown in **b** (theory) and Fig. 3**b** (experiment). From the experimental diffusion coefficients, we estimate mean free paths  $\delta x$  using the velocity  $v = 0.76(1)v_F$  from the ballistic short-time regime (I), and obtain  $\delta x = 3.35(15)a$ ,  $1.07(7)a$  and  $0.66(4)a$  for  $\Delta = -1.02$ ,  $-1.43$  and  $-1.79$ , respectively. **d**, Short-time ( $t \ll \hbar/J_{xy}$ ) decay constant  $\tau = |\Gamma|^{-1}$  obtained from Taylor expansion of the contrast  $c(t) = 1 + \Gamma^2 t^2 + \dots$  as a function of  $Q$ , for  $\Delta = 0$  (red),  $0.55$  (orange),  $0.85$  (yellow),  $0.95$  (purple) and  $1$  (blue). For  $\Delta < 1$  all curves in the log–log plot asymptote to the same slope as  $Q \rightarrow 0$  (continuum limit), whereas there are deviations for larger wavevectors  $Q$ . For  $\Delta = 1$  the slope is instead different. This indicates that the power-law exponent  $\alpha$  in  $\tau \propto Q^{-\alpha}$  depends on the range of wavevectors  $Q$  used to determine it. **e**, Power-law exponents  $\alpha$  determined for the short-wavelength regime between  $\lambda = 6a$  and  $20a$  (filled symbols) as in experiments and numerics, and for the long-wavelength regime between  $\lambda = 150a$  and  $200a$  (open symbols) approaching the continuum limit. In the former case, the exponents show a smooth crossover from superballistic to diffusive as  $\Delta \rightarrow 1$  similar to that in the experiments and numerics, whereas in the latter case the exponents show a sharp jump from ballistic to diffusive occurring exactly at  $\Delta = 1$ .

### Extended Data Fig. 9 Finite-size effects from the initial phase of the spin helix.

**a**, The time evolution of the contrast  $c(t)$  depends strongly on the initial phase  $\theta$ , illustrated here by simulations for  $\Delta = 0$  and  $\lambda = 10.4a$ . **b**, **c**, The dynamics of the local magnetization  $\langle S_i^z(t) \rangle$  for phases  $\theta = 0$  (**b**) and  $\pi/2$  (**c**) reveals that this arises owing to the reflection of ballistically propagating magnetization off the ends of the chain. Depending on the initial phase of the spin helix, the reflected magnetization interferes constructively or destructively with the pattern of the bulk magnetization.

### Extended Data Fig. 10 Finite-size effects from the chain length.

**a**, Contrast  $c(t)$  obtained after a weighted average over all different chain lengths between  $L = 0$  and  $44a$  (shown in **b**), for  $\Delta = 0$  and  $\lambda = 10.4a$ . The

averaged dynamics (orange, yellow, blue) shows almost no dependence on the phase  $\theta$ , in contrast to the dynamics determined from a single chain length  $L = 40a$  (Extended Data Fig. 9a). Also overlaid are the contrasts for a fixed chain length ( $L = 40a$ ) averaged over all initial phases  $0 \leq \theta < 2\pi$  (black solid line), and averaged over only the two phases  $\theta = 0$  and  $\pi/2$  (black dashed line). The close agreement implies that averaging over either chain lengths or phases suppresses the dependence on initial or boundary conditions. **b**, A cut through the spherical Mott insulator with diameter  $L_{\max} = 44a$  (as in the experiment) illustrates the distribution of different chain lengths (oriented along the z direction). Averaging the local magnetization  $S^z$  over the x and y directions provides a 1D magnetization profile (bottom panel), which is an average over all chains. **c**, The number of chains with length  $L$  is given by  $(\pi/2)(L/a)$ . The total number of chains is  $\pi L_{\max}/(2a)^2 \approx 1,500$ . **d**, The number of atoms in chains with length  $L$  is given by  $(\pi/2)(L/a)^2$ . The contribution of each chain to the imaging signal is proportional to the atom number in the chain, and so the relevant average over chain lengths is weighted by the atom number and is  $\langle L \rangle = (3/4)L_{\max} = 33a$ .

## Rights and permissions

[Reprints and Permissions](#)

## About this article



Check for  
updates

## Cite this article

Jepsen, P.N., Amato-Grill, J., Dimitrova, I. *et al.* Spin transport in a tunable Heisenberg model realized with ultracold atoms. *Nature* **588**, 403–407 (2020). <https://doi.org/10.1038/s41586-020-3033-y>

## Download citation

- Received: 18 May 2020
- Accepted: 25 September 2020
- Published: 16 December 2020
- Issue Date: 17 December 2020
- DOI: <https://doi.org/10.1038/s41586-020-3033-y>

## Comments

By submitting a comment you agree to abide by our [Terms](#) and [Community Guidelines](#). If you find something abusive or that does not comply with our terms or guidelines please flag it as inappropriate.

[Access through your institution](#)

[Change institution](#)

[Buy or subscribe](#)

---

This article was downloaded by **calibre** from <https://www.nature.com/articles/s41586-020-3033-y>

- Article
- [Published: 16 December 2020](#)

# Half-minute-scale atomic coherence and high relative stability in a tweezer clock

- [Aaron W. Young](#) [ORCID: orcid.org/0000-0002-3490-4046<sup>1,2</sup>](#),
- [William J. Eckner](#) [ORCID: orcid.org/0000-0003-0833-7137<sup>1,2</sup>](#),
- [William R. Milner<sup>1,2</sup>](#),
- [Dhruv Kedar](#) [ORCID: orcid.org/0000-0003-1117-8616<sup>1,2</sup>](#),
- [Matthew A. Norcia](#) [ORCID: orcid.org/0000-0002-2276-9473<sup>1,2</sup>](#),
- [Eric Oelker](#) [ORCID: orcid.org/0000-0002-3916-1595<sup>1,2</sup>](#),
- [Nathan Schine](#) [ORCID: orcid.org/0000-0001-5903-3200<sup>1,2</sup>](#),
- [Jun Ye](#) [ORCID: orcid.org/0000-0003-0076-2112<sup>1,2</sup>](#) &
- [Adam M. Kaufman](#) [ORCID: orcid.org/0000-0003-4956-5814<sup>1,2</sup>](#)

[Nature](#) volume **588**, pages408–413(2020)[Cite this article](#)

- 777 Accesses
- 76 Altmetric
- [Metrics details](#)

## Subjects

- [Quantum metrology](#)
- [Ultracold gases](#)

## Abstract

The preparation of large, low-entropy, highly coherent ensembles of identical quantum systems is fundamental for many studies in quantum metrology<sup>1</sup>, simulation<sup>2</sup> and information<sup>3</sup>. However, the simultaneous realization of these properties remains a central challenge in quantum science across atomic and condensed-matter systems<sup>2,4,5,6,7</sup>. Here we leverage the favourable properties of tweezer-trapped alkaline-earth (strontium-88) atoms<sup>8,9,10</sup>, and introduce a hybrid approach to tailoring optical potentials that balances scalability, high-fidelity state preparation, site-resolved readout and preservation of atomic coherence. With this approach, we achieve trapping and optical-clock excited-state lifetimes exceeding 40 seconds in ensembles of approximately 150 atoms. This leads to half-minute-scale atomic coherence on an optical-clock transition, corresponding to quality factors well in excess of  $10^{16}$ . These coherence times and atom numbers reduce the effect of quantum projection noise to a level that is comparable with that of leading atomic systems, which use optical lattices to interrogate many thousands of atoms in parallel<sup>11,12</sup>. The result is a relative fractional frequency stability of  $5.2(3) \times 10^{-17} \tau^{-1/2}$  (where  $\tau$  is the averaging time in seconds) for synchronous clock comparisons between sub-ensembles within the tweezer array. When further combined with the microscopic control and readout that are available in this system, these results pave the way towards long-lived engineered entanglement on an optical-clock transition<sup>13</sup> in tailored atom arrays.

[Access through your institution](#)

[Change institution](#)

[Buy or subscribe](#)

## Access options

Subscribe to Journal

Get full journal access for 1 year

185,98 €

only 3,58 € per issue

## Subscribe

All prices are NET prices.  
VAT will be added later in the checkout.

Rent or Buy article

Get time limited or full article access on ReadCube.

from \$8.99

## Rent or Buy

All prices are NET prices.

## **Additional access options:**

- [Log in](#)
- [Access through your institution](#)
- [Learn about institutional subscriptions](#)

**Fig. 1: 3D ground-state cooled strontium atoms in a 320-site magic-wavelength tweezer array.**

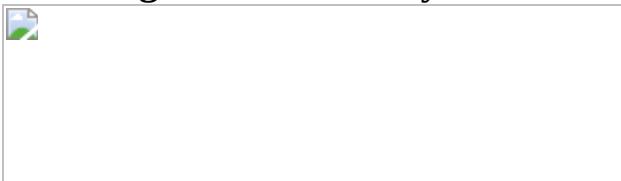


**Fig. 2: Minute-scale atomic lifetime and ensemble coherence studies.**



**Fig. 3: Resolving millihertz shifts of an optical transition.**



**Fig. 4: Microscopic studies of atomic coherence.**



## Data availability

The experimental data presented in this manuscript are available from the corresponding author upon reasonable request. [Source data](#) are provided with this paper.

## Code availability

The code used for analysis and simulation in this work is available from the corresponding author upon reasonable request.

## References

1. 1.

Ludlow, A. D., Boyd, M. M., Ye, J., Peik, E. & Schmidt, P. O. Optical atomic clocks. *Rev. Mod. Phys.* **87**, 637–701 (2015).

[ADS](#) [CAS](#) [Google Scholar](#)

2. 2.

Georgescu, I. M., Ashhab, S. & Nori, F. Quantum simulation. *Rev. Mod. Phys.* **86**, 153–185 (2014).

[ADS](#) [Google Scholar](#)

3. 3.

Preskill, J. Quantum computing and the entanglement frontier. Preprint at <https://arxiv.org/abs/1203.5813> (2012).

4. 4.

Saffman, M., Walker, T. G. & Molmer, K. Quantum information with Rydberg atoms. *Rev. Mod. Phys.* **82**, 2313–2363 (2010).

[ADS](#) [CAS](#) [Google Scholar](#)

5. 5.

Madjarov, I. S. et al. An atomic-array optical clock with single-atom readout. *Phys. Rev. X* **9**, 041052 (2019).

[CAS](#) [Google Scholar](#)

6. 6.

Norcia, M. A. et al. Seconds-scale coherence on an optical clock transition in a tweezer array. *Science* **366**, 93–97 (2019).

[ADS](#) [CAS](#) [PubMed](#) [Google Scholar](#)

7. 7.

Hutson, R. B., Goban, A., Marti, G. E. & Ye, J. Engineering quantum states of matter for atomic clocks in shallow optical lattices. *Phys. Rev. Lett.* **123**, 123401 (2019).

[ADS](#) [CAS](#) [PubMed](#) [Google Scholar](#)

8. 8.

Cooper, A. et al. Alkaline-earth atoms in optical tweezers. *Phys. Rev. X* **8**, 041055 (2018).

[CAS](#) [Google Scholar](#)

9. 9.

Norcia, M. A., Young, A. W. & Kaufman, A. M. Microscopic control and detection of ultracold strontium in optical-tweezer arrays. *Phys. Rev. X* **8**, 041054 (2018).

[Google Scholar](#)

10. 10.

Saskin, S., Wilson, J. T., Grinkemeyer, B. & Thompson, J. D. Narrow-line cooling and imaging of ytterbium atoms in an optical tweezer array. *Phys. Rev. Lett.* **122**, 143002 (2019).

[ADS](#) [CAS](#) [PubMed](#) [Google Scholar](#)

11. 11.

Campbell, S. L. et al. A Fermi-degenerate three-dimensional optical lattice clock. *Science* **358**, 90–94 (2017).

[ADS](#) [CAS](#) [PubMed](#) [Google Scholar](#)

12. 12.

Oelker, E. et al. Demonstration of  $4.8 \times 10^{-17}$  stability at 1 s for two independent optical clocks. *Nat. Photon.* **13**, 714–719 (2019).

[ADS](#) [CAS](#) [Google Scholar](#)

13. 13.

Gil, L. I. R., Mukherjee, R., Bridge, E. M., Jones, M. P. A. & Pohl, T. Spin squeezing in a Rydberg lattice clock. *Phys. Rev. Lett.* **112**, 103601 (2014).

[ADS](#) [CAS](#) [PubMed](#) [Google Scholar](#)

14. 14.

Browaeys, A. & Lahaye, T. Many-body physics with individually controlled Rydberg atoms. *Nat. Phys.* **16**, 132–142 (2020).

[CAS](#) [Google Scholar](#)

15. 15.

Barredo, D., de Léséleuc, S., Lienhard, V., Lahaye, T. & Browaeys, A. An atom-by-atom assembler of defect-free arbitrary two-dimensional atomic arrays. *Science* **354**, 1021–1023 (2016).

[ADS](#) [CAS](#) [PubMed](#) [Google Scholar](#)

16. 16.

Endres, M. et al. Atom-by-atom assembly of defect-free one-dimensional cold atom arrays. *Science* **354**, 1024–1027 (2016).

[ADS](#) [CAS](#) [PubMed](#) [Google Scholar](#)

17. 17.

Kumar, A., Wu, T.-Y., Giraldo, F. & Weiss, D. S. Sorting ultracold atoms in a three-dimensional optical lattice in a realization of

Maxwell's demon. *Nature* **561**, 83–87 (2018).

[ADS](#) [CAS](#) [PubMed](#) [Google Scholar](#)

18. 18.

Brown, M. O., Thiele, T., Kiehl, C., Hsu, T.-W. & Regal, C. A. Gray-molasses optical-tweezer loading: controlling collisions for scaling atom-array assembly. *Phys. Rev. X* **9**, 011057 (2019).

[CAS](#) [Google Scholar](#)

19. 19.

Levine, H. et al. Parallel implementation of high-fidelity multiqubit gates with neutral atoms. *Phys. Rev. Lett.* **123**, 170503 (2019).

[ADS](#) [CAS](#) [PubMed](#) [Google Scholar](#)

20. 20.

Graham, T. M. et al. Rydberg-mediated entanglement in a two-dimensional neutral atom qubit array. *Phys. Rev. Lett.* **123**, 230501 (2019).

[ADS](#) [CAS](#) [PubMed](#) [Google Scholar](#)

21. 21.

Omran, A. et al. Generation and manipulation of Schrödinger cat states in Rydberg atom arrays. *Science* **365**, 570–574 (2019).

[ADS](#) [MathSciNet](#) [CAS](#) [PubMed](#) [Google Scholar](#)

22. 22.

Bernien, H. et al. Probing many-body dynamics on a 51-atom quantum simulator. *Nature* **551**, 579–584 (2017).

[ADS](#) [CAS](#) [PubMed](#) [Google Scholar](#)

23. 23.

de Léséleuc, S. et al. Observation of a symmetry-protected topological phase of interacting bosons with Rydberg atoms. *Science* **365**, 775–780 (2019).

[ADS](#) [MathSciNet](#) [PubMed](#) [MATH](#) [Google Scholar](#)

24. 24.

Madjarov, I. S. et al. High-fidelity entanglement and detection of alkaline-earth Rydberg atoms *Nat. Phys.* **16**, 857–861 (2020).

[CAS](#) [Google Scholar](#)

25. 25.

Wilson, J. et al. Trapped arrays of alkaline earth Rydberg atoms in optical tweezers. Preprint at <https://arxiv.org/abs/1912.08754> (2019).

26. 26.

Chou, C. W., Hume, D. B., Koelemeij, J. C. J., Wineland, D. J. & Rosenband, T. Frequency comparison of two high-accuracy  $\text{Al}^+$  optical clocks. *Phys. Rev. Lett.* **104**, 070802 (2010).

[ADS](#) [CAS](#) [PubMed](#) [Google Scholar](#)

27. 27.

Brewer, S. M. et al.  $^{27}\text{Al}^+$  quantum-logic clock with a systematic uncertainty below  $10^{-18}$ . *Phys. Rev. Lett.* **123**, 033201 (2019).

[ADS](#) [CAS](#) [PubMed](#) [Google Scholar](#)

28. 28.

Ushijima, I., Takamoto, M., Das, M., Ohkubo, T. & Katori, H. Cryogenic optical lattice clocks. *Nat. Photon.* **9**, 185–189 (2015).

[ADS](#) [CAS](#) [Google Scholar](#)

29. 29.

Liu, L. R. et al. Molecular assembly of ground-state cooled single atoms. *Phys. Rev. X* **9**, 021039 (2019).

[CAS](#) [Google Scholar](#)

30. 30.

Dörscher, S. et al. Lattice-induced photon scattering in an optical lattice clock. *Phys. Rev. A* **97**, 063419 (2018).

[ADS](#) [Google Scholar](#)

31. 31.

Takamoto, M., Takano, T. & Katori, H. Frequency comparison of optical lattice clocks beyond the Dick limit. *Nat. Photon.* **5**, 288–292 (2011).

[ADS](#) [CAS](#) [Google Scholar](#)

32. 32.

Marti, G. E. et al. Imaging optical frequencies with 100  $\mu$ Hz precision and 1.1  $\mu$ m resolution. *Phys. Rev. Lett.* **120**, 103201 (2018).

[ADS](#) [CAS](#) [PubMed](#) [Google Scholar](#)

33. 33.

Foster, G. T., Fixler, J. B., McGuirk, J. M. & Kasevich, M. A. Method of phase extraction between coupled atom interferometers using ellipse-specific fitting. *Opt. Lett.* **27**, 951 (2002).

[ADS](#) [CAS](#) [PubMed](#) [Google Scholar](#)

34. 34.

Shi, C. et al. Polarizabilities of the  $^{87}\text{Sr}$  clock transition. *Phys. Rev. A* **92**, 012516 (2015).

[ADS](#) [Google Scholar](#)

35. 35.

Chwalla, M. et al. Precision spectroscopy with two correlated atoms. *Appl. Phys. B* **89**, 483–488 (2007).

[ADS](#) [CAS](#) [Google Scholar](#)

36. 36.

Chou, C. W., Hume, D. B., Thorpe, M. J., Wineland, D. J. & Rosenband, T. Quantum coherence between two atoms beyond  $Q = 10^{15}$ . *Phys. Rev. Lett.* **106**, 160801 (2011).

[ADS](#) [CAS](#) [PubMed](#) [Google Scholar](#)

37. 37.

Hume, D. B. & Leibrandt, D. R. Probing beyond the laser coherence time in optical clock comparisons. *Phys. Rev. A* **93**, 032138 (2016).

[ADS](#) [Google Scholar](#)

38. 38.

Tan, T. R. et al. Suppressing inhomogeneous broadening in a lutetium multi-ion optical clock. *Phys. Rev. Lett.* **123**, 063201 (2019).

[ADS](#) [CAS](#) [PubMed](#) [Google Scholar](#)

39. 39.

Kaufman, A. M. et al. Two-particle quantum interference in tunnel-coupled optical tweezers. *Science* **345**, 306–309 (2014).

[ADS](#) [MathSciNet](#) [CAS](#) [PubMed](#) [MATH](#) [Google Scholar](#)

40. 40.

Murmann, S. et al. Two fermions in a double well: exploring a fundamental building block of the Hubbard model. *Phys. Rev. Lett.* **114**, 080402 (2015).

[ADS](#) [PubMed](#) [Google Scholar](#)

41. 41.

Pedrozo-Peñfiel, E. et al. Entanglement-enhanced optical atomic clock. Preprint at <https://arxiv.org/abs/2006.07501> (2020).

42. 42.

Covey, J. P., Madjarov, I. S., Cooper, A. & Endres, M. 2000-times repeated imaging of strontium atoms in clock-magic tweezer arrays. *Phys. Rev. Lett.* **122**, 173201 (2019).

[ADS](#) [CAS](#) [PubMed](#) [Google Scholar](#)

43. 43.

Kaubruegger, R. et al. Variational spin-squeezing algorithms on programmable quantum sensors. *Phys. Rev. Lett.* **123**, 260505 (2019).

[ADS](#) [CAS](#) [PubMed](#) [Google Scholar](#)

44. 44.

Kessler, E. M. et al. Heisenberg-limited atom clocks based on entangled qubits. *Phys. Rev. Lett.* **112**, 190403 (2014).

[ADS](#) [CAS](#) [PubMed](#) [Google Scholar](#)

45. 45.

Zhang, G. & Song, Z. Topological characterization of extended quantum Ising models. *Phys. Rev. Lett.* **115**, 177204 (2015).

[ADS](#) [CAS](#) [PubMed](#) [Google Scholar](#)

46. 46.

Savary, L. & Balents, L. Quantum spin liquids: a review. *Rep. Prog. Phys.* **80**, 016502 (2017).

[ADS](#) [PubMed](#) [Google Scholar](#)

47. 47.

Titum, P., Iosue, J. T., Garrison, J. R., Gorshkov, A. V. & Gong, Z.-X. Probing ground-state phase transitions through quench dynamics. *Phys. Rev. Lett.* **123**, 115701 (2019).

[ADS](#) [CAS](#) [PubMed](#) [Google Scholar](#)

48. 48.

Briegel, H. J., Browne, D. E., Dür, W., Raussendorf, R. & Van den Nest, M. Measurement-based quantum computation. *Nat. Phys.* **5**, 19–26 (2009).

[CAS](#) [Google Scholar](#)

49. 49.

Monroe, C. et al. Resolved-sideband raman cooling of a bound atom to the 3D zero-point energy. *Phys. Rev. Lett.* **75**, 4011–4014 (1995).

[ADS](#) [MathSciNet](#) [CAS](#) [PubMed](#) [Google Scholar](#)

50. 50.

Kaufman, A. M., Lester, B. J. & Regal, C. A. Cooling a single atom in an optical tweezer to its quantum ground state. *Phys. Rev. X* **2**, 041014 (2012).

[Google Scholar](#)

51. 51.

Thompson, J. D., Tiecke, T. G., Zibrov, A. S., Vuletić, V. & Lukin, M. D. Coherence and Raman sideband cooling of a single atom in an optical tweezer. *Phys. Rev. Lett.* **110**, 133001 (2013).

[ADS](#) [CAS](#) [PubMed](#) [Google Scholar](#)

52. 52.

Taichenachev, A. V. et al. Magnetic field-induced spectroscopy of forbidden optical transitions with application to lattice-based optical atomic clocks. *Phys. Rev. Lett.* **96**, 083001 (2006).

[ADS](#) [CAS](#) [PubMed](#) [Google Scholar](#)

53. 53.

Bali, S., O’Hara, K. M., Gehm, M. E., Granade, S. R. & Thomas, J. E. Quantum-diffractive background gas collisions in atom-trap heating and loss. *Phys. Rev. A* **60**, R29–R32 (1999).

[ADS](#) [CAS](#) [Google Scholar](#)

54. 54.

Van Dongen, J. et al. Trap-depth determination from residual gas collisions. *Phys. Rev. A* **84**, 022708 (2011).

[ADS](#) [Google Scholar](#)

55. 55.

Mitroy, J. & Zhang, J. Y. Dispersion and polarization interactions of the strontium atom. *Mol. Phys.* **108**, 1999–2006 (2010).

[ADS](#) [CAS](#) [Google Scholar](#)

56. 56.

Gibble, K. Scattering of cold-atom coherences by hot atoms: frequency shifts from background-gas collisions. *Phys. Rev. Lett.* **110**, 180802 (2013).

[ADS](#) [PubMed](#) [Google Scholar](#)

57. 57.

Bothwell, T. et al. JILA SrI optical lattice clock with uncertainty of  $2.0 \times 10^{-18}$ . *Metrologia* **56**, 065004 (2019).

[ADS](#) [CAS](#) [Google Scholar](#)

58. 58.

Savard, T. A., O’Hara, K. M. & Thomas, J. E. Laser-noise-induced heating in far-off resonance optical traps. *Phys. Rev. A* **56**, R1095–R1098 (1997).

[ADS](#) [CAS](#) [Google Scholar](#)

59. 59.

Gehm, M. E., O’Hara, K. M., Savard, T. A. & Thomas, J. E. Dynamics of noise-induced heating in atom traps. *Phys. Rev. A* **58**, 3914–3921 (1998).

[ADS](#) [CAS](#) [Google Scholar](#)

60. 60.

Bloom, B. J. et al. An optical lattice clock with accuracy and stability at the  $10^{-18}$  level. *Nature* **506**, 71–75 (2014).

[ADS](#) [CAS](#) [PubMed](#) [Google Scholar](#)

61. 61.

Ovsiannikov, V. D., Pal'chikov, V. G., Taichenachev, A. V., Yudin, V. I. & Katori, H. Multipole, nonlinear, and anharmonic uncertainties of clocks of Sr atoms in an optical lattice. *Phys. Rev. A* **88**, 013405 (2013).

[ADS](#) [Google Scholar](#)

62. 62.

Safronova, M. S., Zuhrianda, Z., Safronova, U. I. & Clark, C. W. Extracting transition rates from zero-polarizability spectroscopy. *Phys. Rev. A* **92**, 040501 (2015).

[ADS](#) [Google Scholar](#)

[Download references](#)

## Acknowledgements

We acknowledge discussions with R. B. Hutson, J. K. Thompson, M. Foss-Feig, S. Kolkowitz and J. Simon. We further acknowledge F. Vietmeyer and M. O. Brown for assistance in the design and development of our FPGA-based tweezer control system. This work was supported by ARO, AFOSR, DARPA, the National Science Foundation Physics Frontier Center at JILA (1734006) and NIST. M.A.N., E.O. and N.S. acknowledge support from the NRC research associateship programme.

## Author information

### Affiliations

1. JILA, University of Colorado and National Institute of Standards and Technology, Boulder, CO, USA

Aaron W. Young, William J. Eckner, William R. Milner, Dhruv Kedar, Matthew A. Norcia, Eric Oelker, Nathan Schine, Jun Ye & Adam M. Kaufman

2. Department of Physics, University of Colorado, Boulder, CO, USA

Aaron W. Young, William J. Eckner, William R. Milner, Dhruv Kedar, Matthew A. Norcia, Eric Oelker, Nathan Schine, Jun Ye & Adam M. Kaufman

## Authors

1. Aaron W. Young

[View author publications](#)

You can also search for this author in [PubMed](#) [Google Scholar](#)

2. William J. Eckner

[View author publications](#)

You can also search for this author in [PubMed](#) [Google Scholar](#)

3. William R. Milner

[View author publications](#)

You can also search for this author in [PubMed](#) [Google Scholar](#)

4. Dhruv Kedar

[View author publications](#)

You can also search for this author in [PubMed](#) [Google Scholar](#)

5. Matthew A. Norcia

[View author publications](#)

You can also search for this author in [PubMed](#) [Google Scholar](#)

6. Eric Oelker

[View author publications](#)

You can also search for this author in [PubMed](#) [Google Scholar](#)

7. Nathan Schine

[View author publications](#)

You can also search for this author in [PubMed](#) [Google Scholar](#)

8. Jun Ye

[View author publications](#)

You can also search for this author in [PubMed](#) [Google Scholar](#)

9. Adam M. Kaufman

[View author publications](#)

You can also search for this author in [PubMed](#) [Google Scholar](#)

## Contributions

A.W.Y., W.J.E., M.A.N., N.S. and A.M.K. built and operated the tweezer apparatus, and the silicon-crystal-stabilized clock laser was operated by W.R.M., D.K., E.O. and J.Y. All authors contributed to the data analysis and the development of the manuscript.

## Corresponding author

Correspondence to [Adam M. Kaufman](#).

## Ethics declarations

## Competing interests

The authors declare no competing interests.

# Additional information

**Peer review information** *Nature* thanks Ahmed Omran and the other, anonymous, reviewer(s) for their contribution to the peer review of this work. Peer reviewer reports are available.

**Publisher's note** Springer Nature remains neutral with regard to jurisdictional claims in published maps and institutional affiliations.

## Extended data figures and tables

### [Extended Data Fig. 1 Sideband cooling and inhomogeneous broadening.](#)

The trap frequency and cooling performance in the radial direction is uniform across the entire array, as further confirmed by spectra taken along a radial axis orthogonal to that of the data presented in Fig. 1d (left).

However, in a reduced  $6 \times 6$  region at the centre of the array (shown in the far-right inset), the axial cooling performance is vastly improved (right), with an average phonon occupation of  $\langle(\bar{n})\rangle = \{0.00\}_{-0.00}^{+0.06}$  before (after) the handoff. This is due to the comparable extent of the lattice beams to the tweezer array (the light-green contour in the far-right inset shows the region over which the lattice intensity stays within 90% of its maximal value). Each data point corresponds to 20 repetitions of the experiment. [Source data](#)

### [Extended Data Fig. 2 Lattice alignment.](#)

**a, b**, Spatial phase of the standing-wave lattice at each tweezer, inferred from measurements at 15 values of the lattice phase averaged over 100 trials (see [Supplementary Information](#)) with an intentional tilt (**a**, left) and properly aligned (**a**, right). These show that it is possible flatten the lattice relative to the entire tweezer array to within 1/10 of a lattice period (**b**). This allows for high-fidelity sideband cooling in all axes. ‘Cts’, counts; ‘arb.’, arbitrary units. [Source data](#)

## Extended Data Fig. 3 Timing of experimental sequence.

**a**, The green and black curves track the depths of the 515-nm and 813-nm tweezers, respectively. The coloured regions above and below the graph categorize each step of the experiment (described in more detail in Methods). We find that maintaining the 813-nm tweezers at a depth greater than  $20E_r$  during the ramp down improves the fidelity of the handoff procedure. Not shown is the time required to load atoms into the 515-nm tweezers from the magneto-optical traps used for initial trapping and cooling, which takes roughly 120 ms. LAC, light-assisted collisions. **b**, Zoomed-in view of our cooling procedure, showing the depth of the axial lattice. We perform two rounds of sideband cooling, indicated by the two regions shaded in grey. The first, done before ramping up the axial lattice, does not cool axial motion to the ground state. Instead, it is important for reducing the size of the atomic wave packet to ensure loading of a single lattice fringe.

## Extended Data Fig. 4 Measuring atom–laser coherence.

Fitting measured Ramsey fringes with fringes of a fixed frequency provides a conservative estimate of atom–laser coherence. Callouts share  $x$ -axis units with the main plot, and show the fitted Ramsey data (the same data as used in Fig. 2b). ‘pop.’, population. [Source data](#)

### **Extended Data Table 1 Relevant optical trapping parameters**

[Full size table](#)

### **Extended Data Table 2 Rates contributing to the predicted Ramsey lifetime**

[Full size table](#)

## **Supplementary information**

### Supplementary Information

This file contains Supplementary Text and Supplementary Figures S1–S5.

## [Peer Review File](#)

## **Source data**

[Source Data Fig. 1](#)

[Source Data Fig. 2](#)

[Source Data Fig. 3](#)

[Source Data Fig. 4](#)

[Source Data Extended Data Fig. 1](#)

[Source Data Extended Data Fig. 2](#)

[Source Data Extended Data Fig. 4](#)

## **Rights and permissions**

[Reprints and Permissions](#)

## **About this article**



Check for  
updates

## **Cite this article**

Young, A.W., Eckner, W.J., Milner, W.R. *et al.* Half-minute-scale atomic coherence and high relative stability in a tweezer clock. *Nature* **588**, 408–413 (2020). <https://doi.org/10.1038/s41586-020-3009-y>

## Download citation

- Received: 18 June 2020
- Accepted: 17 September 2020
- Published: 16 December 2020
- Issue Date: 17 December 2020
- DOI: <https://doi.org/10.1038/s41586-020-3009-y>

## Comments

By submitting a comment you agree to abide by our [Terms](#) and [Community Guidelines](#). If you find something abusive or that does not comply with our terms or guidelines please flag it as inappropriate.

[Access through your institution](#)

[Change institution](#)

[Buy or subscribe](#)

## Associated Content

*Nature* | News & Views

### [Quantum engineering for optical clocks](#)

- Christian Lisdat
- & Carsten Klemp

---

This article was downloaded by **calibre** from <https://www.nature.com/articles/s41586-020-3009-y>.

- Article
- [Published: 16 December 2020](#)

# Entanglement on an optical atomic-clock transition

- [Edwin Pedrozo-Peñaflor](#) [ORCID: orcid.org/0000-0003-4348-9910<sup>1 na1</sup>](#),
- [Simone Colombo](#) [ORCID: orcid.org/0000-0002-7713-6235<sup>1 na1</sup>](#),
- [Chi Shu](#) [ORCID: orcid.org/0000-0001-7294-8878<sup>1,2 na1</sup>](#),
- [Albert F. Adiyatullin](#)<sup>1</sup>,
- [Zeyang Li](#) [ORCID: orcid.org/0000-0001-6841-5905<sup>1</sup>](#),
- [Enrique Mendez](#)<sup>1</sup>,
- [Boris Braverman](#) [ORCID: orcid.org/0000-0001-5193-2711<sup>1 nAff5</sup>](#),
- [Akio Kawasaki](#) [ORCID: orcid.org/0000-0001-8353-8903<sup>1 nAff6</sup>](#),
- [Daisuke Akamatsu](#) [ORCID: orcid.org/0000-0002-3741-1765<sup>1,3</sup>](#),
- [Yanhong Xiao](#) [ORCID: orcid.org/0000-0003-0981-9429<sup>1,4</sup>](#) &
- [Vladan Vuletić](#) [ORCID: orcid.org/0000-0002-9786-0538<sup>1</sup>](#)

[Nature](#) volume 588, pages414–418(2020) [Cite this article](#)

- 1366 Accesses
- 236 Altmetric
- [Metrics details](#)

## Subjects

- [Atomic and molecular interactions with photons](#)
- [Quantum metrology](#)
- [Ultracold gases](#)

# Abstract

State-of-the-art atomic clocks are based on the precise detection of the energy difference between two atomic levels, which is measured in terms of the quantum phase accumulated over a given time interval<sup>1,2,3,4</sup>. The stability of optical-lattice clocks (OLCs) is limited both by the interrupted interrogation of the atomic system by the local-oscillator laser (Dick noise<sup>5</sup>) and by the standard quantum limit (SQL) that arises from the quantum noise associated with discrete measurement outcomes. Although schemes for removing the Dick noise have been recently proposed and implemented<sup>4,6,7,8</sup>, performance beyond the SQL by engineering quantum correlations (entanglement) between atoms<sup>9,10,11,12,13,14,15,16,17,18,19,20</sup> has been demonstrated only in proof-of-principle experiments with microwave clocks of limited stability. The generation of entanglement on an optical-clock transition and operation of an OLC beyond the SQL represent important goals in quantum metrology, but have not yet been demonstrated experimentally<sup>16</sup>. Here we report the creation of a many-atom entangled state on an OLC transition, and use it to demonstrate a Ramsey sequence with an Allan deviation below the SQL after subtraction of the local-oscillator noise. We achieve a metrological gain of  $\sqrt{4.4 \{-0.4\}^{+0.6}}$  decibels over the SQL by using an ensemble consisting of a few hundred ytterbium-171 atoms, corresponding to a reduction of the averaging time by a factor of  $2.8 \pm 0.3$ . Our results are currently limited by the phase noise of the local oscillator and Dick noise, but demonstrate the possible performance improvement in state-of-the-art OLCs<sup>1,2,3,4</sup> through the use of entanglement. This will enable further advances in timekeeping precision and accuracy, with many scientific and technological applications, including precision tests of the fundamental laws of physics<sup>21,22,23</sup>, geodesy<sup>24,25,26</sup> and gravitational-wave detection<sup>27</sup>.

[Access through your institution](#)

[Change institution](#)

[Buy or subscribe](#)

## Access options

## Subscribe to Journal

Get full journal access for 1 year

185,98 €

only 3,58 € per issue

[Subscribe](#)

All prices are NET prices.

VAT will be added later in the checkout.

## Rent or Buy article

Get time limited or full article access on ReadCube.

from \$8.99

[Rent or Buy](#)

All prices are NET prices.

## Additional access options:

- [Log in](#)
- [Access through your institution](#)
- [Learn about institutional subscriptions](#)

**Fig. 1: Setup and squeezed-clock sequence.**



**Fig. 2: Squeezed state tomography.**

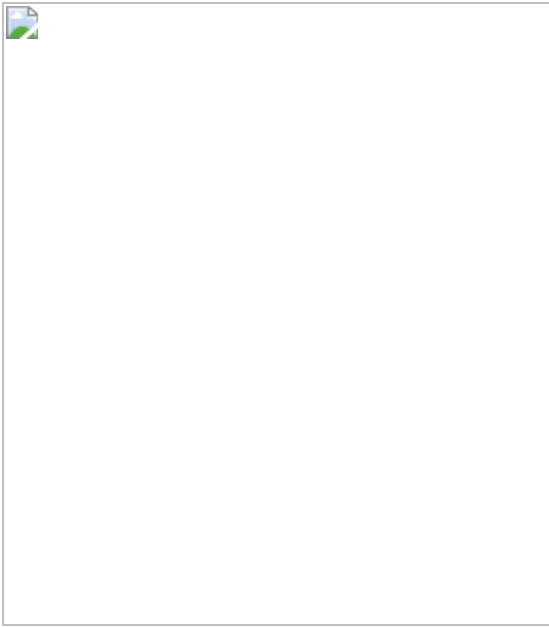


**Fig. 3: Spin noise and Wineland parameter of the clock transition as a function of time.**

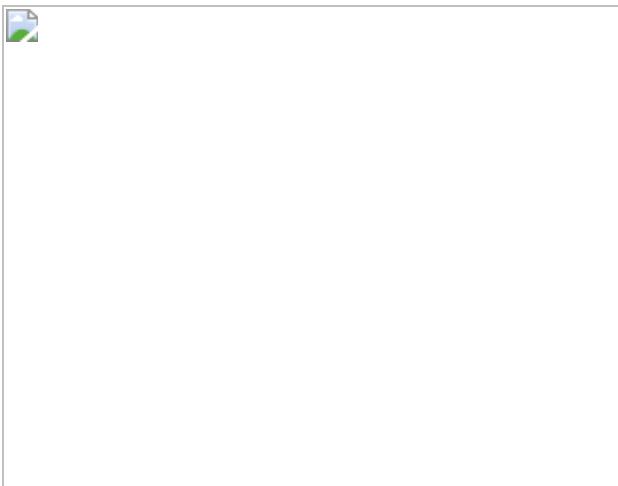


**Fig. 4: Stability improvement with the squeezed clock.**

## Data availability

All data obtained in the study are available from the corresponding author upon reasonable request.

# References

1. 1.

Ludlow, A. D., Boyd, M. M., Ye, J., Peik, E. & Schmidt, P. O. Optical atomic clocks. *Rev. Mod. Phys.* **87**, 637–701 (2015).

[ADS](#) [CAS](#) [Google Scholar](#)

2. 2.

Ushijima, I., Takamoto, M., Das, M., Ohkubo, T. & Katori, H. Cryogenic optical lattice clocks. *Nat. Photon.* **9**, 185–189 (2015).

[ADS](#) [CAS](#) [Google Scholar](#)

3. 3.

Oelker, E. et al. Demonstration of  $4.8 \times 10^{-17}$  stability at 1 s for two independent optical clocks. *Nat. Photon.* **13**, 714–719 (2019).

[ADS](#) [CAS](#) [Google Scholar](#)

4. 4.

Schioppo, M. et al. Ultrastable optical clock with two cold-atom ensembles. *Nat. Photon.* **11**, 48–52 (2017).

[ADS](#) [CAS](#) [Google Scholar](#)

5. 5.

Dick, G. J. *Local Oscillator Induced Instabilities in Trapped Ion Frequency Standards*. Report ADA502386 (California Institute of Technology, Pasadena Jet Propulsion Lab, 1987);  
<https://apps.dtic.mil/sti/citations/ADA502386>.

6. 6.

Norcia, M. A. et al. Seconds-scale coherence on an optical clock transition in a tweezer array. *Science* **366**, 93–97 (2019).

[ADS](#) [CAS](#) [PubMed](#) [Google Scholar](#)

7. 7.

Takamoto, M., Takano, T. & Katori, H. Frequency comparison of optical lattice clocks beyond the dick limit. *Nat. Photon.* **5**, 288–292 (2011).

[ADS](#) [CAS](#) [Google Scholar](#)

8. 8.

Nicholson, T. L. et al. Comparison of two independent Sr optical clocks with  $1 \times 10^{-17}$  stability at  $10^3$  s. *Phys. Rev. Lett.* **109**, 230801 (2012).

[ADS](#) [CAS](#) [PubMed](#) [Google Scholar](#)

9. 9.

Appel, J. et al. Mesoscopic atomic entanglement for precision measurements beyond the standard quantum limit. *Proc. Natl Acad. Sci. USA* **106**, 10960–10965 (2009).

[ADS](#) [CAS](#) [PubMed](#) [Google Scholar](#)

10. 10.

Takano, T., Fuyama, M., Namiki, R. & Takahashi, Y. Spin squeezing of a cold atomic ensemble with the nuclear spin of one-half. *Phys. Rev. Lett.* **102**, 033601 (2009).

[ADS](#) [CAS](#) [PubMed](#) [Google Scholar](#)

11. 11.

Gross, C., Zibold, T., Nicklas, E., Esteve, J. & Oberthaler, M. K. Nonlinear atom interferometer surpasses classical precision limit. *Nature* **464**, 1165–1169 (2010).

[ADS](#) [CAS](#) [PubMed](#) [Google Scholar](#)

12. 12.

Riedel, M. F. et al. Atom-chip-based generation of entanglement for quantum metrology. *Nature* **464**, 1170–1173 (2010).

[ADS](#) [CAS](#) [PubMed](#) [Google Scholar](#)

13. 13.

Schleier-Smith, M. H., Leroux, I. D. & Vuletić, V. Squeezing the collective spin of a dilute atomic ensemble by cavity feedback. *Phys. Rev. A* **81**, 021804 (2010).

[ADS](#) [Google Scholar](#)

14. 14.

Leroux, I. D., Schleier-Smith, M. H. & Vuletić, V. Implementation of cavity squeezing of a collective atomic spin. *Phys. Rev. Lett.* **104**, 073602 (2010).

[ADS](#) [PubMed](#) [Google Scholar](#)

15. 15.

Kruse, I. et al. Improvement of an atomic clock using squeezed vacuum. *Phys. Rev. Lett.* **117**, 143004 (2016).

[ADS](#) [CAS](#) [PubMed](#) [Google Scholar](#)

16. 16.

Pezzè, L., Smerzi, A., Oberthaler, M. K., Schmied, R. & Treutlein, P. Quantum metrology with nonclassical states of atomic ensembles. *Rev. Mod. Phys.* **90**, 035005 (2018).

[ADS](#) [MathSciNet](#) [Google Scholar](#)

17. 17.

Cox, K. C., Greve, G. P., Weiner, J. M. & Thompson, J. K. Deterministic squeezed states with collective measurements and feedback. *Phys. Rev. Lett.* **116**, 093602 (2016).

[ADS](#) [PubMed](#) [Google Scholar](#)

18. 18.

Hosten, O., Engelsen, N. J., Krishnakumar, R. & Kasevich, M. A. Measurement noise 100 times lower than the quantum-projection limit using entangled atoms. *Nature* **529**, 505–508 (2016).

[ADS](#) [CAS](#) [PubMed](#) [MATH](#) [Google Scholar](#)

19. 19.

Bohnet, J. G. et al. Quantum spin dynamics and entanglement generation with hundreds of trapped ions. *Science* **352**, 1297–1301 (2016).

[ADS](#) [MathSciNet](#) [CAS](#) [PubMed](#) [MATH](#) [Google Scholar](#)

20. 20.

Braverman, B. et al. Near-unitary spin squeezing in Yb 171. *Phys. Rev. Lett.* **122**, 223203 (2019).

[ADS](#) [CAS](#) [PubMed](#) [Google Scholar](#)

21. 21.

Wcisło, P. et al. New bounds on dark matter coupling from a global network of optical atomic clocks. *Sci. Adv.* **4**, eaau4869 (2018).

[ADS](#) [PubMed](#) [PubMed Central](#) [Google Scholar](#)

22. 22.

Safronova, M. S. et al. Search for new physics with atoms and molecules. *Rev. Mod. Phys.* **90**, 025008 (2018).

[ADS](#) [MathSciNet](#) [CAS](#) [Google Scholar](#)

23. 23.

Safronova, M. S. The search for variation of fundamental constants with clocks. *Ann. Phys.* **531**, 1800364 (2019).

[Google Scholar](#)

24. 24.

Lisdat, C. et al. A clock network for geodesy and fundamental science. *Nat. Commun.* **7**, 12443 (2016).

[ADS](#) [CAS](#) [PubMed](#) [PubMed Central](#) [Google Scholar](#)

25. 25.

Grotti, J. et al. Geodesy and metrology with a transportable optical clock. *Nat. Phys.* **14**, 437–441 (2018).

[CAS](#) [Google Scholar](#)

26. 26.

Takamoto, M. et al. Test of general relativity by a pair of transportable optical lattice clocks. *Nat. Photon.* **14**, 411–415 (2020).

[ADS](#) [CAS](#) [Google Scholar](#)

27. 27.

Kolkowitz, S. et al. Gravitational wave detection with optical lattice atomic clocks. *Phys. Rev. D* **94**, 124043 (2016).

[ADS](#) [Google Scholar](#)

28. 28.

Wineland, D. J., Bollinger, J. J., Itano, W. M. & Heinzen, D. J. Squeezed atomic states and projection noise in spectroscopy. *Phys. Rev. A* **50**, 67–88 (1994).

[ADS](#) [CAS](#) [PubMed](#) [Google Scholar](#)

29. 29.

Kitagawa, M. & Ueda, M. Squeezed spin states. *Phys. Rev. A* **47**, 5138–5143 (1993).

[ADS](#) [CAS](#) [PubMed](#) [Google Scholar](#)

30. 30.

Hamley, C. D., Gerving, C., Hoang, T., Bookjans, E. & Chapman, M. S. Spin-nematic squeezed vacuum in a quantum gas. *Nat. Phys.* **8**, 305–308 (2012).

[CAS](#) [Google Scholar](#)

31. 31.

Leroux, I. D., Schleier-Smith, M. H. & Vuletić, V. Orientation-dependent entanglement lifetime in a squeezed atomic clock. *Phys. Rev. Lett.* **104**, 250801 (2010).

[ADS](#) [PubMed](#) [Google Scholar](#)

32. 32.

Wineland, D. J. et al. Experimental issues in coherent quantum-state manipulation of trapped atomic ions. *J. Res. Natl. Inst. Stand. Technol.* **103**, 259–328 (1998).

[CAS](#) [PubMed](#) [PubMed Central](#) [Google Scholar](#)

33. 33.

Braverman, B., Kawasaki, A. & Vuletić, V. Impact of non-unitary spin squeezing on atomic clock performance. *New J. Phys.* **20**, 103019 (2018).

[ADS](#) [Google Scholar](#)

34. 34.

Matei, D. G. et al.  $1.5\mu\text{m}$  lasers with sub-10 MHz linewidth. *Phys. Rev. Lett.* **118**, 263202 (2017).

[ADS](#) [CAS](#) [PubMed](#) [Google Scholar](#)

35. 35.

Hu, L., Poli, N., Salvi, L. & Tino, G. M. Atom interferometry with the Sr optical clock transition. *Phys. Rev. Lett.* **119**, 263601 (2017).

[ADS](#) [PubMed](#) [Google Scholar](#)

36. 36.

Pospelov, M. et al. Detecting domain walls of axionlike models using terrestrial experiments. *Phys. Rev. Lett.* **110**, 021803 (2013).

[ADS](#) [CAS](#) [PubMed](#) [Google Scholar](#)

37. 37.

Riehle, F. Optical clock networks. *Nat. Photon.* **11**, 25–31 (2017).

[ADS](#) [CAS](#) [Google Scholar](#)

38. 38.

Al-Masoudi, A., Dörscher, S., Häfner, S., Sterr, U. & Lisdat, C. Noise and instability of an optical lattice clock. *Phys. Rev. A* **92**, 063814 (2015).

[ADS](#) [Google Scholar](#)

39. 39.

Kawasaki, A. et al. Geometrically asymmetric optical cavity for strong atom-photon coupling. *Phys. Rev. A* **99**, 013437 (2019).

[ADS](#) [CAS](#) [Google Scholar](#)

40. 40.

Blatt, S. et al. Rabi spectroscopy and excitation inhomogeneity in a one-dimensional optical lattice clock. *Phys. Rev. A* **80**, 052703 (2009).

[ADS](#) [Google Scholar](#)

41. 41.

Vallet, G. et al. A noise-immune cavity-assisted non-destructive detection for an optical lattice clock in the quantum regime. *New J. Phys.* **19**, 083002 (2017).

[ADS](#) [MathSciNet](#) [Google Scholar](#)

42. 42.

Yamoah, M. et al. Robust kHz-linewidth distributed Bragg reflector laser with optoelectronic feedback. *Opt. Express* **27**, 37714–37720 (2019).

[ADS](#) [CAS](#) [PubMed](#) [Google Scholar](#)

43. 43.

Zhang, W. et al. Reduction of residual amplitude modulation to  $1 \times 10^{-6}$  for frequency modulation and laser stabilization. *Opt. Lett.* **39**, 1980–1983 (2014).

[ADS](#) [CAS](#) [PubMed](#) [Google Scholar](#)

44. 44.

Śliwczyński, Ł., Krehlik, P., Czubla, A., Buczek, Ł. & Lipiński, M. Dissemination of time and RF frequency via a stabilized fibre optic link over a distance of 420 km. *Metrologia* **50**, 133 (2013).

[ADS](#) [Google Scholar](#)

45. 45.

Lee, W. et al. Ultrastable laser system using room-temperature optical cavity with  $4.8 \times 10^{-17}$  thermal noise limit. In *2019 Joint Conference of the IEEE International Frequency Control Symposium and European Frequency and Time Forum* 1–2 (IEEE, 2019).

[Download references](#)

## Acknowledgements

We thank H. Katori, W. Ketterle, A. Ludlow, M. Lukin, J. Ramette, G. Roati, A. Urvoy, Z. Vendeiro and J. Ye for discussions. This work was supported by NSF, DARPA, ONR and the NSF Center for Ultracold Atoms (CUA). S.C. and A.F.A. acknowledge support from the Swiss National Science Foundation (SNSF). B.B. acknowledges support from the National Science and Engineering Research Council of Canada.

## Author information

Author notes

## 1. Boris Braverman

Present address: Department of Physics and Max Planck Centre for Extreme and Quantum Photonics, University of Ottawa, Ottawa, Ontario, Canada

## 2. Akio Kawasaki

Present address: W. W. Hansen Experimental Physics Laboratory and Department of Physics, Stanford University, Stanford, CA, USA

## 3. These authors contributed equally: Edwin Pedrozo-Peñafield, Simone Colombo, Chi Shu

## Affiliations

### 1. Department of Physics, MIT-Harvard Center for Ultracold Atoms and Research Laboratory of Electronics, Massachusetts Institute of Technology, Cambridge, MA, USA

Edwin Pedrozo-Peñafield, Simone Colombo, Chi Shu, Albert F. Adiyatullin, Zeyang Li, Enrique Mendez, Boris Braverman, Akio Kawasaki, Daisuke Akamatsu, Yanhong Xiao & Vladan Vuletić

### 2. Department of Physics, Harvard University, Cambridge, MA, USA

Chi Shu

### 3. National Metrology Institute of Japan (NMIJ), National Institute of Advanced Industrial Science and Technology (AIST), Tsukuba, Japan

Daisuke Akamatsu

### 4. State Key Laboratory of Quantum Optics and Quantum Optics Devices, Institute of Laser Spectroscopy, and Collaborative Innovation Center of Extreme Optics, Shanxi University, Taiyuan, China

Yanhong Xiao

## Authors

1. Edwin Pedrozo-Peñafield  
[View author publications](#)

You can also search for this author in [PubMed](#) [Google Scholar](#)

2. Simone Colombo  
[View author publications](#)

You can also search for this author in [PubMed](#) [Google Scholar](#)

3. Chi Shu  
[View author publications](#)

You can also search for this author in [PubMed](#) [Google Scholar](#)

4. Albert F. Adiyatullin  
[View author publications](#)

You can also search for this author in [PubMed](#) [Google Scholar](#)

5. Zeyang Li  
[View author publications](#)

You can also search for this author in [PubMed](#) [Google Scholar](#)

6. Enrique Mendez  
[View author publications](#)

You can also search for this author in [PubMed](#) [Google Scholar](#)

7. Boris Braverman  
[View author publications](#)

You can also search for this author in [PubMed](#) [Google Scholar](#)

8. Akio Kawasaki  
[View author publications](#)

You can also search for this author in [PubMed](#) [Google Scholar](#)

9. Daisuke Akamatsu

[View author publications](#)

You can also search for this author in [PubMed](#) [Google Scholar](#)

10. Yanhong Xiao

[View author publications](#)

You can also search for this author in [PubMed](#) [Google Scholar](#)

11. Vladan Vuletić

[View author publications](#)

You can also search for this author in [PubMed](#) [Google Scholar](#)

## Contributions

A.K., B.B., C.S., E.P.-P., S.C., A.F.A., Z.L., E.M. and V.V. contributed to the building of the experiment. E.P.-P., S.C. and C.S. led the experimental efforts and simulations. S.C., A.F.A., C.S. and E.P.-P. contributed to the data analysis. V.V. conceived and supervised the experiment. S.C. and V.V. wrote the manuscript. All authors discussed the experiment implementation and results and contributed to the manuscript.

## Corresponding author

Correspondence to [Vladan Vuletić](#).

## Ethics declarations

## Competing interests

The authors declare no competing interests.

# Additional information

**Peer review information** *Nature* thanks the anonymous reviewer(s) for their contribution to the peer review of this work. Peer reviewer reports are available.

**Publisher's note** Springer Nature remains neutral with regard to jurisdictional claims in published maps and institutional affiliations.

## Supplementary information

### [Peer Review File](#)

## Rights and permissions

### [Reprints and Permissions](#)

## About this article



Check for  
updates

## Cite this article

Pedrozo-Peñaflor, E., Colombo, S., Shu, C. *et al.* Entanglement on an optical atomic-clock transition. *Nature* **588**, 414–418 (2020).  
<https://doi.org/10.1038/s41586-020-3006-1>

### [Download citation](#)

- Received: 12 June 2020
- Accepted: 21 October 2020

- Published: 16 December 2020
- Issue Date: 17 December 2020
- DOI: <https://doi.org/10.1038/s41586-020-3006-1>

## Comments

By submitting a comment you agree to abide by our [Terms](#) and [Community Guidelines](#). If you find something abusive or that does not comply with our terms or guidelines please flag it as inappropriate.

[Access through your institution](#)

[Change institution](#)

[Buy or subscribe](#)

## Associated Content

*Nature* | News & Views

### [Quantum engineering for optical clocks](#)

- Christian Lisdat
- & Carsten Klemp

---

This article was downloaded by **calibre** from <https://www.nature.com/articles/s41586-020-3006-1>

- Article
- [Published: 16 December 2020](#)

# Tuning the Chern number in quantum anomalous Hall insulators

- [Yi-Fan Zhao](#) [ORCID: orcid.org/0000-0002-8605-9745<sup>1 na1</sup>](#),
- [Ruoxi Zhang<sup>1 na1</sup>](#),
- [Ruobing Mei<sup>1 na1</sup>](#),
- [Ling-Jie Zhou<sup>1</sup>](#),
- [Hemian Yi<sup>1</sup>](#),
- [Ya-Qi Zhang<sup>1</sup>](#),
- [Jiabin Yu<sup>1</sup>](#),
- [Run Xiao<sup>1</sup>](#),
- [Ke Wang<sup>2</sup>](#),
- [Nitin Samarth<sup>1</sup>](#),
- [Moses H. W. Chan<sup>1</sup>](#),
- [Chao-Xing Liu](#) [ORCID: orcid.org/0000-0003-1881-1365<sup>1</sup>](#) &
- [Cui-Zu Chang](#) [ORCID: orcid.org/0000-0003-3515-2955<sup>1</sup>](#)

[Nature](#) volume 588, pages419–423(2020)[Cite this article](#)

- 1678 Accesses
- 90 Altmetric
- [Metrics details](#)

## Subjects

- [Quantum Hall](#)
- [Surfaces, interfaces and thin films](#)
- [Topological insulators](#)

## Abstract

A quantum anomalous Hall (QAH) state is a two-dimensional topological insulating state that has a quantized Hall resistance of  $h/(Ce^2)$  and vanishing longitudinal resistance under zero magnetic field (where  $h$  is the Planck constant,  $e$  is the elementary charge, and the Chern number  $C$  is an integer)<sup>1,2</sup>. The QAH effect has been realized in magnetic topological insulators<sup>3,4,5,6,7,8,9</sup> and magic-angle twisted bilayer graphene<sup>10,11</sup>. However, the QAH effect at zero magnetic field has so far been realized only for  $C = 1$ . Here we realize a well quantized QAH effect with tunable Chern number (up to  $C = 5$ ) in multilayer structures consisting of alternating magnetic and undoped topological insulator layers, fabricated using molecular beam epitaxy. The Chern number of these QAH insulators is determined by the number of undoped topological insulator layers in the multilayer structure. Moreover, we demonstrate that the Chern number of a given multilayer structure can be tuned by varying either the magnetic doping concentration in the magnetic topological insulator layers or the thickness of the interior magnetic topological insulator layer. We develop a theoretical model to explain our experimental observations and establish phase diagrams for QAH insulators with high, tunable Chern number. The realization of such insulators facilitates the application of dissipationless chiral edge currents in energy-efficient electronic devices, and opens up opportunities for developing multi-channel quantum computing and higher-capacity chiral circuit interconnects.

[Access through your institution](#)

[Change institution](#)

[Buy or subscribe](#)

## Access options

Subscribe to Journal

Get full journal access for 1 year

185,98 €

only 3,58 € per issue

[Subscribe](#)

All prices are NET prices.

VAT will be added later in the checkout.

Rent or Buy article

Get time limited or full article access on ReadCube.

from \$8.99

[Rent or Buy](#)

All prices are NET prices.

### **Additional access options:**

- [Log in](#)
- [Access through your institution](#)
- [Learn about institutional subscriptions](#)

**Fig. 1: The high-C QAH effect in magnetic–undoped topological insulator multilayer structures.**



**Fig. 2: Observations of the high-C QAH effect in magnetic–undoped topological insulator multilayer structures.**



**Fig. 3: Demonstration of high- $C$  QAH states in magnetic–undoped topological insulator multilayer structures.**



**Fig. 4: Tunable Chern number in QAH insulators.**



## Data availability

The datasets generated and/or analysed during this study are available from the corresponding authors on reasonable request.

## Code availability

The codes used in theoretical simulations and calculations are available from the corresponding authors on reasonable request.

## References

1. 1.

Haldane, F. D. M. Model for a quantum Hall effect without Landau levels: condensed-matter realization of the “parity anomaly”. *Phys. Rev. Lett.* **61**, 2015–2018 (1988).

[ADS](#) [CAS](#) [Article](#) [Google Scholar](#)

2. 2.

Yu, R. et al. Quantized anomalous Hall effect in magnetic topological insulators. *Science* **329**, 61–64 (2010).

[ADS](#) [CAS](#) [Article](#) [Google Scholar](#)

3. 3.

Chang, C. Z. et al. Experimental observation of the quantum anomalous Hall effect in a magnetic topological insulator. *Science* **340**, 167–170 (2013).

[ADS](#) [CAS](#) [Article](#) [Google Scholar](#)

4. 4.

Chang, C. Z. et al. High-precision realization of robust quantum anomalous Hall state in a hard ferromagnetic topological insulator. *Nat. Mater.* **14**, 473–477 (2015).

[ADS](#) [CAS](#) [Article](#) [Google Scholar](#)

5. 5.

Deng, Y. et al. Quantum anomalous Hall effect in intrinsic magnetic topological insulator. *Science* **367**, 895–900 (2020).

[ADS](#) [CAS](#) [Article](#) [Google Scholar](#)

6. 6.

Kou, X. F. et al. Scale-invariant quantum anomalous Hall effect in magnetic topological insulators beyond the two-dimensional limit. *Phys. Rev. Lett.* **113**, 137201 (2014).

[ADS](#) [Article](#) [Google Scholar](#)

7. 7.

Checkelsky, J. G. et al. Trajectory of the anomalous Hall effect towards the quantized state in a ferromagnetic topological insulator. *Nat. Phys.* **10**, 731–736 (2014).

[CAS](#) [Article](#) [Google Scholar](#)

8. 8.

Mogi, M. et al. Magnetic modulation doping in topological insulators toward higher-temperature quantum anomalous Hall effect. *Appl. Phys. Lett.* **107**, 182401 (2015).

[ADS](#) [Article](#) [Google Scholar](#)

9. 9.

Ou, Y. et al. Enhancing the quantum anomalous Hall effect by magnetic codoping in a topological insulator. *Adv. Mater.* **30**, 1703062 (2018).

[Article](#) [Google Scholar](#)

10. 10.

Serlin, M. et al. Intrinsic quantized anomalous Hall effect in a moiré heterostructure. *Science* **367**, 900–903 (2020).

[ADS](#) [CAS](#) [Article](#) [Google Scholar](#)

11. 11.

Sharpe, A. L. et al. Emergent ferromagnetism near three-quarters filling in twisted bilayer graphene. *Science* **365**, 605–608 (2019).

[ADS](#) [CAS](#) [Article](#) [Google Scholar](#)

12. 12.

Thouless, D. J. et al. Quantized Hall conductance in a two-dimensional periodic potential. *Phys. Rev. Lett.* **49**, 405–408 (1982).

[ADS](#) [CAS](#) [Article](#) [Google Scholar](#)

13. 13.

Weng, H. M. et al. Quantum anomalous Hall effect and related topological electronic states. *Adv. Phys.* **64**, 227–282 (2015).

[ADS](#) [Article](#) [Google Scholar](#)

14. 14.

Liu, C. X. et al. Quantum anomalous Hall effect in  $Hg_{1-y}Mn_yTe$  quantum wells. *Phys. Rev. Lett.* **101**, 146802 (2008).

[ADS](#) [Article](#) [Google Scholar](#)

15. 15.

Qi, X. L., Hughes, T. L. & Zhang, S. C. Topological field theory of time-reversal invariant insulators. *Phys. Rev. B* **78**, 195424 (2008).

[ADS](#) [Article](#) [Google Scholar](#)

16. 16.

Landauer, R. Spatial variation of currents and fields due to localized scatterers in metallic conduction. *IBM J. Res. Develop.* **1**, 223–231 (1957).

[MathSciNet](#) [Article](#) [Google Scholar](#)

17. 17.

Chang, C. Z. et al. Zero-field dissipationless chiral edge transport and the nature of dissipation in the quantum anomalous Hall state. *Phys. Rev. Lett.* **115**, 057206 (2015).

[ADS](#) [Article](#) [Google Scholar](#)

18. 18.

Wang, J. et al. Quantum anomalous Hall effect with higher plateaus. *Phys. Rev. Lett.* **111**, 136801 (2013).

[ADS](#) [Article](#) [Google Scholar](#)

19. 19.

Fang, C., Gilbert, M. J. & Bernevig, B. A. Large-Chern-number quantum anomalous Hall effect in thin-film topological crystalline insulators. *Phys. Rev. Lett.* **112**, 046801 (2014).

[ADS](#) [Article](#) [Google Scholar](#)

20. 20.

Ge, J. et al. High-Chern-number and high-temperature quantum Hall effect without Landau levels. *Natl Sci. Rev.* **7**, 1280–1287 (2020).

[CAS](#) [Article](#) [Google Scholar](#)

21. 21.

Chen, G. R. et al. Tunable correlated Chern insulator and ferromagnetism in a moiré superlattice. *Nature* **579**, 56–61 (2020); publisher correction **581**, E3 (2020).

[ADS](#) [CAS](#) [Article](#) [Google Scholar](#)

22. 22.

Jiang, H. et al. Quantum anomalous Hall effect with tunable Chern number in magnetic topological insulator film. *Phys. Rev. B* **85**, 045445 (2012).

[ADS](#) [Article](#) [Google Scholar](#)

23. 23.

Zhang, J. S. et al. Topology-driven magnetic quantum phase transition in topological insulators. *Science* **339**, 1582–1586 (2013).

[ADS](#) [CAS](#) [Article](#) [Google Scholar](#)

24. 24.

Chang, C. Z. et al. Chemical-potential-dependent gap opening at the Dirac surface states of  $\text{Bi}_2\text{Se}_3$  induced by aggregated substitutional Cr atoms. *Phys. Rev. Lett.* **112**, 056801 (2014).

[ADS](#) [Article](#) [Google Scholar](#)

25. 25.

Wang, F. et al. Chromium-induced ferromagnetism with perpendicular anisotropy in topological crystalline insulator SnTe (111) thin films. *Phys. Rev. B* **97**, 115414 (2018).

[ADS](#) [CAS](#) [Article](#) [Google Scholar](#)

26. 26.

Burkov, A. A. & Balents, L. Weyl semimetal in a topological insulator multilayer. *Phys. Rev. Lett.* **107**, 127205 (2011).

[ADS](#) [CAS](#) [Article](#) [Google Scholar](#)

27. 27.

Jiang, G. et al. Quantum anomalous Hall multilayers grown by molecular beam epitaxy. *Chin. Phys. Lett.* **35**, 076802 (2018).

[ADS](#) [Article](#) [Google Scholar](#)

28. 28.

Wang, J. et al. Anomalous edge transport in the quantum anomalous Hall state. *Phys. Rev. Lett.* **111**, 086803 (2013).

[ADS](#) [Article](#) [Google Scholar](#)

29. 29.

Feng, X. et al. Thickness dependence of the quantum anomalous Hall effect in magnetic topological insulator films. *Adv. Mater.* **28**, 6386–6390 (2016).

[CAS](#) [Article](#) [Google Scholar](#)

30. 30.

Liu, C. X. et al. Model Hamiltonian for topological insulators. *Phys. Rev. B* **82**, 045122 (2010).

[ADS](#) [Article](#) [Google Scholar](#)

31. 31.

Zhang, H. J. et al. Topological insulators in  $\text{Bi}_2\text{Se}_3$ ,  $\text{Bi}_2\text{Te}_3$  and  $\text{Sb}_2\text{Te}_3$  with a single Dirac cone on the surface. *Nat. Phys.* **5**, 438–442 (2009).

[CAS](#) [Article](#) [Google Scholar](#)

32. 32.

Li, R. D. et al. Dynamical axion field in topological magnetic insulators. *Nat. Phys.* **6**, 284–288 (2010).

[CAS](#) [Article](#) [Google Scholar](#)

33. 33.

Wang, J., Lian, B. & Zhang, S. C. Dynamical axion field in a magnetic topological insulator superlattice. *Phys. Rev. B* **93**, 045115 (2016).

[ADS](#) [Article](#) [Google Scholar](#)

[Download references](#)

## Acknowledgements

We are grateful to Y. T. Cui, J. Jain, W. D. Wu, D. Xiao and X. D. Xu for discussion. This work was primarily supported by a DOE grant (DE-SC0019064), including sample synthesis, transport measurements and theoretical calculations. The sample characterization was partially supported by an ARO Young Investigator Program Award (W911NF1810198), an NSF-CAREER award (DMR-1847811) and the Gordon and Betty Moore Foundation's EPiQS Initiative (GBMF9063 to C.Z.C.). Part of the measurements at dilution-refrigerator temperature is supported by NSF grant DMR-1707340. N.S. and R.X. acknowledge support from DOE EFRC grant DE-SC0019331.

## Author information

Author notes

1. These authors contributed equally: Yi-Fan Zhao, Ruoxi Zhang, Ruobing Mei

## Affiliations

1. Department of Physics, The Pennsylvania State University, University Park, PA, USA

Yi-Fan Zhao, Ruoxi Zhang, Ruobing Mei, Ling-Jie Zhou, Hemian Yi, Ya-Qi Zhang, Jiabin Yu, Run Xiao, Nitin Samarth, Moses H. W. Chan, Chao-Xing Liu & Cui-Zu Chang

2. Materials Research Institute, The Pennsylvania State University, University Park, PA, USA

Ke Wang

## Authors

1. Yi-Fan Zhao

[View author publications](#)

You can also search for this author in [PubMed](#) [Google Scholar](#)

2. Ruoxi Zhang

[View author publications](#)

You can also search for this author in [PubMed](#) [Google Scholar](#)

3. Ruobing Mei

[View author publications](#)

You can also search for this author in [PubMed](#) [Google Scholar](#)

4. Ling-Jie Zhou

[View author publications](#)

You can also search for this author in [PubMed](#) [Google Scholar](#)

5. Hemian Yi

[View author publications](#)

You can also search for this author in [PubMed](#) [Google Scholar](#)

6. Ya-Qi Zhang

[View author publications](#)

You can also search for this author in [PubMed](#) [Google Scholar](#)

7. Jiabin Yu

[View author publications](#)

You can also search for this author in [PubMed](#) [Google Scholar](#)

8. Run Xiao

[View author publications](#)

You can also search for this author in [PubMed](#) [Google Scholar](#)

9. Ke Wang

[View author publications](#)

You can also search for this author in [PubMed](#) [Google Scholar](#)

10. Nitin Samarth

[View author publications](#)

You can also search for this author in [PubMed](#) [Google Scholar](#)

11. Moses H. W. Chan

[View author publications](#)

You can also search for this author in [PubMed](#) [Google Scholar](#)

12. Chao-Xing Liu

[View author publications](#)

You can also search for this author in [PubMed](#) [Google Scholar](#)

13. Cui-Zu Chang

[View author publications](#)

You can also search for this author in [PubMed](#) [Google Scholar](#)

## Contributions

C.-Z.C. conceived and designed the experiment. Y.-F.Z., L.-J.Z. and Y.-Q.Z. grew the magnetic TI/TI multilayer samples and carried out the PPMS transport measurements, with help from C.-Z.C. K.W. performed the TEM measurements. R.Z., L.-J.Z. and Y.-Q.Z. carried out the dilution transport measurements, with help from M.H.W.C. and C.-Z.C. R.M., J.Y. and C.-X.L. did all calculations and provided theoretical support. Y.-F.Z., R.Z., R.M., C.-X.L. and C.-Z.C. analysed the data and wrote the manuscript, with input from all authors.

## Corresponding authors

Correspondence to [Chao-Xing Liu](#) or [Cui-Zu Chang](#).

## Ethics declarations

## Competing interests

The authors declare no competing interests.

## Additional information

**Peer review information** *Nature* thanks Xianhui Chen, Sanfeng Wu and the other, anonymous, reviewer(s) for their contribution to the peer review of this work. Peer reviewer reports are available.

**Publisher's note** Springer Nature remains neutral with regard to jurisdictional claims in published maps and institutional affiliations.

## Extended data figures and tables

### [Extended Data Fig. 1 Characterization of magnetic TI/TI multilayer samples.](#)

**a**, RHEED patterns of the heat-treated SrTiO<sub>3</sub>(111) substrate. The reconstruction pattern indicates its atomic flat surface, which is crucial for

the MBE growth of the high-quality TI films. **b**, RHEED patterns of the [3QL Cr-doped  $(\text{Bi},\text{Sb})_2\text{Te}_3$ –4QL  $(\text{Bi},\text{Sb})_2\text{Te}_3$ ]<sub>2</sub>–3QL Cr-doped  $(\text{Bi},\text{Sb})_2\text{Te}_3$  sample. The sharp and streaky  $1 \times 1$  patterns indicate the high quality of our magnetic TI/TI multilayer samples. **c**, **d**, STEM images of the  $m = 2$  (**c**) and  $m = 3$  (**d**) magnetic TI/TI multilayer samples grown on  $\text{SrTiO}_3$  substrate (left), accompanied by the energy-dispersive spectroscopy maps of Cr distribution (right).

### Extended Data Fig. 2 Transport results for the $C = 1$ sample.

**a**, Dependence of  $\rho_{yx}(0)$  (blue squares) and  $\rho_{xx}(0)$  (red circles) on  $T$ . All measurements were taken at  $\mu_0H = 0$  T after magnetic training. **b**, **c**, Dependence of  $\rho_{yx}$  (**b**) and  $\rho_{xx}$  (**c**) on  $\mu_0H$ , measured at different temperatures and  $V_g = V_{g,0}$ . **d**–**g**, Dependence of  $\rho_{yx}$  (**d**, **e**) and  $\rho_{xx}$  (**f**, **g**) on  $\mu_0H$ , measured at different gate voltages (**d**, **f**,  $V_g < V_{g,0}$ ; **e**, **g**,  $V_g \geq V_{g,0}$ ) and  $T = 25$  mK. When  $V_g$  is tuned away from  $V_{g,0}$ ,  $\rho_{yx}$  and  $\rho_{xx}$  show additional transition features once the external magnetic field changes the polarity. We speculate that these features are probably a result of the heating generated in the dilution fridge and/or the indium contacts used in our samples.

### Extended Data Fig. 3 Transport results for the $C = 2$ sample.

As in Extended Data Fig. 2, but for the  $C = 2$  sample.

### Extended Data Fig. 4 Transport results for the $C = 3$ sample.

As in Extended Data Fig. 2, but for the  $C = 3$  sample.

### Extended Data Fig. 5 Transport results of the $C = 4$ sample.

As in Extended Data Fig. 2, but for the  $C = 4$  sample.

### Extended Data Fig. 6 Transport results of the $C = 5$ sample.

As in Extended Data Fig. 2, but for the  $C = 5$  sample.

## Extended Data Fig. 7 Hall and longitudinal conductance results for the $C = 1\text{--}5$ samples.

**a–e**, Dependence of the longitudinal conductance  $\sigma_{xx}$  (red) and Hall conductance  $\sigma_{xy}$  (blue) on  $\mu_0H$  for the  $C = 1\text{--}5$  samples. All measurements were taken at the charge-neutral point ( $V_g = V_{g,0}$ ) and  $T = 25$  mK. **f–j**, Dependence of  $\sigma_{xy}(0)$  (blue squares) and  $\sigma_{xx}(0)$  (red circles) on gate voltage ( $V_g - V_{g,0}$ ) for the  $C = 1\text{--}5$  samples. All measurements were taken at  $T = 25$  mK and  $\mu_0H = 0$  T after magnetic training.

## Extended Data Fig. 8 The high- $C$ QAH effect observed in another group of magnetic TI/TI multilayer samples.

**a–d**, Dependence of  $\rho_{xx}$  (red) and  $\rho_{yx}$  (blue) on  $\mu_0H$ , measured at the charge-neutral point ( $V_g = V_{g,0}$ ) and  $T = 25$  mK.  $\rho_{yx}(0)$  displays the quantized values of  $0.494h/e^2$ ,  $0.307h/e^2$ ,  $0.231h/e^2$  and  $0.169h/e^2$  for the samples with  $C = 2$ ,  $3$ ,  $4$  and  $5$ , respectively. The corresponding  $\rho_{xx}(0)$  values are  $0.010h/e^2$ ,  $0.050h/e^2$ ,  $0.039h/e^2$  and  $0.087h/e^2$ .  $V_{g,0}$  values for the four samples are  $+15$  V ( $C = 2$ ),  $-3$  V ( $C = 3$ ),  $-15$  V ( $C = 4$ ) and  $+5$  V ( $C = 5$ ). **e–h**, Dependence of  $\rho_{yx}(0)$  (blue squares) and  $\rho_{xx}(0)$  (red circles) on gate voltage ( $V_g - V_{g,0}$ ) for the  $C = 2\text{--}5$  samples. All measurements were taken at  $T = 25$  mK and  $\mu_0H = 0$  T after magnetic training.

## Extended Data Fig. 9 Chern number tuned by varying the Cr doping level in magnetic TI layers.

**a–d**, Dependence of  $\rho_{xx}$  (red) and  $\rho_{yx}$  (blue) on  $\mu_0H$  for the  $m = 2$  sample, with different Cr doping levels  $x$ . All measurements were taken at the charge-neutral point ( $V_g = V_{g,0}$ ) and  $T = 25$  mK.  $\rho_{yx}(0)$  displays the quantized values of  $0.969h/e^2$ ,  $0.994h/e^2$ ,  $0.498h/e^2$  and  $0.497h/e^2$  for the samples with  $x = 0.13$ ,  $0.15$ ,  $0.24$  and  $0.35$ , respectively. The corresponding  $\rho_{xx}(0)$  value are  $0.078h/e^2$ ,  $0.002h/e^2$ ,  $0.008h/e^2$  and  $0.010h/e^2$ . **e–h**, Dependence of  $\rho_{yx}(0)$  (blue squares) and  $\rho_{xx}(0)$  (red circles) on gate voltage

$(V_g - V_{g,0})$  for  $x = 0.13, 0.15, 0.24$  and  $0.35$ . All measurements were taken at  $T = 25$  mK and  $\mu_0 H = 0$  T after magnetic training.

## **Extended Data Fig. 10 Chern number tuned by controlling the thickness of the middle magnetic TI layer.**

**a–d**, Dependence of  $\rho_{xx}$  (red) and  $\rho_{yx}$  (blue) on  $\mu_0 H$  for the  $m = 2$  sample, with different middle magnetic TI layer thicknesses  $d$ . All measurements were taken at the charge-neutral point ( $V_g = V_{g,0}$ ) and  $T = 25$  mK.  $\rho_{yx}(0)$  displays the quantized values of  $0.995h/e^2$ ,  $0.996h/e^2$ ,  $0.469h/e^2$ ,  $0.498h/e^2$  and  $0.490h/e^2$  for the samples with  $d = 0, 1, 2, 3$  and  $4$ , respectively. The corresponding  $\rho_{xx}(0)$  values are  $0.0001h/e^2$ ,  $0.0009h/e^2$ ,  $0.089h/e^2$ ,  $0.008h/e^2$  and  $0.024h/e^2$ . **e–h**, Dependence of  $\rho_{yx}(0)$  (blue squares) and  $\rho_{xx}(0)$  (red circles) on gate voltage ( $V_g - V_{g,0}$ ) for  $d = 0, 1, 2, 3$  and  $4$ . All measurements were taken at  $T = 25$  mK and  $\mu_0 H = 0$  T after magnetic training. Because the  $d = 2$  sample is near the topological phase transition regime and therefore has a smaller hybridization gap (Fig. 4d), it has a larger  $\rho_{xx}$ . For the  $d = 4$  sample, the larger  $\rho_{xx}$  is probably induced by the enhanced dissipative quasi-helical side surface states and/or residual bulk carriers with increasing sample thickness.

## **Supplementary information**

### **Supplementary Information**

This file contains Supplementary Figures, Supplementary Text and References.

### **Peer Review File**

## **Rights and permissions**

### **Reprints and Permissions**

# About this article



Check for  
updates

## Cite this article

Zhao, YF., Zhang, R., Mei, R. *et al.* Tuning the Chern number in quantum anomalous Hall insulators. *Nature* **588**, 419–423 (2020).  
<https://doi.org/10.1038/s41586-020-3020-3>

[Download citation](#)

- Received: 28 June 2020
- Accepted: 02 October 2020
- Published: 16 December 2020
- Issue Date: 17 December 2020
- DOI: <https://doi.org/10.1038/s41586-020-3020-3>

## Comments

By submitting a comment you agree to abide by our [Terms](#) and [Community Guidelines](#). If you find something abusive or that does not comply with our terms or guidelines please flag it as inappropriate.

[Access through your institution](#)

[Change institution](#)

[Buy or subscribe](#)

| [Section menu](#) | [Main menu](#) |

- Article
- [Published: 16 December 2020](#)

# Topological superconductivity in a van der Waals heterostructure

- [Shawulienu Kezilebieke](#) ORCID: [orcid.org/0000-0003-4166-5079<sup>1</sup>](https://orcid.org/0000-0003-4166-5079),
- [Md Nurul Huda<sup>1</sup>](#),
- [Viliam Vaňo](#) ORCID: [orcid.org/0000-0003-1050-3931<sup>1</sup>](https://orcid.org/0000-0003-1050-3931),
- [Markus Aapro<sup>1</sup>](#),
- [Somesh C. Ganguli<sup>1</sup>](#),
- [Orlando J. Silveira<sup>1</sup>](#),
- [Szczepean Głodzik<sup>2</sup>](#),
- [Adam S. Foster](#) ORCID: [orcid.org/0000-0001-5371-5905<sup>1,3</sup>](https://orcid.org/0000-0001-5371-5905),
- [Teemu Ojanen](#) ORCID: [orcid.org/0000-0003-3298-1424<sup>4,5</sup>](https://orcid.org/0000-0003-3298-1424) &
- [Peter Liljeroth](#) ORCID: [orcid.org/0000-0003-1253-8097<sup>1</sup>](https://orcid.org/0000-0003-1253-8097)

[Nature](#) volume 588, pages424–428(2020) [Cite this article](#)

- 2663 Accesses
- 96 Altmetric
- [Metrics details](#)

## Subjects

- [Topological matter](#)
- [Two-dimensional materials](#)

## Abstract

Exotic states such as topological insulators, superconductors and quantum spin liquids are often challenging or impossible to create in a single material<sup>1,2,3</sup>. For example, it is unclear whether topological superconductivity, which has been suggested to be a key ingredient for topological quantum computing, exists in any naturally occurring material<sup>4,5,6,7,8,9</sup>. The problem can be circumvented by deliberately selecting the combination of materials in heterostructures so that the desired physics emerges from interactions between the different components<sup>1,10,11,12,13,14,15</sup>. Here we use this designer approach to fabricate van der Waals heterostructures that combine a two-dimensional (2D) ferromagnet with a superconductor, and we observe 2D topological superconductivity in the system. We use molecular-beam epitaxy to grow 2D islands of ferromagnetic chromium tribromide<sup>16</sup> on superconducting niobium diselenide. We then use low-temperature scanning tunnelling microscopy and spectroscopy to reveal the signatures of one-dimensional Majorana edge modes. The fabricated 2D van der Waals heterostructure provides a high-quality, tunable system that can be readily integrated into device structures that use topological superconductivity. The layered heterostructures can be readily accessed by various external stimuli, potentially allowing external control of 2D topological superconductivity through electrical<sup>17</sup>, mechanical<sup>18</sup>, chemical<sup>19</sup> or optical means<sup>20</sup>.

[Access through your institution](#)

[Change institution](#)

[Buy or subscribe](#)

## Access options

Subscribe to Journal

Get full journal access for 1 year

185,98 €

only 3,58 € per issue

[Subscribe](#)

All prices are NET prices.  
VAT will be added later in the checkout.

Rent or Buy article

Get time limited or full article access on ReadCube.

from \$8.99

[Rent or Buy](#)

All prices are NET prices.

### **Additional access options:**

- [Log in](#)
- [Access through your institution](#)
- [Learn about institutional subscriptions](#)

**Fig. 1: Realization of topological superconductivity in CrBr<sub>3</sub>-NbSe<sub>2</sub> heterostructures.**

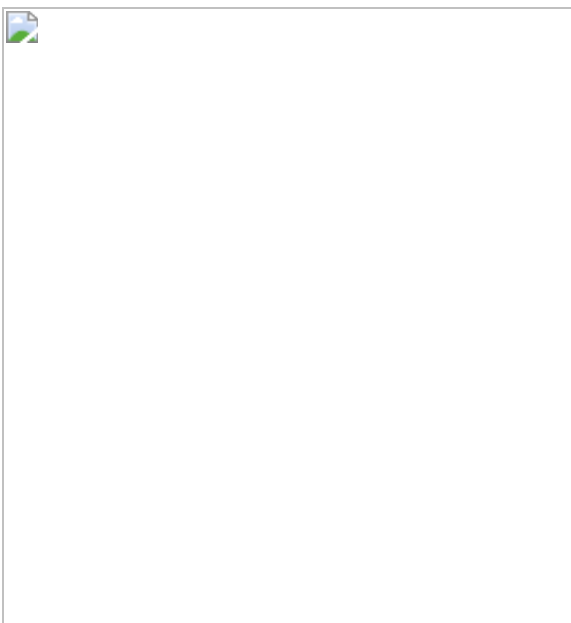


**Fig. 2: Electronic structure of CrBr<sub>3</sub>-NbSe<sub>2</sub> heterostructures.**



**Fig. 3: Spatially resolved spectroscopy of the Majorana zero modes.**



## Data availability

All the data supporting the findings are available from the corresponding authors upon request. The results of the DFT calculations are available on the NOMAD repository (<https://doi.org/10.17172/NOMAD/2020.09.06-1>).

## References

1. 1.

- Lutchyn, R. M. et al. Majorana zero modes in superconductor–semiconductor heterostructures. *Nat. Rev. Mater.* **3**, 52–68 (2018).

[ADS](#) [CAS](#) [Google Scholar](#)

2. 2.

Nayak, C., Simon, S. H., Stern, A., Freedman, M. & Das Sarma, S. Non-Abelian anyons and topological quantum computation. *Rev. Mod. Phys.* **80**, 1083–1159 (2008).

[ADS](#) [MathSciNet](#) [CAS](#) [MATH](#) [Google Scholar](#)

3. 3.

Sato, M. & Ando, Y. Topological superconductors: a review. *Rep. Prog. Phys.* **80**, 076501 (2017).

[ADS](#) [MathSciNet](#) [PubMed](#) [PubMed Central](#) [Google Scholar](#)

4. 4.

Mourik, V. et al. Signatures of Majorana fermions in hybrid superconductor–semiconductor nanowire devices. *Science* **336**, 1003–1007 (2012).

[ADS](#) [CAS](#) [PubMed](#) [PubMed Central](#) [Google Scholar](#)

5. 5.

Nadj-Perge, S. et al. Observation of Majorana fermions in ferromagnetic atomic chains on a superconductor. *Science* **346**, 602–607 (2014).

[ADS](#) [CAS](#) [PubMed](#) [PubMed Central](#) [Google Scholar](#)

6. 6.

Ménard, G. C. et al. Two-dimensional topological superconductivity in Pb/Co/Si(111). *Nat. Commun.* **8**, 2040 (2017).

[ADS](#) [PubMed](#) [PubMed Central](#) [Google Scholar](#)

7. 7.

Kim, H. et al. Toward tailoring Majorana bound states in artificially constructed magnetic atom chains on elemental superconductors. *Sci. Adv.* **4**, eaar5251 (2018).

[ADS](#) [PubMed](#) [PubMed Central](#) [Google Scholar](#)

8. 8.

Palacio-Morales, A. et al. Atomic-scale interface engineering of Majorana edge modes in a 2D magnet–superconductor hybrid system. *Sci. Adv.* **5**, eaav6600 (2019).

[ADS](#) [CAS](#) [PubMed](#) [PubMed Central](#) [Google Scholar](#)

9. 9.

Wang, Z. et al. Evidence for dispersing 1D Majorana channels in an iron-based superconductor. *Science* **367**, 104–108 (2020).

[ADS](#) [CAS](#) [PubMed](#) [PubMed Central](#) [Google Scholar](#)

10. 10.

Geim, A. K. & Grigorieva, I. V. Van der Waals heterostructures. *Nature* **499**, 419–425 (2013).

[CAS](#) [PubMed](#) [PubMed Central](#) [Google Scholar](#)

11. 11.

Novoselov, K. S., Mishchenko, A., Carvalho, A. & Castro Neto, A. H. 2D materials and van der Waals heterostructures. *Science* **353**, aac9439 (2016).

[CAS](#) [PubMed](#) [PubMed Central](#) [Google Scholar](#)

12. 12.

Cao, Y. et al. Unconventional superconductivity in magic-angle graphene superlattices. *Nature* **556**, 43–50 (2018).

[ADS](#) [CAS](#) [PubMed](#) [PubMed Central](#) [Google Scholar](#)

13. 13.

Gibertini, M., Koperski, M., Morpurgo, A. F. & Novoselov, K. S. Magnetic 2D materials and heterostructures. *Nat. Nanotechnol.* **14**, 408–419 (2019).

[ADS](#) [CAS](#) [PubMed](#) [PubMed Central](#) [Google Scholar](#)

14. 14.

Yan, L. & Liljeroth, P. Engineered electronic states in atomically precise artificial lattices and graphene nanoribbons. *Adv. Phys. X* **4**, 1651672 (2019).

[CAS](#) [Google Scholar](#)

15. 15.

Khajetoorians, A. A., Wegner, D., Otte, A. F. & Swart, I. Creating designer quantum states of matter atom-by-atom. *Nat. Rev. Phys.* **1**, 703–715 (2019).

[Google Scholar](#)

16. 16.

Chen, W. et al. Direct observation of van der Waals stacking-dependent interlayer magnetism. *Science* **366**, 983–987 (2019).

[ADS](#) [CAS](#) [PubMed](#) [PubMed Central](#) [Google Scholar](#)

17. 17.

Jiang, S., Shan, J. & Mak, K. F. Electric-field switching of two-dimensional van der Waals magnets. *Nat. Mater.* **17**, 406–410 (2018).

[ADS](#) [CAS](#) [PubMed](#) [PubMed Central](#) [Google Scholar](#)

18. 18.

Wu, Z., Yu, J. & Yuan, S. Strain-tunable magnetic and electronic properties of monolayer CrI<sub>3</sub>. *Phys. Chem. Chem. Phys.* **21**, 7750–7755 (2019).

[CAS](#) [PubMed](#) [PubMed Central](#) [Google Scholar](#)

19. 19.

Jiang, S., Li, L., Wang, Z., Mak, K. F. & Shan, J. Controlling magnetism in 2D CrI<sub>3</sub> by electrostatic doping. *Nat. Nanotechnol.* **13**, 549–553 (2018).

[ADS](#) [CAS](#) [PubMed](#) [PubMed Central](#) [Google Scholar](#)

20. 20.

Zhang, Z. et al. Direct photoluminescence probing of ferromagnetism in monolayer two-dimensional CrBr<sub>3</sub>. *Nano Lett.* **19**, 3138–3142 (2019).

[ADS](#) [CAS](#) [PubMed](#) [PubMed Central](#) [Google Scholar](#)

21. 21.

Liu, P., Williams, J. R. & Cha, J. J. Topological nanomaterials. *Nat. Rev. Mater.* **4**, 479–496 (2019).

[ADS](#) [CAS](#) [Google Scholar](#)

22. 22.

Jäck, B. et al. Observation of a Majorana zero mode in a topologically protected edge channel. *Science* **364**, 1255 (2019).

[ADS](#) [PubMed](#) [PubMed Central](#) [Google Scholar](#)

23. 23.

Fu, L. & Kane, C. L. Superconducting proximity effect and Majorana fermions at the surface of a topological insulator. *Phys. Rev. Lett.* **100**, 096407 (2008).

[ADS](#) [PubMed](#) [PubMed Central](#) [Google Scholar](#)

24. 24.

Sun, H.-H. et al. Majorana zero mode detected with spin selective Andreev reflection in the vortex of a topological superconductor. *Phys. Rev. Lett.* **116**, 257003 (2016).

[ADS](#) [PubMed](#) [PubMed Central](#) [Google Scholar](#)

25. 25.

Zhang, P. et al. Observation of topological superconductivity on the surface of an iron-based superconductor. *Science* **360**, 182–186 (2018).

[ADS](#) [PubMed](#) [PubMed Central](#) [Google Scholar](#)

26. 26.

Wang, D. et al. Evidence for Majorana bound states in an iron-based superconductor. *Science* **362**, 333–335 (2018).

[ADS](#) [CAS](#) [PubMed](#) [PubMed Central](#) [Google Scholar](#)

27. 27.

Zhu, S. et al. Nearly quantized conductance plateau of vortex zero mode in an iron-based superconductor. *Science* **367**, 189–192 (2020).

[ADS](#) [CAS](#) [PubMed](#) [PubMed Central](#) [Google Scholar](#)

28. 28.

Röntynen, J. & Ojanen, T. Topological superconductivity and high Chern numbers in 2D ferromagnetic Shiba lattices. *Phys. Rev. Lett.* **114**, 236803 (2015).

[ADS](#) [PubMed](#) [PubMed Central](#) [Google Scholar](#)

29. 29.

Li, J. et al. Two-dimensional chiral topological superconductivity in Shiba lattices. *Nat. Commun.* **7**, 12297 (2016).

[ADS](#) [CAS](#) [PubMed](#) [PubMed Central](#) [Google Scholar](#)

30. 30.

Rachel, S., Mascot, E., Cocklin, S., Vojta, M. & Morr, D. K. Quantized charge transport in chiral Majorana edge modes. *Phys. Rev. B* **96**, 205131 (2017).

[ADS](#) [Google Scholar](#)

31. 31.

Gong, C. et al. Discovery of intrinsic ferromagnetism in two-dimensional van der Waals crystals. *Nature* **546**, 265–269 (2017).

[ADS](#) [CAS](#) [PubMed](#) [PubMed Central](#) [Google Scholar](#)

32. 32.

Huang, B. et al. Layer-dependent ferromagnetism in a van der Waals crystal down to the monolayer limit. *Nature* **546**, 270–273 (2017).

[ADS](#) [CAS](#) [PubMed](#) [PubMed Central](#) [Google Scholar](#)

33. 33.

Ghazaryan, D. et al. Magnon-assisted tunnelling in van der Waals heterostructures based on CrBr<sub>3</sub>. *Nat. Electron.* **1**, 344–349 (2018).

[CAS](#) [Google Scholar](#)

34. 34.

Liu, S. et al. Wafer-scale two-dimensional ferromagnetic Fe<sub>3</sub>GeTe<sub>2</sub> thin films grown by molecular beam epitaxy. *npj 2D Mater. Appl.* **1**, 30 (2017).

[ADS](#) [Google Scholar](#)

35. 35.

Sato, M. & Fujimoto, S. Topological phases of noncentrosymmetric superconductors: edge states, Majorana fermions, and non-Abelian statistics. *Phys. Rev. B* **79**, 094504 (2009).

[ADS](#) [Google Scholar](#)

36. 36.

Sau, J. D., Lutchyn, R. M., Tewari, S. & Das Sarma, S. Generic new platform for topological quantum computation using semiconductor heterostructures. *Phys. Rev. Lett.* **104**, 040502 (2010).

[ADS](#) [PubMed](#) [PubMed Central](#) [Google Scholar](#)

37. 37.

Noat, Y. et al. Quasiparticle spectra of 2H-NbSe<sub>2</sub>: two-band superconductivity and the role of tunneling selectivity. *Phys. Rev. B* **92**, 134510 (2015).

[ADS](#) [Google Scholar](#)

38. 38.

Ménard, G. C. et al. Coherent long-range magnetic bound states in a superconductor. *Nat. Phys.* **11**, 1013–1016 (2015).

[Google Scholar](#)

39. 39.

Borisenko, S. V. et al. Two energy gaps and Fermi-surface ‘arcs’ in NbSe<sub>2</sub>. *Phys. Rev. Lett.* **102**, 166402 (2009).

[ADS](#) [CAS](#) [PubMed](#) [PubMed Central](#) [Google Scholar](#)

40. 40.

Ugeda, M. M. et al. Characterization of collective ground states in single-layer NbSe<sub>2</sub>. *Nat. Phys.* **12**, 92–97 (2016).

[CAS](#) [Google Scholar](#)

41. 41.

Alicea, J. Majorana fermions in a tunable semiconductor device. *Phys. Rev. B* **81**, 125318 (2010).

[ADS](#) [Google Scholar](#)

42. 42.

Peng, Y., Pientka, F., Glazman, L. I. & von Oppen, F. Strong localization of Majorana end states in chains of magnetic adatoms. *Phys. Rev. Lett.* **114**, 106801 (2015).

[ADS](#) [PubMed](#) [PubMed Central](#) [Google Scholar](#)

43. 43.

Kresse, G. & Furthmüller, J. Efficient iterative schemes for ab initio total-energy calculations using a plane-wave basis set. *Phys. Rev. B* **54**, 11169–11186 (1996).

[ADS](#) [CAS](#) [Google Scholar](#)

44. 44.

Kresse, G. & Furthmüller, J. Efficiency of ab-initio total energy calculations for metals and semiconductors using a plane-wave basis set. *Comput. Mater. Sci.* **6**, 15–50 (1996).

[CAS](#) [Google Scholar](#)

45. 45.

Perdew, J. P., Burke, K. & Ernzerhof, M. Generalized gradient approximation made simple. *Phys. Rev. Lett.* **77**, 3865–3868 (1996).

[ADS](#) [CAS](#) [PubMed](#) [PubMed Central](#) [Google Scholar](#)

46. 46.

Grimme, S., Antony, J., Ehrlich, S. & Krieg, H. A consistent and accurate ab initio parametrization of density functional dispersion correction (DFT-D) for the 94 elements H–Pu. *J. Chem. Phys.* **132**, 154104 (2010).

[ADS](#) [PubMed](#) [PubMed Central](#) [Google Scholar](#)

47. 47.

Medeiros, P. V. C., Stafström, S. & Björk, J. Effects of extrinsic and intrinsic perturbations on the electronic structure of graphene: retaining an effective primitive cell band structure by band unfolding. *Phys. Rev. B* **89**, 041407 (2014).

[ADS](#) [Google Scholar](#)

48. 48.

Medeiros, P. V. C., Tsirkin, S. S., Stafström, S. & Björk, J. Unfolding spinor wave functions and expectation values of general operators: introducing the unfolding-density operator. *Phys. Rev. B* **91**, 041116 (2015).

[ADS](#) [Google Scholar](#)

49. 49.

Webster, L. & Yan, J.-A. Strain-tunable magnetic anisotropy in monolayer CrCl<sub>3</sub>, CrBr<sub>3</sub>, and CrI<sub>3</sub>. *Phys. Rev. B* **98**, 144411 (2018).

[ADS](#) [CAS](#) [Google Scholar](#)

50. 50.

Xu, Y., Liu, X. & Guo, W. Tensile strain induced switching of magnetic states in NbSe<sub>2</sub> and NbS<sub>2</sub> single layers. *Nanoscale* **6**, 12929–12933 (2014).

[ADS](#) [CAS](#) [PubMed](#) [PubMed Central](#) [Google Scholar](#)

51. 51.

Kim, S. & Son, Y.-W. Quasiparticle energy bands and Fermi surfaces of monolayer NbSe<sub>2</sub>. *Phys. Rev. B* **96**, 155439 (2017).

[ADS](#) [Google Scholar](#)

52. 52.

Zhang, H., Yang, W., Ning, Y. & Xu, X. Abundant valley-polarized states in two-dimensional ferromagnetic van der Waals heterostructures. *Phys. Rev. B* **101**, 205404 (2020).

[ADS](#) [CAS](#) [Google Scholar](#)

53. 53.

Zollner, K., Faria, P. E., Jr. & Fabian, J. Proximity exchange effects in MoSe<sub>2</sub> and WSe<sub>2</sub> heterostructures with CrI<sub>3</sub>: twist angle, layer, and gate dependence. *Phys. Rev. B* **100**, 085128 (2019).

[ADS](#) [CAS](#) [Google Scholar](#)

54. 54.

Maaß, H. et al. Spin-texture inversion in the giant Rashba semiconductor BiTeI. *Nat. Commun.* **7**, 11621 (2016).

[ADS](#) [PubMed](#) [PubMed Central](#) [Google Scholar](#)

55. 55.

Feng, Y. et al. Rashba-like spin splitting along three momentum directions in trigonal layered PtBi<sub>2</sub>. *Nat. Commun.* **10**, 4765 (2019).

[ADS](#) [PubMed](#) [PubMed Central](#) [Google Scholar](#)

56. 56.

Klimovskikh, I. I. et al. Giant magnetic band gap in the Rashba-split surface state of vanadium-doped BiTeI: a combined photoemission and ab initio study. *Sci. Rep.* **7**, 3353 (2017).

[ADS](#) [CAS](#) [PubMed](#) [PubMed Central](#) [Google Scholar](#)

57. 57.

Qi, J., Li, X., Niu, Q. & Feng, J. Giant and tunable valley degeneracy splitting in MoTe<sub>2</sub>. *Phys. Rev. B* **92**, 121403 (2015).

[ADS](#) [Google Scholar](#)

58. 58.

Shimada, T., Ohuchi, F. S. & Parkinson, B. A. Work function and photothreshold of layered metal dichalcogenides. *Jpn. J. Appl. Phys.* **33**, 2696 (1994).

[ADS](#) [CAS](#) [Google Scholar](#)

59. 59.

Liu, Y., Stradins, P. & Wei, S.-H. Van der Waals metal–semiconductor junction: weak Fermi level pinning enables effective tuning of Schottky barrier. *Sci. Adv.* **2**, e1600069 (2016).

[ADS](#) [PubMed](#) [PubMed Central](#) [Google Scholar](#)

[Download references](#)

## Acknowledgements

This research made use of the Aalto Nanomicroscopy Center (Aalto NMC) facilities and was supported by the European Research Council (ERC-2017-AdG no. 788185 “Artificial Designer Materials”), Academy of Finland (Academy professor funding no. 318995 and 320555, and Academy postdoctoral researcher no. 309975), and the Aalto University Centre for Quantum Engineering (Aalto CQE). S.G. acknowledges the support of the National Science Centre (NCN, Poland) under grant 2017/27/N/ST3/01762. Computing resources from the Aalto Science-IT project and CSC, Helsinki, are gratefully acknowledged. A.S.F. has been supported by the World Premier International Research Center Initiative (WPI), MEXT, Japan.

## Author information

### Affiliations

1. Department of Applied Physics, Aalto University, Espoo, Finland

Shawlienu Kezilebieke, Md Nurul Huda, Viliam Vaňo, Markus Aapro, Somesh C. Ganguli, Orlando J. Silveira, Adam S.

Foster & Peter Liljeroth

2. Institute of Physics, M. Curie-Skłodowska University, Lublin, Poland

Szczepan Głodzik

3. Nano Life Science Institute (WPI-NanoLSI), Kanazawa University, Kanazawa, Japan

Adam S. Foster

4. Computational Physics Laboratory, Tampere University, Tampere, Finland

Teemu Ojanen

5. Helsinki Institute of Physics, Helsinki, Finland

Teemu Ojanen

## Authors

1. Shawulienu Kezilebieke

[View author publications](#)

You can also search for this author in [PubMed](#) [Google Scholar](#)

2. Md Nurul Huda

[View author publications](#)

You can also search for this author in [PubMed](#) [Google Scholar](#)

3. Viliam Vaňo

[View author publications](#)

You can also search for this author in [PubMed](#) [Google Scholar](#)

4. Markus Aapro

[View author publications](#)

You can also search for this author in [PubMed](#) [Google Scholar](#)

5. Somesh C. Ganguli

[View author publications](#)

You can also search for this author in [PubMed](#) [Google Scholar](#)

6. Orlando J. Silveira

[View author publications](#)

You can also search for this author in [PubMed](#) [Google Scholar](#)

7. Szczepan Głodzik

[View author publications](#)

You can also search for this author in [PubMed](#) [Google Scholar](#)

8. Adam S. Foster

[View author publications](#)

You can also search for this author in [PubMed](#) [Google Scholar](#)

9. Teemu Ojanen

[View author publications](#)

You can also search for this author in [PubMed](#) [Google Scholar](#)

10. Peter Liljeroth

[View author publications](#)

You can also search for this author in [PubMed](#) [Google Scholar](#)

## Contributions

S.K., T.O. and P.L. conceived the experiment. S.K., M.N.H., M.A. and S.C.G. carried out the sample growth. S.K. did the low-temperature STM experiments. S.K. and V.V. analysed the STM data. O.J.S. and A.S.F. planned and carried out the DFT calculations. T.O. and S.G. developed the theoretical model and established its implications. S.G. carried out the

numerical calculations. S.K., T.O. and P.L. wrote the manuscript with input from all co-authors.

## Corresponding authors

Correspondence to [Shawulienu Kezilebieke](#) or [Teemu Ojanen](#) or [Peter Liljeroth](#).

## Ethics declarations

### Competing interests

The authors declare no competing interests.

## Additional information

**Peer review information** *Nature* thanks Jinfeng Jia and the other, anonymous, reviewer(s) for their contribution to the peer review of this work. Peer reviewer reports are available.

**Publisher's note** Springer Nature remains neutral with regard to jurisdictional claims in published maps and institutional affiliations.

## Extended data figures and tables

### [Extended Data Fig. 1 Fitting the bulk NbSe<sub>2</sub> superconducting gap to a two-band model<sup>37</sup>](#)

**a, c, e**, The tunnelling spectra on NbSe<sub>2</sub> (**a**), and in the middle (**c**) and at the edge (**e**) of an CrBr<sub>3</sub> island fitted with the two-band model. **b, d, f**, The corresponding spectra after subtracting the background given by the two-band model fit. Spectra in the middle (**d**) and at the edge (**f**) of an CrBr<sub>3</sub> island show two- and three-peak features within the superconducting gap, respectively. They were fitted by a sum of either two (positioned

symmetrically with respect to zero, green lines) or three Gaussians (two of them positioned symmetrically with respect to zero, green lines; and one centred at zero, red line).

### Extended Data Fig. 2 Shift of the NbSe<sub>2</sub> states under CrBr<sub>3</sub>.

**a**, Blue curve, spectrum recorded on monolayer CrBr<sub>3</sub> island; red curve, spectrum recorded on bare NbSe<sub>2</sub> substrate. Since at these energies there are no CrBr<sub>3</sub> states, this directly probes the states of the underlying NbSe<sub>2</sub> substrate. The results show a clear shift of the Nb *d* band upwards under CrBr<sub>3</sub>. **b**, Spectra recorded along a line from NbSe<sub>2</sub> to CrBr<sub>3</sub>, showing the shift of about 80 meV. Colour scale indicates value of the dI/dV signal (arbitrary units), range (0.05, 0.6).

### Extended Data Fig. 3 Estimating the decay length of the edge states.

**a**, Experimentally measured differential tunnelling conductance maps at zero bias. Colour scale (arbitrary units) range is (0, 1.5). **b**, The corresponding density of states profiles across the edge of the island and corresponding Gaussian fit. ZBC, zero-bias conductance.

### Extended Data Fig. 4 Robustness and reproducibility of the edge mode.

Topography (top row, extracted during grid spectroscopy) and dI/dV maps at different bias voltages (indicated in the different panels) on four different CrBr<sub>3</sub> islands and recorded with different microscopic tip apices. Edge modes are observed in our hybrid van der Waals heterostructures on all CrBr<sub>3</sub> islands, irrespective of their size and shape, or different microscopic tip.

### Extended Data Fig. 5 Measurements in a magnetic field.

**a–e**, Experimentally measured differential tunnelling conductance maps as a function of the bias under an external magnetic field of 4 T. **f**, Corresponding  $dI/dV$  line spectra measured along the line indicated in **a**. Colouring as in Fig. 3a. STM feedback parameters:  $V_{\text{bias}} = +1$  V,  $I = 10$  pA, image size:  $40 \times 40$  nm $^2$ . Zero-bias peaks (ZBPs) can occur because of the formation of a Kondo resonance that appears when many-body interactions screen magnetic impurities in metals. If the ZBPs reported here were not of topological origin but arose from the Kondo effect, they would persist beyond the superconductor-to-normal-metal transition. In our measurements, however, as soon as superconductivity is suppressed, all states (including zero-bias peaks at the edge of the island) disappear, and the spectrum becomes featureless.

### Extended Data Fig. 6 Structures considered in DFT calculations.

**a–e**, Top and side views of the isolated CrBr<sub>3</sub> (**a**) and NbSe<sub>2</sub> (**b**) monolayers, as well as the heterostructures htCrSe (**c**), htCrNbSe (**d**) and htCrNb (**e**).

### Extended Data Fig. 7 Band structures of the isolated monolayers CrBr<sub>3</sub> and NbSe<sub>2</sub>, as well as the most stable CrBr<sub>3</sub>–NbSe<sub>2</sub> heterostructure, htCrSe.

Blue and red lines represent spin up and down, respectively.

### Extended Data Fig. 8 a, Spin-polarized band structure of the htCrSe, where the blue and lines indicate spin up and down, respectively.

**b**, Comparison between the bands of  $2 \times 2$  NbSe<sub>2</sub> and htCrSe near the  $\Gamma$  point. **c**, Unfolded spin-polarized bands. **d**, Band structure of htCrSe with SOC, where the blue (red) circles indicate the positive (negative) projection of the Nb electrons' spin on the quantization axis. **e**, Comparison between

the bands with SOC of the  $2 \times 2$  NbSe<sub>2</sub> and htCrSe near the  $\Gamma$  point. **f**, Unfolded bands obtained with SOC.

**Extended Data Table 1 Parameters for three different heterostructures**  
[Full size table](#)

## Supplementary information

### [Supplementary Information](#)

Supplementary Notes: Description of the phenomenological model for topological superconductivity in the CrBr<sub>3</sub>-NbSe<sub>2</sub> system and additional comparison with experimental data with 5 display items.

### [Peer Review File](#)

## Rights and permissions

### [Reprints and Permissions](#)

## About this article



Check for  
updates

## Cite this article

Kezilebieke, S., Huda, M.N., Vaňo, V. *et al.* Topological superconductivity in a van der Waals heterostructure. *Nature* **588**, 424–428 (2020).  
<https://doi.org/10.1038/s41586-020-2989-y>

### [Download citation](#)

- Received: 06 March 2020

- Accepted: 23 September 2020
- Published: 16 December 2020
- Issue Date: 17 December 2020
- DOI: <https://doi.org/10.1038/s41586-020-2989-y>

## Comments

By submitting a comment you agree to abide by our [Terms](#) and [Community Guidelines](#). If you find something abusive or that does not comply with our terms or guidelines please flag it as inappropriate.

[Access through your institution](#)

[Change institution](#)

[Buy or subscribe](#)

---

This article was downloaded by **calibre** from <https://www.nature.com/articles/s41586-020-2989-y>.

| [Section menu](#) | [Main menu](#) |

- Article
- [Published: 16 December 2020](#)

# Self-assembly of a layered two-dimensional molecularly woven fabric

- [David P. August](#) ORCID: [orcid.org/0000-0002-4049-0759<sup>1</sup>](https://orcid.org/0000-0002-4049-0759),
- [Robert A. W. Dryfe](#) ORCID: [orcid.org/0000-0002-9335-4451<sup>1,2</sup>](https://orcid.org/0000-0002-9335-4451),
- [Sarah J. Haigh](#) ORCID: [orcid.org/0000-0001-5509-6706<sup>3</sup>](https://orcid.org/0000-0001-5509-6706),
- [Paige R. C. Kent](#)<sup>1</sup>,
- [David A. Leigh](#) ORCID: [orcid.org/0000-0002-1202-4507<sup>1</sup>](https://orcid.org/0000-0002-1202-4507),
- [Jean-François Lemonnier](#) ORCID: [orcid.org/0000-0002-2201-2788<sup>1</sup>](https://orcid.org/0000-0002-2201-2788),
- [Zheling Li](#) ORCID: [orcid.org/0000-0001-8412-0234<sup>3</sup>](https://orcid.org/0000-0001-8412-0234),
- [Christopher A. Muryn](#) ORCID: [orcid.org/0000-0002-1581-9778<sup>1</sup>](https://orcid.org/0000-0002-1581-9778),
- [Leoni I. Palmer](#) ORCID: [orcid.org/0000-0001-7894-0674<sup>1</sup>](https://orcid.org/0000-0001-7894-0674),
- [Yiwei Song](#) ORCID: [orcid.org/0000-0003-2471-6516<sup>1</sup>](https://orcid.org/0000-0003-2471-6516),
- [George F. S. Whitehead](#) ORCID: [orcid.org/0000-0003-1949-4250<sup>1</sup>](https://orcid.org/0000-0003-1949-4250) &
- [Robert J. Young](#) ORCID: [orcid.org/0000-0001-6073-9489<sup>3</sup>](https://orcid.org/0000-0001-6073-9489)

[Nature](#) volume 588, pages429–435(2020) [Cite this article](#)

- 3048 Accesses
- 1 Citations
- 80 Altmetric
- [Metrics details](#)

## Subjects

- [Interlocked molecules](#)
- [Supramolecular polymers](#)

## Abstract

Fabrics—materials consisting of layers of woven fibres—are some of the most important materials in everyday life<sup>1</sup>. Previous nanoscale weaves<sup>2,3,4,5,6,7,8,9,10,11,12,13,14,15,16</sup> include isotropic crystalline covalent organic frameworks<sup>12,13,14</sup> that feature rigid helical strands interlaced in all three dimensions, rather than the two-dimensional<sup>17,18</sup> layers of flexible woven strands that give conventional textiles their characteristic flexibility, thinness, anisotropic strength and porosity. A supramolecular two-dimensional kagome weave<sup>15</sup> and a single-layer, surface-supported, interwoven two-dimensional polymer<sup>16</sup> have also been reported. The direct, bottom-up assembly of molecular building blocks into linear organic polymer chains woven in two dimensions has been proposed on a number of occasions<sup>19,20,21,22,23</sup>, but has not previously been achieved. Here we demonstrate that by using an anion and metal ion template, woven molecular ‘tiles’ can be tessellated into a material consisting of alternating aliphatic and aromatic segmented polymer strands, interwoven within discrete layers. Connections between slowly precipitating pre-woven grids, followed by the removal of the ion template, result in a wholly organic molecular material that forms as stacks and clusters of thin sheets—each sheet up to hundreds of micrometres long and wide but only about four nanometres thick—in which warp and weft single-chain polymer strands remain associated through periodic mechanical entanglements within each sheet. Atomic force microscopy and scanning electron microscopy show clusters and, occasionally, isolated individual sheets that, following demetallation, have slid apart from others with which they were stacked during the tessellation and polymerization process. The layered two-dimensional molecularly woven material has long-range order, is birefringent, is twice as stiff as the constituent linear polymer, and delaminates and tears along well-defined lines in the manner of a macroscopic textile. When incorporated into a polymer-supported membrane, it acts as a net, slowing the passage of large ions while letting smaller ions through.

[Access through your institution](#)  
[Change institution](#)  
[Buy or subscribe](#)

## Access options

Subscribe to Journal

Get full journal access for 1 year

185,98 €

only 3,58 € per issue

[Subscribe](#)

All prices are NET prices.  
VAT will be added later in the checkout.

Rent or Buy article

Get time limited or full article access on ReadCube.

from \$8.99

[Rent or Buy](#)

All prices are NET prices.

### Additional access options:

- [Log in](#)
- [Access through your institution](#)
- [Learn about institutional subscriptions](#)

**Fig. 1: X-ray crystal structure of interwoven 3 × 3 molecular grid [Fe<sub>9</sub>1<sub>6</sub>](BF<sub>4</sub>)<sub>18</sub>, and the synthesis of thiol- and disulfide-derivatives 2, 3 and [Fe<sub>9</sub>2<sub>6</sub>](BF<sub>4</sub>)<sub>18</sub>.**

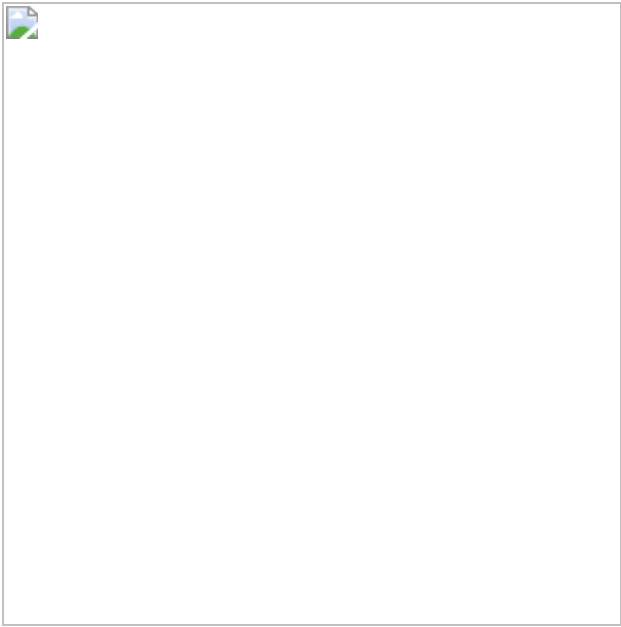


**Fig. 2: Bottom-up self-assembly of layered 2D molecularly woven fabric 4.**

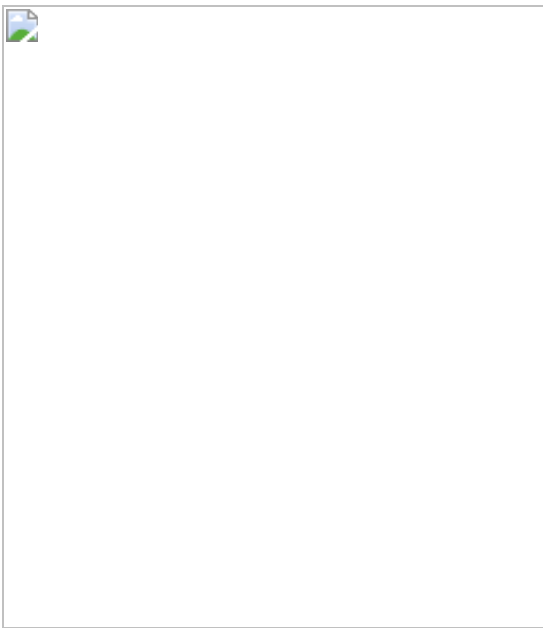


**Fig. 3: Images of layered 2D molecularly woven fabric 4, and evidence for long-range order.**

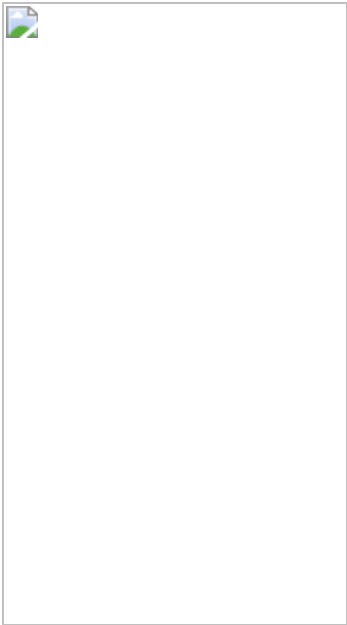


**Fig. 4: Microscopy imaging of layered 2D molecularly woven fabric 4.**

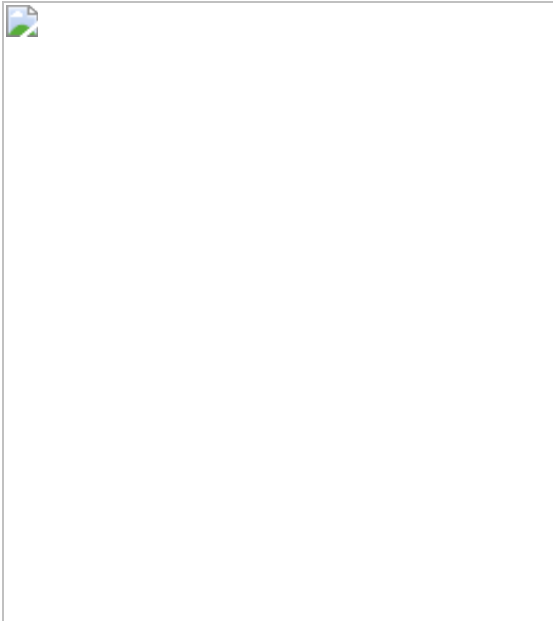
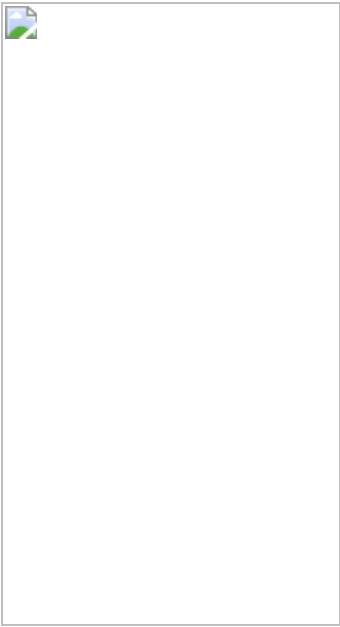


**Fig. 5: Ion permeability studies on PVDF-supported membranes formed from unwoven linear polymer 3 and 2D woven polymer 4.**



## Data availability

The data that support the findings of this study are available within the paper and its [Supplementary Information](#), or are available from the Mendeley data repository (<https://data.mendeley.com/>) with the identifier <https://doi.org/10.17632/zkt5km82r2.2>.

## References

1. 1.

Kadolph, S. J. (ed.) *Textiles* 10th edn (Prentice-Hall, 2007).

2. 2.

Batten, S. R. & Robson, R. Interpenetrating nets: ordered, periodic entanglement. *Angew. Chem. Int. Ed.* **37**, 1460–1494 (1998).

[Google Scholar](#)

3. 3.

Carlucci, L., Ciani, G. & Proserpio, D. M. Polycatenation, polythreading and polyknotting in coordination network chemistry. *Coord. Chem. Rev.* **246**, 247–289 (2003).

[CAS](#) [Google Scholar](#)

4. 4.

Van Calcar, P. M., Olmstead, M. M. & Balch, A. L. Construction of a knitted crystalline polymer through the use of gold(i)–gold(i) interactions. *Chem. Commun.* 1773–1774 (1995).

5. 5.

Axtell, E. A., III, Liao, J.-H. & Kanatzidis, M. G. Flux synthesis of LiAuS and NaAuS: “Chicken-wire-like” layer formation by interweaving of  $(\text{AuS})_n^{n-}$  threads. Comparison with  $\alpha$ -HgS and AAuS (A = K, Rb). *Inorg. Chem.* **37**, 5583–5587 (1998).

[CAS](#) [PubMed](#) [PubMed Central](#) [Google Scholar](#)

6. 6.

Carlucci, L., Ciani, G., Gramaccioli, A., Proserpio, D. M. & Rizzato, S. Crystal engineering of coordination polymers and architectures using the  $[\text{Cu}(2,2'\text{-bipy})]^{2+}$  molecular corner as building block (bipy = 2,2'-bipyridyl). *CrystEngComm* **2**, 154–163 (2000).

[Google Scholar](#)

7. 7.

Li, Y.-H. et al. The first ‘two-over/two-under’ (2O/2U) 2D weave structure assembled from Hg-containing 1D coordination polymer chains. *Chem. Commun.* 1630–1631 (2003).

8. 8.

Han, L. & Zhou, Y. 2D entanglement of 1D flexible zigzag coordination polymers leading to an interwoven network. *Inorg. Chem. Commun.* **11**, 385–387 (2008).

[CAS](#) [Google Scholar](#)

9. 9.

Wu, H., Yang, J., Su, Z.-M., Batten, S. R. & Ma, J.-F. An exceptional 54-fold interpenetrated coordination polymer with  $10^3$ -srs network topology. *J. Am. Chem. Soc.* **133**, 11406–11409 (2011).

[CAS](#) [PubMed](#) [PubMed Central](#) [Google Scholar](#)

10. 10.

Champsaur, A. M. et al. Weaving nanoscale cloth through electrostatic templating. *J. Am. Chem. Soc.* **139**, 11718–11721 (2017).

[CAS](#) [PubMed](#) [PubMed Central](#) [Google Scholar](#)

11. 11.

Ciengshin, T., Sha, R. & Seeman, N. C. Automatic molecular weaving prototyped by using single-stranded DNA. *Angew. Chem. Int. Ed.* **50**, 4419–4422 (2011).

[CAS](#) [Google Scholar](#)

12. 12.

Liu, Y. et al. Weaving of organic threads into a crystalline covalent organic framework. *Science* **351**, 365–369 (2016).

[ADS](#) [CAS](#) [PubMed](#) [PubMed Central](#) [Google Scholar](#)

13. 13.

Zhao, Y. et al. A synthetic route for crystals of woven structures, uniform nanocrystals, and thin films of imine covalent organic frameworks. *J. Am. Chem. Soc.* **139**, 13166–13172 (2017).

[CAS](#) [PubMed](#) [PubMed Central](#) [Google Scholar](#)

14. 14.

Liu, Y. et al. Molecular weaving of covalent organic frameworks for adaptive guest inclusion. *J. Am. Chem. Soc.* **140**, 16015–16019 (2018).

[CAS](#) [PubMed](#) [PubMed Central](#) [Google Scholar](#)

15. 15.

Lewandowska, U. et al. A triaxial supramolecular weave. *Nat. Chem.* **9**, 1068–1072 (2017).

[CAS](#) [PubMed](#) [PubMed Central](#) [Google Scholar](#)

16. 16.

Wang, Z. et al. Molecular weaving via surface-templated epitaxy of crystalline coordination networks. *Nat. Commun.* **8**, 14442 (2017).

[ADS](#) [CAS](#) [PubMed](#) [PubMed Central](#) [Google Scholar](#)

17. 17.

Servalli, M. & Schlüter, A. D. Synthetic two-dimensional polymers. *Annu. Rev. Mater. Res.* **47**, 361–389 (2017).

[CAS](#) [Google Scholar](#)

18. 18.

Mas-Ballesté, R., Gómez-Navarro, C., Gómez-Herrero, J. & Zamora, F. 2D materials: to graphene and beyond. *Nanoscale* **3**, 20–30 (2011).

[ADS](#) [PubMed](#) [PubMed Central](#) [Google Scholar](#)

19. 19.

Busch, D. H. Structural definition of chemical templates and the prediction of new and unusual materials. *J. Incl. Phenom. Macrocycl. Chem* **12**, 389–395 (1992).

[CAS](#) [Google Scholar](#)

20. 20.

Hubin, T. J. & Busch, D. H. Template routes to interlocked molecular structures and orderly molecular entanglements. *Coord. Chem. Rev.* **200–202**, 5–52 (2000).

[Google Scholar](#)

21. 21.

Cockriel, D. L. et al. The design and synthesis of pyrazine amide ligands suitable for the “tiles” approach to molecular weaving with octahedral metal ions. *Inorg. Chem. Commun.* **11**, 1–4 (2008).

[CAS](#) [Google Scholar](#)

22. 22.

Wadhwa, N. R., Hughes, N. C., Hachem, J. A. & Mezei, G. Metal-templated synthesis of intertwined, functionalized strands as precursors to molecularly woven materials. *RSC Adv.* **6**, 11430–11440 (2016).

[CAS](#) [Google Scholar](#)

23. 23.

Mena-Hernando, S. & Pérez, E. M. Mechanically interlocked materials. Rotaxanes and catenanes beyond the small molecule. *Chem.*

*Soc. Rev.* **48**, 5016–5032 (2019).

[CAS](#) [PubMed](#) [PubMed Central](#) [Google Scholar](#)

24. 24.

Forgan, R. S., Sauvage, J.-P. & Stoddart, J. F. Chemical topology: complex molecular knots, links, and entanglements. *Chem. Rev.* **111**, 5434–5464 (2011).

[CAS](#) [PubMed](#) [PubMed Central](#) [Google Scholar](#)

25. 25.

Ayme, J.-F., Beves, J. E., Campbell, C. J. & Leigh, D. A. Template synthesis of molecular knots. *Chem. Soc. Rev.* **42**, 1700–1712 (2013).

[CAS](#) [PubMed](#) [PubMed Central](#) [Google Scholar](#)

26. 26.

Sauvage, J.-P. From chemical topology to molecular machines (Nobel Lecture). *Angew. Chem. Int. Ed.* **56**, 11080–11093 (2017).

[CAS](#) [Google Scholar](#)

27. 27.

Dietrich-Buchecker, C. O. & Sauvage, J.-P. A synthetic molecular trefoil knot. *Angew. Chem. Int. Ed. Engl.* **28**, 189–192 (1989).

[Google Scholar](#)

28. 28.

Chichak, K. S. et al. Molecular Borromean rings. *Science* **304**, 1308–1312 (2004).

[ADS](#) [CAS](#) [PubMed](#) [PubMed Central](#) [Google Scholar](#)

29. 29.

Guo, J., Mayers, P. C., Breault, G. A. & Hunter, C. A. Synthesis of a molecular trefoil knot by folding and closing on an octahedral coordination template. *Nat. Chem.* **2**, 218–222 (2010).

[CAS](#) [PubMed](#) [PubMed Central](#) [Google Scholar](#)

30. 30.

Ayme, J.-F. et al. A synthetic molecular pentafoil knot. *Nat. Chem.* **4**, 15–20 (2012).

[CAS](#) [Google Scholar](#)

31. 31.

Prakasam, T. et al. Simultaneous self-assembly of a [2]catenane, a trefoil knot, and a Solomon link from a simple pair of ligands. *Angew. Chem. Int. Ed.* **52**, 9956–9960 (2013).

[CAS](#) [Google Scholar](#)

32. 32.

Wood, C. S., Ronson, T. K., Belenguer, A. M., Holstein, J. J. & Nitschke, J. R. Two-stage directed self-assembly of a cyclic [3]catenane. *Nat. Chem.* **7**, 354–358 (2015).

[CAS](#) [PubMed](#) [PubMed Central](#) [Google Scholar](#)

33. 33.

Danon, J. J. et al. Braiding a molecular knot with eight crossings. *Science* **355**, 159–162 (2017).

[ADS](#) [CAS](#) [PubMed](#) [PubMed Central](#) [Google Scholar](#)

34. 34.

Zhang, L. et al. Stereoselective synthesis of a composite knot with nine crossings. *Nat. Chem.* **10**, 1083–1088 (2018).

[CAS](#) [PubMed](#) [PubMed Central](#) [Google Scholar](#)

35. 35.

Leigh, D. A. et al. Tying different knots in a molecular strand. *Nature* **584**, 562–568 (2020).

[ADS](#) [CAS](#) [PubMed](#) [PubMed Central](#) [Google Scholar](#)

36. 36.

Ruben, M., Rojo, J., Romero-Salguero, F. J., Uppadine, L. H. & Lehn, J.-M. Grid-type metal ion architectures: functional metallosupramolecular arrays. *Angew. Chem. Int. Ed.* **43**, 3644–3662 (2004).

[CAS](#) [Google Scholar](#)

37. 37.

Dawe, L. N., Abedin, T. S. M. & Thompson, L. K. Ligand directed self-assembly of polynuclear  $[n \times n]$  grids: rational routes to large functional molecular subunits? *Dalton Trans.* 1661–1675 (2008).

38. 38.

Leigh, D. A. et al. A molecular endless ( $7_4$ ) knot. *Nat. Chem.* <https://doi.org/10.1038/s41557-020-00594-x> (2020).

39. 39.

Pakula, A. A. & Simon, M. I. Determination of transmembrane protein structure by disulfide cross-linking: the *Escherichia coli* Tar receptor. *Proc. Natl Acad. Sci. USA* **89**, 4144–4148 (1992).

[ADS](#) [CAS](#) [PubMed](#) [PubMed Central](#) [Google Scholar](#)

40. 40.

Sakamoto, R. et al. Coordination nanosheets (CONASHs): strategies, structures and functions. *Chem. Commun.* **53**, 5781–5801 (2017).

[CAS](#) [Google Scholar](#)

41. 41.

de Gennes, P. G. Reptation of a polymer chain in the presence of fixed obstacles. *J. Chem. Phys.* **55**, 572–579 (1971).

[ADS](#) [Google Scholar](#)

42. 42.

Zhu, W. et al. Structure and electronic transport in graphene wrinkles. *Nano Lett.* **12**, 3431–3436 (2012).

[ADS](#) [CAS](#) [PubMed](#) [PubMed Central](#) [Google Scholar](#)

43. 43.

Young, R. J. & Lovell, P. A. *Introduction to Polymers* 3rd edn (CRC Press, 2011).

44. 44.

de Ruijter, C., Mendes, E., Boerstoel, H. & Picken, S. J. Orientational order and mechanical properties of poly(amide-block-aramid) alternating block copolymer films and fibers. *Polymer* **47**, 8517–8526 (2006).

[Google Scholar](#)

45. 45.

Kontturi, K., Murtomäki, L. & Manzanares, J. A. *Ionic Transport Processes in Electrochemistry and Membrane Science* (Oxford Univ.

Press, 2014).

46. 46.

Li, G. et al. Woven polymer networks via the topological transformation of a [2]catenane. *J. Am. Chem. Soc.* **142**, 14343–14349 (2020).

[CAS](#) [PubMed](#) [PubMed Central](#) [Google Scholar](#)

47. 47.

Hawker, C. J. & Wooley, K. L. The convergence of synthetic organic and polymer chemistries. *Science* **309**, 1200–1205 (2005).

[ADS](#) [CAS](#) [PubMed](#) [PubMed Central](#) [Google Scholar](#)

48. 48.

Sakamoto, J., van Heijst, J., Lukin, O. & Schlüter, A. D. Two-dimensional polymers: just a dream of synthetic chemists? *Angew. Chem. Int. Ed.* **48**, 1030–1069 (2009).

[CAS](#) [Google Scholar](#)

49. 49.

Wu, Q. et al. Poly[*n*]catenanes: synthesis of molecular interlocked chains. *Science* **358**, 1434–1439 (2017).

[ADS](#) [CAS](#) [PubMed](#) [PubMed Central](#) [Google Scholar](#)

50. 50.

Stoddart, J. F. Dawning of the age of molecular nanotopology. *Nano Lett.* **20**, 5597–5600 (2020).

[ADS](#) [CAS](#) [PubMed](#) [PubMed Central](#) [Google Scholar](#)

[Download references](#)

## Acknowledgements

We thank the Engineering and Physical Sciences Research Council (EPSRC; EP/P027067/1), the European Research Council (ERC; Advanced Grant no. 786630), and the Defense Advanced Research Projects Agency (DARPA; Co-operative Agreement W911NF-17-2-0148) for funding; with networking contributions from the COST Action CA17139, EUTOPIA. The views, opinions and/or findings expressed are those of the authors and should not be interpreted as representing the official views or policies of the Department of Defense or the US Government. We also thank the Diamond Light Source (UK) for synchrotron beam time on I19 (XR029), the University of Manchester, Department of Chemistry microanalysis and mass spectrometry services, the Henry Royce Institute for Advanced Materials (funded through EPSRC grants EP/R00661X/1 and EP/P025021/1) for the use of facilities, S. Jantzen/Biocinematics for the video animations, and S. J. Rowan (University of Chicago) and R. P. Sijbesma (Eindhoven University) for comments that improved the draft manuscript. D.A.L. is a Royal Society Research Professor.

## Author information

### Affiliations

#### 1. Department of Chemistry, University of Manchester, Manchester, UK

David P. August, Robert A. W. Dryfe, Paige R. C. Kent, David A. Leigh, Jean-François Lemonnier, Christopher A. Muryn, Leoni I. Palmer, Yiwei Song & George F. S. Whitehead

#### 2. Henry Royce Institute, University of Manchester, Manchester, UK

Robert A. W. Dryfe

3. Department of Materials, National Graphene Institute, University of Manchester, Manchester, UK

Sarah J. Haigh, Zheling Li & Robert J. Young

## Authors

1. David P. August

[View author publications](#)

You can also search for this author in [PubMed](#) [Google Scholar](#)

2. Robert A. W. Dryfe

[View author publications](#)

You can also search for this author in [PubMed](#) [Google Scholar](#)

3. Sarah J. Haigh

[View author publications](#)

You can also search for this author in [PubMed](#) [Google Scholar](#)

4. Paige R. C. Kent

[View author publications](#)

You can also search for this author in [PubMed](#) [Google Scholar](#)

5. David A. Leigh

[View author publications](#)

You can also search for this author in [PubMed](#) [Google Scholar](#)

6. Jean-François Lemonnier

[View author publications](#)

You can also search for this author in [PubMed](#) [Google Scholar](#)

7. Zheling Li

[View author publications](#)

You can also search for this author in [PubMed](#) [Google Scholar](#)

8. Christopher A. Muryn

[View author publications](#)

You can also search for this author in [PubMed](#) [Google Scholar](#)

9. Leoni I. Palmer

[View author publications](#)

You can also search for this author in [PubMed](#) [Google Scholar](#)

10. Yiwei Song

[View author publications](#)

You can also search for this author in [PubMed](#) [Google Scholar](#)

11. George F. S. Whitehead

[View author publications](#)

You can also search for this author in [PubMed](#) [Google Scholar](#)

12. Robert J. Young

[View author publications](#)

You can also search for this author in [PubMed](#) [Google Scholar](#)

## Contributions

D.P.A., L.I.P., J.-F.L. and Y.S. carried out the synthesis and general characterization studies. G.F.S.W. solved the crystal structure of  $[Fe_9\mathbf{1}_6](BF_4)_{18}$ . Z.L., C.A.M. and R.J.Y. carried out the AFM studies. Z.L. and R.J.Y. performed the Young's modulus, polarized optical microscope and deformation experiments. S.J.H. conducted the transmission electron microscopy studies, and R.A.W.D. and P.R.C.K. conducted the ion permeation studies. D.A.L. directed the research. All authors contributed to the analysis of the results and the writing of the manuscript. Authors are

listed alphabetically in view of the broad range of experimental techniques used in this study.

## Corresponding author

Correspondence to [David A. Leigh](#).

## Ethics declarations

### Competing interests

The authors declare no competing interests.

## Additional information

**Peer review information** *Nature* thanks the anonymous reviewer(s) for their contribution to the peer review of this work.

**Publisher's note** Springer Nature remains neutral with regard to jurisdictional claims in published maps and institutional affiliations.

## Supplementary information

### [Supplementary Information](#)

Experimental procedures, methods and characterisation data.

### [Video 1](#)

(MPEG-4) Animation of the assembly of the 2D molecularly woven fabric.  
Video credit: Stuart Jantzen (Biocinematics).

### [Video 2](#)

Supplementary Video 2 (MPEG-4) - Animation of AFM of a layered sheet of the 2D molecularly woven fabric. Video credit: Stuart Jantzen (Biocinematics).

### **Video 3**

Supplementary Video 3 (MPEG-4) - Animation of the fracturing and delamination process of a layered sheet of the 2D molecularly woven fabric on a polyester support under strain. Video credit: Stuart Jantzen (Biocinematics).

### **Video 4**

Supplementary Video 4 (MPEG-4) - Animation of Young's modulus determination by AFM on the 2D molecularly woven fabric and the corresponding unwoven linear polymer. Video credit: Stuart Jantzen (Biocinematics).

### **Video 5**

Supplementary Video 5 (MPEG-4) - Animation of the ion permeability studies on PVDF-supported membranes formed from (i) the 2D molecularly woven fabric and (ii) the corresponding unwoven linear polymer. Video credit: Stuart Jantzen (Biocinematics).

## **Rights and permissions**

[Reprints and Permissions](#)

## **About this article**



Check for  
updates

## Cite this article

August, D.P., Dryfe, R.A.W., Haigh, S.J. *et al.* Self-assembly of a layered two-dimensional molecularly woven fabric. *Nature* **588**, 429–435 (2020). <https://doi.org/10.1038/s41586-020-3019-9>

[Download citation](#)

- Received: 01 July 2020
- Accepted: 28 October 2020
- Published: 16 December 2020
- Issue Date: 17 December 2020
- DOI: <https://doi.org/10.1038/s41586-020-3019-9>

## Further reading

- [A molecular endless \(74\) knot](#)

- David A. Leigh
- , Jonathan J. Danon
- , Stephen D. P. Fielden
- , Jean-FranÃ§ois Lemonnier
- , George F. S. Whitehead
- & Steffen L. Woltering

*Nature Chemistry* (2020)

## Comments

By submitting a comment you agree to abide by our [Terms](#) and [Community Guidelines](#). If you find something abusive or that does not comply with our terms or guidelines please flag it as inappropriate.

[Access through your institution](#)

[Change institution](#)

[Buy or subscribe](#)

## Associated Content

*Nature* | Research Highlight

[\*\*Chemists tie an ‘endless’ knot — one of the most complex ever made\*\*](#)

---

This article was downloaded by **calibre** from <https://www.nature.com/articles/s41586-020-3019-9>

| [Section menu](#) | [Main menu](#) |

- Article
- [Published: 16 December 2020](#)

# More than one million barriers fragment Europe's rivers

- [Barbara Belletti](#) ORCID: [orcid.org/0000-0002-6247-7619<sup>1</sup>](https://orcid.org/0000-0002-6247-7619)<sup>nAff29</sup>,
- [Carlos Garcia de Leaniz](#) ORCID: [orcid.org/0000-0003-1650-2729<sup>2</sup>](https://orcid.org/0000-0003-1650-2729),
- [Joshua Jones](#) ORCID: [orcid.org/0000-0001-9047-9147<sup>2</sup>](https://orcid.org/0000-0001-9047-9147),
- [Simone Buzzi](#)<sup>1</sup><sup>nAff30</sup>,
- [Luca Börger](#) ORCID: [orcid.org/0000-0001-8763-5997<sup>2</sup>](https://orcid.org/0000-0001-8763-5997),
- [Gilles Segura](#)<sup>3,4</sup>,
- [Andrea Castelletti](#) ORCID: [orcid.org/0000-0002-7923-1498<sup>1</sup>](https://orcid.org/0000-0002-7923-1498),
- [Wouter van de Bund](#) ORCID: [orcid.org/0000-0002-2749-0850<sup>5</sup>](https://orcid.org/0000-0002-2749-0850),
- [Kim Aarestrup](#)<sup>6</sup>,
- [James Barry](#)<sup>7</sup>,
- [Kamila Belka](#) ORCID: [orcid.org/0000-0002-3002-0913<sup>8</sup>](https://orcid.org/0000-0002-3002-0913),
- [Arjan Berkhuyzen](#)<sup>9</sup>,
- [Kim Birnie-Gauvin](#) ORCID: [orcid.org/0000-0001-9242-0560<sup>6</sup>](https://orcid.org/0000-0001-9242-0560),
- [Martina Bussettini](#) ORCID: [orcid.org/0000-0002-1346-749X<sup>10</sup>](https://orcid.org/0000-0002-1346-749X),
- [Mauro Carolly](#) ORCID: [orcid.org/0000-0001-9625-8441<sup>11</sup>](https://orcid.org/0000-0001-9625-8441),
- [Sofia Consuegra](#) ORCID: [orcid.org/0000-0003-4403-2509<sup>2</sup>](https://orcid.org/0000-0003-4403-2509),
- [Eduardo Dopico](#) ORCID: [orcid.org/0000-0001-6777-5407<sup>12</sup>](https://orcid.org/0000-0001-6777-5407),
- [Tim Feierfeil](#)<sup>13</sup>,
- [Sara Fernández](#)<sup>12</sup>,
- [Pao Fernandez Garrido](#)<sup>9</sup>,
- [Eva Garcia-Vazquez](#) ORCID: [orcid.org/0000-0002-8429-838X<sup>12</sup>](https://orcid.org/0000-0002-8429-838X),
- [Sara Garrido](#)<sup>14</sup>,
- [Guillermo Giannico](#)<sup>15</sup>,
- [Peter Gough](#)<sup>9</sup>,

- [Niels Jepsen<sup>6</sup>](#),
- [Peter E. Jones<sup>2</sup>](#),
- [Paul Kemp ORCID: orcid.org/0000-0003-4470-0589<sup>16</sup>](#),
- [Jim Kerr ORCID: orcid.org/0000-0002-2990-7293<sup>16</sup>](#),
- [James King<sup>7</sup>](#),
- [Małgorzata Łapińska<sup>8,17</sup>](#),
- [Gloria Lázaro ORCID: orcid.org/0000-0002-3690-4461<sup>14</sup>](#),
- [Martyn C. Lucas ORCID: orcid.org/0000-0002-2009-1785<sup>18</sup>](#),
- [Lucio Marcello<sup>19</sup>](#),
- [Patrick Martin<sup>3</sup>](#),
- [Phillip McGinnity ORCID: orcid.org/0000-0001-5199-5632<sup>20,21</sup>](#),
- [Jesse O'Hanley ORCID: orcid.org/0000-0003-3522-8585<sup>22</sup>](#),
- [Rosa Olivo del Amo ORCID: orcid.org/0000-0003-3014-5625<sup>9 nAff31</sup>](#),
- [Piotr Parasiewicz ORCID: orcid.org/0000-0003-1672-3759<sup>23</sup>](#),
- [Martin Pusch<sup>11</sup>](#),
- [Gonzalo Rincon ORCID: orcid.org/0000-0001-8635-507X<sup>24</sup>](#),
- [Cesar Rodriguez<sup>14</sup>](#),
- [Joshua Royte<sup>25</sup>](#),
- [Claus Till Schneider<sup>26</sup>](#),
- [Jeroen S. Tummers<sup>18</sup>](#),
- [Sergio Vallesi<sup>18 nAff32</sup>](#),
- [Andrew Vowles ORCID: orcid.org/0000-0001-8253-5938<sup>16</sup>](#),
- [Eric Verspoor<sup>19</sup>](#),
- [Herman Wanningen<sup>9</sup>](#),
- [Karl M. Wantzen ORCID: orcid.org/0000-0002-2192-1883<sup>27 nAff33</sup>](#),
- [Laura Wildman<sup>28</sup>](#) &
- [Maciej Zalewski ORCID: orcid.org/0000-0002-4483-6200<sup>8</sup>](#)

[Nature volume 588](#), pages436–441(2020) [Cite this article](#)

- 1666 Accesses
- 379 Altmetric
- [Metrics details](#)

## Subjects

- [Conservation biology](#)
- [Hydrology](#)
- [Water resources](#)

## Abstract

Rivers support some of Earth's richest biodiversity<sup>1</sup> and provide essential ecosystem services to society<sup>2</sup>, but they are often fragmented by barriers to free flow<sup>3</sup>. In Europe, attempts to quantify river connectivity have been hampered by the absence of a harmonized barrier database. Here we show that there are at least 1.2 million instream barriers in 36 European countries (with a mean density of 0.74 barriers per kilometre), 68 per cent of which are structures less than two metres in height that are often overlooked. Standardized walkover surveys along 2,715 kilometres of stream length for 147 rivers indicate that existing records underestimate barrier numbers by about 61 per cent. The highest barrier densities occur in the heavily modified rivers of central Europe and the lowest barrier densities occur in the most remote, sparsely populated alpine areas. Across Europe, the main predictors of barrier density are agricultural pressure, density of river-road crossings, extent of surface water and elevation. Relatively unfragmented rivers are still found in the Balkans, the Baltic states and parts of Scandinavia and southern Europe, but these require urgent protection from proposed dam developments. Our findings could inform the implementation of the EU Biodiversity Strategy, which aims to reconnect 25,000 kilometres of Europe's rivers by 2030, but achieving this will require a paradigm shift in river restoration that recognizes the widespread impacts caused by small barriers.

[Access through your institution](#)

[Change institution](#)

[Buy or subscribe](#)

## Access options

## Subscribe to Journal

Get full journal access for 1 year

185,98 €

only 3,58 € per issue

[Subscribe](#)

All prices are NET prices.

VAT will be added later in the checkout.

## Rent or Buy article

Get time limited or full article access on ReadCube.

from \$8.99

[Rent or Buy](#)

All prices are NET prices.

## Additional access options:

- [Log in](#)
- [Access through your institution](#)
- [Learn about institutional subscriptions](#)

**Fig. 1: Artificial instream barriers in Europe (from the AMBER Barrier Atlas).**



**Fig. 2: Extent of river fragmentation in Europe.**



**Fig. 3: Extent of barrier under-reporting.**



## Data availability

Data for the AMBER Barrier Atlas (Fig. 1), observed barrier densities (Fig. 2a), ground-truthed barrier densities (Fig. 2b) and modelled barrier densities (Fig. 2c) are freely available at <https://amber.international/european-barrier-atlas/> as well as at <https://doi.org/10.6084/m9.figshare.12629051> under a CC-BY-4.0 license. Data for ground-truthed surveyed reaches (Extended Data Table 1, Extended Data Fig. 3) are also available at <https://doi.org/10.6084/m9.figshare.12629051> under a CC-BY-4.0 license. Results of walkover surveys in test rivers (Extended Data Table 1), and barrier database sources (Table 1) are also available at <https://doi.org/10.6084/m9.figshare.12629051>. Source data are provided with this paper.

## Code availability

The Python code used for modelling of barrier abundance, with links to GIS files for visualization, is available under a GNU ([https://en.wikipedia.org/wiki/GNU\\_Project](https://en.wikipedia.org/wiki/GNU_Project)) General Public License at <https://github.com/AMBER-data/atlas-model>. Protocols used for barrier database management, duplicate exclusion and processing were done

manually in SQL and QGIS using ad hoc procedures and are not deposited in a repository.

## References

1. 1.

Reid, A. J. et al. Emerging threats and persistent conservation challenges for freshwater biodiversity. *Biol. Rev. Camb. Phil. Soc.* **94**, 849–873 (2019).

[Google Scholar](#)

2. 2.

Grizzetti, B. et al. Relationship between ecological condition and ecosystem services in European rivers, lakes and coastal waters. *Sci. Total Environ.* **671**, 452–465 (2019).

[ADS](#) [CAS](#) [PubMed](#) [PubMed Central](#) [Google Scholar](#)

3. 3.

Grill, G. et al. Mapping the world's free-flowing rivers. *Nature* **569**, 215–221 (2019).

[ADS](#) [CAS](#) [PubMed](#) [PubMed Central](#) [Google Scholar](#)

4. 4.

Vannote, R. L., Minshall, G. W., Cummins, K. W., Sedell, J. R. & Cushing, C. E. The river continuum concept. *Can. J. Fish. Aquat. Sci.* **37**, 130–137 (1980).

[Google Scholar](#)

5. 5.

Vitousek, P. M., Mooney, H. A., Lubchenco, J. & Melillo, J. M. Human domination of Earth's ecosystems. *Science* **277**, 494–499 (1997).

[CAS](#) [Google Scholar](#)

6. 6.

Carpenter, S. R., Stanley, E. H. & Zanden, M. J. V. State of the world's freshwater ecosystems: physical, chemical, and biological changes. *Annu. Rev. Environ. Resour.* **36**, 75–99 (2011).

[Google Scholar](#)

7. 7.

Fuller, M. R., Doyle, M. W. & Strayer, D. L. Causes and consequences of habitat fragmentation in river networks: river fragmentation. *Ann. NY Acad. Sci.* **1355**, 31–51 (2015).

[ADS](#) [PubMed](#) [Google Scholar](#)

8. 8.

Van Looy, K., Tormos, T. & Souchon, Y. Disentangling dam impacts in river networks. *Ecol. Indic.* **37**, 10–20 (2014).

[Google Scholar](#)

9. 9.

Kemp, P. & O'Hanley, J. Procedures for evaluating and prioritising the removal of fish passage barriers: a synthesis. *Fish. Manag. Ecol.* **17**, 297–322 (2010).

[Google Scholar](#)

10. 10.

Lehner, B. et al. High-resolution mapping of the world's reservoirs and dams for sustainable river-flow management. *Front. Ecol. Environ.* **9**, 494–502 (2011).

[Google Scholar](#)

11. 11.

Lehner, B. et al. *Global Reservoir and Dam Database version 1 (GRanDv1)* <https://doi.org/10.7927/H4N877QK> (NASA Socioeconomic Data and Applications Center, 2011).

12. 12.

Mulligan, M., Soesbergen, A. V. & Sáenz, L. GOODD, a global dataset of more than 38,000 georeferenced dams. *Sci. Data* **7**, 31 (2020).

[PubMed](#) [PubMed Central](#) [Google Scholar](#)

13. 13.

Garcia de Leaniz, C., Berkhuyzen, A. & Belletti, B. Beware small dams, they can do damage too. *Nature* **570**, 164 (2019).

[ADS](#) [Google Scholar](#)

14. 14.

Mantel, S. K., Rivers-Moore, N. & Ramulifho, P. Small dams need consideration in riverscape conservation assessments: small dams and riverscape conservation. *Aqua. Conserv. Mar. Freshw. Ecosyst.* **27**, 748–754 (2017).

[Google Scholar](#)

15. 15.

Lucas, M. C., Bubb, D. H., Jang, M.-H., Ha, K. & Masters, J. E. G. Availability of and access to critical habitats in regulated rivers: effects of low-head barriers on threatened lampreys. *Freshw. Biol.* **54**, 621–634 (2009).

[Google Scholar](#)

16. 16.

Birnie-Gauvin, K., Aarestrup, K., Riis, T. M. O., Jepsen, N. & Koed, A. Shining a light on the loss of rheophilic fish habitat in lowland rivers as a forgotten consequence of barriers, and its implications for management. *Aqua. Conserv. Mar. Freshw. Ecosyst.* **27**, 1345–1349 (2017).

[Google Scholar](#)

17. 17.

Magilligan, F. J., Nislow, K. H. & Renshaw, C. E. in *Treatise on Geomorphology* (ed. Shroder, J. F.) 794–808 (Academic Press, 2013).

18. 18.

Petts, G. E. & Gurnell, A. M. Dams and geomorphology: research progress and future directions. *Geomorphology* **71**, 27–47 (2005).

[ADS](#) [Google Scholar](#)

19. 19.

Bizzi, S. et al. On the control of riverbed incision induced by run-of-river power plant. *Wat. Resour. Res.* **51**, 5023–5040 (2015).

[ADS](#) [Google Scholar](#)

20. 20.

Jones, P. E., Consuegra, S., Börger, L., Jones, J. & Garcia de Leaniz, C. Impacts of artificial barriers on the connectivity and dispersal of vascular macrophytes in rivers: a critical review. *Freshw. Biol.* **65**, 1165–1180 (2020).

[Google Scholar](#)

21. 21.

Carpenter-Bundhoo, L. et al. Effects of a low-head weir on multi-scaled movement and behavior of three riverine fish species. *Sci. Rep.* **10**, 6817 (2020).

[ADS](#) [CAS](#) [PubMed](#) [PubMed Central](#) [Google Scholar](#)

22. 22.

Graf, W. L. Dam nation: a geographic census of American dams and their large-scale hydrologic impacts. *Wat. Resour. Res.* **35**, 1305–1311 (1999).

[ADS](#) [Google Scholar](#)

23. 23.

Jones, J. et al. A comprehensive assessment of stream fragmentation in Great Britain. *Sci. Total Environ.* **673**, 756–762 (2019).

[ADS](#) [CAS](#) [PubMed](#) [Google Scholar](#)

24. 24.

Grizzetti, B. et al. Human pressures and ecological status of European rivers. *Sci. Rep.* **7**, 205 (2017).

[ADS](#) [CAS](#) [PubMed](#) [PubMed Central](#) [Google Scholar](#)

25. 25.

Mauch, C. & Zeller, T. (eds) *Rivers in History: Perspectives on Waterways in Europe and North America* (Univ. of Pittsburgh Press, 2008).

26. 26.

Petts, G. E., Möller, H. & Roux, A. L. *Historical Change of Large Alluvial Rivers: Western Europe* 355 (John Wiley and Sons, 1989).

27. 27.

Kemp, P. S. in *Freshwater Fisheries Ecology* (ed. Craig, J. F.) 717–769 (Wiley, 2015).

28. 28.

European Environment Agency in *European Waters—Assessment of Status and Pressures* 85 (EEA, 2018).

29. 29.

Garcia de Leaniz, C. et al. in *From Sea to Source v2. Protection and Restoration of Fish Migration in Rivers Worldwide* (eds Brink, K. et al.) 142–145 (World Fish Migration Foundation, 2018).

30. 30.

Pistocchi, A. et al. Assessment of the Effectiveness of Reported Water Framework Directive Programmes of Measures. Part II—Development of a System of Europe-wide Pressure Indicators. Report No. EUR 28412 EN (Joint Research Centre, 2017).

31. 31.

Garcia de Leaniz, C. Weir removal in salmonid streams: implications, challenges and practicalities. *Hydrobiologia* **609**, 83–96 (2008).

[Google Scholar](#)

32. 32.

Downward, S. & Skinner, K. Working rivers: the geomorphological legacy of English freshwater mills. *Area* **37**, 138–147 (2005).

[Google Scholar](#)

33. 33.

Sun, J., Galib, S. M. & Lucas, M. C. Are national barrier inventories fit for stream connectivity restoration needs? A test of two catchments. *Wat. Environ. J.* <https://doi.org/10.1111/wej.12578> (2020).

34. 34.

Atkinson, S. et al. An inspection-based assessment of obstacles to salmon, trout, eel and lamprey migration and river channel connectivity in Ireland. *Sci. Total Environ.* **719**, 137215 (2020).

[ADS](#) [CAS](#) [PubMed](#) [Google Scholar](#)

35. 35.

European Environment Agency *European Catchments and Rivers Network System (ECRINS)* (EEA, 2012).

36. 36.

Kristensen, P. & Globevnik, L. European small water bodies. *Biol. Environ.* **114B**, 281–287 (2014).

[Google Scholar](#)

37. 37.

Ferreira, T., Globevnik, L. & Schinegger, R. in *Multiple Stressors in River Ecosystems* 139–155 (Elsevier, 2019).

38. 38.

Schwarz, U. *Hydropower Pressure on European Rivers* 36 (WWF, 2019).

39. 39.

Schiemer, F. et al. The Vjosa River corridor: a model of natural hydro-morphodynamics and a hotspot of highly threatened ecosystems of European significance. *Land. Ecol.* **35**, 953–968 (2020).

[Google Scholar](#)

40. 40.

Duflo, E. & Pande, R. Dams. *Q. J. Econ.* **122**, 601–646 (2007).

[Google Scholar](#)

41. 41.

Grill, G., Ouellet Dallaire, C., Fluet Chouinard, E., Sindorf, N. & Lehner, B. Development of new indicators to evaluate river fragmentation and flow regulation at large scales: a case study for the Mekong River Basin. *Ecol. Indic.* **45**, 148–159 (2014).

[Google Scholar](#)

42. 42.

Zarfl, C., Lumsdon, A. E., Berlekamp, J., Tydecks, L. & Tockner, K. A global boom in hydropower dam construction. *Aquat. Sci.* **77**, 161–170 (2015).

[Google Scholar](#)

43. 43.

Tilt, B., Braun, Y. & He, D. Social impacts of large dam projects: a comparison of international case studies and implications for best practice. *J. Environ. Manage.* **90**, S249–S257 (2009).

[PubMed](#) [Google Scholar](#)

44. 44.

Schmitt, R. J. P., Bizzi, S., Castelletti, A. & Kondolf, G. M. Improved trade-offs of hydropower and sand connectivity by strategic dam planning in the Mekong. *Nature Sust.* **1**, 96–104 (2018).

[Google Scholar](#)

45. 45.

Weibel, D. & Peter, A. Effectiveness of different types of block ramps for fish upstream movement. *Aquat. Sci.* **75**, 251–260 (2013).

[Google Scholar](#)

46. 46.

Cote, D., Kehler, D. G., Bourne, C. & Wiersma, Y. F. A new measure of longitudinal connectivity for stream networks. *Landsc. Ecol.* **24**, 101–113 (2009).

[Google Scholar](#)

47. 47.

Tickner, D. et al. Bending the curve of global freshwater biodiversity loss: an emergency recovery plan. *BioScience* **70**, 330–342 (2020).

[PubMed](#) [PubMed Central](#) [Google Scholar](#)

48. 48.

Bódis, K., Monforti, F. & Szabó, S. Could Europe have more mini hydro sites? A suitability analysis based on continentally harmonized geographical and hydrological data. *Renew. Sust. Energy Rev.* **37**, 794–808 (2014).

[Google Scholar](#)

49. 49.

Huđek, H., Žganec, K. & Pusch, M. T. A review of hydropower dams in Southeast Europe—distribution, trends and availability of monitoring data using the example of a multinational Danube catchment subarea. *Renew. Sust. Energy Rev.* **117**, 109434 (2020).

[Google Scholar](#)

50. 50.

European Union *Bringing Nature Back Into Our Lives. EU 2030 Biodiversity Strategy.* <https://eur-lex.europa.eu/legal-content/EN/TXT/?qid=1590574123338&uri=CELEX:52020DC0380> (European Commission, 2020).

51. 51.

Wohl, E. Connectivity in rivers. *Progr. Phys. Geog. Earth. Env.* **41**, 345–362 (2017).

[Google Scholar](#)

52. 52.

Belletti, B. et al. Datasets for the AMBER Barrier Atlas of Europe. Table S1. Details of test rivers showing number of barriers present in current inventories (Atlas) and those encountered in the field. Table S3. Barrier Database sources. *figshare* <https://doi.org/10.6084/m9.figshare.12629051> (2020).

53. 53.

Jones, J. et al. Quantifying river fragmentation from local to continental scales: data management and modelling methods. Preprint at <https://doi.org/10.22541/au.159612917.72148332> (2020).

54. 54.

*QGIS Geographic Information System* <https://qgis.org/en/site/> (Open Source Geospatial Foundation Project, 2010).

55. 55.

Chao, A., Wang, Y. T. & Jost, L. Entropy and the species accumulation curve: a novel entropy estimator via discovery rates of new species. *Methods Ecol. Evol.* **4**, 1091–1100 (2013).

[Google Scholar](#)

56. 56.

Strahler, A. N. Quantitative analysis of watershed geomorphology. *Trans. AGU* **38**, 913–920 (1957).

[Google Scholar](#)

57. 57.

*R: A Language And Environment For Statistical Computing* Version 4.0.0 (2020-04-24) <https://www.r-project.org/> (R Foundation for Statistical Computing, 2020).

58. 58.

Signorell, A. et al. DescTools: tools for descriptive statistics. R package version 0.99.37 <https://andrisignorell.github.io/DescTools/> (2020).

59. 59.

Januchowski-Hartley, S. R. et al. Restoring aquatic ecosystem connectivity requires expanding inventories of both dams and road crossings. *Front. Ecol. Environ.* **11**, 211–217 (2013).

[Google Scholar](#)

60. 60.

Schmutz, S. & Moog, O. in *Riverine Ecosystem Management* 111–127 (Springer, 2018).

61. 61.

European Environment Agency *CORINE Land Cover (CLC)* Version 20 <https://www.eea.europa.eu/data-and-maps/data/copernicus-land-monitoring-service-corine> (2012).

62. 62.

European Commission *Global Human Settlement—GHS Population Grid* [https://ghsl.jrc.ec.europa.eu/ghs\\_pop.php](https://ghsl.jrc.ec.europa.eu/ghs_pop.php) (2015).

63. 63.

European Environment Agency *EU-DEM* v1.1, <https://land.copernicus.eu/imagery-in-situ/eu-dem/eu-dem-v1.1> (Copernicus Land Monitoring Service, 2016).

64. 64.

Meijer, J. R., Huijbregts, M. A. J., Schotten, K. C. G. J. & Schipper, A. M. Global patterns of current and future road infrastructure. *Environ. Res. Lett.* **13**, 064006 (2018).

[ADS](#) [Google Scholar](#)

65. 65.

Louppe, G., Wehenkel, L., Sutera, A. & Geurts, P. in *Advances in Neural Information Processing Systems* (eds Burges, C. J. C. et al.) 431–439 (Neural Information Processing Systems Foundation, 2013).

66. 66.

*National Inventory of Dams* <http://nid.usace.army.mil/> (2018).

67. 67.

Yoshimura, C., Omura, T., Furumai, H. & Tockner, K. Present state of rivers and streams in Japan. *River Res. Appl.* **21**, 93–112 (2005).

[Google Scholar](#)

68. 68.

*Brazil Dams Safety Report*

<http://www.snisb.gov.br/portal/snisb/relatorio-anual-de-seguranca-de-barragem/2019/rsb19-v0.pdf> (National Water Agency (ANA), Brazil, 2020).

69. 69.

World Commission on Dams *Dams and Development: A New Framework for Decision Making*

<https://pubs.iied.org/pdfs/9126IIED.pdf> (Earthscan Publications, 2000).

70. 70.

International Rivers. The True Cost of Hydropower in China.

[https://www.internationalrivers.org/wp-content/uploads/sites/86/2020/06/truecostofhydro\\_en\\_small.pdf](https://www.internationalrivers.org/wp-content/uploads/sites/86/2020/06/truecostofhydro_en_small.pdf) (2014).

71. 71.

Lehner, B., Verdin, K. & Jarvis, A. New global hydrography derived from spaceborne elevation data. *Trans. AGU* **89**, 93–94 (2008).

[ADS](#) [Google Scholar](#)

[Download references](#)

## Acknowledgements

This study was funded by the EC Horizon 2020 Research and Innovation Programme, AMBER (Adaptive Management of Barriers in European Rivers) Project, grant agreement number 689682, led by C.G.d.L. B.B. was partially supported by EUR H2O'Lyon (ANR-17-EURE-0018) at Université de Lyon. We are indebted to the following institutions, which facilitated barrier data gathering: the International Commission for the Protection of the Danube River (Albania, Croatia, North Macedonia, Serbia, Slovenia); the Ministeri de Medi Ambient, Agricultura i Sostenibilitat. Govern d'Andorra (Andorra); the Bundesministerium für Nachhaltigkeit und Tourismus (Austria); the Service Public de Wallonie, Secrétariat Général (Belgium); the Vlaamse Milieumaatschappij (Belgium); the Agencija za vodno područje Jadranskog mora (Bosnia and Herzegovina); the Balkanka Association (Bulgaria); The Cyprus Conservation Foundation, Terra Cypria (Cyprus); the Ministerstvo Zemědělství (Czech Republic); the Danish Environmental Protection Agency (Denmark); the Keskkonnaministeerium (Estonia); Suomen ympäristökeskus (Finland); the Office national de l'eau et des milieux aquatiques (ONEMA) (France); Landesanstalt für Umwelt Baden-Württemberg (Germany); Bayerisches Landesamt für Umwelt (Germany); Senatsverwaltung für Umwelt, Verkehr und Klimaschutz Berlin (Germany); Landesamt für Umwelt Brandenburg (Germany); Der Senator für Umwelt, Bau und Verkehr Bremen (Germany); Amt für Umweltschutz Hamburg (Germany); Hessisches Landesamt für Naturschutz, Umwelt und Geologie (Germany); Landesamt für Umwelt, Naturschutz und Geologie Mecklenburg-Vorpommern (Germany); Ministerium für Umwelt, Energie, Bauen und Klimaschutz Niedersachsen (Germany); Landesamt für Natur, Umwelt und Verbraucherschutz Nordrhein-Westfalen (Germany); Landesamt für Umwelt Rheinland-Pfalz (Germany); Sächsisches Landesamt für Umwelt, Landwirtschaft und Geologie (Germany); Landesbetrieb für Hochwasserschutz und Wasserwirtschaft Sachsen-Anhalt (Germany); Landesamt für Landwirtschaft, Umwelt und ländliche Räume des Landes Schleswig-Holstein (Germany); Thüringer Landesamt für Umwelt und Geology (Germany); Bundesanstalt für Gewässerkunde (Germany); the Greek Committee on Large Dams (Greece); the WWF Greece; Országos Vízügyi Főigazgatóság (Hungary); the Marine and Freshwater Research Institute (Iceland); Inland Fisheries Ireland (Ireland); Registro Italiano Dighe (Italy); Regione Emilia-Romagna, Lombardia, Piemonte, Toscana (Italy), Latvijas

Vides, ģeoloģijas un meteoroloģijas centrs (Latvia); Aplinkos apsaugos agentūra (Lithuania); the Ministère du Développement durable et des Infrastructures (Luxembourg); the Ministerstvo poljoprivrede i ruralnog razvoja (Montenegro); PDOK (The Netherlands); VISpas (The Netherlands); Norges vassdrags-og energidirektorat (Norway); Gospodarstwo Wody Polskie, National Water Management Board (Poland); the Stanisław Sakowicz Inland Fisheries Institute (Poland); the Universidade de Lisboa, Centro de Estudos Florestais (Portugal); Agência Portuguesa do Ambiente (Portugal); Ministerul Apelor și Pădurilor (Romania); WWF Danube-Carpathian (Romania); Ministerstvo životného prostredia (Slovakia); Confederación Hidrográfica del Júcar (Spain); Confederación Hidrográfica del Cantábrico (Spain); Confederación Hidrográfica del Duero (Spain); Confederación Hidrográfica del Tajo (Spain); Confederación Hidrográfica del Guadiana (Spain); Confederación Hidrográfica del Ebro (Spain); Uraren Euskal Agentzia (Spain); Confederación Hidrográfica del Guadalquivir (Spain); Confederación Hidrográfica del Segura (Spain); Universidad de Murcia (Spain); Universidad de Córdoba (Spain); Universidad de Cantabria (Spain); Ministerio para la Transición Ecológica y el Reto Demográfico (Spain); Agència Catalana de l'Aigua (Spain); SUDOANG (Spain); LST Biotopkartering vandringshinder (Sweden); Nationella Biotopkarteringsdatabasen (Sweden); Federal Office for the Environment (FOEN) (Switzerland); Geocat.ch (Switzerland); the Environment Agency (UK); Natural Resources Wales (UK); and the Scottish Environment Protection Agency (UK). We thank G. Luoni for help in developing the random forest regression model, and many students and colleagues who helped with field surveys across Europe.

## Author information

### Author notes

#### 1. Barbara Belletti

Present address: EVS, CNRS UMR 5600, University of Lyon, Lyon, France

2. Simone Bizzi

Present address: University of Padova, Padua, Italy

3. Rosa Olivo del Amo

Present address: University of Murcia, Murcia, Spain

4. Sergio Vallesi

Present address: HydroneXus, Bologna, Italy

5. Karl M. Wantzen

Present address: CNRS UMR 7362-LIVE, University of Strasbourg,  
Strasbourg, France

## Affiliations

1. Politecnico di Milano, Milan, Italy

Barbara Belletti, Simone Bizzi & Andrea Castelletti

2. Swansea University, Swansea, UK

Carlos Garcia de Leaniz, Joshua Jones, Luca Börger, Sofia  
Consuegra & Peter E. Jones

3. Conservatoire National du Saumon Sauvage, Chanteuges, France

Gilles Segura & Patrick Martin

4. IS Environnement, Saint-Jean, France

Gilles Segura

5. European Commission Joint Research Centre, Ispra, Italy

Wouter van de Bund

6. Technical University of Denmark, Silkeborg, Denmark

Kim Aarestrup, Kim Birnie-Gauvin & Niels Jepsen

7. Inland Fisheries Ireland, Dublin, Ireland

James Barry & James King

8. European Regional Centre for Ecohydrology of the Polish Academy of Sciences, Łódź, Poland

Kamila Belka, Małgorzata Łapińska & Maciej Zalewski

9. World Fish Migration Foundation, Groningen, The Netherlands

Arjan Berkhuysen, Pao Fernandez Garrido, Peter Gough, Rosa Olivo del Amo & Herman Wanningen

10. Italian National Institute for Environmental Protection and Research, Rome, Italy

Martina Bussetti

11. Leibniz Institute of Freshwater Ecology and Inland Fisheries, Berlin, Germany

Mauro Carolly & Martin Pusch

12. University of Oviedo, Oviedo, Spain

Eduardo Dopico, Sara Fernández & Eva Garcia-Vazquez

13. ingenieurbüro kauppert, Karlsruhe, Germany

Tim Feierfeil

14. AEMS-Rios con Vida, Madrid, Spain

Sara Garrido, Gloria Lázaro & Cesar Rodriguez

15. Oregon State University, Corvallis, OR, USA

Guillermo Giannico

16. University of Southampton, Southampton, UK

Paul Kemp, Jim Kerr & Andrew Vowles

17. University of Łódź, Łódź, Poland

Małgorzata Łapińska

18. Durham University, Durham, UK

Martyn C. Lucas, Jeroen S. Tummers & Sergio Vallesi

19. University of Highlands and Islands, Inverness, UK

Lucio Marcello & Eric Verspoor

20. University College Cork, Cork, Ireland

Phillip McGinnity

21. Marine Institute, Newport, Ireland

Phillip McGinnity

22. University of Kent, Canterbury, UK

Jesse O'Hanley

23. Stanisław Sakowicz Inland Fisheries Institute, Olsztyn, Poland

Piotr Parasiewicz

24. Polytechnic University of Madrid, Madrid, Spain

Gonzalo Rincon

25. The Nature Conservancy, Brunswick, ME, USA

Joshua Royte

26. RWE Generation SE, Essen, Germany

Claus Till Schneider

27. University of Tours, Tours, France

Karl M. Wantzen

28. Princeton Hydro, South Glastonbury, CT, USA

Laura Wildman

## Authors

1. Barbara Belletti

[View author publications](#)

You can also search for this author in [PubMed](#) [Google Scholar](#)

2. Carlos Garcia de Leaniz

[View author publications](#)

You can also search for this author in [PubMed](#) [Google Scholar](#)

3. Joshua Jones

[View author publications](#)

You can also search for this author in [PubMed](#) [Google Scholar](#)

4. Simone Bizzi

[View author publications](#)

You can also search for this author in [PubMed](#) [Google Scholar](#)

5. Luca Börger

[View author publications](#)

You can also search for this author in [PubMed](#) [Google Scholar](#)

6. Gilles Segura

[View author publications](#)

You can also search for this author in [PubMed](#) [Google Scholar](#)

7. Andrea Castelletti

[View author publications](#)

You can also search for this author in [PubMed](#) [Google Scholar](#)

8. Wouter van de Bund

[View author publications](#)

You can also search for this author in [PubMed](#) [Google Scholar](#)

9. Kim Aarestrup

[View author publications](#)

You can also search for this author in [PubMed](#) [Google Scholar](#)

10. James Barry

[View author publications](#)

You can also search for this author in [PubMed](#) [Google Scholar](#)

11. Kamila Belka

[View author publications](#)

You can also search for this author in [PubMed](#) [Google Scholar](#)

12. Arjan Berkhuysen

[View author publications](#)

You can also search for this author in [PubMed](#) [Google Scholar](#)

13. Kim Birnie-Gauvin

[View author publications](#)

You can also search for this author in [PubMed](#) [Google Scholar](#)

14. Martina Bussettin

[View author publications](#)

You can also search for this author in [PubMed](#) [Google Scholar](#)

15. Mauro Carolli

[View author publications](#)

You can also search for this author in [PubMed](#) [Google Scholar](#)

16. Sofia Consuegra

[View author publications](#)

You can also search for this author in [PubMed](#) [Google Scholar](#)

17. Eduardo Dopico

[View author publications](#)

You can also search for this author in [PubMed](#) [Google Scholar](#)

18. Tim Feierfeil

[View author publications](#)

You can also search for this author in [PubMed](#) [Google Scholar](#)

19. Sara Fernández

[View author publications](#)

You can also search for this author in [PubMed](#) [Google Scholar](#)

20. Pao Fernandez Garrido

[View author publications](#)

You can also search for this author in [PubMed](#) [Google Scholar](#)

21. Eva Garcia-Vazquez

[View author publications](#)

You can also search for this author in [PubMed](#) [Google Scholar](#)

22. Sara Garrido

[View author publications](#)

You can also search for this author in [PubMed](#) [Google Scholar](#)

23. Guillermo Giannico

[View author publications](#)

You can also search for this author in [PubMed](#) [Google Scholar](#)

24. Peter Gough

[View author publications](#)

You can also search for this author in [PubMed](#) [Google Scholar](#)

25. Niels Jepsen

[View author publications](#)

You can also search for this author in [PubMed](#) [Google Scholar](#)

26. Peter E. Jones

[View author publications](#)

You can also search for this author in [PubMed](#) [Google Scholar](#)

27. Paul Kemp

[View author publications](#)

You can also search for this author in [PubMed](#) [Google Scholar](#)

28. Jim Kerr

[View author publications](#)

You can also search for this author in [PubMed](#) [Google Scholar](#)

29. James King

[View author publications](#)

You can also search for this author in [PubMed](#) [Google Scholar](#)

30. Małgorzata Łapińska

[View author publications](#)

You can also search for this author in [PubMed](#) [Google Scholar](#)

31. Gloria Lázaro

[View author publications](#)

You can also search for this author in [PubMed](#) [Google Scholar](#)

32. Martyn C. Lucas

[View author publications](#)

You can also search for this author in [PubMed](#) [Google Scholar](#)

33. Lucio Marcello

[View author publications](#)

You can also search for this author in [PubMed](#) [Google Scholar](#)

34. Patrick Martin

[View author publications](#)

You can also search for this author in [PubMed](#) [Google Scholar](#)

35. Phillip McGinnity

[View author publications](#)

You can also search for this author in [PubMed](#) [Google Scholar](#)

36. Jesse O'Hanley

[View author publications](#)

You can also search for this author in [PubMed](#) [Google Scholar](#)

37. Rosa Olivo del Amo

[View author publications](#)

You can also search for this author in [PubMed](#) [Google Scholar](#)

38. Piotr Parasiewicz

[View author publications](#)

You can also search for this author in [PubMed](#) [Google Scholar](#)

39. Martin Pusch

[View author publications](#)

You can also search for this author in [PubMed](#) [Google Scholar](#)

40. Gonzalo Rincon

[View author publications](#)

You can also search for this author in [PubMed](#) [Google Scholar](#)

41. Cesar Rodriguez

[View author publications](#)

You can also search for this author in [PubMed](#) [Google Scholar](#)

42. Joshua Royte

[View author publications](#)

You can also search for this author in [PubMed](#) [Google Scholar](#)

43. Claus Till Schneider

[View author publications](#)

You can also search for this author in [PubMed](#) [Google Scholar](#)

44. Jeroen S. Tummers

[View author publications](#)

You can also search for this author in [PubMed](#) [Google Scholar](#)

45. Sergio Vallesi

[View author publications](#)

You can also search for this author in [PubMed](#) [Google Scholar](#)

46. Andrew Vowles

[View author publications](#)

You can also search for this author in [PubMed](#) [Google Scholar](#)

47. Eric Verspoor

[View author publications](#)

You can also search for this author in [PubMed](#) [Google Scholar](#)

48. Herman Wanningen

[View author publications](#)

You can also search for this author in [PubMed](#) [Google Scholar](#)

49. Karl M. Wantzen

[View author publications](#)

You can also search for this author in [PubMed](#) [Google Scholar](#)

50. Laura Wildman

[View author publications](#)

You can also search for this author in [PubMed](#) [Google Scholar](#)

51. Maciej Zalewski

[View author publications](#)

You can also search for this author in [PubMed](#) [Google Scholar](#)

## **Contributions**

B.B., S.B., W.v.d.B. and C.G.d.L. designed the study. B.B., S.B., G.S. and W.v.d.B. led the work and organized the collection of barrier data; B.B.,

S.B., L.B., A.C. and C.G.d.L. carried out the analysis; C.G.d.L. and B.B. wrote the initial drafts of the manuscript with essential input from S.B., L.B, J.J., A.C., S.C. and W.v.d.B.; G.S. and J.J. designed and curated the barrier database; K.M.W. helped to obtain unpublished barrier records from German Länder; B.B., P.F.G., R.O.d.A., G.R. and G.S. cleaned existing barrier inventories. Walkover river surveys were conducted/organized by G.S. and P.M. (Portugal, France); E.D., E.G.-V, C.R., S.F. and G.L. (Spain); B.B. and S.B. (Italy, Lithuania); J.J. and P.E.J. (Wales); K.A., K.B. and N.J. (Denmark), J.B. and J.K. (Ireland), M.C. and M.P. (Balkans, Danube, Estonia, Germany, Scandinavia); T.F., C.T.S. (Germany); P.K., A.V., J.K., M.C.L., S.V. and J.S.T. (England); E.V. and L.M. (Scotland); P.P., M.L. and M.Z. (Poland); H.W. and A.B. (The Netherlands). G.G., J.R., L.W., M.B. and P.G. advised on the development of the Atlas and the policy implications. All co-authors critically revised and approved the edited manuscript.

## Corresponding authors

Correspondence to [Carlos Garcia de Leaniz](#) or [Wouter van de Bund](#).

## Ethics declarations

### Competing interests

The authors declare no competing interests.

## Additional information

**Peer review information** *Nature* thanks Arnout van Soesbergen, Christiane Zarfl and the other, anonymous, reviewer(s) for their contribution to the peer review of this work. Peer reviewer reports are available.

**Publisher's note** Springer Nature remains neutral with regard to jurisdictional claims in published maps and institutional affiliations.

## **Extended data figures and tables**

## Extended Data Fig. 1 Approach used to estimate river fragmentation in Europe.

To correct for under-reporting and derive more accurate estimates of barrier density we used a four-step approach: (1) compilation of georeferenced barrier records from local, regional and national barrier databases (the AMBER Barrier Atlas), (2) data cleaning and removal of duplicate records, (3) ground-truthing barrier densities from walkover river surveys, and (4) statistical barrier modelling via random forest regression.

## Extended Data Fig. 2 Cumulative height distribution of artificial barriers found in European rivers.

The figure shows ( $\log_{10}$  scale) that most barriers (68% of  $n = 117,371$  built structures equal to or greater than 10 cm in height) are low-head structures (such as fords, culverts and sluice gates) smaller than 2 m in height; these are ubiquitous but typically unreported in existing barrier inventories.

[Source data](#)

## Extended Data Fig. 3 Location of test reaches used to ground-truth the AMBER Barrier Atlas during walkover surveys.

We walked 147 test reaches totalling 2,715 km that were representative of river types found in Europe in terms of altitude, slope, stream order, biogeography and land use. River network and country boundaries were sourced from the European Environment Agency<sup>35</sup>.

## Extended Data Fig. 4 Variation in areal barrier density and main drivers of barrier abundance modelled by random forest regression.

**a**, The predicted barrier density at ECRINS sub-catchments (barriers per  $\text{km}^2$ ; number of sub-catchments 8,467). **b**, Agricultural pressure (proportion of agricultural area, Corine Land Cover 2, level 1). **c**, Road crossing density

(crossings per km<sup>2</sup>), **d**, Mean altitude (m.a.s.l., metres above sea level). **e**, Extent of surface water (proportion of area occupied by surface water, Corine Land Cover 5, level 1). **f**, The relative weight (MDI) of the 11 predictors used to model barrier density (detailed in Extended Data Table 4). Country and sub-basin boundaries, CORINE Land Cover and mean altitude were sourced from the European Environment Agency<sup>35,61,63</sup> and road density was sourced from the GRIP database<sup>64</sup>. [Source data](#)

## **Extended Data Fig. 5 Performance of the barrier density model.**

The maps show the distribution of modelling residuals (predicted minus observed barrier density, in units of barriers per km<sup>2</sup>) for the model calibration dataset (number of sub-catchments 2,306) (**a**), and the whole AMBER Barrier Atlas dataset (number of sub-catchments 8,467) (**b**). Country and sub-basin boundaries were sourced from the European Environment Agency<sup>35</sup>.

### **Extended Data Table 1 Results of river walkover surveys used to ground-truth barrier records**

[Full size table](#)

### **Extended Data Table 2 Comparisons of barrier densities (barriers per kilometre) in Europe and elsewhere using a common river network (HydroSHEDS<sup>71</sup>)**

[Full size table](#)

### **Extended Data Table 3 Incidence of barrier duplicates and duplicate exclusion criteria**

[Full size table](#)

### **Extended Data Table 4 Variables used to model barrier density**

[Full size table](#)

### **Extended Data Table 5 Sensitivity analysis for barrier density modelling**

[Full size table](#)

## **Supplementary information**

## [Peer Review File](#)

## **Source data**

[Source Data Fig. 3](#)

[Source Data Extended Data Fig. 2](#)

[Source Data Extended Data Fig. 4](#)

## **Rights and permissions**

[Reprints and Permissions](#)

## **About this article**



Check for  
updates

## **Cite this article**

Belletti, B., Garcia de Leaniz, C., Jones, J. *et al.* More than one million barriers fragment Europe's rivers. *Nature* **588**, 436–441 (2020).  
<https://doi.org/10.1038/s41586-020-3005-2>

[Download citation](#)

- Received: 28 June 2020
- Accepted: 26 October 2020
- Published: 16 December 2020
- Issue Date: 17 December 2020

- DOI: <https://doi.org/10.1038/s41586-020-3005-2>

## Comments

By submitting a comment you agree to abide by our [Terms](#) and [Community Guidelines](#). If you find something abusive or that does not comply with our terms or guidelines please flag it as inappropriate.

[Access through your institution](#)

[Change institution](#)

[Buy or subscribe](#)

## Associated Content

*Nature* | News & Views

### [European rivers are fragmented by many more barriers than had been recorded](#)

- Christiane Zarfl
- & Bernhard Lehner

---

This article was downloaded by **calibre** from <https://www.nature.com/articles/s41586-020-3005-2>

| [Section menu](#) | [Main menu](#) |

- Article
- [Published: 09 December 2020](#)

# Global human-made mass exceeds all living biomass

- [Emily Elhacham](#) ORCID: [orcid.org/0000-0002-0925-0335<sup>1</sup>](https://orcid.org/0000-0002-0925-0335),
- [Liad Ben-Uri<sup>1</sup>](#),
- [Jonathan Grozovski<sup>1</sup>](#),
- [Yinon M. Bar-On<sup>1</sup>](#) &
- [Ron Milo](#) ORCID: [orcid.org/0000-0003-1641-2299<sup>1</sup>](https://orcid.org/0000-0003-1641-2299)

[Nature](#) volume **588**, pages442–444(2020) [Cite this article](#)

- 10k Accesses
- 4562 Altmetric
- [Metrics details](#)

## Subjects

- [Ecology](#)
- [Geology](#)
- [Interdisciplinary studies](#)
- [Materials science](#)
- [Sustainability](#)

## Abstract

Humanity has become a dominant force in shaping the face of Earth<sup>1,2,3,4,5,6,7,8,9</sup>. An emerging question is how the overall material output

of human activities compares to the overall natural biomass. Here we quantify the human-made mass, referred to as ‘anthropogenic mass’, and compare it to the overall living biomass on Earth, which currently equals approximately 1.1 teratonnes<sup>[10,11](#)</sup>. We find that Earth is exactly at the crossover point; in the year 2020 ( $\pm 6$ ), the anthropogenic mass, which has recently doubled roughly every 20 years, will surpass all global living biomass. On average, for each person on the globe, anthropogenic mass equal to more than his or her bodyweight is produced every week. This quantification of the human enterprise gives a mass-based quantitative and symbolic characterization of the human-induced epoch of the Anthropocene.

[Access through your institution](#)

[Change institution](#)

[Buy or subscribe](#)

## Access options

Subscribe to Journal

Get full journal access for 1 year

185,98 €

only 3,58 € per issue

[Subscribe](#)

All prices are NET prices.

VAT will be added later in the checkout.

Rent or Buy article

Get time limited or full article access on ReadCube.

from \$8.99

[Rent or Buy](#)

All prices are NET prices.

### **Additional access options:**

- [Log in](#)
- [Access through your institution](#)
- [Learn about institutional subscriptions](#)

**Fig. 1: Biomass and anthropogenic mass estimates since the beginning of the twentieth century on a dry-mass basis.**

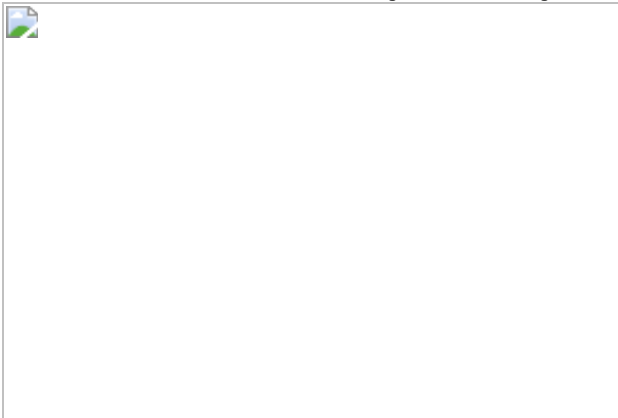


**Fig. 2: Biomass (dry and wet), anthropogenic mass and anthropogenic mass waste estimates since the beginning of the twentieth century.**



**Fig. 3: Contrasting key components of global biomass and anthropogenic mass in the year 2020 (dry-weight basis).**



## Data availability

All data used in this study are available on GitHub, at [https://github.com/milo-lab/anthropogenic\\_mass](https://github.com/milo-lab/anthropogenic_mass). Anthropogenic mass data are available from ref. <sup>22</sup> and at <https://boku.ac.at/wiso/sec/data-download>. TRENDY Dynamic Global Vegetation Models outputs are available at <https://sites.exeter.ac.uk/trendy>. Leaves dry matter content measurements were obtained via TryDB, at <https://www.try-db.org/>. Other datasets used in this study are available from the published literature, as detailed in the Methods and Supplementary Information.

## Code availability

All code used in this study is available on GitHub, at [https://github.com/milo-lab/anthropogenic\\_mass](https://github.com/milo-lab/anthropogenic_mass).

## References

1. 1.

Ramankutty, N. & Foley, J. A. Estimating historical changes in global land cover: croplands from 1700 to 1992. *Glob. Biogeochem. Cycles* **13**, 997–1027 (1999).

[ADS](#) [CAS](#) [Google Scholar](#)

2. 2.

Krausmann, F. et al. Growth in global materials use, GDP and population during the 20th century. *Ecol. Econ.* **68**, 2696–2705 (2009).

[Google Scholar](#)

3. 3.

Matthews, E. *The Weight of Nations: Material Outflows from Industrial Economies* (World Resources Inst., 2000).

4. 4.

Smil, V. *Harvesting the Biosphere: What We Have Taken from Nature* (MIT Press, 2013).

5. 5.

Smil, V. *Making the Modern World: Materials and Dematerialization* (John Wiley & Sons, 2013).

6. 6.

Haff, P. K. Technology as a geological phenomenon: implications for human well-being. *Geol. Soc. Lond. Spec. Publ.* **395**, 301–309 (2014).

[ADS](#) [Google Scholar](#)

7. 7.

Zalasiewicz, J. et al. Scale and diversity of the physical technosphere: a geological perspective. *Anthropocene Rev.* **4**, 9–22 (2017).

[Google Scholar](#)

8. 8.

Zalasiewicz, J., Waters, C. N., Williams, M. & Summerhayes, C. *The Anthropocene as a Geological Time Unit: A Guide to the Scientific Evidence and Current Debate* (Cambridge Univ. Press, 2018).

9. 9.

Stephens, L. et al. Archaeological assessment reveals Earth's early transformation through land use. *Science* **365**, 897–902 (2019).

[ADS](#) [CAS](#) [PubMed](#) [Google Scholar](#)

10. 10.

Erb, K.-H. et al. Unexpectedly large impact of forest management and grazing on global vegetation biomass. *Nature* **553**, 73–76 (2018).

[ADS](#) [CAS](#) [PubMed](#) [Google Scholar](#)

11. 11.

Bar-On, Y. M., Phillips, R. & Milo, R. The biomass distribution on Earth. *Proc. Natl Acad. Sci. USA* **115**, 6506–6511 (2018).

[CAS](#) [PubMed](#) [Google Scholar](#)

12. 12.

Pan, Y. et al. A large and persistent carbon sink in the world's forests. *Science* **333**, 988–993 (2011).

[ADS](#) [CAS](#) [PubMed](#) [Google Scholar](#)

13. 13.

Reddington, C. L. et al. Air quality and human health improvements from reductions in deforestation-related fire in Brazil. *Nat. Geosci.* **8**, 768–771 (2015).

[ADS](#) [CAS](#) [Google Scholar](#)

14. 14.

Ceballos, G. & Ehrlich, P. R. Mammal population losses and the extinction crisis. *Science* **296**, 904–907 (2002).

[ADS](#) [CAS](#) [PubMed](#) [PubMed Central](#) [Google Scholar](#)

15. 15.

WWF. *Living Planet Report–2018: Aiming Higher* (WWF, 2018).

16. 16.

Bar-On, Y. M. & Milo, R. Towards a quantitative view of the global ubiquity of biofilms. *Nat. Rev. Microbiol.* **17**, 199–200 (2019).

[CAS](#) [PubMed](#) [Google Scholar](#)

17. 17.

Pauliuk, S. & Hertwich, E. G. Socioeconomic metabolism as paradigm for studying the biophysical basis of human societies. *Ecol. Econ.* **119**, 83–93 (2015).

[Google Scholar](#)

18. 18.

Haberl, H. et al. Contributions of sociometabolic research to sustainability science. *Nat. Sustainability* **2**, 173–184 (2019).

[Google Scholar](#)

19. 19.

Fischer-Kowalski, M. et al. Methodology and indicators of economy-wide material flow accounting. *J. Ind. Ecol.* **15**, 855–876 (2011).

[Google Scholar](#)

20. 20.

Krausmann, F., Schandl, H., Eisenmenger, N., Giljum, S. & Jackson, T. Material flow accounting: measuring global material use for sustainable development. *Annu. Rev. Environ. Resour.* **42**, 647–675 (2017).

[Google Scholar](#)

21. 21.

Krausmann, F. et al. Global socioeconomic material stocks rise 23-fold over the 20th century and require half of annual resource use. *Proc. Natl Acad. Sci. USA* **114**, 1880–1885 (2017).

[CAS](#) [PubMed](#) [Google Scholar](#)

22. 22.

Krausmann, F., Lauk, C., Haas, W. & Wiedenhofer, D. From resource extraction to outflows of wastes and emissions: the socioeconomic metabolism of the global economy, 1900–2015. *Glob. Environ. Change* **52**, 131–140 (2018).

[PubMed](#) [PubMed Central](#) [Google Scholar](#)

23. 23.

Steffen, W., Broadgate, W., Deutsch, L., Gaffney, O. & Ludwig, C. The trajectory of the Anthropocene: the great acceleration. *Anthropocene Rev.* **2**, 81–98 (2015).

[Google Scholar](#)

24. 24.

Vitousek, P. M., Ehrlich, P. R., Ehrlich, A. H. & Matson, P. A. Human appropriation of the products of photosynthesis. *Bioscience* **36**, 368–373 (1986).

[Google Scholar](#)

25. 25.

Haberl, H. et al. Quantifying and mapping the human appropriation of net primary production in Earth's terrestrial ecosystems. *Proc. Natl Acad. Sci. USA* **104**, 12942–12947 (2007).

[ADS](#) [CAS](#) [PubMed](#) [Google Scholar](#)

26. 26.

Haberl, H., Erb, K.-H. & Krausmann, F. Human appropriation of net primary production: patterns, trends, and planetary boundaries. *Annu. Rev. Environ. Resour.* **39**, 363–391 (2014).

[Google Scholar](#)

27. 27.

Vitousek, P. M. Human domination of Earth's ecosystems. *Science* **277**, 494–499 (1997).

[CAS](#) [Google Scholar](#)

28. 28.

Dirzo, R. et al. Defaunation in the Anthropocene. *Science* **345**, 401–406 (2014).

[ADS](#) [CAS](#) [PubMed](#) [Google Scholar](#)

29. 29.

Crutzen, P. J. in *Earth System Science in the Anthropocene* (eds. Ehlers, E. & Kraft, T.) 13–18 (Springer, 2006).

30. 30.

Steffen, W., Crutzen, J. & McNeill, J. R. The Anthropocene: are humans now overwhelming the great forces of Nature? *Ambio* **36**, 614–621 (2007).

[CAS](#) [PubMed](#) [Google Scholar](#)

31. 31.

Lewis, S. L. & Maslin, M. A. Defining the Anthropocene. *Nature* **519**, 171–180 (2015).

[ADS](#) [CAS](#) [PubMed](#) [Google Scholar](#)

32. 32.

Waters, C. N. et al. The Anthropocene is functionally and stratigraphically distinct from the Holocene. *Science* **351**, aad2622 (2016).

[PubMed](#) [Google Scholar](#)

33. 33.

Krausmann, F. et al. *Economy-wide Material Flow Accounting. Introduction and Guide* Version 1, Social Ecology Working Paper 151 (Alpen-Adria Univ., 2015).

34. 34.

Miatto, A., Schandl, H., Fishman, T. & Tanikawa, H. Global patterns and trends for non-metallic minerals used for construction. *J. Ind. Ecol.* **21**, 924–937 (2017).

[Google Scholar](#)

35. 35.

Cooper, A. H., Brown, T. J., Price, S. J., Ford, J. R. & Waters, C. N. Humans are the most significant global geomorphological driving force of the 21st century. *Anthropocene Rev.* **5**, 222–229 (2018).

[Google Scholar](#)

36. 36.

Food and Agriculture Organization of the United Nations. *Global Forest Resources Assessment 2010: Main Report* (FAO, 2010).

37. 37.

Liu, Y. Y. et al. Recent reversal in loss of global terrestrial biomass. *Nat. Clim. Chang.* **5**, 470–474 (2015).

[ADS](#) [Google Scholar](#)

38. 38.

Sitch, S. et al. Recent trends and drivers of regional sources and sinks of carbon dioxide. *Biogeosciences* **12**, 653–679 (2015).

[ADS](#) [Google Scholar](#)

39. 39.

Friedlingstein, P. et al. Global carbon budget 2019. *Earth Syst. Sci. Data* **11**, 1783–1838 (2019).

[ADS](#) [Google Scholar](#)

40. 40.

Food and Agriculture Organization of the United Nations FAOSTAT  
<http://faostat.fao.org>.

41. 41.

Magnabosco, C. et al. The biomass and biodiversity of the continental subsurface. *Nat. Geosci.* **11**, 707–717 (2018).

[ADS](#) [CAS](#) [Google Scholar](#)

42. 42.

Haverd, V. et al. A new version of the CABLE land surface model (Subversion revision r4601) incorporating land use and land cover change, woody vegetation demography, and a novel optimisation-based approach to plant coordination of photosynthesis. *Geosci. Model Dev.* **11**, 2995–3026 (2018).

[ADS](#) [CAS](#) [Google Scholar](#)

43. 43.

Melton, J. R. & Arora, V. K. Competition between plant functional types in the Canadian Terrestrial Ecosystem Model (CTEM) v. 2.0. *Geosci. Model Dev.* **9**, 323–361 (2016).

[ADS](#) [CAS](#) [Google Scholar](#)

44. 44.

Lawrence, D. M. et al. The community land model version 5: description of new features, benchmarking, and impact of forcing uncertainty. *J. Adv. Model. Earth Syst.* **11**, 4245–4287 (2019).

[ADS](#) [Google Scholar](#)

45. 45.

Tian, H. et al. North American terrestrial CO<sub>2</sub> uptake largely offset by CH<sub>4</sub> and N<sub>2</sub>O emissions: toward a full accounting of the greenhouse gas budget. *Clim. Change* **129**, 413–426 (2015).

[ADS](#) [CAS](#) [PubMed](#) [Google Scholar](#)

46. 46.

Meiyappan, P., Jain, A. K. & House, J. I. Increased influence of nitrogen limitation on CO<sub>2</sub> emissions from future land use and land use change. *Glob. Biogeochem. Cycles* **29**, 1524–1548 (2015).

[ADS](#) [CAS](#) [Google Scholar](#)

47. 47.

Mauritsen, T. et al. Developments in the MPI-M Earth System Model version1.2 (MPI-ESM1.2) and its response to increasing CO<sub>2</sub>. *J. Adv. Model. Earth Syst.* **11**, 998–1038 (2019).

[ADS](#) [PubMed](#) [PubMed Central](#) [Google Scholar](#)

48. 48.

Clark, D. B. et al. The Joint UK Land Environment Simulator (JULES), model description – Part 2: Carbon fluxes and vegetation dynamics. *Geosci. Model Dev.* **4**, 701–722 (2011).

[ADS](#) [Google Scholar](#)

49. 49.

Poulter, B., Frank, D. C., Hodson, E. L. & Zimmermann, N. E. Impacts of land cover and climate data selection on understanding terrestrial carbon dynamics and the CO<sub>2</sub> airborne fraction. *Biogeosciences* **8**, 2027–2036 (2011).

[ADS](#) [CAS](#) [Google Scholar](#)

50. 50.

Smith, B. et al. Implications of incorporating N cycling and N limitations on primary production in an individual-based dynamic vegetation model. *Biogeosciences* **11**, 2027–2054 (2014).

[ADS](#) [Google Scholar](#)

51. 51.

Lienert, S. & Joos, F. A Bayesian ensemble data assimilation to constrain model parameters and land-use carbon emissions. *Biogeosciences* **15**, 2909–2930 (2018).

[ADS](#) [CAS](#) [Google Scholar](#)

52. 52.

Zaehle, S. & Friend, A. D. Carbon and nitrogen cycle dynamics in the O-CN land surface model: 1. Model description, site-scale evaluation, and sensitivity to parameter estimates. *Glob. Biogeochem. Cycles* **24**, GB1005 (2010).

[ADS](#) [Google Scholar](#)

53. 53.

Krinner, G. et al. A dynamic global vegetation model for studies of the coupled atmosphere–biosphere system. *Glob. Biogeochem. Cycles* **19**, GB1015 (2005).

[ADS](#) [Google Scholar](#)

54. 54.

Goll, D. S. et al. Carbon–nitrogen interactions in idealized simulations with JSBACH (version 3.10). *Geosci. Model Dev.* **10**, 2009–2030 (2017).

[ADS](#) [CAS](#) [Google Scholar](#)

55. 55.

Walker, A. P. et al. The impact of alternative trait-scaling hypotheses for the maximum photosynthetic carboxylation rate ( $V_{cmax}$ ) on global gross primary production. *New Phytol.* **215**, 1370–1386 (2017).

[CAS](#) [PubMed](#) [Google Scholar](#)

56. 56.

Kato, E., Kinoshita, T., Ito, A., Kawamiya, M. & Yamagata, Y. Evaluation of spatially explicit emission scenario of land-use change and biomass burning using a process-based biogeochemical model. *J. Land Use Sci.* **8**, 104–122 (2013).

[Google Scholar](#)

57. 57.

Tang, Z. et al. Patterns of plant carbon, nitrogen, and phosphorus concentration in relation to productivity in China's terrestrial ecosystems. *Proc. Natl Acad. Sci. USA* **115**, 4033–4038 (2018).

[PubMed](#) [Google Scholar](#)

58. 58.

Poorter, H. et al. Biomass allocation to leaves, stems and roots: meta-analyses of interspecific variation and environmental control. *New Phytol.* **193**, 30–50 (2012).

[CAS](#) [PubMed](#) [Google Scholar](#)

59. 59.

Heldal, M., Norland, S. & Tumyr, O. X-ray microanalytic method for measurement of dry matter and elemental content of individual

bacteria. *Appl. Environ. Microbiol.* **50**, 1251–1257 (1985).

[CAS](#) [PubMed](#) [PubMed Central](#) [Google Scholar](#)

60. 60.

von Stockar, U. & Liu, J. Does microbial life always feed on negative entropy? Thermodynamic analysis of microbial growth. *Biochim. Biophys. Acta* **1412**, 191–211 (1999).

[Google Scholar](#)

61. 61.

Guo, L., Lin, H., Fan, B., Cui, X. & Chen, J. Impact of root water content on root biomass estimation using ground penetrating radar: evidence from forward simulations and field controlled experiments. *Plant Soil* **371**, 503–520 (2013).

[CAS](#) [Google Scholar](#)

62. 62.

Glass, S. V. & Zelinka, S. L. in *Wood Handbook: Wood as an Engineering Material* Vol. 190, 4.1–4.19 (US Department of Agriculture, 2010).

63. 63.

Loveys, B. R. et al. Thermal acclimation of leaf and root respiration: an investigation comparing inherently fast- and slow-growing plant species. *Glob. Change Biol.* **9**, 895–910 (2003).

[ADS](#) [Google Scholar](#)

64. 64.

Sheremetev, S. N. *Herbs on the Soil Moisture Gradient (Water Relations and the Structural-Functional Organization)* (KMK, 2005).

65. 65.

Michaletz, S. T. & Johnson, E. A. A heat transfer model of crown scorch in forest fires. *Can. J. For. Res.* **36**, 2839–2851 (2006).

[Google Scholar](#)

66. 66.

Messier, J., McGill, B. J. & Lechowicz, M. J. How do traits vary across ecological scales? A case for trait-based ecology. *Ecol. Lett.* **13**, 838–848 (2010).

[PubMed](#) [Google Scholar](#)

67. 67.

Boucher, F. C., Thuiller, W., Arnoldi, C., Albert, C. H. & Lavergne, S. Unravelling the architecture of functional variability in wild populations of *Polygonum viviparum* L. *Funct. Ecol.* **27**, 382–391 (2013).

[PubMed](#) [PubMed Central](#) [Google Scholar](#)

68. 68.

Dahlin, K. M., Asner, G. P. & Field, C. B. Environmental and community controls on plant canopy chemistry in a Mediterranean-type ecosystem. *Proc. Natl Acad. Sci. USA* **110**, 6895–6900 (2013).

[ADS](#) [CAS](#) [PubMed](#) [Google Scholar](#)

69. 69.

Kattge, J. et al. TRY—a global database of plant traits. *Glob. Change Biol.* **17**, 2905–2935 (2011).

[ADS](#) [Google Scholar](#)

70. 70.

Lebigot, E. O. Uncertainties: a Python package for calculations with uncertainties. <https://pythonhosted.org/uncertainties/> (2010).

71. 71.

Wiedenhofer, D., Fishman, T., Lauk, C., Haas, W. & Krausmann, F. Integrating material stock dynamics into economy-wide material flow accounting: concepts, modelling, and global application for 1900–2050. *Ecol. Econ.* **156**, 121–133 (2019).

[Google Scholar](#)

[Download references](#)

## Acknowledgements

We thank U. Alon, S. Dan, G. Eshel, T. Fishman, E. Gelbrieth, T. Kaufmann, T. Klein, A. Knoll, E. Noor, N. Page, R. Phillips, J. Pongratz, M. Shamir, M. Shtein, B. Smith, C. Waters, T. Wiesel, M. Williams and members of our laboratory for help and discussions, and S. Sitch and the TRENDY DGVM community for access to their simulation outputs. This research was supported by the European Research Council (Project NOVCARBFIX 646827); Beck-Canadian Center for Alternative Energy Research; Dana and Yossie Hollander; Ullmann Family Foundation; Helmsley Charitable Foundation; Larson Charitable Foundation; Wolfson Family Charitable Trust; Charles Rothschild; and Selmo Nussenbaum. R.M. is the Charles and Louise Gartner professional chair. Y.M.B.-O is an Azrieli Fellow.

## Author information

### Affiliations

1. Department of Plant and Environmental Sciences, Weizmann Institute of Science, Rehovot, Israel

Emily Elhacham, Liad Ben-Uri, Jonathan Grozovski, Yinon M. Bar-On & Ron Milo

## Authors

1. Emily Elhacham

[View author publications](#)

You can also search for this author in [PubMed](#) [Google Scholar](#)

2. Liad Ben-Uri

[View author publications](#)

You can also search for this author in [PubMed](#) [Google Scholar](#)

3. Jonathan Grozovski

[View author publications](#)

You can also search for this author in [PubMed](#) [Google Scholar](#)

4. Yinon M. Bar-On

[View author publications](#)

You can also search for this author in [PubMed](#) [Google Scholar](#)

5. Ron Milo

[View author publications](#)

You can also search for this author in [PubMed](#) [Google Scholar](#)

## Contributions

E.E., L.B.-U. and R.M. wrote the manuscript. E.E. performed the bulk of the research and data analysis. L.B.-U. contributed to the anthropogenic mass analysis and biomass estimation. Y.M.B.-O. contributed to the biomass estimation and carbon content calculation. J.G. contributed to the water content calculation. E.E., J.G. and Y.M.B.-O. performed the uncertainty analysis. E.E., L.B.-U. and R.M. conceived the study. R.M.

supervised the study. All authors discussed the results, and commented on the manuscript.

## Corresponding author

Correspondence to [Ron Milo](#).

## Ethics declarations

### Competing interests

The authors declare no competing interests.

## Additional information

**Peer review information** *Nature* thanks Fridolin Krausmann, Dominik Wiedenhofer and the other, anonymous, reviewer(s) for their contribution to the peer review of this work.

**Publisher's note** Springer Nature remains neutral with regard to jurisdictional claims in published maps and institutional affiliations.

## Extended data figures and tables

### [Extended Data Fig. 1 Sensitivity analysis of the anthropogenic mass definition.](#)

**a–f**, The effect of adding the following to the anthropogenic mass (dark purple): **a**, mass of the human population, **b**, mass of livestock, **c**, mass of crops and agroforestry, **d**, mass of earthworks, dredging and waste/overburden from mineral and metal production, and **f**, mass of anthropogenic atmospheric CO<sub>2</sub> stocks, as well as **e**, the exclusion of the mass of industrial roundwood. The total biomass weight is depicted by the green line. Black dot indicates the year of intersection based on the alternative anthropogenic mass definition. Violet area and light green-

dashed line indicate extrapolated anthropogenic mass and biomass estimates, respectively. Full description of the sensitivity analysis is provided in Supplementary Information section 1.

**Extended Data Fig. 2 Anthropogenic mass composition since the year 1900, divided into material groups.**

Dataset is based on ref. <sup>22</sup>.

**Extended Data Fig. 3 Anthropogenic mass relative annual change, with highlights of notable global events.**

Relative annual change is calculated as the difference between two consecutive years divided by the earlier year anthropogenic mass value.

**Extended Data Fig. 4 Anthropogenic mass metal estimates since the beginning of the twentieth century, divided into material sub-groups.**

Data are taken from the comprehensive work of the Institute of Social Ecology, Vienna. We used a recent study<sup>71</sup>, which has some minor updates compared to the study used to achieve the main results<sup>22</sup>.

**Extended Data Fig. 5 Anthropogenic mass estimates for (industrial round) wood, glass and plastic since the beginning of the twentieth century, divided into material sub-groups.**

Data are taken from the comprehensive work of the Institute of Social Ecology, Vienna. We used a recent study<sup>71</sup>, which has some minor updates compared to the study used to achieve the main results<sup>22</sup>.

**Extended Data Fig. 6 Calculation steps in plant biomass estimation for 1990–2017.**

As further detailed in the Methods section ‘Biomass change over the years 1900–2017’.

**Extended Data Table 1 The different anthropogenic mass groups and their mass estimates in selected years**

[Full size table](#)

## Supplementary information

### [Supplementary Information](#)

Supplementary Discussions: This file contains Supplementary Section 1 & 2. It includes the sensitivity analysis of the anthropogenic mass definition, as well as an additional discussion on the biomass trend in recent years.

### [Reporting Summary](#)

## Rights and permissions

### [Reprints and Permissions](#)

## About this article



Check for  
updates

## Cite this article

Elhacham, E., Ben-Uri, L., Grozovski, J. *et al.* Global human-made mass exceeds all living biomass. *Nature* **588**, 442–444 (2020).  
<https://doi.org/10.1038/s41586-020-3010-5>

[Download citation](#)

- Received: 01 November 2019
- Accepted: 09 October 2020
- Published: 09 December 2020
- Issue Date: 17 December 2020
- DOI: <https://doi.org/10.1038/s41586-020-3010-5>

## Comments

By submitting a comment you agree to abide by our [Terms](#) and [Community Guidelines](#). If you find something abusive or that does not comply with our terms or guidelines please flag it as inappropriate.

[Access through your institution](#)

[Change institution](#)

[Buy or subscribe](#)

---

This article was downloaded by **calibre** from <https://www.nature.com/articles/s41586-020-3010-5>

| [Section menu](#) | [Main menu](#) |

- Article
- [Published: 09 December 2020](#)

# Enigmatic dinosaur precursors bridge the gap to the origin of Pterosauria

- [Martín D. Ezcurra](#) [ORCID: orcid.org/0000-0002-6000-6450](#)<sup>1,2</sup>,
- [Sterling J. Nesbitt](#) [ORCID: orcid.org/0000-0002-7017-1652](#)<sup>3</sup>,
- [Mario Bronzati](#)<sup>4</sup>,
- [Fabio Marco Dalla Vecchia](#) [ORCID: orcid.org/0000-0003-3914-3896](#)<sup>5,6</sup>,
- [Federico L. Agnolin](#)<sup>7,8</sup>,
- [Roger B. J. Benson](#)<sup>9</sup>,
- [Federico Brissón Egli](#) [ORCID: orcid.org/0000-0001-8037-5467](#)<sup>7</sup>,
- [Sergio F. Cabreira](#)<sup>10</sup>,
- [Serjoscha W. Evers](#)<sup>9,11</sup>,
- [Adriel R. Gentil](#)<sup>7</sup>,
- [Randall B. Irmis](#)<sup>12,13</sup>,
- [Agustín G. Martinelli](#) [ORCID: orcid.org/0000-0003-4489-0888](#)<sup>1</sup>,
- [Fernando E. Novas](#)<sup>7</sup>,
- [Lúcio Roberto da Silva](#)<sup>10</sup>,
- [Nathan D. Smith](#) [ORCID: orcid.org/0000-0001-5554-4994](#)<sup>14</sup>,
- [Michelle R. Stocker](#)<sup>3</sup>,
- [Alan H. Turner](#) [ORCID: orcid.org/0000-0002-4164-6727](#)<sup>15</sup> &
- [Max C. Langer](#)<sup>4</sup>

[Nature](#) volume 588, pages445–449(2020) [Cite this article](#)

- 4048 Accesses

- 995 Altmetric
- [Metrics details](#)

## Subjects

- [Palaeontology](#)
- [Phylogenetics](#)

## Abstract

Pterosaurs were the first vertebrates to evolve powered flight<sup>1</sup> and comprised one of the main evolutionary radiations in terrestrial ecosystems of the Mesozoic era (approximately 252–66 million years ago), but their origin has remained an unresolved enigma in palaeontology since the nineteenth century<sup>2,3,4</sup>. These flying reptiles have been hypothesized to be the close relatives of a wide variety of reptilian clades, including dinosaur relatives<sup>2,3,4,5,6,7,8</sup>, and there is still a major morphological gap between those forms and the oldest, unambiguous pterosaurs from the Upper Triassic series. Here, using recent discoveries of well-preserved cranial remains, microcomputed tomography scans of fragile skull bones (jaws, skull roofs and braincases) and reliably associated postcrania, we demonstrate that lagerpetids—a group of cursorial, non-volant dinosaur precursors—are the sister group of pterosaurs, sharing numerous synapomorphies across the entire skeleton. This finding substantially shortens the temporal and morphological gap between the oldest pterosaurs and their closest relatives and simultaneously strengthens the evidence that pterosaurs belong to the avian line of archosaurs. Neuroanatomical features related to the enhanced sensory abilities of pterosaurs<sup>9</sup> are already present in lagerpetids, which indicates that these features evolved before flight. Our evidence illuminates the first steps of the assembly of the pterosaur body plan, whose conquest of aerial space represents a remarkable morphofunctional innovation in vertebrate evolution.

[Access through your institution](#)

[Change institution](#)

[Buy or subscribe](#)

## Access options

Subscribe to Journal

Get full journal access for 1 year

185,98 €

only 3,58 € per issue

[Subscribe](#)

All prices are NET prices.

VAT will be added later in the checkout.

Rent or Buy article

Get time limited or full article access on ReadCube.

from \$8.99

[Rent or Buy](#)

All prices are NET prices.

### Additional access options:

- [Log in](#)
- [Access through your institution](#)
- [Learn about institutional subscriptions](#)

**Fig. 1: Newly discovered and selected bones characterizing the lagerpetid body plan.**



**Fig. 2: Key comparisons between pterosaur and lagerpetid cranial endocasts and skeletal elements.**



**Fig. 3: Time-calibrated reduced strict consensus tree (after a posteriori pruning of *Kongonaphon*) focused on Pterosauria and Lagerpetidae.**



## Data availability

The data matrices for the phylogenetic analyses in NEXUS and/or TNT formats have been deposited in MorphoBank at <http://morphobank.org/permalink/?P3773>. Three-dimensional models of

lagerpetid bones in STL format are available in MorphoSource at [http://www.morphosource.org/Detail/ProjectDetail>Show/project\\_id/1095](http://www.morphosource.org/Detail/ProjectDetail>Show/project_id/1095) under the following DOIs: <https://doi.org/10.17602/M2/M157269>, <https://doi.org/10.17602/M2/M157271>, <https://doi.org/10.17602/M2/M157273>, <https://doi.org/10.17602/M2/M157275>, <https://doi.org/10.17602/M2/M157280>, <https://doi.org/10.17602/M2/M157282>, <https://doi.org/10.17602/M2/M157283> and <https://doi.org/10.17602/M2/M157284>. [Source data](#) are provided with this paper.

## References

1. 1.

Padian, K. The origins and aerodynamics of flight in extinct vertebrates. *Palaeontology* **28**, 413–433 (1985).

[Article](#) [Google Scholar](#)

2. 2.

Padian, K. in *Third Symposium on Mesozoic Terrestrial Ecosystems: Short Papers* (eds Reif, W.-E. & Westphal, F.) 163–166 (Atempto, 1984).

3. 3.

Sereno, P. C. Basal archosaurs: phylogenetic relationships and functional implications. *Soc. Vertebr. Paleontol. Mem.* **2**, 1–53 (1991).

[Article](#) [Google Scholar](#)

4. 4.

Benton, M. J. *Scleromochlus taylori* and the origin of dinosaurs and pterosaurs. *Phil. Trans. R. Soc. Lond. B* **354**, 1423–1446 (1999).

[Article](#) [Google Scholar](#)

5. 5.

Gauthier, J. A. Saurischian monophyly and the origin of birds. *Mem. Calif. Acad. Sci.* **8**, 1–55 (1986).

[Google Scholar](#)

6. 6.

Nesbitt, S. J. The early evolution of archosaurs: relationships and the origin of major clades. *Bull. Am. Mus. Nat. Hist.* **352**, 1–292 (2011).

[Article](#) [Google Scholar](#)

7. 7.

Ezcurra, M. D. The phylogenetic relationships of basal archosauromorphs, with an emphasis on the systematics of proterosuchian archosauriforms. *PeerJ* **4**, e1778 (2016).

[Article](#) [Google Scholar](#)

8. 8.

Nesbitt, S. J. et al. The earliest bird-line archosaurs and the assembly of the dinosaur body plan. *Nature* **544**, 484–487 (2017).

[ADS](#) [CAS](#) [Article](#) [Google Scholar](#)

9. 9.

Witmer, L. M., Chatterjee, S., Franzosa, J. & Rowe, T. Neuroanatomy of flying reptiles and implications for flight, posture and behaviour. *Nature* **425**, 950–953 (2003).

[ADS](#) [CAS](#) [Article](#) [Google Scholar](#)

10. 10.

Wellnhofer, P. *The Illustrated Encyclopedia of Pterosaurs* (Salamander Books, 1991).

11. 11.

Witton, M. P. *Pterosaurs: Natural History, Evolution, Anatomy* (Princeton Univ. Press, 2013).

12. 12.

Dalla Vecchia, F. M. in *Anatomy, Phylogeny and Palaeobiology of Early Archosaurs and their Kin* (eds Nesbitt, S. J. et al) 119–155 (Geological Society London, 2013).

13. 13.

Britt, B. B. et al. *Caelestiventus hansenii* gen. et sp. nov. extends the desert-dwelling pterosaur record back 65 million years. *Nat. Ecol. Evol.* **2**, 1386–1392 (2018).

[Article](#) [Google Scholar](#)

14. 14.

Butler, R. J., Brusatte, S. L., Andres, B. & Benson, R. B. How do geological sampling biases affect studies of morphological evolution in deep time? A case study of pterosaur (Reptilia: Archosauria) disparity. *Evolution* **66**, 147–162 (2012).

[Article](#) [Google Scholar](#)

15. 15.

Padian, K. Osteology and functional morphology of *Dimorphodon macrouryx* (Buckland) (Pterosauria: Rhamphorhynchoidea) based on new material in the Yale Peabody Museum. *Postilla* **189**, 1–44 (1983).

[Google Scholar](#)

16. 16.

Benton, M. J. Classification and phylogeny of the diapsid reptiles. *Zool. J. Linn. Soc.* **84**, 97–164 (1985).

[Article](#) [Google Scholar](#)

17. 17.

Peters, D. A reexamination of four prolacertiforms with implications for pterosaur phylogenesis. *Riv. Ital. Paleontol. Stratigr.* **106**, 293–336 (2000).

[Google Scholar](#)

18. 18.

Bennett, S. C. Reassessment of the Triassic archosauriform *Scleromochlus taylori*: neither runner nor biped, but hopper. *PeerJ* **8**, e8418 (2020).

[Article](#) [Google Scholar](#)

19. 19.

Renesto, S. & Binelli, G. *Vallesaurus cenensis* Wild 1991, a drepanosaurid (Reptilia, Diapsida) from the Late Triassic of northern Italy. *Riv. Ital. Paleontol. Stratigr.* **112**, 77–94 (2006).

[Google Scholar](#)

20. 20.

Langer, M. C., Nesbitt, S. J., Bittencourt, J. S. & Irmis, R. B. in *Anatomy, Phylogeny and Palaeobiology of Early Archosaurs and their Kin* (eds Nesbitt, S. J. et al.) 156–186 (Geological Society London, 2013).

21. 21.

Cabreira, S. F. et al. A unique Late Triassic dinosauromorph assemblage reveals dinosaur ancestral anatomy and diet. *Curr. Biol.* **26**, 3090–3095 (2016).

[CAS](#) [Article](#) [Google Scholar](#)

22. 22.

Kammerer, C. F., Nesbitt, S. J., Flynn, J. J., Ranivoharimanana, L. & Wyss, A. R. A tiny ornithodiran archosaur from the Triassic of Madagascar and the role of miniaturization in dinosaur and pterosaur ancestry. *Proc. Natl Acad. Sci. USA* **117**, 17932–17936 (2020).

[CAS](#) [Article](#) [Google Scholar](#)

23. 23.

Dalla Vecchia, F. M. *Gli Pterosauri Triassici* (Edizioni del Museo Friulano di Storia Naturale, 2014).

24. 24.

Dalla Vecchia, F. M. *Seazzadactylus venieri* gen. et sp. nov., a new pterosaur (Diapsida: Pterosauria) from the Upper Triassic (Norian) of northeastern Italy. *PeerJ* **7**, e7363 (2019).

[Article](#) [Google Scholar](#)

25. 25.

Codorniú, L., Paulina-Carabajal, A., Pol, D., Unwin, D. & Rauhut, O. W. M. A Jurassic pterosaur from Patagonia and the origin of the pterodactyloid neurocranium. *PeerJ* **4**, e2311 (2016).

[Article](#) [Google Scholar](#)

26. 26.

Goloboff, P. A. & Catalano, S. A. TNT version 1.5, including a full implementation of phylogenetic morphometrics. *Cladistics* **32**, 221–238 (2016).

[Article](#) [Google Scholar](#)

27. 27.

Spoor, F. & Zonneveld, F. Comparative review of the human bony labyrinth. *Am. J. Phys. Anthropol.* **107**, 211–251 (1998).

[Article](#) [Google Scholar](#)

28. 28.

Winship, I. R. & Wylie, D. R. Zonal organization of the vestibulocerebellum in pigeons (*Columba livia*): I. Climbing fiber input to the flocculus. *J. Comp. Neurol.* **456**, 127–139 (2003).

[Article](#) [Google Scholar](#)

29. 29.

Birn-Jeffery, A. V., Miller, C. E., Naish, D., Rayfield, E. J. & Hone, D. W. Pedal claw curvature in birds, lizards and mesozoic dinosaurs—complicated categories and compensating for mass-specific and phylogenetic control. *PLoS ONE* **7**, e50555 (2012).

[ADS](#) [CAS](#) [Article](#) [Google Scholar](#)

30. 30.

Kubo, T. & Kubo, M. O. Associated evolution of bipedality and cursoriality among Triassic archosaurs: a phylogenetically controlled evaluation. *Paleobiology* **38**, 474–485 (2012).

[Article](#) [Google Scholar](#)

31. 31.

Andres, B. & Padian, K. in *Phylonyms: A Companion to the PhyloCode* (eds de Queiroz, K. et al.) 1201–1204 (CRC, 2020).

32. 32.

Langer, M. C., Ezcurra, M. D., Bittencourt, J. S. & Novas, F. E. The origin and early evolution of dinosaurs. *Biol. Rev. Camb. Philos. Soc.* **85**, 55–110 (2010).

[Article](#) [Google Scholar](#)

33. 33.

Nesbitt, S. J. et al. Ecologically distinct dinosaurian sister group shows early diversification of Ornithodira. *Nature* **464**, 95–98 (2010).

[ADS](#) [CAS](#) [Article](#) [Google Scholar](#)

34. 34.

Langer, M. C., Novas, F. E., Bittencourt, J., Ezcurra, M. D. & Gauthier, J. A. in *Phylonyms: A Companion to the PhyloCode* (eds de Queiroz, K. et al.) 1209–1217 (CRC, 2020).

35. 35.

Clarke, J. A. et al. in *Phylonyms: A Companion to the PhyloCode* (eds de Queiroz, K. et al.) 1247–1253 (CRC, 2020).

36. 36.

Fedorov, A. et al. 3D Slicer as an image computing platform for the quantitative imaging network. *Magn. Reson. Imaging* **30**, 1323–1341 (2012).

[Article](#) [Google Scholar](#)

37. 37.

David, R. et al. Motion from the past. A new method to infer vestibular capacities of extinct species. *C. R. Palevol* **9**, 397–410 (2010).

[Article](#) [Google Scholar](#)

38. 38.

Evers, S. W. et al. Neurovascular anatomy of the protostegid turtle *Rhinochelys pulchriceps* and comparisons of membranous and endosseous labyrinth shape in an extant turtle. *Zool. J. Linn. Soc.* **187**, 800–828 (2019).

[Google Scholar](#)

39. 39.

Neenan, J. M. et al. Evolution of the sauropterygian labyrinth with increasingly pelagic lifestyles. *Curr. Biol.* **27**, 3852–3858 (2017).

[CAS](#) [Article](#) [Google Scholar](#)

40. 40.

Adams, D., Collyer, M. & Kaliontzopoulou, A. Geomorph: software for geometric morphometric analyses. R package version 3.2.1  
<https://cran.r-project.org/package=geomorph> (2020).

41. 41.

R Core Team. *R: A Language and Environment for Statistical Computing* (R Foundation for Statistical Computing, 2019).

42. 42.

Butler, R. J., Ezcurra, M. D., Liu, J., Sookias, R. B. & Sullivan, C. The anatomy and phylogenetic position of the erythrosuchid archosauriform *Guchengosuchus shiguaiensis* from the earliest Middle Triassic of China. *PeerJ* **7**, e6435 (2019).

[Article](#) [Google Scholar](#)

43. 43.

Ezcurra, M. D. et al. Deep faunistic turnovers preceded the rise of dinosaurs in southwestern Pangaea. *Nat. Ecol. Evol.* **1**, 1477–1483 (2017).

[Article](#) [Google Scholar](#)

44. 44.

Ezcurra, M. D. & Butler, R. J. The rise of the ruling reptiles and ecosystem recovery from the Permo-Triassic mass extinction. *Proc. R. Soc. Lond. B* **285**, 20180361 (2018).

[Google Scholar](#)

45. 45.

Ronquist, F., van der Mark, P. & Huelsenbeck, J. P. in *The Phylogenetic Handbook: a Practical Approach to Phylogenetic Analysis and Hypothesis Testing* (eds Lemey, P. et al) 210–266 (Cambridge Univ. Press, 2009).

46. 46.

Ezcurra, M. D., Scheyer, T. M. & Butler, R. J. The origin and early evolution of Sauria: reassessing the Permian saurian fossil record and the timing of the crocodile-lizard divergence. *PLoS ONE* **9**, e89165 (2014).

[ADS](#) [Article](#) [Google Scholar](#)

47. 47.

Benton, M. J. et al. Constraints on the timescale of animal evolutionary history. *Palaeontol. Electronica* **18**, 1–106 (2015).

[Google Scholar](#)

48. 48.

Rambaut, A., Drummond, A. J., Xie, D., Baele, G. & Suchard, M. A. Posterior summarization in Bayesian phylogenetics using Tracer 1.7. *Syst. Biol.* **67**, 901–904 (2018).

[CAS Article](#) [Google Scholar](#)

[Download references](#)

## Acknowledgements

We thank C. Alsina and F. De Cianni (MACN) for repreparation, M. B. Epele and M. Cipollone for µCT scanning and F. Tricárico for scanning-electron microscopy microphotographs of PVL 4625; M. Colbert for µCT scanning TMM 31100-1334; D. Cavallari for µCT scanning ULBRA-PVT059; V. Radermacher and J. Choiniere for providing access to the µCT scan of a *Heterodontosaurus* specimen scanned at ESRF, and ESI and SAHRA for permits for that work; A. Paulina-Carabajal for allowing access to the µCT scan of *Allkaruen*; S. Chapman, H. Furrer, Z. Gasparini, M. Moser, G. Muscio, P. Ortíz, A. Paganoni, J. Powell, O. Rauhut, E. Ruigómez, R. Stecher and A. Tintori for access to specimens; J. Gauthier for discussion and suggestions about phylogenetic nomenclature; D. Boyer for assisting us during the uploading of the three-dimensional models of specimens to MorphoSource; S. Hartman allowed the use and modification of the lagerpetid skeletal reconstruction; and S. Brusatte and N. Fraser for comments that improved the overall quality of the manuscript. R. Nogueira digitally assembled and reconstructed the lagerpetid skull and created the life reconstruction. University of Antananarivo, Madagascar, allowed access to three-dimensional data and first-hand study of *Kongonaphon*. This study was supported by the Sepkoski Grant of the Paleontological Society (to M.D.E.), Agencia Nacional de Promoción Científica y Técnica (PICT 2018-01186; to M.D.E.), The Coleman and Susan Burke Foundation (to F.E.N.), Financiadora de Estudos e Projetos, Brazilian Federal Government

(project CT-INFRA 01/2013), and São Paulo Research Foundation (FAPESP 2014/03825-3 to M.C.L. and 2018/18145-9 to M.B.).

## Author information

### Affiliations

1. Sección Paleontología de Vertebrados CONICET–Museo Argentino de Ciencias Naturales ‘Bernardino Rivadavia’, Buenos Aires, Argentina

Martín D. Ezcurra & Agustín G. Martinelli

2. School of Geography, Earth and Environmental Sciences, University of Birmingham, Birmingham, UK

Martín D. Ezcurra

3. Department of Geosciences, Virginia Tech, Blacksburg, VA, USA

Sterling J. Nesbitt & Michelle R. Stocker

4. Departamento de Biología, Universidade de São Paulo, Ribeirão Preto, Brazil

Mario Bronzati & Max C. Langer

5. Research Group of Mesozoic Faunas, Institut Català de Paleontologia Miquel Crusafont (ICP), Sabadell, Spain

Fabio Marco Dalla Vecchia

6. Museo Friulano di Storia Naturale, Udine, Italy

Fabio Marco Dalla Vecchia

7. Laboratorio de Anatomía Comparada y Evolución de los Vertebrados CONICET–Museo Argentino de Ciencias Naturales ‘Bernardino Rivadavia’, Buenos Aires, Argentina

Federico L. Agnolin, Federico Brissón Egli, Adriel R. Gentil & Fernando E. Novas

8. Fundación de Historia Natural ‘Félix de Azara’, Departamento de Ciencias Naturales y Antropología, Universidad Maimónides, Buenos Aires, Argentina

Federico L. Agnolin

9. Department of Earth Sciences, University of Oxford, Oxford, UK

Roger B. J. Benson & Serjoscha W. Evers

10. Associação Sul Brasileira de Paleontologia, Faxinal do Soturno, Brazil

Sergio F. Cabreira & Lúcio Roberto da Silva

11. Department of Geosciences, University of Fribourg, Fribourg, Switzerland

Serjoscha W. Evers

12. Natural History Museum of Utah, University of Utah, Salt Lake City, UT, USA

Randall B. Irmis

13. Department of Geology and Geophysics, University of Utah, Salt Lake City, UT, USA

Randall B. Irmis

14. The Dinosaur Institute, Natural History Museum of Los Angeles County, Los Angeles, CA, USA

Nathan D. Smith

15. Department of Anatomical Sciences, Stony Brook University, Stony Brook, NY, USA

## Alan H. Turner

### Authors

1. Martín D. Ezcurra

[View author publications](#)

You can also search for this author in [PubMed](#) [Google Scholar](#)

2. Sterling J. Nesbitt

[View author publications](#)

You can also search for this author in [PubMed](#) [Google Scholar](#)

3. Mario Bronzati

[View author publications](#)

You can also search for this author in [PubMed](#) [Google Scholar](#)

4. Fabio Marco Dalla Vecchia

[View author publications](#)

You can also search for this author in [PubMed](#) [Google Scholar](#)

5. Federico L. Agnolin

[View author publications](#)

You can also search for this author in [PubMed](#) [Google Scholar](#)

6. Roger B. J. Benson

[View author publications](#)

You can also search for this author in [PubMed](#) [Google Scholar](#)

7. Federico Brissón Egli

[View author publications](#)

You can also search for this author in [PubMed](#) [Google Scholar](#)

8. Sergio F. Cabreira

[View author publications](#)

You can also search for this author in [PubMed](#) [Google Scholar](#)

9. Serjoscha W. Evers

[View author publications](#)

You can also search for this author in [PubMed](#) [Google Scholar](#)

10. Adriel R. Gentil

[View author publications](#)

You can also search for this author in [PubMed](#) [Google Scholar](#)

11. Randall B. Irmis

[View author publications](#)

You can also search for this author in [PubMed](#) [Google Scholar](#)

12. Agustín G. Martinelli

[View author publications](#)

You can also search for this author in [PubMed](#) [Google Scholar](#)

13. Fernando E. Novas

[View author publications](#)

You can also search for this author in [PubMed](#) [Google Scholar](#)

14. Lúcio Roberto da Silva

[View author publications](#)

You can also search for this author in [PubMed](#) [Google Scholar](#)

15. Nathan D. Smith

[View author publications](#)

You can also search for this author in [PubMed](#) [Google Scholar](#)

16. Michelle R. Stocker

[View author publications](#)

You can also search for this author in [PubMed](#) [Google Scholar](#)

17. Alan H. Turner

[View author publications](#)

You can also search for this author in [PubMed](#) [Google Scholar](#)

18. Max C. Langer

[View author publications](#)

You can also search for this author in [PubMed](#) [Google Scholar](#)

## Contributions

M.D.E., S.J.N. and M.C.L. designed the project; M.D.E., S.J.N., M.B., F.L.A., A.G.M. and M.C.L. described the material; M.B., R.B.J.B., S.W.E. and A.R.G. processed and sampled CT and  $\mu$ CT data; M.D.E., S.J.N., M.B., F.L.A., F.M.D.V., S.W.E., N.D.S. and M.C.L. scored phylogenetic matrices; M.D.E. conducted the maximum-parsimony analyses; R.B.J.B. and S.W.E. conducted the Bayesian analyses; M.D.E., S.J.N., M.B. and M.C.L. wrote the bulk of the manuscript; M.D.E., S.J.N., M.B., F.M.D.V. and S.W.E. made figures; all authors collected data and contributed to the writing, discussion and conclusion.

## Corresponding author

Correspondence to [Martín D. Ezcurra](#).

## Ethics declarations

## Competing interests

The authors declare no competing interests.

## Additional information

**Peer review information** Nature thanks Stephen Brusatte, Nicholas Fraser and the other, anonymous, reviewer(s) for their contribution to the peer review of this work. Peer reviewer reports are available.

**Publisher's note** Springer Nature remains neutral with regard to jurisdictional claims in published maps and institutional affiliations.

## Extended data figures and tables

### [Extended Data Fig. 1 Life reconstruction and three-dimensional reconstruction of the skull of the lagerpetid \*I. polesinensis\* \(ULBRA-PVT059, holotype\) with additions of cranial bones of other lagerpetids.](#)

**a–i**, Images are shown in right lateral (**a, f, i**), anterior (**b, g**), posterior (**c**), ventral (**d**), dorsal (**e**) and anterodorsolateral (**h**) views. **f–h**, Images show transparent inferred bones to show the braincase and skull roof bones through them. Bones of *I. polesinensis* are indicated in yellow and those of *K. kely* (UA 10618, holotype), *D. gregorii* (TMM 31100-1334, referred specimen) and *L. chanarensis* (PVL 4625, referred specimen) in red, and inferred bones in light blue. Arrows indicate the anterior direction. Complete scale bar, 5 cm. Life and skull reconstruction by R. Nogueira.

### [Extended Data Fig. 2 Lagerpetid \*L. chanarensis\* \(PVL 4625, referred specimen\), three-dimensional reconstruction from the µCT scan of articulated dentaries and magnifications of dentary tooth crowns.](#)

**a–h**, Images are shown in left lateral (**a**), right dorsolateral (**b**), ventral (**c**), dorsal (**d**), anterodorsal (**e**), apicolingual (**f**) and lingual (**g, h**) views. Horizontal arrows indicate the anterior direction (**a–d, f–h**) and diagonal arrows point to accessory cusps (**f, h**). **a–e**, Three-dimensional models based on µCT scan data. **f**, Scanning electron microscopy photograph. **g, h**,

Binocular microscopy photographs. Scale bars, 5 mm (**a–e**), 0.2 mm (**f**) and 0.5 mm (**g, h**).

**Extended Data Fig. 3 Additional images and comparisons between lagerpetids and pterosaurs.**

**a**, Partial skull roof and braincase of the lagerpetid *D. gregorii* (TMM 31100-1334) in left lateral view. **b**, Right hemipelvis of the lagerpetid *L. chanarensis* (PVL 4619) in lateral view. **c**, Left hemipelvis and articulated proximal end of femur of the pterosaur *Dimorphodon macronyx* (NHMUK PV OR 41212, reversed) in lateral view. **d**, Right femur of the pterosaur *D. macronyx* (YPM 9182) in anterolateral view. Arrows indicate the anterior direction. Scale bars, 3 mm (**a**) and 5 mm (**b–d**).

**Extended Data Fig. 4 Phylogenetic relationships of pterosaurs and lagerpetids among pan-archosaurs using discrete characters.**

Strict consensus of the 280 most-parsimonious trees (tree length = 5,002; consistency index = 0.21431; retention index = 0.65014). Absolute (left) and GC (group present/contradicted) (right) bootstrap frequencies are indicated above each branch and Bremer support values are shown below each branch. The position of *Scleromochlus* in the secondary analysis is indicated with a dotted line.

**Extended Data Fig. 5 Bremer support values in strict reduced consensus tree.**

Strict reduced consensus of the same most-parsimonious trees of Extended Data Fig. 4 after a posteriori pruning of *Spondylosoma*, *Dongusuchus* and PVSJ 883 to avoid reduction of Bremer support values because of missing data in these taxa. Bremer support values are indicated on each branch.

**Extended Data Fig. 6 Majority rule tree recovered from the unconstrained Bayesian phylogenetic analysis.**

Branch colours indicate character state transition rates (that is, the evolutionary rates), numbers at the nodes indicate posterior probabilities, the thin black horizontal line segments indicate the 95% probability distribution of node ages, and dotted vertical lines indicate the boundaries between the Carboniferous, Permian, Triassic and Jurassic geological periods. Thick black vertical bars indicate polytomies and, as a result, transition rates could not be calculated.

**Extended Data Fig. 7 Majority rule tree recovered from the constrained Bayesian phylogenetic analysis.**

The topology of this tree has been constrained a priori after selecting randomly one of the most-parsimonious trees recovered after forcing the position of lagerpetids as the earliest branching dinosauromorphs in the maximum parsimony analysis. Branch colours indicate character state transition rates, the black horizontal line segments indicate the 95% probability distribution of node ages and the dotted vertical lines indicate the boundaries between the Carboniferous, Permian, Triassic and Jurassic geological periods. Posterior probabilities at the nodes are not shown because the topology is fully constrained.

**Extended Data Fig. 8 Phylogenetic relationships of pterosaurs and lagerpetids among pan-archosaurs using discrete characters and the three-dimensional morphogeometric configuration of the inner ear.**

Strict consensus tree generated from the 256 most-parsimonious trees (tree length = 4,927.67960; consistency index = 0.77624; retention index = 0.85756).

**Extended Data Fig. 9 Single most-parsimonious tree found when analysing only the three-dimensional morphogeometric configuration of the inner ear and three-dimensional examples of how distances and angles were measured in the three-dimensional endosseous labyrinth models.**

**a**, Tree rooted with *T. buettneri*. **b**, Three-dimensional model of the left endosseous labyrinth of *Plateosaurus* sp. (HMN R1937) in dorsolateral view. **c**, Labyrinth with reference plane for sectioning indicated. **d**, Landmark scheme for semicircular canal length measurements. **e**, Landmark scheme for asc circumference and labyrinth height measurements. **f**, Landmark scheme for labyrinth width measurements in ventral view on the reference plane. **g**, Landmark constellation explanation. asc, anterior semicircular canal; cc, common crus; enla, endosseous labyrinth; lsc, lateral semicircular canal; psc, posterior semicircular canal; ve, vestibule.

### [Extended Data Fig. 10 Single most-parsimonious tree found when analysing only the three-dimensional morphogeometric configuration of the inner ear and alternative rooting, and morphospace plot of archosauromorph labyrinths.](#)

**a**, Tree rooted with *M. browni*. **b**, Landmark constellation explanation. **c**, Principal component (PC) analyses ( $n = 22$  species) with variation in PC1 plotted against PC2 (showing deformations along PC1–PC2), in which grey dots are non-pan-avian archosauromorphs, pink dots are non-pterosauromorph pan-avians, garnet dots are pterosaurs and orange dots are lagerpetids. [Source Data](#)

## Supplementary information

### [Supplementary Information](#)

This file contains Supplementary Text 1-11.

### [Reporting Summary](#)

### [Peer Review File](#)

## Source data

## [Source Data Extended Data Fig. 10](#)

## Rights and permissions

### [Reprints and Permissions](#)

## About this article



Check for  
updates

## Cite this article

Ezcurra, M.D., Nesbitt, S.J., Bronzati, M. *et al.* Enigmatic dinosaur precursors bridge the gap to the origin of Pterosauria. *Nature* **588**, 445–449 (2020). <https://doi.org/10.1038/s41586-020-3011-4>

### [Download citation](#)

- Received: 20 July 2020
- Accepted: 25 September 2020
- Published: 09 December 2020
- Issue Date: 17 December 2020
- DOI: <https://doi.org/10.1038/s41586-020-3011-4>

## Comments

By submitting a comment you agree to abide by our [Terms](#) and [Community Guidelines](#). If you find something abusive or that does not comply with our terms or guidelines please flag it as inappropriate.

[Access through your institution](#)

[Change institution](#)

[Buy or subscribe](#)

# Associated Content

*Nature* | News & Views

## [Closest relatives found for pterosaurs, the first flying vertebrates](#)

- Kevin Padian

---

This article was downloaded by **calibre** from <https://www.nature.com/articles/s41586-020-3011-4>

| [Section menu](#) | [Main menu](#) |

- Article
- [Published: 02 November 2020](#)

# Values encoded in orbitofrontal cortex are causally related to economic choices

- [Sébastien Ballesta](#)<sup>1 na1 nAff4 nAff5</sup>,
- [Weikang Shi](#) ORCID: [orcid.org/0000-0002-4068-1168](https://orcid.org/0000-0002-4068-1168)<sup>1 na1</sup>,
- [Katherine E. Conen](#) ORCID: [orcid.org/0000-0003-3879-1680](https://orcid.org/0000-0003-3879-1680)<sup>1 nAff6</sup> &
- [Camillo Padoa-Schioppa](#) ORCID: [orcid.org/0000-0002-7519-8790](https://orcid.org/0000-0002-7519-8790)<sup>1,2,3</sup>

[Nature](#) volume 588, pages450–453(2020) [Cite this article](#)

- 4259 Accesses
- 273 Altmetric
- [Metrics details](#)

## Subjects

- [Decision making](#)
- [Economics](#)
- [Neurophysiology](#)
- [Reward](#)

## Abstract

In the eighteenth century, Daniel Bernoulli, Adam Smith and Jeremy Bentham proposed that economic choices rely on the computation and comparison of subjective values<sup>1</sup>. This hypothesis continues to inform modern economic theory<sup>2</sup> and research in behavioural economics<sup>3</sup>, but behavioural measures are ultimately not sufficient to verify the proposal<sup>4</sup>. Consistent with the hypothesis, when agents make choices, neurons in the orbitofrontal cortex (OFC) encode the subjective value of offered and chosen goods<sup>5</sup>. Value-encoding cells integrate multiple dimensions<sup>6,7,8,9</sup>, variability in the activity of each cell group correlates with variability in choices<sup>10,11</sup> and the population dynamics suggests the formation of a decision<sup>12</sup>. However, it is unclear whether these neural processes are causally related to choices. More generally, the evidence linking economic choices to value signals in the brain<sup>13,14,15</sup> remains correlational<sup>16</sup>. Here we show that neuronal activity in the OFC is causal to economic choices. We conducted two experiments using electrical stimulation in rhesus monkeys (*Macaca mulatta*). Low-current stimulation increased the subjective value of individual offers and thus predictably biased choices. Conversely, high-current stimulation disrupted both the computation and the comparison of subjective values, and thus increased choice variability. These results demonstrate a causal chain linking subjective values encoded in OFC to valuation and choice.

[Access through your institution](#)

[Change institution](#)

[Buy or subscribe](#)

## Access options

Subscribe to Journal

Get full journal access for 1 year

185,98 €

only 3,58 € per issue

[Subscribe](#)

All prices are NET prices.  
VAT will be added later in the checkout.

Rent or Buy article

Get time limited or full article access on ReadCube.

from \$8.99

[Rent or Buy](#)

All prices are NET prices.

### **Additional access options:**

- [Log in](#)
- [Access through your institution](#)
- [Learn about institutional subscriptions](#)

**Fig. 1: High-current stimulation of OFC disrupts valuation.**

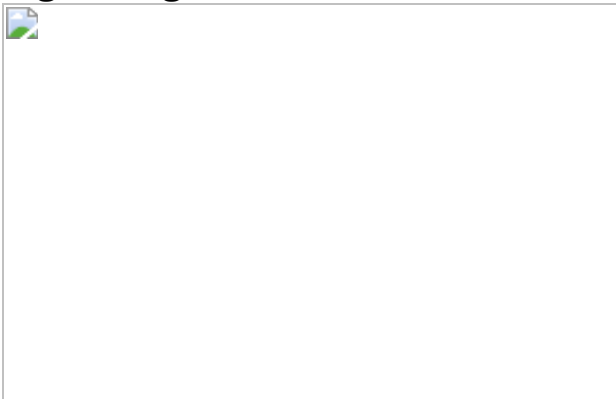


**Fig. 2: Effects of electrical stimulation at different current levels.**

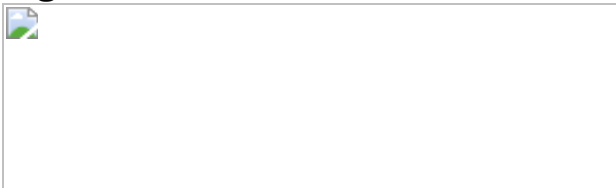


**Fig. 3: Prediction of range-dependent choice bias induced by electrical stimulation.**



**Fig. 4: Range-dependent choice bias induced by neuronal facilitation of OFC.**



## Data availability

The complete dataset is available at  
[https://github.com/PadoaSchioppaLab/2020\\_Ballesta\\_etal\\_Nature\\_Source\\_data](https://github.com/PadoaSchioppaLab/2020_Ballesta_etal_Nature_Source_data) are provided with this paper.

## Code availability

The MATLAB code used for the analysis is available at  
[https://github.com/PadoaSchioppaLab/2020\\_Ballesta\\_etal\\_Nature](https://github.com/PadoaSchioppaLab/2020_Ballesta_etal_Nature).

# References

1. 1.

Niehans, J. *A History of Economic Theory: Classic Contributions, 1720–1980* (Johns Hopkins Univ. Press, 1990).

2. 2.

Kreps, D. M. *A Course in Microeconomic Theory* (Princeton Univ. Press, 1990).

3. 3.

Kahneman, D. & Tversky, A. (eds) *Choices, Values and Frames* (Russell Sage Foundation–Cambridge Univ. Press, 2000).

4. 4.

Camerer, C. F., Loewenstein, G. & Prelec, D. Neuroeconomics: how neuroscience can inform economics. *J. Econ. Lit.* **43**, 9–64 (2005).

[Article](#) [Google Scholar](#)

5. 5.

Padoa-Schioppa, C. & Assad, J. A. Neurons in the orbitofrontal cortex encode economic value. *Nature* **441**, 223–226 (2006).

[ADS](#) [CAS](#) [Article](#) [Google Scholar](#)

6. 6.

Roesch, M. R. & Olson, C. R. Neuronal activity in primate orbitofrontal cortex reflects the value of time. *J. Neurophysiol.* **94**, 2457–2471 (2005).

[Article](#) [Google Scholar](#)

7. 7.

Kennerley, S. W., Dahmubed, A. F., Lara, A. H. & Wallis, J. D. Neurons in the frontal lobe encode the value of multiple decision variables. *J. Cogn. Neurosci.* **21**, 1162–1178 (2009).

[Article](#) [Google Scholar](#)

8. 8.

Pastor-Bernier, A., Stasiak, A. & Schultz, W. Orbitofrontal signals for two-component choice options comply with indifference curves of Revealed Preference Theory. *Nat. Commun.* **10**, 4885 (2019).

[ADS](#) [Article](#) [Google Scholar](#)

9. 9.

Hare, T. A., O'Doherty, J., Camerer, C. F., Schultz, W. & Rangel, A. Dissociating the role of the orbitofrontal cortex and the striatum in the computation of goal values and prediction errors. *J. Neurosci.* **28**, 5623–5630 (2008).

[CAS](#) [Article](#) [Google Scholar](#)

10. 10.

Padoa-Schioppa, C. Neuronal origins of choice variability in economic decisions. *Neuron* **80**, 1322–1336 (2013).

[CAS](#) [Article](#) [Google Scholar](#)

11. 11.

Conen, K. E. & Padoa-Schioppa, C. Neuronal variability in orbitofrontal cortex during economic decisions. *J. Neurophysiol.* **114**, 1367–1381 (2015).

[CAS](#) [Article](#) [Google Scholar](#)

12. 12.

Rich, E. L. & Wallis, J. D. Decoding subjective decisions from orbitofrontal cortex. *Nat. Neurosci.* **19**, 973–980 (2016).

[CAS](#) [Article](#) [Google Scholar](#)

13. 13.

Roesch, M. R. & Olson, C. R. Neuronal activity related to anticipated reward in frontal cortex: does it represent value or reflect motivation? *Ann. NY Acad. Sci.* **1121**, 431–446 (2007).

[ADS](#) [Article](#) [Google Scholar](#)

14. 14.

Schultz, W. Neuronal reward and decision signals: from theories to data. *Physiol. Rev.* **95**, 853–951 (2015).

[CAS](#) [Article](#) [Google Scholar](#)

15. 15.

Bartra, O., McGuire, J. T. & Kable, J. W. The valuation system: a coordinate-based meta-analysis of BOLD fMRI experiments examining neural correlates of subjective value. *Neuroimage* **76**, 412–427 (2013).

[Article](#) [Google Scholar](#)

16. 16.

Stalnaker, T. A., Cooch, N. K. & Schoenbaum, G. What the orbitofrontal cortex does not do. *Nat. Neurosci.* **18**, 620–627 (2015).

[CAS](#) [Article](#) [Google Scholar](#)

17. 17.

Cohen, M. R. & Newsome, W. T. What electrical microstimulation has revealed about the neural basis of cognition. *Curr. Opin. Neurobiol.* **14**, 169–177 (2004).

[CAS](#) [Article](#) [Google Scholar](#)

18. 18.

Clark, K. L., Armstrong, K. M. & Moore, T. Probing neural circuitry and function with electrical microstimulation. *Proc. R. Soc. Lond. B* **278**, 1121–1130 (2011).

[Google Scholar](#)

19. 19.

Salzman, C. D., Britten, K. H. & Newsome, W. T. Cortical microstimulation influences perceptual judgements of motion direction. *Nature* **346**, 174–177 (1990).

[ADS](#) [CAS](#) [Article](#) [Google Scholar](#)

20. 20.

Murasugi, C. M., Salzman, C. D. & Newsome, W. T. Microstimulation in visual area MT: effects of varying pulse amplitude and frequency. *J. Neurosci.* **13**, 1719–1729 (1993).

[CAS](#) [Article](#) [Google Scholar](#)

21. 21.

Kuwabara, M., Kang, N., Holy, T. E. & Padoa-Schioppa, C. Neural mechanisms of economic choices in mice. *eLife* **9**, e49669 (2020).

[CAS](#) [Article](#) [Google Scholar](#)

22. 22.

Wolff, S. B. & Ölveczky, B. P. The promise and perils of causal circuit manipulations. *Curr. Opin. Neurobiol.* **49**, 84–94 (2018).

[CAS Article](#) [Google Scholar](#)

23. 23.

Padoa-Schioppa, C. Range-adapting representation of economic value in the orbitofrontal cortex. *J. Neurosci.* **29**, 14004–14014 (2009).

[CAS Article](#) [Google Scholar](#)

24. 24.

Kobayashi, S., Pinto de Carvalho, O. & Schultz, W. Adaptation of reward sensitivity in orbitofrontal neurons. *J. Neurosci.* **30**, 534–544 (2010).

[CAS Article](#) [Google Scholar](#)

25. 25.

Rustichini, A., Conen, K. E., Cai, X. & Padoa-Schioppa, C. Optimal coding and neuronal adaptation in economic decisions. *Nat. Commun.* **8**, 1208 (2017).

[ADS Article](#) [Google Scholar](#)

26. 26.

Histed, M. H., Bonin, V. & Reid, R. C. Direct activation of sparse, distributed populations of cortical neurons by electrical microstimulation. *Neuron* **63**, 508–522 (2009).

[CAS Article](#) [Google Scholar](#)

27. 27.

Ballesta, S. & Padoa-Schioppa, C. Economic decisions through circuit inhibition. *Curr. Biol.* **29**, 3814–3824 (2019).

[CAS](#) [Article](#) [Google Scholar](#)

28. 28.

Conen, K. E. & Padoa-Schioppa, C. Partial adaptation to the value range in the macaque orbitofrontal cortex. *J. Neurosci.* **39**, 3498–3513 (2019).

[CAS](#) [PubMed](#) [PubMed Central](#) [Google Scholar](#)

29. 29.

Cisek, P. Making decisions through a distributed consensus. *Curr. Opin. Neurobiol.* **22**, 927–936 (2012).

[CAS](#) [Article](#) [Google Scholar](#)

30. 30.

Padoa-Schioppa, C. & Conen, K. E. Orbitofrontal cortex: a neural circuit for economic decisions. *Neuron* **96**, 736–754 (2017).

[CAS](#) [Article](#) [Google Scholar](#)

31. 31.

Rustichini, A. & Padoa-Schioppa, C. A neuro-computational model of economic decisions. *J. Neurophysiol.* **114**, 1382–1398 (2015).

[Article](#) [Google Scholar](#)

32. 32.

Wong, K. F. & Wang, X. J. A recurrent network mechanism of time integration in perceptual decisions. *J. Neurosci.* **26**, 1314–1328 (2006).

[CAS](#) [Article](#) [Google Scholar](#)

33. 33.

Merrill, D. R., Bikson, M. & Jefferys, J. G. Electrical stimulation of excitable tissue: design of efficacious and safe protocols. *J. Neurosci. Methods* **141**, 171–198 (2005).

[Article](#) [Google Scholar](#)

34. 34.

Kim, S. et al. Behavioral assessment of sensitivity to intracortical microstimulation of primate somatosensory cortex. *Proc. Natl Acad. Sci. USA* **112**, 15202–15207 (2015).

[ADS](#) [CAS](#) [Article](#) [Google Scholar](#)

35. 35.

Lee, S. W., Eddington, D. K. & Fried, S. I. Responses to pulsatile subretinal electric stimulation: effects of amplitude and duration. *J. Neurophysiol.* **109**, 1954–1968 (2013).

[Article](#) [Google Scholar](#)

36. 36.

Hussin, A. T., Boychuk, J. A., Brown, A. R., Pittman, Q. J. & Teskey, G. C. Intracortical microstimulation (ICMS) activates motor cortex layer 5 pyramidal neurons mainly transsynaptically. *Brain Stimul.* **8**, 742–750 (2015).

[Article](#) [Google Scholar](#)

37. 37.

Tolias, A. S. et al. Mapping cortical activity elicited with electrical microstimulation using FMRI in the macaque. *Neuron* **48**, 901–911

(2005).

[CAS](#) [Article](#) [Google Scholar](#)

38. 38.

Stoney, S. D. Jr, Thompson, W. D. & Asanuma, H. Excitation of pyramidal tract cells by intracortical microstimulation: effective extent of stimulating current. *J. Neurophysiol.* **31**, 659–669 (1968).

[Article](#) [Google Scholar](#)

39. 39.

Arsiero, M., Lüscher, H. R., Lundstrom, B. N. & Giugliano, M. The impact of input fluctuations on the frequency-current relationships of layer 5 pyramidal neurons in the rat medial prefrontal cortex. *J. Neurosci.* **27**, 3274–3284 (2007).

[CAS](#) [Article](#) [Google Scholar](#)

40. 40.

La Camera, G., Giugliano, M., Senn, W. & Fusi, S. The response of cortical neurons to in vivo-like input current: theory and experiment. I. Noisy inputs with stationary statistics. *Biol. Cybern.* **99**, 279–301 (2008).

[Article](#) [Google Scholar](#)

41. 41.

Ethier, C., Brizzi, L., Darling, W. G. & Capaday, C. Linear summation of cat motor cortex outputs. *J. Neurosci.* **26**, 5574–5581 (2006).

[CAS](#) [Article](#) [Google Scholar](#)

42. 42.

Griffin, D. M., Hudson, H. M., Belhaj-Saïf, A. & Cheney, P. D. Hijacking cortical motor output with repetitive microstimulation. *J. Neurosci.* **31**, 13088–13096 (2011).

[CAS Article](#) [Google Scholar](#)

43. 43.

Van Acker, G. M. III et al. Effective intracortical microstimulation parameters applied to primary motor cortex for evoking forelimb movements to stable spatial end points. *J. Neurophysiol.* **110**, 1180–1189 (2013).

[Article](#) [Google Scholar](#)

[Download references](#)

## Acknowledgements

We thank H. Schoknecht for help with animal training and J. Assad, E. Bromberg-Martin, E. Fehr, D. Freedman, I. Monosov and L. Snyder for comments on the manuscript. This research was supported by the National Institutes of Health (grants number R01-DA032758 and R01-MH104494 to C.P.-S. and grant number F31-MH107111 to K.E.C.) and by the McDonnell Center for Systems Neuroscience (pre-doctoral fellowship to W.S.).

## Author information

Author notes

1. Sébastien Ballesta

Present address: Laboratoire de Neurosciences Cognitives et Adaptatives (UMR 7364), Strasbourg, France

2. Sébastien Ballesta

Present address: Centre de Primatologie de l'Université de Strasbourg,  
Niederhausbergen, France

3. Katherine E. Conen

Present address: Department of Neuroscience, Brown University,  
Providence, RI, USA

4. These authors contributed equally: Sébastien Ballesta, Weikang Shi

## Affiliations

1. Department of Neuroscience, Washington University in St Louis, St Louis, MO, USA

Sébastien Ballesta, Weikang Shi, Katherine E. Conen & Camillo Padoa-Schioppa

2. Department of Economics, Washington University in St Louis, St Louis, MO, USA

Camillo Padoa-Schioppa

3. Department of Biomedical Engineering, Washington University in St Louis, St Louis, MO, USA

Camillo Padoa-Schioppa

4. Laboratoire de Neurosciences Cognitives et Adaptatives (UMR 7364), Strasbourg, France

Sébastien Ballesta

5. Centre de Primatologie de l'Université de Strasbourg,  
Niederhausbergen, France

Sébastien Ballesta

## Authors

1. Sébastien Ballesta

[View author publications](#)

You can also search for this author in [PubMed](#) [Google Scholar](#)

2. Weikang Shi

[View author publications](#)

You can also search for this author in [PubMed](#) [Google Scholar](#)

3. Katherine E. Conen

[View author publications](#)

You can also search for this author in [PubMed](#) [Google Scholar](#)

4. Camillo Padoa-Schioppa

[View author publications](#)

You can also search for this author in [PubMed](#) [Google Scholar](#)

## Contributions

S.B. and W.S. collected and analysed the data; K.E.C. designed experiment 2; and C.P.-S. supervised the project and wrote the manuscript. All of the authors edited the manuscript.

## Corresponding author

Correspondence to [Camillo Padoa-Schioppa](#).

## Ethics declarations

## Competing interests

The authors declare no competing interests.

## Additional information

**Peer review information** *Nature* thanks Tianming Yang and the other, anonymous, reviewer(s) for their contribution to the peer review of this work. Peer reviewer reports are available.

**Publisher's note** Springer Nature remains neutral with regard to jurisdictional claims in published maps and institutional affiliations.

## Extended data figures and tables

### [Extended Data Fig. 1 Experiment 2, control for choice frequency.](#)

We noticed that across sessions the difference in value range ( $\Delta V_A - \Delta V_B$ ) was correlated with the fraction of trials in which the animal chose juice A (% A choice) and with the relative value ( $\rho$ ). In principle, these correlations could represent confounding factors. Indeed, 50  $\mu$ A stimulation could partly disrupt the valuation process. As a result, the animal might respond by defaulting to the juice type most frequently chosen in that session, or to the preferred juice type. If so, the range-dependent bias would be akin to the order bias (experiment 1), in the sense that it would result from functional disruption as opposed to facilitation. To address this concern, we identified a subset of sessions for which choices between the two juices were split almost evenly. In this subset of sessions, the difference in value range and the fraction of A choices were not correlated. We reasoned that if the range-dependent bias observed for the whole dataset was driven by a default to the most frequently chosen option, the bias should disappear when the analysis was restricted to this subset of sessions. However, this was not the case. In fact, the range-dependent bias measured for the selected subset was larger than that measured for the entire population. We concluded that range-dependent biases did not reflect simple heuristics. **a**, Correlation between the difference in value range and the fraction of A choices. Each data point represents one session. Considering the entire dataset (black data points,  $N = 96$  sessions), the two measures were significantly correlated ( $r \geq 0.71$ ,  $P < 10^{-15}$ , Pearson and Spearman correlation tests). We defined a small ellipse centred on coordinates [0, 50] (axes = [9, 14]). The ellipse identified a subset of data (pink data points,  $N = 31$  sessions) for which the difference

in value range and the fraction of A choices were not correlated ( $P \geq 0.69$ , Pearson and Spearman correlation tests). **b**, Correlation between the difference in value range and the relative value. Considering the entire dataset, the two measures were significantly correlated ( $r \geq 0.33$ ,  $P \leq 0.001$ , Pearson and Spearman correlation tests). However, when the analysis was restricted to the subset of sessions identified in **a** (pink data points), the correlation changed sign. **c**, Range-dependent bias, same data as in Fig. 4c, **d**. Considering the entire dataset, the change in relative value was significantly correlated with the difference in value range ( $r \geq 0.34$ ,  $P \leq 0.0007$ , Pearson and Spearman correlation tests). The correlation did not dissipate when the analysis was restricted to the subset of sessions identified in **a** (pink data points;  $r \geq 0.45$ ,  $P \leq 0.01$ , Pearson and Spearman correlation tests). In this figure, data from the two animals are combined. Grey and pink lines in the three panels were obtained from Deming regressions. [Source data](#)

### Extended Data Fig. 2 Experiment 2, results obtained in paired sessions.

In  $N = 33$  instances, we ran two back-to-back sessions offering the same two juices and leaving the electrode in place, but changing the quantity ranges such that  $\Delta V_A - \Delta V_B$  would differ. **a**, Example of paired sessions. **b**, Population analysis. Each pair of sessions in the scatter plot is connected by a line, of which we computed the slope. Data points filled in green correspond to sessions in **a**. Data from the two monkeys are pooled. Across the population, slopes were typically  $>0$  ( $P = 0.007$ , two-tailed Wilcoxon signed-rank test). Hence, range-dependent biases were not dictated by the juice pair or by the location of the electrode within OFC.

### Extended Data Fig. 3 Experiment 2, analysis of response times (RTs).

**a**, Example session 1. Each data point represents one trial type and the two lines were obtained from linear regressions. Under normal conditions (stimOFF, black), RTs decreased as a function of the chosen value (x axis). Electrical stimulation (stimON, red) generally reduced RTs. Linear fits

reveal that lower RTs were due to a lower intercept, as opposed to a steeper (that is, more negative) slope. **b, c**, Population analysis, monkey D ( $N = 35$ ). For each session, we regressed RTs onto the chosen value, separately for stimOFF and stimON trials. We then compared the intercepts and the slopes at the population level. The picture emerging from **a** was confirmed for the population. In **b** (intercept), each data point represents one session. The population is significantly displaced below the identity line ( $P = 0.018$ , two-tailed Wilcoxon test). In **c** (slope), it can be noticed that the slope under stimulation was shallower (less negative), probably due to a floor effect. Filled data points correspond to the session shown in **a**. **d**, Example session 2. Same format as in **a**. **e, f**, Population analysis, monkey G ( $N = 61$ ). Same format as in **b, c**. Electrical stimulation significantly lowered the intercept but did not significantly alter the slope. Filled data points correspond to the session shown in **d**. In **b, c, e, f**, values indicated in the insert refer to the difference between the stimON measure and the stimOFF measure, averaged across the population. All  $P$  values are from two-tailed Wilcoxon tests, and  $t$ -tests provided very similar results. [Source data](#)

### [Extended Data Fig. 4 Experiment 1, range-dependent choice biases.](#)

**a–c**, Results obtained when electric current was delivered at 25  $\mu$ A, 50  $\mu$ A and  $\geq 100 \mu$ A. In each panel,  $x$  and  $y$  axes represent the difference in value range (in uB) and the difference in relative value, respectively. Each data point represents one session. Sessions from the two animals and with different stimulation times (offer 1 or offer 2) were pooled. Grey lines were obtained from linear regressions. Each panel indicates the  $P$  values obtained from Pearson and Spearman correlation tests. In essence, the choice bias imposed by the stimulation ( $\delta\rho$ ) was correlated with the difference in value ranges ( $\Delta V_A - \Delta V_B$ ) at low current (25  $\mu$ A; weakly) and intermediate current (50  $\mu$ A), but not at high current ( $\geq 100 \mu$ A). [Source data](#)

### [Extended Data Fig. 5 Stimulation in experiment 2 did not systematically alter the sigmoid steepness.](#)

For this analysis, the two groups of trials (stimOFF, stimON) were examined separately (see [Methods](#)). The two axes represent the sigmoid steepness in the two conditions. Sessions from the two animals were pooled ( $N = 95$ , 2 outliers removed), and each data point represents one session. The grey ellipse represents the 90% confidence interval. The  $P$  value is from a Wilcoxon test and similar results were obtained with a  $t$ -test. [Source data](#)

## [Extended Data Fig. 6 Experiment 1, interpretation of the order bias.](#)

**a**, Decelerating response function. The black line represents an ideal response function, which relates the number of spikes emitted by a cell in a given time window (y axis) to the synaptic current entering the cell (x axis). In the condition highlighted in yellow,  $I_O$  is the synaptic current due to the offer on the monitor,  $r$  is the corresponding response,  $I_S$  is the synaptic current due to the stimulation, and  $\delta r$  is the corresponding increase in the number of spikes. The condition highlighted in blue is similar, except that  $I_O$  is larger ( $I_{O,\text{blue}} > I_{O,\text{yellow}}$ ). Because the response function is decelerating,  $\delta r$  in the blue condition is smaller ( $\delta r_{\text{blue}} < \delta r_{\text{yellow}}$ ). In experiment 1, only one good was presented at the time. Neurons associated with that good were naturally more active (higher  $I_O$ ) than neurons associated with the other good. Thus deceleration in the response function induced a bias favouring the good not offered during the stimulation (order bias). For given  $I_{O,\text{yellow}}$  and  $I_{O,\text{blue}}$ , the difference  $\delta r_{\text{yellow}} - \delta r_{\text{blue}}$  increases with  $I_S$ . Hence, higher stimulation currents induced larger order biases. **b**, Concurrent presence of order bias and range-dependent bias. The cartoon illustrates an ideal session in experiment 1. We assume that under normal conditions there is no order bias (stimOFF, continuous lines). Thus the two sigmoids for AB trials and BA trials coincide. We also assume that stimulation is delivered during offer 1, and that  $\Delta V_A - \Delta V_B > 0$ . The order bias separates the two sigmoids such that under stimulation the sigmoid for AB trials is on the left of that for BA trials (stimON, dashed lines). The range-dependent bias imposes a shift on the total sigmoid, including both AB and BA trials (not shown), which moves to the right compared to

normal conditions. The two choice biases are complementary and independent.

**Extended Data Table 1** Exact *P* values for the statistical tests used for Fig. 2

[Full size table](#)

**Extended Data Table 2** Dataset for experiment 1

[Full size table](#)

## Supplementary information

[\*\*Reporting Summary\*\*](#)

[\*\*Peer Review File\*\*](#)

## Source data

[\*\*Source Data Fig. 1\*\*](#)

[\*\*Source Data Fig. 2\*\*](#)

[\*\*Source Data Fig. 4\*\*](#)

[\*\*Source Data Extended Data Fig. 1\*\*](#)

[\*\*Source Data Extended Data Fig. 3\*\*](#)

[\*\*Source Data Extended Data Fig. 4\*\*](#)

[\*\*Source Data Extended Data Fig. 5\*\*](#)

## Rights and permissions

[\*\*Reprints and Permissions\*\*](#)

# About this article



Check for  
updates

## Cite this article

Ballesta, S., Shi, W., Conen, K.E. *et al.* Values encoded in orbitofrontal cortex are causally related to economic choices. *Nature* **588**, 450–453 (2020). <https://doi.org/10.1038/s41586-020-2880-x>

[Download citation](#)

- Received: 03 February 2020
- Accepted: 17 August 2020
- Published: 02 November 2020
- Issue Date: 17 December 2020
- DOI: <https://doi.org/10.1038/s41586-020-2880-x>

## Comments

By submitting a comment you agree to abide by our [Terms](#) and [Community Guidelines](#). If you find something abusive or that does not comply with our terms or guidelines please flag it as inappropriate.

[Access through your institution](#)

[Change institution](#)

[Buy or subscribe](#)

| [Section menu](#) | [Main menu](#) |

- Article
- [Published: 18 November 2020](#)

# Assembly of synaptic active zones requires phase separation of scaffold molecules

- [Nathan A. McDonald](#) ORCID: [orcid.org/0000-0003-2716-3881<sup>1</sup>](https://orcid.org/0000-0003-2716-3881),
- [Richard D. Fetter](#) ORCID: [orcid.org/0000-0002-1558-100X<sup>2</sup>](https://orcid.org/0000-0002-1558-100X) &
- [Kang Shen](#) ORCID: [orcid.org/0000-0003-4059-8249<sup>1,2</sup>](https://orcid.org/0000-0003-4059-8249)

[Nature](#) volume 588, pages454–458(2020) [Cite this article](#)

- 4428 Accesses
- 16 Altmetric
- [Metrics details](#)

## Subjects

- [Cell biology](#)
- [Cellular neuroscience](#)

## Abstract

The formation of synapses during neuronal development is essential for establishing neural circuits and a nervous system<sup>1</sup>. Every presynapse builds a core ‘active zone’ structure, where ion channels cluster and synaptic vesicles release their neurotransmitters<sup>2</sup>. Although the composition of active zones is well characterized<sup>2,3</sup>, it is unclear how active-zone proteins

assemble together and recruit the machinery required for vesicle release during development. Here we find that the core active-zone scaffold proteins SYD-2 (also known as liprin- $\alpha$ ) and ELKS-1 undergo phase separation during an early stage of synapse development, and later mature into a solid structure. We directly test the *in vivo* function of phase separation by using mutant SYD-2 and ELKS-1 proteins that specifically lack this activity. These mutant proteins remain enriched at synapses in *Caenorhabditis elegans*, but show defects in active-zone assembly and synapse function. The defects are rescued by introducing a phase-separation motif from an unrelated protein. *In vitro*, we reconstitute the SYD-2 and ELKS-1 liquid-phase scaffold, and find that it is competent to bind and incorporate downstream active-zone components. We find that the fluidity of SYD-2 and ELKS-1 condensates is essential for efficient mixing and incorporation of active-zone components. These data reveal that a developmental liquid phase of scaffold molecules is essential for the assembly of the synaptic active zone, before maturation into a stable final structure.

[Access through your institution](#)

[Change institution](#)

[Buy or subscribe](#)

## Access options

Subscribe to Journal

Get full journal access for 1 year

185,98 €

only 3,58 € per issue

[Subscribe](#)

All prices are NET prices.

VAT will be added later in the checkout.

Rent or Buy article

Get time limited or full article access on ReadCube.

from \$8.99

[Rent or Buy](#)

All prices are NET prices.

### **Additional access options:**

- [Log in](#)
- [Access through your institution](#)
- [Learn about institutional subscriptions](#)

**Fig. 1: The active-zone scaffold proteins SYD-2 and ELKS-1 are dynamic at nascent synapses and capable of phase separation.**



**Fig. 2: Identification and mutation of the phase-separation motifs of SYD-2 and ELKS-1.**



**Fig. 3: Phase separation of SYD-2 and ELKS-1 is required for assembly of the presynaptic active zone.**



**Fig. 4: The fluidity of SYD-2 and ELKS-1 condensates facilitates the incorporation of active-zone components.**



## Data availability

All reagents are available on request. [Source data](#) are provided with this paper.

## References

1. 1.

Südhof, T. C. Towards an understanding of synapse formation. *Neuron* **100**, 276–293 (2018).

[PubMed](#) [PubMed Central](#) [Google Scholar](#)

2. 2.

Südhof, T. C. The presynaptic active zone. *Neuron* **75**, 11–25 (2012).

[PubMed](#) [PubMed Central](#) [Google Scholar](#)

3. 3.

Ghelani, T. & Sigrist, S. J. Coupling the structural and functional assembly of synaptic release sites. *Front. Neuroanat.* **12**, 81 (2018).

[CAS](#) [PubMed](#) [PubMed Central](#) [Google Scholar](#)

4. 4.

Lipton, D. M., Maeder, C. I. & Shen, K. Rapid assembly of presynaptic materials behind the growth cone in dopaminergic neurons is mediated by precise regulation of axonal transport. *Cell Rep.* **24**, 2709–2722 (2018).

[CAS](#) [PubMed](#) [PubMed Central](#) [Google Scholar](#)

5. 5.

Bracha, D., Walls, M. T. & Brangwynne, C. P. Probing and engineering liquid-phase organelles. *Nat. Biotechnol.* **37**, 1435–1445 (2019).

[CAS](#) [PubMed](#) [Google Scholar](#)

6. 6.

Sala, K. et al. The ERC1 scaffold protein implicated in cell motility drives the assembly of a liquid phase. *Sci. Rep.* **9**, 13530 (2019).

[ADS](#) [PubMed](#) [PubMed Central](#) [Google Scholar](#)

7. 7.

Patel, M. R. et al. Hierarchical assembly of presynaptic components in defined *C. elegans* synapses. *Nat. Neurosci.* **9**, 1488–1498 (2006).

[CAS](#) [PubMed](#) [PubMed Central](#) [Google Scholar](#)

8. 8.

Dai, Y. et al. SYD-2 Liprin- $\alpha$  organizes presynaptic active zone formation through ELKS. *Nat. Neurosci.* **9**, 1479–1487 (2006).

[CAS](#) [PubMed](#) [Google Scholar](#)

9. 9.

Zhen, M. & Jin, Y. The liprin protein SYD-2 regulates the differentiation of presynaptic termini in *C. elegans*. *Nature* **401**, 371–375 (1999).

[ADS](#) [CAS](#) [PubMed](#) [Google Scholar](#)

10. 10.

Patel, M. R. & Shen, K. RSY-1 is a local inhibitor of presynaptic assembly in *C. elegans*. *Science* **323**, 1500–1503 (2009).

[ADS](#) [CAS](#) [PubMed](#) [PubMed Central](#) [Google Scholar](#)

11. 11.

Putnam, A., Cassani, M., Smith, J. & Seydoux, G. A gel phase promotes condensation of liquid P granules in *Caenorhabditis elegans* embryos. *Nat. Struct. Mol. Biol.* **26**, 220–226 (2019).

[CAS](#) [PubMed](#) [PubMed Central](#) [Google Scholar](#)

12. 12.

Wheeler, J. R., Matheny, T., Jain, S., Abrisch, R. & Parker, R. Distinct stages in stress granule assembly and disassembly. *eLife* **5**, e18413 (2016).

[PubMed](#) [PubMed Central](#) [Google Scholar](#)

13. 13.

Zeng, M. et al. Phase transition in postsynaptic densities underlies formation of synaptic complexes and synaptic plasticity. *Cell* **166**, 1163–1175 (2016).

[CAS](#) [PubMed](#) [PubMed Central](#) [Google Scholar](#)

14. 14.

Kalla, S. et al. Molecular dynamics of a presynaptic active zone protein studied in Munc13-1-enhanced yellow fluorescent protein knock-in mutant mice. *J. Neurosci.* **26**, 13054–13066 (2006).

[CAS](#) [PubMed](#) [PubMed Central](#) [Google Scholar](#)

15. 15.

Tsuriel, S. et al. Exchange and redistribution dynamics of the cytoskeleton of the active zone molecule bassoon. *J. Neurosci.* **29**, 351–358 (2009).

[CAS](#) [PubMed](#) [PubMed Central](#) [Google Scholar](#)

16. 16.

Deken, S. L. et al. Redundant localization mechanisms of RIM and ELKS in *Caenorhabditis elegans*. *J. Neurosci.* **25**, 5975–5983 (2005).

[CAS](#) [PubMed](#) [PubMed Central](#) [Google Scholar](#)

17. 17.

Kittelmann, M. et al. Liprin- $\alpha$ /SYD-2 determines the size of dense projections in presynaptic active zones in *C. elegans*. *J. Cell Biol.* **203**, 849–863 (2013).

[CAS](#) [PubMed](#) [PubMed Central](#) [Google Scholar](#)

18. 18.

Schwartz, M. L. & Jorgensen, E. M. SapTrap, a toolkit for high-throughput CRISPR/Cas9 gene modification in *Caenorhabditis elegans*. *Genetics* **202**, 1277–1288 (2016).

[CAS](#) [PubMed](#) [PubMed Central](#) [Google Scholar](#)

19. 19.

Wu, Y. E., Huo, L., Maeder, C. I., Feng, W. & Shen, K. The balance between capture and dissociation of presynaptic proteins controls the spatial distribution of synapses. *Neuron* **78**, 994–1011 (2013).

[CAS](#) [PubMed](#) [PubMed Central](#) [Google Scholar](#)

20. 20.

Chia, P. H., Patel, M. R. & Shen, K. NAB-1 instructs synapse assembly by linking adhesion molecules and F-actin to active zone proteins. *Nat. Neurosci.* **15**, 234–242 (2012).

[CAS](#) [PubMed](#) [PubMed Central](#) [Google Scholar](#)

21. 21.

Collins, K. M. et al. Activity of the *C. elegans* egg-laying behavior circuit is controlled by competing activation and feedback inhibition. *eLife* **5**, e21126 (2016).

[PubMed](#) [PubMed Central](#) [Google Scholar](#)

22. 22.

Kato, M. et al. Cell-free formation of RNA granules: low complexity sequence domains form dynamic fibers within hydrogels. *Cell* **149**, 753–767 (2012).

[CAS](#) [PubMed](#) [PubMed Central](#) [Google Scholar](#)

23. 23.

Ryan, V. H. et al. Mechanistic view of hnRNPA2 low-complexity domain structure, interactions, and phase separation altered by mutation and arginine methylation. *Mol. Cell* **69**, 465–479.e7 (2018).

[CAS](#) [PubMed](#) [PubMed Central](#) [Google Scholar](#)

24. 24.

Yamasaki, A. et al. Liquidity is a critical determinant for selective autophagy of protein condensates. *Mol. Cell* **77**, 1163–1175.e9 (2020).

[CAS](#) [PubMed](#) [Google Scholar](#)

25. 25.

Vernon, R. M. et al. Pi-Pi contacts are an overlooked protein feature relevant to phase separation. *eLife* **7**, e31486 (2018).

[PubMed](#) [PubMed Central](#) [Google Scholar](#)

26. 26.

Woodruff, J. B., Hyman, A. A. & Boke, E. Organization and function of non-dynamic biomolecular condensates. *Trends Biochem. Sci.* **43**, 81–94 (2018).

[CAS](#) [PubMed](#) [Google Scholar](#)

27. 27.

Wu, X. et al. RIM and RIM-BP form presynaptic active-zone-like condensates via phase separation. *Mol. Cell* **73**, 971–984.e5 (2019).

[CAS](#) [PubMed](#) [Google Scholar](#)

28. 28.

Milovanovic, D., Wu, Y., Bian, X. & De Camilli, P. A liquid phase of synapsin and lipid vesicles. *Science* **361**, 604–607 (2018).

[ADS](#) [CAS](#) [PubMed](#) [PubMed Central](#) [Google Scholar](#)

29. 29.

Brenner, S. The genetics of *Caenorhabditis elegans*. *Genetics* **77**, 71–94 (1974).

[CAS](#) [PubMed](#) [PubMed Central](#) [Google Scholar](#)

30. 30.

Gibson, D. G. et al. Enzymatic assembly of DNA molecules up to several hundred kilobases. *Nat. Methods* **6**, 343–345 (2009).

[CAS](#) [Google Scholar](#)

31. 31.

Dickinson, D. J., Pani, A. M., Heppert, J. K., Higgins, C. D. & Goldstein, B. Streamlined genome engineering with a self-excising drug selection cassette. *Genetics* **200**, 1035–1049 (2015).

[PubMed](#) [PubMed Central](#) [Google Scholar](#)

32. 32.

Hubbard, E. J. A. FLP/FRT and Cre/lox recombination technology in *C. elegans*. *Methods* **68**, 417–424 (2014).

[CAS](#) [PubMed](#) [PubMed Central](#) [Google Scholar](#)

33. 33.

Kato, M., Lin, Y. & McKnight, S. L. Cross- $\beta$  polymerization and hydrogel formation by low-complexity sequence proteins. *Methods* **126**, 3–11 (2017).

[CAS](#) [PubMed](#) [PubMed Central](#) [Google Scholar](#)

34. 34.

Walther, P. & Ziegler, A. Freeze substitution of high-pressure frozen samples: the visibility of biological membranes is improved when the

substitution medium contains water. *J. Microsc.* **208**, 3–10 (2002).

[MathSciNet](#) [CAS](#) [PubMed](#) [Google Scholar](#)

35. 35.

Buser, C. & Walther, P. Freeze-substitution: the addition of water to polar solvents enhances the retention of structure and acts at temperatures around –60 °C. *J. Microsc.* **230**, 268–277 (2008).

[MathSciNet](#) [CAS](#) [PubMed](#) [Google Scholar](#)

36. 36.

Sato, T. A modified method for lead staining of thin sections. *J. Electron Microsc. (Tokyo)* **17**, 158–159 (1968).

[CAS](#) [Google Scholar](#)

37. 37.

Mészáros, B., Erdős, G. & Dosztányi, Z. IUPred2A: context-dependent prediction of protein disorder as a function of redox state and protein binding. *Nucleic Acids Res.* **46** (W1), W329–W337 (2018).

[PubMed](#) [PubMed Central](#) [Google Scholar](#)

38. 38.

Hanson, J., Paliwal, K. & Zhou, Y. Accurate single-sequence prediction of protein intrinsic disorder by an ensemble of deep recurrent and convolutional architectures. *J. Chem. Inf. Model.* **58**, 2369–2376 (2018).

[CAS](#) [PubMed](#) [Google Scholar](#)

39. 39.

Bolognesi, B. et al. A concentration-dependent liquid phase separation can cause toxicity upon increased protein expression. *Cell Rep.* **16**, 222–231 (2016).

[CAS](#) [PubMed](#) [PubMed Central](#) [Google Scholar](#)

40. 40.

Britton, S. et al. DNA damage triggers SAF-A and RNA biogenesis factors exclusion from chromatin coupled to R-loops removal. *Nucleic Acids Res.* **42**, 9047–9062 (2014).

[CAS](#) [PubMed](#) [PubMed Central](#) [Google Scholar](#)

41. 41.

Monahan, Z. et al. Phosphorylation of the FUS low-complexity domain disrupts phase separation, aggregation, and toxicity. *EMBO J.* **36**, 2951–2967 (2017).

[CAS](#) [PubMed](#) [PubMed Central](#) [Google Scholar](#)

42. 42.

McDonnell, A. V., Jiang, T., Keating, A. E. & Berger, B. Paircoil2: improved prediction of coiled coils from sequence. *Bioinformatics* **22**, 356–358 (2006).

[CAS](#) [PubMed](#) [Google Scholar](#)

43. 43.

Shen, K. & Bargmann, C. I. The immunoglobulin superfamily protein SYG-1 determines the location of specific synapses in *C. elegans*. *Cell* **112**, 619–630 (2003).

[CAS](#) [PubMed](#) [Google Scholar](#)

44. 44.

Schafer, W. F. Genetics of egg-laying in worms. *Annu. Rev. Genet.* **40**, 487–509 (2006).

[CAS](#) [PubMed](#) [Google Scholar](#)

[Download references](#)

## Acknowledgements

We thank L. Luo, S. Chen and members of the Shen laboratory for critical reading of the manuscript; J. Lee for the GFP-SYD-2 strain; K. M. Collins for HSN strains; P. Calsou and N. L. Fawzi for FUS constructs; E. M. Jorgensen and B. Goldstein for FLPon tools; M. Boxem for a tagBFP2 construct; and L. Feng and Y. Xu for assistance with size-exclusion chromatography. This work was funded by Howard Hughes Medical Institute, of which K.S. is an investigator; by NIH grant R37 NS048392 to K.S.; and by a Helen Hay Whitney postdoctoral fellowship to N.A.M.

## Author information

### Affiliations

1. Department of Biology, Stanford University, Stanford, CA, USA

Nathan A. McDonald & Kang Shen

2. Howard Hughes Medical Institute, Department of Biology, Stanford University, Stanford, CA, USA

Richard D. Fetter & Kang Shen

### Authors

1. Nathan A. McDonald

[View author publications](#)

You can also search for this author in [PubMed](#) [Google Scholar](#)

2. Richard D. Fetter

[View author publications](#)

You can also search for this author in [PubMed](#) [Google Scholar](#)

3. Kang Shen

[View author publications](#)

You can also search for this author in [PubMed](#) [Google Scholar](#)

## Contributions

N.A.M. and K.S. conceptualized the study. N.A.M. carried out the experiments and analyses. R.D.F. carried out electron-microscopy experiments and analyses. N.A.M. wrote the paper. N.A.M., R.D.F. and K.S. edited the paper.

## Corresponding author

Correspondence to [Kang Shen](#).

## Ethics declarations

## Competing interests

The authors declare no competing interests.

## Additional information

**Peer review information** *Nature* thanks Erik Jorgensen, Dragomir Milovanovic and the other, anonymous, reviewer(s) for their contribution to the peer review of this work.

**Publisher's note** Springer Nature remains neutral with regard to jurisdictional claims in published maps and institutional affiliations.

# Extended data figures and tables

## Extended Data Fig. 1 Presynaptic active-zone scaffolds display LLPS characteristics.

**a**, Predictions of intrinsic disorder in the sequences of presynaptic active-zone components, using the IUPred2a (ref. [37](#)) and Spot-Disorder2 (ref. [38](#)) algorithms. Values above 0.5 indicate intrinsic disorder. **b**, Predictions of LLPS of active-zone components, using catGRANULE<sup>[39](#)</sup> and Pi–Pi predictor<sup>[25](#)</sup> algorithms. Higher values indicate a propensity towards phase separation. **c**, Expression of GFP- or mCherry-tagged presynaptic active-zone components in COS-7 cells. FUS–GFP is a positive control<sup>[40,41](#)</sup>. Red boxes indicate example puncta that are photobleached in **d**. Scale bar, 10 μm. **d**, FRAP analysis of puncta. Data are means ± 95% CI from two independent experiments. Insets show example recovery kinetics of puncta from **c**. Scale bar, 1 μm. **e**, Time-lapse analysis of in vivo droplets containing SYD-2 or ELKS-1, showing liquid behaviours of fusion and relaxation. Red arrowheads point to droplets before fusion. Liquid behaviour was observed in multiple cells and in different technical replicates. UNC-10 puncta were dynamic when analysed by FRAP, but never showed liquid behaviour. Scale bars, 1 μm. [Source data](#)

## Extended Data Fig. 2 Controls for in vitro phase separation assays.

**a**, In vitro LLPS assay workflow and scoring conditions. **b**, Size-exclusion chromatography of purified mCherry and mCherry–FUS in 20 mM Tris pH 7.4, 500 mM NaCl, indicating that the protein isolated by the high-salt purification method is soluble.  $A_{280}$ , absorption at 280 nm. **c**, In vitro LLPS assay. Left panels, soluble input materials before dilution to physiological salt concentration. Right panels, comparison between the effects of no crowding and 10% PEG conditions on a known phase-separating motif (FUS)<sup>[41](#)</sup> and a negative control (mCherry). **d**, Representative FRAP images (top) and quantified FRAP dynamics (bottom) of FUS and mCherry in vitro condensates formed in 10% PEG. Data are means ± 95% CI from three

independent experiments. **e**, Time-lapse analysis of in vitro condensates containing mCherry and FUS, showing the presence or absence of liquid behaviour. Phase-separation assays were performed in 20 mM Tris pH 7.4, 150 mM NaCl and 10% PEG 3350 where indicated with 10 µM protein. **f**, **g**, Phase diagrams for mCh–SYD-2(Nter) (**f**) and mCh–ELKS-1 (**g**), showing protein concentrations versus NaCl or PEG concentrations. Each combination was tested three times. Scale bars, 5 µm. [Source data](#)

### Extended Data Fig. 3 Purified constructs for in vitro phase separation assays.

SDS–PAGE gels, stained by Coomassie blue, of the purified constructs used for in vitro assays in the indicated figures. Many constructs display a secondary band 10 kDa below the major species, due to mCherry cleavage at the fluorophore centre (Y72)<sup>33</sup>.

### Extended Data Fig. 4 Structure–function analysis of SYD-2 phase separation.

**a**, Diagram showing the structure of SYD-2, including disordered regions and coiled-coils predicted by the indicated algorithms<sup>37,38,42</sup>. LH1/LH2, liprin-homology domains; SAM, sterile alpha motif domains. **b**, Purified recombinant mCherry–SYD-2 constructs tested in an in vitro phase-separation assay. mCherry was fused to the N terminus of each sequence. **c**, Left panels in each column, example time-lapse analyses of in vitro condensates comprising the indicated SYD-2 constructs, showing the presence or absence of liquid fusion behaviour. Right panels, FRAP dynamics of each SYD-2 condensate. Data are means ± 95% CI for at least three condensates from two independent experiments. The y-axes show percentage intensity. Phase-separation assays were performed in 20 mM Tris pH 7.4, 150 mM NaCl with 10 µM protein. FRAP assays were performed on condensates formed in crowding conditions of 10% PEG, except in the case of the blue curves, where there was no crowding agent. Green or blue curves indicate a positive result (scored LLPS+) and black curves a negative result (scored LLPS−). Scale bars, 5 µm. [Source data](#)

## Extended Data Fig. 5 Structure–function analysis of ELKS-1 phase separation.

**a**, Diagram showing the structure of ELKS-1, including disordered regions and coiled-coils predicted by the indicated algorithms<sup>37,38,42</sup>. **b**, Purified recombinant mCherry–ELKS-1 constructs tested in an in vitro phase-separation assay. mCherry was fused to the N terminus of each sequence. **c**, Left panels in each column, example time-lapse analyses of in vitro condensates comprising the indicated ELKS-1 constructs, showing the presence or absence of liquid fusion behaviour. Right panels, FRAP dynamics for each ELKS-1 condensate. Data are means ± 95% CI, for at least three condensates from independent experiments. The y-axes show percentage intensity. Phase-separation assays were performed in 20 mM Tris pH 7.4, 150 mM NaCl with 10 µM protein. FRAP assays were performed on condensates formed in crowding conditions of 10% PEG, except in the case of the blue curves, where there was no crowding agent. Green or blue curves indicate a positive result (scored LLPS+) and black curves a negative result (scored LLPS−). Scale bars, 5 µm. [Source data](#)

## Extended Data Fig. 6 Phase-separation mutants of SYD-2 and ELKS-1 retain the ability to bind partners.

Shown are the results of yeast two-hybrid assays using the indicated bait and prey constructs. Protein–protein interactions are indicated by growth on –His/-Ade media.

## Extended Data Fig. 7 Phase separation of SYD-2 and ELKS-1 is required for the assembly of multiple presynaptic active-zone components.

**a–c**, Cell-specific endogenous markers of presynaptic active zones in GFP–SYD-2 (**a**), GFP–ELKS-1 (**b**) or GFP–SYD-2(IDRΔ) plus *elks-1*(LLPS−) (**c**) worms. **d**, Cell-specific endogenous markers of presynaptic active zones in *syd-2* and *elks-1* complete loss-of-function mutants. **e**, Quantified intensity of endogenous active-zone markers, as well as GFP–SYD-2 and GFP–ELKS, at HSN synapses in the indicated genotypes. Data are

means  $\pm$  95% CI from independent animals. Comparisons were made using one-way ANOVA and Dunnett's test. **f**, Expression of SNB-1 labelled with yellow fluorescent protein (YFP) from the *unc-86* promoter at HSN synapses and cell bodies<sup>43</sup>. **g**, Quantification of SNB-1–YFP at HSN synapses and cell bodies. Data are means  $\pm$  95% CI from independent animals. Comparisons were made using one-way ANOVA and Dunnett's test. **h**, Localization of endogenous GFP–SYD-2 or GFP–SYD-2(IDRΔ) in the indicated genetic backgrounds. **i**, Quantification of endogenous GFP–SYD-2 or GFP–SYD-2(IDRΔ) at HSN synapses in the indicated genetic backgrounds. Data are means  $\pm$  95% CI from independent animals; comparisons were made using one-way ANOVA and Dunnett's (versus wild type) or Tukey's (within genotypes) tests. Data for GFP–SYD-2, GFP–SYD-2(IDRΔ) and GFP–SYD-2; *elks-1(tm1233)* are from Extended Data Fig. 7e. Dotted outlines show synaptic regions. Scale bars, 5  $\mu\text{m}$ . [Source data](#)

### [Extended Data Fig. 8 Phase separation of SYD-2 and ELKS-1 is required for proper synaptic function.](#)

**a**, Left, the *C. elegans* egg-laying neuronal circuit<sup>44</sup>. The hermaphrodite-specific neuron (HSN) extends an axon across the vulval region, making specific synaptic contacts with vm1/2 vulval muscles and inhibitory VC4/5 motor neurons. Right, experimental setup. HSN is activated by channelrhodopsin ChR2 with blue light, while contraction of the vm2 muscle is measured with the  $\text{Ca}^{2+}$  sensor GCaMP5 (ref. <sup>21</sup>). **b**, Representative vulval-muscle  $\text{Ca}^{2+}$  traces, detected by GCaMP5, in the indicated genotypes. ‘–ATR’ conditions lacked the essential ChR2 cofactor all-*trans* retinol. **c**, Quantification of the  $\text{Ca}^{2+}$  spike frequency, measured using GCaMP5, in the indicated genotypes. Data are means  $\pm$  95% CI from independent animals, with comparisons made using one-way ANOVA and Dunnett's test. [Source data](#)

### [Extended Data Fig. 9 Presynaptic assembly phenotypes of syd-2\(IDRΔ\) mutants are rescued by certain exogenous phase-separation motifs only.](#)

**a**, Diagram showing the replacement constructs tested. **b**, Comparison of amino-acid complexity between SYD-2/ELKS-1 and FUS/hnRNPA2 LLPS motifs. **c**, Left, time-lapse analysis of in vitro condensates comprising rescue constructs, showing liquid behaviour. Right, FRAP dynamics of in vitro condensates comprising rescue constructs. Data are means  $\pm$  95% CI across two independent experiments. SAM domains were omitted in these constructs. Assays were performed in 20 mM Tris pH 7.4, 150 mM NaCl with 10  $\mu$ M protein. **d**, **e**, Cell-specific endogenous markers of presynaptic active zones (UNC-10, **d**) or synaptic vesicles (RAB-3, **e**) in the indicated GFP-SYD-2 alleles. Dotted boxes show synaptic regions. **f**, Quantified intensity of UNC-10 and RAB-3 at HSN synapses in the indicated genotypes. Data are means  $\pm$  95% CI from independent animals, with comparisons made using one-way ANOVA and Dunnett's (versus wild type) or Tukey's (IDR $\Delta$  versus IDR $\Delta$  + FUS) tests. Data for wild type, syd-2(IDR $\Delta$ ) and syd-2(IDR $\Delta$  + FUS) are from Fig. 3. **g**, Quantification of egg stages laid by animals of the indicated genotypes. The syd-2(IDR $\Delta$  + hnRNPA2 construct rescues egg laying only in the presence of mScarlet-I-FLPon-RAB-3, for unknown reasons. Data are means  $\pm$  95% CI from independent animals. Data for wild type, syd-2(IDR $\Delta$ ) and syd-2(IDR $\Delta$  + FUS) are from Fig. 3. Scale bars, 5  $\mu$ m. [Source data](#)

### Extended Data Fig. 10 Loss of liquidity of SYD-2 and ELKS-1 impairs the scaffolding of GIT-1.

**a**, Endogenous GFP-ELKS-1(LLPS-) at early (1.5-fold embryo) nerve-ring synapses. Insets show FRAP images of bleached synapses. Main scale bar, 5  $\mu$ m; inset scale bars, 1  $\mu$ m. **b**, Quantification of nerve-ring GFP-ELKS-1 FRAP dynamics. Data are means  $\pm$  95% CI across two independent experiments. Wild-type data are from Fig. 1. **c**, FRAP dynamics of in vitro condensates comprising SYD-2 and ELKS-1 fragments. Data are means  $\pm$  95% CI from two independent experiments. Phase-separation assays were performed in 20 mM Tris pH 7.4, 150 mM NaCl and 10% PEG 3350, with 10  $\mu$ M protein. Data for the '<5 min' curve are from Fig. 2. **d**, Diagram showing the in vitro scaffolding experiment. **e**, **f**, Left, fluorescence images of the indicated condensates. Right, linescans performed through the centre of each condensate. Scale bars, 5  $\mu$ m. **g**, Incorporation index ( $I_{inc}$ ) for GIT-1-Dylight633. Data are means  $\pm$  95% CI

from three independent experiments, with comparisons made using one-way ANOVA and Dunnett's test.

### **Extended Data Fig. 11 Timing of assembly of the presynaptic active zone in early nerve-ring synapses.**

Localization of endogenous GFP-tagged presynaptic active-zone components at sequential stages of embryo development. Each panel shows a maximum z projection of a separate embryo. Embryos are outlined in blue. A zy resliced projection through the nerve-ring region is shown to the right of each image. Red asterisks and arrowheads indicate visible localization to the nerve ring. Most puncta visible throughout the embryo are background autofluorescence, present even in untagged embryos (bottom). The timing of the emergence of fluorescence is stereotypical and was replicated in a second experiment. Scale bars, 10  $\mu$ m. [Source data](#)

## **Supplementary information**

### **Reporting Summary**

### **Supplementary Table**

Supplementary Table 1. *C. elegans* strains used in this study.

### **Supplementary Table**

Supplementary Table 2. Plasmids used in this study.

## **Source data**

### **Source Data Fig. 1**

### **Source Data Fig. 2**

### **Source Data Fig. 3**

[Source Data Fig. 4](#)

[Source Data Extended Data Fig. 1](#)

[Source Data Extended Data Fig. 2](#)

[Source Data Extended Data Fig. 4](#)

[Source Data Extended Data Fig. 5](#)

[Source Data Extended Data Fig. 7](#)

[Source Data Extended Data Fig. 8](#)

[Source Data Extended Data Fig. 9](#)

[Source Data Extended Data Fig. 11](#)

## Rights and permissions

[Reprints and Permissions](#)

## About this article



Check for  
updates

## Cite this article

McDonald, N.A., Fetter, R.D. & Shen, K. Assembly of synaptic active zones requires phase separation of scaffold molecules. *Nature* **588**, 454–458 (2020). <https://doi.org/10.1038/s41586-020-2942-0>

## Download citation

- Received: 07 April 2020
- Accepted: 03 September 2020
- Published: 18 November 2020
- Issue Date: 17 December 2020
- DOI: <https://doi.org/10.1038/s41586-020-2942-0>

## Comments

By submitting a comment you agree to abide by our [Terms](#) and [Community Guidelines](#). If you find something abusive or that does not comply with our terms or guidelines please flag it as inappropriate.

[Access through your institution](#)

[Change institution](#)

[Buy or subscribe](#)

---

This article was downloaded by **calibre** from <https://www.nature.com/articles/s41586-020-2942-0>

| [Section menu](#) | [Main menu](#) |

- Article
- [Published: 31 August 2020](#)

# Neurotoxic microglia promote TDP-43 proteinopathy in progranulin deficiency

- [Jiasheng Zhang<sup>1,2</sup>](#) na1,
- [Dmitry Velmeshev<sup>3</sup>](#) na1,
- [Kei Hashimoto<sup>1</sup>](#) na1,
- [Yu-Hsin Huang<sup>1</sup>](#) na1,
- [Jeffrey W. Hofmann<sup>1</sup>](#),
- [Xiaoyu Shi<sup>4,5</sup>](#),
- [Jiapei Chen<sup>1,6</sup>](#),
- [Andrew M. Leidal<sup>1</sup>](#),
- [Julian G. Dishart](#) [ORCID: orcid.org/0000-0003-0014-6141<sup>1</sup>](#),
- [Michelle K. Cahill<sup>7,8</sup>](#),
- [Kevin W. Kelley<sup>7,8</sup>](#),
- [Shane A. Liddelow<sup>9</sup>](#),
- [William W. Seeley<sup>7,8,10</sup>](#),
- [Bruce L. Miller<sup>10</sup>](#),
- [Tobias C. Walther](#) [ORCID: orcid.org/0000-0003-1442-1327<sup>11,12</sup>](#),
- [Robert V. Farese Jr<sup>11</sup>](#),
- [J. Paul Taylor<sup>13</sup>](#),
- [Erik M. Ullian<sup>14</sup>](#),
- [Bo Huang](#) [ORCID: orcid.org/0000-0003-1704-4141<sup>14,15,16</sup>](#),
- [Jayanta Debnath](#) [ORCID: orcid.org/0000-0002-8745-4069<sup>1,6</sup>](#),
- [Torsten Wittmann](#) [ORCID: orcid.org/0000-0001-9134-691X<sup>6,17</sup>](#),
- [Arnold R. Kriegstein](#) [ORCID: orcid.org/0000-0001-5742-2990<sup>3,6,7</sup>](#) &
- [Eric J. Huang](#) [ORCID: orcid.org/0000-0002-5381-3801<sup>1,2,6,7,8</sup>](#)

- 11k Accesses
- 65 Altmetric
- [Metrics details](#)

## Subjects

- [Microglia](#)
- [Neurodegeneration](#)

## Abstract

Aberrant aggregation of the RNA-binding protein TDP-43 in neurons is a hallmark of frontotemporal lobar degeneration caused by haploinsufficiency in the gene encoding progranulin<sup>1,2</sup>. However, the mechanism leading to TDP-43 proteinopathy remains unclear. Here we use single-nucleus RNA sequencing to show that progranulin deficiency promotes microglial transition from a homeostatic to a disease-specific state that causes endolysosomal dysfunction and neurodegeneration in mice. These defects persist even when *Grn*<sup>-/-</sup> microglia are cultured ex vivo. In addition, single-nucleus RNA sequencing reveals selective loss of excitatory neurons at disease end-stage, which is characterized by prominent nuclear and cytoplasmic TDP-43 granules and nuclear pore defects. Remarkably, conditioned media from *Grn*<sup>-/-</sup> microglia are sufficient to promote TDP-43 granule formation, nuclear pore defects and cell death in excitatory neurons via the complement activation pathway. Consistent with these results, deletion of the genes encoding C1qa and C3 mitigates microglial toxicity and rescues TDP-43 proteinopathy and neurodegeneration. These results uncover previously unappreciated contributions of chronic microglial toxicity to TDP-43 proteinopathy during neurodegeneration.

[Access through your institution](#)

[Change institution](#)

[Buy or subscribe](#)

## Access options

Subscribe to Journal

Get full journal access for 1 year

185,98 €

only 3,58 € per issue

[Subscribe](#)

All prices are NET prices.

VAT will be added later in the checkout.

Rent or Buy article

Get time limited or full article access on ReadCube.

from \$8.99

[Rent or Buy](#)

All prices are NET prices.

### Additional access options:

- [Log in](#)
- [Access through your institution](#)
- [Learn about institutional subscriptions](#)

**Fig. 1: snRNA-seq reveals age-dependent microglial pathology and neuronal vulnerability in the thalamus of *Grn*<sup>-/-</sup> mice.**



**Fig. 2: TDP-43 proteinopathy and nuclear pore defects in  $Grn^{-/-}$  thalamic neurons.**



**Fig. 3: Progranulin-deficient microglia promote TDP-43 proteinopathy in  $Grn^{-/-}$  neurons.**



**Fig. 4: Complements C1q and C3b promote TDP-43 granule formation and neurodegeneration in *Grn*<sup>-/-</sup> mice.**



## Data availability

The raw snRNA-seq and scRNA-seq data have been deposited to the Sequence Read Archive under accession no. [PRJNA507872](#) and no. [PRJNA614533](#), respectively. The data that support the findings of this study are included in the manuscript. Source data are provided for Figs. [1–4](#) and Extended Data Figs. [1–11](#).

## References

1. 1.

Hofmann, J. W., Seeley, W. W. & Huang, E. J. RNA binding proteins and the pathogenesis of frontotemporal lobar degeneration. *Annu. Rev. Pathol.* **14**, 469–495 (2019).

[CAS](#) [PubMed](#) [Google Scholar](#)

2. 2.

Mackenzie, I. R. et al. A harmonized classification system for FTLD-TDP pathology. *Acta Neuropathol.* **122**, 111–113 (2011).

[PubMed](#) [PubMed Central](#) [Google Scholar](#)

3. 3.

Baker, M. et al. Mutations in progranulin cause tau-negative frontotemporal dementia linked to chromosome 17. *Nature* **442**, 916–919 (2006).

[ADS](#) [CAS](#) [PubMed](#) [Google Scholar](#)

4. 4.

Cruts, M. et al. Null mutations in progranulin cause ubiquitin-positive frontotemporal dementia linked to chromosome 17q21. *Nature* **442**, 920–924 (2006).

[ADS](#) [CAS](#) [PubMed](#) [Google Scholar](#)

5. 5.

Kao, A. W., McKay, A., Singh, P. P., Brunet, A. & Huang, E. J. Progranulin, lysosomal regulation and neurodegenerative disease. *Nat. Rev. Neurosci.* **18**, 325–333 (2017).

[CAS](#) [PubMed](#) [PubMed Central](#) [Google Scholar](#)

6. 6.

Lui, H. et al. Progranulin deficiency promotes circuit-specific synaptic pruning by microglia via complement activation. *Cell* **165**, 921–935 (2016).

[CAS](#) [PubMed](#) [PubMed Central](#) [Google Scholar](#)

7. 7.

Chang, M. C. et al. Programulin deficiency causes impairment of autophagy and TDP-43 accumulation. *J. Exp. Med.* **214**, 2611–2628 (2017).

[CAS](#) [PubMed](#) [PubMed Central](#) [Google Scholar](#)

8. 8.

Ward, M. E. et al. Individuals with programulin haploinsufficiency exhibit features of neuronal ceroid lipofuscinosis. *Sci. Transl. Med.* **9**, eaah5642 (2017).

[PubMed](#) [PubMed Central](#) [Google Scholar](#)

9. 9.

Laferrière, F. et al. TDP-43 extracted from frontotemporal lobar degeneration subject brains displays distinct aggregate assemblies and neurotoxic effects reflecting disease progression rates. *Nat. Neurosci.* **22**, 65–77 (2019).

[PubMed](#) [Google Scholar](#)

10. 10.

Habib, N. et al. Div-seq: single-nucleus RNA-seq reveals dynamics of rare adult newborn neurons. *Science* **353**, 925–928 (2016).

[ADS](#) [CAS](#) [PubMed](#) [PubMed Central](#) [Google Scholar](#)

11. 11.

Lake, B. B. et al. Neuronal subtypes and diversity revealed by single-nucleus RNA sequencing of the human brain. *Science* **352**, 1586–1590 (2016).

[ADS](#) [CAS](#) [PubMed](#) [PubMed Central](#) [Google Scholar](#)

12. 12.

Hammond, T. R. et al. Single-cell RNA sequencing of microglia throughout the mouse lifespan and in the injured brain reveals complex cell-state changes. *Immunity* **50**, 253–271.e6 (2019).

[CAS](#) [PubMed](#) [PubMed Central](#) [Google Scholar](#)

13. 13.

Ximerakis, M. et al. Single-cell transcriptomic profiling of the aging mouse brain. *Nat. Neurosci.* **22**, 1696–1708 (2019).

[CAS](#) [PubMed](#) [Google Scholar](#)

14. 14.

Cao, J. et al. Comprehensive single-cell transcriptional profiling of a multicellular organism. *Science* **357**, 661–667 (2017).

[ADS](#) [CAS](#) [PubMed](#) [PubMed Central](#) [Google Scholar](#)

15. 15.

Qiu, X. et al. Reversed graph embedding resolves complex single-cell trajectories. *Nat. Methods* **14**, 979–982 (2017).

[CAS](#) [PubMed](#) [PubMed Central](#) [Google Scholar](#)

16. 16.

Matcovitch-Natan, O. et al. Microglia development follows a stepwise program to regulate brain homeostasis. *Science* **353**, aad8670 (2016).

[PubMed](#) [Google Scholar](#)

17. 17.

Keren-Shaul, H. et al. A unique microglia type associated with restricting development of Alzheimer’s disease. *Cell* **169**, 1276–1290.e17 (2017).

[CAS](#) [PubMed](#) [Google Scholar](#)

18. 18.

Kao, P. F. et al. Detection of TDP-43 oligomers in frontotemporal lobar degeneration-TDP. *Ann. Neurol.* **78**, 211–221 (2015).

[CAS](#) [PubMed](#) [PubMed Central](#) [Google Scholar](#)

19. 19.

Griffis, E. R., Xu, S. & Powers, M. A. Nup98 localizes to both nuclear and cytoplasmic sides of the nuclear pore and binds to two distinct nucleoporin subcomplexes. *Mol. Biol. Cell* **14**, 600–610 (2003).

[CAS](#) [PubMed](#) [PubMed Central](#) [Google Scholar](#)

20. 20.

McGurk, L. et al. Poly(ADP-ribose) prevents pathological phase separation of TDP-43 by promoting liquid demixing and stress granule localization. *Mol. Cell* **71**, 703–717.e9 (2018).

[CAS](#) [PubMed](#) [PubMed Central](#) [Google Scholar](#)

21. 21.

Gasset-Rosa, F. et al. Cytoplasmic TDP-43 de-mixing independent of stress granules drives inhibition of nuclear import, loss of nuclear TDP-43, and cell death. *Neuron* **102**, 339–357.e7 (2019).

[CAS](#) [PubMed](#) [PubMed Central](#) [Google Scholar](#)

22. 22.

Mann, J. R. et al. RNA binding antagonizes neurotoxic phase transitions of TDP-43. *Neuron* **102**, 321–338.e8 (2019).

[CAS](#) [PubMed](#) [PubMed Central](#) [Google Scholar](#)

23. 23.

Liszewski, M. K. et al. Intracellular complement activation sustains T cell homeostasis and mediates effector differentiation. *Immunity* **39**, 1143–1157 (2013).

[CAS](#) [PubMed](#) [PubMed Central](#) [Google Scholar](#)

24. 24.

West, E. E., Afzali, B. & Kemper, C. Unexpected roles for intracellular complement in the regulation of Th1 responses. *Adv. Immunol.* **138**, 35–70 (2018).

[CAS](#) [PubMed](#) [Google Scholar](#)

25. 25.

Liu, G. et al. Endocytosis regulates TDP-43 toxicity and turnover. *Nat. Commun.* **8**, 2092 (2017).

[ADS](#) [PubMed](#) [PubMed Central](#) [Google Scholar](#)

26. 26.

Moisse, K. et al. Divergent patterns of cytosolic TDP-43 and neuronal progranulin expression following axotomy: implications for TDP-43 in the physiological response to neuronal injury. *Brain Res.* **1249**, 202–211 (2009).

[CAS](#) [PubMed](#) [Google Scholar](#)

27. 27.

Wiesner, D. et al. Reversible induction of TDP-43 granules in cortical neurons after traumatic injury. *Exp. Neurol.* **299**, 15–25 (2018).

[CAS](#) [PubMed](#) [Google Scholar](#)

28. 28.

Vogler, T. O. et al. TDP-43 and RNA form amyloid-like myo-granules in regenerating muscle. *Nature* **563**, 508–513 (2018).

[ADS](#) [CAS](#) [PubMed](#) [PubMed Central](#) [Google Scholar](#)

29. 29.

Martens, L. H. et al. Progranulin deficiency promotes neuroinflammation and neuron loss following toxin-induced injury. *J. Clin. Invest.* **122**, 3955–3959 (2012).

[CAS](#) [PubMed](#) [PubMed Central](#) [Google Scholar](#)

30. 30.

Nguyen, A. D. et al. Murine knockin model for progranulin-deficient frontotemporal dementia with nonsense-mediated mRNA decay. *Proc. Natl Acad. Sci. USA* **115**, E2849–E2858 (2018).

[CAS](#) [PubMed](#) [Google Scholar](#)

31. 31.

Botto, M. et al. Homozygous C1q deficiency causes glomerulonephritis associated with multiple apoptotic bodies. *Nat. Genet.* **19**, 56–59 (1998).

[CAS](#) [PubMed](#) [Google Scholar](#)

32. 32.

Bhaduri, A., Nowakowski, T. J., Pollen, A. A. & Kriegstein, A. R. Identification of cell types in a mouse brain single-cell atlas using low sampling coverage. *BMC Biol.* **16**, 113 (2018).

[CAS](#) [PubMed](#) [PubMed Central](#) [Google Scholar](#)

33. 33.

Finak, G. et al. MAST: a flexible statistical framework for assessing transcriptional changes and characterizing heterogeneity in single-cell RNA sequencing data. *Genome Biol.* **16**, 278 (2015).

[PubMed](#) [PubMed Central](#) [Google Scholar](#)

34. 34.

Crowell, H. L. et al. On the discovery of subpopulation-specific state transitions from multi-sample multi-condition single-cell RNA sequencing data. Preprint at *bioRxiv* <https://doi.org/10.1101/713412> (2020).

35. 35.

McCarthy, D. J., Chen, Y. & Smyth, G. K. Differential expression analysis of multifactor RNA-seq experiments with respect to biological variation. *Nucleic Acids Res.* **40**, 4288–4297 (2012).

[CAS](#) [PubMed](#) [PubMed Central](#) [Google Scholar](#)

36. 36.

Mi, H., Muruganujan, A. & Thomas, P. D. PANTHER in 2013: modeling the evolution of gene function, and other gene attributes, in the context of phylogenetic trees. *Nucleic Acids Res.* **41**, D377–D386 (2013).

[CAS](#) [PubMed](#) [Google Scholar](#)

37. 37.

Thomas, P. D. et al. PANTHER: a library of protein families and subfamilies indexed by function. *Genome Res.* **13**, 2129–2141 (2003).

[CAS](#) [PubMed](#) [PubMed Central](#) [Google Scholar](#)

38. 38.

Zhou, Y. et al. Metascape provides a biologist-oriented resource for the analysis of systems-level datasets. *Nat. Commun.* **10**, 1523 (2019).

[ADS](#) [PubMed](#) [PubMed Central](#) [Google Scholar](#)

39. 39.

Stuart, T. et al. Comprehensive integration of single-cell data. *Cell* **177**, 1888–1902.e21 (2019).

[CAS](#) [PubMed](#) [PubMed Central](#) [Google Scholar](#)

40. 40.

Cao, J. et al. The single-cell transcriptional landscape of mammalian organogenesis. *Nature* **566**, 496–502 (2019).

[ADS](#) [CAS](#) [PubMed](#) [PubMed Central](#) [Google Scholar](#)

41. 41.

Huang, E. J. et al. Targeted deletion of numb and numblike in sensory neurons reveals their essential functions in axon arborization. *Genes Dev.* **19**, 138–151 (2005).

[CAS](#) [PubMed](#) [PubMed Central](#) [Google Scholar](#)

42. 42.

Bohlen, C. J. et al. Diverse requirements for microglial survival, specification, and function revealed by defined-medium cultures. *Neuron* **94**, 759–773.e8 (2017).

[CAS](#) [PubMed](#) [PubMed Central](#) [Google Scholar](#)

43. 43.

Lee, S. et al. Activation of HIPK2 promotes ER stress-mediated neurodegeneration in amyotrophic lateral sclerosis. *Neuron* **91**, 41–55 (2016).

[CAS](#) [PubMed](#) [PubMed Central](#) [Google Scholar](#)

44. 44.

Shang, Y., Zhang, J. & Huang, E. J. HIPK2-mediated transcriptional control of NMDA receptor subunit expression regulates neuronal survival and cell death. *J. Neurosci.* **38**, 4006–4019 (2018).

[CAS](#) [PubMed](#) [PubMed Central](#) [Google Scholar](#)

45. 45.

Spiegel, I. et al. Npas4 regulates excitatory–inhibitory balance within neural circuits through cell-type-specific gene programs. *Cell* **157**, 1216–1229 (2014).

[CAS](#) [PubMed](#) [PubMed Central](#) [Google Scholar](#)

46. 46.

Alami, N. H. et al. Axonal transport of TDP-43 mRNA granules is impaired by ALS-causing mutations. *Neuron* **81**, 536–543 (2014).

[CAS](#) [PubMed](#) [PubMed Central](#) [Google Scholar](#)

47. 47.

Stehbens, S., Pemble, H., Murrow, L. & Wittmann, T. Imaging intracellular protein dynamics by spinning disk confocal microscopy. *Methods Enzymol.* **504**, 293–313 (2012).

[CAS](#) [PubMed](#) [PubMed Central](#) [Google Scholar](#)

48. 48.

Schermelleh, L. et al. Subdiffraction multicolor imaging of the nuclear periphery with 3D structured illumination microscopy. *Science* **320**, 1332–1336 (2008).

[ADS](#) [CAS](#) [PubMed](#) [PubMed Central](#) [Google Scholar](#)

49. 49.

Zhang, J. et al. Essential function of HIPK2 in TGF $\beta$ -dependent survival of midbrain dopamine neurons. *Nat. Neurosci.* **10**, 77–86 (2007).

[CAS](#) [PubMed](#) [Google Scholar](#)

50. 50.

Martin, S. et al. Deficiency of G3BP1, the stress granules assembly factor, results in abnormal synaptic plasticity and calcium homeostasis in neurons. *J. Neurochem.* **125**, 175–184 (2013).

[CAS](#) [PubMed](#) [Google Scholar](#)

51. 51.

Sahoo, P. K. et al. Axonal G3BP1 stress granule protein limits axonal mRNA translation and nerve regeneration. *Nat. Commun.* **9**, 3358 (2018).

[ADS](#) [PubMed](#) [PubMed Central](#) [Google Scholar](#)

[Download references](#)

## Acknowledgements

This work has been supported by grants from the US National Institutes of Health (R01 AA027074 to E.J.H. and A.R.K., R01 AG057462 to E.J.H. and J.D., R01 AG068290 to E.J.H., U01 MH105989 to A.R.K. and E.J.H., K99 MH121534 to D.V., K99 GM126136 to X.S., R01 GM124334 to B.H., R01

NS107480 to T.W. and S10 RR026758 to T.W.), the Department of Veterans Affairs (I01 BX002978 to E.J.H.), The Bluefield Project to Cure FTD (to W.W.S., B.L.M., T.C.W., R.V.F. and E.J.H.), NSF Graduate Research Fellowship (to M.K.C.), AHA Predoctoral Fellowship 19PRE3480616 and UCSF Discovery Fellowship (to J.C.), Banting Postdoctoral Fellowship from the Government of Canada 201409BPF-335868 (to A.M.L.), the Glenn Foundation and the Cure Alzheimer's Fund (to S.A.L.), and the Japan Society for the Promotion of Science and Ochanomizu University Scholarship (to K.H.). T.C.W. and J.P.T. are Howard Hughes Medical Institute (HHMI) Investigators, and B.H. is a Chan Zuckerberg Biohub Investigator. S.A.L. thanks anonymous donors for their support. We thank I. Hsieh for IEM, Y. Chen for mouse husbandry and histopathology, UCSF Nikon Imaging Center for 3D structured illumination microscopy, A. Alvarez-Buylla for many helpful advice, and L. Mitic and R. Pearlman for their support.

## Author information

### Author notes

1. These authors contributed equally: Jiasheng Zhang, Dmitry Velmeshev, Kei Hashimoto, Yu-Hsin Huang

## Affiliations

1. Department of Pathology, University of California San Francisco, San Francisco, CA, USA

Jiasheng Zhang, Kei Hashimoto, Yu-Hsin Huang, Jeffrey W. Hofmann, Jiapei Chen, Andrew M. Leidal, Julian G. Dishart, Jayanta Debnath & Eric J. Huang

2. Pathology Service 113B, San Francisco VA Health Care System, San Francisco, CA, USA

Jiasheng Zhang & Eric J. Huang

3. Eli and Edythe Broad Center of Regeneration Medicine and Stem Cell Research, University of California San Francisco, San Francisco, CA, USA

Dmitry Velmeshev & Arnold R. Kriegstein

4. Department of Pharmaceutical Chemistry, University of California San Francisco, San Francisco, CA, USA

Xiaoyu Shi & Bo Huang

5. Department of Developmental and Cell Biology, University of California Irvine, Irvine, CA, USA

Xiaoyu Shi

6. Biomedical Sciences Graduate Program, University of California San Francisco, San Francisco, CA, USA

Jiapei Chen, Jayanta Debnath, Torsten Wittmann, Arnold R. Kriegstein & Eric J. Huang

7. Neuroscience Graduate Program, University of California San Francisco, San Francisco, CA, USA

Michelle K. Cahill, Kevin W. Kelley, William W. Seeley, Arnold R. Kriegstein & Eric J. Huang

8. Weill Institute for Neurosciences, University of California San Francisco, San Francisco, CA, USA

Michelle K. Cahill, Kevin W. Kelley, William W. Seeley & Eric J. Huang

9. Neuroscience Institute, Department of Neuroscience & Physiology, NYU Langone Medical Center, New York, NY, USA

Shane A. Liddelow

10. Department of Neurology, Memory and Aging Center, University of California San Francisco, San Francisco, CA, USA

William W. Seeley & Bruce L. Miller

11. Department of Genetics and Complex Diseases, T.H. Chan School of Public Health, Harvard University, Boston, MA, USA

Tobias C. Walther & Robert V. Farese Jr

12. Howard Hughes Medical Institute, Boston, MA, USA

Tobias C. Walther

13. Department of Cell and Molecular Biology, St Jude Children's Hospital & Howard Hughes Medical Institute, Memphis, TN, USA

J. Paul Taylor

14. Department of Ophthalmology, University of California San Francisco, San Francisco, CA, USA

Erik M. Ullian

15. Department of Biochemistry and Biophysics, University of California San Francisco, San Francisco, CA, USA

Bo Huang

16. Chan Zuckerberg Biohub, San Francisco, CA, USA

Bo Huang

17. Department of Cell and Tissue Biology, University of California San Francisco, San Francisco, CA, USA

Torsten Wittmann

Authors

1. Jiasheng Zhang  
[View author publications](#)

You can also search for this author in [PubMed](#) [Google Scholar](#)

2. Dmitry Velmeshev  
[View author publications](#)

You can also search for this author in [PubMed](#) [Google Scholar](#)

3. Kei Hashimoto  
[View author publications](#)

You can also search for this author in [PubMed](#) [Google Scholar](#)

4. Yu-Hsin Huang  
[View author publications](#)

You can also search for this author in [PubMed](#) [Google Scholar](#)

5. Jeffrey W. Hofmann  
[View author publications](#)

You can also search for this author in [PubMed](#) [Google Scholar](#)

6. Xiaoyu Shi  
[View author publications](#)

You can also search for this author in [PubMed](#) [Google Scholar](#)

7. Jiapei Chen  
[View author publications](#)

You can also search for this author in [PubMed](#) [Google Scholar](#)

8. Andrew M. Leidal  
[View author publications](#)

You can also search for this author in [PubMed](#) [Google Scholar](#)

9. Julian G. Dishart

[View author publications](#)

You can also search for this author in [PubMed](#) [Google Scholar](#)

10. Michelle K. Cahill

[View author publications](#)

You can also search for this author in [PubMed](#) [Google Scholar](#)

11. Kevin W. Kelley

[View author publications](#)

You can also search for this author in [PubMed](#) [Google Scholar](#)

12. Shane A. Liddelow

[View author publications](#)

You can also search for this author in [PubMed](#) [Google Scholar](#)

13. William W. Seeley

[View author publications](#)

You can also search for this author in [PubMed](#) [Google Scholar](#)

14. Bruce L. Miller

[View author publications](#)

You can also search for this author in [PubMed](#) [Google Scholar](#)

15. Tobias C. Walther

[View author publications](#)

You can also search for this author in [PubMed](#) [Google Scholar](#)

16. Robert V. Farese Jr

[View author publications](#)

You can also search for this author in [PubMed](#) [Google Scholar](#)

17. J. Paul Taylor

[View author publications](#)

You can also search for this author in [PubMed](#) [Google Scholar](#)

18. Erik M. Ullian

[View author publications](#)

You can also search for this author in [PubMed](#) [Google Scholar](#)

19. Bo Huang

[View author publications](#)

You can also search for this author in [PubMed](#) [Google Scholar](#)

20. Jayanta Debnath

[View author publications](#)

You can also search for this author in [PubMed](#) [Google Scholar](#)

21. Torsten Wittmann

[View author publications](#)

You can also search for this author in [PubMed](#) [Google Scholar](#)

22. Arnold R. Kriegstein

[View author publications](#)

You can also search for this author in [PubMed](#) [Google Scholar](#)

23. Eric J. Huang

[View author publications](#)

You can also search for this author in [PubMed](#) [Google Scholar](#)

## Contributions

J.Z., D.V., K.H., Y.-H.H., A.R.K. and E.J.H. conceived the project, designed the experiments and wrote the paper. D.V., J.Z. and K.H. performed single-

cell transcriptomics and related work. D.V. performed the bioinformatics analyses. K.H. performed the NanoString nCounter work. J.Z., K.H., Y.-H.H., J.W.H., M.K.C., A.M.L. and J.G.D. performed in vitro cultures, immunohistochemistry and quantifications for cell death, TDP-43 granules and nuclear pore defects. J.Z. performed stereology-based quantifications. A.M.L., E.M.U. and J.D. provided expertise related to stress granule and endolysosomal phenotypes. K.W.K., W.W.S., B.L.M., T.C.W. and R.V.F. contributed expertise, reagents and analyses related to *Grn* mouse models. X.S., J.W.H., J.C. and B.H. provided assistance with 3D structured illumination microscopy. J.P.T. and T.W. provided reagents and assisted with mCherry–TDP-43 live imaging. S.A.L. provided expertise in glial gene expression. All authors reviewed and edited the manuscript.

## Corresponding author

Correspondence to [Eric J. Huang](#).

## Ethics declarations

## Competing interests

The authors declare no competing interests.

## Additional information

**Peer review information** *Nature* thanks the anonymous reviewers for their contribution to the peer review of this work.

**Publisher's note** Springer Nature remains neutral with regard to jurisdictional claims in published maps and institutional affiliations.

## Extended data figures and tables

[Extended Data Fig. 1 snRNA-seq analysis of age-dependent transcriptomic changes in the thalamus of \*Grn\*<sup>-/-</sup> mice.](#)

**a**, Unbiased clustering of snRNA-seq data from the thalamus of 2, 4, 7, 12 and 19 months old *Grn*<sup>+/+</sup> and *Grn*<sup>-/-</sup> mice identify 16 different cell types. The table outlines the number and age of *Grn*<sup>+/+</sup> and *Grn*<sup>-/-</sup> mice used for microdissecting thalamus for snRNA-seq. Two samples, #1 in 2 months old *Grn*<sup>+/+</sup> and #4 in 19 months old *Grn*<sup>-/-</sup>, are excluded due to suboptimal RNA quality. **b, c**, Subtype-specific markers for microglia (*P2ry12*), astrocytes (*Aqp4* and *Gfap*), oligodendroglial precursor cells (OPC) (*Pdgfra*), endothelial cells (*Cldn5*), synaptic marker (*Syt1*), excitatory neurons (*Cux2* and *Satb2*), oligodendroglia (*Plp1*) and inhibitory neurons (*Gad2*, *Sst* and *Reln*). **c**, Individual contribution to different cell clusters from each sample. **d**, Venn diagram shows the overlap of gene expression between cluster 11 and astrocyte and oligodendroglia clusters. These results indicate that cluster 11 contains mixed identity. **e**, Violin plots demonstrate that cells in cluster 11 express markers of myelinating oligodendroglia (*Mog*, *Mag*, *Mbp* and *Plp1*) and astrocytes (*Slc1a2*, *Gja1*, *Nfia* and *Gpc5*). Although cells in cluster 11 express a low level of the neuronal marker *Syt1*, they express very low levels of other neuronal markers, for example, *Rbfox3*, *Gad1* and *Gad2*. **f**, Violin plots that show the cumulative *Grn* mRNA expression from 2 to 19 months in microglia (MG, c4), astrocytes (AST, c7), excitatory neurons (ExNeu, c3, c12, c13), inhibitory neurons (InNeu, c6, c9) and endothelial cells (END, c8). Statistical comparisons using MAST reveal that *Grn* mRNA expression MG is consistently higher than other cell clusters with the following *P* values: MG vs AST:  $2.53 \times 10^{-40}$ , MG vs ExNeu:  $1.15 \times 10^{-8}$ , MG vs InNeu:  $8.79 \times 10^{-17}$  and MG vs END:  $1.45 \times 10^{-17}$ . In addition, comparisons between ExNeu and other cell clusters show the following *P* values: ExNeu vs AST:  $8.46 \times 10^{-75}$ , ExNeu vs InNeu:  $5.57 \times 10^{-13}$  and ExNeu vs END:  $1.38 \times 10^{-09}$ . **g, h**, Normalized cell counts for inhibitory neurons (c6, c9) and astrocytes (c7) in the *Grn*<sup>+/+</sup> and *Grn*<sup>-/-</sup> thalamus. Data represent mean  $\pm$  s.e.m. Statistics use two-tailed, unpaired Student's *t*-test. **i**, Gene burden analysis for glia and neuronal clusters in *Grn*<sup>+/+</sup> and *Grn*<sup>-/-</sup> thalamus at 12 months old. These analyses calculate the number of genes differentially expressed in each cluster in the *Grn*<sup>-/-</sup> thalamus after normalizing the number of nuclei in each cluster. Box plots show the median and 25-75th percentiles. Statistics were performed using Mann-Whitney *U*-test.

## Extended Data Fig. 2 Age-dependent changes in the transcriptomes and subclustering of microglia in the *Grn*<sup>+/+</sup> and *Grn*<sup>-/-</sup> thalamus.

**a**, Heatmap of differentially expressed genes in *Grn*<sup>-/-</sup> thalamic microglia show progressive transcriptomic changes from 7, 12 to 19 months. **b, c**, Pseudotime analyses of snRNA-seq data reveal modest transition of trajectory and subclusters in *Grn*<sup>+/+</sup> thalamic microglia from 2 to 19 months. By contrast, *Grn*<sup>-/-</sup> microglia exhibit drastic changes in trajectory and subcluster distribution, especially at 12 and 19 months. The small clusters towards the right of UMAP graphs in *Grn*<sup>+/+</sup> and *Grn*<sup>-/-</sup> Th-MG most likely represent a small number of microglia-related cells, such as macrophages, or other unidentified cell types. The presence of this very small cluster does not contribute to the pseudotime results for *Grn*<sup>+/+</sup> or *Grn*<sup>-/-</sup> Th-MG. **d, e**, Combined pseudotime analyses show age-dependent downregulation of homeostasis genes, *P2ry12* and *Tmem119*, and upregulation of genes associated with microglial activation, including *Apoe* and *Ctsb*, in *Grn*<sup>-/-</sup> microglia. **f**, Volcano plot showing persistent upregulated or downregulated genes in *Grn*<sup>-/-</sup> microglia from 7 to 19 months. Most differentially expressed genes (DEGs) in *Grn*<sup>-/-</sup> microglia are detected at 7 and 19 months (dark red), 12 and 19 months (light blue), or 7, 12 and 19 months (beige), whereas a smaller number of DEGs are detected only in 7 months (green), 12 months (red) or 19 months (dark blue). Statistics for DEGs in the volcano plot use MAST. See Methods for details of the “Meta Cell” pseudobulk approach to generate the volcano plot. **g**, Venn diagram showing a progressive increase in DEGs in *Grn*<sup>-/-</sup> Th-MG from 7, 12 to 19 months. **h**, Venn diagrams showing limited overlap of DEGs in 19 months *Grn*<sup>-/-</sup> Th-MG and AD DAM genes, and 19 months *Grn*<sup>-/-</sup> Th-MG and ALS DAM genes. Statistics use hypergeometric test. **i**, Metascape interacting map of GO terms of the 32 genes shared by 19 months *Grn*<sup>-/-</sup> Th-MG and AD DAM.

## Extended Data Fig. 3 Immunohistochemical validations of DEGs in the thalamus of *Grn*<sup>-/-</sup> mice.

**a, b**, Validations using immunohistochemistry and confocal microscopy confirm the downregulation of P2Y12 and Tmem119 in *Grn*<sup>-/-</sup> thalamic microglia at 12 and 19 months, respectively (panel **a**). By contrast, *Grn*<sup>-/-</sup> thalamic microglia show marked increases in ApoE and Adam33 protein detected by immunohistochemical staining and confocal microscopy (panel **b**). Insets are high magnification images from the boxed areas in the ventral thalamus. Confocal images on the right panels are obtained from 12 months old *Grn*<sup>+/+</sup> and *Grn*<sup>-/-</sup> thalamus. Immunohistochemistry was performed in 3 independent mice per genotype, whereas the confocal images were from two independent mice. **c**, Confocal images showing upregulated expression of Cathepsin B, IGF-1 and GPNMB in 12 months old *Grn*<sup>-/-</sup> thalamic microglia. By contrast, *Grn*<sup>-/-</sup> thalamic microglia show reduced expression of Numb. The validations were performed in  $N = 3$  independent mice per genotype with similar results. **d**, A proposed model showing the age-dependent transition of *Grn*<sup>-/-</sup> thalamic microglia from a homeostatic state to disease state from 7 to 19 months. The defects in *Grn*<sup>-/-</sup> microglia downregulate homeostatic genes (*C1qa*, *C1qb*, *Mef2c*, *Csf1r*, *Cx3cr1*, *Tgfb1*, *Tmem119*, *Adam33*, *Igf1* and *P2ry12*), and upregulate genes related to lysosomal functions (*Ctsb*), lipid transport (*Apoe*), intracellular trafficking (*Myo1f*, *Myo5a* and *Numb*) and signal pathways (*Arhgap24* and *Dock3*).

#### Extended Data Fig. 4 snRNA-seq analysis of excitatory neuron clusters in the thalamus of *Grn*<sup>+/+</sup> and *Grn*<sup>-/-</sup> mice.

**a–c**, snRNA-seq identifies three distinct clusters of excitatory neurons based on the combined expression of *Ttr* (*Transthyretin*), *Pde4d* (*Phosphodiesterase 4D*) and *Cntnap2* (*Contactin associated protein like 2*) in cluster 3, *Prkcd* (*Protein kinase C Delta*), *Shisa6* (*Shisa family member 6*) and *Pleckhg1* (*Pleckstrin homology and RhoGEF domain containing G1*) in cluster 12, and *Cntn5* (*Contactin 5*), *Foxp2* (*Forkhead Box P2*) and *Nxph1* (*Neurexophilin 1*) in cluster 13. **d**, Heatmaps of cluster 3 and cluster 13 show no definitive age-dependent changes in the transcriptomes. **e**, Comparison of excitatory neuron subtypes in 19 months old *Grn*<sup>+/+</sup> and *Grn*<sup>-/-</sup> thalamus using immunohistochemical stains for PKC $\delta$  (upper panels) and Foxp2 (lower panels) reveals loss of PKC $\delta$ + and Foxp2+

neurons, most prominently affecting neurons in the ventral posterolateral (VPL) and ventral posteromedial (VPM) nuclei of the thalamus. **f**, Stereology quantification of PKC $\delta$ <sup>+</sup> and Foxp2<sup>+</sup> neurons in the ventral thalamus of *Grn*<sup>+/+</sup> and *Grn*<sup>-/-</sup> mice at 7, 12 and 19 months old. Data represent mean  $\pm$  s.e.m., and the number of mice for each age and genotype is indicated at the bottom of each data set. Statistics uses two-tailed, unpaired Student's *t*-test. ns, not significant.

**Extended Data Fig. 5 Characterization of P3 primary microglia from *Grn*<sup>+/+</sup> and *Grn*<sup>-/-</sup> mice using scRNA-seq, NanoString nCounter neuroinflammation panel and western blots.**

**a**, A schematic diagram illustrating the study design to characterize primary microglia from postnatal day 3 (P3) *Grn*<sup>+/+</sup> and *Grn*<sup>-/-</sup> mice using scRNA-seq and NanoString nCounter neuroinflammation panel, and to prepare serum-free conditioned media from *Grn*<sup>+/+</sup> and *Grn*<sup>-/-</sup> P3-MG. In parallel, primary cortical neurons and GABAergic inhibitory neurons are isolated from the developing cortex and ganglionic eminences of embryonic day 15.5 (E15.5) *Grn*<sup>+/+</sup> and *Grn*<sup>-/-</sup> mice. After 14 days in vitro (DIV), *Grn*<sup>+/+</sup> and *Grn*<sup>-/-</sup> microglial conditioned media (MCM) are added to *Grn*<sup>+/+</sup> and *Grn*<sup>-/-</sup> excitatory neurons or GABAergic inhibitory neurons and incubate for 24 h. **b**, *t*-SNE plots of scRNA-seq data from *Grn*<sup>+/+</sup> and *Grn*<sup>-/-</sup> P3-MG revealed 4 distinct clusters and the extent of overlapping in cell density and cluster distribution between *Grn*<sup>+/+</sup> and *Grn*<sup>-/-</sup> P3-MG. **c**, Comparison of cluster A of P3-MG with 2 to 19 months (mo) thalamic microglia (Th-MG) reveals more overlapping between P3-MG (black) and 19 mo Th-MG (red). **d**, Hierarchical clustering of gene expression in *Grn*<sup>+/+</sup> and *Grn*<sup>-/-</sup> P3-MG cluster A and 19 months old Th-MG. **e**, Venn diagrams showing the extent of overlapping between DEGs from 12 and 19 months old Th-MG and DEGs in P3-MG identified by scRNA-seq (upper panel) or DEGs in P3-MG identified by NanoString nCounter Neuroinflammation panel (lower panel). Statistics use the hypergeometric test. **f**, Volcano plot showing the upregulated and downregulated genes in *Grn*<sup>-/-</sup> P3-MG revealed by nCounter neuroinflammation panel. Statistics use nSolver software version 4.0, provided by the NanoString Technologies, Inc. **g**, Quantification of the

DEGs in *Grn*<sup>-/-</sup> P3-MG that are shared with 19 months *Grn*<sup>-/-</sup> Th-MG, including upregulation of *Arhgap24* and *Cables1*, and downregulation of *Chn2*, *Plxdc2*, *C1qa*, *Mef2c*, *Csf1r*, *Cx3cr1*, *Tgfbr1*, *Il6ra*, *Lair1* and *Slco2b1*. Data represent mean ± s.e.m.,  $n = 4$  for each genotype. Statistics uses two-tailed, unpaired Student's *t*-test. **h**, Western blots and quantification show upregulation of cathepsin B, myosin Va, Adam33 and ATG7, but downregulation of Mef2c and Numb. Data represent mean ± s.e.m.,  $n = 3$  for each protein. Statistics uses two-tailed, unpaired Student's *t*-test.

**Extended Data Fig. 6 *Grn*<sup>-/-</sup> MCM-induced cell death in *Grn*<sup>+/+</sup> and *Grn*<sup>-/-</sup> cortical neurons and GABAergic neurons.**

**a**, Representative confocal images of *Grn*<sup>+/+</sup> and *Grn*<sup>-/-</sup> cortical neurons treated with control media, *Grn*<sup>+/+</sup> MCM or *Grn*<sup>-/-</sup> MCM (100 µg/ml) overnight. Immunofluorescent stains are performed using antibodies for MAP2 (green) and cleaved caspase 3 (red). Nuclei are highlighted using DAPI. **b**, Representative confocal microscopic images of GE-derived *Grn*<sup>+/+</sup> and *Grn*<sup>-/-</sup> GABAergic interneurons treated with control media, *Grn*<sup>+/+</sup> MCM or *Grn*<sup>-/-</sup> MCM (100 µg/ml) overnight. Immunofluorescent stains are performed using antibodies for GAD67 (green) and cleaved caspase 3 (red). Nuclei are highlighted using DAPI.

**Extended Data Fig. 7 Nuclear pore defects in *Grn*<sup>-/-</sup> neurons treated with *Grn*<sup>-/-</sup> MCM.**

**a**, 3D structured illumination microscopy (SIM) images of Nup98 and LMN A/B in *Grn*<sup>+/+</sup> and *Grn*<sup>-/-</sup> cortical neurons treated with control media, *Grn*<sup>+/+</sup> MCM and *Grn*<sup>-/-</sup> MCM (250 µg/ml). Nup98 is shown in red, Lamin A/B in green and MAP2 in blue. **b**, Nup98 intensity distribution per intranuclear grid ( $0.44 \times 0.44 \mu\text{m}^2$ ) in *Grn*<sup>+/+</sup> and *Grn*<sup>-/-</sup> cortical neurons treated with control media and *Grn*<sup>-/-</sup> MCM (250 µg/ml) (see Methods for specific algorithms). Nup98 is less evenly distributed in *Grn*<sup>-/-</sup> cortical neurons in control media. When *Grn*<sup>+/+</sup> neurons are treated with *Grn*<sup>-/-</sup>

MCM, they show significant uneven distribution of Nup98 compared to *Grn*<sup>+/+</sup> neurons treated with control media. Interestingly, *Grn*<sup>-/-</sup> neurons treated with *Grn*<sup>-/-</sup> MCM do not show further defects in Nup98 distribution compared to *Grn*<sup>-/-</sup> in control media. Data represent mean ± s.e.m. from 3 independent cultures. Statistics use two-way ANOVA. **c**, Average of Nup98 intensity in the small grids in *Grn*<sup>+/+</sup> and *Grn*<sup>-/-</sup> cortical neurons treated with control media, *Grn*<sup>+/+</sup> MCM and *Grn*<sup>-/-</sup> MCM (250 µg/ml). Data represent mean ± s.e.m. The numbers listed below each data set represent the number of neurons analysed from 3 independent cultures. Statistics uses two-tailed, unpaired Student's *t*-test.

**Extended Data Fig. 8 Overlap between TDP-43 granules in *Grn*<sup>+/+</sup> and *Grn*<sup>-/-</sup> neurons with lysosomal marker LAMP1, but not with the mitochondrial marker Tom20 and the stress granule marker ataxin-2.**

**a–c**, Confocal images of TDP-43 granules and LAMP1+ lysosomes (**a**), Tom20+ mitochondria (**b**), or ataxin-2+ stress granules (**c**) in *Grn*<sup>+/+</sup> and *Grn*<sup>-/-</sup> cortical neurons treated with control media, *Grn*<sup>+/+</sup> MCM and *Grn*<sup>-/-</sup> MCM (250 µg/ml). TDP-43 is shown in red and LAMP1, Tom20 and ataxin-2 in green. Intensity plots shown below confocal images are performed using the Nikon Intensity Profile System. Images were collected in the cytoplasm and dendrites. **d**, Immunogold electron microscopic images of TDP-43 granules in *Grn*<sup>+/+</sup> and *Grn*<sup>-/-</sup> neurons treated with control media, *Grn*<sup>+/+</sup> MCM or *Grn*<sup>-/-</sup> MCM (250 µg/ml). The inset in the right lower panel shows a small spherical structure, which probably represent a cross-section of dendrite that contains many lysosomes with TDP-43 granules attached.

**Extended Data Fig. 9 Sodium arsenite-induced TDP-43 granules in *Grn*<sup>+/+</sup> and *Grn*<sup>-/-</sup> cortical neurons do not colocalize with G3BP1+ stress granules.**

**a**, Sodium arsenite treatment (10 µM, 1 h) induces prominent TDP-43 granules (red) and G3BP1+ granules (green) in *Grn*<sup>+/+</sup> and *Grn*<sup>-/-</sup> cortical neurons. However, the TDP-43 granules and G3BP1+ granules show no evidence of colocalization in these neurons. **b**, Quantification using NIH ImageJ shows that the majority of TDP-43 granules are smaller than 0.05 µm<sup>2</sup>. In contrast to *Grn*<sup>-/-</sup> MCM treatment, sodium arsenite induces similar TDP-43 granule formation in *Grn*<sup>+/+</sup> and *Grn*<sup>-/-</sup> cortical neurons. Images in panel **a** and quantification in panel **b** were obtained from four independent cultures. Data represent mean ± s.e.m. Statistics use two-way ANOVA with multiple comparisons. **c**, Immunogold electron microscopy (IEM) reveals that TDP-43 granules induced by sodium arsenite (500 µM) have morphology similar to those in *Grn*<sup>-/-</sup> thalamic neurons (Fig. 2d) and *Grn*<sup>-/-</sup> cortical neurons treated with *Grn*<sup>-/-</sup> MCM (Extended Data Fig. 8d). At least 8 IEM images were analysed from 2 independent cultures per condition. **d**, *Grn*<sup>+/+</sup> and *Grn*<sup>-/-</sup> cortical neurons are equally vulnerable to sodium arsenite treatment (10 µM, 1 h). Data represent mean ± s.e.m. *N* indicates the number of independent cultures. Statistics use two-tailed, unpaired Student's *t*-test. ns, not significant.

**Extended Data Fig. 10 C1q and C3b produced by *Grn*<sup>-/-</sup> microglia promote TDP-43 granule formation and cell death in *Grn*<sup>-/-</sup> neurons.**

**a**, Immunohistochemical images of *Grn*<sup>+/+</sup>, *Grn*<sup>-/-</sup> and *Grn*<sup>-/-</sup>;C1qa<sup>-/-</sup>;C3<sup>-/-</sup> mice at 7 months show the upregulation of C1q and C3b in the ventral thalamus of *Grn*<sup>-/-</sup> mice. No C1q or C3b staining is detected in *Grn*<sup>-/-</sup>;C1q<sup>-/-</sup>;C3<sup>-/-</sup> mouse brain, confirming the specificity of these antibodies. Insets in *Grn*<sup>-/-</sup> panels represent higher magnification of the boxed regions in the ventral thalamus. Results were analysed in 3 mice per genotype. **b**, ELISA assays for C1q and C3b show increases of both proteins in *Grn*<sup>-/-</sup> MCM, but no C1q or C3b is detected in *Grn*<sup>-/-</sup>;C1qa<sup>-/-</sup>;C3<sup>-/-</sup> MCM. Data represent mean ± s.e.m. from 8 independent microglial cultures for *Grn*<sup>+/+</sup> and *Grn*<sup>-/-</sup> MCM, and 3 independent cultures from *Grn*<sup>-/-</sup>;C1qa<sup>-/-</sup>;C3<sup>-/-</sup> MCM. Statistics use two-tailed, unpaired Student's *t*-test. **c**, Confocal images of cultured *Grn*<sup>+/+</sup> and *Grn*<sup>-/-</sup> cortical neurons treated with purified

human C1q (1 µg/ml) or C1q+C3b (1 µg/ml, each) indicate that complements are sufficient to promote the formation of TDP-43 granules in *Grn*<sup>+/+</sup> and *Grn*<sup>-/-</sup> cortical neurons, whereas *Grn*<sup>-/-</sup>;C1qa<sup>-/-</sup>;C3<sup>-/-</sup> MCM fail to induce TDP-43 granule formation. **d**, Quantification of cytoplasmic TDP-43 intensity (upper panel) and cell death (lower panel) in *Grn*<sup>+/+</sup> and *Grn*<sup>-/-</sup> neurons treated with C1q, C1q+C3b and C4. *N* in the upper panel and the lower panel indicates the number of independent cultures analysed. On average, 6-8 images were obtained from each culture. Statistics use two-tailed, unpaired Student's *t*-test. **e**, Quantification of cytoplasmic TDP-43 intensity (upper panel) and cell death (lower panel) in *Grn*<sup>+/+</sup> and *Grn*<sup>-/-</sup> neurons treated with control media, *Grn*<sup>-/-</sup> MCM, *Grn*<sup>-/-</sup>;C1qa<sup>-/-</sup> MCM or *Grn*<sup>-/-</sup>;C1qa<sup>-/-</sup>;C3<sup>-/-</sup> MCM. Data represent mean ± s.e.m. Statistics use two-tailed, unpaired Student's *t*-test. ns, not significant. *N* in the upper panel and the lower panel indicates the number of independent cultures analysed. On average, 6-8 images were obtained from each culture. **f**, Quantification of cell death of *Grn*<sup>+/+</sup> and *Grn*<sup>-/-</sup> neurons treated with *Grn*<sup>-/-</sup> MCM (250 µg/ml) and two different concentrations of vitronectin (50 or 500 ng/ml), an inhibitor of the complement membrane attack complex. Data represent mean ± s.e.m. Statistics uses two-tailed, unpaired Student's *t*-test. ns, not significant. Data are obtained from 3 independent cultures.

### Extended Data Fig. 11 Proposed model for the neurotoxic properties of *Grn*<sup>-/-</sup> microglia in promoting neurodegeneration in *Grn*<sup>-/-</sup> neurons.

*Grn*<sup>-/-</sup> microglia show progressive transcriptomic changes from 7 to 12 months old. Based on gene burden analysis from snRNA-seq data, *Grn*<sup>-/-</sup> microglia is the first cell cluster in the thalamus to show significant transcriptomic changes at 12 months. By 19 months, *Grn*<sup>-/-</sup> microglia exhibit much more profound changes in their transcriptomes, affecting the expression of genes implicated in plasma membrane bounded cell projection, exocytosis, phagocytosis, protein complex assembly, ion homeostasis/transport, MAPK cascade and receptor tyrosine kinase signalling. Consistent with the snRNA-seq results, immunohistochemistry and in vitro cultures show that *Grn*<sup>-/-</sup> microglia show marked reduction in

proteins required for homeostasis, including Tmem119 and P2Y12, but have elevated expression of lysosomal and pro-inflammatory proteins, including Cathepsin B, ApoE, Adam33 and many others. Our results suggest that the lysosomal defects in *Grn*<sup>-/-</sup> microglia may facilitate the production of complements, C1q and C3b, which promote the accumulation of nuclear and cytoplasmic TDP-43 granules, nuclear pore defects, and ultimately cell death in *Grn*<sup>-/-</sup> neurons. Interestingly, while purified human C1q and C3b can promote TDP-43 granule formation and cell death in *Grn*<sup>-/-</sup> neurons, these effects are less robust than in *Grn*<sup>-/-</sup> MCM. These results suggest that *Grn*<sup>-/-</sup> microglia may produce other unknown factors to facilitate neurodegeneration in *Grn*<sup>-/-</sup> neurons. This model does not exclude the possibility that complements C1q and C3b may have cell-autonomous effects to activate *Grn*<sup>-/-</sup> microglia.

## Supplementary information

### Supplementary Figure 1

Uncropped images for western blots of Cathepsin B, Myosin Va, Adam33, ATG7, Mef2c, Numb and GAPDH in *Grn*<sup>+/+</sup> and *Grn*<sup>-/-</sup> P3 microglia.

Uncropped images of western blots for several key up- or down-regulated genes in *Grn*<sup>-/-</sup> P3 microglia (P3-MG) presented in Extended Data Figure 5h. Each image contains 6 samples, including 3 from *Grn*<sup>+/+</sup> P3-MG (left three lanes) and 3 from *Grn*<sup>-/-</sup> P3-MG (right three lanes). Each sample contains pools of primary microglia from two or more P3 mice, and therefore is considered as a biological replicate. Samples in different lanes are from different pools of microglia. The predicted molecular weight for each protein is presented on top of each panel, and the corresponding position of each protein on the western blot is indicated with an arrow.

### Reporting Summary

### Supplementary Table 1

Meta data for samples and cells in single-nucleus RNA-sequencing (snRNA-seq). This table contains information regarding the samples, the number of nuclei, and the number of reads from the snRNA-seq.

## Supplementary Table 2

Pseudotime analyses of subclusters and subcluster-specific differentially expressed genes in *Grn*<sup>+/+</sup> and *Grn*<sup>-/-</sup> thalamic microglia. This table contains information regarding the pseudotime trajectory analyses of *Grn*<sup>+/+</sup> and *Grn*<sup>-/-</sup> thalamic microglia (Th-MG) using version 3 of Monocle R package. Supplementary Table 2A includes unique gene sets used to identify different subclusters in *Grn*<sup>+/+</sup> and *Grn*<sup>-/-</sup> thalamic microglia (Th-MG). Supplementary Tables 2B and 2C contain the pseudotime trajectory analyses of the differentially expressed genes in each subcluster in *Grn*<sup>+/+</sup> and *Grn*<sup>-/-</sup> Th-MG, respectively. Statistics in 2B and 2C were performed using Moran's I test.

## Supplementary Table 3

Age-specific differentially expressed genes in *Grn*<sup>+/+</sup> and *Grn*<sup>-/-</sup> thalamic microglia at 7, 12 and 19 months. This table contains the lists of differentially expressed genes (DEGs) in *Grn*<sup>-/-</sup> Th-MG at 7 months (Table 3A), 12 months (Table 3B) and 19 months (Table 3C). DEGs were analyzed using two different approaches. The first approach uses MAST and the second approach uses pseudobulk to generate DEGs. Detailed methods and statistics are provided in METHODS.

## Supplementary Video 1

Time-lapse imaging of nuclear mCherry-TDP-43 in *Grn*<sup>+/+</sup> neurons treated with control media. *Grn*<sup>+/+</sup> cortical neurons from E15.5 embryos were transfected with pcDNA-mCherry-FLAG-TDP-43 plasmid. At 18 hours after the transfection, control media (250µg/ml) was added to the neurons and time-laps images of nuclear m-Cherry-TDP-43 were captured for 14 hours at 10 minutes-intervals. Time-lapse sequences were acquired on a Yokogawa CSU-X1 spinning disk confocal microscope system with a

Nikon 60x N.A. 1.49 objective and a Photometrics BSI Prime back-thinned sCMOS camera. A total of 15 *Grn*<sup>+/+</sup> neurons treated with control media were imaged with similar results.

### Supplementary Video 2

Time-lapse imaging of nuclear mCherry-TDP-43 in *Grn*<sup>+/+</sup> neuron treated with *Grn*<sup>-/-</sup> MCM. *Grn*<sup>+/+</sup> cortical neurons were transfected with pcDNA-mCherry-FLAG-TDP-43 plasmid. At 18 hours after the transfection, *Grn*<sup>-/-</sup> MCM (250µg/ml) was added to the neurons and time-laps images of nuclear m-Cherry-TDP-43 were captured for 14 hours at 10 minutes-intervals. Four of 16 *Grn*<sup>+/+</sup> neurons treated with *Grn*<sup>-/-</sup> MCM exhibited >3 folds increase in nuclear mCherry-TDP-43 signal at the end of recording compared with time 0'. Collectively, *Grn*<sup>+/+</sup> neurons treated with *Grn*<sup>-/-</sup> MCM exhibited a modest, but not statistically significant, increase in nuclear m-Cherry-TDP-43 signals.

### Supplementary Video 3

Time-lapse imaging of nuclear mCherry-TDP-43 in *Grn*<sup>-/-</sup> neuron treated with control media. *Grn*<sup>-/-</sup> cortical neurons were transfected with pcDNA-mCherry-FLAG-TDP-43 plasmid. At 18 hours after the transfection, control media (250µg/ml) was added to the neurons and time-laps images of nuclear m-Cherry-TDP-43 were captured for 14 hours at 10 minutes-intervals. A total of 11 *Grn*<sup>-/-</sup> neurons treated with control media were recorded.

### Supplementary Video 4

Time-lapse imaging of nuclear mCherry-TDP-43 in *Grn*<sup>-/-</sup> neuron treated with *Grn*<sup>-/-</sup> MCM. *Grn*<sup>-/-</sup> cortical neurons were transfected with pcDNA-mCherry-FLAG-TDP-43 plasmid. At 18 hours after the transfection, *Grn*<sup>-/-</sup> MCM (250µg/ml) was added to the neurons and time-laps images of nuclear m-Cherry-TDP-43 were captured for 14 hours at 10 minutes-intervals. Five of 17 *Grn*<sup>-/-</sup> neurons treated with *Grn*<sup>-/-</sup> MCM exhibited >5 folds increase, whereas 12 showed variable increases in nuclear m-Cherry-

TDP-43 signals at the end of recording compared with time 0'. Overall, *Grn*<sup>-/-</sup> neurons treated with *Grn*<sup>-/-</sup> MCM exhibited significantly higher nuclear mCherry-TDP-43 signals.

## Supplementary Video 5

Time-lapse imaging of nuclear and cytoplasmic mCherry-TDP-43 in *Grn*<sup>-/-</sup> neuron treated with *Grn*<sup>-/-</sup> MCM. Of the 17 *Grn*<sup>-/-</sup> cortical neurons treated with transfected with *Grn*<sup>-/-</sup> MCM, 5 showed extension of mCherry-TDP43 from the nucleus into the cytoplasm. Supplementary Video 5 represents one of such *Grn*<sup>-/-</sup> cortical neurons. Several of *Grn*<sup>-/-</sup> neurons with extension of nuclear mCherry-TDP-43 into the cytoplasm eventually died at or near the end of recording.

## Rights and permissions

[Reprints and Permissions](#)

## About this article



Check for  
updates

## Cite this article

Zhang, J., Velmeshev, D., Hashimoto, K. *et al.* Neurotoxic microglia promote TDP-43 proteinopathy in progranulin deficiency. *Nature* **588**, 459–465 (2020). <https://doi.org/10.1038/s41586-020-2709-7>

[Download citation](#)

- Received: 10 April 2019
- Accepted: 21 August 2020

- Published: 31 August 2020
- Issue Date: 17 December 2020
- DOI: <https://doi.org/10.1038/s41586-020-2709-7>

## Comments

By submitting a comment you agree to abide by our [Terms](#) and [Community Guidelines](#). If you find something abusive or that does not comply with our terms or guidelines please flag it as inappropriate.

[Access through your institution](#)

[Change institution](#)

[Buy or subscribe](#)

---

This article was downloaded by **calibre** from <https://www.nature.com/articles/s41586-020-2709-7>

| [Section menu](#) | [Main menu](#) |

## Cells of the adult human heart

[Download PDF](#)

- Article
- Published: 24 September 2020

# Cells of the adult human heart

- Monika Litviňuková<sup>1,2 na1</sup>,
- Carlos Talavera-López<sup>1,3 na1</sup>,
- Henrike Maatz<sup>2 na1</sup>,
- Daniel Reichart<sup>4,5 na1</sup>,
- Catherine L. Worth [ORCID: orcid.org/0000-0002-1796-9606](#)<sup>2</sup>,
- Eric L. Lindberg<sup>2</sup>,
- Masatoshi Kanda [ORCID: orcid.org/0000-0003-3468-3586](#)<sup>2,6</sup>,
- Krzysztof Polanski [ORCID: orcid.org/0000-0002-2586-9576](#)<sup>1</sup>,
- Matthias Heinig [ORCID: orcid.org/0000-0002-5612-1720](#)<sup>7,8</sup>,
- Michael Lee [ORCID: orcid.org/0000-0002-0186-4439](#)<sup>9</sup>,
- Emily R. Nadelmann<sup>4</sup>,
- Kenny Roberts [ORCID: orcid.org/0000-0001-6155-0821](#)<sup>1</sup>,
- Liz Tuck<sup>1</sup>,
- Eirini S. Fasouli<sup>1</sup>,
- Daniel M. DeLaughter<sup>4</sup>,
- Barbara McDonough<sup>4,11,16</sup>,
- Hiroko Wakimoto [ORCID: orcid.org/0000-0003-0225-6424](#)<sup>4</sup>,
- Joshua M. Gorham<sup>4</sup>,
- Sara Samari<sup>9</sup>,
- Krishnaa T. Mahbubani [ORCID: orcid.org/0000-0002-1327-2334](#)<sup>12</sup>,
- Kourosh Saeb-Parsy [ORCID: orcid.org/0000-0002-0633-3696](#)<sup>12</sup>,
- Giannino Patone [ORCID: orcid.org/0000-0002-7242-0341](#)<sup>2</sup>,
- Joseph J. Boyle [ORCID: orcid.org/0000-0002-4337-3320](#)<sup>9</sup>,
- Hongbo Zhang<sup>1,13</sup>,
- Hao Zhang<sup>14,15</sup>,
- Anissa Viveiros<sup>14,15</sup>,
- Gavin Y. Oudit<sup>14,15</sup>,
- Omer Ali Bayraktar [ORCID: orcid.org/0000-0001-6055-277X](#)<sup>1</sup>,

- [J. G. Seidman](#)<sup>4 na2</sup>,
- [Christine E. Seidman](#) [ORCID: orcid.org/0000-0001-6380-1209](#)<sup>4,11,16 na2</sup>,
- [Michela Noseda](#) [ORCID: orcid.org/0000-0002-9553-5029](#)<sup>9,17 na2</sup>,
- [Norbert Hubner](#) [ORCID: orcid.org/0000-0002-1218-6223](#)<sup>2,10,18,19 na2</sup> &
- [Sarah A. Teichmann](#) [ORCID: orcid.org/0000-0002-6294-6366](#)<sup>1,20 na2</sup>

[Nature](#) volume 588, pages466–472(2020) [Cite this article](#)

- 48k Accesses
- 6 Citations
- 1320 Altmetric
- [Metrics details](#)

## Subjects

- [Gene expression](#)
- [Genetics research](#)

## Abstract

Cardiovascular disease is the leading cause of death worldwide. Advanced insights into disease mechanisms and therapeutic strategies require a deeper understanding of the molecular processes involved in the healthy heart. Knowledge of the full repertoire of cardiac cells and their gene expression profiles is a fundamental first step in this endeavour. Here, using state-of-the-art analyses of large-scale single-cell and single-nucleus transcriptomes, we characterize six anatomical adult heart regions. Our results highlight the cellular heterogeneity of cardiomyocytes, pericytes and fibroblasts, and reveal distinct atrial and ventricular subsets of cells with diverse developmental origins and specialized properties. We define the complexity of the cardiac vasculature and its changes along the arterio-venous axis. In the immune compartment, we identify cardiac-resident macrophages with inflammatory and protective transcriptional signatures. Furthermore, analyses of cell-to-cell interactions highlight different networks of macrophages, fibroblasts and cardiomyocytes between atria and ventricles that are distinct from those of skeletal muscle. Our human cardiac cell atlas improves our understanding of the human heart and provides a valuable reference for future studies.

[Download PDF](#)

# Main

The heart is a complex organ, composed of four morphologically and functionally distinct chambers (Fig. 1a). Deoxygenated blood from the low-pressure right atrium and ventricle is propelled into the lungs. Oxygenated blood enters the left atrium and ventricle, which propels blood across the body at systemic pressure. Chambers are separated by the interatrial and interventricular septa, and unidirectional flow is established by the atrio-ventricular and ventricular-arterial valves. An intrinsic electrophysiological system rapidly propagates electrical impulses from the sinoatrial node to the atrioventricular node, and along Purkinje fibres to the apex where contraction begins. Cardiac anatomical and functional complexity requires exquisite orchestration of heterogeneous cell populations to enable continuous contraction and relaxation across different pressures, strains and biophysical stimuli in each chamber.

**Fig. 1: Cell composition of the adult human heart.**



**a**, Transmural samples were obtained from left and right atrium, left and right ventricles, apex and interventricular septum from 14 individuals. Single nuclei ( $n = 14$ ) and single cells ( $n = 7$ ) were processed using Chromium 10x 3'DEG chemistry. **b**, Infographic shows donors (women, top; men, bottom), age, and contribution to cells and nuclei datasets (orange circle). Data are available in Supplementary Table 1. **c**, Uniform manifold approximation and projection (UMAP) embedding of 487,106 cells and nuclei delineate 11 cardiac cell types and marker genes. **d**, Distribution of cell populations, identified from nuclei within atria (left and right) and ventricles (left, right, apex and interventricular septum) after subclustering analysis. Colour code as in **c**. Data are available in Supplementary Table 2. Adip, adipocytes; Lym, lymphoid; Meso, mesothelial cells; Myel, myeloid; NC, neuronal cells; PC, pericytes. **e**, Multiplexed smFISH of cell type-specific transcripts in right ventricles (RV; left): *TTN* (green, cardiomyocytes) and *CDH5* (red, EC) right atrium (RA; middle): *NPPA* (green, aCM) and *DCN* (red, FB) and

left atrium (LA; right): *MYH11* (green, SMCs) and *KCNJ8* (red, pericytes). Nuclei are counterstained with DAPI (dark blue). Scale bars, 20  $\mu\text{m}$ . For details on statistics and reproducibility, see [Methods](#).

[Full size image](#)

The heart is derived from multipotent progenitor cells that comprise two heart fields. Cells of the first heart field primarily populate the left ventricle; second heart field cells populate the right ventricle, and both fields contribute to the atria.

Haemodynamics changes in the postnatal period and the distinct gene regulatory networks that operate in each heart field presumably prime gene expression patterns of adult heart cells<sup>1</sup>.

Single-cell and single-nucleus RNA sequencing (scRNA-seq and snRNA-seq, respectively) and multiplex single-molecule fluorescence *in situ* hybridization (smFISH) enable the identification of anatomical specificities, molecular signatures, intercellular networks and spatial relationships by illuminating the coordinated communication of cardiac cells within their microenvironments<sup>2</sup>.

We present comprehensive transcriptomic data on six distinct cardiac regions, providing, to our knowledge, the largest reference framework so far<sup>3,4</sup>. We incorporate snRNA-seq to ensure high-throughput capture of large cardiomyocytes (length and width approximately 100 and 25  $\mu\text{m}$ ) and scRNA-seq to upsample and enrich endothelial and immune cell populations. Using multiplex smFISH imaging, we describe the spatial distribution of selected cell populations and cell–cell co-localizations. We compare cardiac cell and nuclear transcriptomes with those of skeletal muscle and kidney, highlighting cardiac-specific cell signatures. Our study defines the cellular and molecular signatures of the adult healthy heart, and enables functional plasticity in response to varying physiological conditions and diseases.

## Cellular landscape of the adult human heart

We isolate single cells, nuclei and CD45<sup>+</sup> enriched cells from the left and right ventricular free walls, left and right atrium, the left ventricular apex, and interventricular septum, from 14 adults (Fig. [1a, b](#), Supplementary Table [1](#)). After processing with 10X Genomics and a generative deep variational autoencoder, the resulting dataset comprises 45,870 cells, 78,023 CD45<sup>+</sup> enriched cells and 363,213 nuclei for 11 major cell types: atrial cardiomyocytes, ventricular cardiomyocytes, fibroblasts (FBs), endothelial cells (ECs), pericytes, smooth muscle cells (SMCs), immune cells (myeloid and lymphoid), adipocytes, mesothelial cells and neuronal cells (Fig. [1c, e](#), Extended Data Figs. [1, 2](#)).

The distributions of these main cell types, estimated from nuclei data, differ between atrial and ventricular tissues. Atrial tissues contain 30.1% cardiomyocytes, 24.3% FBs, 17.1% mural cells (pericytes and SMCs), 12.2% ECs and 10.4% immune cells (myeloid and lymphoid). By contrast, ventricular regions (apex, interventricular septum, left and ventricle) contain 49.2% ventricular cardiomyocytes, 21.2% mural cells, 15.5% FBs, 7.8% ECs and 5.3% immune cells (Fig. 1d, Supplementary Table 2).

The ventricular proportions of ventricular cardiomyocytes and FBs are negatively correlated, whereas pericytes and SMC proportions are positively correlated, indicating a functional organization (Supplementary Table 3). Cell distributions are generally similar in male and female hearts. However, the mean percentages of ventricular cardiomyocytes from left and right ventricles are higher in female hearts ( $56 \pm 9\%$ ; mean  $\pm$  s.d.) and associated with a stronger negative correlation between ventricular cardiomyocytes and FBs ( $r = -0.8$ ; slope =  $-0.9$ ) compared to male hearts ( $47 \pm 11\%$ ;  $P = 0.03$ ; ventricular cardiomyocytes–FBs,  $r = -0.4$ ; slope =  $-0.3$ ). Differences in the proportions of cardiomyocytes is unexpected given the average smaller female heart mass, and if confirmed might explain higher cardiac stroke volumes in women<sup>5</sup> and lower rates of cardiovascular disease.

## Cardiomyocyte heterogeneity

Cardiomyocytes show high-level expression of genes that encode contractile force-generating sarcomere proteins (*TTN*, *MYBPC3* and *TNNT2*) and calcium-mediated processes (*RYR2*, *PLN* and *SLC8A1*). Consistent with bulk tissue RNA-sequencing (RNA-seq) data<sup>6</sup>, we observe markedly distinct transcriptional signatures in ventricular and atrial cardiomyocytes, reflecting developmental origins and differences in electrophysiological, contractile and secretory processes (Extended Data Fig. 3, Supplementary Table 4).

Ventricular cardiomyocytes are enriched in genes encoding sarcomere proteins (*MYH7* and *MYL2*), transcription factors (*IRX3*, *IRX5*, *IRX6*, *MASP1* and *HEY2*), and *PRDM16*, mutated in left ventricular non-compaction cardiomyopathy<sup>7</sup>. Other abundant transcripts enable tissue integrity despite high ventricular strain: *PCDH7* encodes a calcium-dependent strong adhesive molecule<sup>8</sup>; *SMYD2* encodes a lysine methyltransferase that promotes sarcomere formation and stabilization<sup>9</sup>. Atrial cardiomyocytes abundantly express prototypic genes and also *ALDH1A2*, an enzyme required for retinoic acid synthesis, *ROR2*, which participates in Wnt signalling during lineage differentiation<sup>10</sup>, and *SYNPR*, which functions in the mechanosensing of TRP channels by atrial volume receptors<sup>11</sup>.

We identify five ventricular cardiomyocyte (vCM1–vCM5) populations: vCM1 comprise 63.9% of left ventricular cardiomyocytes but only 36.7% of right ventricular cardiomyocytes (Fig. 2a, b, Extended Data Fig. 3a, c–e, Supplementary Tables 5, 6). vCM2 is more enriched in right ventricles (39.9%) than left ventricles (9.1%). However, differences between vCM1 and vCM2 are small, indicating shared gene programs between left (enriched in vCM1) and right (enriched in vCM2) ventricles. vCM2 shows higher expression of *PRELID2*, a developmental molecule with unknown cardiac function<sup>12</sup> (verified by single-molecule fluorescence in situ hybridization (smFISH) (Fig. 2c, Extended Data Fig. 3c). Among vCMs, vCM2 has the highest expression of the myosin gene *MYH6* and *CDH13*, a cell surface T-cadherin receptor for cardioprotective adiponectin and low density lipoproteins, both associated with several cardiometabolic traits<sup>13</sup>.

**Fig. 2: Cardiomyocytes.**



**a**, UMAP embedding of five ventricular cardiomyocyte (vCM) populations. **b**, Regional distributions of ventricular cardiomyocyte populations. Data are available in Supplementary Table 5. AX, apex; LV, left ventricle; SP, interventricular septum; RV, right ventricle. **c**, **d**, Multiplexed smFISH of *PRELID2* (red) enriched in vCM2 (**c**) and of *FHL1* (red) enriched in vCM3 (**d**). **e**, UMAP embedding of five atrial cardiomyocytes (aCM) populations. **f**, Regional distributions of atrial cardiomyocyte populations. LA, left atrium; RA, right atrium. **g**, **h**, Multiplexed smFISH of *HAMP* (red) enriched in aCM2 (**g**) and of *CNN1* (red) enriched in aCM3 (**h**). In **c**, **d**, **g** and **h**, nuclei are counterstained with DAPI (dark blue). Scale bars, 10 μm. For details on statistics and reproducibility, see [Methods](#).

[Full size image](#)

vCM3 and vCM4 are present across all ventricular regions. The vCM3 transcriptional profile resembles a prominent right atrium population (aCM3, discussed below) with retinoic-acid-responsive SMC gene enrichment (*MYH9*, *NEXN* and *CNN1*)<sup>14,15</sup>. vCM3 also express stress-response genes including *ANKRD1*<sup>16</sup>, *FHL1*<sup>17</sup> (verified by smFISH) (Fig. 2d, Extended Data Fig. 3c), *DUSP27*<sup>18</sup>, and *XIRP1* and *XIRP2*, interacting with intercalated disc ion channel proteins implicated in cardiomyopathy and arrhythmias<sup>19</sup>. The small population vCM4 is enriched for nuclear-encoded mitochondrial genes (*NDUFB11*, *NDUFA4*, *COX7C* and *COX5B*) and Gene Ontology terms indicative of a high energetic state (Extended Data Fig. 3f). vCM4 also demonstrates high levels of *CRYAB*, which encodes a cytoprotective and antioxidant heat shock protein<sup>20</sup>, of sarcomere protein genes and *PLN*, indicating that these ventricular cardiomyocytes are outfitted to perform higher workload than other ventricular cardiomyocytes.

vCM5 (approximately 1%) comprises cells with high levels of *DLC1* and *EBF2*<sup>21</sup>, regulating brown adipocyte differentiation and perhaps cardiac pacemaker activity, and transcripts identified in neuronal lineages (*SOX5*, *EBF1* and *KCNAB1*). As *EBF1*-depleted mice have a profoundly hypoplastic ventricular conduction system<sup>22</sup>, vCM5 may participate in electrophysiology.

We identify five atrial cardiomyocyte populations (aCM1–aCM5) (Fig. 2e,f, Extended Data Fig. 3b–d, Supplementary Tables 6, 7). *HAMP*, a master regulator of iron homeostasis, is considerably enriched in more than 50% of right atrium cardiomyocytes versus 3% left atrium cardiomyocytes (verified by smFISH)<sup>23</sup> (Fig. 2g, Extended Data Fig. 3c), indicating energetic differences<sup>6</sup>. *HAMP* has unknown roles in cardiac biology, but *Hamp*-null mice have deficits in the electron transport chain and lethal cardiomyopathy<sup>24</sup>.

aCM1 shows robust expression of prototypic atrial transcripts, indicative of a basal atrial cardiomyocyte gene program, and lower levels of molecules with neuronal functions (*ADGRL2*, *NFXL1* and *ROBO2*). aCM2 predominantly expresses *HAMP* within the right atrium and is enriched for *SLIT3*, the developmental ligand for cardiac ROBO receptors<sup>25</sup>, *ALDH1A2*<sup>26</sup> and *BRINP3*, involved in retinoic acid signalling, and *GRXCR2*, supporting cilia involved in mechanosensing<sup>27</sup>.

aCM3 and vCM3 share similar transcriptional profiles including enrichment of the SMC gene *CNN1* (verified by smFISH) (Fig. 2h, Extended Data Fig. 3c). The molecular signatures of aCM2, aCM3 and vCM3 indicate derivation from the second heart field<sup>28</sup>. aCM4 transcripts denote high metabolic activity, similar to

vCM4, and have the highest expression of *NPPA*. aCM5 expresses similar transcripts to vCM5.

## Vascular, stromal and mesothelial cells

The vascular compartment includes 17 distinct populations of EC, SMC, pericyte, mesothelial cells with anatomical and arterio-venous specificities (Fig. 3a, b, Supplementary Tables 8, 9). Endothelial cells, identified by pan-EC markers *PECAM1*, *CDH5* and *VWF*, comprise 10 populations (Extended Data Fig. 4a–c, g). Three capillary ECs (EC1-3\_cap), which express *RGCC* and *CA4*<sup>29</sup>, represent 57.4% of all ECs. Capillary-like EC4\_immune ECs express transcripts related to antigen presentation and immune regulation (*CX3CL1*, *CCL2*, *IL6* and *ICAM1*)<sup>30</sup>. Arterial EC5\_art ECs are enriched for *SEMA3G*, *EFNB2* and *DLL4*, whereas EC6\_ven ECs express venous markers *NR2F2*<sup>31</sup> and *ACKR1*<sup>32</sup>, which we confirmed by smFISH (Fig. 3c). Mainly atrial EC7\_atria ECs express the angiogenesis regulator *SMOC1*<sup>33</sup> and *NPR3*, detected in mouse endocardium<sup>34</sup>, suggestive of endocardial cells. Lymphatic EC8\_ln ECs, enriched for *PROX1*, *TBX1* and *PDPN*, represent approximately 1% of the captured ECs<sup>29</sup>.

**Fig. 3: Vascular, stromal and mesothelial cells.**



**a**, UMAP embedding of 17 vascular and mesothelial populations. EC1/2/3\_cap, capillary ECs; EC4\_immune, immune-related ECs; EC5\_art, arterial ECs; EC6\_ven, venous ECs; EC7\_atrial, atria-enriched ECs; EC8\_ln, lymphatic ECs; EC9\_FB-like, ECs with FB features; EC10\_CM-like, ECs with cardiomyocyte features; PC1\_vent, ventricle-enriched pericytes; PC2\_atrial, atria-enriched pericytes; PC3\_str, stromal

pericytes; PC4\_CM-like, pericytes with cardiomyocyte features; SMC1\_basic, basic SMCs; SMC2\_art, arterial SMCs. **b**, Schematic of the vascular cells and their placement in the vasculature. **c**, Multiplexed smFISH of *MYH11* (yellow) in SMC (thick in artery and very thin in small vein), *CDH5* (red) in the endothelium, and *SEMA3G* (cyan) and *ACKR1* (green) in EC5\_art and EC6\_ven, respectively in apex. Nuclei are counterstained with DAPI (dark blue). Scale bar, 20  $\mu$ m. **d**, Predicted cell–cell interactions in arteries and veins. Data are available in Supplementary Table 10. **e, f**, Multiplexed smFISH of pan-FB *DCN* (cyan) and *FAP* (red) in FB4 in interventricular septum (SP) (**e**) and *DCN* (cyan) and *LINC001133* (red) in FB5 in the apex (AX) (**f**). Nuclei are counterstained with DAPI (dark blue). Scale bars, 5  $\mu$ m. **g**, UMAP embedding showing six FB populations and their respective marker genes. **h**, Multiplexed smFISH of *C1QA*<sup>+</sup> macrophages (MP) and *PTX3*<sup>+</sup> FB3, suggesting cross-talk between both cell types. Scale bar, 5  $\mu$ m. For details on statistics and reproducibility, see [Methods](#).

[Full size image](#)

Pericytes express *ABCC9* and *KCNJ8* and segregate into four clusters, with PC1\_vent cells enriched in ventricles and PC2\_atria cells in atria. PC1\_vent cells express adhesion molecules (*NCAM2* and *CD38*), and *CSPG4*, which is involved in microvascular morphogenesis and EC cross-talk<sup>35</sup> (Extended Data Fig. 4d–f). PC3\_str co-express pericyte markers and very low levels of pan-EC transcripts. RNA velocity analyses suggest a directionality that indicates PC3\_str cells as a transitional state between pericytes and ECs (Extended Data Fig. 4h,i). These observations may relate to bidirectional pericyte or endothelial cell (trans)differentiation, which remains controversial<sup>36</sup>.

Vascular SMCs that express *MYH11* split into two populations. SMC1\_basic cells express transcripts that indicate immaturity, including the stem-cell marker *LGR6*<sup>37</sup> and proliferation-associated *RGS5*<sup>38</sup>. SMC2\_art cells express considerably higher levels of *CNN1*, *ACTA2* and *TAGLN*, indicating arterial origin, whereas SMC1\_basic cells may be venous-derived<sup>39</sup> (Extended Data Fig. 4d–f).

Cell–cell interaction analyses indicate connections between ECs and mural cells in different vascular segments (Fig. 3b–d, Extended Data Fig. 4j,k, Supplementary Table 10), including Notch receptor–ligand interactions<sup>40</sup> (NOTCH1 or NOTCH4 with *JAG1*, and NOTCH2 or NOTCH3 with *JAG1*, *JAG2* or *DLL4*) between EC5\_art and SMC2\_art cells. Exploratory spatial transcriptomics (Extended Data Fig. 5) shows co-occurrence of EC5\_art and SMC2\_art markers and *JAG1* and *NOTCH2*, thereby supporting this interaction between ECs and SMCs. A venous-specific *DLL1*–NOTCH3 interaction is predicted for EC6\_ven and SMC1\_basic

cells. Notably, many of the venous and arterial EC predicted interactions are shared with capillary ECs, which suggests gradual changes along the arterio-venous axis<sup>39</sup>.

We define a distinct small population as mesothelial cells that enrich for *MSLN*, *WT1* and *BNC1*<sup>41</sup> but lack EC, FB or mural genes. smFISH confirms this annotation with localization of *BNC1*<sup>+</sup>/*CDH5*<sup>-</sup> cells to the epicardium (Extended Data Fig. 4l–n).

## Cardiac fibroblasts

Cells of the FB compartment show enriched expression of *DCN*, *GSN* and *PDGFRA* within seven populations (Fig. 3g) with regional enrichment in ventricles (FB1) and atria (FB2). This is consistent with distinctive functional properties, including stronger profibrotic responses, by atrial FBs<sup>42</sup>. FB1 and FB2 cells express canonical genes and define a basal, chamber-specific FB expression program (Extended Data Fig. 6a, Supplementary Table 11).

FB4 and FB5 cells are less abundant in the right atrium than other regions, whereas FB3 are less abundant in the left ventricle (Extended Data Fig. 6c). FB4 cells express genes responsive to TGFβ signalling (for example, *POSTN* and *TNC*) (Fig. 3e). FB5 cells have higher expression of genes involved in the production, remodelling and degradation of extracellular matrix (ECM). By contrast, FB3 cells have lower expression of ECM-related genes but higher expression of cytokine receptors such as *OSMR* and *ILST6*<sup>43</sup> (Fig. 3f, Extended Data Fig. 6b, Supplementary Table 12). These distinctive fibroblast gene programs probably govern stress-responsive cardiac remodelling and contribute to homeostasis.

Separate clustering of atrial and ventricular FBs recapitulated the populations described above, including an OSM-signalling population in each chamber (aFB4 and vFB3). In addition, we identify distinct chamber-specific ECM-producing FBs that differ in the expression of collagen isoforms and other ECM-related (aFB2 versus vFB2) (Extended Data Fig. 6g–m, Supplementary Table 13) or connective tissue-related genes (aFB1 versus vFB4).

## Immune cells and cardiac homeostasis

Analysis of cardiac immune cells reveals 21 cell states (Fig. 4a, Extended Data Fig. 7). Myeloid cells comprise 13 populations, including several subtypes of macrophages, monocytes and dendritic cells, whereas the lymphoid compartment comprises 8 populations (Supplementary Tables 14, 15).

**Fig. 4: Cardiac immune populations and cell–cell interactions.**

 figure4

**a**, Manifold of 40,868 myeloid and lymphoid cardiac cells. NP, neutrophils; NK, natural killer; NKT, natural killer T cells; CD4+T\_tem, effector-memory CD4<sup>+</sup> T cells; CD4+T\_cytotoxic, CD4<sup>+</sup> cytotoxic T cells; CD8+T\_tem, CD8<sup>+</sup> effector-memory T cells; CD8+T\_cytotoxic, CD8<sup>+</sup> cytotoxic T cells; DC, dendritic cells; CD14+Mo, CD14<sup>+</sup> monocytes; CD16+Mo, CD16<sup>+</sup> monocytes; Mo\_pi, pro-inflammatory monocytes; IL17RA+Mo, IL17RA<sup>+</sup> monocytes; MP\_AgP, HLA class II antigen-presenting macrophages; MP\_mod, monocyte-derived macrophages; LYVE1+MP1–3, M2-like, LYVE1<sup>+</sup> macrophages sets 1–3; DOCK4+MΦ1–2, DOCK4<sup>+</sup> macrophage sets 1–2; B\_cells, B cells; plasma, plasma B cells. **b**, BioRender infographic summarizes predicted cell–cell interaction circuits between atrial and ventricular cardiomyocytes, FB4 and immune cells involved in tissue repair in the heart and SKM. Data are available in Supplementary Table 17. **c**, Gene expression signature for cardiac-specific LYVE1<sup>+</sup> macrophages compared against predicted matched populations in skeletal muscle and kidney.

[Full size image](#)

Macrophages include three LYVE1<sup>+</sup> macrophage populations: LYVE1<sup>+</sup> MP1–2 enrich for clathrin and cathepsin genes, and LYVE1<sup>+</sup> MP3 for HLA-DQA1/2 and HLA-DQB1. LYVE1<sup>+</sup> macrophages appear related to recently described tissue-resident macrophages associated with cardiovascular remodelling<sup>44</sup>, although negative for TIMD4<sup>45</sup> (Extended Data Fig. 8a, b). Monocyte-derived macrophages express LYVE1 and FOLR2, monocyte-like markers CEBPB and S100A8, and chemoattractant cytokine genes CCL13 and CCL18. Antigen-presenting macrophages are FOLR2<sup>−</sup>, LYVE1<sup>−</sup> and MERTK<sup>−</sup>, and enrich for HLA-DRA, HLA-DMA, HLA-DMB, HLA-DPA1 and TREM2 (described in lipid-associated macrophages)<sup>46</sup>. Although monocytes are abundant in our data and others<sup>47</sup>, these are likely to be circulating, as supported by computational integration of our data with published peripheral blood mononuclear cell (PBMC) single-cell RNA-seq

data (Supplementary Table 16). Two populations of *DOCK4*<sup>+</sup> macrophages differentiated by higher expression of *IL4R*, *STAT3* and *ITGAM* in *DOCK4*<sup>+</sup> MP1 versus *DOCK4*<sup>+</sup> MP2, do not express *C1QA* or *FOLR2* (Extended Data Fig. 8c).

Predicted cell–cell interactions identify receptor–ligand circuits among immune cells, cardiomyocytes, and FBs. *LYVE1*<sup>+</sup>, monocyte-derived and antigen-producing macrophages are predicted to interact with FB4 via CD74–MIF (Fig. 4b, Extended Data Fig. 8d, e, Supplementary Table 17). Inhibition of this interaction leads to fibrosis<sup>48</sup> and tissue damage<sup>49</sup>. FB4 also enrich for *FN1*, *COL4A1* and *TNC*, facilitating cellular proliferation in the fetal heart<sup>50</sup> and predicted to interact with different integrins in atrial and ventricular cardiomyocytes. In skeletal muscle (SKM), predicted cell–cell interactions between *PRG4*<sup>+</sup> FBs (analogous to FB4) and cardiomyocytes involve *COL1A2*, *COL6A2* and  $\alpha 10\beta 1$  integrins, whereas SKM FBs and monocytes appear to interact via the ICAM1–AREG and CXCR4–CXCL12 chemokine pairs (Fig. 4b, Supplementary Table 18), indicating tissue-specific homeostatic transcriptional circuits.

Using a logistic regression model, we find that lymphoid cells are more similar across heart, SKM and kidney, whereas there is less concordance for myeloid cells (Extended Data Fig. 8f, Supplementary Tables 16, 19), probably due to tissue-specific adaptability of myeloid cells<sup>51</sup>. Notably, populations corresponding to cardiac monocyte-derived macrophages, *LYVE1*<sup>+</sup> MP1, *DOCK4*<sup>+</sup> MP1–2 and antigen-presenting macrophages are absent from the SKM and kidney. Cardiac *LYVE1*<sup>+</sup> MP2–3, pro-inflammatory monocytes, classical monocytes and mast cells are more similar to their SKM counterparts, indicating greater similarity of striated muscle and cardiac myeloid populations versus kidney. The transcriptional signature of cardiac *LYVE1*<sup>+</sup> MP2–3 is specific without overlap in SKM and kidney (Fig. 4c).

## Conduction system and neuronal cells

Among 3,961 cells expressing prototypic electrophysiologic transcripts (*NRXN1*, *NRXN3* and *KCNMB4*), we identify six neuronal cell subclusters (Extended Data Fig. 9a–c). NC1 constitutes 75–80% of neuronal cells and exhibits a basal gene program including *LGI4*, required for glia development and axon myelination<sup>52</sup>. NC2 and NC4 show strong expression of the central nervous system marker, *PRKG1*<sup>53</sup>, and co-express typical fibroblast and cardiomyocyte genes, respectively. NC3 has overlapping gene expression signatures with ECs. NC5 expresses *LGR5*, a Wnt signalling, G-protein-coupled receptor and stem-cell marker that promotes cardiomyocyte differentiation in the outflow tract<sup>54</sup>, an arrhythmogenic area<sup>55</sup>. This cluster also expresses the neurodegenerative disease gene *PPP2R2B*<sup>56</sup> (verified by

smFISH) (Extended Data Fig. 9d, Supplementary Table 20); *LSAMP*, which guides the development of specific patterns of neuronal connections<sup>57</sup>; and the lipoprotein transport enzyme *LPL* that remyelinates damaged neurons<sup>58</sup>. NC6 mimics Schwann cells, expressing *MBP*, *PRX* and *MPZ*, which encode myelin constituents<sup>59</sup>.

## Adipocytes

Cardiac adipocytes uniformly express *GPAM*, *FASN* and *ADIPOQ* and at lower levels, *LEP*<sup>60</sup> (Extended Data Fig. 9e–h). ADIP1 expresses genes for PPAR pathways, metabolism of lipids and lipoproteins, and lipolysis. ADIP2 expresses ECM genes such as *LAMA2*, *IGFBP7* and *FBN1*, which encodes both the glycoprotein fibrillin1 and asprosin, a white adipose tissue secreted hormone involved in glucose homeostasis (Supplementary Table 21). Given a stromal-related molecular signature, ADIP2 cells may represent fibrogenic adipocytes and/or precursors<sup>61,62</sup>. ADIP3 transcripts encode inflammatory and cytokine responsive molecules.

## COVID-19 and GWAS disease relevance

Transcripts encoding the severe acute respiratory syndrome coronavirus 2 (SARS-CoV-2) receptor *ACE2*<sup>63</sup> are highest in pericytes, followed by FBs and lowest in cardiomyocytes, where expression is twofold higher in ventricular than atrial cardiomyocytes. Among proteases priming viral entry<sup>63</sup>, *TMPRSS2* transcripts are absent in pericytes, FBs and cardiomyocytes, whereas *CTSB* and *CTSL* are lowly expressed with higher levels in cardiomyocytes. *ACE2* expression in pericytes and fibroblasts is depicted by smFISH (Extended Data Fig. 10a–e).

We define cells enriched for genes from 12 cardiovascular genome-wide association studies (GWAS) and involved in SARS-CoV-2 infection using MAGMA<sup>64</sup> (Extended Data Fig. 10f). Atrial fibrillation GWAS signals are associated with transcriptional profiles in vCM3, owing to higher mean expression of *CAV1*, *CAV2* and *PRRX1*. PR interval GWAS signals are associated with vCM3 and aCM5, with high expression of *SCN5A*, *CAV1*, *ARHGAP24*, *MEIS1*, *TBX5* and *TTN*. GWAS signals for QRS duration are associated with specific gene expression in NC2 (*PRKCA*, *CEP85L*, *SLC35F1*, *SIPA1L1*, *KLF12* and *FADS2*). Coronary artery disease and hypertension GWAS signals are associated with transcripts from many cell lineages, particularly SMCs, FBs, and ECs, reflecting the relevance of vascular cells in both disorders.

## Discussion

Our analyses of approximately half a million single cells and nuclei from six distinct cardiac regions from fourteen donors considerably expand an emerging reference adult heart cell atlas. By combining single-cell and single-nuclear RNA-seq data with machine learning and *in situ* imaging techniques, we provide detailed insights across the repertoire of cardiac cells, including cardiomyocytes (excluded by single-cell RNA-seq) and ECs (underrepresented in cardiac snRNA-seq). We quantify the cellular composition highlighting chamber-specific features and differences between male and female donors. Within each cell compartment, we identify and validate prototypic lineage-specific genes, and genes with previously unknown cardiac expression. Our results begin to unravel the molecular underpinnings of cardiac physiology and the cellular response to stress and disease.

Cardiomyocytes are the most prevalent cardiac cells and comprise higher percentages in ventricles than atria, and in female versus male ventricular tissues. Transcriptional differences between atrial and ventricular cardiomyocyte populations indicate different developmental origins, distinctive haemodynamic forces and specialized functions in cardiac chambers. Cellular diversity of FBs reveals ECM-producing and ECM-organizing activities that with other cells support cardiomyocytes across varying biophysical stimuli. The vascular compartment contains several ECs and pericyte populations and two SMC subtypes with distinct anatomical and arterio-vascular characteristics. Arterial and venous ECs are predicted to interact with mural cells via Notch signalling pathways involved in regulating vascular homeostasis and development. Immune cells interact with FBs and cardiomyocytes. In addition to confirming previous findings<sup>65,66</sup>, we show macrophage complexity and infer paracrine circuits for cardiac homeostasis. Cross-tissue analyses delineate cardiac populations distinct from skeletal muscle and kidney.

We illustrate the relevance of cardiac cell atlas by defining cell lineages enriched in cardiovascular GWAS and molecules involved in SARS-CoV-2 infection. High expression of the viral receptor *ACE2* in pericytes and its correlation with *AGTR1* is consistent with the role of renin–angiotensin–aldosterone system signalling in cardiac haemodynamics<sup>67</sup>.

We recognize limitations associated with cell capture by different data sources and unintended bias from surgical sampling. However, we expect our results will inform studies of other cardiac regions (valves, papillary muscle and conduction system), propel studies with large cohorts to determine the roles of age, gender and ancestry

on normal cardiac physiology and provide crucial insights to enable mechanistic understanding of heart disease.

## Methods

### Data reporting

No statistical methods were used to predetermine sample size. The experiments were not randomized, and investigators were not blinded to allocation during experiments and outcome assessment.

### Research ethics for donor tissues

Heart tissues (donors D1–D7 and D11) were processed at Wellcome Sanger Institute (Hinxton, UK) and obtained from deceased transplant organ donors after Research Ethics Committee approval (ref 15/EE/0152, East of England Cambridge South Research Ethics Committee) and informed consent from the donor families. Heart tissues (donors H2–H7) were processed at Harvard Medical School (Boston, Massachusetts, USA) and obtained from deceased organ donors after Human Research Ethics Board approval Pro00011739 (University of Alberta, Edmonton, Canada). Informed consent from donor families was acquired via the institutional Human Organ Procurement and Exchange Program (HOPE). Cardiovascular history was unremarkable for all donors (Supplementary Table 1).

### Tissue acquisition and processing

Tissues were acquired from UK and North American donors (D1–7 and 11, H2–7) after circulatory death (DCD) (D2, D4–D7 and D11) and after brain death (DBD) (D1, D3, H2–H7). For UK DCD donors, after a five-minute stand-off and for DBD, the chest is opened, the aorta is cross-clamped and cardiac samples are acquired. For North American DBD donors, the aorta is cross-clamped, cold cardioplegia (Celsior) is administered under pressure via the aorta to arrest beating, the heart is excised, rinsed in cold saline and samples acquired. All donor samples were full-thickness myocardial biopsies from the left and right atrium, left and right ventricles, interventricular septum and apex, with intentional exclusion of large epicardial fat deposits. Samples used for single nuclei isolation were flash-frozen and stored at –80 °C. Single-cell isolation and CD45<sup>+</sup> enrichment was carried out on freshly collected samples. Residual tissue after nuclei and cell isolation procedures was formalin-fixed or frozen in OCT for additional studies.

All tissues were stored and transported on ice at all times until freezing or tissue dissociation to minimise any transcriptional degradation. Previous studies on the post-mortem tissue stability of the GTEx consortium on bulk tissues<sup>68</sup> and in single cells<sup>69</sup> suggest only minor changes in tissues within the first 24 h post mortem when stored in cold conditions.

## Single nuclei isolation

Single nuclei were obtained from flash-frozen tissues using mechanical homogenization as previously described<sup>70</sup>. Tissues were homogenized using a 7 ml glass Dounce tissue grinder set (Merck) with 8–10 strokes of a loose pestle (A) and 8–10 strokes of a tight pestle (B) in homogenization buffer (250 mM sucrose, 25 mM KCl, 5 mM MgCl<sub>2</sub>, 10 mM Tris-HCl, 1 mM dithiothreitol (DTT), 1× protease inhibitor, 0.4 U  $\mu\text{l}^{-1}$  RNaseIn, 0.2 U  $\mu\text{l}^{-1}$  SUPERaseIn, 0.1% Triton X-100 in nuclease-free water). Homogenate was filtered through a 40- $\mu\text{m}$  cell strainer (Corning). After centrifugation (500*g*, 5 min, 4 °C) the supernatant was removed and the pellet was resuspended in storage buffer (1× PBS, 4% bovine serum albumin (BSA), 0.2 U  $\mu\text{l}^{-1}$  Protector RNaseIn). Nuclei were stained with NucBlue Live ReadyProbes Reagents (ThermoFisher) and Hoechst-positive single nuclei were purified by fluorescent activated cell sorting (FACS) using influx, XDP or FACSaria (BD Biosciences) (Supplementary Fig. 1). Nuclei purification and integrity was verified under a microscope, and nuclei were further processed using the Chromium Controller (10X Genomics) according to the manufacturer's protocol.

## Single-cell preparation

Heart tissues (0.2–0.9 g) were transferred from cardioplegic solution into gentleMACS C-tubes (Miltenyi Biotec) containing enzymatic digestion base solution (100  $\mu\text{g ml}^{-1}$  liberase TH Research grade and 50  $\mu\text{g ml}^{-1}$  DNase I, HBSS 10 mM HEPES and 30 mM taurine)<sup>71</sup>. Tissues were minced using scissors (FST) and automatically digested using gentleMACS Octo Dissociator (Miltenyi Biotec) with heaters. Cardiomyocyte-depleted single-cell suspension were washed with base solution containing 20% fetal bovine serum (FBS) (Gibco), filtered through 70- $\mu\text{m}$  nylon strainer (BD Falcon), collected by centrifugation (330*g*, 10 min, 4 °C) and resuspended in base solution containing 0.2% FBS (Gibco). Cells were manually counted three times by Trypan blue exclusion after each centrifugation and resuspended at a concentration of at least  $2 \times 10^6 \text{ ml}^{-1}$ . Single cells were processed using Chromium Controller (10X Genomics) according to the manufacturer's protocol.

## **CD45<sup>+</sup> cell enrichment**

Cell suspension was prepared as described above and subsequently labelled using anti-human CD45 monoclonal antibody-conjugated microbeads according to the manufacturer's protocol (Miltenyi Biotec). In brief, up to 10<sup>7</sup> cells were incubated for 15 min at 4 °C in 80 µl of PBS, BSA, EDTA buffer (1× PBS pH 7.2, 0.5% BSA, 2 mM EDTA) containing 20 µl CD45 microbeads. Cell suspension was washed in PBS, BSA, EDTA buffer once and collected by centrifugation (330g, 10 min, 4 °C). Resuspended cells were applied to MACS LS columns (Miltenyi Biotec). CD45-depleted cell fraction was discarded after three washes with PBS, BSA and EDTA buffer and the CD45<sup>+</sup> cell fraction was collected in PBS, BSA and EDTA buffer by removal of the columns from the magnetic field. CD45<sup>+</sup> cells were counted and resuspended in PBS, BSA and EDTA buffer to a concentration of at least 2 × 10<sup>6</sup> per ml before further processing using a Chromium Controller (10X Genomics) according to the manufacturer's protocol.

## **Chromium 10X library preparation**

Single cells and nuclei were manually counted by Trypan blue exclusion or automatically using a Countess II (Life Technologies) using at least two separate counts. Cell or nuclei suspension was adjusted to 400–1,000 cells per microlitre and loaded on the Chromium Controller (10X Genomics) with a targeted cell or nuclei recovery of 4,000–10,000 per reaction. 3' gene expression libraries were prepared according to the manufacturer's instructions of the v2 or v3 Chromium Single Cell Reagent Kits (10X Genomics). Quality control of cDNA and final libraries was done using Bioanalyzer High Sensitivity DNA Analysis (Agilent) or 4200 TapeStation System (Agilent). Libraries were sequenced using HiSeq 4000 (Illumina) at Wellcome Sanger Institute, and NextSeq 500 (Illumina) at Harvard Medical School with a minimum depth of 20,000–30,000 read pairs per cell or nucleus (Supplementary Table 22).

## **Spatial validation using smFISH with RNAscope probes**

During preparation of formalin-fixed paraffin-embedded (FFPE) samples fresh tissue was fixed in neutral-buffered 10% formalin for 18–36 h and subsequently embedded in paraffin blocks. Fixed-frozen tissue samples were fixed in 4% paraformaldehyde (ThermoFisher). Sections were cut at 5-µm thickness using a microtome and placed onto SuperFrost Plus slides (VWR). FFPE tissue slides were automatically stained using BOND RX (Leica) and the RNAscope Multiplex Fluorescent Reagent Kit v2 Assay (ACDBio) according to the manufacturer's

protocol. Fixed-frozen tissue slides were processed according to the protocol of RNAscope Multiplex Fluorescent Assay v1 (ACDBio). RNAscope ready- or custom-made target probes were run in parallel to multiplex positive and negative controls (Extended Data Fig. [12b](#), Supplementary Table [23](#)). All nuclei were DAPI-stained. All FFPE tissue slides were imaged using an Opera Phenix High-Content confocal Screening System (Perkin Elmer) with a 1- $\mu\text{m}$  z-step size and 20 $\times$  water-immersion objective (NA 0.16, 0.299  $\mu\text{m}$  per pixel). Channels: DAPI (excitation 375 nm, emission 435–480 nm), Atto 425 (excitation 425 nm, emission 463–501 nm), opal 520 (excitation 488 nm, emission 500–550 nm), opal 570 (excitation 561 nm, emission 570–630 nm), opal 650 (excitation 640 nm, emission 650–760 nm). Fixed-frozen tissue slides were imaged using a LSM710 confocal microscope (Zeiss) and 40 $\times$  oil-immersion objective (1.3 oil, DIC III). Channels: DAPI (excitation 375 nm, emission 435–480 nm), Alexa Fluor 488 (excitation 492 nm, emission 517 nm), Atto 550 (excitation 560 nm, emission 575 nm) and Atto 647 (excitation 649 nm, emission 662 nm). Visualization and background removal (rolling ball radius) were done using Fiji/ImageJ<sup>[72](#)</sup>. Pseudocolours were used for better visualization.

## Haematoxylin and eosin staining

Tissue samples were fresh-frozen in isopentane (ThermoFisher) at -80 °C and embedded in OCT (VWR). Sections were cut at a thickness of 10  $\mu\text{m}$  using a microtome, placed onto SuperFrostPlus slides (VWR) and further processed according to a standard haematoxylin and eosin staining protocol (Extended Data Fig. [12a](#)).

## Acquisition of skeletal muscle tissue

Intercostal muscle samples were obtained from between the second and third rib on the left side. This is typically from the deepest layer of muscle (furthest away from the skin). Samples were collected directly into the cold preservation solution.

## Nuclei isolation for skeletal muscle

Muscle tissue was washed in 1 $\times$  PBS, cleaned of any visible fat depositions and minced to obtain fragments of approximately 1  $\text{mm}^3$ . Per sample, approximately 0.3 g of minced tissues was homogenized in 3 ml of buffer A (250 mM sucrose, 10 mg  $\text{ml}^{-1}$  BSA, 5 mM MgCl<sub>2</sub>, 0.12 U  $\mu\text{l}^{-1}$  RNaseIn, 0.06 U  $\mu\text{l}^{-1}$  SUPERasIn, 1 $\times$  protease inhibitor) using Dounce tissue grinder set (Merck) with 50 strokes of the loose pestle (A). The homogenate was filtered through a 100- $\mu\text{m}$  cell strainer

(Corning) and the strainer was washed with 1 ml and then 750 µl of buffer A. After the addition of Triton X-100 (final concentration 0.5%), the mixture was further homogenized with 50 strokes of the tight pestle (B). After filtering through a 40-µm strainer, nuclei were centrifuged (3,000*g*, 5 min, 4 °C), resuspended in 1 ml of buffer B (320 mM sucrose, 10 mg ml<sup>-1</sup> BSA, 3 mM CaCl<sub>2</sub>, 2 mM magnesium acetate, 0.1 mM EDTA, 10 mM Tris-HCl, 1 mM DTT, 1× protease inhibitor, 0.12 U µl<sup>-1</sup> RNaseIn, 0.06 U µl<sup>-1</sup> SUPERasin) and purified using a 27% Percoll gradient solution. The Percoll mixture was centrifuged at 20,000*g* (15 min, 4 °C) and the pellet was resuspended in 200 µl of buffer B, followed by centrifugation (20,000*g*, 3 min, 4 °C). After Trypan Blue staining, the intact nuclei were counted using a haemocytometer. Nuclei were profiled using a Chromium Controller (10X Genomics) according to the manufacturer's protocol.

## Single-cell isolation for skeletal muscle

Muscle tissue was washed in 1× PBS, cleaned of any visible fat depositions and finely minced. Then, 2 g of the minced tissue was transferred to digestion buffer 1 (750 U ml<sup>-1</sup> collagenase type 2 in 1× PBS) and incubated at 37 °C in a water bath for 90 min. The partially digested tissue was collected by centrifugation (650*g*, 5 min, 4 °C) and the pellet was resuspended in digestion buffer 2 (100 U ml<sup>-1</sup> collagenase type 2, 2 U ml<sup>-1</sup> dispase in PBS). After 30 min incubation at 37 °C in a water bath, the digestion was stopped by the addition of 2% FBS. Cells were filtered through a 100-µm and a 40-µm nylon strainer (BD Falcon), collected by centrifugation (650*g*, 4 °C, 3 min) and washed with 1× PBS, 2% FBS. Subsequently, a 20% Percoll gradient (15,000*g*, 4 °C, 20 min) was used for cell purification. The layer containing cells was collected, washed in PBS containing 2% FBS, and viable cells were counted by Trypan Blue exclusion using a haemocytometer. Nuclei were profiled using a Chromium Controller (10X Genomics) according to the manufacturer's protocol.

The methods key resources table is in Supplementary Table [24](#).

## Transcriptome mapping

After sequencing, samples were demultiplexed and stored as CRAM files. Each sample was mapped to the human reference genome (GRCh38 v.3.0.0) provided by 10X Genomics, and using the CellRanger suite (v.3.0.1) with default parameters. Single-cell samples were mapped against the reference as it was provided. Single-nuclei samples, the reference for pre-mRNA, was created using the 10X Genomics

instructions (<https://support.10xgenomics.com/single-cell-gene-expression/software/pipelines/latest/advanced/references>).

## Count data processing

After mapping, samples from each data source (single nuclei, single cell and CD45<sup>+</sup> cell) were grouped into individual AnnData objects by concatenating the raw\_feature\_bc\_matrix\_h5.h5 and adding the appropriate metadata information. For each data source object, the mean of unique molecular identifiers (UMIs) (n\_counts) was calculated and used as a threshold for empty droplets.

## Doublet detection

After removal of empty droplets, we applied scrublet<sup>73</sup> to assign a doublet score (scrublet\_score) to each cell. These cells were clustered and visualized using the UMAP method<sup>74</sup>. In addition, each cell was processed for doublet detection using a percolation method to allow for improved detection of doublets<sup>75</sup>.

## Cell quality control and filtering

Each data source was processed and annotated separately to account for source-specific quality differences. These metrics are included as covariates for further processing. Total cells and CD45<sup>+</sup> cells were filtered for counts (500 < n\_counts <15,000), genes (200 < n\_genes), mitochondrial genes (percent\_mito <20%), ribosomal genes (percent\_ribo <20%) and scrublet score (scrublet\_score <0.3). Single nuclei were filtered for counts (500 < n\_counts <15,000), genes (300 < n\_genes <6,000), mitochondrial genes (percent\_mito <5%), ribosomal genes (percent\_ribo <5%) and scrublet score (scrublet\_score <0.3). The same filtering thresholds were applied to the skeletal muscle dataset.

Scanpy toolkit 1.5<sup>76</sup> in Python v.3.7 was used to perform downstream analyses, including normalization (normalize\_per\_cell: counts\_per\_cell\_after = 10,000), log transformation (log1p), variable gene detection (highly\_variable\_genes), regressing out unwanted sources of variation (regress\_out: n\_counts and percent\_mito), data feature scaling (scale: max\_value = 10) and PCA (pca: using highly variable genes) as previously described<sup>77</sup>.

## Batch alignment using deep variational autoencoder

We built a global manifold by aligning all the data sources and donors in our data. This was done in a three-step procedure: (1) Each source was analysed and annotated separately, aligning only for donors using a pericyte-space linear regression step before batch alignment with bbknn<sup>78</sup>. Differentially expressed genes (DEGs) were calculated using a Wilcoxon rank sum test with Bonferroni–Hochberg adjustment as implemented in the Scanpy framework. (2) To annotate each cluster, we used an integrative approach by searching the top significant DEGs ( $P < 1 \times 10^{-5}$ ) with a logFC  $> 1$  against the ToppFun<sup>79</sup> and EnrichR<sup>80</sup> databases. Significant hits on pathways, transcriptional regulation and biological processes were prioritized to annotate a given cluster. Each cellular compartment was labelled under the adata.obs[‘cell\_type’] slot after grouping source-specific cell states. (3) All sources were combined into a single AnnData object under the label adata.obs[‘cell\_sources’]. Batches were aligned using the batch\_correction function from the scGen variational autoencoder<sup>81</sup>. First we align for adata.obs[‘cell\_sources’], using adata.obs[‘cell\_type’] as an anchor. Next, we aligned for adata.obs[‘donor’], using adata.obs[‘cell\_type’] as an anchor. Each batch alignment round was run for 50 epochs.

Manifolds for the adipocytes, vascular and immune cardiac populations, as well as the skeletal muscle analysis, were created using this method and the clustering accuracy was evaluated with SCCAF<sup>82</sup> (Extended Data Fig. 12d).

## DEGs

To help with the annotation of the subpopulations of each cell compartment, we calculated the DEGs using the Wilcoxon rank sum test as implemented in the scanpy workflow and recommended by recent benchmarking studies<sup>83</sup>. A gene was considered to be differentially expressed if it has a log<sub>2</sub>-transformed fold change  $> 1$  and a  $P < 1 \times 10^{-5}$ , unless stated otherwise in the analysis section.

## Cell–cell interactions

Expression matrices of the populations under study were exported from the AnnData, together with a metadata table that contained the cell-barcodes as indices. We then ran CellPhoneDB as follows: cellphonedb method statistical\_analysis meta.tsv counts.tsv=counts-data = gene\_name\_threads = 60. CellPhoneDB raw predictions were filtered by removing those interactions with a  $P > 1.0 \times 10^{-5}$ . Significant pairs were then submitted for gene set enrichment analysis into ReactomeDB, enrichR and ToppFun for functional classification. The vascular cells were randomly sub-sampled to 39,000 cells before the analysis, and the cardiac

repair group (atrial and ventricular cardiomyocytes, FBs, and immune cells) was randomly sub-sampled to 69,295 cells before the analysis.

## Visualization of gene expression on 10X Genomics Visium data

We processed the publicly available left ventricular myocardium Visium data from 10X Genomics ([https://support.10xgenomics.com/spatial-gene-expression/datasets/1.0.0/V1\\_Human\\_Heart](https://support.10xgenomics.com/spatial-gene-expression/datasets/1.0.0/V1_Human_Heart)) using the Scanpy v.1.5 workflow adapted for the analysis of 10X Genomics Visium data (<https://scanpy-tutorials.readthedocs.io/en/latest/spatial/basic-analysis.html>). In brief, spots were removed with less than 500 UMIs or more than 20,000 UMIs, and less than 200 genes. Data were log-transformed and normalized before plotting.

## Estimation of RNA velocity

To calculate the RNA velocity of the single cells and CD45<sup>+</sup> enriched single cells, we used the CellRanger output BAM file and the GENCODE v33 GTF (ftp://ftp.ebi.ac.uk/pub/databases/gencode/Gencode\_human/release\_33/gencode.v33.chr\_patch\_hapl\_scaff.annotation.gtf.gz) file together with the velocyto<sup>84</sup> CLI v.0.17.17 to generate a loom file containing the quantification of spliced and unspliced RNA. Next, we built a manifold, cluster the cells and visualize the RNA velocities using scVelo<sup>85</sup>.

## Subpopulation analyses of atrial and ventricular cardiomyocytes, FBs and neuronal cells

All barcodes labelled in the global object as cardiomyocytes, fibroblasts and neural cells were selected for further subpopulation analyses. Additional cell population-specific filtering criteria were applied to nuclei as follows: cardiomyocyte counts (n\_counts <12,500), genes (n\_genes <4,000), mitochondrial genes (percent\_mito <1%), ribosomal genes (percent\_ribo <1%) and scrublet score (scrublet\_score <0.25); FB mitochondrial genes (percent\_mito <1%), ribosomal genes (percent\_ribo <1%); neuronal cell genes (n\_genes <4000), mitochondrial genes (percent\_mito <1%), ribosomal genes (percent\_ribo <1%). Total and CD45<sup>+</sup> cells were excluded in the atrial and ventricular cardiomyocytes datasets and did not contribute to subpopulation analysis. No further filtering of FBs or neuronal cell total and CD45<sup>+</sup> cells was applied. Cardiomyocytes and FBs were then further split into two groupings based on the region of origin: (1) left and right atrium, and (2) left and right ventricles, apex and interventricular septum.

Donor effects were aligned as described in step (1) above. For FB and neuronal cells, sources were aligned as described in step (3) above. Leiden clustering and UMAP visualization were performed for identifying subpopulations and visualization<sup>86</sup>. Differentially expressed genes were calculated using the Wilcoxon rank sum test. Genes were ranked by score.

## Cross-tissue comparison of cardiac immune populations with skeletal muscle, kidney and blood immune populations

We collected single-cell transcriptome data for adult kidneys from ref. <sup>99</sup> (<https://www.kidneycellatlas.org/>), and subset all immune cells reported in their study. For the SKM we selected the annotated immune cells from the merged manifold. For the human blood, we used the publicly available 10,000 single PBMC cells dataset provided by 10X Genomics ([https://support.10xgenomics.com/single-cell-gene-expression/datasets/3.0.0/pbmc\\_10k\\_v3](https://support.10xgenomics.com/single-cell-gene-expression/datasets/3.0.0/pbmc_10k_v3)). As previously described<sup>87</sup>, we trained a logistic regression model on the cardiac immune cells using 80% of the expression data and tested its accuracy on the remaining 20% to produce a model with an accuracy of 0.6862 (Extended Data Fig. 8f, Supplementary Table 16). We then applied this model to predict analogue cardiac immune populations in the adult kidney, SKM and PBMCs. Predictions with a probability less than 0.8 were excluded from downstream comparative analyses.

## Gene Ontology enrichment analysis

For the ventricular cardiomyocyte population, we used the R package gProfileR (<https://cran.r-project.org/web/packages/gProfileR/index.html>) with the score-ranked gene list of vCM4 as input and the set of genes expressed in ventricular cardiomyocytes as background (those genes having a UMI count >1). To perform the Gene Ontology analysis on the vascular cells, the top 500 significant DEGs ( $P < 1 \times 10^{-5}$ ) with a log-transformed fold change  $> 1$  were searched against the Gene Ontology biological process database using ToppFun<sup>79</sup> (Supplementary Table 25). The top five significantly enriched terms ( $q < 0.05$ ) for each subpopulation were selected and plotted on a heat map. To perform the pathway analysis on the adipocytes, the top 500 significant DEGs ( $P < 1 \times 10^{-5}$ ) with a log-transformed fold change  $> 0.5$  were searched against ToppFun<sup>79</sup> pathway databases (Supplementary Table 26). The top five significantly enriched pathways ( $q < 0.05$ ) for each subpopulation were selected and plotted on a heat map.

## Gene set score

We use the score\_genes function as implemented in scanpy to calculate the enrichment of genes involved in the Oncostatin M pathway. A list of genes was collected upon literature research<sup>88,89</sup>. For gene set enrichment, only highly expressed genes were considered to reduce noise (more than 500 UMIs across all cells). The same analysis was performed for comparison of cardiac immune cells in our study with the observations of previous studies on cardiac-resident macrophages<sup>51</sup>, mouse tissue-remodelling macrophage<sup>45</sup> and yolk sac lineage origin<sup>90</sup>.

## Statistics and reproducibility

All analyses were performed using R Software, v.3.6.1. Student's *t*-tests were used to compare cell type distributions at each site.  $P < 0.05$  was considered statistically significant. Linear regression models (correlations) were obtained using the R linear model function (lm), which estimates statistical likelihood ( $P$  value) of a linear relationship. Bonferroni correction was applied for multiple testing.

The depicted RNAscope micrographs in the figures are representative. The micrographs in Figs. 2g, 3c, h and Extended Data Fig. 3c (HAMP), Extended Data Fig. 3e (CNN1), Extended Data Figs. 4g, m, 6f were repeated with similar results in two individual tissue sections. The micrographs in Figs. 2h, 3f and Extended Data Fig. 3c (CNN1), Extended Data Fig. 3e (PCDH7), Extended Data Figs. 6e, h, 9d were repeated with similar results in three individual tissue sections. The micrographs in Figs. 1e, 2d, 3e and Extended Data Figs. 1f, 3c (FHL1) and Extended Data Fig. 6d were repeated with similar results in four individual tissue sections. The micrographs in Fig. 2c and Extended Data Fig. 3c (PRELID2), Extended Data Figs. 10e, 12a were repeated with similar results in six or more individual tissue sections. Positive and negative controls were done once per used samples.

## GWAS enrichment analysis

We downloaded GWAS summary statistics from broad cvdi, EBI GWAS catalogue and GWAS atlas. We selected traits with well-powered GWAS ( $n > 5,000$  and number of significant loci  $> 10$ ). GWAS datasets are summarized in Supplementary Table 27. Gene expression data of protein-coding genes were mapped onto Entrez gene ids and these gene annotations were used on the human genome assembly hg19/37. We only used gene expression data from nuclei. We implemented the analysis previously described<sup>64</sup> in python and in R. The log-transformed counts (plus one pseudocount) were used to compute average cell type-specific expression profiles. We performed individual magma analyses for each cell type, always

conditioning on default gene level covariates (for example, gene length) and average gene expression across all cells. Subsequently, we applied the Benjamini–Hochberg method and selected cell type trait associations with FDR < 10%. These pairs were then subjected to conditional analysis as previously described<sup>64</sup> to define ‘independent’, ‘jointly explained’ and ‘partially jointly explained’ pairs of associations (Supplementary Table 28).

## Distributions of dispersed cells and isolated nuclei

The different procedures for obtaining isolated nuclei and dispersed cells resulted in significantly different distributions of cell types (Supplementary Table 29, Extended Data Fig. 2). Notably, 30.1% and 49.2% of isolated nuclei were derived from atrial and ventricular cardiomyocytes in the atrial and ventricular regions, whereas these cells were mostly excluded from preparations of isolated and CD45-selected cells (Supplementary Table 2).

Excluding cardiomyocytes, the distribution of cell types identified from isolated nuclei and dispersed cells remained distinct (Supplementary Table 30). Although 59.0% of dispersed cells were ECs, only 15.7% of nuclei were derived from ECs. By contrast, 64.2% of nuclei were from FBs (31.2%) and pericytes (33.0%), whereas only 17.1% of dispersed cells were FBs (2.3%) and pericytes (14.8%). These differences may reflect sensitivity of EC nuclei to isolation procedures or resistance of pericytes and FBs to cellular enzymatic digestion.

Despite differences in cell distributions between isolated nuclei and dispersed cells, the gene expression profiles of cell lineages were reasonably correlated ( $r > 0.4$  for each cell type). To address the concordance of the genes captured by cells and nuclei, we compared the expression of the major cell type markers from Fig. 1c across the three sources (Extended Data Fig. 1c). As nuclei lack cytoplasmic RNA, the expression of certain genes, especially immune genes *NKG7* and *C1QA*, was lower in nuclei than in cells. Nevertheless, the general trend with respect to marker genes was consistent across the three sources, and the same genes distinguished individual cell types independent of the source.

## Further analysis of vascular cells

The PC3\_str contained similar contribution of cells and nuclei, and had a scrublet score below the stringent threshold used; nevertheless, the average number of genes and counts in this cluster was higher than average. Thus, despite our stringent quality filtering, we cannot exclude the possibility that there might be doublets in this cluster. EC10\_CMC-like and PC4\_CMC-like co-express EC or pericyte genes with cardiomyocyte markers and further studies are required to understand whether they represent previously unknown cell states or doublets.

The observations of the arterial and venous SMC are supported by previous studies, which predict that arterial SMCs are more contractile, and venous SMCs are less differentiated<sup>[91](#)</sup>.

EC3\_cap enrich for transcripts encoding components of AP1 (*JUN* and *FOS*), which mediates multiple EC fate decisions including response to VEGF, inflammatory and stress signals, and *ATF3*, an adaptive-response gene induced by diverse signals<sup>[92,93,94](#)</sup>.

## Skeletal muscle characterization

We collected intercostal skeletal muscle samples from five healthy individuals, including one donor with matched cardiac tissue, and profiled the transcriptome of 35,665 single cells and 39,597 single nuclei. Analogous to the heart, the combination of cells and nuclei allowed us to capture and resolve major cell lineages, including cardiomyocyte, fibroblasts, endothelial cells, smooth muscle cells, pericytes, myeloid and lymphoid immune cells and satellite cells (Extended Data Fig. [11a,b](#), Supplementary Table [31](#)).

Further analysis of the vascular cells of the skeletal muscle identified ten distinct populations. The endothelial cells showed five clusters separated based on their respective vascular beds with signatures similar to the ones we observe in the heart. The EC\_cap expresses *VWF* and *RGCC*. Venous EC\_ven express *ACKR1* and *PLVAP*, whereas arterial EC\_art show

*SEMA3G* and *HEY1*, in line with our heart data (Extended Data Fig. [11c, d](#), Supplementary Table [32](#)).

The overall distributions of vascular and stromal cell populations in skeletal and cardiac muscle were similar, including the arterial and venous features of ECs; however; skeletal muscle contained a single SMC cluster, potentially related to the smaller size of the dataset. In skeletal muscle, the predicted cell–cell interactions of the EC\_art and SMCs included NOTCH1/4–JAG1 as well as JAG1/JAG2/DLL4–NOTCH3, but not JAG1/JAG2/DLL4–NOTCH2, inferred in the heart (Extended Data Fig. [11e, f](#), Supplementary Table [33](#)).

## Cardiac immune cells

Using the logistic regression model, we did not identify any counterpart of the cardiac *IL17RA*<sup>+</sup> monocytes in SKM or kidney, possibly owing to the small size of this population.

Naive T cells (CD4+T\_naive) identified expressed *CCR7* and *SELL*, indicative of their naive and tissue-resident nature<sup>[95](#)</sup>. Memory T cells (CD8+T\_tem) expressed *BACH2*, *STAT4* and *IL7R*, associated with long-term immune memory<sup>[96,97](#)</sup>. We further characterized the lymphoid cells using scNym<sup>[98](#)</sup>, and trained it using published data<sup>[99,100](#)</sup>. The resulting model was applied to our cardiac immune cells and those cells, with a predicted score higher than 0.8 were presumed to be likely candidates for re-annotation. Using this approach, we identified candidates for plasma B cells (109), dendritic cells (645), innate lymphoid cells (89), MAIT T cells (219), T helper cells (80) T regulatory cells (11), T central memory cells (103),  $\gamma\delta$  T cells (30) and plasmacytoid dendritic cells (27). These annotations can be found in the cardiac immune object annotations under the label ‘scNym’ at [www.heartcellatlas.org](http://www.heartcellatlas.org).

## Reporting summary

Further information on research design is available in the [Nature Research Reporting Summary](#) linked to this paper.

## Data availability

Data objects with the raw counts matrices and annotation are available via the www.heartcellatlas.org webportal. Raw data are available through the Human Cell Atlas (HCA) Data Coordination Platform (DCP) with accession number: ERP123138

(<https://www.ebi.ac.uk/ena/browser/view/ERP123138>). The 10X Genomics Visium data for the heart left ventricle tissue can be accessed at: [https://support.10xgenomics.com/spatial-gene-expression/datasets/1.1.0/V1\\_Human\\_Heart](https://support.10xgenomics.com/spatial-gene-expression/datasets/1.1.0/V1_Human_Heart). GWAS data used in this study can be found in [Supplementary Table 27](#). All of our data can be explored at [www.heartcellatlas.org](http://www.heartcellatlas.org).

## Code availability

All code used for this study can be accessed as Jupyter notebooks in the project GitHub repository: [https://github.com/cartal/HCA\\_Heart](https://github.com/cartal/HCA_Heart).

# References

1. 1.

Meilhac, S. M. & Buckingham, M. E. The deployment of cell lineages that form the mammalian heart. *Nat. Rev. Cardiol.* **15**, 705–724 (2018).

[PubMed](#) [Google Scholar](#)

2. 2.

Svensson, V., Vento-Tormo, R. & Teichmann, S. A. Exponential scaling of single-cell RNA-seq in the past decade. *Nat. Protocols* **13**, 599–604 (2018).

[CAS](#) [PubMed](#) [Google Scholar](#)

3. 3.

Wang, L. et al. Single-cell reconstruction of the adult human heart during heart failure and recovery reveals the cellular landscape underlying cardiac function. *Nat. Cell Biol.* **22**, 108–119 (2020).

[CAS](#) [PubMed](#) [Google Scholar](#)

4. 4.

Tucker, N. R. et al. Transcriptional and cellular diversity of the human heart. *Circulation* **142**, 466–482 (2020).

[CAS](#) [PubMed](#) [Google Scholar](#)

5. 5.

Chung, A. K. et al. Women have higher left ventricular ejection fractions than men independent of differences in left ventricular volume: the Dallas Heart Study. *Circulation* **113**, 1597–1604 (2006).

[PubMed](#) [Google Scholar](#)

6. 6.

Johnson, E. K., Matkovich, S. J. & Nerbonne, J. M. Regional differences in mRNA and lncRNA expression profiles in non-failing human atria and ventricles. *Sci. Rep.* **8**, 13919 (2018).

[ADS](#) [PubMed](#) [PubMed Central](#) [Google Scholar](#)

7. 7.

Delplancq, G. et al. Cardiomyopathy due to PRDM16 mutation: first description of a fetal presentation, with possible modifier genes. *Am. J. Med. Genet. C. Semin. Med. Genet.* **184**, 129–135 (2020).

[CAS](#) [PubMed](#) [Google Scholar](#)

8. 8.

Kim, S.-Y., Yasuda, S., Tanaka, H., Yamagata, K. & Kim, H. Non-clustered protocadherin. *Cell Adhes. Migr.* **5**, 97–105 (2011).

[Google Scholar](#)

9. 9.

Donlin, L. T. et al. Smyd2 controls cytoplasmic lysine methylation of Hsp90 and myofilament organization. *Genes Dev.* **26**, 114–119 (2012).

[CAS](#) [PubMed](#) [PubMed Central](#) [Google Scholar](#)

10. 10.

Mazzotta, S. et al. Distinctive roles of canonical and noncanonical Wnt signaling in human embryonic cardiomyocyte development. *Stem Cell Reports* **7**, 764–776 (2016).

[CAS](#) [PubMed](#) [PubMed Central](#) [Google Scholar](#)

11. 11.

Shenton, F. C. & Pyner, S. Expression of transient receptor potential channels TRPC1 and TRPV4 in venoatrial endocardium of the rat heart. *Neuroscience* **267**, 195–204 (2014).

[CAS](#) [PubMed](#) [Google Scholar](#)

12. 12.

Gao, M. et al. Conserved expression of the PRELI domain containing 2 gene (Prelid2) during mid-later-gestation mouse embryogenesis. *J. Mol. Histol.* **40**, 227–233 (2009).

[CAS](#) [PubMed](#) [Google Scholar](#)

13. 13.

Putku, M. et al. CDH13 promoter SNPs with pleiotropic effect on cardiometabolic parameters represent methylation QTLs. *Hum. Genet.* **134**, 291–303 (2015).

[CAS](#) [PubMed](#) [Google Scholar](#)

14. 14.

Liu, R. & Jin, J.-P. Calponin isoforms CNN1, CNN2 and CNN3: regulators for actin cytoskeleton functions in smooth muscle and non-muscle cells. *Gene* **585**, 143–153 (2016).

[CAS](#) [PubMed](#) [PubMed Central](#) [Google Scholar](#)

15. 15.

Besnard, S. et al. Smooth muscle dysfunction in resistance arteries of the staggerer mouse, a mutant of the nuclear receptor ROR $\alpha$ . *Circ. Res.* **90**, 820–825 (2002).

[CAS](#) [PubMed](#) [Google Scholar](#)

16. 16.

Mikhailov, A. T. & Torrado, M. The enigmatic role of the ankyrin repeat domain 1 gene in heart development and disease. *Int. J. Dev. Biol.* **52**, 811–821 (2008).

[CAS](#) [PubMed](#) [Google Scholar](#)

17. 17.

Kwapiszewska, G. et al. Fhl-1, a new key protein in pulmonary hypertension. *Circulation* **118**, 1183–1194 (2008).

[CAS](#) [PubMed](#) [Google Scholar](#)

18. 18.

Geng, T. et al. H19 lncRNA promotes skeletal muscle insulin sensitivity in part by targeting AMPK. *Diabetes* **67**, 2183–2198 (2018).

[CAS](#) [PubMed](#) [PubMed Central](#) [Google Scholar](#)

19. 19.

Huang, L. et al. Critical roles of Xirp proteins in cardiac conduction and their rare variants identified in sudden unexplained nocturnal death syndrome and Brugada syndrome in Chinese Han population. *J. Am. Heart Assoc.* **7**, e006320 (2018).

[PubMed](#) [PubMed Central](#) [Google Scholar](#)

20. 20.

Fittipaldi, S. et al. Alpha B-crystallin induction in skeletal muscle cells under redox imbalance is mediated by a JNK-dependent regulatory mechanism. *Free Radic. Biol. Med.* **86**, 331–342 (2015).

[CAS](#) [PubMed](#) [Google Scholar](#)

21. 21.

Rajakumari, S. et al. EBF2 determines and maintains brown adipocyte identity. *Cell Metab.* **17**, 562–574 (2013).

[CAS](#) [PubMed](#) [PubMed Central](#) [Google Scholar](#)

22. 22.

2016 AHA late-breaking basic science abstracts. *Circ. Res.* **119**, e160–e171 (2016).

23. 23.

Bolotta, A. et al. New insights into the hepcidin-ferroportin axis and iron homeostasis in iPSC-derived cardiomyocytes from Friedreich's ataxia patient. *Oxid. Med. Cell. Longev.* **2019**, 7623023 (2019).

[PubMed](#) [PubMed Central](#) [Google Scholar](#)

24. 24.

Lakhal-Littleton, S. et al. An essential cell-autonomous role for hepcidin in cardiac iron homeostasis. *eLife* **5**, e19804 (2016).

[PubMed](#) [PubMed Central](#) [Google Scholar](#)

25. 25.

Medioni, C. et al. Expression of Slit and Robo genes in the developing mouse heart. *Dev. Dyn.* **239**, 3303–3311 (2010).

[CAS](#) [PubMed](#) [PubMed Central](#) [Google Scholar](#)

26. 26.

Lee, J. H., Protze, S. I., Laksman, Z., Backx, P. H. & Keller, G. M. Human pluripotent stem cell-derived atrial and ventricular

cardiomyocytes develop from distinct mesoderm populations. *Cell Stem Cell* **21**, 179–194.e4 (2017).

[CAS](#) [PubMed](#) [Google Scholar](#)

27. 27.

Liu, C., Luo, N., Tung, C.-Y., Perrin, B. J. & Zhao, B. GRXCR2 regulates taperin localization critical for stereocilia morphology and hearing. *Cell Rep.* **25**, 1268–1280.e4 (2018).

[CAS](#) [PubMed](#) [PubMed Central](#) [Google Scholar](#)

28. 28.

Liu, X. et al. Single-cell RNA-Seq of the developing cardiac outflow tract reveals convergent development of the vascular smooth muscle cells. *Cell Rep.* **28**, 1346–1361.e4 (2019).

[CAS](#) [PubMed](#) [Google Scholar](#)

29. 29.

Kalucka, J. et al. Single-cell transcriptome atlas of murine endothelial cells. *Cell* **180**, 764–779.e20 (2020).

[CAS](#) [PubMed](#) [Google Scholar](#)

30. 30.

Pober, J. S., Merola, J., Liu, R. & Manes, T. D. Antigen presentation by vascular cells. *Front. Immunol.* **8**, 1907 (2017).

[PubMed](#) [PubMed Central](#) [Google Scholar](#)

31. 31.

Corada, M., Morini, M. F. & Dejana, E. Signaling pathways in the specification of arteries and veins. *Arterioscler. Thromb. Vasc. Biol.*

34, 2372–2377 (2014).

[CAS](#) [PubMed](#) [Google Scholar](#)

32. 32.

Kashiwazaki, M. et al. A high endothelial venule-expressing promiscuous chemokine receptor DARC can bind inflammatory, but not lymphoid, chemokines and is dispensable for lymphocyte homing under physiological conditions. *Int. Immunol.* **15**, 1219–1227 (2003).

[CAS](#) [PubMed](#) [Google Scholar](#)

33. 33.

Awwad, K. et al. Role of secreted modular calcium-binding protein 1 (SMOC1) in transforming growth factor  $\beta$  signalling and angiogenesis. *Cardiovasc. Res.* **106**, 284–294 (2015).

[CAS](#) [PubMed](#) [Google Scholar](#)

34. 34.

Tang, J. et al. Genetic fate mapping defines the vascular potential of endocardial cells in the adult heart. *Circ. Res.* **122**, 984–993 (2018).

[CAS](#) [PubMed](#) [Google Scholar](#)

35. 35.

Stallcup, W. B. The NG2 proteoglycan in pericyte biology. *Adv. Exp. Med. Biol.* **1109**, 5–19 (2018).

[CAS](#) [PubMed](#) [Google Scholar](#)

36. 36.

Chen, Q. et al. Endothelial cells are progenitors of cardiac pericytes and vascular smooth muscle cells. *Nat. Commun.* **7**, 12422 (2016).

[ADS](#) [CAS](#) [PubMed](#) [PubMed Central](#) [Google Scholar](#)

37. 37.

Barker, N. & Clevers, H. Leucine-rich repeat-containing G-protein-coupled receptors as markers of adult stem cells. *Gastroenterology* **138**, 1681–1696 (2010).

[CAS](#) [PubMed](#) [Google Scholar](#)

38. 38.

Daniel, J.-M. et al. Regulator of G-protein signaling 5 prevents smooth muscle cell proliferation and attenuates neointima formation. *Arterioscler. Thromb. Vasc. Biol.* **36**, 317–327 (2016).

[CAS](#) [PubMed](#) [Google Scholar](#)

39. 39.

Vanlandewijck, M. et al. A molecular atlas of cell types and zonation in the brain vasculature. *Nature* **554**, 475–480 (2018).

[ADS](#) [CAS](#) [PubMed](#) [Google Scholar](#)

40. 40.

Sweeney, M. & Foldes, G. It takes two: endothelial-perivascular cell cross-talk in vascular development and disease. *Front. Cardiovasc. Med.* **5**, 154 (2018).

[CAS](#) [PubMed](#) [PubMed Central](#) [Google Scholar](#)

41. 41.

Zhou, B. et al. Adult mouse epicardium modulates myocardial injury by secreting paracrine factors. *J. Clin. Invest.* **121**, 1894–1904 (2011).

[CAS](#) [PubMed](#) [PubMed Central](#) [Google Scholar](#)

42. 42.

Burstein, B., Libby, E., Calderone, A. & Nattel, S. Differential behaviors of atrial versus ventricular fibroblasts: a potential role for platelet-derived growth factor in atrial-ventricular remodeling differences. *Circulation* **117**, 1630–1641 (2008).

[PubMed](#) [Google Scholar](#)

43. 43.

Zhang, F., Li, C., Halfter, H. & Liu, J. Delineating an oncostatin M-activated STAT3 signaling pathway that coordinates the expression of genes involved in cell cycle regulation and extracellular matrix deposition of MCF-7 cells. *Oncogene* **22**, 894–905 (2003).

[CAS](#) [PubMed](#) [Google Scholar](#)

44. 44.

Lim, H. Y. et al. Hyaluronan receptor LYVE-1-expressing macrophages maintain arterial tone through hyaluronan-mediated regulation of smooth muscle cell collagen. *Immunity* **49**, 326–341.e7 (2018).

[CAS](#) [PubMed](#) [Google Scholar](#)

45. 45.

Dick, S. A. et al. Self-renewing resident cardiac macrophages limit adverse remodeling following myocardial infarction. *Nat. Immunol.* **20**, 29–39 (2019).

[CAS](#) [PubMed](#) [Google Scholar](#)

46. 46.

Jaitin, D. A. et al. Lipid-associated macrophages control metabolic homeostasis in a Trem2-dependent manner. *Cell* **178**, 686–698.e14

(2019).

[CAS](#) [PubMed](#) [PubMed Central](#) [Google Scholar](#)

47. 47.

Nahrendorf, M., Pittet, M. J. & Swirski, F. K. Monocytes: protagonists of infarct inflammation and repair after myocardial infarction. *Circulation* **121**, 2437–2445 (2010).

[PubMed](#) [PubMed Central](#) [Google Scholar](#)

48. 48.

Heinrichs, D. et al. Macrophage migration inhibitory factor (MIF) exerts antifibrotic effects in experimental liver fibrosis via CD74. *Proc. Natl Acad. Sci. USA* **108**, 17444–17449 (2011).

[ADS](#) [CAS](#) [PubMed](#) [Google Scholar](#)

49. 49.

Valiño-Rivas, L. et al. CD74 in kidney disease. *Front. Immunol.* **6**, 483 (2015).

[PubMed](#) [PubMed Central](#) [Google Scholar](#)

50. 50.

Hortells, L., Johansen, A. K. Z. & Yutzey, K. E. Cardiac fibroblasts and the extracellular matrix in regenerative and nonregenerative hearts. *J. Cardiovasc. Dev. Dis.* **6**, 29 (2019).

[CAS](#) [PubMed Central](#) [Google Scholar](#)

51. 51.

Bajpai, G. et al. The human heart contains distinct macrophage subsets with divergent origins and functions. *Nat. Med.* **24**, 1234–1245 (2018).

[CAS](#) [PubMed](#) [PubMed Central](#) [Google Scholar](#)

52. 52.

Kegel, L., Aunin, E., Meijer, D. & Bermingham, J. R. LGI proteins in the nervous system. *ASN Neuro* **5**, 167–181 (2013).

[CAS](#) [PubMed](#) [Google Scholar](#)

53. 53.

Struk, A. A. et al. Self-regulation and the *foraging* gene (*PRKG1*) in humans. *Proc. Natl Acad. Sci. USA* **116**, 4434–4439 (2019).

[CAS](#) [PubMed](#) [Google Scholar](#)

54. 54.

Sahara, M. et al. Population and single-cell analysis of human cardiogenesis reveals unique LGR5 ventricular progenitors in embryonic outflow tract. *Dev. Cell* **48**, 475–490.e7 (2019).

[CAS](#) [PubMed](#) [Google Scholar](#)

55. 55.

Lerman, B. B. Outflow tract ventricular arrhythmias: an update. *Trends Cardiovasc. Med.* **25**, 550–558 (2015).

[PubMed](#) [Google Scholar](#)

56. 56.

Dagda, R. K. et al. The spinocerebellar ataxia 12 gene product and protein phosphatase 2A regulatory subunit B $\beta$ 2 antagonizes neuronal survival by promoting mitochondrial fission. *J. Biol. Chem.* **283**, 36241–36248 (2008).

[CAS](#) [PubMed](#) [PubMed Central](#) [Google Scholar](#)

57. 57.

Wang, L. et al. Polymorphisms of the tumor suppressor gene LSAMP are associated with left main coronary artery disease. *Ann. Hum. Genet.* **72**, 443–453 (2008).

[CAS](#) [PubMed](#) [PubMed Central](#) [Google Scholar](#)

58. 58.

Bruce, K. D. et al. Lipoprotein lipase is a feature of alternatively-activated microglia and may facilitate lipid uptake in the CNS during demyelination. *Front. Mol. Neurosci.* **11**, 57 (2018).

[PubMed](#) [PubMed Central](#) [Google Scholar](#)

59. 59.

Kim, H.-S. et al. Schwann cell precursors from human pluripotent stem cells as a potential therapeutic target for myelin repair. *Stem Cell Reports* **8**, 1714–1726 (2017).

[CAS](#) [PubMed](#) [PubMed Central](#) [Google Scholar](#)

60. 60.

Antonopoulos, A. S. & Antoniades, C. The role of epicardial adipose tissue in cardiac biology: classic concepts and emerging roles. *J. Physiol. (Lond.)* **595**, 3907–3917 (2017).

[CAS](#) [Google Scholar](#)

61. 61.

Vijay, J. et al. Single-cell analysis of human adipose tissue identifies depot and disease specific cell types. *Nat. Metab.* **2**, 97–109 (2020).

[PubMed](#) [Google Scholar](#)

62. 62.

Hepler, C. et al. Identification of functionally distinct fibro-inflammatory and adipogenic stromal subpopulations in visceral adipose tissue of adult mice. *eLife* **7**, e39636 (2018).

[PubMed](#) [PubMed Central](#) [Google Scholar](#)

63. 63.

Hoffmann, M. et al. SARS-CoV-2 cell entry depends on ACE2 and TMPRSS2 and is blocked by a clinically proven protease inhibitor. *Cell* **181**, 271–280 (2020).

[CAS](#) [PubMed](#) [PubMed Central](#) [Google Scholar](#)

64. 64.

Watanabe, K., Umićević Mirkov, M., de Leeuw, C. A., van den Heuvel, M. P. & Posthuma, D. Genetic mapping of cell type specificity for complex traits. *Nat. Commun.* **10**, 3222 (2019).

[ADS](#) [CAS](#) [PubMed](#) [PubMed Central](#) [Google Scholar](#)

65. 65.

Leid, J. et al. Primitive embryonic macrophages are required for coronary development and maturation. *Circ. Res.* **118**, 1498–1511 (2016).

[CAS](#) [PubMed](#) [PubMed Central](#) [Google Scholar](#)

66. 66.

Chen, B., Brickshawana, A. & Frangogiannis, N. G. The functional heterogeneity of resident cardiac macrophages in myocardial injury CCR2<sup>+</sup> cells promote inflammation, whereas CCR2<sup>-</sup> cells protect. *Circ. Res.* **124**, 183–185 (2019).

[CAS](#) [PubMed](#) [PubMed Central](#) [Google Scholar](#)

67. 67.

Vaduganathan, M. et al. Renin-angiotensin-aldosterone system inhibitors in patients with Covid-19. *N. Engl. J. Med.* **382**, 1653–1659 (2020).

[CAS](#) [PubMed](#) [Google Scholar](#)

68. 68.

Ferreira, P. G. et al. The effects of death and post-mortem cold ischemia on human tissue transcriptomes. *Nat. Commun.* **9**, 490 (2018).

[ADS](#) [PubMed](#) [PubMed Central](#) [Google Scholar](#)

69. 69.

Madissoon, E. et al. scRNA-seq assessment of the human lung, spleen, and esophagus tissue stability after cold preservation. *Genome Biol.* **21**, 1 (2019).

[CAS](#) [PubMed](#) [PubMed Central](#) [Google Scholar](#)

70. 70.

Litvinukova, M. et al. Single cell and single nuclei analysis human heart tissue. <https://doi.org/10.17504/protocols.io.veae3ae> (2018).

71. 71.

Noseda, M. et al. PDGFR $\alpha$  demarcates the cardiogenic clonogenic Sca1 $^+$  stem/progenitor cell in adult murine myocardium. *Nat. Commun.* **6**, 6930 (2015).

[ADS](#) [CAS](#) [PubMed](#) [PubMed Central](#) [Google Scholar](#)

72. 72.

Schindelin, J. et al. Fiji: an open-source platform for biological-image analysis. *Nat. Methods* **9**, 676–682 (2012).

[CAS](#) [Google Scholar](#)

73. 73.

Wolock, S. L., Lopez, R. & Klein, A. M. Scrublet: computational identification of cell doublets in single-cell transcriptomic data. *Cell Syst.* **8**, 281–291.e9 (2019).

[CAS](#) [PubMed](#) [PubMed Central](#) [Google Scholar](#)

74. 74.

McInnes, L. & Healy, J. UMAP: Uniform manifold approximation and projection for dimension reduction. Preprint at <https://arxiv.org/abs/1802.03426> (2018).

75. 75.

Popescu, D.-M. et al. Decoding human fetal liver haematopoiesis. *Nature* **574**, 365–371 (2019).

[ADS](#) [CAS](#) [PubMed](#) [PubMed Central](#) [Google Scholar](#)

76. 76.

Wolf, F. A., Angerer, P. & Theis, F. J. SCANPY: large-scale single-cell gene expression data analysis. *Genome Biol.* **19**, 15 (2018).

[PubMed](#) [PubMed Central](#) [Google Scholar](#)

77. 77.

Luecken, M. D. & Theis, F. J. Current best practices in single-cell RNA-seq analysis: a tutorial. *Mol. Syst. Biol.* **15**, e8746 (2019).

[PubMed](#) [PubMed Central](#) [Google Scholar](#)

78. 78.

Polański, K. et al. BBKNN: fast batch alignment of single cell transcriptomes. *Bioinformatics* **36**, 964–965 (2019).

[Google Scholar](#)

79. 79.

Chen, J., Bardes, E. E., Aronow, B. J. & Jegga, A. G. ToppGene Suite for gene list enrichment analysis and candidate gene prioritization. *Nucleic Acids Res.* **37**, W305–W311 (2009).

[CAS](#) [PubMed](#) [PubMed Central](#) [Google Scholar](#)

80. 80.

Kuleshov, M. V. et al. Enrichr: a comprehensive gene set enrichment analysis web server 2016 update. *Nucleic Acids Res.* **44** (W1), W90–W97 (2016).

[CAS](#) [PubMed](#) [PubMed Central](#) [Google Scholar](#)

81. 81.

Lotfollahi, M., Wolf, F. A. & Theis, F. J. scGen predicts single-cell perturbation responses. *Nat. Methods* **16**, 715–721 (2019).

[CAS](#) [PubMed](#) [Google Scholar](#)

82. 82.

Miao, Z. et al. Putative cell type discovery from single-cell gene expression data. *Nat. Methods* **17**, 621–628 (2020).

[CAS](#) [PubMed](#) [Google Scholar](#)

83. 83.

Soneson, C. & Robinson, M. D. Bias, robustness and scalability in single-cell differential expression analysis. *Nat. Methods* **15**, 255–261 (2018).

[CAS](#) [PubMed](#) [Google Scholar](#)

84. 84.

La Manno, G. et al. RNA velocity of single cells. *Nature* **560**, 494–498 (2018).

[ADS](#) [PubMed](#) [PubMed Central](#) [Google Scholar](#)

85. 85.

Bergen, V., Lange, M., Peidli, S., Alexander Wolf, F. & Theis, F. J. Generalizing RNA velocity to transient cell states through dynamical modeling. *Nat. Biotechnol.* <https://doi.org/10.1038/s41587-020-0591-3> (2020).

86. 86.

Traag, V. A., Waltman, L. & van Eck, N. J. From Louvain to Leiden: guaranteeing well-connected communities. *Sci. Rep.* **9**, 5233 (2019).

[ADS](#) [CAS](#) [PubMed](#) [PubMed Central](#) [Google Scholar](#)

87. 87.

Miragaia, R. J. et al. Single-cell transcriptomics of regulatory T cells reveals trajectories of tissue adaptation. *Immunity* **50**, 493–504.e7 (2019).

[CAS](#) [PubMed](#) [PubMed Central](#) [Google Scholar](#)

88. 88.

Dey, G. et al. Signaling network of oncostatin M pathway. *J. Cell Commun. Signal.* **7**, 103–108 (2013).

[PubMed](#) [Google Scholar](#)

89. 89.

Abe, H. et al. Macrophage hypoxia signaling regulates cardiac fibrosis via oncostatin M. *Nat. Commun.* **10**, 2824 (2019).

[ADS](#) [PubMed](#) [PubMed Central](#) [Google Scholar](#)

90. 90.

Bian, Z. et al. Deciphering human macrophage development at single-cell resolution. *Nature* **582**, 571–576 (2020).

[ADS](#) [CAS](#) [PubMed](#) [Google Scholar](#)

91. 91.

Wong, A. P., Nili, N. & Strauss, B. H. In vitro differences between venous and arterial-derived smooth muscle cells: potential modulatory role of decorin. *Cardiovasc. Res.* **65**, 702–710 (2005).

[CAS](#) [PubMed](#) [Google Scholar](#)

92. 92.

Pober, J. S. & Sessa, W. C. Evolving functions of endothelial cells in inflammation. *Nat. Rev. Immunol.* **7**, 803–815 (2007).

[CAS](#) [PubMed](#) [PubMed Central](#) [Google Scholar](#)

93. 93.

McDonald, A. I. et al. Endothelial regeneration of large vessels is a biphasic process driven by local cells with distinct proliferative capacities. *Cell Stem Cell* **23**, 210–225.e6 (2018).

[CAS](#) [PubMed](#) [PubMed Central](#) [Google Scholar](#)

94. 94.

Chen, S.-C., Liu, Y.-C., Shyu, K.-G. & Wang, D. L. Acute hypoxia to endothelial cells induces activating transcription factor 3 (ATF3) expression that is mediated via nitric oxide. *Atherosclerosis* **201**, 281–288 (2008).

[CAS](#) [PubMed](#) [Google Scholar](#)

95. 95.

Hashimoto, K. et al. Single-cell transcriptomics reveals expansion of cytotoxic CD4 T cells in supercentenarians. *Proc. Natl Acad. Sci. USA* **116**, 24242–24251 (2019).

[CAS](#) [PubMed](#) [PubMed Central](#) [Google Scholar](#)

96. 96.

Roychoudhuri, R. et al. BACH2 regulates CD8<sup>+</sup> T cell differentiation by controlling access of AP-1 factors to enhancers. *Nat. Immunol.* **17**, 851–860 (2016).

[CAS](#) [PubMed](#) [PubMed Central](#) [Google Scholar](#)

97. 97.

Ahrends, T. et al. CD4<sup>+</sup> T cell help creates memory CD8<sup>+</sup> T cells with innate and help-independent recall capacities. *Nat. Commun.* **10**, 5531 (2019).

[ADS](#) [CAS](#) [PubMed](#) [PubMed Central](#) [Google Scholar](#)

98. 98.

Kimmel, J. C. & Kelley, D. R. scNym: Semi-supervised adversarial neural networks for single cell classification. Preprint at

<https://doi.org/10.1101/2020.06.04.132324> (2020).

99. 99.

Stewart, B. J. et al. Spatiotemporal immune zonation of the human kidney. *Science* **365**, 1461–1466 (2019).

[ADS](#) [CAS](#) [PubMed](#) [PubMed Central](#) [Google Scholar](#)

100. 100.

James, K. R. et al. Distinct microbial and immune niches of the human colon. *Nat. Immunol.* **21**, 343–353 (2020).

[CAS](#) [PubMed](#) [PubMed Central](#) [Google Scholar](#)

[Download references](#)

## Acknowledgements

This publication is part of the Human Cell Atlas ([www.humancellatlas.org/publications](http://www.humancellatlas.org/publications)). We acknowledge the Sanger Flow Cytometry Facility, Sanger Cellular Generation and Phenotyping (CGaP) Core Facility, and Sanger Core Sequencing pipeline for support with sample processing and sequencing library preparation. We acknowledge the HMS MiRoN Core for their support and assistance in this work. We thank J. Eliasova for graphical images; M. Prete, V. Kiselev and O. Tarkowska for IT support; S. Aldridge for editing the manuscript; C. Domínguez-Conde, J. Park, K. James, K. Tuong, R. Elmentait and M. Haniffa for discussions about immune cell annotation, and M. Luecken, M. Lotfollahi, D. Fischer and F. Theis for discussions on computational analyses. We thank T. R. W. Oliver and L. Campos for their assistance with orientation of basic cardiac histology. M.N. is the recipient of a British Heart Foundation (BHF) grant (PG/16/47/32156) and J.J.B. is recipient of a BHF grant (FS/13/12/30037, PG/15/57/31580, PG/17/71/33242). M.N., N.H. and S.A.T. are funded by a BHF/DZHK grant (SP/19/1/34461). N.H. is the recipient of an ERC Advanced Grant under the European Union Horizon 2020 Research and

Innovation Program (grant agreement AdG788970) and the Federal Ministry of Education and Research of Germany in the framework of CaRNAtion (031L0075A). N.H., C.E.S. and J.G.S. are supported by grants from the Leducq Fondation (16CVD03). D.R. is supported by the German Research Foundation (DFG). H.Z. is supported by the long-term Chinese Council Scholarship (CSC). M.K. received funding provided by the Alexander von Humboldt Foundation. H.Z. was supported by an EMBO long-term postdoctoral fellowship. G.O. received funding provided by the CIHR Canadian Institutes for Health Research, HSF Heart and Stroke Foundation and AI Alberta Innovates. This project has been made possible in part by grant number 2019-202666 from the Chan Zuckerberg Initiative (C.E.S., J.G.S., M.N., M.H., N.H. and S.A.T.). C.T.-L., K.P., E.F., E.T., K.R., O.B., H.Z. and S.A.T. are supported by the Wellcome Sanger Institute grant (WT206194) and the Wellcome Science Strategic Support for a Pilot for the Human Cell Atlas (WT211276/Z/18/Z)). J.G.S. and C.E.S. are supported by NIH grants (2R01HL080494, 2R01HL080494, 1UM1HL098166). J.G.S. and C.E.S. are supported by Engineering Research Centers Program of the National Science Foundation under NSF Cooperative Agreement no. EEC-1647837. C.E.S. and B.M. are supported by the Howard Hughes Medical Institute. We are grateful to the deceased donors and their families, the Human Organ Procurement and Exchange Program (HOPE) and to the Cambridge Biorepository for Translational Medicine (CBTM) for access to human tissue. E.R.N. was supported by a fellowship from the Sarnoff Cardiovascular Research Foundation.

## Author information

### Author notes

1. These authors contributed equally: Monika Litviňuková, Carlos Talavera-López, Henrike Maatz, Daniel Reichart
2. These authors jointly supervised this work: J. G. Seidman, Christine E. Seidman, Michela Noseda, Norbert Hubner, Sarah A. Teichmann

## Affiliations

1. Cellular Genetics Programme, Wellcome Sanger Institute, Wellcome Genome Campus, Hinxton, UK

Monika Litviňuková, Carlos Talavera-López, Krzysztof Polanski, Kenny Roberts, Liz Tuck, Eirini S. Fasouli, Hongbo Zhang, Omer Ali Bayraktar & Sarah A. Teichmann

2. Cardiovascular and Metabolic Sciences, Max Delbrück Center for Molecular Medicine in the Helmholtz Association (MDC), Berlin, Germany

Monika Litviňuková, Henrike Maatz, Catherine L. Worth, Eric L. Lindberg, Masatoshi Kanda, Giannino Patone & Norbert Hubner

3. EMBL - EBI, Wellcome Genome Campus, Hinxton, UK

Carlos Talavera-López

4. Department of Genetics, Harvard Medical School, Boston, MA, USA

Daniel Reichart, Emily R. Nadelmann, Daniel M. DeLaughter, Barbara McDonough, Hiroko Wakimoto, Joshua M. Gorham, J. G. Seidman & Christine E. Seidman

5. Department of Cardiology, University Heart & Vascular Center, University of Hamburg, Hamburg, Germany

Daniel Reichart

6. Department of Rheumatology and Clinical Immunology, Sapporo Medical University, Sapporo, Japan

Masatoshi Kanda

7. Institute of Computational Biology (ICB), HMGU, Neuherberg, Germany

Matthias Heinig

8. Department of Informatics, Technische Universitaet Muenchen (TUM), Munich, Germany

Matthias Heinig

9. National Heart and Lung Institute, Imperial College London, London, UK

Michael Lee, Sara Samari, Joseph J. Boyle & Michela Noseda

10. DZHK (German Centre for Cardiovascular Research), Partner Site Berlin, Berlin, Germany

Norbert Hubner

11. Cardiovascular Division, Brigham and Women's Hospital, Boston, MA, USA

Barbara McDonough & Christine E. Seidman

12. Department of Surgery, University of Cambridge, NIHR Cambridge Biomedical Centre, Cambridge Biorepository for Translational Medicine, Cambridge, UK

Krishnaa T. Mahbubani & Kourosh Saeb-Parsy

13. Department of Histology and Embryology of Zhongshan School of Medicine, Sun-Yat Sen University, Guangzhou, China

Hongbo Zhang

14. Division of Cardiology, Department of Medicine, Faculty of Medicine and Dentistry, University of Alberta, Edmonton, Alberta, Canada

Hao Zhang, Anissa Viveiros & Gavin Y. Oudit

15. Mazankowski Alberta Heart Institute, Faculty of Medicine and Dentistry, University of Alberta, Edmonton, Alberta, Canada

Hao Zhang, Anissa Viveiros & Gavin Y. Oudit

16. Howard Hughes Medical Institute, Chevy Chase, MD, USA

Barbara McDonough & Christine E. Seidman

17. British Heart Foundation Centre of Regenerative Medicine, British Heart Foundation Centre of Research Excellence, Imperial College London, London, UK

Michela Noseda

18. Charité-Universitätsmedizin, Berlin, Germany

Norbert Hubner

19. Berlin Institute of Health (BIH), Berlin, Germany

Norbert Hubner

20. Department of Physics, Cavendish Laboratory, University of Cambridge, Cambridge, UK

Sarah A. Teichmann

## Authors

1. Monika Litviňuková

[View author publications](#)

You can also search for this author in [PubMed](#) [Google Scholar](#)

2. Carlos Talavera-López

[View author publications](#)

You can also search for this author in [PubMed](#) [Google Scholar](#)

3. Henrike Maatz

[View author publications](#)

You can also search for this author in [PubMed](#) [Google Scholar](#)

4. Daniel Reichart

[View author publications](#)

You can also search for this author in [PubMed](#) [Google Scholar](#)

5. Catherine L. Worth

[View author publications](#)

You can also search for this author in [PubMed](#) [Google Scholar](#)

6. Eric L. Lindberg

[View author publications](#)

You can also search for this author in [PubMed](#) [Google Scholar](#)

7. Masatoshi Kanda

[View author publications](#)

You can also search for this author in [PubMed](#) [Google Scholar](#)

8. Krzysztof Polanski

[View author publications](#)

You can also search for this author in [PubMed](#) [Google Scholar](#)

9. Matthias Heinig

[View author publications](#)

You can also search for this author in [PubMed](#) [Google Scholar](#)

10. Michael Lee

[View author publications](#)

You can also search for this author in [PubMed](#) [Google Scholar](#)

11. Emily R. Nadelmann

[View author publications](#)

You can also search for this author in [PubMed](#) [Google Scholar](#)

12. Kenny Roberts

[View author publications](#)

You can also search for this author in [PubMed](#) [Google Scholar](#)

13. Liz Tuck

[View author publications](#)

You can also search for this author in [PubMed](#) [Google Scholar](#)

14. Eirini S. Fasouli

[View author publications](#)

You can also search for this author in [PubMed](#) [Google Scholar](#)

15. Daniel M. DeLaughter

[View author publications](#)

You can also search for this author in [PubMed](#) [Google Scholar](#)

16. Barbara McDonough

[View author publications](#)

You can also search for this author in [PubMed](#) [Google Scholar](#)

17. Hiroko Wakimoto

[View author publications](#)

You can also search for this author in [PubMed](#) [Google Scholar](#)

18. Joshua M. Gorham

[View author publications](#)

You can also search for this author in [PubMed](#) [Google Scholar](#)

19. Sara Samari

[View author publications](#)

You can also search for this author in [PubMed](#) [Google Scholar](#)

20. Krishnaa T. Mahbubani  
[View author publications](#)

You can also search for this author in [PubMed](#) [Google Scholar](#)

21. Kourosh Saeb-Parsy  
[View author publications](#)

You can also search for this author in [PubMed](#) [Google Scholar](#)

22. Giannino Patone  
[View author publications](#)

You can also search for this author in [PubMed](#) [Google Scholar](#)

23. Joseph J. Boyle  
[View author publications](#)

You can also search for this author in [PubMed](#) [Google Scholar](#)

24. Hongbo Zhang  
[View author publications](#)

You can also search for this author in [PubMed](#) [Google Scholar](#)

25. Hao Zhang  
[View author publications](#)

You can also search for this author in [PubMed](#) [Google Scholar](#)

26. Anissa Viveiros  
[View author publications](#)

You can also search for this author in [PubMed](#) [Google Scholar](#)

27. Gavin Y. Oudit  
[View author publications](#)

You can also search for this author in [PubMed](#) [Google Scholar](#)

28. Omer Ali Bayraktar

[View author publications](#)

You can also search for this author in [PubMed](#) [Google Scholar](#)

29. J. G. Seidman

[View author publications](#)

You can also search for this author in [PubMed](#) [Google Scholar](#)

30. Christine E. Seidman

[View author publications](#)

You can also search for this author in [PubMed](#) [Google Scholar](#)

31. Michela Noseda

[View author publications](#)

You can also search for this author in [PubMed](#) [Google Scholar](#)

32. Norbert Hubner

[View author publications](#)

You can also search for this author in [PubMed](#) [Google Scholar](#)

33. Sarah A. Teichmann

[View author publications](#)

You can also search for this author in [PubMed](#) [Google Scholar](#)

## Contributions

Conceived the study: N.H., S.A.T., M.N., C.E.S., J.G.S., H.M. Acquired tissue: K.M., K.S.P., G.O., H.Z., A.V. Processed tissue: M. Litviňuková, D.R., S.S., E.F., L.T., H.W., J.M.G., B.M., D.M.D., K.R., M.N.

Computational methods development: C.T.-L., K.P., M.H., J.G.S. Cell biology methods development: M. Litviňuková, E.L.L., M.N., H.M., D.R.

Histopathological evaluation: J.J.B., M.N. Data processing: C.T.-L., K.P., G.P. Global analysis: C.T.-L., D.R., M. Litviňuková, C.L.W., E.L.L., J.G.S. Cardiomyocyte analysis: D.R., C.L.W., E.R.N., H.M., D.M.D., N.H., J.G.S., C.E.S. Vascular analysis: M. Litviňuková, M.N., C.T.-L., M.K., S.A.T. Fibroblast analysis: E.L.L., H.M., D.R., M. Litviňuková, M.K., M.N., J.G.S., C.E.S., N.H. Immune analysis: C.T.-L., S.A.T. Neuronal analysis: E.R.N., D.R., C.L.W., J.G.S., C.E.S. Adipocyte analysis: M. Lee, M.N. Comparative analysis: C.T.-L., M. Litviňuková, M.N., S.A.T. GWAS analysis: M.H., C.T.-L., N.H., S.A.T. Interpreted results: M. Litviňuková, C.T.-L., D.R., H.M., C.L.W, E.L.L., M.H., J.B., M.N., C.E.S., J.G.S., S.A.T., N.H. Wrote the manuscript: M. Litviňuková, C.T.-L., H.M., D.R., C.L.W., E.L.L., M.K., M.H., J.G.S., C.E.S., M.N., N.H., S.A.T.

## Corresponding authors

Correspondence to [J. G. Seidman](#) or [Christine E. Seidman](#) or [Michela Noseda](#) or [Norbert Hubner](#) or [Sarah A. Teichmann](#).

## Ethics declarations

### Competing interests

The authors declare no competing interests.

## Additional information

**Peer review information** *Nature* thanks the anonymous reviewers for their contribution to the peer review of this work. Peer reviewer reports are available.

**Publisher's note** Springer Nature remains neutral with regard to jurisdictional claims in published maps and institutional affiliations.

## Extended data figures and tables

### [Extended Data Fig. 1 Expression of the canonical markers.](#)

**a**, UMAP embedding of selected canonical markers shown in Fig. [1c](#). **b**, Scaled expression ( $\log_2$ -transformed fold change,  $\log_2\text{FC}$ ) of selected canonical markers shown in Fig. [1c](#). **c**, Expression ( $\log_2\text{FC}$ ) of marker genes from Fig. [1c](#) in each source highlighting that the same marker genes are used for identification of the same cell types in both cells and nuclei. **d**, Multiplexed smFISH staining of cell type-specific transcripts from Fig. [1e](#) in right ventricles (top): *TTN* (green, cardiomyocytes) and *CDH5* (red, EC) right atrium (middle): *NPPA* (green, aCM) and *DCN* (red, FB) and LA (bottom): *MYH11* (green, SMC) and *KCNJ8* (red, pericytes), nuclei are

DAPI-stained (dark blue). Scale bars, 20 µm. For details on statistics and reproducibility, see [Methods](#).

## Extended Data Fig. 2 Source and region covariates of the global dataset.

**a**, UMAP embedding of the major cell types coloured by source. **b**, UMAP embedding highlighting the individual sources **c**, Distribution of cell types obtained by each source. Data are available in Supplementary Table [29](#). Further analyses and descriptions are available in the Methods and Supplementary Table [30](#). **d**, UMAP embedding of the major cell types coloured by region. **e**, UMAP embedding highlighting the individual regions **f**, Distribution of cell types across the six sampled regions (nuclei only). Data are available in Supplementary Table [2](#).

## Extended Data Fig. 3 Ventricular and atrial cardiomyocytes.

**a**, Expression ( $\log_2\text{FC}$ ) of selected marker genes in ventricular cardiomyocyte subpopulations. **b**, Expression ( $\log_2\text{FC}$ ) of selected marker genes in atrial cardiomyocyte subpopulations **c**, Single channel multiplexed smFISH images of overlay shown in Fig. [2c](#), [d](#), [g](#), [h](#). **d**, Expression ( $\log_2\text{FC}$ ) of specific markers in cardiomyocyte subpopulations. I and II, *PCDH7* expression in ventricular and atrial cardiomyocytes, respectively. III, *PRELID2* expression is highest in vCM2 and is enriched in right ventricles. IV and V, *CNN1* expression is enriched in both vCM3 and aCM3. VI and VII, *HAMP* expression is enriched in the right atrium. **e**, Multiplexed smFISH of transcripts enriched in cardiomyocyte subpopulations. Left, expression of *TNNT2* (green) and *PCDH7* (red) in left ventricles. Right, expression of *TNNT2* (green) and *CNN1* (red) in right ventricles, nuclei are DAPI-stained (dark blue). Scale bars, 10 µm. **f**, Gene Ontology analysis results for vCM4 showing significant terms related to energy metabolism and muscle contraction. Data are available in Supplementary Table [6](#). **g**, Multiplexed smFISH of positive and negative RNAscope control probes. Scale bars, 5 µm. For details on statistics and reproducibility, see [Methods](#).

## Extended Data Fig. 4 Vascular and mesothelial populations.

**a**, Scaled expression ( $\log_2\text{FC}$ ) of selected marker genes for EC subpopulations. **b, c**, Distribution of the EC subpopulations across the sources (**b**) and the regions (**c**) (nuclei only). Data are available in Supplementary Table 9. **d**, Scaled expression ( $\log_2\text{FC}$ ) of selected marker genes of pericytes and smooth muscle cell subpopulations. **e, f**, Distribution of the mural subpopulations across the sources (**e**) and the regions (**f**) (nuclei only). Data are available in Supplementary Table 9. **g**, Multiplexed smFISH in apex section shows *MYH11* (yellow) expression in vascular SMC (thick in artery and very thin in nearby small calibre vein), *CDH5* (red) in the endothelium, and *SEMA3G* (cyan) and *ACKR1* (green) expression respectively in arterial and venous ECs, nuclei are DAPI-stained (dark blue). Scale bars, 20  $\mu\text{m}$ . **h**, UMAP embedding of vascular and mesothelial cells with stochastic representation of the RNA velocity. **i**, Latent time of the vascular cells showing predicted directionalities of the cell populations based on the RNA splicing dynamics. The analysis uses only cells, nuclei are omitted. EC\_cap, capillary ECs; EC\_art, arterial ECs; EC\_ven, venous ECs; EC\_atrial, atrial endothelial cells; EC\_ln, lymphatic endothelial cells; PC, pericytes; PC\_str, stromal pericytes; SMC\_basic, smooth muscle cells; SMC\_art, arterial smooth muscle cells. **j**, Predicted cell–cell interactions using the CellphoneDB statistical inference framework on 39,000 cells from 14 biologically independent individuals ( $n = 14$ ). Selected ligand–receptor interactions show specificity of NOTCH ligands-receptors pairing in defined vasculature beds. Mean of combined gene expression of interacting pairs ( $\log_2\text{FC}$ ). CellPhoneDB  $P$  value of the specificity of the interactions =  $10 \times 10^{-5}$ . The red rectangles highlight the arterial interactions and the blue rectangle highlights venous interactions depicted in Fig. 3d. Notably, even though the EC6\_ven and SMC2\_art interaction is unexpected, we cannot exclude that those cell states are restricted to their respective vascular beds. Further validation is needed to determine the exact spatial distribution of EC6\_ven and SMC2\_art and subsequently verify whether the interaction is plausible *in vivo*. Data are available in Supplementary Table 10. **k**, Scaled expression ( $\log_2\text{FC}$ ) of the ligands and receptors from **g** across the vascular populations described in Fig. 3a. **l**, Scaled expression ( $\log_2\text{FC}$ ) of selected marker genes of mesothelial cells. **m**, Multiplexed smFISH localizes the mesothelial cells expressing *BNC1* into the epicardium of the left atria. *CDH5* shows

endothelial cells in the tissue and is absent from the mesothelial cells, nuclei are DAPI-stained (dark blue). Scale bars, 20  $\mu$ m. **n**, Distribution of the mural subpopulations across the sampled regions (nuclei only). Data are available in Supplementary Table 9. For details on statistics and reproducibility, see [Methods](#).

### Extended Data Fig. 5 Vascular markers visualized on 10X Genomics Visium data.

**a–d**, Spatial expression ( $\log_2\text{FC}$ ) of *CDH5* (pan-EC marker), *SEMA3G* and *GJA5* (arterial EC markers) (a), *ACKR1* and *PLVAP* (venous EC markers) (b), *MYH11* and *ACTA2* (pan-SMC markers) (c), and *JAG1* and *NOTCH2* (d) on publicly available 10X Visium section of human left ventricle. *JAG1* and *NOTCH2* are the predicted interaction partners for arterial ECs and SMCs, respectively.

## Extended Data Fig. 6 Fibroblasts.

**a**, Scaled expression ( $\log_2\text{FC}$ ) of selected marker genes of identified FB populations. **b**, Enrichment for oncostatin M pathway for FB populations showing enriched activity in FB3. A list of genes with which the score was calculated is in Supplementary Table 12. **c**, Regional distribution per FB population. Some FB populations show enrichment in the atria (left and right), such as FB2 and FB3. FB1, FB4–FB6 are enriched in the ventricles (left, right, apex and interventricular septum). Data are available in Supplementary Table 35. **d–f**, Multiplexed smFISH for probes targeting *FAP*, *LINC01133* and *PTX3* confirming FB4, FB5 and FB3 subpopulations. *FAP* (red) is imaged in interventricular septum, *LINC01133* (red) in apex and *PTX3* (red) in right atrium tissue section. *DCN* (cyan) is used as a pan-FB marker, *C1QA* (green) as a pan-macrophage marker, nuclei are DAPI-stained (dark blue). Scale bars, 5  $\mu\text{m}$ . **g**, Scaled expression ( $\log_2\text{FC}$ ) of *APOD* and *CFH* genes, which represent differences between ventricular and atrial fibroblasts. **h**, Multiplexed smFISH of apex section representing *DCN* (cyan), *APOD* (red) and *CFH* (green), nuclei are DAPI-stained (dark blue). Although the *APOD* signal colocalized with *DCN*, expression of *CFH* was absent. Scale bars, 5  $\mu\text{m}$ . **i**, UMAP embedding of the ventricular fibroblast cell-states. **j**, UMAP embedding of atrial fibroblasts cell types. **k**, Scaled expression ( $\log_2\text{FC}$ ) of marker genes for ventricular fibroblast subpopulations. **l**, Scaled expression ( $\log_2\text{FC}$ ) of marker genes for atrial fibroblast subpopulations. **m**, Scaled expression ( $\log_2\text{FC}$ ) of ECM genes differentiating atrial (aFB1, aFB2) and ventricular (vFB2, vFB4) clusters which suggest different ECM mechanisms. For details on statistics and reproducibility, see [Methods](#).

## Extended Data Fig. 7 Covariates of immune cardiac populations.

**a–j**, UMAP embedding of cell source (**a**), donor (**b**), gender (**c**), type (**d**), number of genes (**e**), number of counts (**f**), percentage of mitochondrial genes (**g**), percentage of ribosomal genes (**h**), scrublet score (**i**) and annotation of the cell populations of the immune cells (**j**).

## Extended Data Fig. 8 Immune cardiac populations.

**a**, Visualization of transcriptional signatures from published studies. The score values represent the likelihood of the external transcriptional signature to be present when comparing it against the transcriptional background of a cardiac immune population. Bajpai\_2018 = *CCR2-MERTK*<sup>+</sup> tissue-resident macrophages from ref. <sup>51</sup>. Dick\_2019 = self-renewing tissue macrophages from ref. <sup>45</sup>. Bian\_2020 = yolk sac-derived macrophages from ref. <sup>90</sup>. The complete signature can be found in Supplementary Table <sup>19</sup>. **b**, Expression ( $\log_2\text{FC}$ ) of *LYVE1*, *FOLR2* and *TIMD4* characteristic of the self-renewing tissue-resident murine macrophages previously described<sup>45</sup>, as well as *MERTK* as previously described<sup>51</sup> and the *TREM2* expression associated to lipid-associated macrophages (LAM) previously described<sup>46</sup>. Complete signatures can be found in Supplementary Table <sup>19</sup>. **c**, Scaled expression ( $\log_2\text{FC}$ ) of genes differentiating DOCK4<sup>+</sup> MP1 from DOCK4<sup>+</sup> MP2: *IL4R*, *ITGAM*, *STAT3*, *DOCK1*, *HIF1A* and *RASA2*. **d**, Predicted cell–cell interactions calculated for 69,295 cardiomyocytes, fibroblasts and myeloid cells from 14 donors ( $n = 14$ ) and enriched for ‘extracellular matrix organization’. Mean of combined gene expression of interacting pairs ( $\log_2\text{FC}$ ). Data are available in Supplementary Table <sup>17</sup>. **e**, Spatial mapping of the *CD74–MIF* interaction between LYVE1<sup>+</sup>MP and FB4 on a publicly available 10X Genomics Visium dataset for left ventricular myocardium. We identified four spots where we observe co-expression of *FN1*, *LYVE1*, *CD74* and *MIF*, as predicted from the cell–cell interactions. The bar represents the  $\log_2\text{FC}$ . **f**, Confusion matrix for the logistic regression model trained on cardiac immune cells. This model reached an accuracy score of 0.6862, showing a stronger accuracy with lymphoid cells, compared with the myeloid ones.

## Extended Data Fig. 9 Neuronal and adipocyte populations.

**a**, UMAP embedding identifies six neuronal subpopulations. **b**, Regional distribution of neuronal cell subpopulations identified in **a**. Data are available in Supplementary Table <sup>20</sup>. **c**, Expression ( $\log_2\text{FC}$ ) dot plot of selected marker genes in neuronal cell subpopulations. **d**, Multiplexed

smFISH of *NRXN1* (green) and *PPP2R2B* (red), nuclei were DAPI-stained (dark blue). Scale bars, 5  $\mu\text{m}$ . For details on statistics and reproducibility, see [Methods](#). **e**, UMAP embedding showing four adipocyte subpopulations. **f**, UMAP embedding of expression of gene markers associated with adipocytes (*GPAM*, *FASN*, *ADIPOQ*, *LEP*). **g**, Top five significantly enriched pathways for each adipocyte subpopulation, using differentially expressed genes calculated using the Wilcoxon rank sum test with Benjamini–Hochberg correction ( $\log_{\text{FC}} > 0.5$ ,  $P < 1.0 \times 10^{-5}$ ) and tested using a hypergeometric distribution with Bonferroni correction as implemented in ToppFun. Data are available in Supplementary Table [21](#). **h**, Expression ( $\log_2\text{FC}$ ) of adipocyte associated genes and select marker genes from the top enriched pathway for each adipocyte subpopulation.

## **Extended Data Fig. 10 Relevance for COVID-19 and GWAS studies.**

**a**, Global expression ( $\log_2\text{FC}$ ) of *ACE2* in all cardiac cells. **b–d**, Gene expression of *ACE2*, *TMPRSS2*, *CTSB* and *CTSL* in cardiomyocytes (**b**), FBs (**c**) and vascular cells (**d**). **e**, Multiplexed smFISH expression of *DCN* (cyan), *KCNJ8* (green) and *ACE2* (red), nuclei are DAPI-stained (dark blue) marking fibroblasts (#; expression of *DCN*) and pericytes (\*; co-expression of *DCN* and *KCNJ8*) in right ventricular tissue section. Scale bars, 5  $\mu\text{m}$ . For statistics and reproducibility, see [Methods](#). **f**, The colour coding of the heat map shows the  $-\log_{10}(P \text{ value})$  of the MAGMA GWAS enrichment analysis for the association between cell type-specific expression (y axis) and GWAS signals (x axis). The cell types refer to the subcluster annotations and GWAS studies refer to Supplementary Table [27](#). AF, atrial fibrillation; CAD, coronary artery disease; HF, heart failure; HR, heart rate; HT, hypertension; LVD, left ventricular diameter; NICM, non-ischaemic cardiomyopathy; PR, PR interval; PWAVE, P-wave duration; T2D, type 2 diabetes; QRS, QRS complex duration; QT, QT interval. Dots mark significant associations ( $\text{FDR} < 10\%$ ). The colour of the dots indicates the type of association as determined by pairwise conditional analysis (green: independent association, blue: partially jointly explained with other cell types, grey: explained away by other cell types). Data are available in Supplementary Table [28](#).

## Extended Data Fig. 11 Skeletal muscle populations.

**a**, UMAP embedding of transcriptional data from skeletal muscle using cells and nuclei. Mural, pericytes and smooth muscle cells. **b**, Scaled expression ( $\log_2\text{FC}$ ) of selected markers for the major skeletal muscle populations. **c**, UMAP embedding of vascular and stromal populations of skeletal muscle. **d**, Scaled expression ( $\log_2\text{FC}$ ) of marker genes used in Extended Data Fig. 3 for identification of vascular cell states. **e**, Predicted cell–cell interactions inferred using CellphoneDB statistical inference framework in skeletal muscle cells with 9,220 cells from five donors ( $n = 5$ ) depicting cell states from **c**. Selected ligand–receptor interactions show specificity of NOTCH ligand–receptor pairing in defined vasculature beds. The interactions of EC\_art-SMC are highlighted by a red rectangle and EC\_ven-SMC are highlighted by a blue rectangle. Colour of the dots indicates the mean expression level of interacting molecule in partner 1 and interacting molecule partner 2. Mean of combined gene expression of interacting pairs ( $\log_2\text{FC}$ ). CellPhoneDB  $P$  value of the specificity of the interactions =  $10 \times 10^{-5}$ . Data are available in Supplementary Table 10. **f**, Scaled expression ( $\log_2\text{FC}$ ) of the ligands and receptors from Extended Data Fig. 3 depicted on vascular populations of skeletal muscle.

## Extended Data Fig. 12 Analysis technical information.

**a**, Locations and representative histology section of six cardiac regions sampled, including right and left atrium, right and left ventricular free wall and left ventricular apex and interventricular septum. H&E, magnification  $\times 10$ ; scale bars, 500  $\mu\text{m}$ . **b**, Spatial visualization of positive and negative RNAscope control probes. Scale bars, 5  $\mu\text{m}$ . For statistics and reproducibility, see [Methods](#). **c**, Heat map of top five significantly enriched Gene Ontology Biological Processes term for each of the vascular subpopulations from Fig. 3a. Data are available in Supplementary Table 25. **d**, SCCAF scores for each batch aligned manifold. For each population, we plotted the true positive (TPR) versus false positive (FPR) learning ratios from the subpopulation in each manifold. Next, we plotted how accurately the manifold represents each learned subpopulation based on the test

training set and the CV cross-validation set. The closer the CV value to the test value, the better the manifold is at representing the subpopulations.

## Supplementary information

### Supplementary Figure 1

FACS gating strategy for removal of cell debris and purification of nuclei.

**a.** Size gating to remove doublets and aggregates was applied (SSC-A, FSC-A, SSC-W, SSC-H, FSC-H, FSC-W), followed by sorts for Hoechst-positive nuclei (purple population). Used for all nuclei processed in North America **b.** Example of negative control (no NucBlue Live ReadyProbes Reagent applied, ThermoFisher) with the same parameters as **a.** **c.** Gating strategy used for all nuclei processed in the United Kingdom. The Hoechst-positive nuclei were selected in P1. Further gating for size was applied (P2, P3) to remove doublets and aggregates. **d.** Example of a negative control with the same parameters as **c.**

### Reporting Summary

### Supplementary Tables

This zipped file contains Supplementary Tables 1-35 and their legends.

### Peer Review File

## Rights and permissions

### Reprints and Permissions

## About this article



Check for  
updates

## Cite this article

Litviňuková, M., Talavera-López, C., Maatz, H. *et al.* Cells of the adult human heart. *Nature* **588**, 466–472 (2020). <https://doi.org/10.1038/s41586-020-2797-4>

### [Download citation](#)

- Received: 10 February 2020
- Accepted: 18 September 2020
- Published: 24 September 2020
- Issue Date: 17 December 2020
- DOI: <https://doi.org/10.1038/s41586-020-2797-4>

## Further reading

- [\*\*The Human Explanted Heart Program: A translational bridge for cardiovascular medicine\*\*](#)
  - Hao Zhang
  - , Anissa Viveiros
  - , Anish Nikhanj
  - , Quynh Nguyen
  - , Kaiming Wang
  - , Wei Wang
  - , Darren H. Freed
  - , John C. Mullen
  - , Roderick MacArthur
  - , Daniel H. Kim
  - , Wayne Tymchak
  - , Consolato M. Sergi
  - , Zamaneh Kassiri
  - , Shaohua Wang

- & Gavin Y. Oudit

*Biochimica et Biophysica Acta (BBA) - Molecular Basis of Disease*  
(2021)

- **Complexity and plasticity of cardiac cellular composition**

- Gregory B. Lim

*Nature Reviews Cardiology* (2020)

- **Using Cardiovascular Cells from Human Pluripotent Stem Cells for COVID-19 Research: Why the Heart Fails**

- Loukia Yianguou
- , Richard P. Davis
- & Christine L. Mummery

*Stem Cell Reports* (2020)

- **GATA6 mutations in hiPSCs inform mechanisms for maldevelopment of the heart, pancreas, and diaphragm**

- Arun Sharma
- , Lauren K Wasson
- , Jon AL Willcox
- , Sarah U Morton
- , Joshua M Gorham
- , Daniel M DeLaughter
- , Meraj Neyazi
- , Manuel Schmid
- , Radhika Agarwal
- , Min Young Jang
- , Christopher N Toepfer
- , Tarsha Ward
- , Yuri Kim
- , Alexandre C Pereira

- , Steven R DePalma
- , Angela Tai
- , Seongwon Kim
- , David Conner
- , Daniel Bernstein
- , Bruce D Gelb
- , Wendy K Chung
- , Elizabeth Goldmuntz
- , George Porter
- , Martin Tristani-Firouzi
- , Deepak Srivastava
- , Jonathan G Seidman
- & Christine E Seidman

*eLife* (2020)

## Comments

By submitting a comment you agree to abide by our [Terms](#) and [Community Guidelines](#). If you find something abusive or that does not comply with our terms or guidelines please flag it as inappropriate.

[Download PDF](#)

---

This article was downloaded by **calibre** from <https://www.nature.com/articles/s41586-020-2797-4>

- Article
- [Published: 09 December 2020](#)

# The functional proteome landscape of *Escherichia coli*

- [André Mateus](#) ORCID: [orcid.org/0000-0001-6870-0677<sup>1</sup>](https://orcid.org/0000-0001-6870-0677),
- [Johannes Heyler](#) ORCID: [orcid.org/0000-0001-6636-7145<sup>1</sup>](https://orcid.org/0000-0001-6636-7145),
- [Jacob Bobonis](#) ORCID: [orcid.org/0000-0001-9293-9733<sup>1,2</sup>](https://orcid.org/0000-0001-9293-9733),
- [Nils Kurzawa](#) ORCID: [orcid.org/0000-0002-7846-2817<sup>1,2</sup>](https://orcid.org/0000-0002-7846-2817),
- [Malay Shah<sup>1</sup>](#),
- [Karin Mitosch<sup>1</sup>](#),
- [Camille V. Goemans](#) ORCID: [orcid.org/0000-0002-5564-1644<sup>1</sup>](https://orcid.org/0000-0002-5564-1644),
- [Dominic Helm](#) ORCID: [orcid.org/0000-0001-9321-2069<sup>3</sup>](https://orcid.org/0000-0001-9321-2069),
- [Frank Stein](#) ORCID: [orcid.org/0000-0001-9695-1692<sup>3</sup>](https://orcid.org/0000-0001-9695-1692),
- [Athanasios Typas](#) ORCID: [orcid.org/0000-0002-0797-9018<sup>1</sup>](https://orcid.org/0000-0002-0797-9018) &
- [Mikhail M. Savitski](#) ORCID: [orcid.org/0000-0003-2011-9247<sup>1</sup>](https://orcid.org/0000-0003-2011-9247)

[Nature](#) volume 588, pages473–478(2020) [Cite this article](#)

- 4632 Accesses
- 104 Altmetric
- [Metrics details](#)

## Subjects

- [Bacterial genes](#)
- [Bacterial systems biology](#).
- [Systems analysis](#)

# Abstract

Recent developments in high-throughput reverse genetics<sup>1,2</sup> have revolutionized our ability to map gene function and interactions<sup>3,4,5,6</sup>. The power of these approaches depends on their ability to identify functionally associated genes, which elicit similar phenotypic changes across several perturbations (chemical, environmental or genetic) when knocked out<sup>7,8,9</sup>. However, owing to the large number of perturbations, these approaches have been limited to growth or morphological readouts<sup>10</sup>. Here we use a high-content biochemical readout, thermal proteome profiling<sup>11</sup>, to measure the proteome-wide protein abundance and thermal stability in response to 121 genetic perturbations in *Escherichia coli*. We show that thermal stability, and therefore the state and interactions of essential proteins, is commonly modulated, raising the possibility of studying a protein group that is particularly inaccessible to genetics. We find that functionally associated proteins have coordinated changes in abundance and thermal stability across perturbations, owing to their co-regulation and physical interactions (with proteins, metabolites or cofactors). Finally, we provide mechanistic insights into previously determined growth phenotypes<sup>12</sup> that go beyond the deleted gene. These data represent a rich resource for inferring protein functions and interactions.

[Access through your institution](#)

[Change institution](#)

[Buy or subscribe](#)

## Access options

Subscribe to Journal

Get full journal access for 1 year

185,98 €

only 3,58 € per issue

## Subscribe

All prices are NET prices.  
VAT will be added later in the checkout.

Rent or Buy article

Get time limited or full article access on ReadCube.

from \$8.99

## Rent or Buy

All prices are NET prices.

## **Additional access options:**

- [Log in](#)
- [Access through your institution](#)
- [Learn about institutional subscriptions](#)

**Fig. 1: TPP of 121 *E. coli* mutants.**

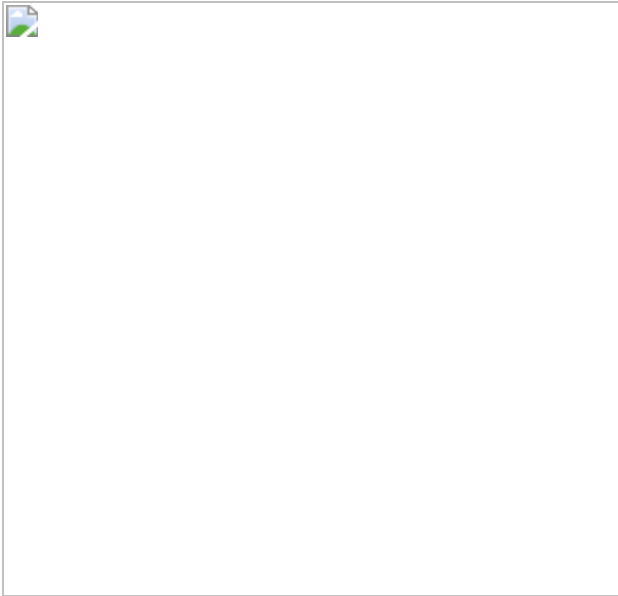


**Fig. 2: Essential proteins change state, not abundance, in different genetic backgrounds.**



**Fig. 3: Co-changes in protein abundance and thermal stability are strong identifiers of functional relationships.**



**Fig. 4: Protein thermal stability captures enzymatic activity.**



## Data availability

The thermal proteome profiling data are available at <http://ecoliTPP.shiny.embl.de>. The mass spectrometry proteomics data have been deposited to the ProteomeXchange Consortium via the PRIDE partner repository with the dataset identifier PXD016589. The mass spectrometry metabolomics data have been deposited to the MassIVE repository with the dataset identifier MSV000084632. Data for protein complexes, pathways, and operons were retrieved from Ecocyc v21.1 (<https://ecocyc.org/>)<sup>56</sup>. STRING database v10.5 was used (<https://string-db.org/>)<sup>57</sup>. Data referring to protein localization were retrieved from STEPdb v1.0 (<http://stepdb.eu/>)<sup>61</sup>. Cellular processes targeted by mutants in this study were derived from Clusters of Orthologous Groups (COG) database (<https://www.ncbi.nlm.nih.gov/research/cog-project/>)<sup>62</sup>. Gene ontology annotations (release: 2020-01-01) were downloaded from <http://geneontology.org>.

## Code availability

The code to process raw mass spectrometry data (available at PRIDE partner repository with the dataset identifier PXD016589) and to calculate

abundance and thermal stability scores and *q*-values (Supplementary Data 3) is available at <https://github.com/fstein/EcoliTPP>.

## References

1. 1.

Beltrao, P., Cagney, G. & Krogan, N. J. Quantitative genetic interactions reveal biological modularity. *Cell* **141**, 739–745 (2010).

[CAS](#) [PubMed](#) [PubMed Central](#) [Google Scholar](#)

2. 2.

Costanzo, M. et al. Global genetic networks and the genotype-to-phenotype relationship. *Cell* **177**, 85–100 (2019).

[CAS](#) [PubMed](#) [Google Scholar](#)

3. 3.

Typas, A. et al. Regulation of peptidoglycan synthesis by outer-membrane proteins. *Cell* **143**, 1097–1109 (2010).

[CAS](#) [PubMed](#) [PubMed Central](#) [Google Scholar](#)

4. 4.

Gray, A. N. et al. Coordination of peptidoglycan synthesis and outer membrane constriction during *Escherichia coli* cell division. *eLife* **4**, (2015).

5. 5.

Surma, M. A. et al. A lipid E-MAP identifies Ubx2 as a critical regulator of lipid saturation and lipid bilayer stress. *Mol. Cell* **51**, 519–530 (2013).

[CAS](#) [PubMed](#) [PubMed Central](#) [Google Scholar](#)

6. 6.

Collins, S. R. et al. Functional dissection of protein complexes involved in yeast chromosome biology using a genetic interaction map. *Nature* **446**, 806–810 (2007).

[CAS](#) [PubMed](#) [ADS](#) [Google Scholar](#)

7. 7.

Nichols, R. J. et al. Phenotypic landscape of a bacterial cell. *Cell* **144**, 143–156 (2011).

[CAS](#) [PubMed](#) [Google Scholar](#)

8. 8.

Costanzo, M. et al. A global genetic interaction network maps a wiring diagram of cellular function. *Science* **353**, aaf1420 (2016).

[PubMed](#) [PubMed Central](#) [Google Scholar](#)

9. 9.

Price, M. N. et al. Mutant phenotypes for thousands of bacterial genes of unknown function. *Nature* **557**, 503–509 (2018).

[CAS](#) [PubMed](#) [ADS](#) [Google Scholar](#)

10. 10.

Kritikos, G. et al. A tool named Iris for versatile high-throughput phenotyping in microorganisms. *Nat. Microbiol.* **2**, 17014 (2017).

[CAS](#) [PubMed](#) [PubMed Central](#) [Google Scholar](#)

11. 11.

Savitski, M. M. et al. Tracking cancer drugs in living cells by thermal profiling of the proteome. *Science* **346**, 1255784 (2014).

[PubMed](#) [Google Scholar](#)

12. 12.

Herrera-Dominguez, L. & Typas, A. Exploring the dark (and not so dark) genome of *E. coli*, <https://ecoli-darkgen.shinyapps.io/app-1/> (2020).

13. 13.

Babu, M. et al. Global landscape of cell envelope protein complexes in *Escherichia coli*. *Nat. Biotechnol.* **36**, 103–112 (2018).

[CAS](#) [PubMed](#) [Google Scholar](#)

14. 14.

Wan, C. et al. Panorama of ancient metazoan macromolecular complexes. *Nature* **525**, 339–344 (2015).

[CAS](#) [PubMed](#) [PubMed Central](#) [ADS](#) [Google Scholar](#)

15. 15.

Tan, C. S. H. et al. Thermal proximity coaggregation for system-wide profiling of protein complex dynamics in cells. *Science* **359**, 1170–1177 (2018).

[CAS](#) [PubMed](#) [ADS](#) [Google Scholar](#)

16. 16.

Martinez Molina, D. et al. Monitoring drug target engagement in cells and tissues using the cellular thermal shift assay. *Science* **341**, 84–87 (2013).

[PubMed](#) [ADS](#) [Google Scholar](#)

17. 17.

Bantscheff, M., Lemeer, S., Savitski, M. M. & Kuster, B. Quantitative mass spectrometry in proteomics: critical review update from 2007 to the present. *Anal. Bioanal. Chem.* **404**, 939–965 (2012).

[CAS](#) [PubMed](#) [Google Scholar](#)

18. 18.

Mateus, A. et al. Thermal proteome profiling for interrogating protein interactions. *Mol. Syst. Biol.* **16**, e9232 (2020).

[CAS](#) [PubMed](#) [PubMed Central](#) [Google Scholar](#)

19. 19.

Sridharan, S. et al. Proteome-wide solubility and thermal stability profiling reveals distinct regulatory roles for ATP. *Nat. Commun.* **10**, 1155 (2019).

20. 20.

Mateus, A. et al. Thermal proteome profiling in bacteria: probing protein state *in vivo*. *Mol. Syst. Biol.* **14**, e8242 (2018).

[PubMed](#) [PubMed Central](#) [Google Scholar](#)

21. 21.

Becher, I. et al. Pervasive protein thermal stability variation during the cell cycle. *Cell* **173**, 1495–1507 (2018).

[CAS](#) [PubMed](#) [PubMed Central](#) [Google Scholar](#)

22. 22.

Huang, J. X. et al. High throughput discovery of functional protein modifications by hotspot thermal profiling. *Nat. Methods* **16**, 894–901 (2019).

[CAS](#) [PubMed](#) [PubMed Central](#) [Google Scholar](#)

23. 23.

Potel, C. M. et al. Impact of phosphorylation on thermal stability of proteins. Preprint at <https://doi.org/10.1101/2020.01.14.903849> (2020).

24. 24.

Smith, I. R. et al. Identification of phosphosites that alter protein thermal stability. Preprint at <https://doi.org/10.1101/2020.01.14.904300> (2020).

25. 25.

Becher, I. et al. Thermal profiling reveals phenylalanine hydroxylase as an off-target of panobinostat. *Nat. Chem. Biol.* **12**, 908–910 (2016).

[CAS](#) [PubMed](#) [Google Scholar](#)

26. 26.

Baba, T. et al. Construction of *Escherichia coli* K-12 in-frame, single-gene knockout mutants: the Keio collection. *Mol. Syst. Biol.* **2**, 2006.0008, (2006).

[PubMed](#) [PubMed Central](#) [Google Scholar](#)

27. 27.

Werner, T. et al. Ion coalescence of neutron encoded TMT 10-plex reporter ions. *Anal. Chem.* **86**, 3594–3601 (2014).

[CAS](#) [PubMed](#) [Google Scholar](#)

28. 28.

Parker, D. J., Demetci, P. & Li, G. W. Rapid accumulation of motility-activating mutations in resting liquid culture of *Escherichia coli*. *J. Bacteriol.* **201**, e00259-19 (2019).

[CAS](#) [PubMed](#) [PubMed Central](#) [Google Scholar](#)

29. 29.

Palmer, T. & Berks, B. C. The twin-arginine translocation (Tat) protein export pathway. *Nat. Rev. Microbiol.* **10**, 483–496 (2012).

[CAS](#) [PubMed](#) [Google Scholar](#)

30. 30.

Koo, B. M. et al. Construction and analysis of two genome-scale deletion libraries for *Bacillus subtilis*. *Cell Syst.* **4**, 291–305 (2017).

[CAS](#) [PubMed](#) [PubMed Central](#) [Google Scholar](#)

31. 31.

Qi, L. S. et al. Repurposing CRISPR as an RNA-guided platform for sequence-specific control of gene expression. *Cell* **152**, 1173–1183 (2013).

[CAS](#) [PubMed](#) [PubMed Central](#) [Google Scholar](#)

32. 32.

Lawson, M. J. et al. *In situ* genotyping of a pooled strain library after characterizing complex phenotypes. *Mol. Syst. Biol.* **13**, 947 (2017).

[PubMed](#) [PubMed Central](#) [Google Scholar](#)

33. 33.

Peters, J. M. et al. A Comprehensive, CRISPR-based functional analysis of essential genes in bacteria. *Cell* **165**, 1493–1506 (2016).

[CAS](#) [PubMed](#) [PubMed Central](#) [Google Scholar](#)

34. 34.

Kustatscher, G. et al. Co-regulation map of the human proteome enables identification of protein functions. *Nat. Biotechnol.* **37**, 1361–1371 (2019).

[CAS](#) [PubMed](#) [PubMed Central](#) [Google Scholar](#)

35. 35.

Romanov, N. et al. Disentangling genetic and environmental effects on the proteotypes of individuals. *Cell* **177**, 1308–1318 (2019).

[CAS](#) [PubMed](#) [PubMed Central](#) [Google Scholar](#)

36. 36.

Havugimana, P. C. et al. A census of human soluble protein complexes. *Cell* **150**, 1068–1081 (2012).

[CAS](#) [PubMed](#) [PubMed Central](#) [Google Scholar](#)

37. 37.

Lalanne, J. B. et al. Evolutionary convergence of pathway-specific enzyme expression stoichiometry. *Cell* **173**, 749–761 (2018).

[CAS](#) [PubMed](#) [PubMed Central](#) [Google Scholar](#)

38. 38.

Ghatak, S., King, Z. A., Sastry, A. & Palsson, B. O. The y-ome defines the 35% of *Escherichia coli* genes that lack experimental evidence of function. *Nucleic Acids Res.* **47**, 2446–2454 (2019).

[CAS](#) [PubMed](#) [PubMed Central](#) [Google Scholar](#)

39. 39.

Mateus, A., Määttä, T. A. & Savitski, M. M. Thermal proteome profiling: unbiased assessment of protein state through heat-induced stability changes. *Proteome Sci.* **15**, 13 (2017).

[PubMed](#) [PubMed Central](#) [Google Scholar](#)

40. 40.

Shiver, A. L. et al. A chemical-genomic screen of neglected antibiotics reveals illicit transport of kasugamycin and blasticidin S. *PLoS Genet.* **12**, e1006124 (2016).

[PubMed](#) [PubMed Central](#) [Google Scholar](#)

41. 41.

Rousset, F. et al. Genome-wide CRISPR-dCas9 screens in *E. coli* identify essential genes and phage host factors. *PLoS Genet.* **14**, e1007749 (2018).

[PubMed](#) [PubMed Central](#) [Google Scholar](#)

42. 42.

Liu, X. et al. High-throughput CRISPRi phenotyping identifies new essential genes in *Streptococcus pneumoniae*. *Mol. Syst. Biol.* **13**, 931 (2017).

[PubMed](#) [PubMed Central](#) [Google Scholar](#)

43. 43.

Aoki, S. K. et al. Contact-dependent growth inhibition requires the essential outer membrane protein BamA (YaeT) as the receptor and the

inner membrane transport protein AcrB. *Mol. Microbiol.* **70**, 323–340 (2008).

[CAS](#) [PubMed](#) [PubMed Central](#) [Google Scholar](#)

44. 44.

Bernard, C. S., Sadasivam, M., Shiomi, D. & Margolin, W. An altered FtsA can compensate for the loss of essential cell division protein FtsN in *Escherichia coli*. *Mol. Microbiol.* **64**, 1289–1305 (2007).

[CAS](#) [PubMed](#) [PubMed Central](#) [Google Scholar](#)

45. 45.

Malinvernini, J. C. et al. YfiO stabilizes the YaeT complex and is essential for outer membrane protein assembly in *Escherichia coli*. *Mol. Microbiol.* **61**, 151–164 (2006).

[CAS](#) [PubMed](#) [Google Scholar](#)

46. 46.

Sampson, B. A., Misra, R. & Benson, S. A. Identification and characterization of a new gene of *Escherichia coli* K-12 involved in outer membrane permeability. *Genetics* **122**, 491–501 (1989).

[CAS](#) [PubMed](#) [PubMed Central](#) [Google Scholar](#)

47. 47.

Grenier, F., Matteau, D., Baby, V. & Rodrigue, S. Complete genome sequence of *Escherichia coli* BW25113. *Genome Announc.* **2**, e01038-14 (2014).

[PubMed](#) [PubMed Central](#) [Google Scholar](#)

48. 48.

Hughes, C. S. et al. Ultrasensitive proteome analysis using paramagnetic bead technology. *Mol. Syst. Biol.* **10**, 757 (2014).

[PubMed](#) [Google Scholar](#)

49. 49.

Hughes, C. S. et al. Single-pot, solid-phase-enhanced sample preparation for proteomics experiments. *Nat. Protocols* **14**, 68–85 (2019).

[CAS](#) [PubMed](#) [Google Scholar](#)

50. 50.

Franken, H. et al. Thermal proteome profiling for unbiased identification of direct and indirect drug targets using multiplexed quantitative mass spectrometry. *Nat. Protocols* **10**, 1567–1593 (2015).

[CAS](#) [PubMed](#) [Google Scholar](#)

51. 51.

Huber, W., von Heydebreck, A., Sültmann, H., Poustka, A. & Vingron, M. Variance stabilization applied to microarray data calibration and to the quantification of differential expression. *Bioinformatics* **18** (Suppl 1), S96–S104 (2002).

[PubMed](#) [Google Scholar](#)

52. 52.

Ritchie, M. E. et al. limma powers differential expression analyses for RNA-sequencing and microarray studies. *Nucleic Acids Res.* **43**, e47 (2015).

[PubMed](#) [PubMed Central](#) [Google Scholar](#)

53. 53.

Cui, L. et al. A CRISPRi screen in *E. coli* reveals sequence-specific toxicity of dCas9. *Nat. Commun.* **9**, 1912 (2018).

[PubMed](#) [PubMed Central](#) [ADS](#) [Google Scholar](#)

54. 54.

Haeussler, M. et al. Evaluation of off-target and on-target scoring algorithms and integration into the guide RNA selection tool CRISPOR. *Genome Biol.* **17**, 148 (2016).

[PubMed](#) [PubMed Central](#) [Google Scholar](#)

55. 55.

Robin, X. et al. pROC: an open-source package for R and S+ to analyze and compare ROC curves. *BMC Bioinformatics* **12**, 77 (2011).

[PubMed](#) [PubMed Central](#) [Google Scholar](#)

56. 56.

Keseler, I. M. et al. The EcoCyc database: reflecting new knowledge about *Escherichia coli* K-12. *Nucleic Acids Res.* **45** (D1), D543–D550 (2017).

[CAS](#) [PubMed](#) [Google Scholar](#)

57. 57.

Szklarczyk, D. et al. STRING v11: protein-protein association networks with increased coverage, supporting functional discovery in genome-wide experimental datasets. *Nucleic Acids Res.* **47** (D1), D607–D613 (2019).

[CAS](#) [Google Scholar](#)

58. 58.

Guzman, L. M., Belin, D., Carson, M. J. & Beckwith, J. Tight regulation, modulation, and high-level expression by vectors containing the arabinose PBAD promoter. *J. Bacteriol.* **177**, 4121–4130 (1995).

[CAS](#) [PubMed](#) [PubMed Central](#) [Google Scholar](#)

59. 59.

Otsuka, Y. et al. GenoBase: comprehensive resource database of *Escherichia coli* K-12. *Nucleic Acids Res.* **43**, D606–D617 (2015).

[CAS](#) [PubMed](#) [Google Scholar](#)

60. 60.

Saka, K. et al. A complete set of *Escherichia coli* open reading frames in mobile plasmids facilitating genetic studies. *DNA Res.* **12**, 63–68 (2005).

[CAS](#) [PubMed](#) [Google Scholar](#)

61. 61.

Orfanoudaki, G. & Economou, A. Proteome-wide subcellular topologies of *E. coli* polypeptides database (STEPdb). *Mol. Cell. Proteomics* **13**, 3674–3687 (2014).

[CAS](#) [PubMed](#) [PubMed Central](#) [Google Scholar](#)

62. 62.

Tatusov, R. L., Galperin, M. Y., Natale, D. A. & Koonin, E. V. The COG database: a tool for genome-scale analysis of protein functions and evolution. *Nucleic Acids Res.* **28** 33–36 (2000).

[CAS](#) [PubMed](#) [PubMed Central](#) [Google Scholar](#)

[Download references](#)

# Acknowledgements

We thank P. Phapale for help with metabolomics analysis, and H. Link and D. Bikard for strains and plasmids for the dCas9 work. This work was supported by the European Molecular Biology Laboratory. A.M. and K.M. were supported by a fellowship from the EMBL Interdisciplinary Postdoc (EI3POD) programme under Marie Skłodowska-Curie Actions COFUND (grant number 664726). C.V.G. is recipient of an EMBO long-term postdoctoral fellowship and an add-on fellowship from the Christiane Nüsslein-Volhard-Stiftung. AT is supported by an ERC consolidator grant, uCARE.

# Author information

## Affiliations

1. Genome Biology Unit, European Molecular Biology Laboratory (EMBL), Heidelberg, Germany

André Mateus, Johannes Hevler, Jacob Bobonis, Nils Kurzawa, Malay Shah, Karin Mitosch, Camille V. Goemans, Athanasios Typas & Mikhail M. Savitski

2. Faculty of Biosciences, Heidelberg University, Heidelberg, Germany

Jacob Bobonis & Nils Kurzawa

3. Proteomics Core Facility, European Molecular Biology Laboratory (EMBL), Heidelberg, Germany

Dominic Helm & Frank Stein

## Authors

1. André Mateus

[View author publications](#)

You can also search for this author in [PubMed](#) [Google Scholar](#)

2. Johannes Hevler

[View author publications](#)

You can also search for this author in [PubMed](#) [Google Scholar](#)

3. Jacob Bobonis

[View author publications](#)

You can also search for this author in [PubMed](#) [Google Scholar](#)

4. Nils Kurzawa

[View author publications](#)

You can also search for this author in [PubMed](#) [Google Scholar](#)

5. Malay Shah

[View author publications](#)

You can also search for this author in [PubMed](#) [Google Scholar](#)

6. Karin Mitosch

[View author publications](#)

You can also search for this author in [PubMed](#) [Google Scholar](#)

7. Camille V. Goemans

[View author publications](#)

You can also search for this author in [PubMed](#) [Google Scholar](#)

8. Dominic Helm

[View author publications](#)

You can also search for this author in [PubMed](#) [Google Scholar](#)

9. Frank Stein

[View author publications](#)

You can also search for this author in [PubMed](#) [Google Scholar](#)

10. Athanasios Typas

[View author publications](#)

You can also search for this author in [PubMed](#) [Google Scholar](#)

11. Mikhail M. Savitski

[View author publications](#)

You can also search for this author in [PubMed](#) [Google Scholar](#)

## Contributions

A.M., N.K., F.S., M.M.S. and A.T. designed the study. A.M. and J.H. performed the thermal proteome profiling experiments. A.M., J.H. and D.H. performed the proteomics mass spectrometry analysis. A.M., and K.M. performed the metabolomics mass spectrometry analysis. A.M., J.B., M.S., C.V.G. performed follow-up molecular work: *flhDC* (A.M.), CueO (A.M. and J.B.), CRISPRi (A.M. and M.S.), MdtK and RecR (A.M., M.S. and J.B.), other genetics and biochemistry (A.M., J.B. and C.V.G.). A.M., N.K. and F.S. performed the data analysis. A.M., A.T. and M.M.S. drafted the manuscript, which was reviewed and edited by all authors. A.T. and M.M.S. supervised the study.

## Corresponding authors

Correspondence to [Athanasios Typas](#) or [Mikhail M. Savitski](#).

## Ethics declarations

## Competing interests

The authors declare no competing interests.

## Additional information

**Peer review information** *Nature* thanks the anonymous reviewer(s) for their contribution to the peer review of this work. Peer reviewer reports are available.

**Publisher's note** Springer Nature remains neutral with regard to jurisdictional claims in published maps and institutional affiliations.

## Extended data figures and tables

### Extended Data Fig. 1 Biological replicates show good reproducibility, with differences revealing biological phenomena.

**a**, Rarefaction analysis of the proteome coverage (proteins with at least two unique peptides in each mass spectrometry run) as a function of the number of mass spectrometry runs. **b**, Distribution of  $\log_2$ -transformed fold change differences between the two biological replicates. **c**, Scatter plot of protein fold changes between all biological replicate measurements ( $n = 1,512,475$ ; all proteins, all temperatures, all mutants).  $r$  depicts Pearson correlation. **d**, Reproducibility of protein fold changes between biological replicate measurements at each temperature. **e**, Examples of replicate correlation for specific mutants, highlighting that flagellar proteins are common outliers in one of the two clones ( $n_{\Delta hemX} = 13,150$ ,  $n_{\Delta ybaB} = 12,313$ ,  $n_{\Delta clpA} = 12,950$ ,  $n_{\Delta mrcB} = 12,604$ ,  $n_{\Delta fur} = 12,543$ ,  $n_{\Delta mlaA} = 12,559$ ,  $n_{\Delta lpp} = 12,719$ ; all proteins, all temperatures). **f**, Polymerase chain reaction of the promoter region of the *flhDC* operon (schematic on top) demonstrates the presence of insertions in mutant clones (gel on bottom,  $n = 1$ ; for gel source data see Supplementary Fig. 2) with high flagellar protein expression (FliC fold-changes at the two lowest temperatures of each mutant replicate used as a proxy for abundance). **g**, Scatter plot of abundance and thermal stability z-scores of all proteins in all mutants ( $n = 170,150$ ).  $r$  depicts Pearson correlation. **h**, Distribution of the number of mutants in which a protein is significantly altered ( $n = 1,764$  proteins). Box plots as in Fig. 2a. **i**, Distribution of the number of proteins that are significantly altered in each mutant ( $n = 121$  mutants). Box plots as in Fig. 2a.

**Extended Data Fig. 2 Cellular processes targeted in this study and changes in thermal stability reflect protein complex architecture in *E. coli* mutants.**

**a**, Distribution of cellular processes targeted in this study compared to the general distribution of the *E. coli* genome using Clusters of Orthologous Groups (COG). **b, c**, Schematic representation of protein complexes targeted by genetic perturbations in this study. Protein missing (encoded by gene deleted) is highlighted by a dashed line and other complex members are coloured according to their thermal stability (**b**) or abundance (**c**) in that mutant. \* $|z\text{-score}| > 1.96$  and with  $q\text{-value} \leq 0.05$ .  $\Delta tolC$  data are from ref. [20](#).

**Extended Data Fig. 3 Protein co-expression patterns provide insight into gene expression regulation.**

**a**, Correlation of DegP and OmpF log<sub>2</sub>-transformed fold changes to control in each of the genetic perturbations probed here ( $n = 120$ , as OmpF is not detected in  $\Delta ompF$ ) at each temperature (colour coded;  $n = 10$ ). Mutants that lead to cell envelope stress (highlighted), and therefore activation of stress response (see also **b**) lead to upregulation of DegP and downregulation of OmpF. **b**, Schematic representation of regulation of *degP* and *ompF* genes. CpxAR two-component system regulates both genes, while EnvZ/OmpR regulates only *ompF*. Heatmap shows Spearman's rank correlation (calculated as in Fig. [3a](#)) for proteins involved in regulation of *degP* and *ompF*.

**Extended Data Fig. 4 Cofactor binding leads to changes in protein thermal stability.**

**a**, Distribution of thermal stability z-scores of all proteins in the iron-sulfur cluster biosynthesis mutants,  $\Delta iscA$ ,  $\Delta iscS$  and  $\Delta iscU$  according to their Gene Ontology annotation as iron-sulfur cluster binding proteins ( $n_{\Delta iscA} = 41$ ,  $n_{\Delta iscS} = 41$ ,  $n_{\Delta iscU} = 40$ ) or not ( $n_{\Delta iscA} = 1,400$ ,  $n_{\Delta iscS} = 1,415$ ,  $n_{\Delta iscU} = 1,314$ ). Box plots as in Fig. [2a](#). Significance assessed with two-

sided Wilcoxon signed-rank test ( $P_{\Delta iscA} = 3.9 \times 10^{-5}$ ,  $P_{\Delta iscS} = 9.5 \times 10^{-11}$ ,  $P_{\Delta iscU} = 7.7 \times 10^{-5}$ ). **b**, Volcano plot showing proteins that significantly change in their thermal stability (highlighted in red) in  $\Delta tatB$  shows that CueO is thermally destabilized. **c**, Total and periplasmic protein extraction of different CueO constructs shows that deletion of Tat signal peptide ( $\Delta 28$ ) and full-length construct in  $\Delta tatB$  retain CueO protein levels, but only a small fraction makes it to the periplasm. CueO was detected using mouse monoclonal anti-Flag antibody and goat anti-mouse IgG-HRP ( $n = 1$ ). An SDS-PAGE gel was run in parallel and stained with Coomassie to ensure that periplasmic extraction was successful ( $n = 1$ ). **d**, Cellular thermal shift assay (CETSA) of CueO fused to Flag peptide, either using the full-length protein (WT) or a version lacking the first 28 amino acids ( $\Delta 28$ ; corresponding to the Tat signal peptide). Experiments performed in living cells in  $\Delta cueO$  strain. CueO was detected using mouse monoclonal anti-Flag antibody and goat anti-mouse IgG-HRP ( $n = 1$ ). As a loading control, run on the same gel, rabbit anti-LpoB antibody<sup>3</sup> and goat anti-rabbit IgG-HRP were used ( $n = 1$ ). **e**, As in **d**, but comparing the thermal stability of CueO fused to Flag peptide, either in  $\Delta cueO$  (WT) or  $\Delta cueO\Delta tatB$  ( $\Delta$ ) live cells ( $n = 1$ ). **f**, As in **d**, but comparing thermal stability of  $\Delta 28$ -CueO in  $\Delta cueO$  strain and full-length CueO in  $\Delta cueO\Delta tatB$  ( $n = 1$ ). **g**, CETSA of  $\Delta 28$ -CueO in lysate of  $\Delta cueO$  strain after addition of 4 mM CuCl<sub>2</sub> or the same volume of vehicle ( $n = 1$ ). For gel source data see Supplementary Fig. 2.

### Extended Data Fig. 5 Changes in thermal stability of essential proteins.

**a**, log<sub>2</sub>-transformed fold change of FtsK protein levels in each mutant compared to control at each temperature. FtsK is strongly thermally destabilized in the  $\Delta phoP$  mutant and the *ftsK* knockdown is synthetically lethal with the *phoP* deletion (Fig. 2d). **b**, As in **a** for *parC*. ParC is strongly thermally stabilized in the  $\Delta clpS$  mutant and thermally destabilized in the  $\Delta phoP$  mutant and the *parC* knockdown is synthetically lethal with both. Synthetic lethality is also apparent in the  $\Delta ahpC$ ,  $\Delta amiA$  and  $\Delta envC$  mutants, despite the absence in changes in ParC thermal stability (Fig. 2e).

**Extended Data Fig. 6 Protein correlation profiling recapitulates known biological interactions with abundance and thermal stability data having different contribution to functional associations.**

**a**, Distribution of Spearman's rank correlation of all protein pair comparisons compared to known operons, protein complexes, and metabolic pathways. Distribution statistics refer to all protein pairs. **b**, ROC analysis based on the decreasing absolute Spearman's rank correlation compared to interactions in STRING database at different cut-offs of the combined STRING score. **c–e**, Spearman's rank correlation of protein pairs belonging to the same operon (**c**), protein complex (**d**), or metabolic pathway (**e**) using solely changes in abundance (x axis) or changes in thermal stability (y axis). Protein pairs belonging to the same operon are highlighted in purple. Distribution of Spearman's rank correlation are shown outside the axes.  $n = 446$  for operons,  $n = 348$  for protein complexes, and  $n = 801$  for metabolic pathways. Proteins belonging to the same operon or complex mostly have coordinated abundance changes, while proteins belonging to the same pathway have also often coordinated thermal stability. **f**, Schematic representation of UDP-*N*-acetylmuramoyl-pentapeptide biosynthesis pathway. **g**, Example of protein pair (DdlA and MurC) co-changing in their thermal stability ( $r_S = 0.79$ ), but not abundance ( $r_S = -0.13$ ) across 81 genetic perturbations. Each data point corresponds to the abundance or thermal stability z-score in one of the genetic perturbations (colour-coded). **h**, Heat map of Spearman's rank correlation of all quantified members of UDP-*N*-acetylmuramoyl-pentapeptide biosynthesis pathway based on co-changes in abundance (top triangle) or thermal stability alone (bottom triangle).

**Extended Data Fig. 7 Protein correlation profiling reflects substructures of protein complexes.**

**a**, Heat map of Spearman's rank correlation (lower triangle; based on protein abundance and thermal stability data across 121 mutants, as in Fig. 3a) and the physical distance (upper triangle; based on ribosome structure, PDB: 4YBB, and using the centres of mass of each protein) between the

ribosome members. At the bottom, 30S and 50S ribosomal subunits are shown in purple and green, respectively, and lower triangle data are clustered hierarchically. **b, c**, High-resolution structure of the ribosome coloured according to the heat map clusters from **a** (**b**) or 30S and 50S ribosomal subunits (**c**). **d–g**, ATP synthase members (**d, e**; PDB: 5T4O) and respiratory complex I (**f, g**; PDB: 4HEA), as in **a–c**. **h**, Closely located members of protein complexes are more likely to be similarly regulated across different conditions. Spearman's rank correlation plotted against the distance between complex subunits for the three complexes represented in the figure, with an apparent negative correlation. Box plots are as in Fig. 2a.

### [Extended Data Fig. 8 GO enrichments of co-changing partners of proteins of unknown function can reveal their function.](#)

Examples of links between proteins of unknown function and GO terms that their co-changing proteins are enriched in. Some of these links are supported by external evidence (node colour, see [Supplementary Discussion](#)). Edges are coloured according to the enrichment *P* value using the Fisher's exact test after correction for multiple comparison with the Benjamini–Hochberg procedure.

### [Extended Data Fig. 9 Metabolite levels correlate with thermal stability of enzyme producing or using the metabolite.](#)

**a, b**, Scatter plot of metabolite  $\log_2$  fold-changes in mutant compared to wild-type strain (y axis) and protein abundance (**a**) or thermal stability (**b**) in each mutant for enzymes that directly interact with the metabolite (x axis) ( $n = 19$  mutants, except for G6P/F6P–PhoA ( $n = 7$ ), 2-oxoglutarate–SucA ( $n = 18$ ), succinate–SdhD ( $n = 12$ ), malate–FumA ( $n = 6$ ), and malate–FumB ( $n = 12$ ))).  $r$  depicts the Pearson correlation coefficient for each metabolite–enzyme pair. Black line represents the linear fit and grey shades the 95% confidence interval of the fit. **c**, Twenty strains used for targeted metabolomics analysis. **d**, Distribution of Pearson correlation coefficients for metabolite levels in each mutant and abundance or thermal stability of enzymes that directly interact with the metabolite (upstream and downstream of metabolite, as in **a** and **b**). Box plots are as in

Fig. 2a. With all data represented on top of the box plots ( $n_{\text{G6P/F6P}} = 6$ ,  $n_{\text{PEP}} = 5$ ,  $n_{\text{Pyruvate}} = 8$ ,  $n_{\text{2-oxoglutarate}} = 4$ ,  $n_{\text{Succinate}} = 6$ ,  $n_{\text{Malate}} = 9$ ).

## Extended Data Fig. 10 Changes in protein abundance and thermal stability explain growth phenotypes of *E. coli* mutants.

**a**, Scatter plot of number of significantly affected proteins (abundance or thermal stability) in each mutant (x axis) and the number of significant growth phenotypes of the same mutant (y axis; data from ref. 12).  $P$  refers to the correlation  $P$  value and  $n$  to the number of mutants. **b**, Scatter plot of MdtK abundance in mutants profiled in this study and their sensitivity to 80 mM metformin<sup>12</sup> ( $r = 0.44$ ;  $n = 119$  mutants). **c, d**, Spot assay for the indicated strains overexpressing *mdtK*, *ahpC* or *cpxA*, or a control empty plasmid in plates containing 0–80 mM metformin. Cells were diluted to  $\text{OD}_{578} = 0.5$ , serially diluted in tenfold steps, and spotted on LB agar plates containing 10  $\mu\text{g ml}^{-1}$  tetracycline (to maintain plasmid), 0.1 mM IPTG (to induce expression of encoded gene), and metformin as indicated. **e**, As in b, but showing correlation of RecR abundance and UV exposure for 18 s ( $r = 0.53$ ;  $n = 99$  mutants). **f**, Schematic representation of the *ybaB-recR* operon and protein abundance scores in the  $\Delta ybaB$  mutant. **g**, Spot assay for the indicated strains overexpressing *ybaB*, *recR*, or a control empty plasmid after exposure to UV with a total energy of 85 mJ  $\text{cm}^{-2}$  or control non-exposed plate. Cells were diluted to  $\text{OD}_{578} = 0.1$  and then serially diluted in tenfold steps, and spotted on LB agar plates containing 50  $\mu\text{g ml}^{-1}$  ampicillin (to maintain plasmid) and 0.1 mM IPTG (to induce expression of encoded gene).

## Supplementary information

### Supplementary Information

This file contains Supplementary Figures 1-2 and Supplementary Discussion.

### Reporting Summary

## Peer Review File

### Supplementary Data 1

Details on mutants used in this study.

### Supplementary Data 2

Proteins identified in this study.

### Supplementary Data 3

Results from mass spectrometry experiments. Relative log2 fold-changes of mutant vs control.

### Supplementary Data 4

GO enrichment of highly variable proteins.

### Supplementary Data 5

Abundance and thermal stability scores.

### Supplementary Data 6

Protein correlation profiling.

### Supplementary Data 7

GO enrichment of highly correlated proteins for each protein.

### Supplementary Data 8

Glycolysis and TCA cycle metabolite levels in 19 mutants.

### Supplementary Data 9

Significant correlations between growth phenotypes in different chemical and environmental perturbations and protein abundance or thermal stability. Only correlations with at least 60 data points and adjusted p-value <0.01 were considered significant.

## Rights and permissions

[Reprints and Permissions](#)

## About this article



Check for  
updates

## Cite this article

Mateus, A., Hevler, J., Bobonis, J. *et al.* The functional proteome landscape of *Escherichia coli*. *Nature* **588**, 473–478 (2020).  
<https://doi.org/10.1038/s41586-020-3002-5>

[Download citation](#)

- Received: 13 March 2020
- Accepted: 08 October 2020
- Published: 09 December 2020
- Issue Date: 17 December 2020
- DOI: <https://doi.org/10.1038/s41586-020-3002-5>

## Comments

By submitting a comment you agree to abide by our [Terms](#) and [Community Guidelines](#). If you find something abusive or that does not comply with our terms or guidelines please flag it as inappropriate.

[Access through your institution](#)

[Change institution](#)

[Buy or subscribe](#)

---

This article was downloaded by **calibre** from <https://www.nature.com/articles/s41586-020-3002-5>

| [Section menu](#) | [Main menu](#) |

- Article
- [Published: 11 November 2020](#)

# Feeding induces cholesterol biosynthesis via the mTORC1–USP20–HMGCR axis

- [Xiao-Yi Lu<sup>1 na1</sup>](#),
- [Xiong-Jie Shi ORCID: orcid.org/0000-0002-3750-6676<sup>1 na1</sup>](#),
- [Ao Hu<sup>1 na1</sup>](#),
- [Ju-Qiong Wang<sup>1 na1</sup>](#),
- [Yi Ding<sup>1</sup>](#),
- [Wei Jiang<sup>1</sup>](#),
- [Ming Sun<sup>1</sup>](#),
- [Xiaolu Zhao ORCID: orcid.org/0000-0003-1535-3880<sup>1</sup>](#),
- [Jie Luo ORCID: orcid.org/0000-0003-1899-3111<sup>1</sup>](#),
- [Wei Qi<sup>2</sup>](#) &
- [Bao-Liang Song ORCID: orcid.org/0000-0002-6397-5935<sup>1</sup>](#)

[Nature](#) volume 588, pages479–484(2020) [Cite this article](#)

- 10k Accesses
- 68 Altmetric
- [Metrics details](#)

## Subjects

- [Lipids](#)
- [Metabolic disorders](#)

# Abstract

Cholesterol is an essential lipid and its synthesis is nutritionally and energetically costly<sup>1,2</sup>. In mammals, cholesterol biosynthesis increases after feeding and is inhibited under fasting conditions<sup>3</sup>. However, the regulatory mechanisms of cholesterol biosynthesis at the fasting–feeding transition remain poorly understood. Here we show that the deubiquitylase ubiquitin-specific peptidase 20 (USP20) stabilizes HMG-CoA reductase (HMGCR), the rate-limiting enzyme in the cholesterol biosynthetic pathway, in the feeding state. The post-prandial increase in insulin and glucose concentration stimulates mTORC1 to phosphorylate USP20 at S132 and S134; USP20 is recruited to the HMGCR complex and antagonizes its degradation. The feeding-induced stabilization of HMGCR is abolished in mice with liver-specific *Usp20* deletion and in USP20(S132A/S134A) knock-in mice. Genetic deletion or pharmacological inhibition of USP20 markedly decreases diet-induced body weight gain, reduces lipid levels in the serum and liver, improves insulin sensitivity and increases energy expenditure. These metabolic changes are reversed by expression of the constitutively stable HMGCR(K248R). This study reveals an unexpected regulatory axis from mTORC1 to HMGCR via USP20 phosphorylation and suggests that inhibitors of USP20 could be used to lower cholesterol levels to treat metabolic diseases including hyperlipidaemia, liver steatosis, obesity and diabetes.

[Access through your institution](#)

[Change institution](#)

[Buy or subscribe](#)

## Access options

Subscribe to Journal

Get full journal access for 1 year

185,98 €

only 3,58 € per issue

[Subscribe](#)

All prices are NET prices.  
VAT will be added later in the checkout.

Rent or Buy article

Get time limited or full article access on ReadCube.  
from \$8.99

[Rent or Buy](#)

All prices are NET prices.

### **Additional access options:**

- [Log in](#)
- [Access through your institution](#)
- [Learn about institutional subscriptions](#)

**Fig. 1: USP20 is required for feeding-induced increase of HMGCR.**

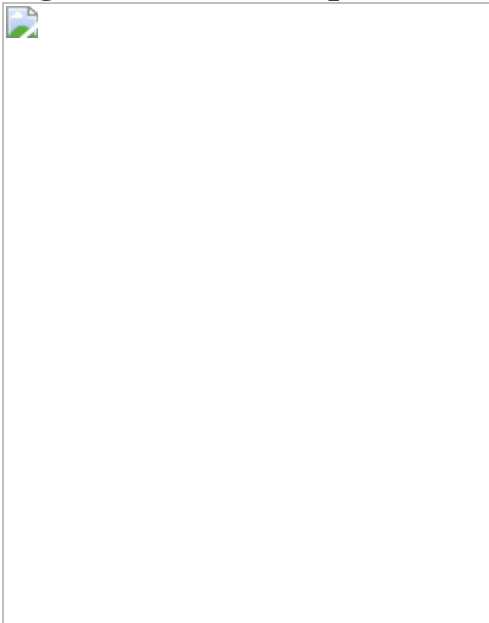


**Fig. 2: Insulin and glucose regulate USP20 through mTORC1-mediated phosphorylation at S132 and S134.**



**Fig. 3: L-*Usp20*<sup>-/-</sup> mice display improved metabolism.**



**Fig. 4: Pharmacological USP20 inhibition improves metabolism in mice.**





## Data availability

All source data for immunoblotting are shown in Supplementary Fig. 1. [Source data](#) are provided with this paper.

## References

1. 1.

Luo, J., Yang, H. & Song, B. L. Mechanisms and regulation of cholesterol homeostasis. *Nat. Rev. Mol. Cell Biol.* **21**, 225–245 (2020).

[CAS Article](#) [Google Scholar](#)

2. 2.

Repa, J. J. & Mangelsdorf, D. J. The role of orphan nuclear receptors in the regulation of cholesterol homeostasis. *Annu. Rev. Cell Dev. Biol.* **16**, 459–481 (2000).

[CAS Article](#) [Google Scholar](#)

3. 3.

Edwards, P. A., Muroya, H. & Gould, R. G. In vivo demonstration of the circadian rhythm of cholesterol biosynthesis in the liver and intestine of the rat. *J. Lipid Res.* **13**, 396–401 (1972).

[CAS](#) [PubMed](#) [Google Scholar](#)

4. 4.

Porter, J. A., Young, K. E. & Beachy, P. A. Cholesterol modification of hedgehog signaling proteins in animal development. *Science* **274**, 255–259 (1996).

[CAS](#) [Article](#) [ADS](#) [Google Scholar](#)

5. 5.

Xiao, X. et al. Cholesterol modification of smoothened is required for hedgehog signaling. *Mol. Cell* **66**, 154–162 (2017).

[CAS](#) [Article](#) [Google Scholar](#)

6. 6.

Hu, A. & Song, B. L. The interplay of Patched, Smoothened and cholesterol in Hedgehog signaling. *Curr. Opin. Cell Biol.* **61**, 31–38 (2019).

[CAS](#) [Article](#) [Google Scholar](#)

7. 7.

Chen, L. et al. Regulation of glucose and lipid metabolism in health and disease. *Sci. China Life Sci.* **60**, 1765–1775 (2019).

[CAS](#) [Google Scholar](#)

8. 8.

Goldstein, J. L. & Brown, M. S. Regulation of the mevalonate pathway. *Nature* **343**, 425–430 (1990).

[CAS](#) [Article](#) [ADS](#) [Google Scholar](#)

9. 9.

Brown, M. S. & Goldstein, J. L. The SREBP pathway: regulation of cholesterol metabolism by proteolysis of a membrane-bound transcription factor. *Cell* **89**, 331–340 (1997).

[CAS](#) [Article](#) [Google Scholar](#)

10. 10.

DeBose-Boyd, R. A. & Ye, J. SREBPs in lipid metabolism, insulin signaling, and beyond. *Trends Biochem. Sci.* **43**, 358–368 (2018).

[CAS](#) [Article](#) [Google Scholar](#)

11. 11.

Cahill, G. F., Jr. Fuel metabolism in starvation. *Annu. Rev. Nutr.* **26**, 1–22 (2006).

[CAS](#) [Article](#) [Google Scholar](#)

12. 12.

Song, B. L., Sever, N. & DeBose-Boyd, R. A. Gp78, a membrane-anchored ubiquitin ligase, associates with Insig-1 and couples sterol-regulated ubiquitination to degradation of HMG CoA reductase. *Mol. Cell* **19**, 829–840 (2005).

[CAS](#) [Article](#) [Google Scholar](#)

13. 13.

Liu, T.-F. et al. Ablation of gp78 in liver improves hyperlipidemia and insulin resistance by inhibiting SREBP to decrease lipid biosynthesis. *Cell Metab.* **16**, 213–225 (2012).

[CAS](#) [Article](#) [Google Scholar](#)

14. 14.

Jiang, L. Y. et al. Ring finger protein 145 (RNF145) is a ubiquitin ligase for sterol-induced degradation of HMG-CoA reductase. *J. Biol. Chem.* **293**, 4047–4055 (2018).

[CAS](#) [Article](#) [Google Scholar](#)

15. 15.

Song, B.-L. & DeBose-Boyd, R. A. Ubiquitination of 3-hydroxy-3-methylglutaryl-CoA reductase in permeabilized cells mediated by cytosolic E1 and a putative membrane-bound ubiquitin ligase. *J. Biol. Chem.* **279**, 28798–28806 (2004).

[CAS](#) [Article](#) [Google Scholar](#)

16. 16.

Song, B.-L., Javitt, N. B. & DeBose-Boyd, R. A. Insig-mediated degradation of HMG CoA reductase stimulated by lanosterol, an intermediate in the synthesis of cholesterol. *Cell Metab.* **1**, 179–189 (2005).

[CAS](#) [Article](#) [Google Scholar](#)

17. 17.

Cao, J. et al. Ufd1 is a cofactor of gp78 and plays a key role in cholesterol metabolism by regulating the stability of HMG-CoA reductase. *Cell Metab.* **6**, 115–128 (2007).

[CAS](#) [Article](#) [Google Scholar](#)

18. 18.

Nijman, S. M. B. et al. A genomic and functional inventory of deubiquitinating enzymes. *Cell* **123**, 773–786 (2005).

[CAS](#) [Article](#) [Google Scholar](#)

19. 19.

Sever, N. et al. Insig-dependent ubiquitination and degradation of mammalian 3-hydroxy-3-methylglutaryl-CoA reductase stimulated by sterols and geranylgeraniol. *J. Biol. Chem.* **278**, 52479–52490 (2003).

[CAS](#) [Article](#) [Google Scholar](#)

20. 20.

Rong, S. et al. Expression of SREBP-1c requires SREBP-2-mediated generation of a sterol ligand for LXR in livers of mice. *eLife* **6**, e25015 (2017).

[Article](#) [Google Scholar](#)

21. 21.

Yang, C. et al. Sterol intermediates from cholesterol biosynthetic pathway as liver X receptor ligands. *J. Biol. Chem.* **281**, 27816–27826 (2006).

[CAS](#) [Article](#) [Google Scholar](#)

22. 22.

Hillgartner, F. B., Salati, L. M. & Goodridge, A. G. Physiological and molecular mechanisms involved in nutritional regulation of fatty acid synthesis. *Physiol. Rev.* **75**, 47–76 (1995).

[CAS](#) [Article](#) [Google Scholar](#)

23. 23.

Li, S., Brown, M. S. & Goldstein, J. L. Bifurcation of insulin signaling pathway in rat liver: mTORC1 required for stimulation of lipogenesis, but not inhibition of gluconeogenesis. *Proc. Natl Acad. Sci. USA* **107**, 3441–3446 (2010).

[CAS](#) [Article](#) [ADS](#) [Google Scholar](#)

24. 24.

Condon, K. J. & Sabatini, D. M. Nutrient regulation of mTORC1 at a glance. *J. Cell Sci.* **132**, 222570 (2019).

[Article](#) [Google Scholar](#)

25. 25.

Gwinn, D. M. et al. AMPK phosphorylation of raptor mediates a metabolic checkpoint. *Mol. Cell* **30**, 214–226 (2008).

[CAS](#) [Article](#) [Google Scholar](#)

26. 26.

Inoki, K., Zhu, T. & Guan, K. L. TSC2 mediates cellular energy response to control cell growth and survival. *Cell* **115**, 577–590 (2003).

[CAS](#) [Article](#) [Google Scholar](#)

27. 27.

González, A., Hall, M. N., Lin, S. C. & Hardie, D. G. AMPK and TOR: the yin and yang of cellular nutrient sensing and growth control. *Cell Metab.* **31**, 472–492 (2020).

[Article](#) [Google Scholar](#)

28. 28.

Inoki, K., Kim, J. & Guan, K. L. AMPK and mTOR in cellular energy homeostasis and drug targets. *Annu. Rev. Pharmacol. Toxicol.* **52**, 381–400 (2012).

[CAS](#) [Article](#) [Google Scholar](#)

29. 29.

Yu, Y. et al. Phosphoproteomic analysis identifies Grb10 as an mTORC1 substrate that negatively regulates insulin signaling. *Science* **332**, 1322–1326 (2011).

[CAS](#) [Article](#) [ADS](#) [Google Scholar](#)

30. 30.

Hsu, P. P. et al. The mTOR-regulated phosphoproteome reveals a mechanism of mTORC1-mediated inhibition of growth factor signaling. *Science* **332**, 1317–1322 (2011).

[CAS](#) [Article](#) [ADS](#) [Google Scholar](#)

31. 31.

Arnedo, M. et al. More than one HMG-CoA lyase: The classical mitochondrial enzyme plus the peroxisomal and the cytosolic ones. *Int. J. Mol. Sci.* **20**, 6124 (2019).

[CAS](#) [Article](#) [Google Scholar](#)

32. 32.

Puchalska, P. et al. Hepatocyte–macrophage acetoacetate shuttle protects against tissue fibrosis. *Cell Metab.* **29**, 383–398.e7 (2019).

[CAS](#) [Article](#) [Google Scholar](#)

33. 33.

Mills, E. L. et al. Accumulation of succinate controls activation of adipose tissue thermogenesis. *Nature* **560**, 102–106 (2018).

[CAS](#) [Article](#) [ADS](#) [Google Scholar](#)

34. 34.

Liu, K. et al. Scd1 controls de novo beige fat biogenesis through succinate-dependent regulation of mitochondrial complex II. *Proc. Natl Acad. Sci. USA* **117**, 2462–2472 (2020).

[CAS](#) [Article](#) [Google Scholar](#)

35. 35.

Harrigan, J. A., Jacq, X., Martin, N. M. & Jackson, S. P. Deubiquitylating enzymes and drug discovery: emerging opportunities. *Nat. Rev. Drug Discov.* **17**, 57–78 (2018).

[CAS](#) [Article](#) [Google Scholar](#)

36. 36.

Paseban, M., Butler, A. E. & Sahebkar, A. Mechanisms of statin-induced new-onset diabetes. *J. Cell. Physiol.* **234**, 12551–12561 (2019).

[CAS](#) [Article](#) [Google Scholar](#)

37. 37.

Balaz, M. et al. Inhibition of mevalonate pathway prevents adipocyte browning in mice and men by affecting protein prenylation. *Cell Metab.* **29**, 901–916.e8 (2019).

[CAS](#) [Article](#) [Google Scholar](#)

[Download references](#)

## Acknowledgements

We thank D. Liang and B.-Y. Xiang for technical assistance; Y. Qiu and S. Fu for reagents; and X. Zhou and L. Deng for bomb calorimetry. This work was supported by grants from the National Natural Science Foundation China (91957103, 91954203, 31690102 and 32021003) and Ministry of Science and Technology China (2016YFA0500100). B.-L.S. acknowledges the support from the Tencent Foundation through the Xplorer Prize.

## Author information

### Author notes

1. These authors contributed equally: Xiao-Yi Lu, Xiong-Jie Shi, Ao Hu, Ju-Qiong Wang

### Affiliations

1. Hubei Key Laboratory of Cell Homeostasis, College of Life Sciences, Frontier Science Center for Immunology and Metabolism, the Institute for Advanced Studies, Wuhan University, Wuhan, China

Xiao-Yi Lu, Xiong-Jie Shi, Ao Hu, Ju-Qiong Wang, Yi Ding, Wei Jiang, Ming Sun, Xiaolu Zhao, Jie Luo & Bao-Liang Song

2. School of Life Science and Technology, ShanghaiTech University, Shanghai, China

Wei Qi

### Authors

1. Xiao-Yi Lu  
[View author publications](#)

You can also search for this author in [PubMed](#) [Google Scholar](#)

2. Xiong-Jie Shi

[View author publications](#)

You can also search for this author in [PubMed](#) [Google Scholar](#)

3. Ao Hu

[View author publications](#)

You can also search for this author in [PubMed](#) [Google Scholar](#)

4. Ju-Qiong Wang

[View author publications](#)

You can also search for this author in [PubMed](#) [Google Scholar](#)

5. Yi Ding

[View author publications](#)

You can also search for this author in [PubMed](#) [Google Scholar](#)

6. Wei Jiang

[View author publications](#)

You can also search for this author in [PubMed](#) [Google Scholar](#)

7. Ming Sun

[View author publications](#)

You can also search for this author in [PubMed](#) [Google Scholar](#)

8. Xiaolu Zhao

[View author publications](#)

You can also search for this author in [PubMed](#) [Google Scholar](#)

9. Jie Luo

[View author publications](#)

You can also search for this author in [PubMed](#) [Google Scholar](#)

10. Wei Qi

[View author publications](#)

You can also search for this author in [PubMed](#) [Google Scholar](#)

11. Bao-Liang Song

[View author publications](#)

You can also search for this author in [PubMed](#) [Google Scholar](#)

## Contributions

X.-Y.L. and X.-J.S. carried out the overall experiments and analysed the data. A.H., Y.D., and W.J. performed the screening of the DUB expression library. A.H. performed the in vitro kinase assay and in vitro deubiquitination assay. J.-Q.W. performed experiments in UCP1-knockout mice and HMGCR(K248R) knock-in mice. Y.D. and M.S. assisted with the animal and cell experiments. X.Z. performed metabolites analysis and analysed the data. B.-L.S. conceived the project and directed the research. B.-L.S., X.-Y.L., X.-J.S., W.Q. and J.L. wrote the paper with input from the other authors.

## Corresponding author

Correspondence to [Bao-Liang Song](#).

## Ethics declarations

## Competing interests

The authors declare no competing interests.

## Additional information

**Peer review information** *Nature* thanks Wayne Hancock and the other, anonymous, reviewer(s) for their contribution to the peer review of this work.

**Publisher's note** Springer Nature remains neutral with regard to jurisdictional claims in published maps and institutional affiliations.

## Extended data figures and tables

### Extended Data Fig. 1 In vitro ubiquitination assay of HMGCR.

**a**, Quantification of the proteins in Fig. 1a. The signals of HMGCR, FDFT1, LSS and DHCR24 were normalized to that of GAPDH. The amount of each protein in fasted state was defined as 1. **b**, Relative amounts of mRNAs in the livers of the mice in Fig. 1a measured by qPCR. **c**, Immunoblot analysis of HMGCR, FDFT1, LSS and DHCR24 in the livers of mice fasted (F) for 12 h, or fasted for 12 h and then refed (R) with a high-carbohydrate/low-fat diet for 3 h, 6 h, or 12 h ( $n = 3$  per group) respectively. **d**, Quantification of proteins in (c). **e**, The mRNA levels of indicated genes in mouse liver ( $n = 4$  per group) treated as in (c). **f**, Schematic representation of the experimental design for in vitro ubiquitination assays. Membrane fractions were prepared from the sterol-depleted CHO-7 cells to provide un-ubiquitinated HMGCR and E3 complex. The liver cytosols were prepared from mice under fasted or refed conditions. The membrane fractions were incubated with E1, UBE2G2, ATP, FLAG-Ubiquitin, the indicated cytosol and 25-hydroxycholesterol (25-HC) at 37 °C for 30 min. Samples were solubilized and HMGCR was immunoprecipitated with polyclonal anti-HMGCR antibodies. Immunoblotting was carried out with monoclonal anti-FLAG or monoclonal anti-HMGCR antibodies. **g**, In vitro ubiquitination of HMGCR as described in (f). Experiments were performed as indicated three times with similar results. All values are presented as mean ± SEM. Data were analysed by unpaired two-tailed Student's *t*-test (**a**, **b**), or one-way ANOVA with Tukey's multiple comparisons test (**d**, **e**). [Source data](#)

## Extended Data Fig. 2 The screening of the DUB expression library.

Experiments were performed as indicated three times with similar results. **a–p**, CHO-7 cells were set up for experiments on day 0 at  $4 \times 10^5$  cells per 60-mm dish in DMEM/F12 supplemented with 5% FBS. On day 1, cells were transfected in 3 ml of DMEM/F12 supplemented with 5% FBS containing 1  $\mu$ g of pCMV-HMGCR-T7, 30 ng of pCMV-Insig-1-Myc and 0.3  $\mu$ g indicated Dub. The total DNA was adjusted to 2  $\mu$ g dish $^{-1}$  using pcDNA3 mock vector. Eight hours after transfection, cells were incubated in 3 ml of DMEM/F12 supplemented with 5% FBS. On day 2, cells were washed with phosphate-buffered saline (PBS) and then switched to DMEM/F12 containing 5% lipoprotein-deficient serum (LPDS), 1  $\mu$ M lovastatin, and 10  $\mu$ M mevalonate. After incubation for 16 h at 37 °C, the cells were treated with 1  $\mu$ g ml $^{-1}$  25-HC plus 10 mM mevalonate as indicated. After 5 h at 37 °C, cells from 2 dishes were pooled and collected, lysed, and subjected to immunoblotting. Immunoblot analysis was carried out with anti-T7 IgG (against HMGCR) and anti-FLAG IgG (against DUBs) as described. Mev., mevalonate.

## Extended Data Fig. 3 Characterization of the deubiquitylase USP20.

**a**, In vitro activities of USP20 variants indicated by the hydrolysis of a fluorogenic substrate Ubiquitin-7-amino-4-trifluoromethylcoumarin (Ub-AFC). The WT USP20 and USP20(C154S) proteins were purified from HEK 293T cells. Negative control (NC) means no protein added. Inset western blotting shows the similar amount of the proteins. **b**, Hydrolysis of various linked di-ubiquitin (Ub2) by USP20 in vitro. **c**, USP20 decreases sterol-induced ubiquitination of HMGCR. CHO-7 cells were transfected with the indicated plasmids, depleted of sterols as in Extended Data Fig. 2 and then treated with 25-HC plus 10  $\mu$ M MG132 for 2 h. Cells lysates were immunoprecipitated with anti-T7 beads. The pellet was immunoblotted with anti-HA antibody and anti-HMGCR. The input was immunoblotted with anti-FLAG. **d**, GSK2643943A inhibits USP20-mediated deubiquitination of HMGCR. CHO-7 cells were transfected with plasmids and depleted of

sterols. Then the cells were treated with 1 µg ml<sup>-1</sup> 25-HC in the presence of MG132 for 2 h. Cell lysates were immunoprecipitated with anti-T7 beads. The pellet was immunoblotted with anti-HA and anti-HMGCR antibodies. The input was immunoblotted with anti-FLAG. **e**, GSK2643943A inhibits USP20-mediated HMGCR deubiquitination in vitro. The sterol-depleted CHO-7 cells were treated with 25-HC plus MG132. Cells lysates were immunoprecipitated with anti-HMGCR antibody-coupled agarose. The pellet samples were then incubated with recombinant USP20 protein for 30 min at 37 °C. \*: non-specific band. USP20 was inactivated by boiling for 10 min as a control. Experiments in (**a–e**) were performed as indicated three times with similar results. **f–h**, Knockdown of *Usp20* accelerated sterol-induced degradation of HMGCR. Huh7 cells were transfected with scrambled (negative control, NC) or USP20-targeting siRNA, treated as in Fig. [1d](#). The experiments were repeated for three times. **i**, Quantification of HMGCR in (**f–h**). Data are mean ± SEM and were analysed by two-way ANOVA. [Source data](#)

#### [Extended Data Fig. 4 Characterization of L-\*Usp20\*<sup>-/-</sup> mice and the regulation of hepatic HMGCR by glucose and insulin.](#)

**a**, Tissue distribution of mouse USP20 protein. **b**, Schematic of L-*Usp20*<sup>-/-</sup> gene-targeting strategy. **c**, Immunoblotting analysis of different tissues of WT and L-*Usp20*<sup>-/-</sup> mice. **d–f**, Body weight (**d**), food intake (**e**) and serum AST (**f**) of male WT and L-*Usp20*<sup>-/-</sup> (*n* = 5 per group) mice fed chow diet ad libitum. **g**, Incorporation of tritium-labelled H<sub>2</sub>O into sterol in kidney of the mice (*n* = 4 per group) as in Fig. [1f](#). **h**, Eight-week-old male L-*Usp20*<sup>-/-</sup> and their male WT littermates were fed chow diet and subjected to fasting and refeeding treatment. The metabolic parameters were measured. Each value represents mean ± SEM of data from five mice. \**P* < 0.05, \*\**P* < 0.01, \*\*\**P* < 0.001 for the level of statistical significance (unpaired two-tailed Student's *t*-test) between WT and L-*Usp20*<sup>-/-</sup> mice under the same condition. The “a” means refed WT mice versus fasted WT mice; “b” means refed L-*Usp20*<sup>-/-</sup> versus fasted L-*Usp20*<sup>-/-</sup>; “c” means fasted L-*Usp20*<sup>-/-</sup> versus fasted WT mice; “d” means refed L-*Usp20*<sup>-/-</sup> versus refed WT mice. **i**, Relative amounts of mRNAs in the livers of the mice treated as in (**h**). Each value represents mean of data from three mice. **j**,

Immunoblotting analysis of hepatic HMGCR protein upon glucose and insulin stimulation. Eight-week-old male WT mice were fasted overnight and intraperitoneally injected with 2 mg g<sup>-1</sup> glucose or 0.75 mU g<sup>-1</sup> insulin or both. After 3 h, liver samples were subjected to immunoblotting. **k**, qPCR analysis of the mRNAs in mice livers ( $n = 3$  per group) treated as in **(j)**. **l**, WT mouse primary hepatocytes were untreated (-) or treated (+) with 25.5 mM glucose or 10 nM insulin for 3 h or 5 h. **m**, qPCR analysis of the mouse primary hepatocytes ( $n = 3$  per group) treated as in **(l)**. **n**, Inhibition of mTOR signalling antagonizes insulin-induced stabilization of HMGCR. WT primary hepatocytes were grown in M199 medium. On day 1, cells were transfected plasmids and depleted of cholesterol by incubating in M199 medium containing 5% LPDS, 1 μM lovastatin and 10 μM mevalonate for 16 h. Then, the cells were switched to the same medium with indicated inhibitor (Wort. wortmannin, 0.2 μM; AKTi, AKT1/2 kinase inhibitor 10 μM; Rap. Rapamycin, 0.1 μM). After 2 h, cells were treated with or without 1 μg ml<sup>-1</sup> 25-HC plus 10 mM mevalonate in the absence (-) or presence (+) of insulin and the indicated inhibitors for 5 h. Immunoblots were performed with the indicated antibodies. **o**, Effect of AMPK inhibition Dorsomorphin. WT primary hepatocytes were transfected, depleted of sterol, treated with 1 μM Dorsomorphin, 5.5 mM (-) or 25.5 mM (+) glucose combined with 1 μg ml<sup>-1</sup> 25-HC plus 10 mM mevalonate for 5 h. **p**, Effect of AMPK activation A-769662. WT primary hepatocytes were transfected, depleted of sterol, treated with 1 μM AMPK activator A-769662, 25.5 mM (+) glucose combined with 1 μg ml<sup>-1</sup> 25-HC plus 10 mM mevalonate for 5 h. Experiments in **(a, c, l–p)** were performed as indicated twice with similar results. Statistical significance was determined using unpaired two-tailed Student's *t*-test **(d–g, k, m)**. Bars represent mean ± SEM. [Source data](#)

## Extended Data Fig. 5 Analysis the phosphorylation sites of USP20 and its interaction with gp78.

**a**, Procedure to identify the phosphorylated sites of USP20. **b**, The top 10 of phosphorylated USP20 peptides. H: high glucose; L: low glucose. **c**, Mass spectrum showing that USP20 was phosphorylated at S132 and S134. **d**, Domain organization of USP20. zf-UBP: zinc-finger ubiquitin binding

domain; DUSP: domain present in ubiquitin-specific protease. **e**, Validation of the home-made phospho-specific antibody recognizing p-S132/p-S134 of USP20 (p-USP20). USP20 was immunoprecipitated from HEK 293T cells, treated with or without 1U  $\mu\text{l}^{-1}$   $\lambda$ -phosphatase and 5U  $\text{ml}^{-1}$  CIP (PPase), eluted with FLAG peptide and subjected to immunoblotting. **f**, Rapamycin attenuates USP20 phosphorylation. WT primary hepatocytes were transfected with the indicated plasmid, pre-treated with 100 nM rapamycin for 30 min, and then stimulated with 25.5 mM glucose plus 10 nM insulin for additional 1 h. Cells were lysed with 0.5% NP-40 containing protease and phosphatase inhibitors and immunoprecipitated with anti-FLAG agarose. **g**, Eight-week-old male WT mice were subjected to fasting and refeeding. Vehicle or rapamycin ( $5 \text{ mg kg}^{-1}$ ) were intraperitoneally injected 1 h before fasting or refeeding respectively. Immunoblot analysis of liver samples was performed. F: fasted; R: refed; V: vehicle; Rapa.: rapamycin. **h, i**, Serum total cholesterol (**h**) and triglyceride (**i**) of the mice in (**g**) ( $n = 5$  per group). **j, k**, Liver total cholesterol (**j**) and triglyceride (**k**) of the mice in (**g**) ( $n = 5$  per group). **l**, In vitro activities of USP20 variants. The inset demonstrated equal amounts of USP20 proteins. **m**, Immunoblot analysis of endogenous Insig-1 and 2 in WT and gp78-KO CHO cells. **n, o**, Overexpression of Insig-1 (**n**) or Insig-2 (**o**) does not block HMGCR-USP20 interaction. **p**, Mapping the region of gp78 that interacts with USP20. **q**, The interaction of gp78 and USP20 is unresponsive to 25-HC and mevalonate. Experiments in (**e, f, l–q**) were performed as indicated twice with similar results. All values are presented as mean  $\pm$  SEM. Data were analysed by unpaired two-tailed Student's *t*-test (**h–k**). [Source data](#)

## Extended Data Fig. 6 Characterization of the *Usp20*<sup>KI/KI</sup> mice and analysis the metabolism of L-*Usp20*<sup>−/−</sup> and *Usp20*<sup>KI/KI</sup> mice on HFHS.

**a**, Strategy to generate *Usp20*<sup>KI/KI</sup> mice expressing USP20(S132A/S134A). **b–f**, Eight-week-old male *Usp20*<sup>KI/KI</sup> mice and their male WT littermates under chow diet were subjected to fasting and refeeding ( $n = 5$  per group). TC (**b**), TG (**c**), free FA (**d**), insulin (**e**) and glucose (**f**) in the serum were measured. **g**, Relative amounts of mRNAs in the livers of WT and *Usp20*<sup>KI/KI</sup> mice subjected to fasting and refeeding treatments measured by

qPCR. Each value represents mean of data from five mice. **h, i**, In vitro HMGCR deubiquitination assay performed as depicted in Fig. [1b](#). **j–n**, Eight-week-old male L-*Usp20*<sup>-/-</sup> mice and their male WT littermates were randomly grouped ( $n = 6$  per group) and allowed ad libitum access to water and the HFHS diet for 23 weeks as in Fig. [3a](#). **j**, Representative image of the mice after 23-week of HFHS diet. **k**, Cumulative food intake ( $n = 6$  per group). **l**, Measurement of fecal energy by bomb calorimetry ( $n = 5$  per group). **m, n**, Respiratory exchange ratio (RER) (**m**) and movement (**n**) as determined by metabolic cages ( $n = 6$  per group). **o–u**, Eight-week-old male *Usp20*<sup>KI/KI</sup> mice and their male WT littermates were randomly grouped ( $n = 5$  per group) and allowed ad libitum access to water and the HFHS Diet for 14 weeks. **o**, Representative images after 14-week of HFHS diet. **p**, Body weight ( $n = 5$  per group). **q, r**, Whole-body composition ( $n = 5$  per group). **s**, Liver weight ( $n = 5$  per group). **t**, GTT ( $n = 5$  per group). **u**, ITT ( $n = 5$  per group). **v, w**, Effect of chronic HFHS diet. Eight-week-old male L-*Usp20*<sup>-/-</sup> mice and their male WT littermates were randomly grouped and allowed ad libitum access to water and normal chow diet or HFHS diet for 8 weeks. **v**, Mice were fasted for 4 h and then sacrificed. **w**, Mice were subjected to fasting and refeeding treatment as in Fig. [1a](#). Liver samples were analysed by western blotting. CD: chow diet; HFHS: high-fat and high sucrose diet; F: fasted; R: refed. Each value represents mean  $\pm$  SEM. Experiments in (**h, i, v, w**) were performed as indicated twice with similar results. Statistical significance was determined using unpaired two-tailed Student's *t*-test (**b–f, l, m, q–s**); or two-way ANOVA (**n, p, t, u**). [Source data](#)

## [Extended Data Fig. 7 Expression of HMGCR\(K248R\) by AAV or knock-in reverses the phenotypes of L-\*Usp20\*<sup>-/-</sup> mice.](#)

**a**, HMGCR(K248R) was resistant to sterol-induced degradation. +: 0.3  $\mu$ g ml<sup>-1</sup> 25-HC and 3 mM Mev; ++: 1  $\mu$ g ml<sup>-1</sup> 25-HC and 10 mM Mev. The experiments were carried out as described in Fig. [1d](#). **b**, USP20 did not increase the level of HMGCR(K248R). 1  $\mu$ g ml<sup>-1</sup> 25-HC and 10 mM Mev were used. **c–j**, Eight-week-old male L-*Usp20*<sup>-/-</sup> mice and their male WT littermates were injected with  $1 \times 10^{10}$  viral genome (v.g.) of AAV-HMGCR(K248R) or AAV-control (Ctr). After HFHS diet for 8 weeks, the

mice were analysed. **c**, Immunoblotting analysis of liver samples. **d**, Body weight ( $n = 3$  for WT injected with AAV-Ctr,  $n = 4$  for other groups). **e**, Total cholesterol in serum ( $n = 3$  for WT injected with AAV-Ctr,  $n = 4$  for other groups). **f**, Triglyceride in serum ( $n = 3$  for WT injected with AAV-Ctr,  $n = 4$  for other groups). **g**, **h**, Whole-body oxygen consumption of mice over dark and light cycles ( $n = 3$  for WT injected with AAV-Ctr,  $n = 4$  for other groups). **i**, GTT ( $n = 3$  for WT injected with AAV-Ctr,  $n = 4$  for other groups). **j**, Strategy to generate *Hmgcr*<sup>KI/KI</sup> mice expressing HMGCR(K248R). **k–p**, Eight-week-old male mice were fed the HFHS diet for 7 weeks and then subjected to fasting-refeeding treatment. **k**, western blotting analysis of liver samples. **l**, Total cholesterol in serum ( $n = 3$  per group). **m**, Triglyceride in serum ( $n = 3$  per group). **n**, **o**, Whole-body oxygen consumption of mice ( $n = 4$  per group). **p**, GTT ( $n = 5$  per group). Each value represents mean  $\pm$  SEM. Experiments in (**a–c**, **k**) were performed as indicated twice with similar results. Statistical significance was determined using unpaired two-tailed Student's *t*-test (**d–f**, **h**, **i** (right), **l**, **m**, **o**, **p** (right)); or two-way ANOVA (**g**, **i** (left), **n**, **p** (left)). F: fasted; R: refed. [Source data](#)

## Extended Data Fig. 8 Level of tricarboxylic acid metabolites and some factors.

**a**, Proposed link between cholesterol biosynthetic pathway and succinate. **b**, Levels of the metabolites in liver. The male WT and L-*Usp20*<sup>−/−</sup> littermates ( $n = 4$  per group) were fasted for 12 h and then refed for 6 h. The metabolites were measured by liquid chromatography-tandem mass spectrometry (LC-MS/MS). **c**, Changes in the metabolites associated with the tricarboxylic acid cycle in liver. The male WT and L-*Usp20*<sup>−/−</sup> littermates ( $n = 4$  per group) were fasted for 12 h and then refed for 6 h. Liver metabolites were measured by LC-MS/MS. The fold change was calculated through dividing the L-*Usp20*<sup>−/−</sup> mice value by the WT mice mean value. \* $P < 0.05$  for the level of statistical significance (unpaired two-tailed Student's *t*-test) between WT and L-*Usp20*<sup>−/−</sup> mice. **d–l**, The epinephrine (**d**), norepinephrine (**e**), triiodothyronine (T3) (**f**), thyroxine (T4) (**g**), secretin (**h**), thyroid-stimulating hormone (TSH) (**i**), FGF21 (**j**), ALT (**k**) and AST (**l**) of L-*Usp20*<sup>−/−</sup> and WT mice ( $n = 6$  per group). The

data were analysed by unpaired two-tailed Student's *t*-test (**b**, **d–l**). The values present as mean ± SEM. [Source data](#)

### Extended Data Fig. 9 Analysis of the mice receiving GSK2643943A.

**a**, Chemical structure of GSK2643943A. **b**, In vitro deubiquitylase activity of USP20 inhibited by 1, 3, or 10 µM GSK2643943. NC: no USP20 control. **c–i**, The mice were treated as in Fig. 4a. TC (**c**) and TG (**d**) in serum of mice treated with vehicle (V) or GSK2643943A (G) were measured after fasting and refeeding ( $n = 4$  per group). **e**, **f**, GTT ( $n = 6$  per group). **g**, Quantification of whole-body oxygen consumption of mice ( $n = 6$  per group) in Fig. 4e. **h**, **i**, Serum ALT (**h**) and AST (**i**) of the mice ( $n = 6$  per group). **j–y**, The mice were treated as in Fig. 4f. **j**, Food intake ( $n = 6$  per group). **k**, Measurement of fecal energy ( $n = 5$  per group) by bomb calorimetry. Fat mass (**l**), lean mass (**m**) of the mice ( $n = 6$  per group) measured at the indicated time. Liver weight (**n**), BAT weight (**o**), heart weight (**p**) and kidney weight (**q**) of the mice ( $n = 6$  per group) measured on Day 14. **r**, On Day 14 shown in Fig. 4f, the mice were fasted for 4 h and then sacrificed. The tissue samples were analysed by western blotting. Experiments in (**r**) were performed as indicated twice with similar results. **s**, **t**, Whole-body oxygen consumption of the mice ( $n = 6$  per group) measured by metabolic cages. **u–w**, AST (**u**), ALT (**v**) and creatinine (**w**) in serum of the mice ( $n = 6$  per group). **x**, Serum TNF $\alpha$  ( $n = 5$  per group). **y**, Expression of the genes including macrophage markers (CD68, F4/80 and Arg1) and inflammatory markers (TNF $\alpha$  and IL6) of the mice ( $n = 6$  per group) determined by qPCR. All values are expressed as means ± SEM. Data were analysed by two-way ANOVA (**e**, **l**, **s**), or unpaired two-tailed Student's *t*-test (**c**, **d**, **f–k**, **n–q**, **t–y**). [Source data](#)

### Extended Data Fig. 10 Analysis the effects of GSK2643943A on Ucp1 KO or L-Usp20<sup>−/−</sup> mice.

**a–l**, Eight-week-old male *Ucp1* KO mice and their male WT littermates were randomly grouped, fed the HFHS diet and gavaged with vehicle or 30 mg kg<sup>−1</sup> GSK2643943A daily for 13 days. GTT and metabolic cage analysis

were performed on day 7 and 10, respectively. **a**, Immunoblotting analysis. \*: non-specific band. **b**, Body weight per mouse ( $n = 3$  per group) during the experiments. **c**, Cumulative food intake for each treatment. Each value represents mean of data from three mice. **d**, **e**, Whole-body oxygen consumption of the mice ( $n = 3$  per group) measured by metabolic cages. **f**, Respiratory exchange ratio (RER) over dark and light cycles ( $n = 3$  per group). **g**, **h**, GTT analysis ( $n = 3$  per group). **i–l**, TC (**i**), TG (**j**), AST (**k**), and ALT (**l**) in the serum ( $n = 3$  per group). **m–s**, Eight-week-old male L-*Usp20*<sup>-/-</sup> mice and their male WT littermates were randomly grouped, fed the HFHS diet and gavaged with vehicle or 30 mg kg<sup>-1</sup> GSK2643943A daily for 13 days. GTT and metabolic cage analysis were performed on day 7 and 10, respectively. **m**, Immunoblotting analysis. **n**, **o**, Whole-body oxygen consumption of the mice ( $n = 4$  per group) measured by metabolic cages. **p**, **q**, GTT analysis ( $n = 4$  per group). **r**, Total cholesterol in serum ( $n = 4$  per group). **s**, Triglyceride in serum ( $n = 4$  per group). All values are expressed as means  $\pm$  SEM. Experiments in (**a**, **m**) were performed as indicated twice with similar results. Data were analysed by unpaired two-tailed Student's *t*-test (**e**, **f**, **h–l**, **o**, **q–s**), or two-way ANOVA (**b**, **d**, **g**, **n**, **p**).

[Source data](#)

## Supplementary information

### [Supplementary Information](#)

This file contains Supplementary Fig. 1 (raw gel data) and Supplementary Table 1 (a list of the sequences of primers and siRNAs).

### [Reporting Summary](#)

## Source data

### [Source Data Fig. 1](#)

### [Source Data Fig. 3](#)

[Source Data Fig. 4](#)

[Source Data Extended Data Fig. 1](#)

[Source Data Extended Data Fig. 3](#)

[Source Data Extended Data Fig. 4](#)

[Source Data Extended Data Fig. 5](#)

[Source Data Extended Data Fig. 6](#)

[Source Data Extended Data Fig. 7](#)

[Source Data Extended Data Fig. 8](#)

[Source Data Extended Data Fig. 9](#)

[Source Data Extended Data Fig. 10](#)

## Rights and permissions

[Reprints and Permissions](#)

## About this article



Check for  
updates

## Cite this article

Lu, XY., Shi, XJ., Hu, A. *et al.* Feeding induces cholesterol biosynthesis via the mTORC1–USP20–HMGCR axis. *Nature* **588**, 479–484 (2020).

<https://doi.org/10.1038/s41586-020-2928-y>

[Download citation](#)

- Received: 13 November 2019
- Accepted: 19 August 2020
- Published: 11 November 2020
- Issue Date: 17 December 2020
- DOI: <https://doi.org/10.1038/s41586-020-2928-y>

## Comments

By submitting a comment you agree to abide by our [Terms](#) and [Community Guidelines](#). If you find something abusive or that does not comply with our terms or guidelines please flag it as inappropriate.

[Access through your institution](#)

[Change institution](#)

[Buy or subscribe](#)

---

This article was downloaded by **calibre** from <https://www.nature.com/articles/s41586-020-2928-y>.

Fc-optimized antibodies elicit CD8 immunity to viral respiratory infection

[Download PDF](#)

- Article
- [Published: 08 October 2020](#)

# Fc-optimized antibodies elicit CD8 immunity to viral respiratory infection

- [Stylianos Bournazos](#) ORCID: orcid.org/0000-0001-5466-5620<sup>1</sup>,
- [Davide Corti](#) ORCID: orcid.org/0000-0002-5797-1364<sup>2</sup>,
- [Herbert W. Virgin](#) ORCID: orcid.org/0000-0001-8580-7628<sup>3</sup> &
- [Jeffrey V. Ravetch](#) ORCID: orcid.org/0000-0003-2024-9041<sup>1</sup>

[Nature](#) volume 588, pages485–490(2020) [Cite this article](#)

- 10k Accesses
- 1 Citations
- 155 Altmetric
- [Metrics details](#)

## Subjects

- [Antibody therapy](#)
- [Immunization](#)
- [Viral infection](#)

## Abstract

Antibodies against viral pathogens represent promising therapeutic agents for the control of infection, and their antiviral efficacy has been shown to require the coordinated function of both the Fab and Fc domains<sup>1</sup>. The Fc domain engages a wide spectrum of receptors on discrete cells of the immune system to trigger the clearance of viruses and subsequent killing of infected cells<sup>1,2,3,4</sup>. Here we report

that Fc engineering of anti-influenza IgG monoclonal antibodies for selective binding to the activating Fc $\gamma$  receptor Fc $\gamma$ RIIa results in enhanced ability to prevent or treat lethal viral respiratory infection in mice, with increased maturation of dendritic cells and the induction of protective CD8 $^{+}$  T cell responses. These findings highlight the capacity for IgG antibodies to induce protective adaptive immunity to viral infection when they selectively activate a dendritic cell and T cell pathway, with important implications for the development of therapeutic antibodies with improved antiviral efficacy against viral respiratory pathogens.

[Download PDF](#)

## Main

Several monoclonal antibodies to influenza virus epitopes from the globular head and the stalk domains of influenza hemagglutinin (HA) and neuraminidase (NA) (Fig. 1a) have been shown to confer broad and potent antiviral activity against diverse influenza strains<sup>5,6,7,8</sup>. These broadly protective monoclonal antibodies require Fc effector activity to provide full protection from lethal viral challenge, as mutant Fc domain variants that are unable to interact with Fc receptors (Fc $\gamma$ Rs) expressed on effector leukocytes are associated with reduced *in vivo* antiviral potency<sup>5,6</sup>. Although previous studies clearly demonstrated that broadly protective anti-influenza monoclonal antibodies depend on activating, but not inhibitory, Fc $\gamma$ Rs for activity<sup>5,6</sup>, the cell types and specific Fc $\gamma$ Rs that contribute to the antiviral activity of these monoclonal antibodies remains to be determined. The diversity of Fc $\gamma$ R expression on immune cells, the structural complexity of the Fc $\gamma$ R family, and the divergence of these receptors in different species (reviewed in ref. <sup>9</sup>) pose particular challenges in resolving the mechanistic details of how Fc $\gamma$ R dependence of anti-influenza antibodies result in enhanced protection *in vivo*.

**Fig. 1: Anti-HA stalk monoclonal antibodies engineered for increased Fc $\gamma$ RIIa affinity exhibit improved protective activity.**

 **figure1**

**a**, Influenza virus antigens (HA and NA) and the names of the tested monoclonal antibodies. **b**, Fc variants with differential Fc $\gamma$ R binding affinity were generated for anti-influenza monoclonal antibodies. WT, wild type. **c**, **d**, Fc variants of anti-HA stalk monoclonal antibodies FI6v3 (**c**) and FY1 (**d**) were administered intraperitoneally (4 mg kg $^{-1}$  for FI6v3 and 2 mg kg $^{-1}$  for FY1) to Fc $\gamma$ R-humanized mice before challenge with influenza (H1N1 PR8) ( $n = 6$  mice per group for PBS-treated;  $n = 10$  for WT FI6v3, GA, ALIE, GRLR and WT FY1;  $n = 9$  for FI6v3 GAALIE and FY1 V11; and  $n = 8$  for FY1 GA, afucosylated (Afuc), and GAALIE in two independent experiments). Weight loss (left; mean  $\pm$  s.e.m.) and survival curves (right) were compared to the corresponding wild-type human IgG1 antibody-treated group by two-way ANOVA (Bonferroni post hoc analysis adjusted for multiple comparisons) (**c**: \*\* $P = 0.0072$ , # $P = 0.0029$ , \* $P = 0.014$ , \*\*\* $P = 0.0035$ ) and log-rank (Mantel–Cox) test, respectively (**c**: \* $P = 0.019654$ ; \*\* $P = 0.006759$ ; \*\*\* $P = 0.000303$ ; **d**: \* $P = 0.0494$ , \*\* $P = 0.0045$ ). NS, not significant.

[Source data](#)

[Full size image](#)

To address this problem, we previously described a mouse model in which only human Fc $\gamma$ Rs are expressed in a pattern that recapitulates the expression pattern seen in human tissues as accurately as possible<sup>10</sup>. Despite the inherent limitations of the use of animal models to study human infection and disease, as well as differences in the absolute Fc $\gamma$ R expression levels and pattern of expression between humans and Fc $\gamma$ R-humanized mice (for example, the expression of Fc $\gamma$ RIIb on

monocytes and neutrophils that are commonly absent in humans), this strain represents a suitable platform to perform studies on human IgG antibody function with translational relevance to humans. This *in vivo* system is combined with anti-influenza antibodies (Fig. 1a) in which the human IgG1 Fc is expressed as a series of variants with selective binding affinity to specific human Fc $\gamma$ Rs (Fig. 1b, Extended Data Fig. 1a–j). These antibodies are administered to Fc $\gamma$ R-humanized mice before lethal challenge with influenza virus (intranasally, with five mouse lethal doses at 50% (mLD<sub>50</sub>)) and weight loss and survival were monitored over 14 days. Mice treated with broadly protective monoclonal antibodies that target the stalk domain of HA (FI6v3<sup>8</sup> or FY1<sup>7</sup>) showed enhanced protection when the Fc is modified to selectively engage the Fc $\gamma$ RIIa receptor (GA variant<sup>11,12</sup>), alone or in combination with enhanced Fc $\gamma$ RIIIa binding (GAALIE variant<sup>13</sup>) (Fig. 1c,d). Although Fc $\gamma$ RIIa-enhanced variants (GA) of FY1 fully protect mice that express only human Fc $\gamma$ RIIa under the conditions tested, they are unable to confer antiviral protection of Fc $\gamma$ R-deficient mice, confirming the dependence on Fc $\gamma$ RIIa engagement in the enhanced protection mediated by GA variants (Extended Data Fig. 5a–d). Similarly, the administration of a blocking monoclonal antibody with relative selectivity against Fc $\gamma$ RIIa (clone IV.3) reduces the ability of Fc $\gamma$ RIIa-enhanced variants (GA) of FI6v3 to protect Fc $\gamma$ R-humanized mice against lethal influenza challenge (Extended Data Fig. 5e,f). Enhancing Fc $\gamma$ RIIIa binding alone—using two complementary approaches: (i) protein engineering (ALIE variant<sup>12,14</sup>) or (ii) glycoengineering (afucosylated glycoforms<sup>15</sup>)—does not provide enhanced protection compared with the wild-type human IgG1 at the selected monoclonal antibody dose (determined based on titration studies that established the antibody dose at which wild-type IgG1 offers sub-optimal protection) (Extended Data Fig. 2). Consistent with previous studies that determined a key role for activating Fc $\gamma$ R engagement in the anti-viral activity of the selected monoclonal antibodies<sup>5,6</sup>, no protection is observed when the Fc is modified to abrogate Fc $\gamma$ R binding (GRLR variant) or engineered to engage the inhibitory Fc $\gamma$ RIIb (V11 variant<sup>16</sup>) (Fig. 1c,d). None of these Fc modifications affect the *in vitro* neutralization activity and target antigen-binding specificity (Extended Data Fig. 3a–f) or cause protein aggregation and altered pharmacokinetics *in vivo* (Extended Data Figs. 1c, d, 4a). In addition, quantification of the serum levels of anti-influenza monoclonal antibodies on day 3 after infection revealed comparable levels among the different Fc domain variants, which indicates that the observed effects could not be attributed to differential monoclonal antibody half-lives or *in vivo* stability (Extended Data Fig. 4b,c).

To determine whether the dependence on Fc $\gamma$ RIIa for the antiviral protection conferred by anti-HA stalk antibodies also extends to antibodies against other viral epitopes, we generated Fc domain variants for the 4G05<sup>5</sup> and 1A01<sup>5</sup> antibodies,

which target the globular head of HA and exhibit differential neutralization and haemagglutination inhibition (HAI) activity, as well as for the broadly reactive anti-NA monoclonal antibody, 3C05<sup>17</sup> (Extended Data Fig. [3g–o](#)). Similar to anti-HA stalk antibodies, Fc variants with enhanced affinity for FcγRIIa (GA or GAALIE variants) demonstrate enhanced protective activity compared with their wild-type human IgG1 counterparts (Fig. [2](#), Extended Data Fig. [4d–f](#)), which suggest that the FcγR mechanisms by which anti-influenza monoclonal antibodies confer protection against infection are conserved among antibodies with differential in vitro neutralization potency and epitope specificity.

**Fig. 2: Anti-HA globular head and anti-NA antibodies depend on FcγRIIa to confer protective activity in vivo.**

 figure2

**a–c**, Fc variants with differential Fc $\gamma$ R affinity (Fig. 1b) were generated for the anti-HA head monoclonal antibodies 4G05 (**a**) and 1A01 (**b**), and the anti-NA monoclonal antibody 3C05 (**c**). Fc $\gamma$ R-humanized mice were administered

intravenously with Fc domain variants of 4G05 ( $0.5 \text{ mg kg}^{-1}$ ) ( $n = 10$  mice per group for antibody-treated groups;  $n = 5$  for PBS group in two independent experiments) (a), 1A01 ( $2 \text{ mg kg}^{-1}$ ) ( $n = 8$  mice per group for WT, GA, ALIE and GAALIE groups;  $n = 6$  for GRLR;  $n = 4$  for PBS in two independent experiments) (b), and 3C05 ( $20 \text{ mg kg}^{-1}$ ) ( $n = 12$  mice per group for WT and GA groups;  $n = 10$  for GRLR and ALIE;  $n = 9$  for GAALIE;  $n = 6$  for PBS in two independent experiments) (c) before lethal challenge with influenza (H1N1 Neth/09). Weight loss (left; mean  $\pm$  s.e.m.) and survival curves (right) were compared to the corresponding wild-type unmodified IgG1-treated group by two-way ANOVA (Bonferroni post hoc analysis adjusted for multiple comparisons) (a: \* $P = 0.0034$ , # $P = 0.0052$ ;  $^P = 0.02$ ; ¶ $P = 0.03$ ; b: \* $P = 0.03$ , \*\* $P = 0.02$ , # $P = 0.01$ ,  $^P = 0.001$ , ## $P = 0.005$ , § $P = 0.002$ ,  $^{^P}P = 0.006$ , ¶ $P = 0.04$ ,  $^{^P}P = 0.009$ ; c: \* $P = 0.03$ ,  $^P = 0.02$ , # $P = 0.04$ ) and log-rank (Mantel–Cox) test, respectively (a: \*\* $P = 0.0042$ , b: \*\* $P = 0.0032$ , \* $P = 0.01285$ , c: \* $P = 0.0167$ , \*\* $P = 0.0055$ ).

[Source data](#)

[Full size image](#)

Our findings demonstrate that although Fc $\gamma$ RIIa is the major receptor that drives the protective activity of anti-influenza monoclonal antibodies, Fc $\gamma$ RIIIa has paradoxically limited contribution to the antibody-mediated protection, despite numerous studies that have previously determined that the cytotoxic clearance of malignant or virus-infected cells is predominantly mediated by Fc $\gamma$ RIIIa<sup>2,12</sup>. In addition, despite the abundant expression of Fc $\gamma$ RIIIa on alveolar macrophages at baseline as well as the influx of Fc $\gamma$ RIIIa-expressing natural killer cells in response to infection (Extended Data Fig. 6a–c), selective engagement of this receptor does not enhance protection, suggesting that enhancing the clearance of viral particles by alveolar macrophages or killing of infected cells by natural killer cells does not improve the ability of these antibodies to protect against lethal influenza challenge.

Fc $\gamma$ Rs can either activate (Fc $\gamma$ RI, Fc $\gamma$ RIIa and Fc $\gamma$ RIIIa) or inhibit (Fc $\gamma$ RIIb) cellular responses. Activating Fc $\gamma$ Rs trigger intracellular signalling subsequent to crosslinking of the extracellular ligand binding domains by IgG immune complexes by either intrinsic cytoplasmic ITAM motifs (Fc $\gamma$ RIIa) or  $\gamma$  or  $\zeta$  chain-associated ITAM motifs (Fc $\gamma$ RIIIa), recruiting SYK family tyrosine kinases (reviewed in ref. 1). Because Fc $\gamma$ RIIa and Fc $\gamma$ RIIIa are redundantly expressed on a variety of innate immune cells, including monocytes and macrophages (Extended Data Fig. 6d–f), it is unlikely that the unique dependence on Fc $\gamma$ RIIa engagement that results in enhanced antiviral protection is mediated by these cells. Although neutrophils co-express Fc $\gamma$ RIIa and Fc $\gamma$ RIIIb, the latter lacks intracellular signalling domains and

has limited ability to mediate effector activities<sup>1</sup>, even when engaged by variants (ALIE and afucosylated) that exhibit increased affinity for this receptor. It is therefore possible that neutrophils, through specific activation of Fc $\gamma$ RIIa, might contribute to the observed antiviral potency of Fc $\gamma$ RIIa-enhanced variants. To test this hypothesis, we assessed whether or not neutrophil depletion influences the ability of Fc $\gamma$ RIIa-enhanced variants (GA) of FY1 to protect Fc $\gamma$ R-humanized mice from lethal influenza challenge. We found that depletion of neutrophils had no effect on the antiviral activity of Fc $\gamma$ RIIa-enhanced FY1 (Extended Data Fig. 5*h, i*), which suggests that neutrophils are unlikely to contribute notably to the Fc $\gamma$ RIIa-mediated antiviral protection we observe.

In contrast to alveolar macrophages and monocytes, conventional dendritic cells (such as cDC1 (CD11c $^+$ CD11b $^-$ CD103 $^+$ ) and cDC2 (CD11c $^+$ CD11b $^+$ CD103 $^-$ ) subsets) (Extended Data Fig. 7*a–f*) express Fc $\gamma$ RIIa and the inhibitory receptor Fc $\gamma$ RIIb, but not Fc $\gamma$ RIIIa, and are found both at baseline and after infection in the lung (Extended Data Fig. 7*b*). To investigate the effect of Fc $\gamma$ RIIa engagement by Fc-engineered monoclonal antibodies on the functional activity of the various dendritic cell subsets (cDC1, cDC2 and Fc $\gamma$ RIII-expressing TNF/iNOS-producing dendritic cells (tipDCs) that emerge in response to influenza infection; defined as MHCII $^+$ CD11c $^+$ CD11b $^+$ CD103 $^-$ Gr-1 $^+$ ) (Extended Data Fig. 7*a*), we analysed dendritic cells in the lungs of Fc $\gamma$ R-humanized mice infected with influenza that have previously received Fc variants of the anti-HA stalk monoclonal antibody FI6v3. The treatment of mice with the Fc $\gamma$ RIIa-enhancing variant (GAALIE) before influenza challenge resulted in dendritic cell maturation (Fig. 3*a, b*, Extended Data Fig. 7*g–i, l–n*), as seen by the increased frequency of CD80 $^{high}$ CD86 $^{high}$  cells on cDC1 and cDC2 subsets, and upregulation of CD40 expression in the cDC1 subset—the dendritic cell population specialized for cross-presentation and CD8 T cell stimulation<sup>18</sup>. By contrast, the same antibody (FI6v3) expressed either as wild-type or with an Fc modified to abrogate Fc $\gamma$ R binding (GRLR) did not result in dendritic cell maturation. Unlike the cDC1 and cDC2 subsets, treatment with the GAALIE variant is not associated with increased maturation of tipDCs, which suggests a limited role for this population in the antibody-mediated protection against influenza infection conferred by Fc $\gamma$ RIIa-enhanced variants (Extended Data Fig. 7*i*). Consistent with these in vivo data from Fc $\gamma$ R-humanized mice, ex vivo stimulation of human monocyte-derived dendritic cells with IgG immune complexes revealed improved capacity for Fc $\gamma$ RIIa-enhanced variants (GA and GAALIE) to induce cellular maturation (Extended Data Fig. 7*j, k*).

**Fig. 3: Engagement of Fc $\gamma$ RIIa by Fc-engineered monoclonal antibodies drives dendritic cell maturation and protective CD8 $^+$  T cell responses.**

 figure3

**a–c**, Fc $\gamma$ R-humanized mice ( $n = 4$  mice per group for all groups, except  $n = 3$  for day 7 WT and GRLR) were treated with FI6v3 monoclonal antibody Fc variants (intraperitoneally 3 mg kg $^{-1}$ ), infected with H1N1 (PR8), and then lung-resident dendritic cells and T cells were analysed on days 4 ( $n = 4$  mice per group) or 7 ( $n = 3$  mice per group for WT and GRLR,  $n = 4$  for GAALIE in two independent experiments) after infection. One-way ANOVA (Bonferroni post hoc analysis adjusted for multiple comparisons) was used to compare the frequency of mature conventional dendritic cell subsets (CD80 $^{\text{high}}$ CD86 $^{\text{high}}$ ) on day 4 after infection (\* $P = 0.0384$ , \*\* $P = 0.0075$ , \*\*\* $P = 0.0008$ , \*\*\*\* $P = 0.0002$ ) (a), CD40 expression in cDC1 subsets (\* $P = 0.0261$ , \*\* $P = 0.0139$ , \*\*\* $P = 0.0061$ , \*\*\*\* $P = 0.0007$ ) (b), and the frequency of activated (CD44 $^{\text{hi}}$ CD69 $^+$ ) CD8 $^+$  and CD4 $^+$  T cells (day 4 after infection) (^ $P = 0.0412$ , \* $P = 0.0232$ , \*\* $P = 0.0018$ , \*\*\* $P = 0.0003$ ) (c). MFI, mean fluorescence intensity. **d–f**, Fc variants of the FY1 monoclonal antibody (mAb) were

administered intraperitoneally ( $2 \text{ mg kg}^{-1}$ ) to Fc $\gamma$ R-humanized mice before influenza challenge (H1N1 PR8). Isotype or anti-mouse CD8 monoclonal antibodies were administered on day 3 after infection (isotype-treated groups:  $n = 12$  mice per group for WT, GAALIE and PBS groups,  $n = 8$  mice for GA; anti-CD8-treated groups:  $n = 11$  mice per group for WT,  $n = 8$  for GA,  $n = 10$  for PBS, and  $n = 12$  for GAALIE in three independent experiments). **e, f**, Weight loss (mean  $\pm$  s.e.m.) (**e**) and survival curves (**f**) were compared against the corresponding isotype-treated group by two-way ANOVA (Bonferroni post hoc analysis adjusted for multiple comparisons) ( $*P = 0.03$ ,  $^{\wedge}P = 0.0220$ ) and log-rank (Mantel–Cox) test, respectively ( $^{**}P = 0.00199$ ,  $*P = 0.0477$ ).

[Source data](#)

[Full size image](#)

Maturation of dendritic cells and the induction of the accessory molecules CD80, CD86 and CD40 in the virally challenged lung is a prerequisite to the activation of antigen-specific naive T cells. This would indicate that an anti-viral antibody modified to enhance dendritic cell maturation by Fc $\gamma$ RIIa engagement can induce an adaptive response that results in the induction of protective T cell immunity. To explore this hypothesis, we characterized the T cell responses in the lungs of Fc $\gamma$ R-humanized mice treated with anti-influenza monoclonal antibodies with selective Fc $\gamma$ R-binding properties before viral challenge. We found that the GAALIE variant induced increased activation of both CD8 $^{+}$  and CD4 $^{+}$  T cells (Fig. [3c](#), Extended Data Fig. [8](#)), whereas neither wild-type IgG1 nor the GRLR variant showed evidence of robust induction of T cell responses. To determine whether the observed induction of T cell activation also contributes to the enhanced protection we observed with the Fc $\gamma$ RIIa-binding variants (Figs. [1](#), [2](#)), we repeated the FY1 antibody pre-treatment and viral challenge protocol, modifying it to include a CD8 $^{+}$  or CD4 $^{+}$  cellular depletion step on day 3 after infection (Fig. [3d](#), Extended Data Fig. [10a–c](#)). Depletion of CD8 $^{+}$ , but not CD4 $^{+}$ , T cells resulted in the loss of enhancement of the GA or GAALIE Fc variant, demonstrating that the improved protection observed for Fc $\gamma$ RIIa-enhanced variants is mediated by the induction of protective CD8 $^{+}$  T cell responses (Fig. [3e,f](#), Extended Data Figs. [4g](#), [10a–e](#)).

Because recent reports have suggested Fc $\gamma$ RIIa expression by subsets of T cells [19,20,21](#), we analysed Fc $\gamma$ R expression in human peripheral T cells, as well as in T cells obtained from the blood, spleen or lung of naive or influenza-infected Fc $\gamma$ R-humanized mice (Extended Data Fig. [9](#)) to determine whether the improved protective activity of Fc $\gamma$ RIIa-enhanced variants is the outcome of direct T cell activation by Fc $\gamma$ R crosslinking. With the exception of a minor (10%) subset of

CD8<sup>+</sup> T cells in the lung of infected mice that is positive for FcγRIII (Extended Data Fig. 9*l*), T cells from human or FcγR-humanized mice were negative for all FcγRs, which suggests that the antibody-mediated anti-viral protection is not due to direct effects on T cells.

Because FcγRIIa-enhanced variants induce the activation of both CD8<sup>+</sup> and CD4<sup>+</sup> T cells, we tested whether these effects also drive improved antiviral IgG responses. IgG responses were characterized in mice treated with wild-type or GAALIE variants of the non-neutralizing anti-HA monoclonal antibody 1A01 at a dose that both variants offer comparable protection. Treatment with either wild-type or FcγRIIa-enhanced variants resulted in robust and comparable IgG responses against HA and NP from homologous or heterologous virus strains, as well as serum HAI activity (Extended Data Fig. 10*f–m*).

Through interactions with effector leukocytes, antibodies against viral antigens can enhance disease and contribute to specific histopathologic manifestations. Although this phenomenon, termed antibody-dependent enhancement, has been shown specifically for flaviviruses, such as dengue<sup>22</sup>, clinical experience from severe cases of viral respiratory infections, such as influenza and SARS-CoV-2, also raise the possibility that antibodies might have a pathogenic role through uncontrolled or inappropriate amplification of local inflammatory responses. For example, studies during the 2009 influenza pandemic have shown that severe disease was associated with evidence of IgG-mediated inflammation in the lung parenchyma through IgG immune complex and complement deposition to the lung tissue<sup>23</sup>. Similarly, severe cases of COVID-19 disease are often characterized by excessive pro-inflammatory cytokine expression and T cell responses, as well as by clinical manifestations that resemble secondary haemophagocytic lymphohistiocytosis<sup>24</sup>. Given that Fc-engineered variants with increased affinity for FcγRIIa can enhance adaptive T cell responses by activation of FcγRIIa-expressing dendritic cells, it is important to determine whether such variants could also modulate disease pathogenesis through inappropriate amplification of host inflammatory responses that are elicited in response to virus infection. To determine whether FcγRIIa-enhanced variants could lead to severe disease, we assessed the in vivo activity of these variants in FcγR-humanized mice with established influenza infection (Fig. 4*a*). Mice were infected with influenza and 3 days after infection, FY1 monoclonal antibody (either wild-type or GAALIE) was administered at different doses (5–15 mg kg<sup>-1</sup>). Although wild-type IgG1 FY1 was unable to rescue mice from lethal influenza infection, GAALIE variants exhibited a dose-dependent therapeutic benefit. These findings suggest that the unique FcγR-binding profile of the GAALIE variant (increased for activating FcγRIIa and FcγRIIIa receptors, but reduced for the inhibitory FcγRIIb receptor), and its ability to stimulate CD8 T cell responses has no pathogenic

consequences, instead it provides meaningful and robust protection from established infection (Fig. [4b](#),[c](#)).

**Fig. 4: Evaluation of GAALIE variants of the FY1 monoclonal antibody in models of therapy or prevention of influenza infection.**

 [figure4](#)

**a–c**, Fc $\gamma$ R-humanized mice ( $n = 6$  mice per group for antibody-treated groups;  $n = 3$  for PBS-treated in two independent experiments) were infected with influenza (H1N1 PR8), and FY1 Fc variants were administered intraperitoneally 3 days after infection at the indicated dose. **b, c**, Weight loss (mean  $\pm$  s.e.m.) (**b**) and survival curves (**c**) of GAALIE-treated mice were compared with the PBS-treated group at the corresponding antibody dose by two-way ANOVA (Bonferroni post hoc analysis adjusted for multiple comparisons) ( ${}^*P = 0.0456$ ,  ${}^\wedge P = 0.041$ ,  ${}^{**}P = 0.0014$ ,  ${}^{\wedge\wedge}P = 0.0003$ ,  ${}^{\#}P = 0.0005$ ,  ${}^{***}P < 0.0001$ ) and log-rank (Mantel–Cox) test, respectively ( ${}^{**}P = 0.000911$ ). **d–h**, The protective activity of LS and GAALIE–LS variants of FY1 was evaluated in a model of antibody-mediated prophylaxis. Fc $\gamma$ R/FcRn-humanized mice ( $n = 8$  mice per group for GAALIE–LS at 1.6 and

$0.4 \text{ mg kg}^{-1}$ ;  $n = 10$  for LS at  $0.1 \text{ mg kg}^{-1}$ ,  $n = 3$  for PBS,  $n = 9$  for the remaining treatment groups in two independent experiments) were administered intravenously with the indicated dose of FY1 2 days before influenza challenge (H1N1 PR8). **e, f**, Weight loss (mean  $\pm$  s.e.m.) (**e**) and survival curves (**f**) of GAALIE–LS-treated mice were compared against the LS group at the corresponding antibody dose by two-way ANOVA (Bonferroni post hoc analysis adjusted for multiple comparisons) ( $*P < 0.001$ ,  $^{\wedge}P = 0.01$ ,  $\#P = 0.02$ ,  $\$P = 0.006$ ,  $\P P = 0.002$ ) and log-rank (Mantel–Cox) test, respectively ( $*P = 0.0283$ ,  $^{**}P = 0.0266$ ,  $^{***}P = 0.00377$ ,  $^{****}P = 0.000143$ ). **h**, The enhanced potency conferred by the GAALIE–LS variant was quantified by plotting the maximum weight change after infection against the serum antibody concentration at the time of challenge. Data were fitted by nonlinear regression analysis (four-parameter, variable slope).

[Source data](#)

[Full size image](#)

In addition to their therapeutic potential, monoclonal antibodies engineered for increased Fc $\gamma$ RIIa affinity could provide long-term prophylaxis from influenza infection, especially when combined with Fc domain mutations (for example, the LS (M428L/N434S) variant<sup>25</sup>) that increase affinity for human FcRn and extend IgG half-life *in vivo*<sup>25</sup>. Using a mouse model of antibody-mediated prophylaxis of influenza infection (Fig. 4d), we compared the ability of LS (enhanced for FcRn) and GAALIE–LS (enhanced for FcRn, Fc $\gamma$ RIIa and Fc $\gamma$ RIIIa) variants of FY1 to protect Fc $\gamma$ R- or FcRn-humanized mice from influenza infection. At all doses tested ( $0.1\text{--}1.6 \text{ mg kg}^{-1}$ ), GAALIE–LS variants demonstrated superior protective activity over their LS counterparts (Fig. 4e–g, Extended Data Fig. 4h). In addition, quantification of the protective activity of the two FY1 Fc variants over a wide range of doses revealed that the GAALIE–LS variant exhibited at least 5.5-fold improvement in *in vivo* antiviral potency (Fig. 4h), which suggests that Fc engineering for increased affinity to specific Fc $\gamma$ Rs represents a promising approach that could substantially improve the clinical efficacy of antiviral monoclonal antibodies.

IgG antibodies can mediate pleiotropic effects, resulting from the diversity of Fc binding molecules that engage the Fc domain. The Fc domain is structurally diverse, the consequence of subclasses and Fc glycosylation, and results in differential Fc receptor binding activities for various Fc structural variants (reviewed in ref. 1). This natural heterogeneity contributes to the efficacy of polyclonal IgG responses to viral infections, and provides a mechanism for the recognition of diverse viral epitopes and triggering of several effector pathways. The development of monoclonal

antibodies for the selective binding to specific neutralizing viral epitopes can now be coupled to Fc modifications to facilitate the engagement of specific Fc $\gamma$ Rs to optimize the potency of these therapeutic agents. As demonstrated for anti-tumour therapeutic antibodies, enhancing their affinity for Fc $\gamma$ RIIIa results in improved phagocytosis of tumour cells by macrophages (antibody-dependent cell phagocytosis, ADCP), as well as enhanced killing by natural killer cells (antibody-dependent cell cytotoxicity, ADCC), which translates to improved clinical efficacy<sup>26</sup>. On the basis of these findings, it has been presumed that enhancing the ability of the Fc domain to engage and activate Fc $\gamma$ RIIIa would also lead to increased therapeutic efficacy of protective anti-viral antibodies. However, this does not seem to be the case. Antibody treatment of HIV infection has been shown to induce a CD8 $^{+}$  response both in chronically infected macaques and humans, which contributes to the control of viraemia<sup>27,28</sup>. Our present results show that selective engagement of the activating Fc $\gamma$ R on dendritic cells, Fc $\gamma$ RIIa, by a variety of anti-influenza monoclonal antibodies results in the induction of a protective CD8 $^{+}$  response, mechanistically similar to the ‘vaccinal’ response we have observed for anti-tumour antibody treatment<sup>12</sup>. The ability of an antibody to not only couple to innate effector responses through its Fc domain, but also induce an adaptive response by engaging and activating dendritic cells, provides a potent new approach to the design of therapeutic antibodies for the prevention and treatment of viral diseases. This approach to Fc engineering is particularly relevant to pandemic viruses, such as influenza and SARS-CoV-2. Neutralizing antibodies to these viruses, engineered to enhance dendritic cell activation and CD8 $^{+}$  T cell responses, as shown here for the GAALIE variant, are predicted to provide considerable enhancement of protection by stimulating a variety of synergistic immunological pathways.

## Methods

### Viruses, cell lines and mouse strains

The A/Puerto Rico/8/34 (PR8) and A/Netherlands/602/09 (Neth09) H1N1 viruses were grown as previously described<sup>6</sup>. MDCK cells (ATCC) were maintained at 37 °C, 5% CO<sub>2</sub> in DMEM supplemented with 10% FBS, 50 U ml<sup>-1</sup> penicillin and 50 µg ml<sup>-1</sup> streptomycin (ThermoFisher). Expi293F cells (ThermoFisher) were maintained at 37 °C, 8% CO<sub>2</sub> in Expi293 expression medium (ThermoFisher) supplemented with 10 U ml<sup>-1</sup> penicillin and 10 µg ml<sup>-1</sup> streptomycin. Fc $\gamma$ RIIa- and Fc $\gamma$ RIIIa-expressing NFAT reporter cells were purchased from Promega and have been authenticated by the vendor by STR analysis. All cell lines tested negative for

mycoplasma contamination. All in vivo experiments were performed in compliance with federal laws and institutional guidelines and have been approved by the Rockefeller University Institutional Animal Care and Use Committee. Mice were bred and maintained at the Comparative Bioscience Center at the Rockefeller University at a controlled ambient temperature environment with 12-h dark/light cycle. C57BL/6 mice were purchased from The Jackson Laboratory. Fc $\gamma$ R-humanized mice ( $mFc\gamma R\alpha^{-/-}$ ,  $Fcgr1^{-/-}$ , hFc $\gamma$ RI $^+$ , hFc $\gamma$ RIIa $R131^+$ , hFc $\gamma$ RIIb $^+$ , hFc $\gamma$ RIIIa $F158^+$ , and hFc $\gamma$ RIIIb $^+$ ) and Fc $\gamma$ R knockout mice ( $mFc\gamma R\alpha^{-/-}$ ;  $Fcgr1^{-/-}$ ) were generated in the C57BL/6 background and extensively characterized in previous studies<sup>10</sup>. Human Fc $\gamma$ RIIa-only mice (hFc $\gamma$ RIIa $^+$ ) were generated in a mouse Fc $\gamma$ R-deficient background (C57BL/6;  $Fc\gamma R\alpha^{-/-}$ ;  $Fcgr1^{-/-}$ )<sup>10</sup>. FcRn-humanized mice (B6.Cg-*Fcgrt*<sup>tm1Dcr</sup> Tg(*FCGRT*)32Dcr/DcrJ) were purchased from The Jackson Laboratory and are deficient in mouse FcRn and express human FcRn as a transgene<sup>29,30</sup>. Fc $\gamma$ R/FcRn-humanized mice were generated by crossing the Fc $\gamma$ R-humanized strain to the FcRn-humanized mice<sup>31</sup>.

## Cloning, expression and purification of recombinant IgG antibodies

For the generation of Fc domain variants of human IgG1 Fc domain variants, site-directed mutagenesis using specific primers was performed as previously described<sup>4</sup>. Recombinant antibodies were generated by transient transfection of Expi293 or Expi-CHO cells with heavy and light chain expression plasmids using previously described protocols<sup>13</sup>. Before transfection, plasmid sequences were validated by direct sequencing (Genewiz). Recombinant IgG antibodies were purified from cell-free supernatants by affinity purification using protein G or protein A sepharose beads (GE Healthcare). Purified proteins were dialysed in PBS, filter-sterilized (0.22  $\mu$ m), and purity was assessed by SDS-PAGE followed by SafeStain blue staining (ThermoFisher). All antibody preparations were more than 90% pure and endotoxin levels were less than 0.05 EU mg $^{-1}$ , as measured by the limulus amebocyte lysate assay. For the generation of afucosylated Fc domain variants, CHO cells were transfected with heavy chain and light chain expression plasmids in the presence of 100  $\mu$ M 2-fluorofucose peracetate<sup>32</sup>. To confirm the absence of fucose, glycans were released with PNGase F, labelled with Waters RapiFluor-MS, cleaned up with a HILIC microElution plate, injected onto a Waters Glycan BEH Amide column, using a Thermo Vanquish UHPLC with FLD detection. Chromatograms were integrated and the relative contribution of each glycan calculated as a percentage. Peaks were identified by mass spec using a Thermo Q Exactive Plus mass spectrometer and through comparison to the NIST monoclonal antibody standard. Size exclusion chromatography (SEC) was

performed using a Superdex 200 Increase 10/300GL column (GE Healthcare) on an Äkta Pure 25 HPLC system and analysed using Unicorn v.6.3 software.

### **ELISA-based Fc $\gamma$ R binding assay**

Recombinant human Fc $\gamma$ R ectodomains (Sinobiological) ( $5\text{ }\mu\text{g ml}^{-1}$ ) were immobilized into high-binding 96-well microtitre plates (Nunc), and after overnight incubation at  $4\text{ }^\circ\text{C}$ , plates were blocked with PBS plus 2% (w/v) BSA and 0.05% (v/v) Tween20 for 2 h. IgG immune complexes were prepared by incubating for 1 h at  $4\text{ }^\circ\text{C}$  Fc variants of the anti-NP (4-hydroxy-3-nitrophenylacetyl) monoclonal antibody Ab 3B62 with NP-BSA (27 conjugation ratio, Biosearch Technologies) at a molar ratio of 1:10 (antigen:antibody). IgG immune complexes or monomeric IgG (for Fc $\gamma$ RI) were serially diluted (1:3 consecutive dilutions in PBS starting at  $10\text{ }\mu\text{g ml}^{-1}$  (IgG concentration) for immune complexes or  $1\text{ }\mu\text{g ml}^{-1}$  for monomeric IgG) and applied to Fc $\gamma$ R-coated plates. After 1 h incubation at room temperature, bound IgG was detected using horseradish peroxidase (HRP)-conjugated goat F(ab') $_2$  anti-human IgG (1 h; 1:5,000; Jackson Immunoresearch). Plates were developed using the TMB (3,3',5,5'-tetramethylbenzidine) two-component peroxidase substrate kit (KPL) and reactions were stopped with the addition of 1 M phosphoric acid. Absorbance at 450 nm was immediately recorded using a SpectraMax Plus spectrophotometer (Molecular Devices) and background absorbance from negative control samples was subtracted. Data were collected and analysed using SoftMax Pro v.7.0.2 software (Molecular Devices).

### **Surface plasmon resonance**

All experiments were performed with a Biacore T200 SPR system (GE Healthcare) at  $25\text{ }^\circ\text{C}$  in HBS-EP $^+$  buffer (10 mM HEPES, pH 7.4, 150 mM NaCl, 3.4 mM EDTA, 0.005% (v/v) surfactant P20). IgG antibodies (clone 3B62) were immobilized on Series S Protein G sensor chip (GE Healthcare) at a density of 2,000 response units (RU). Serial dilutions of recombinant soluble human Fc $\gamma$ RI ectodomain (Sinobiological) were injected to the flow cells at  $20\text{ }\mu\text{l min}^{-1}$ , with the concentration ranging from 250 to 0.488 nM (1:2 successive dilutions). Association time was 60 s followed by a 900-s dissociation step. At the end of each cycle, sensor surface was regenerated with a glycine HCl buffer (10 mM, pH 2.0;  $50\text{ }\mu\text{l min}^{-1}$ , 30 s). Background binding to blank immobilized flow cells was subtracted, and affinity constants were calculated using BIACore T200 evaluation software v.2.0 (GE Healthcare) using the 1:1 Langmuir binding model.

### **Determination of antibody-dependent activation of human Fc $\gamma$ RIIIa**

Monoclonal antibodies were serially diluted in ADCC assay buffer (Promega). Target cells (A549-H1 HA, A/California/04/2009) were added in a white flat-bottom 96-well plate at  $1.25 \times 10^4$  cells per well in 25  $\mu\text{l}$ , then serially diluted antibodies were added to each well (25  $\mu\text{l}$  per well), and the antibody and cell mixture was incubated for 10 min at room temperature. Effector cells (Jurkat-Fc $\gamma$ RIIIa) for the ADCC Bioassay are thawed and added at a cell density of  $7.5 \times 10^4$  per well in 25  $\mu\text{l}$  (effector to target ratio of 6:1). Plates were incubated for 20 h at 37 °C with 5% CO<sub>2</sub>. Activation of human Fc $\gamma$ RIIIa (V158 or F158 variants) in this bioassay results in the NFAT-mediated expression of the luciferase reporter gene. Luminescence is therefore measured with a luminometer (Synergy H1, Bioteck) using the BioGlo Luciferase Assay Reagent according to the manufacturer's instructions. The data (that is, specific Fc $\gamma$ RIIIa activation) are expressed as the average of relative luminescence units (RLU) over the background by applying the following formula: (RLU at concentration x of monoclonal antibodies – RLU of background).

## Determination of antibody-dependent activation of human Fc $\gamma$ RIIa

Monoclonal antibodies were serially diluted in ADCP assay buffer (Promega). Target cells (A549-H1HA, A/California/04/2009) were added in a white flat-bottom 96-well plate at  $10^4$  cells per well in 25  $\mu\text{l}$ , then serially diluted antibodies were added to each well (25  $\mu\text{l}$  per well), and the antibody and cell mixture was incubated for 10 min at room temperature. Effector cells (Jurkat-Fc $\gamma$ RIIa) for the ADCP Bioassay are thawed and added at a cell density of  $5 \times 10^4$  per well in 25  $\mu\text{l}$  (effector to target ratio of 5:1). Plates were incubated for 20 h at 37 °C with 5% CO<sub>2</sub>.

Activation of human Fc $\gamma$ RIIa (H131 variant) in this bioassay results in the NFAT-mediated expression of the luciferase reporter gene. Luminescence is therefore measured with a luminometer (Synergy H1, Bioteck) using the BioGlo Luciferase Assay Reagent according to the manufacturer's instructions. The data (that is, specific Fc $\gamma$ RIIa activation) are expressed as the average of relative luminescence units (RLU) over the background by applying the following formula: (RLU at concentration x of antibodies – RLU of background).

## ADCC assay

Natural killer cells were freshly isolated from whole EDTA blood using the MACSxpress NK isolation kit following the manufacturer instruction. Monoclonal antibodies were serially diluted tenfold in AIM-V medium from 1  $\mu\text{g ml}^{-1}$  to 0.001  $\mu\text{g ml}^{-1}$ . Target cells (A549-H1HA, A/California/04/2009) were added in a round-bottom 384-well plate at  $7.5 \times 10^3$  cells per well in 23  $\mu\text{l}$ , then serially diluted antibodies were added to each well (23  $\mu\text{l}$  per well), and the antibody–cell mixture

was incubated for 10 min at room temperature. After incubation, human natural killer cells were added at a cell density of  $4.5 \times 10^4$  per well in 23 µl (effector to target ratio of 6:1). Control wells were also included that were used to measure maximal lysis (containing target cells with 23 µl of 3% Triton X-100) and spontaneous lysis (containing target cells and effector cells without antibody). Plates were incubated for 4 h at 37 °C with 5% CO<sub>2</sub>. Cell death was determined by measuring lactate dehydrogenase (LDH) release using an LDH detection kit (Roche) according to the manufacturer's instructions. Using a kinetic protocol, the absorbance at 490 nm and 650 nm was measured once every 2 min for 8 min. The percentage of specific lysis was determined by applying the following formula: (specific release – spontaneous release)/(maximum release – spontaneous release) × 100.

## Anti-HA, NA and NP ELISA

Recombinant HA (Influenza A H1N1 (A/California/04/2009 or A/Puerto Rico/8/34) or H3N2 (A/x31)), or NA (A/California/04/2009) or NP (H1N1 (A/California/04/2009) or H3N2 (A/x31)) (Sinobiological) (3 µg ml<sup>-1</sup>) were immobilized into high-binding 96-well microtitre plates (Nunc) and after overnight incubation at 4 °C, plates were blocked with PBS plus 2% (w/v) BSA and 0.05% (v/v) Tween20 for 2 h. After blocking, plates were incubated for 1 h with serially diluted IgG antibodies or serum samples (1:3 consecutive dilutions in PBS starting at 1 µg ml<sup>-1</sup> for monoclonal antibodies or 1:10 for serum samples), followed by HRP-conjugated goat anti-human IgG (minimal cross-reactivity to mouse IgG) for human monoclonal antibodies or goat anti-mouse IgG (minimal cross-reactivity to human IgG) for serum samples (1 h; 1:5,000; Jackson Immunoresearch). Plates were developed using the TMB two-component peroxidase substrate kit (KPL) and reactions were stopped with the addition of 1 M phosphoric acid. Absorbance at 450 nm was immediately recorded using a SpectraMax Plus spectrophotometer (Molecular Devices) and background absorbance from negative control samples was subtracted. Data were collected and analysed using SoftMax Pro v.7.0.2 software (Molecular Devices).

## Microneutralization assay

The neutralizing activity of anti-HA and NA monoclonal antibody Fc variants was evaluated in microneutralization assays, using previously described protocols<sup>33</sup>. Virus input was titrated to maximize the signal-to-noise ratio. Fc domain variants (starting concentration at 100 µg ml<sup>-1</sup> followed by 1:3 serial dilutions) and viruses ( $1.8 \times 10^3$  pfu ml<sup>-1</sup> for A/Puerto Rico/8/34 and  $3.2 \times 10^4$  pfu ml<sup>-1</sup> for

A/Netherlands/602/09) were prepared in DMEM supplemented with 50 U ml<sup>-1</sup> penicillin, 50 µg ml<sup>-1</sup> streptomycin, 25 mM HEPES and 1 µg ml<sup>-1</sup> TPCK-treated trypsin (Sigma). The virus–antibody mixture was pre-incubated for 1 h at 37 °C and added to a monolayer of MDCK cells (70–80% confluent in 96-well plates). After incubation at 37 °C for 1 h to allow for virus adsorption, the cell monolayer was washed three times with PBS and re-incubated for 18–20 h at 37 °C with medium (DMEM supplemented with 50 U ml<sup>-1</sup> penicillin, 50 µg ml<sup>-1</sup> streptomycin, 25 mM HEPES and 1 µg ml<sup>-1</sup> TPCK-treated trypsin) containing monoclonal antibodies (at equivalent concentrations as during the virus co-incubation). Cells were fixed with 80% (v/v) acetone, blocked with 5% (w/v) non-fat milk diluted in PBS for 30 min at room temperature, and quenched with 3% (v/v) hydrogen peroxide (in PBS) by incubating for a further 20 min at room temperature. Cells were stained with biotinylated anti-NP antibody (EMD Millipore; 1:2,000), followed by HRP-conjugated streptavidin (Jackson Immunoresearch; 1:5,000). Plates were developed using the TMB two-component peroxidase substrate kit (KPL) and reactions stopped with the addition of 1 M phosphoric acid. Absorbance at 450 nm was immediately recorded using a SpectraMax Plus spectrophotometer (Molecular Devices) and background absorbance from negative control samples was subtracted. Data were collected and analysed using SoftMax Pro v.7.0.2 software (Molecular Devices).

### **Haemagglutination inhibition assay**

HAI activity was evaluated using previously described protocols<sup>34</sup>. In brief, serum samples (diluted 1:3 in cholera filtrate) or Fc domain variants of antibodies (starting concentration at 100 µg ml<sup>-1</sup> followed by 1:3 serial dilutions) and viruses (A/Puerto Rico/8/34 or A/Netherlands/602/09; 10<sup>7</sup> pfu ml<sup>-1</sup>) were incubated in V-bottom 96 microtitre plates for 30 min at room temperature. Turkey red blood cells (0.75% (v/v); Rockland) were added to the antibody–virus mixture, mixed gently, and incubated for 30 min at room temperature. Plates were scored for the number of wells exhibiting HAI activity.

### **Quantification of serum IgG levels**

Blood from mice was collected into gel microvette tubes, serum was fractionated by centrifugation (10,000*g*, 5 min) and stored at –20 °C. IgG levels in serum samples were determined by ELISA following previously published protocols<sup>13,31</sup>.

### **Mouse influenza infection models**

No statistical method was used to predetermine sample size. On the basis of preliminary studies that determined experimental variation in survival after infection and antibody treatment, we performed power calculations and determined that at least  $n = 6$  mice per group is sufficient to detect differences among experimental groups (powered at 80% for 5% significance level; survival assessed by log-rank (Mantel–Cox) test). Mice (females; 6–12 weeks old) were anaesthetized with a ketamine ( $75 \text{ mg kg}^{-1}$ ) and xylazine ( $15 \text{ mg kg}^{-1}$ ) mixture (administered intraperitoneally) and viruses (diluted in PBS) were administered intranasally (five mLD<sub>50</sub>) in 30  $\mu\text{l}$ . After infection, mice were monitored daily, and their weights were recorded for 14 days. Death was determined by a 20% body weight loss threshold that was authorized by the Rockefeller University Institutional Animal Care and Use Committee. Mice were randomized based on age and weight. Before treatment, we ensured that the mean weight and age were comparable among the various treatment groups. Whenever possible (not always, due to limited access of laboratory staff in BSL-2 animal facilities), the treatment groups were blinded to the person involved in monitoring mouse survival and weight upon challenge (applicable to data presented in Figs. 1d, 4). For antibody-mediated prophylaxis, antibodies were administered intraperitoneally or intravenously 4 h before virus challenge (except for experiments with FcRn/FcγR-humanized mice, in which antibodies were administered 2 days before infection), whereas for antibody-mediated therapy, antibodies were administered on day 3 after infection. Antibody dose was calculated as  $\text{mg kg}^{-1}$ . For FcγRIIa-blocking experiments, recombinant anti-FcγRIIa (clone IV.3) expressed as human IgG1 GRLR variant to abrogate FcγR binding or isotype control (anti-hapten (NP) monoclonal antibody; clone 3C13) was administered (80  $\mu\text{g}$ ) intranasally to mice 1 day after virus challenge.

### **Ex vivo stimulation of human monocyte-derived dendritic cells**

Leukocyte packs (buffy coats) were purchased from the New York Blood Center, mononuclear cells were isolated by Ficoll gradient centrifugation, and CD14<sup>+</sup> monocytes were purified using CD14 microbeads (Miltenyi Biotech). Cells were cultured at 37 °C, 5% CO<sub>2</sub> for 6 days in RPMI supplemented with 50 U ml<sup>-1</sup> penicillin, 50  $\mu\text{g ml}^{-1}$  streptomycin, 10% heat-inactivated FBS, 100 ng ml<sup>-1</sup> GM-CSF, and 100 ng ml<sup>-1</sup> IL-4. Cells were then seeded in 96-well plates at  $8 \times 10^4$  cells per well in RPMI supplemented with 50 U ml<sup>-1</sup> penicillin, 50  $\mu\text{g ml}^{-1}$  streptomycin, 5% ultra-low IgG, heat-inactivated FBS and stimulated overnight with IgG immune complexes (100  $\mu\text{g ml}^{-1}$ ). The following immune complexes were used: (i) heat-aggregated IgG complexes generated by incubation of IgG (1A01 monoclonal antibody) at 63 °C for 60 min; or (ii) anti-NP:NP-BSA immune complexes generated as described for the ELISA-based FcγR binding assay. After overnight

stimulation, dendritic cell maturation was assessed by flow cytometry. Cells were stained with the following fluorochrome-conjugated antibodies (diluted at 1:100 unless otherwise stated): anti-DC-SIGN-BrilliantViolet 421, anti-CD40-BrilliantViolet 510, anti-human Fc $\gamma$ RI-BrilliantViolet 605 (clone 10.1), anti-CD11b-BrilliantViolet 650, anti-CD86-BrilliantViolet 711, anti-human Fc $\gamma$ RIIa-FITC (clone IV.3, used at 1:50 dilution), anti-CD11c-PerCP-Cy5.5, anti-human Fc $\gamma$ RIIIa/b-PE (clone 3G8), anti-CD80-PE/Cy7, anti-human Fc $\gamma$ RIIb-Dylight 650 (clone 2B6) (used at 10  $\mu$ g ml $^{-1}$ ), anti-HLA-DR-AlexaFluor700, and anti-CD83-APC/Cy7. Samples were collected on an Attune NxT flow cytometer (ThermoFisher) using Attune NxT software v.3.1.2 and analysed using FlowJo (v.10.6) software.

### **In vivo neutrophil, CD8 $^{+}$ or CD4 $^{+}$ T cell depletion**

Neutrophils, CD8 $^{+}$  or CD4 $^{+}$  cells were depleted in mice by administration of anti-Gr-1, anti-CD8 or anti-CD4 monoclonal antibodies, respectively. To establish the efficiency of antibody-mediated cell depletion, Fc $\gamma$ R-humanized mice were injected intravenously with 150  $\mu$ g anti-mouse Gr-1 monoclonal antibody (clone RB6-8C5; rat IgG2b; Bioxcell), anti-mouse CD8 $\alpha$  monoclonal antibody (clone 2.43; rat IgG2b; Bioxcell), anti-mouse CD4 monoclonal antibody (clone GK1.5; rat IgG2b; Bioxcell), or isotype control (clone LTF-2; rat IgG2b; Bioxcell). The abundance of neutrophils, CD8 $^{+}$  and CD4 $^{+}$  T cells in peripheral blood was determined at various time points after antibody administration by flow cytometry. Baseline CD8 $^{+}$  and CD4 $^{+}$  T cell frequencies were determined in blood samples obtained before antibody administration. For the flow cytometry analysis, fluorescently conjugated monoclonal antibodies targeting Ly6G (clone 1A8; Biolegend), the  $\beta$  subunit of mouse CD8 (clone YTS156.7.7; Biolegend) or epitopes non-overlapping with the GK1.5 epitope (clone RM4-4; Thermofisher) were used to avoid competition with the depleting antibodies. Neutrophil, CD8 $^{+}$  or CD4 $^{+}$  T cell depletion of influenza-infected mice was performed using the aforementioned conditions and depleting antibodies or isotype were administered intravenously (150  $\mu$ g) on day 1 (for neutrophils) or 3 (for CD8 $^{+}$  or CD4 $^{+}$  T cells) after infection.

### **Processing of mouse tissues and flow cytometry analysis**

Mice were euthanized and lungs were perfused by injection of PBS (containing 10 U ml $^{-1}$  heparin) into the right cardiac ventricle. Lungs were excised and homogenized using the gentleMACS dissociator (mouse lung dissociation kit, Miltenyi), according to the manufacturer's recommendations. Spleens were homogenized by mechanical shearing. After lysis of red blood cells (RBC lysis buffer; Biolegend), single-cell suspensions were labelled with the LIVE/DEAD

Fixable Near-IR (ThermoFisher) and resuspended in PBS containing 0.5% (w/v) BSA and 5 mM EDTA. Cells were labelled with mixtures of fluorescently labelled antibodies including (all used at 1:250 dilution unless otherwise stated): (i) for the characterization of the Fc $\gamma$ RIIa expression of the Fc $\gamma$ RIIa $^+$  mouse strain: anti-CD11c-eFluor506, anti-CD11b-BrilliantViolet605, anti-SiglecF-SuperBright645, anti-CD8 $\beta$ -BrilliantViolet711, anti-MHCII- BrilliantViolet785, anti-human Fc $\gamma$ RIIa (clone IV.3)-FITC (used at 1:50 dilution), anti-Gr-1-PerCP/Cy5.5, anti-CD3-PE, anti-CD103-PE/eFluor610, anti-NK1.1-PE/Cy7, anti-CD4-AlexaFluor647, and anti-CD19-AlexaFluor700; (ii) for the evaluation of Fc $\gamma$ R expression on innate effector leukocytes: anti-CD11c-eFluor506, anti-human Fc $\gamma$ RI (clone 10.1)-BrilliantViolet605 (used at 1:100 dilution), anti-SiglecF-SuperBright645, anti-Ly6G-BrilliantViolet711, anti-CD11b-BrilliantViolet785, anti-human Fc $\gamma$ RIIa (clone IV.3)-FITC (used at 1:50 dilution), anti-Ly6C-PerCP/Cy5.5, anti-human Fc $\gamma$ RIIIa/b (clone 3G8)-PE (used at 1:100 dilution), anti-CD103-PE/eFluor610, anti-NK1.1-PE/Cy7, and anti-human Fc $\gamma$ RIIb (clone 2B6)-Dylight650 (used at 10  $\mu$ g/ml); (iii) for the evaluation of Fc $\gamma$ R expression and activation status of DCs: anti-CD11c-eFluor506, anti-human Fc $\gamma$ RI (clone 10.1)-BrilliantViolet605 (used at 1:100 dilution), anti-SiglecF-SuperBright645, anti-CD80-BrilliantViolet711, anti-CD11b-BrilliantViolet785, anti-human Fc $\gamma$ RIIa (clone IV.3)-FITC (used at 1:50 dilution), anti-Gr-1-PerCP/Cy5.5, anti-human Fc $\gamma$ RIIIa/b (clone 3G8)-PE (used at 1:100 dilution), anti-CD103-PE/eFluor610, anti-CD86-PE/Cy7, anti-human Fc $\gamma$ RIIb (clone 2B6)-Dylight650 (used at 10  $\mu$ g ml $^{-1}$ ), and anti-MHCII-AlexaFluor700; (iv) for the evaluation of CD8 or CD4 depletion: anti-CD3e-eFluor506, anti-CD19-BrilliantViolet605, anti-CD8 $\beta$ -BrilliantViolet711, anti-CD11b-PE, anti-NK1.1-PE/Cy7, anti-CD4-FITC, anti-Gr-1-PerCP/Cy5.5, anti-NKp46-eFluor660, and anti-B220-APC/eFluor780; (v) for the evaluation of neutrophil depletion: anti-CD11c-eFluor506, anti-CD19-BrilliantViolet605, anti-SiglecF- SuperBright645, anti-Ly6G-BrilliantViolet711, anti-CD11b-BrilliantViolet785, anti-CD8a-FITC, anti-Ly6C-PerCP/Cy5.5, anti-CD3-PE, anti-NK1.1-PE/Cy7, anti-CD4-AlexaFluor647, anti-CD45-AlexaFluor700; (vi) for the assessment of Fc $\gamma$ R expression on T cells: anti-B220-BrilliantViolet421, anti-CD3-BrilliantViolet510, anti-human Fc $\gamma$ RI (clone 10.1)-BrilliantViolet605 (used at 1:100 dilution), anti-CD8-BrilliantViolet711, anti-CD4-BrilliantViolet785, anti-human Fc $\gamma$ RIIa (clone IV.3)-FITC (used at 1:50 dilution), anti-NK1.1-PerCP/Cy5.5, anti-human Fc $\gamma$ RIIIa/b (clone 3G8)-PE (used at 1:100 dilution), anti-CD11b-PE/Cy7, anti-human Fc $\gamma$ RIIb (clone 2B6)-Dylight650 (used at 10  $\mu$ g ml $^{-1}$ ), and anti-Gr-1-AlexaFluor 700; (vii) for the characterization of dendritic cell populations after antibody treatment: anti-CD103-FITC, anti-Ly6C-PerCP/Cy5.5, anti-NK1.1-AlexaFluor647, anti-CD45-AlexaFluor700, anti-CD11c-eFluor506, anti-CD86-BrilliantViolet605, anti-SiglecF-SuperBright645, anti-Ly6G-BrilliantViolet711, anti-CD11b-BrilliantViolet785, anti-CD40-PE, anti-MHCII-PE/eFluor610, and anti-CD80-PE/Cy7; (viii) for the characterization of T cell

populations after antibody treatment: anti-CD4-AlexaFluor488, anti-CD3e-PerCP/Cy5.5, anti-NK1.1-AlexaFluor647, anti-CD45-AlexaFluor700, anti-CD44-BrilliantViolet421, anti-CD62L-BrilliantViolet510, anti-CD25-BrilliantViolet605, anti-CD27-BrilliantViolet650, anti-CD8-BrilliantViolet711, anti-CD11a-PE, anti-CCR7-PE/eFluor610, and anti-CD69-PE/Cy7. For experiments assessing Fc $\gamma$ R expression, relevant isotype control antibodies were used and included: mouse IgG1 isotype control-Dylight650 (used at 10  $\mu$ g ml $^{-1}$ ), mouse IgG2b kappa isotype control-FITC (used at 1:50 dilution), mouse IgG1 kappa isotype control-PE (used at 1:100 dilution), mouse IgG1 kappa isotype control-BrilliantViolet605 (used at 1:100 dilution). Cell counts were determined using CountBright absolute counting beads (ThermoFisher). Samples were collected on an Attune NxT flow cytometer (ThermoFisher) using Attune NxT software v3.1.2 and analysed using FlowJo (v10.6) software. For cluster analysis, dendritic cells (defined as Live/Lin $^{+}$ /CD45 $^{+}$ /CD11c $^{+}$ /MHCII $^{+}$ ) and T cells (defined as Live/CD45 $^{+}$ /NK1.1 $^{-}$ /CD3 $^{+}$ ) from individual mice were downsampled using the Downsample v.3.2 plugin (3,000 (dendritic cells) or 6,000 (T cells) events/mouse; 12,000 (dendritic cells) or 24,000 (T cells)/ treatment condition) and concatenated. Cells were clustered and visualized using UMAP reduction (UMAP plugin v2.2) and populations were identified by KNN density estimation (X-shift, v.1.3)<sup>35</sup>.

## Analysis of Fc $\gamma$ R expression on human T cells

Leukocyte packs (buffy coats) were purchased from the New York Blood Center, mononuclear cells were isolated by Ficoll gradient centrifugation and stained with the following fluorochrome-conjugated anti-human antibodies: anti-CD14-BrilliantViolet510, anti-CD19-BrilliantViolet510, anti-human Fc $\gamma$ RI-BrilliantViolet605 (clone 10.1), anti-CD8-BrilliantViolet650, anti-CD3-BrilliantViolet711, anti-CD11b-BrilliantViolet785, anti-human Fc $\gamma$ RIIa-FITC (clone IV.3) (used at 1:50 dilution), anti-CD4-PerCP-Cy5.5, anti-human Fc $\gamma$ RIIa/b-PE (clone 3G8), anti-CD56-PE/Cy7, anti-human Fc $\gamma$ RIIb-Dylight650 (clone 2B6) (used at 10  $\mu$ g ml $^{-1}$ ), anti-CD41-AlexaFluor700, and anti-CD42b-AlexaFluor700. The following isotype controls were used: mouse IgG1 isotype control-Dylight650 (used at 10  $\mu$ g ml $^{-1}$ ), mouse IgG2b kappa isotype control-FITC (used at 1:50 dilution), mouse IgG1 kappa isotype control-PE (used at 1:100 dilution), mouse IgG1 kappa isotype control-BrilliantViolet605 (used at 1:100 dilution). Samples were collected on an Attune NxT flow cytometer (ThermoFisher) using Attune NxT software v3.1.2 and analysed using FlowJo (v.10.6) software.

## Statistical analysis

Results from multiple experiments are presented as mean  $\pm$  s.e.m. One- or two-way ANOVA was used to test for differences in the mean values of quantitative variables, and where statistically significant effects were found, post hoc analysis using Bonferroni (adjusted for multiple comparisons) test was performed. Two-tailed *t*-test was used to test for differences in datasets with two groups. Statistical differences between survival rates were analysed by comparing Kaplan–Meier curves using the log-rank (Mantel–Cox) test. Data were analysed with GraphPad Prism v.8.4 software (GraphPad) and  $P < 0.05$  were considered to be statistically significant.

## Reporting summary

Further information on research design is available in the [Nature Research Reporting Summary](#) linked to this paper.

## Data availability

[Source data](#) are provided with this paper.

## References

1. 1.

Bournazos, S., Wang, T. T., Dahan, R., Maamary, J. & Ravetch, J. V. Signaling by antibodies: recent progress. *Annu. Rev. Immunol.* **35**, 285–311 (2017).

[CAS Article](#) [Google Scholar](#)

2. 2.

Lu, C. L. et al. Enhanced clearance of HIV-1-infected cells by broadly neutralizing antibodies against HIV-1 in vivo. *Science* **352**, 1001–1004 (2016).

[CAS Article](#) [ADS](#) [Google Scholar](#)

3. 3.

Bournazos, S., DiLillo, D. J. & Ravetch, J. V. The role of Fc-FcγR interactions in IgG-mediated microbial neutralization. *J. Exp. Med.* **212**, 1361–1369 (2015).

[CAS Article](#) [Google Scholar](#)

4. 4.

Bournazos, S. et al. Broadly neutralizing anti-HIV-1 antibodies require Fc effector functions for in vivo activity. *Cell* **158**, 1243–1253 (2014).

[CAS](#) [Article](#) [Google Scholar](#)

5. 5.

DiLillo, D. J., Palese, P., Wilson, P. C. & Ravetch, J. V. Broadly neutralizing anti-influenza antibodies require Fc receptor engagement for in vivo protection. *J. Clin. Invest.* **126**, 605–610 (2016).

[Article](#) [Google Scholar](#)

6. 6.

DiLillo, D. J., Tan, G. S., Palese, P. & Ravetch, J. V. Broadly neutralizing hemagglutinin stalk-specific antibodies require Fc $\gamma$ R interactions for protection against influenza virus in vivo. *Nat. Med.* **20**, 143–151 (2014).

[CAS](#) [Article](#) [Google Scholar](#)

7. 7.

Kallewaard, N. L. et al. Structure and function analysis of an antibody recognizing all influenza A subtypes. *Cell* **166**, 596–608 (2016).

[CAS](#) [Article](#) [Google Scholar](#)

8. 8.

Corti, D. et al. A neutralizing antibody selected from plasma cells that binds to group 1 and group 2 influenza A hemagglutinins. *Science* **333**, 850–856 (2011).

[CAS](#) [Article](#) [ADS](#) [Google Scholar](#)

9. 9.

Bournazos, S. IgG Fc receptors: evolutionary considerations. *Curr. Top. Microbiol. Immunol.* **423**, 1–11 (2019).

[PubMed](#) [Google Scholar](#)

10. 10.  
Smith, P., DiLillo, D. J., Bournazos, S., Li, F. & Ravetch, J. V. Mouse model recapitulating human Fc $\gamma$  receptor structural and functional diversity. *Proc. Natl Acad. Sci. USA* **109**, 6181–6186 (2012).

[CAS](#) [Article](#) [ADS](#) [Google Scholar](#)

11. 11.  
Richards, J. O. et al. Optimization of antibody binding to Fc $\gamma$ RIIa enhances macrophage phagocytosis of tumor cells. *Mol. Cancer Ther.* **7**, 2517–2527 (2008).

[CAS](#) [Article](#) [Google Scholar](#)

12. 12.  
DiLillo, D. J. & Ravetch, J. V. Differential Fc-receptor engagement drives an anti-tumor vaccinal effect. *Cell* **161**, 1035–1045 (2015).

[CAS](#) [Article](#) [Google Scholar](#)

13. 13.  
Weitzenfeld, P., Bournazos, S. & Ravetch, J. V. Antibodies targeting sialyl Lewis A mediate tumor clearance through distinct effector pathways. *J. Clin. Invest.* **129**, 3952–3962 (2019).

[Article](#) [Google Scholar](#)

14. 14.  
Lazar, G. A. et al. Engineered antibody Fc variants with enhanced effector function. *Proc. Natl Acad. Sci. USA* **103**, 4005–4010 (2006).

[CAS](#) [Article](#) [ADS](#) [Google Scholar](#)

15. 15.  
Ferrara, C. et al. Unique carbohydrate-carbohydrate interactions are required for high affinity binding between Fc $\gamma$ RIII and antibodies lacking core fucose. *Proc. Natl Acad. Sci. USA* **108**, 12669–12674 (2011).

[CAS](#) [Article](#) [ADS](#) [Google Scholar](#)

16. 16.

Mimoto, F. et al. Engineered antibody Fc variant with selectively enhanced Fc $\gamma$ RIIb binding over both Fc $\gamma$ RIIa(R131) and Fc $\gamma$ RIIa(H131). *Protein Eng. Des. Sel.* **26**, 589–598 (2013).

[CAS](#) [Article](#) [Google Scholar](#)

17. 17.

Wrammert, J. et al. Broadly cross-reactive antibodies dominate the human B cell response against 2009 pandemic H1N1 influenza virus infection. *J. Exp. Med.* **208**, 181–193 (2011).

[CAS](#) [Article](#) [Google Scholar](#)

18. 18.

Eisenbarth, S. C. Dendritic cell subsets in T cell programming: location dictates function. *Nat. Rev. Immunol.* **19**, 89–103 (2019).

[CAS](#) [Article](#) [Google Scholar](#)

19. 19.

Badia, R. et al. CD32 expression is associated to T-cell activation and is not a marker of the HIV-1 reservoir. *Nat. Commun.* **9**, 2739 (2018).

[Article](#) [ADS](#) [Google Scholar](#)

20. 20.

Martin, G. E. et al. CD32-expressing CD4 T cells are phenotypically diverse and can contain proviral HIV DNA. *Front. Immunol.* **9**, 928 (2018).

[Article](#) [Google Scholar](#)

21. 21.

Descours, B. et al. CD32a is a marker of a CD4 T-cell HIV reservoir harbouring replication-competent proviruses. *Nature* **543**, 564–567 (2017).

[CAS](#) [Article](#) [ADS](#) [Google Scholar](#)

22. 22.

Wang, T. T. et al. IgG antibodies to dengue enhanced for Fc $\gamma$ RIIIA binding determine disease severity. *Science* **355**, 395–398 (2017).

[CAS](#) [Article](#) [ADS](#) [Google Scholar](#)

23. 23.

Monsalvo, A. C. et al. Severe pandemic 2009 H1N1 influenza disease due to pathogenic immune complexes. *Nat. Med.* **17**, 195–199 (2011).

[CAS](#) [Article](#) [Google Scholar](#)

24. 24.

Mehta, P. et al. COVID-19: consider cytokine storm syndromes and immunosuppression. *Lancet* **395**, 1033–1034 (2020).

[CAS](#) [Article](#) [Google Scholar](#)

25. 25.

Zalevsky, J. et al. Enhanced antibody half-life improves in vivo activity. *Nat. Biotechnol.* **28**, 157–159 (2010).

[CAS](#) [Article](#) [Google Scholar](#)

26. 26.

Goede, V. et al. Obinutuzumab plus chlorambucil in patients with CLL and coexisting conditions. *N. Engl. J. Med.* **370**, 1101–1110 (2014).

[CAS](#) [Article](#) [Google Scholar](#)

27. 27.

Nishimura, Y. et al. Early antibody therapy can induce long-lasting immunity to SHIV. *Nature* **543**, 559–563 (2017).

[CAS](#) [Article](#) [ADS](#) [Google Scholar](#)

28. 28.

Niessl, J. et al. Combination anti-HIV-1 antibody therapy is associated with increased virus-specific T cell immunity. *Nat. Med.* **26**, 222–227 (2020).

[CAS](#) [Article](#) [Google Scholar](#)

29. 29.

Petkova, S. B. et al. Enhanced half-life of genetically engineered human IgG1 antibodies in a humanized FcRn mouse model: potential application in humorally mediated autoimmune disease. *Int. Immunol.* **18**, 1759–1769 (2006).

[CAS](#) [Article](#) [Google Scholar](#)

30. 30.

Roopenian, D. C., Christianson, G. J. & Sproule, T. J. Human FcRn transgenic mice for pharmacokinetic evaluation of therapeutic antibodies. *Methods Mol. Biol.* **602**, 93–104 (2010).

[CAS](#) [Article](#) [Google Scholar](#)

31. 31.

Borghi, S. et al. FcRn, but not FcγRs, drives maternal-fetal transplacental transport of human IgG antibodies. *Proc. Natl Acad. Sci. USA* **117**, 12943–12951 (2020).

[CAS](#) [Article](#) [Google Scholar](#)

32. 32.

Okeley, N. M. et al. Development of orally active inhibitors of protein and cellular fucosylation. *Proc. Natl Acad. Sci. USA* **110**, 5404–5409 (2013).

[CAS](#) [Article](#) [ADS](#) [Google Scholar](#)

33. 33.

He, W., Mullarkey, C. E. & Miller, M. S. Measuring the neutralization potency of influenza A virus hemagglutinin stalk/stem-binding antibodies in polyclonal preparations by microneutralization assay. *Methods* **90**, 95–100 (2015).

[CAS Article](#) [Google Scholar](#)

34. 34.

Kaufmann, L. et al. An optimized hemagglutination inhibition (HI) assay to quantify influenza-specific antibody titers. *J. Vis. Exp.* **130**, 55833 (2017).

[Google Scholar](#)

35. 35.

Samusik, N., Good, Z., Spitzer, M. H., Davis, K. L. & Nolan, G. P. Automated mapping of phenotype space with single-cell data. *Nat. Methods* **13**, 493–496 (2016).

[CAS Article](#) [Google Scholar](#)

36. 36.

Dahan, R. et al. Therapeutic activity of agonistic, human anti-CD40 monoclonal antibodies requires selective Fc $\gamma$ R engagement. *Cancer Cell* **29**, 820–831 (2016).

[CAS Article](#) [Google Scholar](#)

[Download references](#)

## Acknowledgements

We thank R. Francis for technical assistance in antibody cloning and expression, in vitro experiments, flow cytometry, and in vivo influenza challenge studies, M. Ye and E. Lam for maintaining the mouse colonies and for assisting with in vitro and in vivo experiments, P. Smith for maintaining the humanized mouse strains and all the members of the Laboratory of the Molecular Genetics and Immunology for discussions. We also thank S. Jaconi, K. Culap, E. Cameroni and B. Guarino for providing the FY1 monoclonal antibody Fc variants and for technical assistance in characterizing the in vitro ADCC/ADCP activity of Fc variants. Research reported in this publication was supported by the National Institute of Allergy and Infectious Diseases (R01AI129795 and R01AI145870). We acknowledge support from the Rockefeller University and Vir Biotechnology Inc. The content is solely the responsibility of the authors and does not necessarily represent the official views of the NIH.

# Author information

## Affiliations

1. Laboratory of Molecular Genetics and Immunology, The Rockefeller University, New York, NY, USA

Stylianos Bournazos & Jeffrey V. Ravetch

2. Humabs Biomed SA, a subsidiary of Vir Biotechnology Inc., Bellinzona, Switzerland

Davide Corti

3. Vir Biotechnology Inc., San Francisco, CA, USA

Herbert W. Virgin

## Authors

1. Stylianos Bournazos

[View author publications](#)

You can also search for this author in [PubMed](#) [Google Scholar](#)

2. Davide Corti

[View author publications](#)

You can also search for this author in [PubMed](#) [Google Scholar](#)

3. Herbert W. Virgin

[View author publications](#)

You can also search for this author in [PubMed](#) [Google Scholar](#)

4. Jeffrey V. Ravetch

[View author publications](#)

You can also search for this author in [PubMed](#) [Google Scholar](#)

## Contributions

S.B. designed the study, performed experiments, analysed data, and wrote the manuscript; D.C. and H.W.V. provided intellectual input; J.V.R. designed the study and wrote the manuscript.

## Corresponding author

Correspondence to [Jeffrey V. Ravetch](#).

## Ethics declarations

### Competing interests

S.B. and J.V.R. are inventors on a patent (WO2019125846A1) describing the GAALIE variant and its use in therapeutic monoclonal antibodies; D.C. and H.W.V. are employees of Vir Biotechnology Inc. and may hold shares in Vir Biotechnology Inc.; J.V.R. is a member of the scientific advisory board and a consultant of Vir Biotechnology Inc.

## Additional information

**Peer review information** *Nature* thanks George Georgiou and the other, anonymous, reviewer(s) for their contribution to the peer review of this work. Peer reviewer reports are available.

**Publisher's note** Springer Nature remains neutral with regard to jurisdictional claims in published maps and institutional affiliations.

## Extended data figures and tables

## **Extended Data Fig. 1 Characterization of the Fc $\gamma$ R binding profile and Fc effector activity of Fc domain variants.**

Fc domain variants with differential Fc $\gamma$ R binding affinity were generated through the introduction of amino acid substitutions at the hinge proximal region of the CH2 domain of human IgG1. **a**, The positions of the mutated residues for the different Fc domain variants are highlighted. **b**, The affinity of these human IgG1 Fc variants for the different human Fc $\gamma$ Rs was assessed by surface plasmon resonance and the dissociation constant ( $K_d$ ) (in M) is presented. The following references are cited in the table: refs. [13,36](#). **c, d**, HPLC analysis of Fc domain variants using size-exclusion chromatography (SEC) columns was performed to determine whether mutations at the Fc domain are associated with increased antibody aggregation. The SEC profiles (**c**: overlay; **d**: individual Fc variants) and the abundance (percentage) of monomeric IgG is presented for the different Fc variants. **e**, Fc variants for the anti-NP monoclonal antibody 3B62 were generated and their binding (monomeric for Fc $\gamma$ RI or as IgG immune complexes using NP-BSA for all other Fc $\gamma$ Rs) to immobilized human Fc $\gamma$ RI, Fc $\gamma$ RIIa, Fc $\gamma$ RIIb and Fc $\gamma$ RIIIa was assessed by ELISA. Results are from one experiment performed in duplicates. The Fc effector activity of anti-influenza monoclonal antibody FY1 Fc variants was assessed in vitro using Fc $\gamma$ RIIa-expressing (**f**:  $n = 2$  independent experiments for wild type,  $n = 1$  for other groups, **i**:  $n = 2$  independent experiments) and Fc $\gamma$ RIIIa-expressing (**g** ( $F^{158}$  allele), **j** ( $V^{158}$  allele);  $n = 1$  for each variant, except for GAALIE-LS ( $n = 2$  independent experiments)) NFAT reporter cell lines. Fc variants with enhanced affinity for Fc $\gamma$ RIIa or Fc $\gamma$ RIIIa demonstrated increased capacity to induce NFAT reporter activation. **h**, Similarly, FY1 Fc variants engineered for Fc $\gamma$ RIIIa binding exhibited improved primary human natural killer cell-mediated ADCC activity against HA-expressing cells. Results are the mean from two independent experiments using different natural killer cell donors. [Source data](#)

## **Extended Data Fig. 2 Anti-HA and NA monoclonal antibody titration studies to determine the optimal dose required for protection against mouse influenza infection.**

Given the differential epitope specificities and in vitro neutralization potency of the selected anti-influenza monoclonal antibodies, titration studies were performed to assess the capacity of these antibodies to protect mice against lethal influenza infection. Anti-HA and NA antibodies (**a**, FI6v3 ( $n = 5$  mice per group for  $8 \text{ mg kg}^{-1}$  group,  $n = 6$  mice per group for all other groups); **b**, FY1 ( $n = 6$  mice per group for 4 and  $2 \text{ mg kg}^{-1}$ ,  $n = 5$  mice per group for 1 and  $0.5 \text{ mg kg}^{-1}$ ,  $n = 4$  mice per group for PBS); **c**, 4G05 ( $n = 7$  mice per group for  $0.5 \text{ mg kg}^{-1}$  group,  $n = 6$  mice per group for all other groups); **d**, 1A01 ( $n = 4$  mice per group for  $1 \text{ mg kg}^{-1}$  group,  $n = 5$  mice per group for all other groups); **e**, 3C05 ( $n = 5$  mice per group for 20 and  $5 \text{ mg kg}^{-1}$ ,  $n = 4$  mice per group for  $10 \text{ mg kg}^{-1}$  and PBS groups)). All antibodies were expressed as human IgG1 and administered intraperitoneally (for FI6v3 and FY1) or intravenously (for 4G05, 1A01, and 3C05) at the dose indicated to mice (C57BL/6) 4 h before lethal challenge with influenza (five mLD<sub>50</sub>; H1N1 PR8 for **a**, **b**; H1N1 Neth/09 for **c–e**). Survival was monitored for 14 days. [Source data](#)

### **Extended Data Fig. 3 In vitro characterization of the antigenic specificity, neutralization potency, and HAI activity of Fc domain variants of anti-influenza monoclonal antibodies.**

**a–l**, To study the role of Fc–FcγR interactions in the antibody-mediated protection against influenza infection, Fc domain variants with differential FcγR affinities (Fig. [1b](#)) were generated for antibodies that target distinct epitopes on influenza antigens (Fig. [1a](#)). These antibodies include FI6v3 (**a–c**) and FY1 (**d–f**), which both recognize the stalk region of influenza HA and exhibit broad and potent neutralizing activity against group 1 and 2 influenza strains, 4G05 (**g–i**), which is a pan-H1 monoclonal antibody against the globular head of HA and exhibits potent neutralizing and HAI activity, 1A01 (**j–l**), which is a pan-H1 anti-globular head HA antibody with no neutralizing or HAI activity, and 3C05 (**m–o**), a broadly (pan-H1) protective antibody against NA. To confirm that changes in the Fc domain have no effect on the antigenic activity and Fab-mediated functions of these antibodies, Fc domain variants were characterized by ELISA (**a**, **d**, **g**, **j**, **m**;  $n = 1$  experiment performed in duplicates) to assess their specificity against purified HA (H1N1 PR8 strain for FI6v3 and FY1; Cal/09 strain for 4G05,

1A01 and 3C05), by microneutralization assay (**b**, **e**, **h**, **k** and **n**; **c**, **f**, **i**, **l** and **o** for IC<sub>50</sub> values;  $n = 2$  independent experiments; data were fitted with nonlinear regression analysis (four-parameter) to calculate IC<sub>50</sub> values) to evaluate their neutralizing activity against H1N1 (H1N1 PR8 strain for FI6v3 and FY1; Neth/09 strain for 4G05, 1A01, and 3C05), and by HAI assay (H1N1 PR8 strain for FI6v3 and FY1; Neth/09 strain for 4G05, 1A01, and 3C05;  $n = 2$  independent experiments) to determine their HAI titre (**c**, **f**, **i**, **l** and **o**). [Source data](#)

### Extended Data Fig. 4 In vivo half-life of Fc domain variants.

**a**, Fc variants of an anti-HIV antibody (3BNC117) were administered (intravenously; 100 µg) to FcγR-humanized mice and antibody serum levels were determined by ELISA at various time points after antibody administration.  $n = 4$  mice per group in two independent experiments. Data are mean ± s.e.m. **b–f**, To ensure that the observed differences in the protective activity of Fc variants of anti-HA and NA antibodies (Figs. [1](#) and [2](#)) were not due to differential in vivo antibody half-lives, serum was obtained from influenza-infected mice (day 3 after infection) and analysed by ELISA to quantify antibody levels. (**b**:  $n = 9$  mice per group for GAALIE,  $n = 10$  mice per group for all other groups; **c**:  $n = 10$  mice per group for wild type,  $n = 8$  mice per group for all other groups ; **d**:  $n = 10$  mice per group; **e**:  $n = 6$  mice per group for GRLR,  $n = 8$  mice per group for all other groups; **f**:  $n = 12$  mice per group for wild type and GA;  $n = 10$  mice per group for GRLR and ALIE;  $n = 9$  mice per group for GAALIE). **g**, To ensure that the observed differences in the protective activity of Fc variants of FY1 antibodies (Fig. [3e,f](#), Extended Data Fig. [10d,e](#)) were not due to differential in vivo antibody half-lives, serum was obtained from influenza-infected mice (day 3 after infection) and analysed by ELISA to quantify FY1 antibody levels.  $n = 12$  mice per group for wild type/isotype, GAALIE/isotype, and GAALIE/anti-CD8 groups,  $n = 11$  mice per group for wild-type/anti-CD8,  $n = 8$  mice per group for GA/isotype, GA/anti-CD4, and GA/anti-CD4 groups,  $n = 6$  mice per group for wild-type/anti-CD4 group. **h**, Titration studies were performed in a mouse model of antibody-mediated prophylaxis of influenza infection (Fig. [4d](#)) and serum was obtained at the time of virus challenge and analysed by ELISA to quantify FY1 antibody levels.  $n = 10$  mice per group for LS 0.1 mg kg<sup>-1</sup> dose,  $n = 8$

for GAALIE–LS at 1.6 and 0.4 mg kg<sup>-1</sup> doses,  $n = 9$  mice per group for all other groups. [Source data](#)

## Extended Data Fig. 5 Evaluation of the role of FcγRIIa and the contribution of neutrophils in the antibody-mediated protection against influenza infection.

**a, b,** To confirm the dependence of FcγRIIa engagement in driving the protective activity of the GA variant, mice expressing the human FcγRIIa transgene on an FcγR<sub>null</sub> background (hFcγRIIa<sup>+</sup>; gating strategy **(a)** and representative flow cytometry histograms **(b)** of FcγRIIa expression in lung-resident leukocytes) or deficient for all classes of FcγRs (hFcγRIIa<sup>-</sup>) were administered with GA variants of FY1 (intraperitoneally 2 mg kg<sup>-1</sup>) ( $n = 7$  mice per group for FcγRIIa<sup>+</sup>,  $n = 6$  mice per group for FcγRIIa<sup>-</sup> in two independent experiments) or PBS ( $n = 4$  mice per group for FcγRIIa<sup>+</sup>,  $n = 5$  mice per group for FcγRIIa<sup>-</sup> in two independent experiments) 4 h before lethal challenge with influenza (H1N1; PR8, 5 mLD<sub>50</sub>). **c, d,** Weight loss **(c)** (mean ± s.e.m.) and survival **(d)** were monitored for 14 days and compared by two-way ANOVA (Bonferroni post hoc analysis adjusted for multiple comparisons) (**c**: \* $P = 0.02$  § $P = 0.03$ , ¶ $P = 0.006$ , ^ $P < 0.0001$ , # $P = 0.0002$ , ▲ $P = 0.0006$ , \*\* $P = 0.001$ , ## $P = 0.002$  versus GA-treated FcγRIIa<sup>-</sup>) and log-rank (Mantel–Cox) test, respectively (**d**: \* $P = 0.0006$  versus GA-treated FcγRIIa<sup>-</sup>). **e, f,** FcγR-humanized mice were administered with GA variants of FI6v3 (intraperitoneally 4 mg kg<sup>-1</sup>) before challenge with PR8 (as described in **c, d**). To block the ligand binding activity of FcγRIIa, recombinant anti-FcγRIIa (clone IV.3) expressed as human IgG1 GRLR variant to abrogate FcγR binding or isotype control (anti-hapten (NP) monoclonal antibody; clone 3C13) was administered intranasally (80 µg) to mice 1 day after virus challenge ( $n = 7$  mice per group for GA/IV.3-treated group,  $n = 5$  mice per group for all other groups in two independent experiments) and weight loss **(e)** (mean ± s.e.m.) and survival **(f)** were monitored. **g,** To establish the efficiency of antibody-mediated neutrophil depletion, FcγR-humanized mice ( $n = 3$  mice per group in one experiment) were injected intravenously with 150 µg anti-mouse Gr-1 monoclonal antibody (clone RB6-8C5) or isotype control (clone LTF-2). The abundance

of neutrophils ( $\text{Ly6G}^+$ ) in peripheral blood was determined 2 days after antibody administration by flow cytometry.  $**P = 0.0053$ , two-sided unpaired *t*-test. **h, i**, To assess the contribution of neutrophils to the protective activity of Fc $\gamma$ RIIa-enhanced variants of anti-influenza antibodies, GA variants of the anti-HA stalk antibody FY1 were administered intraperitoneally ( $2 \text{ mg kg}^{-1}$ ) to Fc $\gamma$ R-humanized mice ( $n = 6$  mice per group, except for PBS/Gr-1 treated ( $n = 5$  mice per group) in two independent experiments) 4 h before lethal challenge with PR8. Isotype or anti-mouse Gr-1 monoclonal antibodies ( $150 \mu\text{g}$  intravenously) were administered on day 1 after infection and weight loss (**h**) (mean  $\pm$  s.e.m.) and survival (**i**) were recorded. [Source data](#)

**Extended Data Fig. 6 Abundance and Fc $\gamma$ R expression profile of leukocyte populations in the lungs of influenza-infected Fc $\gamma$ R-humanized mice at different time points after infection.**

**a–f**, To determine the abundance and Fc $\gamma$ R expression profile of lung resident and infiltrated leukocytes during the course of influenza infection, cohorts of Fc $\gamma$ R-humanized mice were infected (intranasally with H1N1 PR8;  $5 \text{ mL D}_{50}$ ) and euthanized at different time points after infection (day 0 to 6). Lungs were homogenized and analysed by flow cytometry (**a**: gating strategy) to determine the frequency (**b, c**) and Fc $\gamma$ R expression profile (**f**) of innate effector leukocytes.  $n = 3$  and  $n = 4$  mice per time point for day 0–2 and day 3–6 time points, respectively. Influenza infection was associated with the recruitment of natural killer (NK) cells, neutrophils and monocytes, whereas the number of alveolar macrophages was reduced at the later stages of infection. Owing to the high degree of sequence similarity between Fc $\gamma$ RIIa and Fc $\gamma$ RIIb, expression of these Fc $\gamma$ Rs was assessed using antibody clones (**d**: IV.3 for Fc $\gamma$ RIIa; **e**: 2B6 for Fc $\gamma$ RIIb) that exhibit high specificity, as assessed by ELISA using recombinant Fc $\gamma$ Rs ( $n = 1$  experiment performed in duplicates). Analysis of the Fc $\gamma$ R expression profile (MFI) revealed that influenza infection had no effect on the levels of Fc $\gamma$ Rs expressed by the various leukocyte types. With the exception of natural killer cells, which expressed only Fc $\gamma$ RIIIa, most innate effector leukocytes co-expressed multiple Fc $\gamma$ Rs, including the activating Fc $\gamma$ Rs, Fc $\gamma$ RIIa and Fc $\gamma$ RIIIa/b, as well as the inhibitory Fc $\gamma$ RIIb.

$n = 3$  and  $n = 4$  mice per time point for day 0–2 and day 3–6 time points, respectively. [Source data](#)

### Extended Data Fig. 7 Treatment of Fc $\gamma$ R-humanized mice with GAALIE variants of anti-HA antibodies is associated with increased frequency of activated dendritic cells.

**a–f**, To determine the abundance and Fc $\gamma$ R expression profile of dendritic cell subsets during the course of influenza infection, cohorts of Fc $\gamma$ R-humanized mice were infected (intranasally with H1N1 PR8; 5 mLD<sub>50</sub>) and euthanized at different time points after infection (day 0 to 6). Lungs were homogenized and analysed by flow cytometry (**a**: gating strategy) to determine the frequency (**b**) and Fc $\gamma$ R expression profile (**c**: representative flow cytometry overlay; **d–f**: MFI) of the three major dendritic cell subsets identified: cDC1, cDC2 and tipDCs. Influenza infection was not associated with any major changes in the number of lung-resident cDC1 and cDC2, whereas tipDCs were almost absent at baseline, but their number increased markedly after infection. cDC1 and cDC2 expressed Fc $\gamma$ RIIa and Fc $\gamma$ RIIb, but they were negative for Fc $\gamma$ RIIIa. By contrast, tipDCs expressed Fc $\gamma$ RIIa and Fc $\gamma$ RIIIa, along with the inhibitory Fc $\gamma$ RIIb. Owing to the very low number of tipDCs at baseline, Fc $\gamma$ R expression (MFI) was omitted.  $n = 4$  mice per time point assessed. **g–i**, To investigate the effect of enhanced Fc $\gamma$ RIIa engagement by GAALIE variants on the maturation status of dendritic cells, Fc $\gamma$ R-humanized mice were treated with Fc domain variants of the anti-HA stalk antibody FI6v3, exhibiting differential Fc $\gamma$ R affinity—wild type IgG1 (baseline Fc $\gamma$ R affinity), GRLR (diminished binding to all classes of Fc $\gamma$ Rs), and GAALIE (increased Fc $\gamma$ RIIa and Fc $\gamma$ RIIIa affinity). Fc domain variants were administered intraperitoneally (3 mg kg<sup>-1</sup>) to Fc $\gamma$ R-humanized mice ( $n = 4$  mice per treatment group in two independent experiments) 4 h before lethal challenge with H1N1 (PR8; 5 mLD<sub>50</sub>). Mice were euthanized on day 4 and lung-resident dendritic cells were analysed by flow cytometry. The abundance of mature (defined as CD80<sup>high</sup>CD86<sup>high</sup>) cDC1 (**g**), cDC2 (**h**), and tipDCs (**i**) was compared between mice treated with the various Fc domain variants of FI6v3. Representative flow cytometry plots from data presented in Fig. [3a](#). In contrast to cDC1 and cDC2, no differences were observed in the maturation status of tipDCs

among mice treated with different FI6v3 Fc variants (one-way ANOVA). **j**, **k**, In vitro differentiated monocyte-derived dendritic cells ( $n = 4$  peripheral blood mononuclear cell donors performed in two independent experiments) were stimulated overnight with IgG immune complexes (anti-NP–NP-BSA immune complexes (**j**) and heat-aggregated IgG complexes (**k**)). The abundance (percentage) of mature dendritic cells (defined as CD80<sup>high</sup>CD86<sup>high</sup>) was assessed by multicolour flow cytometry and compared against the corresponding wild-type-treated group by one-way ANOVA (Bonferroni post hoc analysis adjusted for multiple comparisons) \* $P = 0.0417$ , \*\* $P = 0.0134$ , \*\*\* $P < 0.0001$ , ^ $P = 0.0049$ . **l–n**, Cluster analysis of dendritic cell populations present in the lungs of influenza-infected mice treated with Fc domain variants of anti-HA monoclonal antibodies. Mice ( $n = 4$  mice per group in two independent experiments) were treated as described in **g–i**, euthanized on day 4 after infection and dendritic cells (Lin<sup>+</sup>MHCII<sup>+</sup>CD11c<sup>+</sup>) were analysed by multicolour flow cytometry. Data were dimensionally reduced and visualized using the UMAP algorithm. **l**, UMAP plots of dendritic cells in mice treated with the different Fc domain variants are presented. Populations were identified by X-shift using KNN density estimation and assigned IDs (A–J). **m**, The abundance of the various dendritic cell clusters in the different treatment groups was plotted and populations that are enriched or reduced in GAALIE-treated mice were identified. **n**, Histogram plots of the expression of CD80, CD86, CD40 and MHCII in dendritic cell populations that are enriched (red, A; and orange, H) or reduced (cyan, D; purple, E; and blue, F) in GAALIE-treated mice. GAALIE treatment was associated with the enrichment of dendritic cell populations characterized by high levels of CD86 and CD40 expression. Results are from four mice per treatment condition in two independent experiments. [Source data](#)

### **Extended Data Fig. 8 Treatment of FcγR-humanized mice with GAALIE variants of anti-HA stalk antibodies is associated with increased activation of CD8<sup>+</sup> and CD4<sup>+</sup> T cells.**

To investigate whether the observed increase in the frequency of mature dendritic cells in mice treated with GAALIE variants of anti-HA monoclonal antibodies was associated with enhanced T cell responses, the

activation status of CD8<sup>+</sup> and CD4<sup>+</sup> T cells was analysed and compared between mice treated with anti-HA Fc domain variants with differential Fc $\gamma$ R affinity (wild-type IgG1, GRLR and GAALIE). Fc domain variants of the anti-HA stalk antibody FI6v3 were administered (intraperitoneally 3 mg kg<sup>-1</sup>) to Fc $\gamma$ R-humanized mice before lethal challenge with H1N1 (PR8; 5 mLD<sub>50</sub>). Mice ( $n = 4$  mice per group in two independent experiments) were euthanized on day 4 after infection and T cell populations were analysed by multicolour flow cytometry. **a, b**, The frequency of activated (defined as CD44<sup>hi</sup>CD69<sup>+</sup>) CD8<sup>+</sup> (**a**) and CD4<sup>+</sup> (**b**) T cells was compared between mice treated with the various Fc domain variants of FI6v3. Representative flow cytometry plots from data in Fig. [3c](#). In addition, cluster analysis of T cell populations present in the lungs of influenza-infected mice treated with Fc domain variants of anti-HA monoclonal antibodies was performed. Flow cytometry data were dimensionally reduced and visualized using the UMAP algorithm. **c**, UMAP plots of T cells in mice treated with the different Fc domain variants are presented. Populations were identified by X-shift using KNN density estimation and assigned IDs (A-M). **d**, Heat map of the abundance of the various T cell clusters in the different treatment groups. Populations that are enriched or reduced in GAALIE-treated mice were identified. **e**, Histogram plots of the expression of CD69, CD25, CD44 and CD62L in T cell populations that are enriched (red, G; green, E; orange, J) or reduced (cyan, C; blue, D; magenta, L) in GAALIE-treated mice. GAALIE treatment was associated with the enrichment of T cell populations characterized by high levels of CD69, CD44 and CD25 expression. Results are from four mice per treatment condition. [Source data](#)

### Extended Data Fig. 9 Fc $\gamma$ R expression analysis of T cells.

To determine whether human T cells express human Fc $\gamma$ Rs, human peripheral blood mononuclear cells were analysed by multicolour flow cytometry. **a**, Gating strategy for identifying human T cells. Monocytes (CD14<sup>+</sup>CD11b<sup>+</sup>) and B cells (CD19<sup>+</sup>CD11b<sup>-</sup>) were included as controls for Fc $\gamma$ R immunofluorescence staining. **b, g**, Analysis of Fc $\gamma$ R expression revealed that human T cells are negative for Fc $\gamma$ R expression (**b**: representative flow cytometry histogram overlays; **g**: quantification of

Fc $\gamma$ R $^+$  cells;  $n = 3$  donors). **c–f, h–l**, Human Fc $\gamma$ R expression on peripheral blood (**c, d, h, i**), spleen (**e, f, j, k**), or lung (**l**) T cells from naive (**h, j**) or influenza-infected (**i, k, l**; day 6 after infection (5 mLD<sub>50</sub>; H1N1 PR8))

Fc $\gamma$ R-humanized mice was assessed by multicolour flow cytometry. Gating strategy for identifying T cells in mouse blood (**c**), spleen or lungs (**e**).

Myeloid cells (CD11b $^+$ ) and B cells (B220 $^+$ ) were included as controls for Fc $\gamma$ R immunofluorescence staining. Analysis of Fc $\gamma$ R expression on T cells from naive or influenza-infected Fc $\gamma$ R-humanized mice revealed minimal expression of Fc $\gamma$ Rs on T cell (**d, f**: representative flow cytometry histogram overlays; **h–l**: quantification of Fc $\gamma$ R $^+$  cells ( $n = 2$  mice per group in one experiment) in the blood (**h, i**), spleen (**j, k**) and lungs (**l**) of naive or influenza-infected mice). Although a small fraction of B cells appears positive for Fc $\gamma$ RIIa expression, this is probably due to the cross-reactivity of the anti-Fc $\gamma$ RIIa antibody (clone IV.3) to Fc $\gamma$ RIIb (see Extended Data Fig. [6d](#)). [Source data](#)

### Extended Data Fig. 10 T cell depletion experiments and the effect of Fc $\gamma$ RIIa-enhanced variants on anti-influenza IgG responses.

**a, b**, To establish the efficiency of antibody-mediated CD8 $^+$  or CD4 $^+$  T cell depletion, Fc $\gamma$ R-humanized mice were injected intravenously with 150  $\mu$ g anti-mouse CD8 $\alpha$  monoclonal antibody (clone 2.43) or anti-mouse CD4 (clone GK1.5), or isotype control (clone LTF-2). The abundance of CD8 $^+$  (**a**) or CD4 $^+$  (**b**) T cells in peripheral blood was determined at various time points after antibody administration by flow cytometry. Baseline CD8 $^+$  or CD4 $^+$  T cell frequencies were determined in blood samples obtained before antibody administration. Results are expressed as the percentage of CD8 $^+$ CD3 $^+$  or CD4 $^+$ CD3 $^+$  T cells ( $n = 6$  for anti-CD8 and anti-CD4-treated groups,  $n = 7$  mice per group for isotype groups in two independent experiments). **c–e**, To determine the contribution of CD4 $^+$  T cells in the protective activity of Fc $\gamma$ RIIa-enhanced variants of anti-influenza monoclonal antibodies, CD4 $^+$  depletion studies were performed. **c**, Wild-type or GA variants of the anti-HA stalk antibody FY1 were administered intraperitoneally (2 mg kg $^{-1}$ ) to Fc $\gamma$ R-humanized mice 4 h before lethal

challenge with influenza (5 mLD<sub>50</sub>; H1N1 PR8). Isotype or anti-mouse CD4 antibodies (150 µg intravenously) were administered on day 3 after infection. Isotype-treated groups:  $n = 12$  mice per group for wild-type and PBS groups,  $n = 8$  mice per group for GA group; anti-CD4-treated groups:  $n = 6$  mice per group for wild type,  $n = 8$  mice/group for GA,  $n = 4$  mice per group for PBS in two independent experiments. **d, e**, Weight loss (**d**) (mean ± s.e.m.) and survival (**e**) were monitored for 14 days. Data for isotype-treated mice are also in Fig. 3e,f. **f–m**, Wild-type or GAALIE Fc variants for the anti-HA globular head antibody 1A01 were administered (intravenously 4 mg kg<sup>-1</sup>) to FcγR-humanized mice ( $n = 7$  mice per group for wild-type group,  $n = 11$  mice per group for GAALIE-treated group,  $n = 5$  mice per group for PBS-treated in two independent experiments) 4 h before lethal challenge with influenza (5 mLD<sub>50</sub>; H1N1 Neth/09). **f, g**, Weight loss (mean ± s.e.m.) and survival (**g**) were monitored for 14 days. **h–k**, IgG responses against HA (**h, i**) and NP (**j, k**) from homologous (H1N1; A/California/04/2009) or heterologous (H3N2; A/x31) strains were evaluated in surviving mice. **l**, Analysis of IgG titres against homologous or heterologous HA or NP revealed no differences among mice previously treated with wild-type or GAALIE Fc variants of 1A01 antibody. **m**, Similarly, comparable HAI titres were noted among the treatment groups.

[Source data](#)

## Supplementary information

### [Reporting Summary](#)

### [Peer Review File](#)

### Source data

#### [Source Data Fig. 1](#)

#### [Source Data Fig. 2](#)

#### [Source Data Fig. 3](#)

[Source Data Fig. 4](#)

[Source Data Extended Data Fig. 1](#)

[Source Data Extended Data Fig. 2](#)

[Source Data Extended Data Fig. 3](#)

[Source Data Extended Data Fig. 4](#)

[Source Data Extended Data Fig. 5](#)

[Source Data Extended Data Fig. 6](#)

[Source Data Extended Data Fig. 7](#)

[Source Data Extended Data Fig. 8](#)

[Source Data Extended Data Fig. 9](#)

[Source Data Extended Data Fig. 10](#)

## Rights and permissions

[Reprints and Permissions](#)

## About this article



Check for  
updates

## Cite this article

Bournazos, S., Corti, D., Virgin, H.W. *et al.* Fc-optimized antibodies elicit CD8 immunity to viral respiratory infection. *Nature* **588**, 485–490 (2020). <https://doi.org/10.1038/s41586-020-2838-z>

## [Download citation](#)

- Received: 18 April 2020
- Accepted: 02 October 2020
- Published: 08 October 2020
- Issue Date: 17 December 2020
- DOI: <https://doi.org/10.1038/s41586-020-2838-z>

## Further reading

- [\*\*Engineered antibodies to combat viral threats\*\*](#)
  - Xiaojie Yu
  - & Mark S. Cragg

*Nature* (2020)

## Comments

By submitting a comment you agree to abide by our [Terms](#) and [Community Guidelines](#). If you find something abusive or that does not comply with our terms or guidelines please flag it as inappropriate.

## [Download PDF](#)

---

This article was downloaded by **calibre** from <https://www.nature.com/articles/s41586-020-2838-z>

IFITM3 functions as a PIP3 scaffold to amplify PI3K signalling in B cells  
[Download PDF](#)

- Article
- [Published: 04 November 2020](#)

# IFITM3 functions as a PIP3 scaffold to amplify PI3K signalling in B cells

- [Jaewoong Lee<sup>1</sup>](#),
- [Mark E. Robinson](#) [ORCID: orcid.org/0000-0003-2363-6047<sup>1</sup>](#),
- [Ning Ma<sup>2</sup>](#),
- [Dewan Artadji](#) [ORCID: orcid.org/0000-0002-1189-6936<sup>1</sup>](#),
- [Mohamed A. Ahmed](#) [ORCID: orcid.org/0000-0003-4476-0768<sup>3</sup>](#),
- [Gang Xiao<sup>3</sup>](#),
- [Teresa Sadras<sup>1</sup>](#),
- [Gauri Deb<sup>3</sup>](#),
- [Janet Winchester<sup>3</sup>](#),
- [Kadriye Nehir Cosgun<sup>1</sup>](#),
- [Huimin Geng<sup>4</sup>](#),
- [Lai N. Chan<sup>1</sup>](#),
- [Kohei Kume](#) [ORCID: orcid.org/0000-0003-2856-5970<sup>1</sup>](#),
- [Teemu P. Miettinen](#) [ORCID: orcid.org/0000-0002-5975-200X<sup>5,6</sup>](#),
- [Ye Zhang<sup>5</sup>](#),
- [Matthew A. Nix](#) [ORCID: orcid.org/0000-0001-7741-5368<sup>4</sup>](#),
- [Lars Klemm<sup>1</sup>](#),
- [Chun Wei Chen](#) [ORCID: orcid.org/0000-0002-8737-6830<sup>3</sup>](#),
- [Jianjun Chen](#) [ORCID: orcid.org/0000-0003-3749-2902<sup>3</sup>](#),
- [Vishal Khairnar<sup>3</sup>](#),
- [Arun P. Wiita](#) [ORCID: orcid.org/0000-0002-7465-6964<sup>4</sup>](#),
- [Andrei Thomas-Tikhonenko<sup>7</sup>](#),
- [Michael Farzan](#) [ORCID: orcid.org/0000-0002-2990-5319<sup>8</sup>](#),
- [Jae U. Jung](#) [ORCID: orcid.org/0000-0003-4559-8774<sup>9</sup>](#),
- [David M. Weinstock<sup>10,11</sup>](#),
- [Scott R. Manalis](#) [ORCID: orcid.org/0000-0001-5223-9433<sup>5,12</sup>](#),

- [Michael S. Diamond](#) ORCID: [orcid.org/0000-0002-8791-3165](https://orcid.org/0000-0002-8791-3165)<sup>13,14,15</sup>,
- [Nagarajan Vaidehi](#) ORCID: [orcid.org/0000-0001-8100-8132](https://orcid.org/0000-0001-8100-8132)<sup>2</sup> &
- [Markus Müschen](#) ORCID: [orcid.org/0000-0002-6064-8613](https://orcid.org/0000-0002-6064-8613)<sup>1,16</sup>

[Nature](#) volume 588, pages491–497(2020)[Cite this article](#)

- 7764 Accesses
- 34 Altmetric
- [Metrics details](#)

## Subjects

- [B-cell lymphoma](#)
- [B cells](#)
- [Signal transduction](#)

## Abstract

Interferon-induced transmembrane protein 3 (IFITM3) has previously been identified as an endosomal protein that blocks viral infection<sup>1,2,3</sup>. Here we studied clinical cohorts of patients with B cell leukaemia and lymphoma, and identified *IFITM3* as a strong predictor of poor outcome. In normal resting B cells, IFITM3 was minimally expressed and mainly localized in endosomes. However, engagement of the B cell receptor (BCR) induced both expression of IFITM3 and phosphorylation of this protein at Tyr20, which resulted in the accumulation of IFITM3 at the cell surface. In B cell leukaemia, oncogenic kinases phosphorylate IFITM3 at Tyr20, which causes constitutive localization of this protein at the plasma membrane. In a mouse model, *Ifitm3*<sup>-/-</sup> naive B cells developed in normal numbers; however, the formation of germinal centres and the production of antigen-specific antibodies were compromised. Oncogenes that induce the development of leukaemia and lymphoma did not transform *Ifitm3*<sup>-/-</sup> B cells. Conversely, the phosphomimetic IFITM3(Y20E) mutant induced oncogenic PI3K signalling and initiated the transformation of premalignant B cells. Mechanistic experiments revealed that IFITM3 functions as a PIP3 scaffold and central amplifier of PI3K signalling. The amplification of PI3K signals depends on IFITM3 using two lysine residues (Lys83 and Lys104) in its conserved intracellular loop as a scaffold for the accumulation of PIP3. In *Ifitm3*<sup>-/-</sup> B cells, lipid rafts were depleted of PIP3, which resulted in the defective expression of over 60 lipid-raft-associated surface receptors, and impaired

BCR signalling and cellular adhesion. We conclude that the phosphorylation of IFITM3 that occurs after B cells encounter antigen induces a dynamic switch from antiviral effector functions in endosomes to a PI3K amplification loop at the cell surface. IFITM3-dependent amplification of PI3K signalling, which in part acts downstream of the BCR, is critical for the rapid expansion of B cells with high affinity to antigen. In addition, multiple oncogenes depend on IFITM3 to assemble PIP3-dependent signalling complexes and amplify PI3K signalling for malignant transformation.

[Download PDF](#)

## Main

IFITM3 is a small antiviral membrane protein (133 amino acids in size) with activity against influenza A virus, severe acute respiratory syndrome (SARS) coronavirus and many other viruses<sup>1,2,3,4,5</sup>. Endocytosis and preferential endosomal localization of IFITM3 are mediated by its N-terminal AP2 sorting motif, YEML<sup>1</sup>. Phosphorylation of this motif at Y20 by SRC kinases prevents not only endocytosis but also proteasomal degradation<sup>6,7</sup>. Individuals with the *IFITM3* single-nucleotide polymorphism (SNP) rs12252-C allele show increased morbidity and mortality from H1N1 strains of influenza A virus<sup>8</sup> and SARS coronavirus 2<sup>4</sup>. *IFITM3* SNP rs12252-C was predicted through mRNA splicing to encode a 21-amino-acid truncation of the N terminus (which includes Y20), although a recent transcript analysis found no evidence for such processed mRNA<sup>9</sup>. IFITM3 probably functions as an antiviral effector molecule by limiting viral fusion through increasing the ‘rigidity’ of endosomal cell membranes<sup>10,11</sup>. IFITM3 is overexpressed in multiple types of cancer, and its expression levels correlated with histopathological grading and staging<sup>12,13</sup>. Although IFITM3-dependent antiviral effector functions are restricted to endosomal compartments<sup>14</sup>, we report here on IFITM3-dependent functions at the cell surface of B cells, where IFITM3 functions as amplifier of PI3K signalling.

## IFITM3 is essential for B cell affinity maturation

Although IFITM3 is only minimally expressed in normal resting B cells, BCR engagement and acute activation of the PI3K pathway strongly induced the expression of this protein (Extended Data Fig. 1a–c). Expression of IFITM proteins has recently been established as a diagnostic biomarker of high-risk B cell-lineage acute lymphoblastic leukaemia (B-ALL) that expresses the oncogenic BCR–ABL1 tyrosine kinase or related kinases<sup>15</sup>; we found that BCR–ABL1 kinase inhibition

decreased levels of IFITM3 expression (Extended Data Fig. 1d). Levels of *IFITM3* mRNA were generally higher in B cell malignancies than in their normal counterparts (Extended Data Fig. 1f,g) and elevated *IFITM3* mRNA levels were associated with poor clinical outcomes in multiple clinical cohorts of patients with B cell malignancies (including paediatric and adult B-ALL and mantle cell lymphoma) (Extended Data Fig. 1h-l). *IFITM3* was previously identified as a transcriptional target of the transcriptional repressor IKZF1<sup>16</sup>, which suggests that high levels of *IFITM3* expression may be the result of genetic lesions in *IKZF1*. Our results confirmed that reconstitution of IKZF1 suppresses IFITM3 expression, and that inducible deletion of *Ikzf1* in mice relieves transcriptional repression (Extended Data Fig. 1m,n). However, a multivariate analysis of risk factors in B-ALL showed that high *IFITM3* mRNA levels are an independent predictor of poor outcome, regardless of *IKZF1* deletion (Extended Data Fig. 1o). We next examined how the genetic deletion of *Ifitm3* affects normal B cell development in mice. Surface expression of CD19—a common B cell surface receptor that promotes SRC kinase and PI3K signalling<sup>17</sup>—was substantially diminished in *Ifitm3*<sup>-/-</sup> pre-B cells (Fig. 1a). Consistent with increased apoptosis and reduced proliferation, expression of MYC and BCL2 as well as PI3K signalling were reduced in *Ifitm3*<sup>-/-</sup> pre-B cells (Fig. 1a-c). The development of resting *Ifitm3*<sup>-/-</sup> B cell populations was largely unperturbed (Extended Data Fig. 2), whereas B1 cell and marginal-zone B cell populations were decreased (Fig. 1d, Extended Data Fig. 2). To assess B-cell-specific effects of IFITM3 during humoral immune responses, we performed adoptive transfer experiments: *Ifitm3*<sup>+/+</sup> or *Ifitm3*<sup>-/-</sup> splenic B cells were transferred into congenic μMT mice that lack endogenous mature B cells. After reconstitution of mature B cell development, recipient μMT mice were immunized with the hapten 4-hydroxy-3-nitrophenyl acetyl (NP) conjugated to keyhole limpet haemocyanin (KLH) (NP-KLH). Upon immunization, μMT mice reconstituted with *Ifitm3*<sup>+/+</sup> B cells developed about 5% NP-specific germinal-centre B cells, which were largely absent in μMT mice reconstituted with *Ifitm3*<sup>-/-</sup> B cells (Fig. 1e-h). Similarly, the number of follicles in the spleen, PNA<sup>+</sup> germinal-centre B cells and production of IgM, IgG1 and IgG2b antibodies were reduced in the absence of *Ifitm3* (Fig. 1i). These abnormalities in *Ifitm3*-deficient B cells phenocopy B cell defects seen in mice upon deletion of *Pik3cd*<sup>18</sup> and *Cd19*<sup>19</sup>.

**Fig. 1: *Ifitm3* is essential for B cell activation and affinity maturation in germinal centres.**

 **figure1**

**a**, CD19 surface expression (top), cell cycle progression (middle) (percentages in S phase) and cell viability (bottom) (percentages of annexin V<sup>+</sup>7-AAD<sup>+</sup> cells) were measured. **b**, Number of viable *Ifitm3*<sup>+/+</sup> and *Ifitm3*<sup>-/-</sup> pre-B cells were counted

at the times indicated. **c**, Levels of AKT phosphorylated at S473 (AKT-pS473), AKT, MYC, p53, p21 and BCL2 were assessed in *Ifitm3*<sup>+/+</sup> and *Ifitm3*<sup>-/-</sup> pre-B cells. **d**, Splenic B cells from *Ifitm3*<sup>+/+</sup> and *Ifitm3*<sup>-/-</sup> mice ( $n = 5$ ) were analysed for CD21<sup>high</sup>CD23<sup>low</sup> or CD21<sup>high</sup>CD23<sup>-</sup> marginal-zone B cells (MZB), peritoneal-cavity B cells for MAC1<sup>+</sup>IgM<sup>+</sup> B1 cells and CD5<sup>+</sup>IgM<sup>+</sup> B1a cells. **e**, Splenic B cells from *Ifitm3*<sup>+/+</sup> and *Ifitm3*<sup>-/-</sup> mice were adoptively transferred to  $\mu$ MT recipient mice ( $n = 10$ ) followed by immunization with 0.5 mg of NP-KLH or vehicle. Spleens were collected on day 12 after immunization and subjected to immunofluorescence staining of tissue sections with B220, CD3 and peanut agglutinin (PNA). Scale bar, 500  $\mu$ m. **f–h**, Splenocytes collected from  $\mu$ MT mice ( $n = 10$ ) were analysed by flow cytometry 12 days after immunization for CD95, GL7 and NP to identify NP-specific germinal-centre B cells. Relative fractions (**f**), absolute numbers (**g**) and representative flow cytometry plots (**h**) are shown. **i**, Levels of serum immunoglobulin isotypes in  $\mu$ MT recipient mice transplanted with *Ifitm3*<sup>+/+</sup> or *Ifitm3*<sup>-/-</sup> B cells are shown before and after immunization ( $n = 10$ ; day 12). Serum levels of IgM, IgG1 and IgG2b were determined by enzyme-linked immunosorbent assay (ELISA). For gel source data for **a–c**, see Supplementary Fig. 1. In **b, f, g, i**, mean  $\pm$  s.d. indicated; significance determined by two-tailed *t*-test.

[Source data](#)

[Full size image](#)

## Role of *Ifitm3* in oncogenic signalling

To elucidate a potential contribution of *Ifitm3* to oncogenic signalling, we studied the transformation of *Ifitm3*<sup>+/+</sup> and *Ifitm3*<sup>-/-</sup> pre-B cells by *BCR-ABL1* and *NRAS<sup>G12D</sup>* (Fig. 2a, b). As in normal B cells, *Ifitm3*<sup>-/-</sup> leukaemia cells in a mouse model of B-ALL (*Ifitm3*<sup>-/-</sup> B-ALL cells) showed multiple defects in survival and proliferation, and a markedly reduced ability to form colonies in semi-solid methylcellulose (Fig. 2b, c). Consistent with a 70-fold reduction of the frequency of leukaemia-initiating cells ( $P = 3.7 \times 10^{-7}$ ), *Ifitm3*<sup>-/-</sup> B-ALL cells did not initiate overt leukaemia in immunodeficient transplant recipient mice (Fig. 2d, e). Similar to B-ALL cells, deletion of *IFITM3* in mantle cell lymphoma (MCL) cells reduced competitive fitness and proliferation (Fig. 2f). Both mouse *Ifitm3*<sup>-/-</sup> B cells and human *IFITM3*-deficient MCL cells showed defective Ca<sup>2+</sup> release in response to BCR engagement, and partially lost CD19 surface expression (Extended Data Fig. 2c, d). In addition, BCR engagement in *IFITM3*<sup>-/-</sup> MCL cells did not induce processive signal amplification between CD19 and LYN<sup>17</sup>, as CD19 was not phosphorylated and did not interact with LYN. *IFITM3*-deficient MCL cells

expressed lower levels of LYN and did not activate SRC kinases in response to BCR engagement (Extended Data Fig. [2e](#)). RNA-sequencing gene-expression studies revealed upregulation of *Ifitm1* in *Ifitm3*<sup>-/-</sup> B-ALL cells, presumably to compensate for loss of *Ifitm3*. Gene set enrichment analyses showed that *Ifitm3* deficiency was associated with reduced expression of components of the BCR signalling pathway and a phenotype reminiscent of B cell anergy (Extended Data Fig. [3a–c](#)).

**Fig. 2: Essential role of IFITM3 in oncogenic signalling and B cell transformation.**

 **figure2**

**a**, CD19 surface expression (top), cell cycle progression (middle) (percentages in S phase) and cell viability (bottom) (percentages of annexin V<sup>+</sup>7-AAD<sup>+</sup> cells) were measured. **b, c**, *Ifitm3*<sup>+/+</sup> and *Ifitm3*<sup>-/-</sup> B-ALL cells transformed with human *BCR-ABL1* or *NRAS*<sup>G12D</sup> were assayed for levels of AKT-pS473, AKT, MYC, p53, p21 and BCL2 ( $n = 3$ ) (**b**) and plated in semi-solid methylcellulose (**c**). Scale bars, 7 mm

**(c**, top row), 2.5 mm (**c**, bottom row). **d**, Kaplan–Meier analyses of NOD-SCID-gamma (NSG) recipient mice injected with the indicated numbers of *Ifitm3*<sup>+/+</sup> and *Ifitm3*<sup>-/-</sup> *BCR-ABL1* (left) or *NRAS*<sup>G12D</sup> (right) B-ALL cells ( $n = 5$ ). **e**, Frequencies of leukaemia-initiating cells (LIC) estimated with extreme limiting dilution analysis (ELDA) (90% confidence interval; likelihood ratio test). **f**, Jeko1 MCL cells expressing doxycycline (Dox)-inducible Cas9 were transduced with *IFITM3*-targeting or non-targeting (NT) single-guide RNAs. Enrichment or depletion of targeted cells (Cas9<sup>+</sup>gRNA<sup>+</sup>) was monitored by flow cytometry upon treatment with doxycycline (mean  $\pm$  s.d.), and IFITM3 levels were measured by western blot. **g**, Premalignant LSL-*Bcr*<sup>BCR-ABL1</sup> × *Mb1-cre* pre-B cells expressing IFITM3, IFITM3(Y20E) or empty vector (EV) were plated for colony-forming assays (7 days). Representative images shown at 1× (top) and 10× (bottom) magnification. **h**, Survival analyses ( $P = 0.0001$ , log-rank test) of congenic recipient mice transplanted with LSL-*Bcr*<sup>BCR-ABL1</sup> × *Mb1-cre* B cells transduced with empty vector, IFITM3 or IFITM3(Y20E) ( $n = 7$ ). **i**, The engraftment and expansion of luciferase-labelled leukaemia cells were monitored by luciferase bioimaging at the times indicated. **j**, Effects of IFITM3 or IFITM3(Y20E) on oncogenic signalling in LSL-*Bcr*<sup>BCR-ABL1</sup> × *Mb1-cre* B cell precursors measured by western blot and compared to empty vector. Phosphorylation of CD19 at Y531 (CD19-pY531), of SRC at Y416 (SRC-pY416) and AKT at S473 were examined. Gel source data for **a–c**, **f**, **g**, **j** are shown in Supplementary Fig. 1. In **c**, **g**, two-tailed *t*-test.

[Source data](#)

[Full size image](#)

## Effect of phosphorylation of IFITM3 at Y20

Combinations of surface and intracellular staining revealed the cytoplasmic localization of the N terminus of IFITM3, with a short extracellular portion of the C terminus (Extended Data Fig. 3d). Previous studies have shown that phosphorylation of IFITM3 at Y20 prevents both endocytosis and degradation<sup>6,7</sup>. Phosphomimetic IFITM3(Y20E) was constitutively localized at the cell surface. Similarly, phosphorylation by BCR–ABL1 induced the accumulation of IFITM3 at the cell membrane, in a process that was sensitive to inhibition of BCR–ABL1 or SRC kinases (Extended Data Fig. 3e). Therefore, the phosphorylation of Y20 induces a dynamic switch from antiviral functions in endosomes to BCR or oncogene signalling at the cell surface (Extended Data Fig. 3e,f). To test whether phosphorylation of IFITM3 at Y20 and constitutive membrane localization are sufficient to enable oncogenic signalling, we overexpressed wild-type and

IFITM3(Y20E) in premalignant B cells carrying a *BCR-ABL1*-knock-in allele, which did not readily give rise to leukaemia<sup>20</sup>. Expression of IFITM3(Y20E) increased the ability of pre-B cells to form colonies by 129-fold ( $P = 2.1 \times 10^{-8}$ ) (Fig. 2g), induced oncogenic signalling and initiated fatal leukaemia in congenic transplant recipient mice (Fig. 2h–j). To elucidate how membrane-bound IFITM3(Y20E) promotes malignant transformation, we performed phosphoproteomic analyses of IFITM3 Y20 signalling in patient-derived B-ALL cells. Consistent with processive signal amplification<sup>17</sup>, engagement of IFITM3 induced phosphorylation of CD19 on multiple residues—including Y531, which mediates PI3K activation. In addition, Y20 of IFITM3 engaged multiple components of the BCR and integrin receptor signalling pathways (Fig. 3a, Extended Data Fig. 4a), which converge with CD19 at the level of PI3K activation. A comprehensive analysis of phosphosites showed a significant enrichment of phosphorylation in the PI3K, BCR and integrin receptor pathways, which we confirmed for SRC, CD19 and PI3K signalling by western blot (Fig. 3a–c). IFITM3(Y20E) required crosslinking by a full antibody, as the engagement of Y20 of monomeric IFITM3 using F(ab) fragments did not elicit PI3K activation (Extended Data Fig. 4b). Because PI3K signalling in mouse B-ALL cells increased *Ifitm3* mRNA levels by 10-fold and protein levels by more than 50-fold, these observations suggest a feed-forward loop of signal amplification between IFITM3 and PI3K signalling (Extended Data Fig. 1b–e). Comparable to effects on BCR signalling and CD19 surface expression in B cells, genetic deletion of *IFITM3* in human Jurkat T cells compromised T cell receptor signalling and CD3 surface expression (Extended Data Fig. 4c), which suggests that IFITM3 may have a similar role in T cells.

**Fig. 3: IFITM3 links components of the BCR and integrin receptor pathways to PI3K signalling.**

 **figure3**

**a**, Levels of proteins phosphorylated at the indicated residues in PDX2 B-ALL cells transduced with HA-tagged IFITM3(Y20E) or empty vector (EV) control were identified by mass spectrometry upon IFITM3 crosslinking with anti-HA antibodies. **b**, Feature set enrichment analysis (FSEA) for phosphorylated proteins in the BCR (red), integrin (blue) and PI3K (grey) pathways, ranked by  $\log_2$ -transformed fold change (Kolmogorov–Smirnov). **c**, Levels of SRC-pY416, LYN, CD19-pY531, CD19, AKT-pS473 and AKT assessed in ICN12 cells expressing IFITM3–HA, IFITM3(Y20E)–HA or HA-tagged empty vector upon IFITM3 crosslinking. **d, e**, Interactomes of BirA–IFITM3(Y20E) or empty vector control expressed in PDX2 B-ALL (**d**) and Jeko1 MCL (**e**) cells. **f, g**, Validation of IFITM3-interacting proteins

by anti-Flag co-immunoprecipitation (IP) in PDX2 cells transduced with Flag–IFITM3 or Flag-tagged empty vector, followed by western blotting for validation of interacting proteins, and STAT5 and eIF4E as specificity controls. WCL, whole-cell lysates. **h, i**, Proximity ligation assay (PLA) in Jeko1 cells upon BCR stimulation, assessed for proximity of CD79B to IFITM3. Representative images with PLA signal (red), nuclei (DAPI) and plasma membrane (WGA) (green). Scale bars, 5 μm (**i**). **j**, Quantification of PLA signals per cell (two-tailed *t*-test). **j**, Structural model of IFITM3-mediated signal amplification between CD19 and LYN. In resting B cells (left), IFITM3 is localized in endosomes. Upon antigen encounter (right), LYN-mediated phosphorylation of IFITM3 induces membrane translocation, acting as a scaffold for CD19 and LYN in proximity to BCR molecules. BCR–CD19–IFITM3 complexes form clusters for PI3K activation and accumulation of PIP3 in lipid rafts. In **a–i**, *n* = 3. For gel source data, see Supplementary Fig. 1. In **a, d, e**, row-scaled protein abundance ranked by fold change; key proteins of interest are highlighted.

[Source data](#)

[Full size image](#)

## IFITM3 enables CD19–PI3K signalling

By enriching for cell-surface proteins using N-linked glycosylation-site biotin labelling, we identified 65 surface receptors—most of which were associated with lipid rafts—that were downregulated in *Ifitm3*<sup>−/−</sup> B-ALL cells, including CD19, BCR-associated and adhesion receptors. Only five surface proteins were upregulated—including the IFITM family member IFITM2, which suggests a possible compensation mechanism (Extended Data Fig. 4d). We performed validation by flow cytometry for 17 surface receptors for IFITM3 loss-of-function (*Ifitm3*<sup>−/−</sup>) and gain-of-function (IFITM3(Y20E)) (Extended Data Fig. 4e–g). Continuous forced expression of CD19 (for more than one week) in *Ifitm3*<sup>−/−</sup> B cells partially restored defective survival and proliferation, which required the PI3K-activation motif Y531 of CD19 (ref. 21) (Extended Data Fig. 5a–e). However, inducible translocation of CD19 to the cell membrane did not restore any defects in *Ifitm3*<sup>−/−</sup> B cells, which suggests that IFITM3 is still required to integrate CD19 into signalling complexes for SRC kinase and PI3K signalling (Extended Data Fig. 5f–h). To study complexes that interact with IFITM3, we performed enzyme-catalysed proximity labelling studies on the basis of N-terminal fusions of the BirA biotin ligase with IFITM3(Y20E) carrying an extracellular haemagglutinin (HA) tag in B-ALL and IgM<sup>+</sup> MCL cells. After engagement with IFITM3 (anti-HA) or BCR (anti-IgM),

IFITM3-interacting proteins were biotinylated on the basis of their proximity to the cytoplasmic BirA moiety, collected using streptavidin-coated beads and identified by mass spectrometry. Consistent with phosphoproteomic analyses (Fig. 3a), and across different cell types (B-ALL and MCL) and stimulations (anti-HA and anti-IgM), IFITM3-interacting proteins included BCR, integrin receptor and PI3K signalling elements (Fig. 3d,e, Extended Data Fig. 6a–d). We transduced MCL cells with Flag-IFITM3 for validation by co-immunoprecipitation and western blotting (Fig. 3f,g). Using proximity ligation assays, we confirmed the inducible formation of a complex between IFITM3 and the BCR signalling chain CD79B upon engagement of the BCR. Interactions between BCR and IFITM3 were induced within minutes and dissociated after 30 min (Fig. 3h,i). Consistent with endosomal BCR functions<sup>22</sup>, interactions between BCR and IFITM3 occasionally colocalized with LAMP1<sup>+</sup> endosomal compartments (Extended Data Fig. 6e). Therefore, BCR-mediated activation of SRC-mediated phosphorylation of Y20 of IFITM3 induces the accumulation of IFITM3 at the plasma membrane, where IFITM3 functions as a scaffold for CD19 and LYN in proximity to BCR molecules to enable processive signal amplification (Fig. 3j). In resting B cells, IgM BCRs are excluded from lipid rafts and recruited upon encounters with antigen<sup>23</sup>. By contrast, IgD BCRs are already in close proximity to CD19 within lipid rafts in resting B cells, which suggests that IFITM3 may specifically enable IgM BCRs.

## IFITM3-PIP3 binding is needed to form lipid rafts

Reduced expression of integrins and adhesion receptors was associated with decreased homotypic adhesion of *Ifitm3*<sup>-/-</sup> pre-B cells, whereas membrane-bound IFITM3(Y20E) triggered the formation of large clusters (Extended Data Fig. 7). Because IKZF1 negatively regulates adhesion<sup>24,25</sup>, we examined whether this regulation is mediated by transcriptional repression of *Ifitm3*<sup>16</sup>. Overexpression of a dominant-negative IKZF1-mutant (termed IK6) markedly increased colony formation, adhesion to stroma and surface expression of adhesion receptors in the presence—but not in the absence—of IFITM3. Although dominant-negative inhibition of IKZF1 relieved transcriptional repression of adhesion receptors, the normal expression and function of these receptors at the cell surface still required IFITM3 and its ability to link integrins and adhesion receptors to the PI3K pathway. Loss of IFITM3, and reduced activity of the SRC kinase LYN and CD19-PI3K signalling, could broadly affect lipid rafts and short-circuit BCR signalling. Consistent with this scenario, the lipid-raft components cholesterol and ganglioside GM1 were markedly reduced in *Ifitm3*<sup>-/-</sup> B cells (Fig. 4a). In addition, BCR engagement increased membrane rigidity in *IFITM3*<sup>+/+</sup> MCL cells. However, membrane stiffening in response to BCR engagement was significantly reduced in

*IFITM3*<sup>-/-</sup> MCL cells (Extended Data Fig. 8a). Consistent with defects in PI3K signalling, the ratios of PIP3 to the PI3K substrate PIP2 were reduced substantially in mouse *Ifitm3*<sup>-/-</sup> B cells and patient-derived *IFITM3*<sup>-/-</sup> B-ALL cells. By contrast, overexpression of IFITM3 and IFITM3(Y20E) increased PIP3:PIP2 ratios by about 3-fold and 5.5-fold, respectively (Fig. 4b,c). To elucidate how IFITM3 interacts with plasma membrane lipids, we probed 15 distinct lipid classes for binding to IFITM3 in vitro. IFITM3 bound selectively to PIP3, but not to any of the other 14 lipids (Fig. 4d). Because IFITM3 function is required to retain normal PIP3 levels, we tested whether exogenous delivery of PIP3 could rescue *Ifitm3* deficiency in mice. Insertion of exogenous PIP3 into the cell membrane partially restored AKT and MYC activation and colony formation, but not CD19 and SRC phosphorylation or surface expression of lipid-raft-associated receptors (Extended Data Fig. 8b-d). Therefore, IFITM3 promotes PI3K signalling not only by increasing the amount of PIP3 but also by integrating PIP3 into signalling complexes in lipid rafts.

**Fig. 4: Structural basis of IFITM3-mediated regulation of PIP3 signalling from lipid rafts.**

 **figure4**

**a**, Ganglioside GM1 and cholesterol (stained with filipin III) levels measured in *Ifitm3*<sup>+/+</sup> and *Ifitm3*<sup>-/-</sup> pre-B (top) and B-ALL (bottom) cells. **b, c**, Ratios of PIP3 and PIP2 were measured in *Ifitm3*<sup>+/+</sup> and *Ifitm3*<sup>-/-</sup> mouse (**b**, left), and human B-

ALL cells (PDX2) (**b**, right), and upon expression of empty vector, IFITM3 or IFITM3(Y20E) (**c**). **d**, In vitro lipid-binding assays for glutathione-S-transferase-tagged IFITM3 (GST–IFITM3) and 15 lipid classes. Recombinant GST tag was used as baseline. **e**, Lipid-binding assays were performed for biotin–IFITM3 N terminus (amino acids 1–57), the first intramembrane  $\alpha$ -helix (IM- $\alpha$ ) (amino acids 58–70), conserved intracellular loop (CIL) (amino acids 71–105) and transmembrane  $\alpha$ -helix (TM- $\alpha$ ) (amino acids 89–105). **f**, Lipid-binding assays to study interactions of PIP3 with biotinylated fragments of the IFITM3 conserved intracellular loop that carry mutations of basic residues. **g–i**, PIP3 binding to K83 and K104, and to R85, R87 and K88, basic residue patches (**g**). Dashed lines indicate PIP3 contacts within 3.5 Å. **h**, Interaction energies of PIP3 with basic residues K83 or R85 averaged over molecular dynamics simulation trajectories (median levels indicated by red dotted line) (Methods). **i**, Binding affinity for PIP3 as shown as a heat map of contact frequencies between PIP3 and each residue. **j–l**, Levels of AKT-pS473, AKT, S6K phosphorylated at T389 (S6K-pT389), S6K phosphorylated at T421 and S424 (S6K-pT421/S424), CD19-pY531, CD19, SRC-pY416, LYN, PAK1 and PAK3 phosphorylated at S199 and S204 (PAK1/3-pS199/204), PAK2 phosphorylated at S192 and S197 (PAK2-pS192/197), PAK1, FAK phosphorylated at Y397 (FAK-pY397), FAK phosphorylated at Y576 and Y577 (FAK-pY576/577), FAK, CXCR4 phosphorylated at S339 (CXCR4-pS339), CXCR4 and integrin- $\beta$ 1 in PDX2 cells expressing empty vector, IFITM3–HA, IFITM3(Y20E)–HA, and the R85A, K83A, R85A/R87A/K88A and K83A/K104A mutants of IFITM3, upon IFITM3 crosslinking with anti-HA antibodies. In **a–f, j–l**,  $n = 3$ , For gel source data, see Supplementary Fig. 1. In **b, c, e, h**, two-tailed *t*-test.

[Source data](#)

[Full size image](#)

## Structural basis of IFITM3 binding to PIP3

Proteins that contain a cluster of four or more basic residues located at the membrane–solution interface can laterally sequester PIP3, which does not require a PH domain or any other specific structure<sup>26</sup>. To map PIP3 binding to specific portions of IFITM3, we repeated lipid-binding assays with biotin-tagged fragments, including the N terminus, the first intramembrane  $\alpha$ -helix and the conserved intracellular loop. PIP3 binding was detected only for the conserved intracellular loop (Fig. 4e), which contains five basic residues that are in close proximity in sequence and that spatially cluster into two distinct basic patches. To address why IFITM3 preferentially binds to PIP3 over PIP2, we performed multi-scale molecular dynamics simulations of IFITM3 in multi-component lipid bilayers that mimic the

plasma membrane. All-atom molecular dynamics simulations revealed that the representative binding pose of PIP2 from its most populated conformation cluster showed a charge interaction with one single basic residue (R85) ( $-213 \text{ kJ mol}^{-1}$ ), which was energetically weaker than the two charge interactions with PIP3 at K83 and K104 ( $-704 \text{ kJ mol}^{-1}$ ) ( $P = 0.0008$ ). Two-residue contacts were rare for PIP2 and more common for PIP3 ( $P = 0.011$ ) (Extended Data Fig. 9). To experimentally test the predicted function of the basic residues of the conserved intracellular loop, we performed PIP3 binding assays for biotinylated fragments of the IFITM3 conserved intracellular loop that carried mutations of these residues. The R85A and R85A/R87A/K88A mutants largely retained the ability to bind PIP3, which was abrogated for the K83A/K104A mutant (Fig. 4f). To understand the structural basis of this difference, we modelled the interaction of PIP3 with each of the mutants of the basic residues (K83A/K104A, R85A/R87A/K88A and R85A/R87A) using all-atom molecular dynamics simulations. PIP3 shows an interaction energy that is three times stronger with K83 and K104 than with R85, R87 and K88 (Fig. 4g-i). PIP3 makes dual-pronged salt-bridge interactions with K83 and K104, whereas it interacts only with R85 and not with R87 and K88 in the other basic patch. The R87 and K88 residues form intra-protein salt bridges with D92 and D86, respectively, and are not available for interaction with PIP3.

## IFITM3 amplifies PI3K, integrin and BCR signalling

To experimentally validate this model, we globally identified changes in signal transduction that depend on K83 and R85 residues in human B-ALL and MCL B cells. The most prominent differences were enrichments for phosphorylation sites associated with PI3K, BCR and adhesion receptor signalling (Extended Data Fig. 10a,b). Although most phosphorylation events induced by membrane-bound IFITM3(Y20E) were lost upon mutation of K83, this was not the case for substitution of the R85 residue (Extended Data Fig. 10c,d). Proximity ligation assays revealed IFITM3-dependent recruitment of multiple proteins in the PI3K, BCR and integrin signalling pathways. However, almost all of these interactions were lost upon mutation of K83 (Extended Data Fig. 10e-h). Biochemical studies revealed that crosslinking of IFITM3(Y20E) resulted in massive activation of PI3K and integrin receptor pathways, whereas CD19 and SRC were constitutively phosphorylated in the presence of IFITM3(Y20E) (Fig. 4j-l). The R85A mutation had only minor effects, whereas the substitution of K83 almost entirely abolished IFITM3-dependent signal transduction. In contrast to the triple-mutant IFITM3(R85A/R87A/K88A), the IFITM3(K83A/K104A) double mutant lost all activity in PI3K, BCR and adhesion receptor pathways (Fig. 4j-l).

In summary, we have revealed a function for IFITM3 as a PIP3 scaffold in the amplification of PI3K signalling. In *Ifitm3*<sup>-/-</sup> B cells, lipid rafts were depleted of PIP3, which resulted in marked defects in lipid-raft-associated BCR and integrin receptor signalling. IFITM3-dependent amplification of PI3K signalling, acting—in part—downstream of the BCR and adhesion receptors, is critical for the rapid expansion of B cells with high affinity to antigen. In addition, multiple oncogenes depend on IFITM3 to assemble PIP3-dependent signalling complexes and amplify PI3K signalling for malignant transformation.

## Methods

No statistical methods were used to predetermine sample size. The experiments were not randomized and investigators were not blinded to allocation during experiments and outcome assessment.

### Analysis of patient gene expression and outcome data

Gene expression microarray data from three large cohorts of patients with pre-B ALL were downloaded from GSE5314<sup>27</sup> (the Eastern Cooperative Oncology Group (ECOG) Clinical Trial E2993), GSE11877<sup>28</sup> (the Children's Oncology Group (COG) Clinical Trial P9906), St. Jude Research Hospital paediatric ALL<sup>29</sup> (<http://www.stjuderesearch.org/site/data/ALL3/>). In ECOG E2993, pretreatment bone marrow or peripheral blood samples were obtained at diagnosis before any treatment from 83 patients with Ph<sup>+</sup> B-ALL enrolled in the Medical Research Council (MRC) UKALLXII/Eastern Cooperative Oncology Group (ECOG) E2993 phase III trial. In data set from St. Jude childhood, 15 cases of Ph<sup>+</sup> B-ALL were selected from the original 327 diagnostic bone marrow aspirates. Minimal residual disease (MRD) data were available for patients with paediatric high-risk B-ALL (COG P9906). *IFITM3* expression levels were measured in patients with either a MRD positive (MRD<sup>+</sup>) status or a MRD negative (MRD<sup>-</sup>) status. In COG P9906 clinical outcome, expression profiles were obtained in pretreatment leukaemic samples from 207 uniformly treated children with high-risk ALL<sup>30</sup>, a risk category largely defined by pretreatment clinical characteristics. Patients had MRD tested by flow cytometry with two combinations (CD20/CD10/CD45 or CD9/CD19/CD34/CD45), and were defined as MRD positive or MRD negative at the end of induction therapy (day 29) using a threshold of 0.01% as previously described<sup>31</sup>. Then, RNA was purified from 207 pretreatment diagnostic samples with more than 80% blasts (131 bone marrow, 76 peripheral blood) and subjected to microarrays. Log-rank test was used to assess statistical significance.

## Primary human samples and cell lines

Patient samples (Supplementary Table 2) were sourced ethically from patients who gave informed consent, and were in compliance with the internal review boards of the Beckman Research Institute of City of Hope. We have complied with all relevant ethical regulations. Patient samples were harvested from biopsy of bone marrow from patients with ALL at the time of diagnosis or relapse. All samples were transplanted into sublethally irradiated NOD.Cg-*Prkdc*<sup>scid</sup> *Il2rg*<sup>tm1Wjl</sup>/SzJ mice (NSG mice, The Jackson Laboratory) through tail-vein injection. After samples were collected, patient-derived primary human pre-B ALL xenografts were cultured on OP9 stroma in Alpha Minimum Essential Medium (MEMα; Life Technologies) with GlutaMAX containing 20% fetal bovine serum (FBS), 100 IU ml<sup>-1</sup> penicillin, 100 µg ml<sup>-1</sup> streptomycin and 1 mM sodium pyruvate. The human cell lines (Supplementary Table 8) were cultured in RPMI-1640 (GIBCO) with GlutaMAX containing 20%FBS, 100 IU ml<sup>-1</sup> penicillin, 100 µg ml<sup>-1</sup> streptomycin at 37 °C in a humidified incubator with 5% CO<sub>2</sub>. All human primary samples and cell lines were tested negative for mycoplasma by detection kit (MycoAlert PLUS, LONZA).

## Genetic mouse models

Genetic mouse models used in this study are listed in Supplementary Table 9. NOD.Cg-*Prkdc*<sup>scid</sup> *Il2rg*<sup>tm1Wjl</sup>/SzJ (NSG) mice were purchased from Jackson Laboratory. *Ifitm3*<sup>tm1Masu</sup> (ref. 32) mice were backcrossed to the C57BL/6J background for more than eight generations. B6.C(Cg)-*Cd79a*<sup>tm1(cre)Reth</sup>/EhobJ (Mb1-Cre) mice were purchased from Jackson Laboratory. B6.129S2-*Ighm*<sup>tm1Cgn</sup>/J (μMT) mice were purchased from Jackson Laboratory. C129S4-*Pten*<sup>tm1Hwu</sup>/J (*Pten*<sup>fl/fl</sup>) mice were purchased from Jackson Laboratory. For mice bred in-house, littermates of the same sex were randomized to experimental groups. For the in vivo leukaemia initiation assay, 8- to 10-week-old female NSG mice were randomly allocated before injection. To generate a model for pre-leukaemic B cell precursors expressing BCR-ABL1, LSL-*Bcr*<sup>+/BCR-ABL1</sup> mice<sup>33</sup> were crossed with *Mb1-cre* strain (*Mb1-cre* × LSL-*Bcr*<sup>+/BCR-ABL1</sup>) for excision of a stop-cassette in early pre-B cells. For in vivo oncogenic priming assay with *Mb1-cre* × LSL-*Bcr*<sup>+/BCR-ABL1</sup> B cell precursors, 8- to 10-week-old female NSG mice were randomly allocated before injection. Temperatures of 18–23 °C with 40–60% humidity were maintained with 14-h light/10-h dark cycle. The following scores were considered as end-point: (1) a failure to eat food or drink water for 24 h; (2) a failure to make normal postural adjustments or to display normal behaviour; and (3) when tumour burden reached 1.5 cm × 1.5 cm × 1.5 cm (tumour ulceration was not expected). If a mouse lost 25% of its initial body weight (or reached 16 g of body weight, regardless of the

initial weight), or if we observed a weight loss of 15% on 2 sequential weight measurements, we euthanized the mouse immediately. All mouse experiments were subject to institutional approval by the Beckman Research Institute of City of Hope Animal Care and Use Committee.

## Mouse primary and leukaemia cells

Bone marrow cells from 6–10-week-old mice were collected by flushing cavities of the femur and tibia with chilled PBS, followed by filtering through 40- $\mu\text{m}$  strainer to yield a single-cell suspension. Spleen or thymus cells were directly extracted by forcing tissues through a 40- $\mu\text{m}$  strainer into chilled PBS. Filtered cells were further incubated with lysis buffer (RBC Lysis Buffer, BioLegend) to lyse erythrocytes. After washing with PBS, cells were subjected to further experiments. For IL-7-dependent pre-B cell culture, bone marrow cells were collected and cultured in Iscove's modified Dulbecco's medium (IMDM) (GIBCO) with GlutaMAX containing 20% FBS, 50  $\mu\text{M}$  2-mercaptoethanol, 100 IU  $\text{ml}^{-1}$  penicillin, 100  $\mu\text{g}$   $\text{ml}^{-1}$  streptomycin in the presence of 10 ng  $\text{ml}^{-1}$  recombinant mouse IL-7 (Peprotech). For the *BCR-ABL1* leukaemia model, pre-B cells were retrovirally transformed with *BCR-ABL1* and then IL-7 was removed to select the transduced cells. *Nras*<sup>G12D</sup> ALL cells were selected with puromycin (GIBCO) and were maintained with IL-7-supplemented IMDM.

## Retroviral and lentiviral transduction

Retroviral supernatant was generated by cotransfection of HEK 293FT cells with retroviral constructs together with pHIT60 (gag-pol) and pHIT123 (for mouse) or pHIT456 (for human ecotropic envelope) using Lipofectamine 2000 (Invitrogen). Lentiviral supernatant for CRISPR-mediated gene editing was produced by cotransfection of HEK 293FT cells with lentiviral constructs together with pCDNL/BH and EM140. Transfected HEK 293FT cells were cultured in high-glucose Dulbecco's modified Eagle's medium (DMEM) (GIBCO) with GlutaMAX containing 10% fetal bovine serum, 100 IU  $\text{ml}^{-1}$  penicillin, 100  $\mu\text{g}$   $\text{ml}^{-1}$  streptomycin, 25 mmol  $\text{l}^{-1}$  HEPES, 1 mmol  $\text{l}^{-1}$  sodium pyruvate and 0.1 mmol  $\text{l}^{-1}$  non-essential amino acids for 16 h. After sodium butyrate (10 mM) induction for 8 h, the virus supernatant was collected and filtered through a 0.45- $\mu\text{m}$  filter. The virus-containing supernatants were loaded by centrifugation (2,000*g*, 90 min at 32 °C) on 50  $\mu\text{g}$   $\text{ml}^{-1}$  retronectin (Takara)-coated non-tissue culture 6-well plates. For retroviral transduction, 3–5 × 10<sup>6</sup> cells were transduced per well by centrifugation at 600*g* for 30 min in the appropriate culture medium and maintained at 37 °C at 5% CO<sub>2</sub> for 48 h. For lentiviral transduction, 3–5 × 10<sup>6</sup> cells per well were centrifuged

at 600g for 30 min in the presence of lentiviral supernatant and maintained at 37 °C at 5% CO<sub>2</sub>. The lentiviral supernatant was replaced with fresh medium the next day.

## Western blotting

PBS-washed cells were lysed in CelLytic buffer (Sigma-Aldrich) supplemented with 1% protease inhibitor cocktail (Roche Diagnostics), 1% phosphatase inhibitor cocktail (EMD Millipore) and 1 mM PMSF on ice. A total of 10 µg of cell lysates was separated on mini-precast gels (Bio-Rad) and transferred onto nitrocellulose membranes (Bio-Rad). Membranes were probed with the appropriate primary antibodies. Membranes were then incubated with alkaline-phosphatase conjugated secondary antibodies (Invitrogen) and chemiluminescent substrate (Invitrogen) and were further detected by film exposure, UVP BioSpectrum 810 Imaging System (Thermo Fisher Scientific) or by using the ChemiDoc MP Imaging System (BioRad). Antibodies used in this study are provided in Supplementary Table 10, and were used at 1:750 to 1:1,000 dilution in blocking buffer.

## Flow cytometry

PBS-washed cells were blocked with Fc blocker for 10 min on ice and then stained with the appropriate antibodies listed in Supplementary Table 10, or with isotype control, for 25 min on ice. Cells were then washed and resuspended in chilled PBS containing 0.75 µg ml<sup>-1</sup> of DAPI to exclude dead cells. Acquisition was performed by LSRII flow cytometer (BD Biosciences) with BD FACSDIVA software. The fluorescence-based cell sorting was performed by FACSAria II (BD Biosciences) with BD FACSDIVA software. FACS data were analysed with FlowJo software (FlowJo). For apoptosis analyses, annexin V and 7-AAD (BD Biosciences) were used. For cell cycle analysis, the BrdU flow cytometry kit (BD Biosciences) was used according to manufacturer's instructions. For intracellular staining of cytoplasmic proteins, cells were first stained for cell surface antigens and subsequently fixed in fixation and permeabilization solution (BD Biosciences) containing 4% paraformaldehyde and the detergent saponin. Cells were then washed and resuspended in Perm/Wash Buffer (BD Biosciences) and stained with the appropriate antibodies. For statistical quantification, data were plotted with GraphPad Prism 7 or SigmaPlot. FACS antibodies, listed in Supplementary Table 10, were pre-diluted 1:5–1:10. Two µl of diluted antibody was added to 1–2 million cells per 50 µl in PBS for final dilution of 1:50 for human cells or 1:200 for mouse cells.

## Pharmacological inhibitors and reagents

Imatinib was purchased from LC Laboratories. Stock solutions were prepared in sterile water at 10 mmol l<sup>-1</sup> and administered at 10 µmol l<sup>-1</sup>. Dasatinib was purchased from SelleckChem. Stock solutions were prepared in sterile DMSO at 25 µmol l<sup>-1</sup> and administered at 25 nmol l<sup>-1</sup> (Supplementary Table 11).

## Analysis of chromatin immunoprecipitation with sequencing data

IKZF1 chromatin immunoprecipitation with sequencing (ChIP-seq) was performed as previously described<sup>34</sup> with a patient-derived human B-ALL xenograft cell line (LAX2), which expresses wild-type full-length IKZF1 and no detectable level of the dominant-negative IKZF1 isoform. ChIP-seq tracks (GSE58825) for the IKZF1 antibody in LAX2 on *IFITM3* gene promoter regions are shown in the bottom of Extended Data Fig. 1m. The y axis represents the normalized number of reads per million reads for peak summit for each track. ChIP-seq tracks (GSE86897) for the enrichment of RNAPII and H3K4me3 at the *Ifitm3* locus in pre-B cells from *Ikzf1*<sup>exon5fl/fl</sup> mice upon Cre-mediated deletion of *Ikzf1* are shown in the top of Extended Data Fig. 1m. The ChIP-seq peaks were called by the MACS peak-caller by comparing read density in the ChIP experiment relative to the input chromatin control reads, and are shown as bars under each wiggle track. Gene models are shown in UCSC genome browser hg19. Integrative Genomics Viewer (IGV) was used to visualize ChIP-seq tracks.

## Inducible expression of IKZF1

Human Philadelphia chromosome-positive (*Ph*<sup>+</sup>) pre-B ALL cells (BV173) carrying deletions of *IKZF1* were transduced with pRetroX-Tet3G-Neo. Neomycin-resistant cells were transduced with pRetroX-TRE3G-wild-type IKZF1-Puro. Expression of wild-type IKZF1 in puromycin-resistant cells was initiated by treatment with 1 µg ml<sup>-1</sup> of doxycycline (TetOn).

## Inducible reconstitution of CD19

For inducible CD19 reconstitution, mouse CD19 was fused to the ligand-binding domain of a mutant oestrogen receptor (ER<sup>T2</sup>) at the C terminus of CD19. BCR-ABL1-transformed mouse B-lineage ALL cells were retrovirally transduced with MSCV CD19-ER<sup>T2</sup>-Puro. Puromycin-resistant cells were treated with 4-hydroxytamoxifen (4-OHT) (Sigma-Aldrich) or vehicle control to induce reconstitution of CD19.

## Cell viability assay

One hundred thousand BCR–ABL1-transformed mouse B-lineage ALL cells were seeded in a volume of 100 µl in medium in 1 well of a 96-well plate (BD Biosciences). Imatinib (LC Laboratories) was added at the indicated concentration in a total volume of 150 µl. After culturing for 3 days, 15 µl of resazurin (R&D) was added into each well and incubated for 4 h at 37 °C. Medium without cells was used as blank. The fluorescence was read at 535 nm and the reference wavelength was 590 nm. Relative viability was calculated using baseline values of vehicle-treated cells as a reference.

## Colony-forming assay

The methylcellulose colony-forming assays were performed with 10,000 cells. Cells were resuspended in mouse MethoCult medium (without cytokines for *BCR-ABL1*-transformed cells; with IL-7 for *NRAS<sup>G12D</sup>*-expressing cells) and cultured on 3-cm-diameter dishes, with an extra water supply dish to prevent evaporation. Colonies were imaged and counted after seven days using GelCount (Oxford Optronix), Olympus IX71 microscope and Q-Capture pro 7.

## In vitro IFITM3–HA crosslinking

Eight million patient-derived B-ALL cells per sample were resuspended into complete medium and treated with either 2.5 µg ml<sup>-1</sup> polyclonal anti-HA (Abcam) or isotype control for the indicated times. F(ab) fragments for the anti-HA antibody were generated by using the F(ab) preparation kit following the manufacturer's instructions (Thermo Fisher Scientific). F(ab) fragmentation was confirmed by Criterion TGX Stain-Free Precast Gels (Bio-Rad).

## Measurement of intracellular calcium mobilization

In Extended Data Fig. 2f, 1 million fresh splenocytes were incubated with the 4 µM Rhod-2-AM Ca<sup>2+</sup>-binding dye (Thermo Fisher Scientific) for 15 min at room temperature in dark. Cells were then resuspended in PBS and maintained at 37 °C, and Ca<sup>2+</sup> response was induced by adding 10 µg ml<sup>-1</sup> of polyclonal anti-IgM (Southern Biotech) at 50 s after acquisition of background fluorescence.

Intracellular Ca<sup>2+</sup> mobilization in response to crosslinked IgM was measured up to 300 s by flow cytometry. In Extended Data Fig. 4c, 1 × 10<sup>6</sup> viable Jurkat cells were incubated with the 4 µM Fluo4-AM Ca<sup>2+</sup>-binding dye (Thermo Fisher Scientific) for 15 min at room temperature in dark. Cells were then resuspended in PBS and maintained at 37 °C, and Ca<sup>2+</sup> response was induced by adding 10 µg ml<sup>-1</sup> of monoclonal (OKT3) purified NA/LE anti-human CD3 (Biolegend) at 50 s after

acquisition of background fluorescence. Intracellular  $\text{Ca}^{2+}$  mobilization in response to crosslinked IFITM3 was measured up to 300 s by flow cytometry. The same procedure was performed for Extended Data Fig. 6f;  $1 \times 10^6$  viable Jeko1 cells were incubated with the 4  $\mu\text{M}$  Fluo4-AM (Thermo Fisher Scientific).  $\text{Ca}^{2+}$  response was induced by adding 10  $\mu\text{g ml}^{-1}$  of polyclonal F(ab')<sub>2</sub> anti-human  $\mu$  chain (Jackson Immunoresearch).

## Homotypic aggregation assay

*Ifitm3*<sup>-/-</sup> B-ALL cells expressing C-terminal HA-tagged wild-type IFITM3, IFITM3 mutant vector (Y20E) or an empty vector were incubated with 2.5  $\mu\text{g ml}^{-1}$  of monoclonal (1D3) purified LEAF anti-mouse CD19 (Biolegend) or 2.5  $\mu\text{g ml}^{-1}$  polyclonal anti-HA (Abcam) or isotype controls at 37 °C at 5% CO<sub>2</sub>. After culturing for 24 h, homotypic aggregation was visualized using light microscopy.

## In vivo oncogenic priming assay with *Mb1-cre;LSL-Bcr*<sup>+/BCR-ABL1</sup> B cell precursors

To generate a model for pre-leukaemic B cell precursors expressing BCR–ABL1, BCR–ABL1 knock-in mice were crossed with Mb1–Cre strain (*Mb1-cre* × LSL-*Bcr*<sup>+/BCR-ABL1</sup>) for excision of a stop cassette in early pre-B cells. Bone marrow cells collected from *Mb1-cre* × LSL-*Bcr*<sup>+/BCR-ABL1</sup> mice, cultured in the presence of 10 ng  $\text{ml}^{-1}$  recombinant mouse IL-7 (Peprotech). IL-7 dependent pre-leukaemic B cells were labelled with retroviral firefly luciferase and selected by blasticidin for 7 days. After selection, cells were further transduced with MSCV-IFITM3-HA-IRES-Puro, MSCV-IFITM3<sup>Y20E</sup>-HA-IRES-Puro or empty vector and selected by puromycin for 3 days. Viable cells ( $1 \times 10^7$ ) were injected via the tail vein into sublethally irradiated (200 cGy) NSG recipient mice. In vivo expansion and leukaemia burden were monitored by luciferase bioimaging (IVIS 100 bioluminescence and optical imaging system; Xenogen) at the indicated time points. In brief, d-luciferin (Promega) dissolved in PBS was injected intraperitoneally at a dose of 2.5 mg per mouse 15 min before measuring luminescence. All mice were anaesthetized by 5% isoflurane and continued during detection of light emission with 2% isoflurane introduced through a nose cone. A mouse was euthanized when they showed signs of leukaemia burden such as a hunched back, weight loss and inability to move. Kaplan–Meier survival analysis was performed using GraphPad Prism 7 (GraphPad Software) to compare overall survival. Mantel–Cox log-rank test was used as statistical analysis using GraphPad Prism 7 (Supplementary Table 4).

## Cell adhesion assay

*Ifitm3<sup>+/+</sup>* or *Ifitm3<sup>-/-</sup>* BCR-ABL1 B-ALL cells were transduced with MSCV-IK6-IRES-GFP or MSCV-IRES-GFP as negative control. GFP<sup>+</sup> cells ( $1 \times 10^5$ ) sorted by FACS were cultured on  $1.5 \times 10^5$  OP9 stroma on a 6-well plate with IMDM-GlutaMAX containing 20% FBS, 50 µM 2-mercaptoethanol, 100 IU ml<sup>-1</sup> penicillin and 100 µg ml<sup>-1</sup> streptomycin. For calculation of the ratio of adherent cells to nonadherent cells, nonadherent cells were collected and counted with the trypan blue exclusion method using the Countess II FL Automated Cell Counter (Life Technologies). After washing the plate with PBS twice, adherent cells were detached with trypsinization and GFP<sup>+</sup> B-ALL cells and were counted with the trypan blue exclusion method using the Countess II FL Automated Cell Counter (Life Technologies) and ratios were calculated.

## Adoptive transfer of purified B cells into µMT mice

For the adoptive transfer of B cells, splenocytes from 7- to 10-week-old *Ifitm3<sup>+/+</sup>* or *Ifitm3<sup>-/-</sup>* mice were negatively selected by MojoSort Mouse Pan B Cell Isolation Kit II (Miltenyi Biotec) using immunomagnetic beads against CD3, CD4, CD8a, CD11c, CD49b, Ly6G/Ly6C (GR1) and TER119. Ten million flow-sorted splenic B cells were intravenously injected into µMT mice (B6.129S2-*Ighm<sup>tm1Cgn</sup>*/J) that lack the Cµ exon and mature B cell development as a result of defective surface IgM expression. Reconstitution of donor B cells was determined by flow cytometry 20 days after injection. Recipient µMT mice were immunized with the hapten NP coupled to a carrier protein (KLH) on day 0 and day 7, and spleens were collected on day 12.

## Immunization and immunohistology

*Ifitm3<sup>+/+</sup>* and *Ifitm3<sup>-/-</sup>* littermate mice were immunized with 0.5 mg NP-KLH (Biosearch Technologies) in alum (Sigma-Aldrich) intraperitoneally. Seven days later, mice were immunized a second time for five days. Spleens were isolated at day 12 after immunization. The spleen was embedded in optimum cutting temperature compound and 5-µm-thick cryosections were used for staining. Sections were fixed with acetone for 10 min, and nonspecific antigens were blocked in DPBS containing 2% FBS for 15 min. Sections were stained with 1:200 diluted polyclonal (RA3-6B2) anti-CD45R (B220, BD Biosciences), monoclonal anti-mouse CD3 (17A2, BioLegend) antibodies and biotinylated peanut agglutinin (B-1075, Vector Laboratories) for 45 min. Sections were washed and further stained with Alexa Fluor 647 streptavidin (BioLegend) antibody for 45 min. All antibodies were diluted

1:100 to their original concentration in blocking buffer. After washing with blocking buffer, sections were mounted in ProLong Diamond Antifade Mountant (ThermoFisher Scientific). Images were acquired on a ZEISS LSL 880 confocal microscope and analysed on ZEN 2.3 (Zeiss) software.

## ELISA measurements

For determination of the concentrations of immunoglobulin isotypes in sera, ELISAs were carried out according to the manufacturer's protocol (Ig Isotyping Mouse Instant ELISA Kit for IgG1, IgG2b and IgM) (Supplementary Table 11). NP-specific antibodies were measured by ELISA using 10 µg/ml of NP(24)-BSA (Biosearch Technologies) as the coating reagent. NP-specific IgM and IgG1 was detected using goat anti-mouse IgM and IgG1 Fc-specific antibodies conjugated to horseradish peroxidase and developed with tetramethylbenzidine (Sigma). Optical densities were determined by using an ELISA reader at 450 nm (SpectraMax M3, Molecular Devices).

## RNA-sequencing analysis

Total mRNA from *Ifitm3*<sup>+/+</sup> and *Ifitm3*<sup>-/-</sup> BCR-ABL1 or NRAS<sup>G12D</sup> B-ALL cells was extracted using RNeasy Kit (Qiagen) according to the manufacturer's instructions. Sequencing was performed on an Illumina Hiseq 2500 (Illumina) instrument using the TruSeq SR Cluster Kit v.4-cBot-HS (Illumina) with v.4 chemistry. Quality control of RNA-sequencing reads was performed using FastQC. For analysis, raw sequence reads were mapped to the mouse genome (mm10) using STAR v.2.5.3<sup>35</sup>, and the frequency of genes was counted using featureCounts v.1.5.1<sup>36</sup>. The raw counts were then normalized using the trimmed mean of *M* values method and compared using Bioconductor package 'edgeR'<sup>37</sup>. Reads per kilobase per million (RPKM) mapped reads were also calculated from the raw counts. For differential expression analysis, transcripts were quantified using Salmon v.1.1.0 against gencode GRCh38 v.M24 transcript annotations; normalization and statistical analysis were done in R using DESeq2 v.1.28.1. Differentially expressed genes were identified if RPKM ≥ 1 in at least one sample, fold change ≥ 2 and *P* ≤ 0.05 (Extended Data Fig. 3b). RPKM data were later used in the gene set enrichment analysis (GSEA). GSEA was performed using the DOSE package in R<sup>38</sup>; genes were ranked by log<sub>2</sub>-transformed fold change; and gene sets were obtained from MSigDB or from internal data, as indicated.

## CRISPR-mediated gene deletion

All lentiviral constructs expressing Cas9 nuclease and guide RNA were purchased from Transomic Technologies. For gene deletion, cells were transduced with pTOL-hCMV-Tet3G-Hygromycin. Hygromycin-resistant cells were subsequently transduced with pCLIP-Tre3g-hCMV-Cas9-P2A-zsGreen. Expression of Cas9–P2A–zsGreen was induced at 1 µg ml<sup>-1</sup> of doxycycline for 16 h, and zsGreen<sup>+</sup> cells were sorted by flow cytometry. Cells were washed out to remove doxycycline to turn off Cas9 expression (TetOff) and then subsequently transduced with pCLIP-gRNA-hCMV-RFP-gRNA. Sorted RFP<sup>+</sup> cells were subjected to further experiments. Gene deletion was initiated by treatment with 1 µg ml<sup>-1</sup> of doxycycline (TetOn). Non-targeting guide RNA was used as control.

## Gene deletion by non-viral genome targeting

Chemically synthesized CRISPR RNAs (160 µM) and *trans*-activating CRISPR RNAs (160 µM) were mixed 1:1 by volume and annealed by incubation at 37 °C for 30 min. Recombinantly produced Cas9 (40 µM) was then mixed 1:1 by volume with gRNA to produce RNA ribonucleoprotein (RNP) complexes. RNPs were freshly complexed before electroporation. Electroporation was performed by using pulse code EH-115 on a Lonza 4D 96-well electroporation system. Predesigned Alt-R CRISPR–Cas9 guide RNAs were purchased from IDT. Non-targeting control guide RNAs were purchased from IDT.

## Co-immunoprecipitation

Co-immunoprecipitation was performed with the Pierce Crosslink Magnetic IP/Co-IP kit according to manufacturer's instructions (Thermo Fisher Scientific). In brief, patient-derived *Ph*<sup>+</sup> ALL cells (PDX2) were transduced with MSCV Flag-IRES-Puro or MSCV Flag-IFITM3-IRES-Puro and selected in puromycin for 3 days. Viable cells ( $5 \times 10^7$ ) were collected and washed by PBS before lysis using IP lysis/Wash buffer (Thermo Fisher Scientific). Then, 5 µg of anti-Flag antibody M2 (F1804, Sigma-Aldrich) per sample was coupled to protein A/G magnetic beads and covalently crosslinked with 20 µM disuccinimidyl suberate. The antibody crosslinked beads were incubated with cell lysate, washed to remove non-bound material and eluted in a low-pH elution buffer that dissociates bound antigen from the antibody crosslinked beads. The enriched antigen in low pH was immediately neutralized and subjected to western blotting. Jeko1 cells electroporated with either non-targeting RNP or *IFITM3*-targeting RNP complex were stimulated with 10 µg ml<sup>-1</sup> F(ab')<sub>2</sub> fragment goat anti-human µ chain (Jackson Immunoresearch) for the indicated time points at 37 °C and 5% CO<sub>2</sub>. Cells were immediately washed with

chilled PBS and subjected to co-immunoprecipitation with anti-CD19 antibody (no. 90176, CST).

## PLA

For PLA of pre-BCR or BCR–IFITM3, cells were incubated with  $10 \mu\text{g ml}^{-1}$  F(ab')<sub>2</sub> fragment goat anti-human  $\mu$  chain (Jackson Immunoresearch) for 5 min at 37 °C and 5% CO<sub>2</sub>. Cells were immediately washed with chilled PBS and subsequently fixed in fixation buffer (Biolegend) containing 4% paraformaldehyde for 25 min on ice and then washed with chilled PBS. For cellular membrane staining, cells were labelled with  $5 \mu\text{g ml}^{-1}$  WGA conjugated to Alexa Fluor 488 (Thermo Fisher Scientific) for 5 min at room temperature. Cells were then permeabilized in Perm/Wash Buffer (BD Biosciences) and then blocked in Duolink Blocking buffer for 30 min at room temperature. Cells were incubated with 1:150 diluted primary antibodies listed in Supplementary Table 10 overnight at 4 °C. For late endosome staining, cells were incubated with anti-human LAMP1 conjugated to Alexa Fluor 488 (R&D Systems) with the primary antibodies. Cells were washed and settled on Cell-Tak (Corning)-coated Shandon Single Cytoslide by cytopsin at 400g for 5 min. PLA reactions were carried out according to the manufacturer's protocol (Duolink, Sigma). In brief, primary antibodies were coupled with Duolink in situ PLA PLUS or MINUS probes (Sigma-Aldrich), and then probes were visualized with Duolink Detection Reagent Red (Sigma-Aldrich). Cells were mounted with Duolink in situ mounting medium with DAPI (Sigma-Aldrich). Microscopy images were acquired using an Olympus IX3-55 and analysed by CellSens imaging software (Olympus) and ImageJ. For quantification of PLA signals, one dot was defined as pixel size of 5 × 5 by BlobFinder software. Statistical significance was calculated using unpaired Student's *t*-test with Excel and plotted with GraphPad Prism 7.

## Phosphoproteomic analysis

Patient-derived B-ALL (PDX2) cells transduced with HA-tagged IFITM3(Y20E) or empty vector control were incubated with  $2.5 \mu\text{g ml}^{-1}$  of polyclonal anti-HA (Abcam) for 5 min at 37 °C at 5% CO<sub>2</sub>. Cellular extracts were prepared in urea lysis buffer, sonicated, centrifuged, reduced with DTT and alkylated with iodoacetamide. Fifteen mg total protein for each sample was digested with trypsin, and 500  $\mu\text{g}$  total protein for each sample was digested with LysC and trypsin mix for IMAC analysis. Samples were purified over C18 columns and dried in a lyophilizer. Dried samples were resuspended and enriched with Fe-IMAC beads, purified over C18 STAGE tips (Rappsilber). Replicate injections of each sample were run nonsequentially on the instrument. Peptides were eluted using a 150-min (IMAC) linear gradient of

acetonitrile in 0.125% formic acid delivered at 280 nl/min. Tandem mass spectra (MS/MS) were collected in a data-dependent manner with a Thermo Orbitrap Fusion Lumos Tribrid mass spectrometer using a top-twenty MS/MS method, a dynamic repeat count of one and a repeat duration of 30 s. Real-time recalibration of mass error was performed using lock mass (Olsen) with a singly charged polysiloxane ion of  $m/z$  = 371.101237. MS/MS spectra were evaluated using SEQUEST and the Core platform from Harvard University (by J. K. Eng, E. L. Huttlin and J. Villen). Files were searched against the SwissProt *Homo sapiens* FASTA database. A mass accuracy of  $\pm 5$  ppm was used for precursor ions and 0.02 Da for product ions. Enzyme specificity was limited to trypsin, with at least one tryptic (K- or R-containing) terminus required per peptide and up to four miscleavages allowed. Cysteine carboxamidomethylation was specified as a static modification, and oxidation of methionine and phosphorylation on serine, threonine and tyrosine residues were allowed as variable modifications. Reverse decoy databases were included for all searches to estimate false discovery rates, and filtered using a 1% false-discovery rate in the linear discriminant module of Core. Peptides were also manually filtered using a  $\pm 5$  ppm mass error range and presence of a phosphorylated residue. All quantitative results were generated using Skyline (MacLean) to extract the integrated peak area of the corresponding peptide assignments. Accuracy of quantitative data was ensured by manual review in Skyline or in the ion chromatogram files.

## Bio-ID proteomics

Patient-derived PDX2 B-ALL cells and Jeko1 MCL cells were transduced with Flag-tagged IFITM3(Y20E) or IFITM3(K83A/K104A) mutant constructs with N-terminal Turbo-ID BirA (engineered biotin ligase) and selected by puromycin for three days. Turbo-ID BirA-expressing construct tagged with Flag was used as negative control. To induce biotinylation of proteins proximal to IFITM3, cells were treated with 50  $\mu$ mol l<sup>-1</sup> biotin and with anti-HA antibody for simultaneous induction of IFITM3 crosslinking for 10 min. Cells were washed three times with chilled PBS and lysed in IP/WASH buffer (Thermo Fisher Scientific) with 1× HALT protease inhibitor (Thermo Fisher Scientific). The lysates were incubated by streptavidin C1 MyOne Dynabeads (Invitrogen) for 16 h at 4 °C. Unbound proteins were washed 3 times by 2% SDS-PBS, 3 times by PBS and 3 times with pure water. The eluted proteins were gel-purified, followed by in-gel digestion and subjected to mass spectrometry. For liquid chromatography (LC)-MS/MS analysis, peptides were analysed using a Dionex UltiMate 3000 Rapid Separation LC system and a Orbitrap mass spectrometer (ThermoFisher Scientific). Six- $\mu$ l peptide samples were loaded onto the trap column, which was 150  $\mu$ m × 3 cm and in-house-packed with 3- $\mu$ m C18 beads. The analytical column was a 75  $\mu$ m × 10.5-cm PicoChip column

packed with 3- $\mu$ m C18 beads (New Objectives). The flow rate was kept at 300 nl/min. Solvent A was 0.1% formic acid (FA) in water and solvent B was 0.1% FA in ACN. The peptide was separated on a 120-min analytical gradient from 5% ACN and 0.1% FA to 40% ACN and 0.1% FA. The mass spectrometer was operated in data-dependent mode. The source voltage was 2.40 kV and the capillary temperature was 275 °C. MS1 scans were acquired from 400–2,000 *m/z* at 60,000 resolving power and automatic gain control (AGC) set to  $1 \times 10^6$ . The 15 most abundant precursor ions in each MS1 scan were selected for fragmentation. Precursors were selected with an isolation width of 1 Da and fragmented by collision-induced dissociation at 35% normalized collision energy in the ion trap; previously selected ions were dynamically excluded from reselection for 60 s. The MS2 AGC was set to  $3 \times 10^5$ . For data analysis, proteins were identified from the mass spectrometry raw files using Mascot search engine (Matrix science). MS/MS spectra were searched against the SwissProt human database. All searches included carbamidomethyl cysteine as a fixed modification and oxidized Met, deamidated Asn and Gln, and acetylated N terminus as variable modifications. Three missed tryptic cleavages were allowed. The MS1 precursor mass tolerance was set to 10 ppm and the MS2 tolerance was set to 0.6 Da. A 1% false discovery rate cut-off was applied at the peptide level. Only proteins with a minimum of two peptides above the cut-off were considered for further study. For comparison to empty vector control, background peptide abundances for missing values were imputed from a Gaussian distribution centred around the minimum observed abundance using the MinProb method from MSnbase package in R.

## Cell-surface proteome analyses

Cell-surface proteins were labelled with biotin using the N-linked glycosylation-site biotin labelling method<sup>39</sup>. In brief, 40 million *Ifitm3<sup>+/+</sup>* or *Ifitm3<sup>-/-</sup>* B-ALL cells were washed twice and resuspended in 1 ml of ice-cold PBS, and treated with 1.6 mM sodium metaperiodate (VWR) at 4 °C for 20 min to oxidize the vicinal diols of sugar residues linked to surface proteins. The cells were then washed twice in PBS to remove excess sodium metaperiodate. Cells were resuspended in 1ml of ice-cold PBS and treated with 1 mM biocytin hydrazide (Biotium) and 10 mM aniline (Sigma-Aldrich) at 4 °C for 90 min with gentle mixing to biotinylate free aldehydes exposed on the sugar residues. After labelling, cells were washed 3 times with ice-cold PBS to removed excess biotin, frozen in liquid nitrogen and stored at -80 °C until further processing for mass spectrometry. All experiments were performed in biological triplicates with replicates collected from consecutive passages. Frozen cell pellets were thawed on ice in 1 ml of RIPA buffer (Millipore) with the addition of 1× HALT protease inhibitors (Pierce). After incubation on ice for 10 min, cells were disrupted by sonication and the lysates were clarified by centrifugation at

17,000 rcf at 4 °C for 10 min. Clarified lysate was mixed with 500 µl of neutravidin agarose resin (Thermo Fisher Scientific) and incubated at 4 °C for 2 h with end-over-end mixing. Neutravidin beads with captured biotinylated surface proteins were washed extensively by gravity flow to remove unbound proteins using 50 ml of 1× RIPA + 1 mM EDTA, followed by 50 ml of PBS + 1 M NaCl and finally 50 ml of 50 mM ABC + 2 M urea buffer. Washed beads were resuspended in digestion buffer (50 mM Tris pH 8.5, 10 mM TCEP, 20 mM 2-iodoacetamide and 1.6 M Urea) with 10 µg of added trypsin protease (Pierce, 90057) to perform simultaneous disulfide reduction, alkylation and on-bead peptide digestion at room temperature overnight (16–20 h). After digestion, the pH was dropped to about 2 with neat trifluoroacetic acid (Sigma-Aldrich) and the peptide mixture was desalting using a SOLA-HRP column (Thermo Fisher Scientific) on a vacuum manifold. Desalted peptides were eluted with 50% acetonitrile (Sigma-Aldrich) and 50% water with 0.1% TFA and dried down completely in a speedvac. Dried peptides were resuspended in LC–MS grade water (Fisher) with 2% ACN and 0.1% FA. Peptide concentration was measured using 280 nm absorbance on a Nanodrop, and the peptide concentration was adjusted to 0.2 µg µl<sup>-1</sup> for mass spectrometry runs.

## LC–MS and data analysis for cell-surface proteome

For each replicate, 1 µg of peptide was injected onto a Dionex Ultimate 3000 NanoRSCLC instrument with a 15-cm Acclaim PEPMAP C18 (Thermo Fisher Scientific, 164534) reverse-phase column. The samples were separated on a 3.5-h nonlinear gradient using a mixture of buffer A (0.1% FA) and B (80% ACN/0.1% FA), from 2.4% ACN to 32% ACN. Eluted peptides were analysed with a Thermo Q-Exactive Plus mass spectrometer. The mass spectrometry survey scan was performed over a mass range of 350–1500 *m/z* with a resolution of 70,000, with a maximum injection time of 100 ms. We performed a data-dependent MS2 acquisition at a resolution of 17,500, AGC of  $5 \times 10^4$ , and injection time of 150 ms. The 15 most intense precursor ions were fragmented in the higher-energy collisional dissociation at a normalized collision energy of 27. Dynamic exclusion was set to 20 s to avoid over-sampling of highly abundant species. The raw spectral data files are available at the ProteomeXchange PRIDE repository (accession number PXD014691). Raw spectral data were analysed using MaxQuant v.1.5.1.2<sup>40</sup> to identify and quantify peptide abundance and searched against the human Swiss-Prot annotated human proteome from Uniprot (downloaded with 20,303 entries). The ‘match-between-runs’ option was selected to increase peptide identifications and the ‘fast LFQ’ option was selected to calculate label-free quantification values of identified proteins. All other settings were left at the default MaxQuant values. The MaxQuant output data were analysed using Perseus<sup>41</sup> and the R program (version 3.4.0). Proteins annotated as ‘reverse’, ‘only identified by site’ and ‘potential

contaminant' were filtered out, as were proteins that were quantified in less than two out of three biological replicates in at least one experimental group. Missing values were imputed on the basis of the normal distribution of the dataset as implemented by Perseus. Volcano plots were generated using output from a two-sample *t*-test comparing the log<sub>2</sub>-transformed label-free quantification protein abundance values from different cell lines with a false-discovery rate set to 0.01. Validation was performed by flow cytometry (Supplementary Table 1).

## Cholesterol and lipid raft measurement

For the depletion of cholesterol, cells were preincubated with 5 mM of methyl-β-cyclodextrin for 30 min at 37 °C before filipin staining. For ganglioside GM1 staining, cells were labelled with cholera toxin B using Vybrant lipid raft labelling kit (Molecular Probes), according to the manufacturer's protocol. In brief, cells were labelled with cholera toxin unit B conjugated with Alexa Fluor 594 on ice for 15 min, washed twice with PBS. Cholera-toxin-B-labelled lipid rafts were crosslinked with anti-cholera-toxin-B antibody on ice for 15 min, washed twice with PBS and analysed by flow cytometry.

## In vivo transplantation of leukaemia cells

Mouse pre-B ALL cells transformed by BCR–ABL1 or NRAS(G12D) were injected into sublethally irradiated (200 cGy) NOD-*scid* IL2R $\gamma$ <sup>null</sup> (NSG) mice via the tail vein. Eight- to ten-week-old female NSG mice were randomly allocated before injection. A mouse was euthanized when they showed signs of leukaemia burden, such as a hunched back, weight loss and inability to move, and then the bone marrow and/or spleen were collected to test leukaemia infiltration by flow cytometry. Kaplan–Meier survival analysis was performed using GraphPad Prism 7 (GraphPad Software) to compare overall survival. The Mantel–Cox log-rank test was used as statistical analysis using GraphPad Prism 7 (Supplementary Table 3). The minimal number of mice in each group was calculated by using the 'cpower' function in Hmisc package of R. No blinding was used. All mouse experiments were subject to institutional approval by the Beckman Research Institute of City of Hope Animal Care and Use Committee.

## PIP3 quantification

For Fig. 4, 60 million viable cells were resuspended in chilled 0.5 M trichloroacetic acid (TCA) in a total volume of 1 ml and incubated on ice for 5 min. Cells were centrifuged at 3,000 rpm for 7 min at 4 °C and resuspended in 5% TCA and 1 mM EDTA in a total volume of 1 ml. After vortexing for 30 s, cells were washed again

with 5% TCA and 1 mM EDTA. To extract neutral lipids, cells were resuspended in 1 ml of MeOH:CHCl<sub>3</sub> (2:1) and vortexed for 10 min at room temperature and centrifuged at 3,000 rpm for 5 min. After 1 more extraction of neutral lipids, the acidic lipids were extracted by adding 750 µl MeOH:CHCl<sub>3</sub>:12 M HCl (80:40:1) with vigorous vortexing for 25 min at room temperature. After centrifugation at 3,000 rpm for 5 min, supernatant was transferred to a 2-ml centrifuge tube and mixed with 250 µl of CHCl<sub>3</sub> and 450 µl of 0.1 M HCl, vortexed for 30 s, and centrifuged at 3,000 rpm for 5 min to separate organic and aqueous phases. Five hundred µl of the lower organic phases was collected into a clean 1.5-ml vial and dried in a vacuum dryer for 1 h. Dried lipid was stored at -20 °C. On the day of assay, lipid samples were reconstituted with 200 µl of PBS containing 0.25% protein stabilizer; 20 µl was used for PI(4,5)P<sub>2</sub> measurement and the rest (180 µl) was used for PI(3,4,5)P<sub>3</sub> measurement using an ELISA kit (Echelon Biosciences) according to the manufacturer's instructions.

## Exogenous delivery of PIP3

Phosphatidylinositol 3,4,5-trisphosphate diC16 (Echelon Biosciences) was freshly reconstituted with PBS at 2 mM. Unlabelled shuttle PIP carrier 2 (histone H1) was freshly reconstituted with water at 2 mM. PIP<sub>3</sub> in a volume of 75 µl was mixed with 25 µl of PIP carrier and incubated at room temperature for 10 min. One hundred µl of PIP<sub>3</sub>-carrier complex was added into *Ifitm3*<sup>+/+</sup> or *Ifitm3*<sup>-/-</sup> B-ALL cells in a total volume of 5 ml and incubated for 24 h. PIP<sub>3</sub>-loaded *Ifitm3*<sup>+/+</sup> or *Ifitm3*<sup>-/-</sup> B-ALL cells were subjected to colony-forming assay, as shown in Extended Data Fig. 8.

## Lipid-binding assay

To assess the direct binding of IFITM3 to lipids, a lipid-binding assay was performed using Membrane Lipid Strips (Echelon Biosciences) according to the manufacturer's instructions. In brief, membranes were blocked in 5% fatty acid-free BSA (Sigma-Aldrich) in TBST (50 mM Tris-HCl, 150 mM NaCl, and 0.1% Tween 20) for 1 h at room temperature in the dark followed by overnight incubation with 0.5 µg/ml of recombinant proteins in blocking buffer at 4 °C with gentle agitation. After washing membranes 3 times for 30 min in TBST, membranes were incubated for 1 h with anti-GST tag polyclonal Ab (Thermo Fisher Scientific) or anti-biotin monoclonal antibody (Cell Signaling Technology) antibodies, listed in Supplementary Table 10. Membranes were incubated with alkaline-phosphatase-conjugated secondary antibodies (Invitrogen) and chemiluminescent substrate (Invitrogen) and were further detected by UVP BioSpectrum 810 Imaging System

(Thermo Fisher Scientific). Recombinant GST-tagged protein was purchased from Sigma-Aldrich. Recombinant human GST–IFITM3 protein was purchased from Abnova. Recombinant human IFITM3 fragments listed in Supplementary Table 5 were synthesized at LifeTein.

## Preferential PIP3 accumulation and binding to IFITM3 using multi-scale molecular dynamics simulations

The IFITM3 protein structure from residues 58 to 128 was modelled by coarse-grained molecular dynamics simulation method in GROMACS, in explicit cell membrane mimic bilayer. There is no structure available for IFITM3 or for any close homologue. We calculated the hydrophobicity for each position using the hydrophobic index of amino acids<sup>42</sup> and averaged hydrophobicity over a sliding window of seven amino acids. Previous structural studies on IFITM3 structure<sup>43</sup> have shown there is only one transmembrane domain 2 that is inserted into the membrane. On the basis of this evidence, we used the topology shown in Supplementary Fig. 9 as the starting structure. TM1 was generated as an  $\alpha$ -helix structure, and the CRAC motifs and linker region were built as fully extended chain. The linker region was relaxed using 5,000 steps of coarse-grained simulation using GROMACS program<sup>44</sup> with Martini force field<sup>45</sup> to remove stress in the system. We then added the TM2 region as a helix and inserted TM2 into a cell-membrane-mimicking bilayer<sup>46</sup>. The composition and ratio of lipids for the mixed bilayer is POPC:DOPC:POPE:DOPE:CHOL:Sph:GM1 = 0.2:0.2:0.05:0.05:0.25:0.15:0.1 for the outer leaflet of the bilayer, and 0.05:0.05:0.20:0.2:0.08:0.08:0.25:0.03:0.03 of POPC: DOPC: POPE: DOPE: POPS: DOPS: CHOL: PIP1:PIP2:PIP3 for the inner leaflet. We generated three possible starting setup for the mixed lipid bilayer with water in the upper and inner regions with CHARMM-GUI<sup>47,48</sup>. The charges in the system were neutralized with 0.15 M NaCl. We used nine replicates of the protein IFITM3 structure in the simulation box (Supplementary Fig. 9a). The initial configuration was minimized using steepest decent method for 5,000 steps, and then equilibrated in NPT ensemble for 5 ns, at 303-K temperature and 1 bar pressure. The temperature was controlled by Berendsen thermostat<sup>49</sup> with coupling constant of 1 ps, and the pressure was controlled by Berendsen barostat<sup>49</sup> in semi-isotropic type with a coupling constant of 5 ps and a compressibility of  $3 \times 10^{-4}$  bar<sup>-1</sup>. The reaction field coulomb<sup>50</sup> was applied to describe electrostatics, with cut-off at 1.1 nm. The cut-off for van der Waals interactions used was also 1.1 nm. We used the Leap-frog integrator, and a 20-fs time step for integration. All systems were solvated in coarse-grained water model adopted in the Martini forcefield water, neutralized with 0.15 M NaCl. Ten  $\mu$ s of production simulation was performed for each of the three starting conformations of the lipid bilayer. The final 1  $\mu$ s of the trajectory from

each of the 3 setups was used to analyse the folded structure of the CRAC1–basic patch–CRAC2 region of the IFITM3 model. We clustered the conformations of IFITM3 by the root mean square deviation cut-off of 0.3 nm in the backbone coarse-grained particles in the coarse-grained simulations. We analysed the binding patterns of PIP2 and PIP3 in this most populated conformational cluster. We observed that both PIP2 and PIP3 compete for the ‘basic patch’ of residues shown in the amino acid sequence in Extended Data Fig. 9. We extracted three snapshots from this conformational cluster that represent the most diverse patterns in PIP2 and PIP3 binding.

## Details of the all-atom molecular dynamics simulations for phospholipid binding

To better understand the detailed binding conformation of PIP2 and PIP3 to IFITM3 and to calculate their binding energies to IFITM3, we converted the three snapshots extracted from the coarse-grained simulations to an all-atom system using Martini tools<sup>51</sup>. The three chosen snapshots were cut into  $9 \times 9\text{-nm}^2$  box centred at the IFITM3 unit from the coarse-grained simulations to preserve the local optimized lipid environment. The lipid and protein were converted to an all-atom model, and were resolvated into a  $9 \times 9 \times 9\text{-nm}^3$  simulation box, neutralized by 0.15 M NaCl. Extended Data Figure 9 shows the detailed interaction between PIP2 or PIP3 with IFITM3 protein in an all-atom resolution base on these snapshots. The all-atom simulations were performed using GROMACS package<sup>44</sup> and CHARMM36 force field<sup>52</sup>, with the TIP3 water model. The nonbond interactions were calculated with a cut-off of 12 Å, and the particle-mesh Ewald method<sup>51</sup> was applied to solve long-range van der Waals interactions. Each system was gradually heated to 310 K with random initial velocities sampled from a Boltzmann distribution. The heating process lasted for 1 ns, with temperature controlled by a Nosé–Hoover thermostat<sup>53</sup>, followed by 30-ns equilibration in NPT ensemble with harmonic position restraints on protein heavy atoms. The pressure was maintained at 1 bar in semi-isotropic environment, controlled by the Parrinello–Rahman method. The restraint force was gradually reduced from 5 kcal/mol to 0 kcal/mol with a -1 kcal/mol step per 5-ns window. The final frame of equilibration was taken for a production run. The production run was performed twice for 50 ns each, with 2 different random initial velocities assigned to the equilibrated structure. An integration time step of 2 fs was used. The interaction energy between PIP3 with IFITM3 protein was calculated as the sum of electrostatic Coulombic energy and van der Waals potential energy averaged over the two 50-ns trajectories, totalling 100 ns.

## **Interaction of PIP3 with the two basic residue patches**

The PIP3-binding and AKT-signalling activation assays showed that mutation of the K83/K104 patch to K83A/K104A had higher effect than mutating the R85/R87/K88 patch to R85A/R87A/K88A. To further validate the interaction strength difference between PIP3 and the two basic patches, we converted all PIP1 and PIP2 in the simulation box to PIP3. We further performed simulations on the IFITM3(K83A/K104A) and on IFITM3(R85A/R87A/K88A) in the PIP3-only simulation box. Starting from this structure, we performed equilibration of the system and 5 all-atom molecular dynamics production simulations (each 200-ns long), using the protocol for all-atom molecular dynamics simulations described in ‘Details of the all-atom molecular dynamics simulations for phospholipid binding’. We aggregated the final 100 ns of simulation trajectories from each of the 5 runs, which we added to 500 ns of molecular dynamics simulation trajectories for analysis. We calculated the interaction energy as the sum of electrostatic Coulombic and van der Waals potential energies between PIP3 and residues forming the basic patch only (K83/K104 or R85/R87/K88). The interaction energies were averaged over the 500 ns of aggregated molecular dynamics simulation trajectories for each system. We repeated these interaction energy calculations for the wild-type IFITM3 and for the mutant K83A/K104A and R85A/R87A/K88A constructs.

## **Contact-frequency heat-map calculations from molecular dynamics simulations**

The important information that can be extracted from molecular dynamics simulations is the temporal frequency of PIP3 contacts with the two basic residue patches. The persistence of these interactions has an important role in the accumulation of PIP3 by IFITM3. We calculated the percentage of molecular dynamics snapshots that show contacts between each of the residues in the basic patch. This is termed the contact frequency. We also calculated the percentage of molecular dynamics snapshots that show simultaneous contacts made by PIP3 with two or more residues in the two basic residue patches. We generated a heat map using the frequencies calculated for the wild-type IFITM3 and in the alanine mutants.

## Quantitative real-time PCR

Bone marrow from a healthy donor was stained and sorted as previously described<sup>54</sup>. Total RNA from cells was extracted using the RNA isolation kit from Macherey–Nagel. Complementary DNA was generated with the qScript cDNA SuperMix (Quanta Biosciences). Quantitative real-time PCR was performed with FAST SYBR Green Master Mix (Applied Biosystems) and the Vii7 real-time PCR system (Applied Biosystems) according to standard PCR conditions. *COX6B* was used as a reference gene.

## Acoustic scattering measurements

Single-cell size-normalized acoustic scattering (SNACS) was measured using a previously established microfluidic method, which has been shown to be specifically sensitive to cell-surface stiffness<sup>55</sup>. Full measurement details can be found in a previous publication<sup>55</sup>. In brief, cells were flowed through a standing acoustic wave generated inside a vibrating suspended microchannel resonator (SMR). The SMR is a cantilever-based mass measurement tool<sup>56</sup>, which can also detect acoustic scattering from cells when the cells transit through the acoustic wave. The cantilever vibration frequency was monitored, and its shift was used to quantify the acoustic scattering from the cells as well as the buoyant mass of the cells. Before taking a set of measurements, the SMR was cleaned with 0.25% trypsin–EDTA for 20 min, followed by 5% bleach for 3-min and then a 5-min rinse with deionized H<sub>2</sub>O, to remove persistent biological debris. After cleaning, the SMR was passivated with 1 mg/ml PLL-g-PEG in H<sub>2</sub>O for 10 min at room temperature, followed by a 5-min rinse with normal cell culture medium. During the measurement, all the samples were loaded into the SMR through 0.005-inch-inner-diameter fluorinated ethylene propylene tubing. The fluid flow across the SMR was driven by three independent electronic pressure regulators and three solenoid valves. A consistent differential pressure was applied across the SMR to maintain constant shear and data rate for cell measurement. The data displayed in Extended Data Fig. 8a were obtained using a 350-μm-long cantilever with a 15 × 20-μm-sized channel inside of the cantilever and an approximately 200-ms transit time through the cantilever. All the regulators, valves and data acquisition

were controlled by custom software coded in LabVIEW 2017 (National Instruments) as detailed in a previous publication<sup>55</sup>. A parallel volume measurement using Coulter Counter (Beckman Coulter) was carried out to quantify average cell volume, which was used together with the single-cell buoyant mass measurements to calculate SNACS for each cell, as previously reported<sup>55</sup>. All measurements were carried out in normal cell culture medium at room temperature within 10 min of taking cells out of the cell culture incubator. After a measurement of the untreated Jeko1 cells, a new patch of same cells was obtained from the incubator, treated with 10 µg ml<sup>-1</sup> F(ab')<sub>2</sub> fragment goat anti-human µ chain (Jackson Immunoresearch) and the cells were immediately (within about 1 min) loaded into the SMR for measurement. Antibody-treated Jeko1 cells were measured for about 7 min to ensure that the anti-human µ chain stimulated changes were not reversed during the experiment. The SMR was briefly washed with PBS between each experiment. Wild-type Jeko1 cells were also measured after fixation to obtain a positive control for cell stiffness. For fixation, the cells were washed twice with PBS, mixed with 8% PFA for 30 min, washed twice with PBS and stored at 4 °C before the acoustic scattering measurements.

## Quantification and statistical analysis

Data are shown as mean ± s.d. unless stated. Statistical analysis was performed by GraphPad Prism 7 (GraphPad Software) using unpaired two-tailed *t* test, or as indicated in figure legends. Significance was considered at *P* < 0.05. For in vivo transplantation experiments, the minimal number of mice in each group was calculated through use of the ‘cpower’ function in the Hmisc package of R. Kaplan–Meier survival analysis was used to estimate overall survival with GraphPad Prism 7. Mantel–Cox log-rank test was used to compare the difference between two groups. No mice were excluded. For patient overall survival analysis, patients in each dataset were divided into two groups on the basis of whether their expression was above or below the median level of *IFITM3* and Kaplan–Meier survival analysis was used to estimate overall survival. The datasets used include patient-outcome data for B-ALL (Children’s Oncology Group (COG) P9906, *n* = 207; Eastern Cooperative Oncology Group (ECOG) E2993, *n* = 83; and St Jude, *n* = 15), mantle cell lymphoma (Lymphoma/Leukemia

Molecular Profiling Project (LLMPP),  $n = 92$ ) and acute myeloid leukaemia (The Cancer Genome Atlas (TCGA),  $n = 200$ ). A log-rank test was used to compare survival differences between patient groups. The R package ‘survival’ (version 2.35-8) was used for the survival analysis and Cox proportional hazards regression model in the R package for the multivariate analysis (<https://www.r-project.org/>). The investigators were not blinded to allocation during experiments and outcome assessment. Experiments were repeated to ensure reproducibility of the observations.

## Reporting summary

Further information on research design is available in the [Nature Research Reporting Summary](#) linked to this paper.

## Data availability

Patient-outcome data for B-ALL were obtained from the National Cancer Institute TARGET DATA Matrix of the COG Clinical Trial P9906 (GSE11877) (refs. [28,30](#)), ECOG Clinical Trial E2993 (GSE5314) (ref. [57](#)) and St Jude Children’s Research Hospital (<https://www.stjude.org/site/data/ALL3/>) (ref. [29](#)). Patient-outcome data for mantle cell lymphoma were obtained from <https://llmpp.nih.gov/MCL/> (ref. [58](#)). Patient-outcome data for AML were obtained from TCGA Acute Myeloid Leukaemia Project ([http://www.ncbi.nlm.nih.gov/geo/study/summary?id=laml\\_tcga\\_pub#clinical](http://www.ncbi.nlm.nih.gov/geo/study/summary?id=laml_tcga_pub#clinical))[59](#). Proteomics data have been deposited to the ProteomeXchange Consortium via the PRIDE partner repository with the following accession numbers: cell-surface proteome, PXD014691; phosphoproteome, PXD020696; and IFITM3 interactomes, PXD020697. Levels of *IFITM3* mRNA across human normal and malignant B-lymphoid samples were obtained from <http://Amazonia.transcriptome.eu/>. All other data are available from the corresponding author upon reasonable request. Genome binding and occupancy profiling from wild-type and IKDN stromal adherent pre-B cells were obtained from GSE86897. Immunohistochemistry images for IFITM3 levels in normal or malignant B cells were obtained from The Human Protein Atlas <https://www.proteinatlas.org/>. ChIP-seq data of the genome-

wide mapping of IKZF1 binding in patient-derived B-ALL xenograft cells were obtained from GSE58825. ChIP-seq data of the genetic analysis of IKZF1 target genes and tumour suppressor function in *Ph*<sup>+</sup> pre-B ALL cells were obtained from GSE90656. RNA-sequencing data for *Ifitm3*<sup>+/+</sup> and *Ifitm3*<sup>-/-</sup> *BCR-ABL1* or *NRAS*<sup>G12D</sup> B-ALL cells are available at [GSE155305](#). RNA-sequencing data for *Pten*<sup>f/f</sup> pre-B cells carrying 4-OHT-inducible Cre-ER<sup>T2</sup> or ER<sup>T2</sup> are available at [GSE155618](#). Supplementary Table 12 summarizes the accession numbers and publicly deposited data from this study. All other data needed to evaluate the conclusions in the paper are available within the Article and its Supplementary Information. [Source data](#) are provided with this paper.

## References

1. 1.

Bailey, C. C., Zhong, G., Huang, I. C. & Farzan, M. IFITM-family proteins: the cell's first line of antiviral defense. *Annu. Rev. Virol.* **1**, 261–283 (2014).

[PubMed](#) [PubMed Central](#) [Google Scholar](#)

2. 2.

Diamond, M. S. & Farzan, M. The broad-spectrum antiviral functions of IFIT and IFITM proteins. *Nat. Rev. Immunol.* **13**, 46–57 (2013).

[CAS](#) [PubMed](#) [Google Scholar](#)

3. 3.

Brass, A. L. et al. The IFITM proteins mediate cellular resistance to influenza A H1N1 virus, West Nile virus, and dengue virus. *Cell* **139**, 1243–1254 (2009).

[PubMed](#) [PubMed Central](#) [Google Scholar](#)

4. 4.

Zhang, Y. et al. Interferon-induced transmembrane protein 3 genetic variant rs12252-C associated with disease severity in coronavirus disease 2019. *J. Infect. Dis.* **222**, 34–37 (2020).

[PubMed](#) [Google Scholar](#)

5. 5.

Zhao, X. et al. Identification of residues controlling restriction versus enhancing activities of IFITM proteins on entry of human coronaviruses. *J. Virol.* **92**, e01535-17 (2018).

[CAS](#) [PubMed](#) [PubMed Central](#) [Google Scholar](#)

6. 6.

Jia, R. et al. The N-terminal region of IFITM3 modulates its antiviral activity by regulating IFITM3 cellular localization. *J. Virol.* **86**, 13697–13707 (2012).

[CAS](#) [PubMed](#) [PubMed Central](#) [Google Scholar](#)

7. 7.

Chesarino, N. M., McMichael, T. M., Hach, J. C. & Yount, J. S. Phosphorylation of the antiviral protein interferon-inducible transmembrane protein 3 (IFITM3) dually regulates its endocytosis and ubiquitination. *J. Biol. Chem.* **289**, 11986–11992 (2014).

[CAS](#) [PubMed](#) [PubMed Central](#) [Google Scholar](#)

8. 8.

Everitt, A. R. et al. IFITM3 restricts the morbidity and mortality associated with influenza. *Nature* **484**, 519–523 (2012).

[CAS](#) [PubMed](#) [PubMed Central](#) [Google Scholar](#)

9. 9.

Makvandi-Nejad, S. et al. Lack of truncated IFITM3 transcripts in cells homozygous for the rs12252-C variant that is associated with severe influenza infection. *J. Infect. Dis.* **217**, 257–262 (2018).

[CAS](#) [PubMed](#) [Google Scholar](#)

10. 10.

Kohn, A. Early interactions of viruses with cellular membranes. *Adv. Virus Res.* **24**, 223–276 (1979).

[CAS](#) [PubMed](#) [Google Scholar](#)

11. 11.

Liu, S. Y., Sanchez, D. J. & Cheng, G. New developments in the induction and antiviral effectors of type I interferon. *Curr. Opin. Immunol.* **23**, 57–64 (2011).

[PubMed](#) [Google Scholar](#)

12. 12.

Li, D. et al. KLF4-mediated negative regulation of IFITM3 expression plays a critical role in colon cancer pathogenesis. *Clin. Cancer Res.* **17**, 3558–3568 (2011).

[ADS](#) [CAS](#) [PubMed](#) [PubMed Central](#) [Google Scholar](#)

13. 13.

Zhang, D., Wang, H., He, H., Niu, H. & Li, Y. Interferon induced transmembrane protein 3 regulates the growth and invasion of human lung adenocarcinoma. *Thorac. Cancer* **8**, 337–343 (2017).

[CAS](#) [PubMed](#) [PubMed Central](#) [Google Scholar](#)

14. 14.

Spence, J. S. et al. IFITM3 directly engages and shuttles incoming virus particles to lysosomes. *Nat. Chem. Biol.* **15**, 259–268 (2019).

[CAS](#) [PubMed](#) [PubMed Central](#) [Google Scholar](#)

15. 15.

Harvey, R. C. et al. Identification of novel cluster groups in pediatric high-risk B-precursor acute lymphoblastic leukemia with gene expression profiling: correlation with genome-wide DNA copy number alterations, clinical characteristics, and outcome. *Blood* **116**, 4874–4884 (2010).

[CAS](#) [PubMed](#) [PubMed Central](#) [Google Scholar](#)

16. 16.

Witkowski, M. T. et al. Conserved IKAROS-regulated genes associated with B-progenitor acute lymphoblastic leukemia outcome. *J. Exp. Med.* **214**, 773–791 (2017).

[CAS](#) [PubMed](#) [PubMed Central](#) [Google Scholar](#)

17. 17.

Fujimoto, M. et al. CD19 regulates Src family protein tyrosine kinase activation in B lymphocytes through processive amplification. *Immunity* **13**, 47–57 (2000).

[CAS](#) [PubMed](#) [Google Scholar](#)

18. 18.

Okkenhaug, K. et al. Impaired B and T cell antigen receptor signaling in p110 $\delta$  PI 3-kinase mutant mice. *Science* **297**, 1031–1034 (2002).

[ADS](#) [CAS](#) [PubMed](#) [Google Scholar](#)

19. 19.

Engel, P. et al. Abnormal B lymphocyte development, activation, and differentiation in mice that lack or overexpress the CD19 signal transduction molecule. *Immunity* **3**, 39–50 (1995).

[CAS](#) [PubMed](#) [Google Scholar](#)

20. 20.

Chan, L. N. et al. Metabolic gatekeeper function of B-lymphoid transcription factors. *Nature* **542**, 479–483 (2017).

[ADS](#) [CAS](#) [PubMed](#) [PubMed Central](#) [Google Scholar](#)

21. 21.

Wang, Y. et al. The physiologic role of CD19 cytoplasmic tyrosines. *Immunity* **17**, 501–514 (2002).

[CAS](#) [PubMed](#) [Google Scholar](#)

22. 22.

Phelan, J. D. et al. A multiprotein supercomplex controlling oncogenic signalling in lymphoma. *Nature* **560**, 387–391 (2018).

[ADS](#) [CAS](#) [PubMed](#) [PubMed Central](#) [Google Scholar](#)

23. 23.

Kläsener, K., Maity, P. C., Hobeika, E., Yang, J. & Reth, M. B cell activation involves nanoscale receptor reorganizations and inside-out signaling by Syk. *eLife* **3**, e02069 (2014).

[PubMed](#) [PubMed Central](#) [Google Scholar](#)

24. 24.

Schwickert, T. A. et al. Stage-specific control of early B cell development by the transcription factor Ikaros. *Nat. Immunol.* **15**, 283–293 (2014).

[CAS](#) [PubMed](#) [PubMed Central](#) [Google Scholar](#)

25. 25.

Joshi, I. et al. Loss of Ikaros DNA-binding function confers integrin-dependent survival on pre-B cells and progression to acute lymphoblastic leukemia. *Nat. Immunol.* **15**, 294–304 (2014).

[CAS](#) [PubMed](#) [PubMed Central](#) [Google Scholar](#)

26. 26.

McLaughlin, S. & Murray, D. Plasma membrane phosphoinositide organization by protein electrostatics. *Nature* **438**, 605–611 (2005).

[ADS](#) [CAS](#) [PubMed](#) [Google Scholar](#)

27. 27.

Geng, H. et al. Integrative epigenomic analysis identifies biomarkers and therapeutic targets in adult B-acute lymphoblastic leukemia. *Cancer Discov.* **2**, 1004–1023 (2012).

[CAS](#) [PubMed](#) [PubMed Central](#) [Google Scholar](#)

28. 28.

Harvey, R. C. et al. Identification of novel cluster groups in pediatric high-risk B-precursor acute lymphoblastic leukemia with gene expression profiling: correlation with genome-wide DNA copy number alterations, clinical characteristics, and outcome. *Blood* **116**, 4874–4884 (2010).

[CAS](#) [PubMed](#) [PubMed Central](#) [Google Scholar](#)

29. 29.

Ross, M. E. et al. Classification of pediatric acute lymphoblastic leukemia by gene expression profiling. *Blood* **102**, 2951–2959 (2003).

[CAS](#) [PubMed](#) [Google Scholar](#)

30. 30.

Kang, H. et al. Gene expression classifiers for relapse-free survival and minimal residual disease improve risk classification and outcome prediction in pediatric B-precursor acute lymphoblastic leukemia. *Blood* **115**, 1394–1405 (2010).

[CAS](#) [PubMed](#) [PubMed Central](#) [Google Scholar](#)

31. 31.

Borowitz, M. J. et al. Clinical significance of minimal residual disease in childhood acute lymphoblastic leukemia and its relationship to other prognostic factors: a Children's Oncology Group study. *Blood* **111**, 5477–5485 (2008).

[CAS](#) [PubMed](#) [PubMed Central](#) [Google Scholar](#)

32. 32.

Poddar, S., Hyde, J. L., Gorman, M. J., Farzan, M. & Diamond, M. S. The interferon-stimulated gene *IFITM3* restricts infection and pathogenesis of arthritogenic and encephalitic alphaviruses. *J. Virol.* **90**, 8780–8794 (2016).

[CAS](#) [PubMed](#) [PubMed Central](#) [Google Scholar](#)

33. 33.

Foley, S. B. et al. Expression of BCR/ABL p210 from a knockin allele enhances bone marrow engraftment without inducing neoplasia. *Cell Rep.* **5**, 51–60 (2013).

[CAS](#) [PubMed](#) [Google Scholar](#)

34. 34.

Schjerven, H. et al. Genetic analysis of Ikaros target genes and tumor suppressor function in BCR-ABL1<sup>+</sup> pre-B ALL. *J. Exp. Med.* **214**, 793–814 (2017).

[CAS](#) [PubMed](#) [PubMed Central](#) [Google Scholar](#)

35. 35.

Dobin, A. et al. STAR: ultrafast universal RNA-seq aligner. *Bioinformatics* **29**, 15–21 (2013).

[CAS](#) [Google Scholar](#)

36. 36.

Liao, Y., Smyth, G. K. & Shi, W. featureCounts: an efficient general purpose program for assigning sequence reads to genomic features. *Bioinformatics* **30**, 923–930 (2014).

[CAS](#) [Google Scholar](#)

37. 37.

Robinson, M. D., McCarthy, D. J. & Smyth, G. K. edgeR: a Bioconductor package for differential expression analysis of digital gene expression data. *Bioinformatics* **26**, 139–140 (2010).

[CAS](#) [Google Scholar](#)

38. 38.

Yu, G., Wang, L.-G. & He, Q.-Y. ChIPseeker: an R/Bioconductor package for ChIP peak annotation, comparison and visualization. *Bioinformatics* **31**, 2382–2383 (2015).

[CAS](#) [PubMed](#) [Google Scholar](#)

39. 39.

Wollscheid, B. et al. Mass-spectrometric identification and relative quantification of N-linked cell surface glycoproteins. *Nat. Biotechnol.* **27**, 378–386 (2009).

[CAS](#) [PubMed](#) [PubMed Central](#) [Google Scholar](#)

40. 40.

Tyanova, S., Temu, T. & Cox, J. The MaxQuant computational platform for mass spectrometry-based shotgun proteomics. *Nat. Protocols* **11**, 2301–2319 (2016).

[CAS](#) [PubMed](#) [Google Scholar](#)

41. 41.

Tyanova, S. et al. The Perseus computational platform for comprehensive analysis of (prote)omics data. *Nat. Methods* **13**, 731–740 (2016).

[CAS](#) [PubMed](#) [Google Scholar](#)

42. 42.

Monera, O. D., Sereda, T. J., Zhou, N. E., Kay, C. M. & Hodges, R. S. Relationship of sidechain hydrophobicity and  $\alpha$ -helical propensity on the stability of the single-stranded amphipathic  $\alpha$ -helix. *J. Pept. Sci.* **1**, 319–329 (1995).

[CAS](#) [PubMed](#) [Google Scholar](#)

43. 43.

Ling, S. et al. Combined approaches of EPR and NMR illustrate only one transmembrane helix in the human IFITM3. *Sci. Rep.* **6**, 24029

(2016).

[ADS](#) [CAS](#) [PubMed](#) [PubMed Central](#) [Google Scholar](#)

44. 44.

Berendsen, H. J. C., van der Spoel, D. & van Drunen, R. GROMACS: a message-passing parallel molecular dynamics implementation. *Comput. Phys. Commun.* **91**, 43–56 (1995).

[ADS](#) [CAS](#) [Google Scholar](#)

45. 45.

de Jong, D. H. et al. Improved parameters for the Martini coarse-grained protein force field. *J. Chem. Theory Comput.* **9**, 687–697 (2013).

[PubMed](#) [Google Scholar](#)

46. 46.

Yen, H.-Y. et al. PtdIns(4,5)P<sub>2</sub> stabilizes active states of GPCRs and enhances selectivity of G-protein coupling. *Nature* **559**, 423–427 (2018).

[ADS](#) [CAS](#) [PubMed](#) [PubMed Central](#) [Google Scholar](#)

47. 47.

Hsu, P.-C. et al. CHARMM-GUI Martini maker for modeling and simulation of complex bacterial membranes with lipopolysaccharides. *J. Comput. Chem.* **38**, 2354–2363 (2017).

[CAS](#) [PubMed](#) [PubMed Central](#) [Google Scholar](#)

48. 48.

Qi, Y. et al. CHARMM-GUI Martini maker for coarse-grained simulations with the Martini force field. *J. Chem. Theory Comput.* **11**, 4486–4494 (2015).

[CAS](#) [PubMed](#) [Google Scholar](#)

49. 49.

Berendsen, H. J. C., Postma, J. P. M., van Gunsteren, W. F., DiNola, A. & Haak, J. R. Molecular dynamics with coupling to an external bath. *J. Chem. Phys.* **81**, 3684–3690 (1984).

[ADS](#) [CAS](#) [Google Scholar](#)

50. 50.

Tironi, I. G., Sperb, R., Smith, P. E. & van Gunsteren, W. F. A generalized reaction field method for molecular dynamics simulations. *J. Chem. Phys.* **102**, 5451–5459 (1995).

[ADS](#) [CAS](#) [Google Scholar](#)

51. 51.

Wassenaar, T. A., Pluhackova, K., Böckmann, R. A., Marrink, S. J. & Tieleman, D. P. Going backward: a flexible geometric approach to reverse transformation from coarse grained to atomistic models. *J. Chem. Theory Comput.* **10**, 676–690 (2014).

[CAS](#) [PubMed](#) [Google Scholar](#)

52. 52.

Huang, J. & MacKerell, A. D. Jr. CHARMM36 all-atom additive protein force field: validation based on comparison to NMR data. *J. Comput. Chem.* **34**, 2135–2145 (2013).

[CAS](#) [PubMed](#) [PubMed Central](#) [Google Scholar](#)

53. 53.

Martyna, G. J., Klein, M. L. & Tuckerman, M. Nosé–Hoover chains: the canonical ensemble via continuous dynamics. *J. Chem. Phys.* **97**, 2635–2643 (1992).

[ADS](#) [Google Scholar](#)

54. 54.

Buchner, M. et al. Identification of FOXM1 as a therapeutic target in B-cell lineage acute lymphoblastic leukaemia. *Nat. Commun.* **6**, 6471 (2015).

[ADS](#) [CAS](#) [PubMed](#) [PubMed Central](#) [Google Scholar](#)

55. 55.

Kang, J. H. et al. Noninvasive monitoring of single-cell mechanics by acoustic scattering. *Nat. Methods* **16**, 263–269 (2019).

[CAS](#) [PubMed](#) [PubMed Central](#) [Google Scholar](#)

56. 56.

Burg, T. P. et al. Weighing of biomolecules, single cells and single nanoparticles in fluid. *Nature* **446**, 1066–1069 (2007).

[ADS](#) [CAS](#) [PubMed](#) [Google Scholar](#)

57. 57.

Juric, D. et al. Differential gene expression patterns and interaction networks in *BCR-ABL*-positive and -negative adult acute lymphoblastic leukemias. *J. Clin. Oncol.* **25**, 1341–1349 (2007).

[CAS](#) [PubMed](#) [Google Scholar](#)

58. 58.

Rosenwald, A. et al. The proliferation gene expression signature is a quantitative integrator of oncogenic events that predicts survival in mantle cell lymphoma. *Cancer Cell* **3**, 185–197 (2003).

[CAS](#) [PubMed](#) [Google Scholar](#)

59. 59.

The Cancer Genome Atlas Research Network. Genomic and epigenomic landscapes of adult de novo acute myeloid leukemia. *N. Engl. J. Med.* **368**, 2059–2074 (2013).

[PubMed Central](#) [Google Scholar](#)

[Download references](#)

## Acknowledgements

We thank M. A. Lemmon for critical discussion and advice, and current and former members of the Müschen laboratory for their support and helpful discussions. Research in the Müschen laboratory is funded by the NIH/NCI through R35CA197628, R01CA157644, R01CA213138 and P01CA233412, the Dr. Ralph and Marian Falk Medical Research Trust Transformational Awards Program through MCG-18447-19, the Leukemia and Lymphoma Society through MCL-7000-18 and Blood Cancer Discoveries Grant BCDG-20327-20, as well the Howard Hughes Medical Institute HHMI-55108547 (to M.M.). This work was partly supported by NIH grants R35CA200422, R01CA251275, AI116585, AI116585S, AI140718, AI140705, DE023926 and DE028521 (to J.U.J.), R01 AI104002 and R01 AI127513 (to M.S.D.), R01 GM117923 and R01 GM097261 (to N.V.), NCI R35 CA231958 (to D.M.W.), Wellcome Trust 110275/Z/15/Z (to T.P.M.) and the Paul G. Allen Frontiers Group and the Cancer Systems Biology Consortium funding (U54-CA217377) from the National Cancer Institute (to S.R.M.). Relevant research in the A.T.-T. laboratory was supported by the Cancer Moonshot grant U01 CA232563. T.S. is a fellow of the Lymphoma Research Foundation. V.K. is supported by a Career Development Fellow grant (5491-20) from the Leukemia and Lymphoma

Society, and by a Young Investigator Award from Alex's Lemonade Stand Foundation. Proteomics services were performed by the Northwestern Proteomics Core Facility, generously supported by NCI CCSG P30 CA060553 awarded to the Robert H Lurie Comprehensive Cancer Center, instrumentation award (S10OD025194) from NIH Office of Director, and the National Resource for Translational and Developmental Proteomics supported by P41 GM108569. M.M. is a Howard Hughes Medical Institute (HHMI) Faculty Scholar. J.C. is a Leukemia and Lymphoma Society (LLS) Scholar.

## Author information

### Affiliations

1. Center of Molecular and Cellular Oncology, Yale Cancer Center, Yale School of Medicine, New Haven, CT, USA

Jaewoong Lee, Mark E. Robinson, Dewan Artadji, Teresa Sadras, Kadriye Nehir Cosgun, Lai N. Chan, Kohei Kume, Lars Klemm & Markus Müschen

2. Department of Computational and Quantitative Medicine, City of Hope Comprehensive Cancer Center, Duarte, CA, USA

Ning Ma & Nagarajan Vaidehi

3. Department of Systems Biology, City of Hope Comprehensive Cancer Center, Duarte, CA, USA

Mohamed A. Ahmed, Gang Xiao, Gauri Deb, Janet Winchester, Chun Wei Chen, Jianjun Chen & Vishal Khairnar

4. Department of Laboratory Medicine, University of California San Francisco, San Francisco, CA, USA

Huimin Geng, Matthew A. Nix & Arun P. Wiita

5. Koch Institute for Integrative Cancer Research, Massachusetts Institute of Technology, Cambridge, MA, USA

Teemu P. Miettinen, Ye Zhang & Scott R. Manalis

6. Medical Research Council Laboratory for Molecular Cell Biology, University College London, London, UK

Teemu P. Miettinen

7. Department of Pathology and Laboratory Medicine, Children's Hospital of Philadelphia and Perelman School of Medicine, University of Pennsylvania, Philadelphia, PA, USA

Andrei Thomas-Tikhonenko

8. Department of Immunology and Microbiology, The Scripps Research Institute, Jupiter, FL, USA

Michael Farzan

9. Department of Cancer Biology, Lerner Research Institute, Cleveland Clinic, Cleveland, OH, USA

Jae U. Jung

10. Dana Farber Cancer Institute, Boston, MA, USA

David M. Weinstock

11. Harvard Medical School, Boston, MA, USA

David M. Weinstock

12. Department of Biological Engineering, Massachusetts Institute of Technology, Cambridge, MA, USA

Scott R. Manalis

13. Department of Medicine, Washington University School of Medicine in St Louis, St Louis, MO, USA

Michael S. Diamond

14. Department of Molecular Microbiology, Washington University School of Medicine in St Louis, St Louis, MO, USA

Michael S. Diamond

15. Department of Pathology and Immunology, Washington University School of Medicine in St Louis, St Louis, MO, USA

Michael S. Diamond

16. Department of Immunobiology, Yale University, New Haven, CT, USA

Markus Müschen

## Authors

1. Jaewoong Lee

[View author publications](#)

You can also search for this author in [PubMed](#) [Google Scholar](#)

2. Mark E. Robinson

[View author publications](#)

You can also search for this author in [PubMed](#) [Google Scholar](#)

3. Ning Ma

[View author publications](#)

You can also search for this author in [PubMed](#) [Google Scholar](#)

4. Dewan Artadji

[View author publications](#)

You can also search for this author in [PubMed](#) [Google Scholar](#)

5. Mohamed A. Ahmed

[View author publications](#)

You can also search for this author in [PubMed](#) [Google Scholar](#)

6. Gang Xiao

[View author publications](#)

You can also search for this author in [PubMed](#) [Google Scholar](#)

7. Teresa Sadras

[View author publications](#)

You can also search for this author in [PubMed](#) [Google Scholar](#)

8. Gauri Deb

[View author publications](#)

You can also search for this author in [PubMed](#) [Google Scholar](#)

9. Janet Winchester

[View author publications](#)

You can also search for this author in [PubMed](#) [Google Scholar](#)

10. Kadriye Nehir Cosgun

[View author publications](#)

You can also search for this author in [PubMed](#) [Google Scholar](#)

11. Huimin Geng

[View author publications](#)

You can also search for this author in [PubMed](#) [Google Scholar](#)

12. Lai N. Chan

[View author publications](#)

You can also search for this author in [PubMed](#) [Google Scholar](#)

13. Kohei Kume

[View author publications](#)

You can also search for this author in [PubMed](#) [Google Scholar](#)

14. Teemu P. Miettinen

[View author publications](#)

You can also search for this author in [PubMed](#) [Google Scholar](#)

15. Ye Zhang

[View author publications](#)

You can also search for this author in [PubMed](#) [Google Scholar](#)

16. Matthew A. Nix

[View author publications](#)

You can also search for this author in [PubMed](#) [Google Scholar](#)

17. Lars Klemm

[View author publications](#)

You can also search for this author in [PubMed](#) [Google Scholar](#)

18. Chun Wei Chen

[View author publications](#)

You can also search for this author in [PubMed](#) [Google Scholar](#)

19. Jianjun Chen

[View author publications](#)

You can also search for this author in [PubMed](#) [Google Scholar](#)

20. Vishal Khairnar

[View author publications](#)

You can also search for this author in [PubMed](#) [Google Scholar](#)

21. Arun P. Wiita

[View author publications](#)

You can also search for this author in [PubMed](#) [Google Scholar](#)

22. Andrei Thomas-Tikhonenko

[View author publications](#)

You can also search for this author in [PubMed](#) [Google Scholar](#)

23. Michael Farzan

[View author publications](#)

You can also search for this author in [PubMed](#) [Google Scholar](#)

24. Jae U. Jung

[View author publications](#)

You can also search for this author in [PubMed](#) [Google Scholar](#)

25. David M. Weinstock

[View author publications](#)

You can also search for this author in [PubMed](#) [Google Scholar](#)

26. Scott R. Manalis

[View author publications](#)

You can also search for this author in [PubMed](#) [Google Scholar](#)

27. Michael S. Diamond

[View author publications](#)

You can also search for this author in [PubMed](#) [Google Scholar](#)

28. Nagarajan Vaidehi

[View author publications](#)

You can also search for this author in [PubMed](#) [Google Scholar](#)

29. Markus Müschen

[View author publications](#)

You can also search for this author in [PubMed](#) [Google Scholar](#)

## Contributions

J.L. performed experiments and contributed to all aspects of the study; in particular, western blotting, flow cytometry analysis, viable cell counts, growth competition assays, immunization assays, ELISA, colony-forming assays, CRISPR-mediated gene deletion, cell sorting, *in vivo* transplantation experiments, bio-imaging, bio-ID, immunoprecipitation assays, lipid strip assays, lipid raft analysis, calcium flux measurements and data analysis. M.E.R. and H.G. performed all bioinformatic and biostatistical analyses and power calculations for experimental design. N.M. and N.V. performed molecular dynamics simulations and structural analysis of IFITM3–PIP3 interactions. D.A. performed western blotting, flow cytometry analysis, viable cell counts, cell adhesion assays, CRISPR-mediated gene deletion and immunization assays. G.D., J.W., K.N.C., L.N.C., K.K. and V.K. performed flow cytometry analysis and viable cell counts. L.K. performed gene cloning, virus generation and flow cytometry analysis and cell sorting. M.A.A. performed RNA isolation for RNA sequencing, western blotting and CRISPR-mediated gene deletion. G.X. performed RNA-sequencing analysis with *Pten*<sup>f/f</sup> ER<sup>T2</sup> and Cre-ER<sup>T2</sup> mouse models and measured PIP3:PIP2 ratios. T.S. performed PLA. V.K. also performed immunofluorescence staining after immunization assays. C.W.C. and J.C. provided expertise in gene-editing experiments. M.A.N. and A.P.W. provided expertise in cell-surface proteomics. A.T.-T. provided expertise in CD19 signalling, and M.F., M.S.D. and J.U.J. contributed expertise and reagents in antiviral effector functions of IFITM3. T.P.M., Y.Z., D.M.W. and S.R.M. performed SNACS cell-stiffness assays. M.M. secured funding, developed the amplification loop concept and wrote the manuscript. All co-authors reviewed and edited the manuscript.

## Corresponding author

Correspondence to [Markus Müschen](#).

## Ethics declarations

### Competing interests

M.S.D. is a consultant for Inbios, Vir Biotechnology and NGM Biopharmaceuticals, and on the Scientific Advisory Board of Moderna and Immunome. The Diamond laboratory at Washington University School of Medicine has received unrelated sponsored research agreements from Moderna, Vir Biotechnology, and Emergent BioSolutions.

## Additional information

**Peer review information** *Nature* thanks Marcus Clark, Paul Kellam, Michael Reth and the other, anonymous, reviewer(s) for their contribution to the peer review of this work.

**Publisher's note** Springer Nature remains neutral with regard to jurisdictional claims in published maps and institutional affiliations.

## Extended data figures and tables

### [Extended Data Fig. 1 \*Ifitm3\* expression is induced by oncogenic PI3K signalling and repressed by IKZF1.](#)

**a**, Changes of *Ifitm3* mRNA levels were monitored in mouse splenic B cells upon BCR engagement (mean  $\pm$  s.e.;  $n = 2$ ). **b, c**, *Pten*<sup>f/f</sup> pre-B ALL cells carrying 4-OHT-inducible Cre-ER<sup>T2</sup> or ER<sup>T2</sup> were treated with 4-OHT and studied by RNA sequencing for *Ifitm3* transcript expression (**b**) and western blot for protein levels of PTEN, AKT-pS<sup>473</sup>, AKT and IFITM3 (**c**;  $n = 3$ ). **d**, STAT5 phosphorylated at Y694 (STAT5-pY<sup>694</sup>), STAT5 and IFITM3 levels in patient-derived B-ALL cells (PDX2) measured by western blotting upon imatinib treatment ( $n = 3$ ). **e**, Scenario of the PI3K pathway as a positive regulator of IFITM3, which in turn amplifies BCR and oncogenic

signalling. **f**, *IFITM3* mRNA levels across human normal and malignant haematopoietic and B-lymphoid samples (source data and statistics are given in Supplementary Table 2). Two-tailed *t*-test. **g**, *IFITM3* mRNA levels in pre-B cells from healthy donors and samples from patients with B-ALL were compared for two clinical cohorts (ECOG E2993 and St Jude). In ECOG E2993, bone marrow samples were obtained at diagnosis before treatment from 83 adults with B-ALL with a confirmed purity of >90% leukaemic blasts. For the St Jude datasets, 15 samples from children with B-ALL before treatment were compared to flow-sorted pre-B cells from bone marrow aspirates of healthy donors. Two-tailed Wilcoxon. **h**, Minimal residual disease (MRD) was determined in the COG P9906 cohort, *IFITM3* mRNA levels were compared in patients who were positive ( $n = 67$ ) and negative ( $n = 124$ ) for MRD. Two-tailed Wilcoxon. **i–l**, Patients with leukaemia and lymphoma from five clinical cohorts were segregated into two groups based on higher (*IFITM3*<sup>high</sup>) or lower (*IFITM3*<sup>low</sup>) than median *IFITM3* mRNA levels. Overall survival was compared by two-tailed log-rank test. **m**, ChIP-seq enrichment of RNAPII and H3K4me3 at the *Ifitm3* locus in pre-B cells (top) from *Ikzf1*<sup>exon5fl/fl</sup> mice upon Cre-mediated deletion of *Ikzf1* (GSE86897). Binding of IKZF1 to the promoter region of *IFITM3* was also analysed in ChIP-seq data from patient-derived B-ALL cells (bottom, LAX2, GSE58825). **n**, Human B-ALL cells (BV173) carrying *IKZF1* deletions were reconstituted with doxycycline-inducible IKZF1 or EV. Levels of IFITM3 were assessed by western blotting upon doxycycline-induction ( $n = 3$ ). **o**, Multivariate analysis of established risk factors in children with B-ALL (COG P9906,  $n = 207$ ) including mutation or deletion of *IKZF1*. Patients ( $n = 207$ ) were separated into *IKZF*<sup>+/+</sup> or *IKZF*-deleted groups, then further segregated based on higher or lower than median expression levels of *IFITM3*. The comparison of these four groups established *IFITM3* mRNA levels as an independent risk factor regardless of *IKZF1*-deletion status (two-sided log-rank test;  $P = 0.0045$ ). **c, d, n**, For gel source data, see Supplementary Fig. 1. [Source data](#)

**Extended Data Fig. 2 *Ifitm3* is essential for the development of B1 and germinal centre B cells.**

**a**, Hardy fractions of B cell subsets isolated from bone marrow of *Ifitm3*<sup>+/+</sup> and *Ifitm3*<sup>-/-</sup> littermates analysed by flow cytometry ( $n = 3$ ). **b**, Surface expression of IgM, CD20, CD19, IgD, CD2 and CD21 measured by flow cytometry in enriched bone marrow (GR1<sup>-</sup>, Nk1.1<sup>-</sup> and B220<sup>+</sup>) and splenic B cells (CD3<sup>-</sup> and B220<sup>+</sup>) from *Ifitm3*<sup>+/+</sup> or *Ifitm3*<sup>-/-</sup> mice ( $n = 7$ ; mean ± s.d.). Mean fluorescence intensities (MFI) values for individual measurement compared by two-tailed *t*-test. **c**, Ca<sup>2+</sup> mobilization from cytoplasmic stores in response to BCR (IgM) engagement was measured in *Ifitm3*<sup>+/+</sup> and *Ifitm3*<sup>-/-</sup> splenic B cells. Ca<sup>2+</sup> release was induced by addition of 10 µg ml<sup>-1</sup> anti-mouse IgM 60 s after acquisition of background fluorescence. Ca<sup>2+</sup> release was measured over 300 s with cell-permeant Rhod-2 dye; MFI compared between replicates ( $n = 3$ ). **d**, Ca<sup>2+</sup> mobilization in response to BCR engagement measured upon CRISPR–Cas9-mediated deletion of *IFITM3* in Jeko1 MCL cells. Ca<sup>2+</sup> release upon addition of 10 µg ml<sup>-1</sup> of polyclonal F(ab')<sub>2</sub> anti-human IgM was measured for 300 s with cell-permeant Fluo-4 dye; MFI compared between replicates (left;  $n = 3$ ). Surface expression of CD19 following deletion of *IFITM3* in Jeko1 MCL cells, MFIs for CD19 indicated (right;  $n = 3$ ). **e**, Jeko1 MCL cells were electroporated with non-targeting RNP (Cas9-gRNA ribonucleoproteins, gNT) or IFITM3-targeting RNP complex (gIFITM3). Following electroporation, MCL cells were treated with vehicle (DMSO) or 25 nmol l<sup>-1</sup> of dasatinib for 3 h. Cells were stimulated with 10 µg ml<sup>-1</sup> of anti-human IgM F(ab')<sub>2</sub> for the indicated time points and subjected to co-immunoprecipitation with an anti-CD19 antibody. Immunoblots were performed to measure levels of CD19 tyrosine phosphorylation and binding of LYN to CD19. Levels of IFITM3, SRC-pY<sup>416</sup> and LYN were assessed in whole-cell lysates (10% input) with β-actin as loading control. ( $n = 3$ ; gel source data in Supplementary Fig. 1). **f–h**, Relative fractions (left) and absolute cell counts (right) of total B1 (**f**) and B1a (**g**) cells in the peritoneal cavity and marginal-zone B cells (**h**) in spleen of *Ifitm3*<sup>+/+</sup> and *Ifitm3*<sup>-/-</sup> littermates ( $n = 5$ ) are shown (means ± s.d.; two-tailed *t*-test). [Source data](#)

**Extended Data Fig. 3 *Ifitm3*-deficient B-ALL cells exhibit an anergic phenotype and compensatory upregulation of *Ifitm1* and PI3K signalling molecules.**

**a**, Numbers of viable *Ifitm3*<sup>+/+</sup> and *Ifitm3*<sup>-/-</sup> *BCR-ABL1* or *NRAS*<sup>G12D</sup> B-ALL cells were counted by Trypan blue dye exclusion ( $n = 3$ ; mean  $\pm$  s.d.; two-tailed *t*-test). **b**, RNA sequencing was performed for *Ifitm3*<sup>+/+</sup> and *Ifitm3*<sup>-/-</sup> *BCR-ABL1* and *NRAS*<sup>G12D</sup> B-ALL cells. Relative rlog-normalized gene expression values for all strongly differentially expressed genes ( $P < 1 \times 10^{-5}$  and log<sub>2</sub>-transformed fold change  $> 1$ ; Wald test with Benjamini–Hochberg correction) in both *BCR-ABL1* and *NRAS*<sup>G12D</sup> conditions plotted as a heat map with row scaling. B-cell-signalling-related genes are labelled in red, anergy-related genes are labelled in blue and PI3K-signalling-related genes are labelled in grey. **c**, Gene set enrichment analysis for genes ranked by ratio of *Ifitm3*<sup>-/-</sup> to *Ifitm3*<sup>+/+</sup> as log<sub>2</sub>-transformed fold change; red lines indicate running enrichment score (right axis), grey bars indicate fold change (left axis). Statistical significance was determined by two-tailed Kolmogorov–Smirnov test. **d**, Patient-derived B-ALL cells (PDX2) were transduced with N-terminally Flag-tagged or C-terminally HA-tagged IFITM3 constructs. Combinations of intracellular and surface staining were performed to examine IFITM3 topology at the cell membrane. **e**, Patient-derived B-ALL cells (PDX2) were transduced with C-terminal HA-tagged IFITM3 or the IFITM3(Y20E) phosphomimetic. Combinations of intracellular and surface staining, with or without SRC-kinase inhibition by dasatinib, were performed to examine IFITM3 topology at the cell membrane and its regulation by SRC kinases. **d, e**, Representative plots from three independent experiments. **f**, A scenario of the topology of IFITM3 regulated by SRC (LYN) or oncogenic tyrosine kinases (BCR–ABL1) at the plasma membrane is shown. Phosphorylation of Y20 hinders the recognition of <sup>20</sup>YEM<sup>23</sup> endocytosis motif by the AP-2 complex, thereby antagonizing endocytosis and endosomal trafficking of IFITM3. [Source data](#)

## Extended Data Fig. 4 IFITM3 amplifies PI3K signalling downstream of BCR and integrin receptors.

**a**, Volcano plot of differentially phosphorylated proteins in patient-derived B-ALL (PDX2) cells transduced with IFITM3(Y20E) compared to empty vector (EV) control ( $n = 3$ ; Wald test with Benjamini–Hochberg correction). **b**, F(ab) fragments of the anti-HA antibody or isotype control were purified

and their identity confirmed by western blot (left). Eight million patient-derived B-ALL (PDX2) cells carrying IFITM3–HA, IFITM3(Y20E)–HA or EV control were resuspended in complete medium and treated with either 2.5 µg ml<sup>-1</sup> of full antibodies, F(ab) fragments of anti-HA or isotype control for the indicated times. Levels of AKT-pS<sup>473</sup>, AKT and HA-tagged IFITM3 were assessed by western blots using β-actin as loading control (right). Data from three independent experiments. For gel source data, see Supplementary Fig. 1. **c**, Ca<sup>2+</sup> mobilization in response to TCR engagement using CD3ε-specific antibodies was measured upon CRISPR–Cas9-mediated deletion of *IFITM3* in T-ALL cells (Jurkat) (left). Ca<sup>2+</sup> release from cytoplasmic stores was induced by adding 10 µg ml<sup>-1</sup> of monoclonal (OKT3) anti-human CD3ε at 50 s after acquisition of background fluorescence. Surface expression of CD3 was measured following deletion of IFITM3 in Jurkat cells (right). MFIs for CD3 are indicated.

Representative plots from three independent biological experiments are shown. MFI values for individual measurement were compared by two-tailed *t*-test. **d**, Surface proteins on *Ifitm3*<sup>+/+</sup> and *Ifitm3*<sup>-/-</sup> B-ALL cells were labelled with biotin and enriched with streptavidin affinity pull-down followed by on-bead trypsin digestion, mass spectrometry and quantified with label-free quantification. Differentially expressed cell surface proteins on *Ifitm3*<sup>+/+</sup> and *Ifitm3*<sup>-/-</sup> B-ALL cells are shown with the mean difference of label-free quantification plotted against the *P* value (Welch's *t*-test). All experiments were performed in biological triplicates. **e–g**, Validation of differential expression of surface receptors between *Ifitm3*<sup>+/+</sup>, *Ifitm3*<sup>-/-</sup> and *Ifitm3*<sup>Y20E</sup>-overexpressing B-ALL cells. Flow cytometry analyses show surface expression of BCR signalling components (**e**), integrins and adhesion receptors (**f**) and other surface receptors (**g**) in *Ifitm3*<sup>+/+</sup>, *Ifitm3*<sup>-/-</sup> and B-ALL cells expressing IFITM3(Y20E) (*n* = 3). [Source data](#)

### **Extended Data Fig. 5 Inducible membrane translocation of CD19 does not rescue defective SRC and PI3K signalling in *Ifitm3*-deficient B cells.**

**a**, Surface expression of CD19 was assessed by flow cytometry following forced expression of CD19 for >1 week in *Ifitm3*<sup>+/+</sup> and *Ifitm3*<sup>-/-</sup> B-ALL

cells. **b**, Western blot analyses of AKT-pS<sup>473</sup>, AKT, MYC and BCL2 upon forced expression of CD19 for >1 week in mouse *Ifitm3*<sup>+/+</sup> and *Ifitm3*<sup>-/-</sup> B-ALL cells. **c, d**, Colony-forming ability (**c**) and cell cycle progression (**d**) of *Ifitm3*<sup>+/+</sup> and *Ifitm3*<sup>-/-</sup> B-ALL cells upon forced expression of CD19 for >1 week was examined. **c**, Colony numbers for individual measurement were compared by two-tailed *t*-test. **d**, Numbers indicate percentage of cells in S phase. **e**, Numbers of viable *Ifitm3*<sup>+/+</sup> and *Ifitm3*<sup>-/-</sup> B-ALL cells following forced expression of CD19 were counted using the Trypan blue dye exclusion method (left). *Ifitm3*<sup>-/-</sup> B-ALL cells were transduced with GFP-tagged constructs for expression of CD19 with an intact (Y531) or mutant (Y531F) PI3K-activation motif in its cytoplasmic tail. Relative changes of GFP<sup>+</sup> cells (transduced with CD19 or CD19(Y531F)) were plotted over time (means ± s.d.). **a–e**, Data from three independent experiments. **b**, For gel source data, see Supplementary Fig. 1. **f**, Mouse *Cd19*<sup>-/-</sup> B-ALL clones were generated by electroporation of mouse B-ALL cells with CD19-targeting RNP (Cas9-gRNA ribonucleoproteins, gCd19 ALL) and single-cell clones with biallelic deletion were selected. *Cd19*<sup>-/-</sup> B-ALL cells were transduced with CD19-ER<sup>T2</sup>, a fusion of the ER-ligand binding domain to the C terminus of CD19, or ER<sup>T2</sup> as empty vector control. Reconstitution of *Cd19*<sup>-/-</sup> B-ALL cells with CD19-ER<sup>T2</sup> resulted in stable expression of the fusion proteins that were retained in complex with cytoplasmic heatshock proteins. Addition of 4-OHT released CD19-ER<sup>T2</sup> from its cytoplasmic heatshock chaperone and enable cell surface expression within 30 min of 4-OHT addition. **g**, To test the effect of inducible CD19 membrane translocation in *Ifitm3*<sup>-/-</sup> B-ALL cells, *Ifitm3*<sup>+/+</sup> and *Ifitm3*<sup>-/-</sup> B-ALL cells were transduced with CD19-ER<sup>T2</sup> or ER<sup>T2</sup> empty vector control. 4-OHT-mediated translocation of CD19 to the cell surface was assessed by flow cytometry for the indicated times (0 to 3 h). **h**, *Ifitm3*<sup>+/+</sup> and *Ifitm3*<sup>-/-</sup> B-ALL cells were transduced with CD19-ER<sup>T2</sup> or ER<sup>T2</sup> empty vector control. Cells were treated for 0, 1 and 3 h with 4-OHT for surface-translocation of CD19. Cell lysates from these populations were analysed by western blot for CD19-pY<sup>531</sup>, CD19, SRC-pY416, LYN, AKT-pS<sup>473</sup>, AKT, MYC and BCL2. While CD19-ER<sup>T2</sup> reconstitutes CD19 protein levels in *Ifitm3*<sup>-/-</sup> B-ALL cells and restores rapid translocation to the cell surface (**g**), this change alone was not sufficient to induce proper phosphorylation of CD19, SRC kinases and PI3K signalling via AKT. **f–h**, Data from three

independent experiments. **h**, For gel source data, see Supplementary Fig. 1.  
[Source data](#)

**Extended Data Fig. 6 IFITM3 links components of the BCR and integrin receptor pathways to PI3K signalling.**

**a**, Schematic of HA-tagged-IFITM3(Y20E)–BirA fusion proteins used for TurboID interactome analyses. BirA (biotin ligase) was fused to N-terminal IFITM3 carrying the phosphomimetic Y20E mutation for membrane localization. **b–d**, HA–IFITM3(Y20E)–BirA or HA–BirA controls were expressed in PDX2 B-ALL (**b**) or Jeko1 MCL cells (**c, d**). **c, d**, Cells were incubated with exogenous biotin for 10 min upon IFITM3 (anti-HA) or BCR (anti-IgM) engagement. IFITM3(Y20E) interactome analyses identified interacting proteins by mass spectrometry, plotted based on significance and log<sub>2</sub>-transformed fold enrichment over EV control. Essential interactors as BCR component (red), integrin (blue) and PI3K signalling (grey) are highlighted. Data from three independent biological replicates. **e**, PLAs were performed with Jeko1 MCL cells upon engagement of BCR. Jeko1 MCL cells were stimulated by BCR engagement for 0, 3 and 30 min, then fixed, permeabilized and assessed for the proximity of CD79B to IFITM3. Representative microscopic images with PLA signal (red dot) and nuclei stained with DAPI as blue are shown. LAMP1 was used as a marker for endosomes to distinguish plasma-membrane-bound from endosomal localization of CD79B:IFITM3 complexes. Scale bars, 5 μm. Data from three independent replicates.

[Source data](#)

**Extended Data Fig. 7 Ifitm3 functions as a central effector of B cell adhesion.**

**a**, Homotypic aggregation was studied in *Ifitm3*<sup>−/−</sup> B-ALL cells that were reconstituted with C-terminal HA-tagged IFITM3, IFITM3(Y20E) or empty vector (EV) and incubated with anti-CD19, anti-HA antibodies or isotype control for 24 h. Data from three independent experiments. **b**, *Ifitm3*<sup>+/+</sup> or *Ifitm3*<sup>−/−</sup> B-ALL cells were transduced with GFP-tagged IK6 or GFP alone. IK6 levels in flow-sorted GFP<sup>+</sup> cells assessed by western blot analysis

using β-actin as loading control (right). Ten thousand *Ifitm3*<sup>+/+</sup> or *Ifitm3*<sup>-/-</sup> B-ALL cells carrying IK6 or EV were plated for colony forming assays. Colonies were imaged and counted after 7 days. Representative images are shown with colony numbers. Data from three independent experiments and assessed by two-tailed *t*-test (means ± s.d.). For gel source data, see Supplementary Fig. 1. **c**, One hundred thousand *Ifitm3*<sup>+/+</sup> or *Ifitm3*<sup>-/-</sup> B-ALL cells carrying IK6 or EV were cultured on OP9 stroma cells. Ratios of adherent cells to nonadherent cells were calculated. Data from three independent biological experiments (right) were analysed and assessed by two-tailed *t*-test (means ± s.d.). **d**, Representative images of adherent B-ALL cells on OP9 stroma are shown. Round and light-refracting cells are adherent B-ALL cells attached to stroma cells. Dark and round cells are adherent B-ALL cells incorporated into stromal layer. Data from three independent biological replicates. **e**, Surface expression levels of integrins on adherent B-ALL cells were measured by flow cytometry. MFI values are indicated for individual measurements. Data from three independent biological replicates. [Source data](#)

## Extended Data Fig. 8 IFITM3 functions as a PIP3 scaffold and mediated cell-membrane stiffening upon BCR engagement.

**a**, SNACS was measured using a previously established microfluidic method as a metric for cell surface stiffness. Jeko1 mantle cell lymphoma cells were flown through a standing acoustic wave generated inside a vibrating suspended microchannel resonator. The cantilever vibration frequency was monitored, and its shift was used to quantify the acoustic scattering from the cells as well as the buoyant mass of the cells. The data displayed was obtained using a 350-μm-long cantilever with 15 × 20-μm-sized channel inside of the cantilever and an approximately 200-ms transit time through the cantilever. All the regulators, valves and data acquisition were controlled by custom software coded in LabVIEW 2017 (National Instruments). A parallel volume measurement using Coulter Counter was carried out to quantify average cell volume, which was used together with the single-cell buoyant mass measurements to calculate SNACS for each cell. Jeko1 mantle cell lymphoma cells without (*IFITM3*<sup>+/+</sup>) and with (*IFITM3*<sup>-/-</sup>) CRISPR–Cas9-mediated deletion of IFITM3 were kept under

cell culture conditions and treated with an anti-IgM antibody. Fixation with paraformaldehyde (PFA) was used as a positive control. Representative plots from three independent experiments are shown (median levels in red dotted line). Statistical significance was determined by two-tailed *t*-test. Numbers indicated cells studied for SNACS measurement. **b**, *Ifitm3*<sup>+/+</sup> and *Ifitm3*<sup>-/-</sup> B-ALL cells were incubated with 30 µM of the PIP3 carrier histone H1 or PIP3–histone H1 complex for 30 min. Levels of CD19-pY<sup>531</sup>, CD19, SRC-pY<sup>416</sup>, LYN, AKT-pS<sup>473</sup>, AKT and MYC were measured by western blot using β-actin as loading control. Data from three independent replicates. For gel source data, see Supplementary Fig. 1. **c**, Colony-formation assays were performed for *Ifitm3*<sup>+/+</sup> and *Ifitm3*<sup>-/-</sup> B-ALL cells that were treated with 30 µM of PIP3–histone H1 or the shuttle protein histone H1 (H1) alone. Photomicrographs and colony numbers per 10,000 plated cells are shown. Data are presented as means ± standard derivation (s.d.) from three independent experiments. Statistical significance was determined by two-tailed *t*-test. **d**, Flow cytometry analyses of surface expression of CD19, CD44, CD25 and CD44 on *Ifitm3*<sup>+/+</sup> and *Ifitm3*<sup>-/-</sup> B-ALL cells treated with 30 µM of PIP3–histone H1 or the shuttle protein histone H1 (H1) alone for 72 h. Data from three independent replicates.

[Source data](#)

## [Extended Data Fig. 9 Modelling of binding of IFITM3 to PIP2 and PIP3.](#)

**a–c**, The hierarchical scheme of molecular dynamics simulations to delineate the structural and dynamical basis of PIP2 and PIP3 binding to IFITM3 (yellow). **a**, Coarse grained simulations of IFITM3 in composite cell membrane. The side views of the lipid bilayer are shown. The lipid raft markers are shown in colour with GM1 (pink), cholesterol (green) and sphingomyelin (blue). The grey surface represents all the other lipids. **b**, The simulation cell extracted from the coarse grained simulation as the starting structure for all-atom molecular dynamics simulations. The IFITM3 protein is shown in yellow and the PIP2 and PIP3 are shown in green and red stick representations. **c**, Close up view of one of the predicted binding poses of PIP2 and PIP3 in the most populated conformation of IFITM3. The dashed lines shown are the PIP2 or PIP3 contacts with the basic residues in

IFITM3 (top). The amino acid sequence of IFITM3 in the stretch of residues between TM1 and TM2 from 57 to 128 modelled in this work is shown. The CIL region is boxed and basic amino acids are highlighted with blue. The average interaction energy of PIP2 or PIP3 with the two basic batches measured in all-atom molecular dynamics simulations is indicated (Supplementary Table 6). **d**, **e**, The average interaction energy of PIP2 (green) or PIP3 (red) with IFITM3 (residues 57–128) was measured in all-atom molecular dynamics simulations. The one-residue contact indicates the conformation of PIP2 or PIP3 binding with only one basic residue in the basic amino patch KSRDRK of IFITM3. The two-residue contact refers to the binding conformation of PIP2 or PIP3 that show contacts with two basic residues. Representative plots from at least four independent experiments are shown (mean ± s.d.). In **d**, *P* values were determined by two-tailed *t*-test. Populations showing one- or two-residue contacts of PIP2 (green) or PIP3 (red) to IFITM3 were quantitated from all-atom molecular dynamics simulations. The population density was assessed by the normalization of number of events with the total number of frames. Representative plots from three independent experiments are shown (mean ± s.d.). In **e**, statistical significance was determined by two-tailed *t*-test. [Source data](#)

### [Extended Data Fig. 10 IFITM3-mediated PI3K signalling downstream of BCR and integrin receptors depends on K83–K104 but not on R85, R87 and K88 residues.](#)

**a–c**, Levels of differentially phosphorylated proteins in patient-derived B-ALL (PDX2) cells transduced with IFITM3(Y20E), IFITM3(Y20E/K83A), IFITM3(Y20E/R85A) or empty vector (EV) control were identified by mass spectrometry ( $n = 3$ ). Relative abundance values are plotted for all sites ranked by fold change as indicated; phosphosites of interest are highlighted. **b**, FSEA ranked by  $\log_2$ -transformed fold change are shown for phosphosites in PI3K signalling (grey), BCR signalling (red) and integrin and adhesion receptor elements (blue). Statistical significance was determined by two-tailed Kolmogorov–Smirnov test. **d**, Cumulative distribution frequencies for  $\log_2$ -transformed fold changes in phosphosite abundance between IFITM3-transduced and EV conditions were calculated for all sites and globally increased in IFITM3(Y20E) over EV. The analysis

was repeated for the K83A (red) and R85A (green) mutants of IFITM3. The light grey line indicates background variance observed between EV replicates. Shifts that were caused by the K83A and R85A mutants are indicated by arrows. Overall changes in distribution (shifts) between IFITM3(Y20E) and IFITM3(Y20E/K83A) and IFITM3(Y20E/R85A) mutants were measured by two-tailed Kolmogorov–Smirnov test. **e**, Schematic of BirA (engineered biotin ligase) was fused at N-terminal ends of HA-tagged IFITM3(Y20E) or its K83A mutant and expressed in PDX2 B-ALL or Jeko1 MCL cells. **e–g**, Interactomes of IFITM3(Y20E) and its K83A mutant were compared in PDX2 B-ALL cells upon IFITM3 engagement (anti-HA) (**e**) or in Jeko1 MCL cells upon IFITM3 (anti-HA) (**f**) or BCR (anti-IgM) (**g**) engagement. Phosphosites of interest, including BCR signalling, PI3K signalling and integrins and adhesion receptor elements are highlighted. [Source data](#)

## Supplementary information

### [Supplementary Tables](#)

This file contains Supplementary Tables S1-S12.

### [Reporting Summary](#)

### [Supplementary Figure](#)

Supplementary Figure 1: Source Data (Immunoblots).

## Source data

### [Source Data Fig. 1](#)

### [Source Data Fig. 2](#)

### [Source Data Fig. 3](#)

[Source Data Fig. 4](#)

[Source Data Extended Data Fig. 1](#)

[Source Data Extended Data Fig. 2](#)

[Source Data Extended Data Fig. 3](#)

[Source Data Extended Data Fig. 4](#)

[Source Data Extended Data Fig. 5](#)

[Source Data Extended Data Fig. 6](#)

[Source Data Extended Data Fig. 7](#)

[Source Data Extended Data Fig. 8](#)

[Source Data Extended Data Fig. 9](#)

[Source Data Extended Data Fig. 10](#)

## Rights and permissions

[Reprints and Permissions](#)

## About this article



Check for  
updates

## Cite this article

Lee, J., Robinson, M.E., Ma, N. *et al.* IFITM3 functions as a PIP3 scaffold to amplify PI3K signalling in B cells. *Nature* **588**, 491–497 (2020).  
<https://doi.org/10.1038/s41586-020-2884-6>

## [Download citation](#)

- Received: 11 September 2019
- Accepted: 13 August 2020
- Published: 04 November 2020
- Issue Date: 17 December 2020
- DOI: <https://doi.org/10.1038/s41586-020-2884-6>

## Comments

By submitting a comment you agree to abide by our [Terms](#) and [Community Guidelines](#). If you find something abusive or that does not comply with our terms or guidelines please flag it as inappropriate.

## [Download PDF](#)

---

This article was downloaded by **calibre** from <https://www.nature.com/articles/s41586-020-2884-6>

Structures and distributions of SARS-CoV-2 spike proteins on intact virions  
[Download PDF](#)

- Article
- [Published: 17 August 2020](#)

# Structures and distributions of SARS-CoV-2 spike proteins on intact virions

- [Zunlong Ke](#) [ORCID: orcid.org/0000-0002-8408-850X](#)<sup>1 na1</sup>,
- [Joaquin Oton](#) [ORCID: orcid.org/0000-0002-2195-4730](#)<sup>1 na1</sup>,
- [Kun Qu](#)<sup>1 na1</sup>,
- [Mirko Cortese](#) [ORCID: orcid.org/0000-0003-1786-4211](#)<sup>2</sup>,
- [Vojtech Zila](#) [ORCID: orcid.org/0000-0003-2032-3600](#)<sup>3</sup>,
- [Lesley McKeane](#)<sup>4</sup>,
- [Takanori Nakane](#) [ORCID: orcid.org/0000-0003-2697-2767](#)<sup>1</sup>,
- [Jasenko Zivanov](#)<sup>1</sup>,
- [Christopher J. Neufeldt](#) [ORCID: orcid.org/0000-0002-4551-1811](#)<sup>2</sup>,
- [Berati Cerikan](#)<sup>2</sup>,
- [John M. Lu](#) [ORCID: orcid.org/0000-0002-3972-8854](#)<sup>1</sup>,
- [Julia Peukes](#)<sup>1</sup>,
- [Xiaoli Xiong](#) [ORCID: orcid.org/0000-0002-4632-9122](#)<sup>1</sup>,
- [Hans-Georg Kräusslich](#)<sup>3,5</sup>,
- [Sjors H. W. Scheres](#) [ORCID: orcid.org/0000-0002-0462-6540](#)<sup>1</sup>,
- [Ralf Bartenschlager](#) [ORCID: orcid.org/0000-0001-5601-9307](#)<sup>2,5,6</sup> &
- [John A. G. Briggs](#) [ORCID: orcid.org/0000-0003-3990-6910](#)<sup>1</sup>

[Nature](#) volume 588, pages498–502(2020)[Cite this article](#)

- 44k Accesses
- 23 Citations
- 542 Altmetric
- [Metrics details](#)

## Subjects

- [Cryoelectron microscopy](#)
- [Cryoelectron tomography](#)
- [SARS-CoV-2](#)

## Abstract

Severe acute respiratory syndrome coronavirus 2 (SARS-CoV-2) virions are surrounded by a lipid bilayer from which spike (S) protein trimers protrude<sup>1</sup>. Heavily glycosylated S trimers bind to the angiotensin-converting enzyme 2 receptor and mediate entry of virions into target cells<sup>2,3,4,5,6</sup>. S exhibits extensive conformational flexibility: it modulates exposure of its receptor-binding site and subsequently undergoes complete structural rearrangement to drive fusion of viral and cellular membranes<sup>2,7,8</sup>. The structures and conformations of soluble, overexpressed, purified S proteins have been studied in detail using cryo-electron microscopy<sup>2,7,9,10,11,12</sup>, but the structure and distribution of S on the virion surface remain unknown. Here we applied cryo-electron microscopy and tomography to image intact SARS-CoV-2 virions and determine the high-resolution structure, conformational flexibility and distribution of S trimers *in situ* on the virion surface. These results reveal the conformations of S on the virion, and provide a basis from which to understand interactions between S and neutralizing antibodies during infection or vaccination.

[Download PDF](#)

## Main

The *Betacoronavirus* SARS-CoV-2<sup>13,14</sup> is an enveloped virus containing a large nucleoprotein (N)-encapsidated positive-sense RNA genome<sup>15</sup>. Three transmembrane proteins are incorporated into the viral lipid envelope: S and two smaller proteins, membrane protein (M) and envelope protein (E)<sup>1,15</sup>. When imaged by cryo-electron microscopy (cryo-EM), betacoronaviruses appear as approximately spherical particles with variable diameters centred around 100 nm, containing a dense viroplasm and bounded by a lipid bilayer from which prominent S trimers protrude<sup>16,17</sup>. S trimers of SARS-CoV-2 bind to its receptor on the surface of target cells—angiotensin-converting enzyme 2 (ACE2)—and mediate subsequent viral uptake and fusion<sup>2,3,4,5,7</sup>. In so doing, S undergoes a substantial structural rearrangement from the prefusion form to the postfusion form<sup>8</sup>. The overall

architectures of both prefusion and postfusion forms are highly conserved among coronaviruses<sup>8,18,19</sup>.

During infection, coronaviruses extensively remodel the internal membrane organization of the cell, generating viral replication organelles in which replication takes place<sup>20,21,22</sup>. The S, M and E proteins are inserted into membranes of the endoplasmic reticulum and traffic to the endoplasmic reticulum–Golgi intermediate compartment (ERGIC). The encapsidated genome buds into the ERGIC to form virions, which are then trafficked to the plasma membrane and released<sup>20,21,22</sup>. S is primed for membrane fusion by proteolytic cleavage at the S1–S2 site, and subsequently the S2' site<sup>23</sup>.

The prefusion structures of S proteins from coronaviruses, including SARS-CoV-2 S, have been extensively studied using ectopic expression of soluble, secreted forms of S, followed by purification and cryo-EM<sup>2,7,9,10,11</sup>. In the prefusion form, the receptor-binding domain (RBD) sits at the top of a broad, trimeric spike above the fusion core. Three copies of the RBD are surrounded by three copies of the N-terminal domain (NTD) which display some mobility<sup>2,7,8,9</sup>. In the closed prefusion conformation, all three copies of the RBD lie flat on the spike surface, largely occluding the receptor-binding site, whereas in the open prefusion conformation, one or multiple RBDs lift to expose the receptor-binding site<sup>2,7,9,10</sup>. The surface of the trimer is extensively glycosylated with 22 potential N-linked glycosylation sites per monomer<sup>2,6,7</sup>. After receptor binding, structural transition of the prefusion form to the postfusion form brings the fusion peptide and the transmembrane domain together at one end of a long, needle-like structure centred around a three-helix bundle<sup>8</sup>. Five N-linked glycans are spaced along the length of the postfusion spike<sup>8</sup>.

Fully understanding how S proteins function and how they interact with the immune system requires knowledge of the structures, conformations and distributions of S trimers within virions. In this study, we apply cryo-EM methods to study the structure, conformations and distributions of S trimers *in situ* on the virion surface.

To avoid artefacts associated with virus concentration or purification, we aimed to image SARS-CoV-2 virions from the supernatant of infected cells without further concentrating or purifying the virus. Vero E6 cells were infected with SARS-CoV-2 (isolate Germany/BavPat1/2020)<sup>24</sup>. At 48 h after infection, the supernatant was clarified, inactivated by fixation with formaldehyde and stored at –80 °C. Western blot analysis revealed that approximately 45% of the total S protein monomers on virions had been cleaved at the multibasic cleavage site, resulting in S1 and S2 peptides (Fig. 1a). The fixed supernatant was vitrified by plunge freezing and imaged by cryo-EM. Fixation may help to stabilize some protein conformations by

crosslinking, but is not expected to give rise to any new conformations. As expected, given the concentration of virus in cellular supernatants (around  $10^7$  plaque-forming units per ml), small numbers of individual virions were found scattered around the grid—these were imaged by cryo-electron tomography (cryo-ET) (Fig. [1b](#)).

**Fig. 1: Characterization of virus production and images of SARS-CoV-2 virions.**



[figure1](#)

**a**, Western blot analysis of SARS-CoV-2 non-structural protein 3 (nsp3), S and N in lysates of Vero E6 cells and in virus preparations, representative of three experiments. In released virions, S is present in both cleaved and uncleaved forms. The positions of S<sub>0</sub>, S<sub>2</sub> and the S<sub>2</sub>–S<sub>2'</sub> cleavage product are marked. **b**, Four representative tomographic slices of SARS-CoV-2 virions from the supernatant of infected cells. Virions are approximately spherical, contain granular density corresponding to N-packaged genome, and have S trimers protruding at variable angles from their surfaces. Scale bar, 50 nm. **c**, Three S trimers from the dataset, shown as projections through the trimer to illustrate variable tilt towards the membrane. Scale bars, 10 nm.

[Full size image](#)

Virions were approximately spherical, with a diameter to the outside of the lipid bilayer of  $91 \pm 11$  nm ( $n = 179$ ) (Extended Data Fig. [1a](#)). They contained granular

densities corresponding to N, and were studded with S trimers (Fig. 1b,c). These features are generally consistent with those of other coronaviruses imaged using cryo-EM<sup>1,16,17</sup>. S trimers protruding from the viral surface displayed two distinct morphologies—a minority were extended thin structures reminiscent of the postfusion form, whereas the majority were wider structures reminiscent of the prefusion form. This observation is in contrast to a study showing cryo-EM images of purified SARS-CoV-2 virions inactivated with the nucleic acid modifier  $\beta$ -propiolactone, in which only thin protrusions were seen on the viral surface<sup>25</sup>, but is consistent with in situ observations of virus assembly<sup>21</sup>.

We also collected tomograms of SARS-CoV-2 virions produced by infection of Calu-3 cells, a human lung carcinoma cell line that supports virus production with a similar titre to Vero E6 cells. The morphology of the virions and the appearance of the S trimers on the surface were consistent with those for virions produced from Vero E6 cells (Extended Data Fig. 2a–c). Western blot analysis showed that approximately 73% of S from Calu-3 supernatant was in the cleaved form (Extended Data Fig. 2d).

Individual virions contained  $24 \pm 9$  S trimers (Extended Data Fig. 1b). This is fewer than previous estimates that assumed a uniform distribution of S<sup>21</sup>, because S was not uniformly distributed over the virus surface. A small sub-population of virions contained only few S trimers whereas larger virions contained higher numbers of S trimers (Extended Data Fig. 1b). We identified 4,104 wide-structure S trimers and 116 thin-structure S trimers from 179 virions and analysed them using subtomogram averaging. The averaged structures, at 7.7 and 22 Å resolution, respectively, correspond closely to published structures of purified S trimers in the prefusion and postfusion forms<sup>2,7,8</sup> (Fig. 2a). Overall, approximately 97% of S trimers were in the prefusion form and 3% were in the postfusion form. Prefusion and postfusion forms were evenly distributed among virions.

**Fig. 2: Structural analysis of SARS-CoV-2 S trimers on intact virions.**

 **figure2**

**a**, Structures of prefusion (left) and postfusion (right) trimers from intact virions, determined by subtomogram averaging. Structures are shown as transparent grey isosurfaces fitted with structures of the closed, prefusion trimer (Protein Data Bank (PDB) 6VXX) and the postfusion trimer (PDB 6XRA). One prefusion monomer is coloured blue (N terminus) to red (C terminus). The NTD is blue, the RBD is cyan. The NTD does not fully occupy the cryo-EM density because some loops are not resolved or built in the template structure (PDB 6VXX). **b**, Three conformations of

the prefusion trimer observed on intact virions: all RBDs in the closed position (left, fitted with PDB 6VXX); one RBD in the open position (centre, fitted with PDB 6VYB); two RBDs in the open position (right, fitted with PDB 6X2B, which lacks modelled glycans). The two-open conformation has only been observed in vitro after inserting multiple stabilizing mutations. S monomers with closed RBDs are green, and those with open RBDs are blue. **c**, Averaging of subsets of trimers grouped according to their orientation relative to the membrane shows flexibility in the stalk region. Examples are shown for pools centred at 0°, 30° and 60° from the perpendicular, and for two rotations of the trimer relative to the tilt direction. **d**, Three-dimensional models of two individual SARS-CoV-2 virions with a membrane (blue) of the measured radius, and all spike proteins shown in the conformations, positions and orientations determined by subtomogram averaging. Different S conformations are distributed over the virion surface and can be tilted by up to approximately 90° relative to the membrane (Extended Data Fig. [1c,d](#)).

[Full size image](#)

Prefusion S trimers on the virus surface may be predominantly in the closed conformation, with the open conformation induced or stabilized only with ACE2 binding; alternatively, both closed and open prefusion trimers may be present in the absence of ACE2. Open or closed conformations may induce different antibody responses when used as immunogens, and there are ongoing efforts to generate S protein constructs that are stabilized in specific conformations [9,11,12](#). To assess whether S trimers are present in open and/or closed conformations, we classified the RBD regions of individual monomers within trimers. We identified three classes of RBD, one with the RBD in the closed position, one with the RBD in the open position, and one in which the RBD was predominantly in the closed position, but showed some weakening of the density, suggesting the presence of more mobile conformations (Extended Data Fig. [3](#)). On the basis of our assignment of individual monomers to these classes, we derived structures of fully closed trimers and of trimers in which one RBD was open, representing approximately 31% and 55% of 3,854 prefusion trimers, respectively (Fig. [2b](#), Extended Data Fig. [4](#)). We also identified a small number of trimers (around 14% of 3,854 prefusion trimers) in which two RBDs were in the open conformation (Fig. [2b](#)). These observations confirmed that the opening of the RBD observed in recombinant S trimers also takes place on the virus surface, and that artificial S protein constructs stabilized in the closed and open conformations both represent structures present in situ. The receptor-binding site is therefore stochastically exposed in situ and available to interact with ACE2 and with antibodies.

The trimers did not all protrude perpendicularly from the viral surface. They were tilted by up to 90° towards the membrane, although the frequency of observed tilt angles decreased above 50° (Extended Data Fig. 1c, d). We grouped trimers according to their orientation relative to the membrane, and averaged these groups independently. The averaged structures reveal that the membrane-proximal stalk region acts as a hinge with sufficient flexibility to allow tilting in all directions (Fig. 2c).

We generated models of individual virus particles, with S trimers located at the position, orientation and conformation that were determined by subtomogram averaging (Fig. 2d). S trimers appear to be distributed randomly on the viral surface, with no obvious clustering or relationship between location, orientation and conformation. There is approximately one trimer per 1,000 nm<sup>2</sup> of membrane surface, compared with approximately one per 100 nm<sup>2</sup> for influenza A virus<sup>26</sup>. The sparse distribution of S, together with the predominantly closed state, suggest that receptor binding may be less dependent on avidity effects than in the case of pandemic influenza viruses<sup>27</sup>. This is consistent with the higher affinity between S and ACE2 (in the nM range<sup>27</sup>) than between haemagglutinin and sialic acid (mM range<sup>27</sup>).

The low concentration of particles in supernatant makes high-resolution structure determination difficult. We therefore concentrated the virus by pelleting through a sucrose cushion. Concentrated virions deviated from the spherical morphology (Extended Data Fig. 5), but the overall features were preserved. We performed cryo-ET and subtomogram averaging on the particles and observed predominantly prefusion S trimers, with occasional postfusion S trimers. Upon classification of the prefusion S trimers, we were able to identify the RBD only in the closed position; weak RBD density was observed in monomers (Extended Data Fig. 3c).

Virions in the supernatant from infected cells exhibited primarily prefusion S trimers in either closed or open prefusion conformations. Virions concentrated through a sucrose cushion also exhibited prefusion conformations, but we did not observe the open conformation. Previous studies have shown that virions inactivated with β-propiolactone rather than formaldehyde are primarily in a postfusion state<sup>25</sup>. S trimers purified from membranes are found only in the closed prefusion and postfusion conformations<sup>8</sup>, whereas the open RBD in soluble S trimers has been found to exhibit a wide range of different conformations<sup>28</sup>. These observations suggest that the open prefusion conformations of the spike protein that we observed before, but not after concentration, are fragile (despite the fixation applied here) and may be affected by the purification procedures.

Our data indicate that inactivation and purification methods can alter the ratio of prefusion and postfusion forms, as well as the ratio of open and closed conformations. It has been suggested that substantial amounts of postfusion S on the virus surface may protect the virus by shielding the prefusion form, or may shift the host response towards non-neutralizing antibodies<sup>8</sup>. Our observation that intact virions harbour only a small fraction of postfusion spikes suggest that this is unlikely to be an important defence mechanism for the virus during infection, but it may be an important consideration for vaccination. Candidate vaccines based on inactivated virus particles are under development. These may present different S protein epitopes to the immune system depending on how they are prepared, and may therefore differ in their ability to induce a neutralizing response. For example,  $\beta$ -propiolactone is frequently used in vaccine production (such as for influenza virus subunit vaccines<sup>29</sup>), but if postfusion S induces non-neutralizing responses,  $\beta$ -propiolactone may not be optimal for inactivation during SARS-CoV-2 S vaccine formulation.

We next imaged the concentrated virus in 2D using cryo-EM and performed single-particle analysis on prefusion S trimers that protruded from the sides of the virus particles, generating a consensus structure of the prefusion trimer at 3.4 Å resolution. Focused classification with partial signal subtraction on individual RBD monomers led to two classes (Extended Data Fig. 5). Consistent with the absence of open conformations in this sample in cryo-ET images, 81% of the monomers showed the RBD in the closed conformation and 19% showed weaker density for the RBD, which remained predominantly in the closed position. We refined the structures of S trimers in which all three RBDs are in the closed conformation (53% of the data), and those in which at least one RBD has weak density (47% of the data), to resolutions of 3.5 Å and 4.1 Å, respectively (Fig. 3a, Extended Data Fig. 6). The two structures are highly similar, differing only in the density levels for one RBD. We used the structure with three closed RBDs to build and refine an atomic model of the S protein trimer *in situ* on the viral surface.

**Fig. 3: Structures of SARS-CoV-2 S trimers on intact virions by single-particle reconstruction.**

 **figure3**

**a**, Top and side views of trimers with three closed RBDs (left, 3.5 Å resolution) and one RBD with weaker density (right, 4.1 Å resolution). Individual monomers are coloured white, blue and green. Comparison of the left and right structures shows

the weaker density for the RBD of the green monomer in the region indicated by the red arrowheads. **b**, Glycosylation profile of the S protein. Colour scheme as in **a**; glycans are shown in orange. Boxes indicates the regions shown in **c** and **d**. **c**, Enlarged view of the base of the trimer at lower isosurface threshold to highlight the glycan ring and the extended C-terminal density. **d**, Enlarged view of the region of the spike where the D614G variation abolishes a salt bridge to K854.

[Full size image](#)

The positions of glycans on the surface of S are well resolved in our structure, with density at 17 of the 22 predicted N-glycosylation sites (Fig. 3b). The other five glycosylation sites are in disordered NTD loops or in the stalk region and are not resolved at high resolution. At the base of the trimer, a clear ring of glycans forms a collar above the stalk region. The density for the stalk region is extended by two helical turns compared with published structures of soluble ectodomain, and further at lower resolution before fading owing to stalk flexibility (Fig. 3c). SARS-CoV-2 S trimers are sparsely distributed and can be highly tilted towards the membrane. This implies that epitopes at the base of the head domain and in the stalk region would be accessible to antibodies where they are not protected by the extensive glycan shell.

We compared the *in situ* structure of the S trimer with structures previously obtained using exogenously expressed purified protein. A recent study of full-length trimeric S solubilized in detergent micelles<sup>8</sup> identified two features that are not seen in most structures of soluble S ectodomain trimers: well-defined density for residues 14–26 of S, and a folded loop between residues 833 and 853. This loop is folded in the structure of the ‘locked’ conformation of the ectodomain<sup>9</sup>, and may become folded in the low-pH conditions in the endosome<sup>30</sup>. We observed only weak density for residues 14–26, and no folded structure for the 833–853 region. The SARS-CoV-2 strain that we have imaged contains the widely circulating D614G substitution<sup>31</sup>, which abolishes a salt bridge to K854 (Fig. 3d) and may reduce folding of the 833–854 loop<sup>9,30</sup>. We did not observe additional density that would correspond to bound lipids, as described recently<sup>10</sup>, or other bound co-factors. These may be present sub-stoichiometrically or in rare conformations, but are not a general feature of the S trimer *in situ*. Overall, our structure is very similar to that of the soluble trimeric ectodomain in the closed prefusion form stabilized by a double proline mutation<sup>2,7</sup> (Extended Data Fig. 7). This validates the ongoing use of recombinant, purified S trimers for research, diagnostics and vaccination—they indeed represent the *in situ* structure of S. In this study, we have determined the structure of S trimers on the virion surface to 3.4 Å resolution using cryo-EM (Fig. 3), supporting the further use of this technique to study antibody binding to S in the context of the viral surface. Such studies could provide insights into how neutralizing antibodies block virus

infection, particularly for antibodies against membrane-proximal regions of S, and thus can inform the design of immunogens for vaccination.

## Methods

No statistical methods were used to predetermine sample size. For Cryo-ET, division of dataset into two random halves was done based on virus number. For Cryo-EM, division of datasets into two random halves was done based on the standard approach in RELION 3. Other experiments did not involve randomization. The investigators were not blinded to allocation during experiments and outcome assessment.

### Cells and virus

Vero E6 cells were obtained from ATCC and were cultured in Dulbecco's modified Eagle medium (DMEM, Life Technologies) containing 10% fetal bovine serum, 100 U ml<sup>-1</sup> penicillin, 100 µg ml<sup>-1</sup> streptomycin and 1% non-essential amino acids (complete medium). The Germany/BavPat1/2020 SARS-CoV-2 strain was isolated by C. Drosten (Charité, Berlin, distributed by the European Virology Archive (Ref-SKU: 026V-03883)) at passage (P)2. A stock of SARS-CoV-2 was obtained by passaging the virus once in Vero E6 cells (P3). To produce SARS-CoV-2 virions, Vero E6 cells grown on 75 cm<sup>2</sup> side-bottom tissue culture flasks were infected with SARS-CoV-2 (P3) at a multiplicity of infection (MOI) of 0.5. Culture medium from infected cells was collected at 48 h after infection, clarified by centrifugation at 1,000g for 10 min, cleared through a 0.45-µm nitrocellulose filter and fixed with 4% formaldehyde for 30 min at room temperature. Culture medium was supplemented with 10 mM HEPES (pH 7.2) before fixation. Virus-containing medium was subsequently split into aliquots and stored at -80 °C. Infectious supernatants containing SARS-CoV-2 virions were obtained from Calu-3 cells infected with P3 virus at an MOI of 5 for 48 h and processed as described above.

To obtain SARS-CoV-2 virions at high concentration, infection and collection of Vero E6 culture medium were performed as above, followed by concentration of fixation-inactivated virions from medium by ultracentrifugation through a 20% (wt/wt) sucrose cushion (120 min at 27,000 rpm in a Beckman SW32 rotor; Beckman Coulter Life Sciences). Pelleted particles were resuspended in PBS and stored in aliquots at -80 °C.

### Western blot

Vero E6 or Calu-3 cells mock infected or infected for 48 h with SARS-CoV-2 (MOI = 5) were washed twice in PBS, scraped, pelleted at 700g for 5 min and lysed in PBS pH 7.4, containing 1% Triton X-100 and protease inhibitors (Merck) for 30 min at 4 °C. Samples were centrifuged at 4 °C for 30 min and supernatants were collected. Total protein concentration was calculated using the Bio-Rad Protein Assay kit (Bio-Rad). Purified viruses were prepared for western blot by centrifugation of 32 ml of virus containing supernatants on a 10% sucrose cushion in a Beckmann J25 centrifuge. Centrifugation was performed at 10,000g for 4 h at 4 °C. Supernatants were discarded and purified virus pellet were resuspended in 500 µl PBS. For western blotting, 10 µg of total cell lysates and 5 µl purified viruses were diluted in Laemmli buffer and loaded on a pre-cast Criterion XT 4–12% gradient gel (Bio-Rad). Gels were transferred to PVDF membrane using a wet-electroblotting chamber system (Bio-Rad) in Towbin buffer containing 10% methanol. Transfer was performed overnight at 4 °C. Membranes were washed in PBS and blocked with 10% milk in PBS containing 0.2% tween-20 (PBS-T) for 1 h. Membranes were incubated for 1 h at room temperature with primary antibodies specific for an epitope in the C-terminal region of S (Abcam, ab252690; diluted 1:1,000 in PBS-T), for N protein (Sino Biological, 40143-MM05; diluted 1:1,000 in PBS-T) or nsp3 (Abcam, ab181620; diluted 1:500 in PBS-T). Next, the membranes were washed 3 times in PBS-T, incubated with horseradish peroxidase-conjugated anti-mouse or anti-rabbit antibodies at 1:10,000 dilution for 1 h, washed again 3 times in PBS-T, incubated with western Lightning Plus-ECL reagent (Perkin Elmer) and imaged using an Intas ChemoCam Imager 3.2 (Intas). Densitometric analysis of western blot assays was performed using LabImage 1D L340 software v.4.1 (Intas). The blot shown is representative of three independent experiments. Uncropped, unprocessed blots are presented in the Source Data.

## PCR with reverse transcription and spike sequencing

Total RNA was isolated from infected Vero E6 cells 48 h after infection with Germany/BavPat1/2020 SARS-CoV-2 (P2). Spike cDNA was produced from the total RNA using Superscript III (ThermoFisher) with specific reverse transcription primer (CAATTGTGAAGATTCTCATA). The cDNA was amplified by PCR using specific primers (Fwrd, ATGTTGTTTCTTGTTTATT; rev, TTATGTGTAATGTAATTGA) and the resulting amplicon was sent for Sanger sequencing. Sequences were compared to the Germany/BatPat1/2020 SARS-CoV-2 reference sequence (Ref-SKU: 026V-03883) and found to be identical. Specific sequencing primers: Fwrd1, ATGTTGTTTCTTGTTTATT; Fwrd2, GGTTGGACAGCTGGTGC; Fwrd3, CCAACCATACAGAGTAGTAGTA; Rev1, GTAGCAGCAAGATTAGCAGAA; and Rev2, TTATGTGTAATGTAATTGA.

## Cryo-ET sample preparation

Fixed virus samples from the supernatant of infected cells without any concentration step (unconc) or concentrated by pelleting through a sucrose cushion (conc) were prepared, imaged, and processed in parallel. The virus suspension was mixed with 10-nm colloidal gold (in PBS solution) in 10:1 ratio. Then, 3  $\mu$ l of the solution was added to a glow-discharged copper grid (C-Flat 2/2, Protochips). Grids were plunge frozen into liquid ethane by back-side blotting using a LeicaGP cryo plunger (Leica) and stored in liquid nitrogen until imaging.

## Cryo-ET data collection

Cryo-ET data collection was performed essentially as described previously<sup>32</sup>. Cryo-grids were loaded into an FEI Titan Krios transmission electron microscope operated at 300 kV and images were recorded on a Gatan K2 Summit direct detection camera in counting mode with a 20 eV energy slit in zero-loss mode. Tomographic tilt series between  $-60^\circ$  and  $+60^\circ$  were collected using SerialEM 3.8.0 software<sup>33</sup> in a dose-symmetric scheme<sup>34</sup> with a  $3^\circ$  angular increment. A total dose of  $120 \text{ e}^- \text{ Å}^{-2}$  per tilt series was distributed evenly among 41 tilt images. The nominal magnification was 81,000 $\times$ , giving a pixel size of 1.532 Å on the specimen. The defocus range was between  $-2 \mu\text{m}$  and  $-6 \mu\text{m}$  and 10 frames were saved for each tilt angle. All data acquisition parameters are listed in Extended Data Table 1.

Frames were motion-corrected in IMOD 4.10.30<sup>35</sup> and images were dose-filtered using the alignframes function in IMOD. Exposure filtering was implemented according to the cumulative dose per tilt as described elsewhere<sup>36</sup>. The contrast transfer function (CTF) was measured using non-dose-filtered images using the ctfplotter package within IMOD<sup>37</sup>. Tilt series stacks were sorted using IMOD newstack function and fiducial-alignment of all tilt series was performed in IMOD/etomo. Tomograms with less than three trackable gold fiducials were discarded. Motion-corrected and dose-filtered tilt stacks were CTF-corrected by CTF multiplication and tomograms were reconstructed by weighted back-projection in novaCTF<sup>38</sup>. Tomograms were low-pass filtered to 50 Å for better visualization in EMAN2.2<sup>39</sup> and tomographic slices were visualized with IMOD.

## Extraction of S trimers from tomograms

The initial steps of subtomogram alignment and averaging were implemented using MATLAB (MathWorks) scripts, which were derived from the TOM<sup>40</sup> and AV3<sup>41</sup> packages as described previously<sup>32</sup>. The missing wedge was modelled as the

summed amplitude spectrum of background subtomograms for each tomogram, and was applied during alignment and averaging.

To generate an initial template model of the spike protein from the viral surface, 68 spikes were manually picked from four virions of tomograms that were down-scaled by 4 $\times$  binning of the voxels. The 68 spikes' initial Euler angles (2 out of 3) were determined on the basis of the vector between two points, one on the head of the spike and one on the membrane where the spike anchors, respectively. The 68 spikes were iteratively aligned to one another for four iterations, applying three-fold symmetry to generate a low-resolution template that resembled a prefusion conformation of the spike. This template was used as an alignment reference for all virions (below). All postfusion spikes were manually identified and picked, and initial Euler angles were assigned in the same manner.

The centre of each virion was then marked manually using the Volume Tracer function in UCSF Chimera (v.1.13.1)<sup>42</sup> and the radius of the virion was determined centred at the membrane using the Pick Particle Chimera Plugin<sup>43</sup>. An oversampled spherical grid of points was generated on the virion surface with ~9 nm spacing, and subtomograms were extracted for all grid points with a box size of 96 pixels (approximately 60 nm) centred at a radius 14 nm above these grid positions (approximately the radius of the expected centre of the spike). Initial Euler angles were assigned to each subtomogram based on the orientation of the normal vectors relative to the sphere surface.

Subtomograms were aligned against the low-resolution template (from the above average of 68 spikes). During this alignment, subtomogram positions converged onto clusters at the true spike positions. One subtomogram position was kept for each cluster, excluding particles within a distance of ~60 Å (10 pixels at 4 $\times$  binning) and removing particles with cross-correlation coefficients below 0.11.

Subtomograms that had tilted by more than 90° relative to their perpendicular positions were excluded. Visual inspection of the tomograms using the Place Object Chimera Plugin<sup>43</sup> confirmed that subtomograms selected in this manner corresponded to S trimers on the viral surface (see below). Subtomograms were divided into two halves on the basis of virion number. From this point on the two halves were processed independently.

## Subtomogram averaging

Subsequent processing was performed in RELION<sup>44</sup>. For this purpose, subtomograms were reconstructed from the original tilt series images after motion correction using relion\_reconstruct. Using dedicated Python scripts, the S trimer

positions in the 3D tomograms from the procedure outlined above were converted into 2D positions and defocus values in the corresponding tilt series images, as well as Euler angles in the RELION convention. Individual sub-tomograms were reconstructed at a  $2\times$  downsampled pixel size of 3.064 Å, by 3D insertion of Fourier slices of the cropped regions of the tilt series images, each multiplied by their corresponding CTF, which included the dose filter. Similarly, 3D-CTF volumes were generated by 3D insertion of the corresponding CTF<sup>2</sup> slices. Subtomograms were reconstructed in a box size of 128 voxels for prefusion trimers and a box size of 192 voxels for averages of tilted prefusion trimers and for postfusion trimers.

To deal with the CTF pre-multiplied sub-tomograms, as well as the multiplicity of each 3D voxel in the tilt series, a modified version of RELION was used for subtomogram refinement and classification (details to be described elsewhere). Standard 3D auto-refinement was performed with C3 symmetry and a soft-edged mask around the trimers, using a 30 Å lowpass-filtered map as an initial reference. Using 3,854 of the 4,104 subtomograms (excluding those that had tilted by more than 90° relative to the perpendicular position (Extended Data Fig. 1c)), a 7.7 Å consensus map was calculated for the prefusion trimers; 116 postfusion trimers led to a 22 Å map.

Angular density (Extended Data Fig. 1c) was illustrated by dividing the number of spikes per histogram bin by the sine of the tilt angle. From this histogram, the noise level in the distribution due to incorrectly aligned spikes was estimated assuming they are uniformly distributed (red dashed line in Extended Data Fig. 1c), and based on averaging over the range 140–180°. Such angles must be incorrectly alignments because they orient the spike towards the inside of the virus.

Based on the subtomograms that contributed to the consensus map we estimated that there are  $23 \pm 9$  prefusion S trimers per virion. For a subset of 28 virions, we visually compared the trimers identified by subtomogram averaging with the tomograms to identify false positives or false negatives, finding that the number of S trimers identified by subtomogram averaging is an underestimate of the number of observed S trimers by 0.9 trimers per virion. On this basis we estimate there are  $24 \pm 9$  prefusion S trimers per virion.

Next, we performed symmetry expansion<sup>45</sup>, followed by focused classification without alignment and with partial signal subtraction, while keeping the orientations from the consensus refinement fixed. The mask used for focused classification was generated manually and enclosed the RBD of one monomer (Extended Data Fig. 3a), including the closest NTD of the neighbouring monomer. Classification of the primary dataset (unconc1) led to three different RBD states: closed (45% of the monomers); open (28%) and with weak density (27%) (Extended Data Fig. 3a).

Classification of a second, smaller dataset of virus particles in supernatant (unconc2), comprising 1,224 trimers yielded 39% closed RBD, 22% open RBD and 39% weak RBD, in general agreement with the unconc1 results (Extended Data Fig. [3b](#)). Classification of a dataset of virus particles after concentration through a sucrose cushion (conc), comprising 3,788 trimers, yielded 67% of the monomers corresponding to closed RBDs and 33% to RBDs with weak density. For this dataset, no RBDs in the open conformation were identified (Extended Data Fig. [3c](#)).

The classification of the RBDs as closed, open or with weaker density was used to divide the unconc1 dataset into three subsets: 31% (1,175 trimers) have no open RBDs; 55% (2,121 trimers) have one RBD in the open state; and 14% (525 trimers) have two open RBDs. The remaining 33 trimers have three RBDs in the open state and not further processed. In the class with weaker density, the RBD appears to be predominantly in the closed state and was treated as closed for this assignment. For each of the three subsets, reconstruction of the two independently refined half sets was performed using the orientations from the consensus refinement that gave the 7.7 Å consensus map described above. Subsequent standard post-processing procedures for resolution estimation, map sharpening and local-resolution filtering in RELION led to three final maps. The subset with no open RBDs gave a reconstruction with C3 symmetry in which all three RBDs were closed at 8.6 Å resolution. The other two subsets yielded structures with C1 symmetry and either one or two open RBDs, with resolutions of 8.6 Å and 9.9 Å, respectively (Extended Data Figs. [3](#), [4](#)). Note, that while fixation is not expected to give rise to any new conformations, we cannot rule out that it differentially stabilizes different conformations, and the position of the equilibrium between open and closed conformations in unfixed samples may differ from those estimated from fixed samples.

Averages of tilted prefusion trimers were generated by grouping according to the tilt and rotation of the subtomogram away from the normal vector to the membrane. Subtomograms were included in a group for averaging if they were within 15° of the displayed tilt (0°, 30° and 60°) and rotation (0°, 60°). The pools illustrated in Fig. [2c](#) contain 14.5, 14.1, 12.0 and 10.0% of the subtomograms.

## Cryo-EM sample preparation and data collection

Virus solution concentrated through a 20% (wt/wt) sucrose cushion was plunge-frozen on C-Flat 2/2 3C grids (Protochips) following the same procedure as for cryo-ET, but without adding gold fiducials. Grids were imaged on a Thermo Fisher Scientific Titan Krios transmission electron microscope that was operated at 300 kV, using a Gatan K3 direct electron detector and a Gatan BioQuantum energy filter with a 20 eV energy slit. Movies with 48 frames and an accumulated dose of  $50 \text{ e}^- \text{ \AA}^{-2}$  were acquired in counting mode using SerialEM-3.8.0<sup>33</sup> at a nominal magnification of 81,000 $\times$ , corresponding to a calibrated pixel size of 1.061  $\text{\AA}$  per pixel. Detailed data acquisition parameters are summarized in Extended Data Table 2.

## Cryo-EM image processing

The scheduler functionality in RELION-3.1 was used for fully automated real-time processing during data collection<sup>9,46</sup>. Movies were motion-corrected and dose-weighted using the RELION implementation of the MotionCor2 algorithm<sup>47</sup>. Subsequently, non-dose-weighted sums were used to estimate the CTF in CTFFIND-4.1.13<sup>48</sup>. S trimers that were extending from the sides of virus particles were picked manually (4,493 particles from the first 100 micrographs) and then used as a training set for optimisation of the convolutional neural network in the automated particle picking software Topaz<sup>49</sup>. Extracted particles were subjected to 3D classification using a previously determined structure of the S trimer<sup>9</sup>, low-pass-filtered to 30  $\text{\AA}$ , as initial 3D reference. The selected 286,407 particles that contributed to 3D classes corresponding to S trimers were submitted to Bayesian polishing to correct for per-particle beam-induced motions and a second round of 3D classification to select the 55,159 particles that contributed to the best class. This final consensus set of particles was subjected to CTF refinement of per-particle defocus, per-micrograph astigmatism and beam tilt, followed by a second round of Bayesian polishing. 3D auto-refinements were performed with the selected particles after each round of 3D classification, CTF

refinement or Bayesian polishing. The consensus structure had a resolution of 3.4 Å.

Subsequently, symmetry expansion<sup>45</sup> was performed, followed by focused 3D classification with partial signal subtraction<sup>50</sup>. Using a mask on a single RBD to focus classification into six classes while keeping the orientations of the last consensus refinement fixed resulted in the identification of two RBD states: closed or with weak density. S trimers with all three RBDs in the closed state were refined separately from S trimers with one RBD with weak density, resulting in two final maps with resolutions. Standard RELION post-processing was used for resolution estimation, map sharpening and local-resolution filtering. The C3 symmetric map with three closed RBDs had an estimated overall resolution of 3.5 Å; the C1 map with one weaker RBD extended to 4.1 Å resolution (Extended Data Fig. [6b](#)).

## Model building and refinement

The SARS-CoV-2 S trimer structure<sup>9</sup> (PDB 6ZP0) was used as an initial model for building into the model with three closed RBDs (Extended Data Fig. [6a](#), middle). Residues were adjusted manually in Coot 0.9<sup>51</sup>. Steric clash and sidechain rotamer conformations were improved using the Namdinator web server<sup>52</sup>. After further iterations of manual adjustment, the structure was refined in PHENIX-1.18.2<sup>53</sup>. The geometry and statistics are given in Extended Data Table [2](#). The unmasked model-to-map FSC was calculated in PHENIX for the refined model against the full reconstruction.

## 3D model of spikes on authentic virions

To visualize the spike protein on the authentic SARS-CoV-2 virions, the coordinates, orientations and conformational classes determined by subtomogram averaging were converted into a format compatible with Maxon Cinema 4D (v.S22.116), and imported together with the 3D models of the different conformational states determined by subtomogram averaging. To generate representative virion images in Fig. [2d](#) we removed the three false positives from one virion and positioned the three false negatives on each virion that had been identified by visual inspection of the

data (see above). The HR2 region was modelled as a cylinder. Images of individual virions from the dataset were rendered into Adobe Photoshop to generate images for presentation.

## Reporting summary

Further information on research design is available in the [Nature Research Reporting Summary](#) linked to this paper.

## Data availability

Published structures for comparison or initial model building were obtained from the PDB with accession codes [6VXX<sup>2</sup>](#), [6VYB<sup>2</sup>](#), [6X2B<sup>11</sup>](#), [6XRA<sup>8</sup>](#) and [6ZP0<sup>9</sup>](#). The cryo-EM and cryo-ET structures determined here and representative tomograms are deposited in the Electron Microscopy Data Bank (EMDB) under accession codes [EMD-11493](#) (prefusion consensus structure), [EMD-11494](#) (three closed RBDs from subtomogram averaging), [EMD-11495](#) (one open RBD), [EMD-11496](#) (two open RBDs), [EMD-11497](#) (three closed RBDs from cryo-EM), and [EMD-11498](#) (two open RBDs and one weak RBD). The associated molecular models are deposited in the PDB under accession code [6ZWV](#) (three closed RBDs from cryo-EM). The raw micrographs are deposited in the Electron Microscopy Public Image Archive under accession codes [EMPIAR-10492](#) (cryo-EM) and [EMPIAR-10493](#) (cryo-ET).

## References

1. 1.

Neuman, B. W. & Buchmeier, M. J. Supramolecular architecture of the coronavirus particle. *Adv. Virus Res.* **96**, 1–27 (2016).

[CAS](#) [PubMed](#) [PubMed Central](#) [Google Scholar](#)

2. 2.

Walls, A. C. et al. Structure, function, and antigenicity of the SARS-CoV-2 spike glycoprotein. *Cell* **181**, 281–292 (2020).

[CAS](#) [PubMed](#) [PubMed Central](#) [Google Scholar](#)

3. 3.

Hoffmann, M. et al. SARS-CoV-2 cell entry depends on ACE2 and TMPRSS2 and is blocked by a clinically proven protease inhibitor. *Cell* **181**, 271–280 (2020).

[CAS](#) [PubMed](#) [PubMed Central](#) [Google Scholar](#)

4. 4.

Shang, J. et al. Structural basis of receptor recognition by SARS-CoV-2. *Nature* **581**, 221–224 (2020).

[ADS](#) [CAS](#) [PubMed](#) [PubMed Central](#) [Google Scholar](#)

5. 5.

Wang, Q. et al. Structural and functional basis of SARS-CoV-2 entry by using human ACE2. *Cell* **181**, 894–904 (2020).

[CAS](#) [PubMed](#) [PubMed Central](#) [Google Scholar](#)

6. 6.

Watanabe, Y., Allen, J. D., Wrapp, D., McLellan, J. S. & Crispin, M. Site-specific glycan analysis of the SARS-CoV-2 spike. *Science* **369**, 330–333 (2020).

[ADS](#) [CAS](#) [PubMed](#) [PubMed Central](#) [Google Scholar](#)

7. 7.

Wrapp, D. et al. Cryo-EM structure of the 2019-nCoV spike in the prefusion conformation. *Science* **367**, 1260–1263 (2020).

[ADS](#) [CAS](#) [PubMed](#) [PubMed Central](#) [Google Scholar](#)

8. 8.

Cai, Y. et al. Distinct conformational states of SARS-CoV-2 spike protein. *Science* **369**, 1586–1592 (2020).

9. 9.

Xiong, X. et al. A thermostable, closed SARS-CoV-2 spike protein trimer. *Nat. Struct. Mol. Biol.* **27**, 934–941 (2020).

10. 10.

Toelzer, C. et al. Free fatty acid binding pocket in the locked structure of SARS-CoV-2 spike protein. *Science* eabd3255 (2020).

11. 11.

Henderson, R. et al. Controlling the SARS-CoV-2 spike glycoprotein conformation. *Nat. Struct. Mol. Biol.* **27**, 925–933 (2020).

12. 12.

McCallum, M., Walls, A. C., Bowen, J. E., Corti, D. & Veesler, D. Structure-guided covalent stabilization of coronavirus spike glycoprotein trimers in the closed conformation. *Nat. Struct. Mol. Biol.* **27**, 942–949 (2020).

13. 13.

Zhu, N. et al. A novel coronavirus from patients with pneumonia in China, 2019. *N. Engl. J. Med.* **382**, 727–733 (2020).

[CAS](#) [PubMed](#) [Google Scholar](#)

14. 14.

Zhou, P. et al. A pneumonia outbreak associated with a new coronavirus of probable bat origin. *Nature* **579**, 270–273 (2020).

[ADS](#) [CAS](#) [PubMed](#) [PubMed Central](#) [Google Scholar](#)

15. 15.

Masters, P. S. & Perlman, S. in *Fields Virology* 6th edn (eds Knipe, D. M. & Howley, P. M.) 826–858 (Elsevier, 2013).

16. 16.

Neuman, B. W. et al. Supramolecular architecture of severe acute respiratory syndrome coronavirus revealed by electron cryomicroscopy. *J. Virol.* **80**, 7918–7928 (2006).

[CAS](#) [PubMed](#) [PubMed Central](#) [Google Scholar](#)

17. 17.

Bárcena, M. et al. Cryo-electron tomography of mouse hepatitis virus: insights into the structure of the coronavirion. *Proc. Natl Acad. Sci. USA* **106**, 582–587 (2009).

[ADS](#) [PubMed](#) [Google Scholar](#)

18. 18.

Walls, A. C. et al. Tectonic conformational changes of a coronavirus spike glycoprotein promote membrane fusion. *Proc. Natl Acad. Sci. USA* **114**, 11157–11162 (2017).

[CAS](#) [PubMed](#) [Google Scholar](#)

19. 19.

Yuan, Y. et al. Cryo-EM structures of MERS-CoV and SARS-CoV spike glycoproteins reveal the dynamic receptor binding domains. *Nat. Commun.* **8**, 15092 (2017).

[ADS](#) [CAS](#) [PubMed](#) [PubMed Central](#) [Google Scholar](#)

20. 20.

Fehr, A. R. & Perlman, S. Coronaviruses: an overview of their replication and pathogenesis. *Methods Mol. Biol.* **1282**, 1–23 (2015).

[CAS](#) [PubMed](#) [PubMed Central](#) [Google Scholar](#)

21. 21.

Klein, S. et al. SARS-CoV-2 structure and replication characterized by *in situ* cryo-electron tomography. Preprint at <https://doi.org/10.1101/2020.06.23.167064> (2020).

22. 22.

Snijder, E. J. et al. A unifying structural and functional model of the coronavirus replication organelle: tracking down RNA synthesis. *PLoS Biol.* **18**, e3000715 (2020).

[CAS](#) [PubMed](#) [PubMed Central](#) [Google Scholar](#)

23. 23.

Hoffmann, M., Hofmann-Winkler, H. & Pöhlmann, S. in *Activation of Viruses by Host Proteases* (eds Böttcher-Friebertshäuser, E. et al.) 71–98 (2018).

24. 24.

Rothe, C. et al. Transmission of 2019-nCoV infection from an asymptomatic contact in Germany. *N. Engl. J. Med.* **382**, 970–971 (2020).

[PubMed](#) [PubMed Central](#) [Google Scholar](#)

25. 25.

Liu, C. et al. Viral architecture of SARS-CoV-2 with post-fusion spike revealed by cryo-EM. Preprint at <https://doi.org/10.1101/2020.03.02.972927> (2020).

26. 26.

Chlonda, P. et al. The hemifusion structure induced by influenza virus haemagglutinin is determined by physical properties of the target membranes. *Nat. Microbiol.* **1**, 16050 (2016).

[CAS](#) [PubMed](#) [PubMed Central](#) [Google Scholar](#)

27. 27.

Xiong, X. et al. Receptor binding by a ferret-transmissible H5 avian influenza virus. *Nature* **497**, 392–396 (2013).

[ADS](#) [CAS](#) [PubMed](#) [Google Scholar](#)

28. 28.

Gui, M. et al. Cryo-electron microscopy structures of the SARS-CoV spike glycoprotein reveal a prerequisite conformational state for receptor binding. *Cell Res.* **27**, 119–129 (2017).

[CAS](#) [PubMed](#) [Google Scholar](#)

29. 29.

Bonafous, P. et al. Treatment of influenza virus with beta-propiolactone alters viral membrane fusion. *Biochim. Biophys. Acta* **1838**, 355–363 (2014).

[CAS](#) [PubMed](#) [Google Scholar](#)

30. 30.

Zhou, T. et al. A pH-dependent switch mediates conformational masking of SARS-CoV-2 spike. Preprint at

<https://doi.org/10.1101/2020.07.04.187989> (2020).

31. 31.

Korber, B. et al. Tracking changes in SARS-CoV-2 spike: evidence that D614G increases infectivity of the COVID-19 virus. *Cell* **182**, 812–827 (2020).

[CAS](#) [PubMed](#) [PubMed Central](#) [Google Scholar](#)

32. 32.

Wan, W. et al. Structure and assembly of the Ebola virus nucleocapsid. *Nature* **551**, 394–397 (2017).

[ADS](#) [CAS](#) [PubMed](#) [PubMed Central](#) [Google Scholar](#)

33. 33.

Mastronarde, D. N. Automated electron microscope tomography using robust prediction of specimen movements. *J. Struct. Biol.* **152**, 36–51 (2005).

[PubMed](#) [Google Scholar](#)

34. 34.

Hagen, W. J. H., Wan, W. & Briggs, J. A. G. Implementation of a cryo-electron tomography tilt-scheme optimized for high resolution subtomogram averaging. *J. Struct. Biol.* **197**, 191–198 (2017).

[PubMed](#) [PubMed Central](#) [Google Scholar](#)

35. 35.

Kremer, J. R., Mastronarde, D. N. & McIntosh, J. R. Computer visualization of three-dimensional image data using IMOD. *J. Struct. Biol.* **116**, 71–76 (1996).

[CAS](#) [PubMed](#) [Google Scholar](#)

36. 36.

Grant, T. & Grigorieff, N. Measuring the optimal exposure for single particle cryo-EM using a 2.6 Å reconstruction of rotavirus VP6. *eLife* **4**, e06980 (2015).

[PubMed](#) [PubMed Central](#) [Google Scholar](#)

37. 37.

Xiong, Q., Morphew, M. K., Schwartz, C. L., Hoenger, A. H. & Mastronarde, D. N. CTF determination and correction for low dose tomographic tilt series. *J. Struct. Biol.* **168**, 378–387 (2009).

[PubMed](#) [PubMed Central](#) [Google Scholar](#)

38. 38.

Turoňová, B., Schur, F. K. M., Wan, W. & Briggs, J. A. G. Efficient 3D-CTF correction for cryo-electron tomography using NovaCTF improves subtomogram averaging resolution to 3.4 Å. *J. Struct. Biol.* **199**, 187–195 (2017).

[PubMed](#) [PubMed Central](#) [Google Scholar](#)

39. 39.

Galaz-Montoya, J. G., Flanagan, J., Schmid, M. F. & Ludtke, S. J. Single particle tomography in EMAN2. *J. Struct. Biol.* **190**, 279–290 (2015).

[CAS](#) [PubMed](#) [PubMed Central](#) [Google Scholar](#)

40. 40.

Nickell, S. et al. TOM software toolbox: acquisition and analysis for electron tomography. *J. Struct. Biol.* **149**, 227–234 (2005).

[PubMed](#) [Google Scholar](#)

41. 41.

Förster, F., Medalia, O., Zauberman, N., Baumeister, W. & Fass, D. Retrovirus envelope protein complex structure in situ studied by cryo-electron tomography. *Proc. Natl Acad. Sci. USA* **102**, 4729–4734 (2005).

[ADS](#) [PubMed](#) [Google Scholar](#)

42. 42.

Pettersen, E. F. et al. UCSF Chimera—a visualization system for exploratory research and analysis. *J. Comput. Chem.* **25**, 1605–1612 (2004).

[CAS](#) [Google Scholar](#)

43. 43.

Qu, K. et al. Structure and architecture of immature and mature murine leukemia virus capsids. *Proc. Natl Acad. Sci. USA* **115**, E11751–E11760 (2018).

[CAS](#) [PubMed](#) [Google Scholar](#)

44. 44.

Bharat, T. A. M., Russo, C. J., Löwe, J., Passmore, L. A. & Scheres, S. H. W. Advances in single-particle electron cryomicroscopy structure determination applied to sub-tomogram averaging. *Structure* **23**, 1743–1753 (2015).

[CAS](#) [PubMed](#) [PubMed Central](#) [Google Scholar](#)

45. 45.

Scheres, S. H. W. Processing of structurally heterogeneous cryo-EM data in RELION. *Methods Enzymol.* **579**, 125–157 (2016).

[CAS](#) [PubMed](#) [Google Scholar](#)

46. 46.

Zivanov, J. et al. New tools for automated high-resolution cryo-EM structure determination in RELION-3. *eLife* **7**, e42166 (2018).

[PubMed](#) [PubMed Central](#) [Google Scholar](#)

47. 47.

Zheng, S. Q. et al. MotionCor2: anisotropic correction of beam-induced motion for improved cryo-electron microscopy. *Nat. Methods* **14**, 331–332 (2017).

[CAS](#) [PubMed](#) [PubMed Central](#) [Google Scholar](#)

48. 48.

Rohou, A. & Grigorieff, N. CTFFIND4: fast and accurate defocus estimation from electron micrographs. *J. Struct. Biol.* **192**, 216–221 (2015).

[PubMed](#) [PubMed Central](#) [Google Scholar](#)

49. 49.

Bepler, T. et al. Positive-unlabeled convolutional neural networks for particle picking in cryo-electron micrographs. *Nat. Methods* **16**, 1153–1160 (2019).

[CAS](#) [PubMed](#) [PubMed Central](#) [Google Scholar](#)

50. 50.

Bai, X. C., Rajendra, E., Yang, G., Shi, Y. & Scheres, S. H. W. Sampling the conformational space of the catalytic subunit of human  $\gamma$ -secretase. *eLife* **4**, e11182 (2015).

[PubMed](#) [PubMed Central](#) [Google Scholar](#)

51. 51.

Emsley, P. & Cowtan, K. Coot: model-building tools for molecular graphics. *Acta Crystallogr. D* **60**, 2126–2132 (2004).

[PubMed](#) [Google Scholar](#)

52. 52.

Kidmose, R. T. et al. Namdinator—automatic molecular dynamics flexible fitting of structural models into cryo-EM and crystallography experimental maps. *IUCrJ* **6**, 526–531 (2019).

[CAS](#) [PubMed](#) [PubMed Central](#) [Google Scholar](#)

53. 53.

Afonine, P. V. et al. Real-space refinement in PHENIX for cryo-EM and crystallography. *Acta Crystallogr. D* **74**, 531–544 (2018).

[CAS](#) [Google Scholar](#)

[Download references](#)

## Acknowledgements

We thank the staff of the MRC-LMB for generous support during the COVID-19 pandemic lockdown; all of the staff of the MRC-LMB EM Facility, in particular A. Yeates, G. Sharov and G. Cannone, for supporting the EM experiments; J. Grimmett and T. Darling for supporting scientific computing; C. Drosten and EVAg for provision of the SARS-CoV-2 strain used here; and M. Frey for the Calu-3 cell line. We acknowledge

microscopy support from the Infectious Diseases Imaging Platform (IDIP) at the Center for Integrative Infectious Disease Research Heidelberg. This study was supported by funding from the European Research Council (ERC) under the European Union's Horizon 2020 research and innovation programme (ERC-CoG-648432 MEMBRANEFUSION to J.A.G.B.), the Medical Research Council as part of UK Research and Innovation (MC\_UP\_A025\_1013 to S.H.W.S.; MC\_UP\_1201/16 to J.A.G.B.), the Deutsche Forschungsgemeinschaft (240245660–SFB 1129 project 5 to H.-G.K. and project 11 to R.B.) and the Japan Society for the Promotion of Science (overseas research fellowship to T.N.).

## Author information

### Author notes

1. These authors contributed equally: Zunlong Ke, Joaquin Oton, Kun Qu

## Affiliations

1. Structural Studies Division, Medical Research Council Laboratory of Molecular Biology, Cambridge, UK

Zunlong Ke, Joaquin Oton, Kun Qu, Takanori Nakane, Jasenko Zivanov, John M. Lu, Julia Peukes, Xiaoli Xiong, Sjors H. W. Scheres & John A. G. Briggs

2. Department of Infectious Diseases, Molecular Virology, Heidelberg University, Heidelberg, Germany

Mirko Cortese, Christopher J. Neufeldt, Berati Cerikan & Ralf Bartenschlager

3. Department of Infectious Diseases, Virology, Heidelberg University, Heidelberg, Germany

Vojtech Zila & Hans-Georg Kräusslich

4. Visual Aids Department, Medical Research Council Laboratory of Molecular Biology, Cambridge, UK

Lesley McKeane

5. German Center for Infection Research, Heidelberg Partner Site, Heidelberg, Germany

Hans-Georg Kräusslich & Ralf Bartenschlager

6. Division of Virus-Associated Carcinogenesis, German Cancer Research Center (DKFZ), Heidelberg, Germany

Ralf Bartenschlager

## Authors

1. Zunlong Ke

[View author publications](#)

You can also search for this author in [PubMed](#) [Google Scholar](#)

2. Joaquin Oton

[View author publications](#)

You can also search for this author in [PubMed](#) [Google Scholar](#)

3. Kun Qu

[View author publications](#)

You can also search for this author in [PubMed](#) [Google Scholar](#)

4. Mirko Cortese

[View author publications](#)

You can also search for this author in [PubMed](#) [Google Scholar](#)

5. Vojtech Zila

[View author publications](#)

You can also search for this author in [PubMed](#) [Google Scholar](#)

6. Lesley McKeane

[View author publications](#)

You can also search for this author in [PubMed](#) [Google Scholar](#)

7. Takanori Nakane

[View author publications](#)

You can also search for this author in [PubMed](#) [Google Scholar](#)

8. Jasenko Zivanov

[View author publications](#)

You can also search for this author in [PubMed](#) [Google Scholar](#)

9. Christopher J. Neufeldt

[View author publications](#)

You can also search for this author in [PubMed](#) [Google Scholar](#)

10. Berati Cerikan

[View author publications](#)

You can also search for this author in [PubMed](#) [Google Scholar](#)

11. John M. Lu

[View author publications](#)

You can also search for this author in [PubMed](#) [Google Scholar](#)

12. Julia Peukes

[View author publications](#)

You can also search for this author in [PubMed](#) [Google Scholar](#)

13. Xiaoli Xiong

[View author publications](#)

You can also search for this author in [PubMed](#) [Google Scholar](#)

14. Hans-Georg Kräusslich  
[View author publications](#)

You can also search for this author in [PubMed](#) [Google Scholar](#)

15. Sjors H. W. Scheres  
[View author publications](#)

You can also search for this author in [PubMed](#) [Google Scholar](#)

16. Ralf Bartenschlager  
[View author publications](#)

You can also search for this author in [PubMed](#) [Google Scholar](#)

17. John A. G. Briggs  
[View author publications](#)

You can also search for this author in [PubMed](#) [Google Scholar](#)

## Contributions

Z.K. and J.A.G.B. conceived the study. Z.K., J.O., K.Q., M.C., V.Z., H.-G.K., R.B. and J.A.G.B. designed the study. M.C., V.Z., C.J.N. and B.C. prepared and characterized virus samples with supervision from H.-G.K. and R.B. Z.K. and K.Q. collected cryo-EM data. Z.K., J.O. and K.Q. processed cryo-EM data with assistance from T.N., J.Z., J.M.L. and J.P., supervised by S.H.W.S. and J.A.G.B. Z.K., J.O., K.Q., M.C. and L.M. made figures. Z.K., J.O., K.Q., M.C., X.X. and J.A.G.B. interpreted data. J.A.G.B. prepared the initial draft and managed the project. Z.K., J.O., K.Q., M.C. and J.A.G.B. wrote the manuscript with input from all authors. S.H.W.S., H.-G.K., R.B. and J.A.G.B. obtained funding.

## Corresponding author

Correspondence to [John A. G. Briggs](#).

# Ethics declarations

## Competing interests

The authors declare no competing interests.

## Additional information

**Peer review information** *Nature* thanks Jason McLellan and the other, anonymous, reviewer(s) for their contribution to the peer review of this work. Peer reviewer reports are available.

**Publisher's note** Springer Nature remains neutral with regard to jurisdictional claims in published maps and institutional affiliations.

## Extended data figures and tables

### [Extended Data Fig. 1 Characterization of SARS-CoV-2 virion morphology.](#)

**a**, Histogram of virion diameters for unconcentrated extracellular virions in the supernatant of two independent preparations (top and middle), and for extracellular virions after concentration through a sucrose cushion (bottom). After concentration the virions become less spherical. Mean and standard deviation for diameters are  $91 \pm 11$  nm ( $n = 179$ ),  $94 \pm 9$  nm ( $n = 68$ ) and  $92 \pm 8$  nm ( $n = 227$ ) for the three preparations. **b**, Scatter plot of number of spikes identified per virion during subtomogram averaging against virion diameter for the same virions shown in **a**. Visual inspection indicates that almost all spikes were identified for virions in the supernatant, but that not all spikes are identified in the concentrated preparation leading to an underestimate of the number of spikes. **c**, Histogram of spike tilt angle towards the membrane for the larger supernatant virus dataset (unconc1). The vertical black dashed line indicates  $90^\circ$ . 97% of particles have tilts below  $90^\circ$ ; particles with tilts above  $90^\circ$  were not included in image

analysis. The angular density (right) is calculated by dividing the number of spikes by the sine of the determined angle. If spikes were unconstrained in tilt, this distribution would be uniform. The angular density decreases from  $\sim 50^\circ$ , indicating that higher tilts are disfavoured. The horizontal red dashed line indicates the angular distribution of noise (spikes which have failed to align), estimated based on the angular density between  $140^\circ$  and  $180^\circ$ . **d**, Schematic diagram and examples of individual tilted spikes on virions. The schematic indicates the angle that was measured. Five examples of individual tilted spikes are marked on tomographic slices through an intact virion, with their associated angle. Scale bar 50 nm.

### Extended Data Fig. 2 Morphology of SARS-CoV-2 virions released from infected Calu-3 cells.

As in Extended Data Fig. 1. **a**, Histogram of virion diameters. Mean and standard deviation for diameters are  $104 \pm 13$  nm ( $n = 67$ ). **b**, Scatter plot of number of spikes identified per virion during subtomogram averaging against virion diameter for the same virions shown in **a**. **c**, Central slices through three representative viruses from 67 imaged in one experiment. Virions from Calu-3 cells had a slightly broader diameter distribution than those from Vero E6 cells. Scale bar 50 nm. **d**, Western blot analysis of SARS-CoV-2 nsp3, S and N in cell lysates and in virus preparations. In released virions, S is present in both cleaved (S2, 73%) and uncleaved forms (S0, 27%).

### Extended Data Fig. 3 Classification of SARS-CoV-2 spike RBDs.

**a**, Class averages obtained after focused classification on the RBD of the left monomer after symmetry expansion of the unconc1 dataset. Top views and side views are shown for closed, open and weak classes. The region subjected to classification is indicated by a transparent red mask surface in the left hand panel. **b**, Equivalent analysis for a smaller, independent dataset (unconc2). **c**, Equivalent analysis for a dataset obtained after concentrating virus through a sucrose cushion (conc). Only closed and weak classes were obtained. **d–f**, Cut-open local resolution maps for structures shown in **a–c**.

**Extended Data Fig. 4 Resolution assessment of subtomogram averaging structures.**

**a**, Local resolution map for the consensus structure obtained for the prefusion S trimers. **b**, Local resolution maps for the prefusion S trimer in three different conformations. **c**, Global resolution assessment by Fourier shell correlation (FSC) at the 0.143 criterion for the four structures shown in **a** and **b**, as well as the postfusion S trimer.

**Extended Data Fig. 5 Single particle cryo-EM image processing workflow.**

Automatically picked particles (green circles) were subjected to 3D classification. Scale bar 100 nm. Selected 3D classes are indicated by black boxes. RBDs from individual asymmetric units from the S trimer (red dashed circles) were locally classified to sort different conformations of RBD. The asymmetric unit subjected to local classification is shown in a top view, the RDB of the green monomer is weak in the right-hand class (red arrowhead). S trimers with all three RBDs in the closed state were further refined with C3 symmetry. S trimers where one RBD had weak density were refined with C1 symmetry. For further details see materials and methods.

**Extended Data Fig. 6 Single particle Cryo-EM structure validation.**

**a**, Cut-open cryo-EM maps obtained using all prefusion S trimers, S trimers with 3 closed RBDs or S trimers with 2 closed and 1 weak RBDs, coloured according to the local resolution. **b**, FSC curves for the three structures in **a**, and for the atomic model against the map.

**Extended Data Fig. 7 Structural comparison of in situ structure with recombinant soluble structure.**

Structural superposition of S trimer modelled into the structure of the trimer with three closed RBDs (green, this study) with the published structure of

recombinant, soluble closed trimer (blue, PDB 6VXX). Top and side views are shown. The structures are very similar.

### Extended Data Table 1 Cryo-ET data acquisition and image processing

[Full size table](#)

### Extended Data Table 2 Cryo-EM data collection, refinement and validation statistics

[Full size table](#)

## Supplementary information

### [Supplementary Information](#)

This source data file contains the uncropped blots for Figure 1a and Extended Data Figure 2d.

### [Reporting Summary](#)

### [Peer Review File](#)

## Rights and permissions

### [Reprints and Permissions](#)

## About this article



Check for  
updates

## Cite this article

Ke, Z., Oton, J., Qu, K. *et al.* Structures and distributions of SARS-CoV-2 spike proteins on intact virions. *Nature* **588**, 498–502 (2020).  
<https://doi.org/10.1038/s41586-020-2665-2>

## Download citation

- Received: 02 July 2020
- Accepted: 10 August 2020
- Published: 17 August 2020
- Issue Date: 17 December 2020
- DOI: <https://doi.org/10.1038/s41586-020-2665-2>

## Further reading

- [\*\*SARS-CoV-2 spike behavior in situ: a Cryo-EM images for a better understanding of the COVID-19 pandemic\*\*](#)
  - Alaa M. Ismail
  - & Abdo A. Elfiky
- [\*\*Man-Specific, GalNAc/T/Tn-Specific and Neu5Ac-Specific Seaweed Lectins as Glycan Probes for the SARS-CoV-2 \(COVID-19\) Coronavirus\*\*](#)
  - Annick Barre
  - , Els J.M. Van Damme
  - , Mathias Simplicien
  - , Hervé Benoist
  - & Pierre Roug  

*Marine Drugs* (2020)

- [\*\*A Novel In-Cell ELISA Assay Allows Rapid and Automated Quantification of SARS-CoV-2 to Analyze\*\*](#)

## Neutralizing Antibodies and Antiviral Compounds

- Lara Schöler
- , Vu Thuy Khanh Le-Trilling
- , Mareike Eilbrecht
- , Denise Mennerich
- , Olympia E. Anastasiou
- , Adalbert Krawczyk
- , Anke Herrmann
- , Ulf Dittmer
- & Mirko Trilling

*Frontiers in Immunology* (2020)

- Continuous flexibility analysis of SARS-CoV-2 spike prefusion structures

- Roberto Melero
- , Carlos Oscar S. Sorzano
- , Brent Foster
- , José-Luis Vilas
- , Marta Martínez
- , Roberto Marabini
- , Erney Ramírez-Aportela
- , Ruben Sanchez-Garcia
- , David Herreros
- , Laura del Caño
- , Patricia Losana
- , Yunior C. Fonseca-Reyna
- , Pablo Conesa
- , Daniel Wrapp
- , Pablo Chacon
- , Jason S. McLellan
- , Hemant D. Tagare
- & Jose-Maria Carazo

*IUCrJ* (2020)

- **Interaction of Human ACE2 to Membrane-Bound SARS-CoV-1 and SARS-CoV-2 S Glycoproteins**

- Sai Priya Anand
- , Yaozong Chen
- , Jérémie Prévost
- , Romain Gasser
- , Guillaume Beaudoin-Bussières
- , Cameron F. Abrams
- , Marzena Pazgier
- & Andrés Finzi

*Viruses* (2020)

## Comments

By submitting a comment you agree to abide by our [Terms](#) and [Community Guidelines](#). If you find something abusive or that does not comply with our terms or guidelines please flag it as inappropriate.

[Download PDF](#)

---

This article was downloaded by **calibre** from <https://www.nature.com/articles/s41586-020-2665-2>

- Article
- [Published: 09 December 2020](#)

# A hydrophobic ratchet entrenches molecular complexes

- [Georg K. A. Hochberg](#)<sup>1</sup>,
- [Yang Liu](#) [ORCID: orcid.org/0000-0003-4994-5200](#)<sup>2</sup>,
- [Erik G. Marklund](#) [ORCID: orcid.org/0000-0002-9804-5009](#)<sup>3</sup>,
- [Brian P. H. Metzger](#)<sup>1</sup>,
- [Arthur Laganowsky](#) [ORCID: orcid.org/0000-0001-5012-5547](#)<sup>2</sup> &
- [Joseph W. Thornton](#) [ORCID: orcid.org/0000-0001-9589-6994](#)<sup>1,4</sup>

[Nature](#) volume 588, pages503–508(2020) [Cite this article](#)

- 8882 Accesses
- 464 Altmetric
- [Metrics details](#)

## Subjects

- [Biochemistry](#)
- [Molecular evolution](#)

## Abstract

Most proteins assemble into multisubunit complexes<sup>1</sup>. The persistence of these complexes across evolutionary time is usually explained as the result of natural selection for functional properties that depend on multimerization, such as intersubunit allostery or the capacity to do

mechanical work<sup>2</sup>. In many complexes, however, multimerization does not enable any known function<sup>3</sup>. An alternative explanation is that multimers could become entrenched if substitutions accumulate that are neutral in multimers but deleterious in monomers; purifying selection would then prevent reversion to the unassembled form, even if assembly per se does not enhance biological function<sup>3,4,5,6,7</sup>. Here we show that a hydrophobic mutational ratchet systematically entrenches molecular complexes. By applying ancestral protein reconstruction and biochemical assays to the evolution of steroid hormone receptors, we show that an ancient hydrophobic interface, conserved for hundreds of millions of years, is entrenched because exposure of this interface to solvent reduces protein stability and causes aggregation, even though the interface makes no detectable contribution to function. Using structural bioinformatics, we show that a universal mutational propensity drives sites that are buried in multimeric interfaces to accumulate hydrophobic substitutions to levels that are not tolerated in monomers. In a database of hundreds of families of multimers, most show signatures of long-term hydrophobic entrenchment. It is therefore likely that many protein complexes persist because a simple ratchet-like mechanism entrenches them across evolutionary time, even when they are functionally gratuitous.

[Access through your institution](#)

[Change institution](#)

[Buy or subscribe](#)

## Access options

Subscribe to Journal

Get full journal access for 1 year

185,98 €

only 3,58 € per issue

[Subscribe](#)

All prices are NET prices.  
VAT will be added later in the checkout.

Rent or Buy article

Get time limited or full article access on ReadCube.

from \$8.99

[Rent or Buy](#)

All prices are NET prices.

### **Additional access options:**

- [Log in](#)
- [Access through your institution](#)
- [Learn about institutional subscriptions](#)

**Fig. 1: Evolution of self-assembly in SRs.**

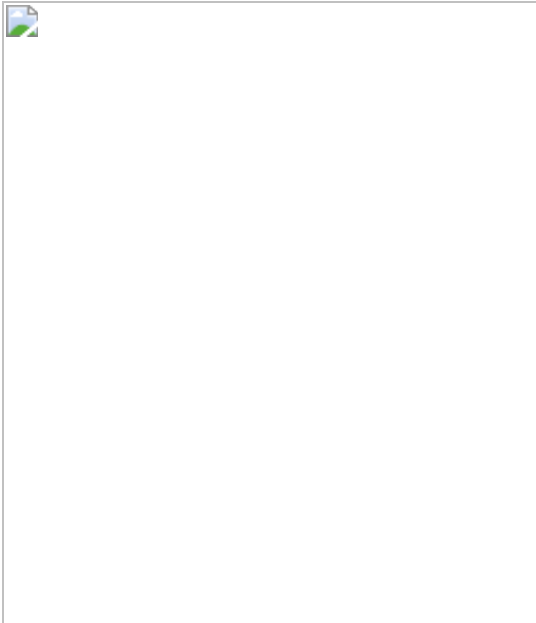


**Fig. 2: The ancestral LBD interface was hydrophobically entrenched.**



**Fig. 3: AncSR2 traded intermolecular for intramolecular entrenchment.**



**Fig. 4: Pervasive hydrophobic entrenchment of molecular complexes.**



## Data availability

Data have been deposited in the Open Science Framework (<https://osf.io/>) under accession GTJ86, including alignment, phylogeny, sequences and posterior probability of ancestral reconstructions; list of PDB identifiers for coordinates of dimers and monomers in our structural database; and molecular dynamics trajectories.

## Code availability

Scripts and code for structural bioinformatics analysis have been deposited at github (<https://github.com/JoeThorntonLab>).

## References

1. 1.

Marsh, J. A. & Teichmann, S. A. Structure, dynamics, assembly, and evolution of protein complexes. *Annu. Rev. Biochem.* **84**, 551–575 (2015).

[CAS](#) [PubMed](#) [Google Scholar](#)

2. 2.

Goodsell, D. S. & Olson, A. J. Structural symmetry and protein function. *Annu. Rev. Biophys. Biomol. Struct.* **29**, 105–153 (2000).

[CAS](#) [PubMed](#) [Google Scholar](#)

3. 3.

Lynch, M. Evolutionary diversification of the multimeric states of proteins. *Proc. Natl Acad. Sci. USA* **110**, E2821–E2828 (2013).

[ADS](#) [CAS](#) [PubMed](#) [Google Scholar](#)

4. 4.

Lukeš, J., Archibald, J. M., Keeling, P. J., Doolittle, W. F. & Gray, M. W. How a neutral evolutionary ratchet can build cellular complexity. *IUBMB Life* **63**, 528–537 (2011).

[PubMed](#) [Google Scholar](#)

5. 5.

Manhart, M. & Morozov, A. V. Protein folding and binding can emerge as evolutionary spandrels through structural coupling. *Proc. Natl Acad. Sci. USA* **112**, 1797–1802 (2015).

[ADS](#) [CAS](#) [PubMed](#) [Google Scholar](#)

6. 6.

Schank, J. C. & Wimsatt, W. C. Generative entrenchment and evolution. *PSA: Proc. Biennial Meeting Philos. Sci. Assoc.* 1986, 33–60 (1986).

7. 7.

Muller, H. J. Genetic variability, twin hybrids and constant hybrids, in a case of balanced lethal factors. *Genetics* **3**, 422–499 (1918).

[CAS](#) [PubMed](#) [PubMed Central](#) [Google Scholar](#)

8. 8.

Moody, A. D., Miura, M. T., Connaghan, K. D. & Bain, D. L. Thermodynamic dissection of estrogen receptor-promoter interactions reveals that steroid receptors differentially partition their self-association and promoter binding energetics. *Biochemistry* **51**, 739–749 (2012).

[CAS](#) [PubMed](#) [PubMed Central](#) [Google Scholar](#)

9. 9.

Tamrazi, A., Carlson, K. E., Daniels, J. R., Hurth, K. M. & Katzenellenbogen, J. A. Estrogen receptor dimerization: ligand binding regulates dimer affinity and dimer dissociation rate. *Mol. Endocrinol.* **16**, 2706–2719 (2002).

[CAS](#) [PubMed](#) [Google Scholar](#)

10. 10.

Robblee, J. P., Miura, M. T. & Bain, D. L. Glucocorticoid receptor-promoter interactions: energetic dissection suggests a framework for the specificity of steroid receptor-mediated gene regulation. *Biochemistry* **51**, 4463–4472 (2012).

[CAS](#) [PubMed](#) [PubMed Central](#) [Google Scholar](#)

11. 11.

Alroy, I. & Freedman, L. P. DNA binding analysis of glucocorticoid receptor specificity mutants. *Nucleic Acids Res.* **20**, 1045–1052 (1992).

[CAS](#) [PubMed](#) [PubMed Central](#) [Google Scholar](#)

12. 12.

McKeown, A. N. et al. Evolution of DNA specificity in a transcription factor family produced a new gene regulatory module. *Cell* **159**, 58–68 (2014).

[CAS](#) [PubMed](#) [PubMed Central](#) [Google Scholar](#)

13. 13.

Harms, M. J. et al. Biophysical mechanisms for large-effect mutations in the evolution of steroid hormone receptors. *Proc. Natl Acad. Sci. USA* **110**, 11475–11480 (2013).

[ADS](#) [CAS](#) [PubMed](#) [Google Scholar](#)

14. 14.

Eick, G. N., Colucci, J. K., Harms, M. J., Ortlund, E. A. & Thornton, J. W. Evolution of minimal specificity and promiscuity in steroid hormone receptors. *PLoS Genet.* **8**, e1003072 (2012).

[CAS](#) [PubMed](#) [PubMed Central](#) [Google Scholar](#)

15. 15.

Fagart, J. et al. Crystal structure of a mutant mineralocorticoid receptor responsible for hypertension. *Nat. Struct. Mol. Biol.* **12**, 554–555 (2005).

[CAS](#) [PubMed](#) [Google Scholar](#)

16. 16.

Kauppi, B. et al. The three-dimensional structures of antagonistic and agonistic forms of the glucocorticoid receptor ligand-binding domain: RU-486 induces a transconformation that leads to active antagonism. *J. Biol. Chem.* **278**, 22748–22754 (2003).

[CAS](#) [PubMed](#) [Google Scholar](#)

17. 17.

Sack, J. S. et al. Crystallographic structures of the ligand-binding domains of the androgen receptor and its T877A mutant complexed with the natural agonist dihydrotestosterone. *Proc. Natl Acad. Sci. USA* **98**, 4904–4909 (2001).

[ADS](#) [CAS](#) [PubMed](#) [Google Scholar](#)

18. 18.

Williams, S. P. & Sigler, P. B. Atomic structure of progesterone complexed with its receptor. *Nature* **393**, 392–396 (1998).

[ADS](#) [CAS](#) [PubMed](#) [Google Scholar](#)

19. 19.

Bowie, J. U., Reidhaar-Olson, J. F., Lim, W. A. & Sauer, R. T. Deciphering the message in protein sequences: tolerance to amino acid substitutions. *Science* **247**, 1306–1310 (1990).

[ADS](#) [CAS](#) [PubMed](#) [Google Scholar](#)

20. 20.

Pakula, A. A. & Sauer, R. T. Reverse hydrophobic effects relieved by amino-acid substitutions at a protein surface. *Nature* **344**, 363–364 (1990).

[ADS](#) [CAS](#) [PubMed](#) [Google Scholar](#)

21. 21.

Valentine, J. E., Kalkhoven, E., White, R., Hoare, S. & Parker, M. G. Mutations in the estrogen receptor ligand binding domain discriminate

between hormone-dependent transactivation and transrepression. *J. Biol. Chem.* **275**, 25322–25329 (2000).

[CAS](#) [PubMed](#) [Google Scholar](#)

22. 22.

Ince, B. A., Zhuang, Y., Wrenn, C. K., Shapiro, D. J. & Katzenellenbogen, B. S. Powerful dominant negative mutants of the human estrogen receptor. *J. Biol. Chem.* **268**, 14026–14032 (1993).

[CAS](#) [PubMed](#) [Google Scholar](#)

23. 23.

Xu, J., Nawaz, Z., Tsai, S. Y., Tsai, M. J. & O’Malley, B. W. The extreme C terminus of progesterone receptor contains a transcriptional repressor domain that functions through a putative corepressor. *Proc. Natl Acad. Sci. USA* **93**, 12195–12199 (1996).

[ADS](#) [CAS](#) [PubMed](#) [Google Scholar](#)

24. 24.

Zhang, S., Liang, X. & Danielsen, M. Role of the C terminus of the glucocorticoid receptor in hormone binding and agonist/antagonist discrimination. *Mol. Endocrinol.* **10**, 24–34 (1996).

[CAS](#) [PubMed](#) [Google Scholar](#)

25. 25.

Ahnert, S. E., Marsh, J. A., Hernández, H., Robinson, C. V. & Teichmann, S. A. Principles of assembly reveal a periodic table of protein complexes. *Science* **350**, aaa2245 (2015).

[PubMed](#) [Google Scholar](#)

26. 26.

Finnigan, G. C., Hanson-Smith, V., Stevens, T. H. & Thornton, J. W. Evolution of increased complexity in a molecular machine. *Nature* **481**, 360–364 (2012).

[ADS](#) [CAS](#) [PubMed](#) [PubMed Central](#) [Google Scholar](#)

27. 27.

Force, A. et al. Preservation of duplicate genes by complementary, degenerative mutations. *Genetics* **151**, 1531–1545 (1999).

[CAS](#) [PubMed](#) [PubMed Central](#) [Google Scholar](#)

28. 28.

Gray, M. W., Lukes, J., Archibald, J. M., Keeling, P. J. & Doolittle, W. F. Irremediable complexity? *Science* **330**, 920–921 (2010).

[ADS](#) [CAS](#) [PubMed](#) [Google Scholar](#)

29. 29.

Lynch, M. The frailty of adaptive hypotheses for the origins of organismal complexity. *Proc. Natl Acad. Sci. USA* **104** (Suppl. 1), 8597–8604 (2007).

[ADS](#) [CAS](#) [PubMed](#) [Google Scholar](#)

30. 30.

Stoltzfus, A. On the possibility of constructive neutral evolution. *J. Mol. Evol.* **49**, 169–181 (1999).

[ADS](#) [CAS](#) [PubMed](#) [Google Scholar](#)

31. 31.

Hershberg, R. & Petrov, D. A. Evidence that mutation is universally biased towards AT in bacteria. *PLoS Genet.* **6**, e1001115 (2010).

[PubMed](#) [PubMed Central](#) [Google Scholar](#)

32. 32.

Hochberg, G. K. A. et al. Structural principles that enable oligomeric small heat-shock protein paralogs to evolve distinct functions. *Science* **359**, 930–935 (2018).

[ADS](#) [CAS](#) [PubMed](#) [PubMed Central](#) [Google Scholar](#)

33. 33.

Kaltenegger, E. & Ober, D. Parologue interference affects the dynamics after gene duplication. *Trends Plant Sci.* **20**, 814–821 (2015).

[CAS](#) [PubMed](#) [Google Scholar](#)

34. 34.

Edgar, R. C. MUSCLE: a multiple sequence alignment method with reduced time and space complexity. *BMC Bioinformatics* **5**, 113 (2004).

[PubMed](#) [PubMed Central](#) [Google Scholar](#)

35. 35.

Darriba, D., Taboada, G. L., Doallo, R. & Posada, D. ProtTest 3: fast selection of best-fit models of protein evolution. *Bioinformatics* **27**, 1164–1165 (2011).

[CAS](#) [PubMed](#) [PubMed Central](#) [Google Scholar](#)

36. 36.

Guindon, S. et al. New algorithms and methods to estimate maximum-likelihood phylogenies: assessing the performance of PhyML 3.0. *Syst. Biol.* **59**, 307–321 (2010).

[CAS](#) [PubMed](#) [Google Scholar](#)

37. 37.

Katsu, Y. et al. A second estrogen receptor from Japanese lamprey (*Lethenteron japonicum*) does not have activities for estrogen binding and transcription. *Gen. Comp. Endocrinol.* **236**, 105–114 (2016).

[CAS](#) [PubMed](#) [Google Scholar](#)

38. 38.

Simakov, O. et al. Deeply conserved synteny resolves early events in vertebrate evolution. *Nat. Ecol. Evol.* **4**, 820–830 (2020).

[PubMed](#) [PubMed Central](#) [Google Scholar](#)

39. 39.

Philippe, H. et al. Acoelomorph flatworms are deuterostomes related to *Xenoturbella*. *Nature* **470**, 255–258 (2011).

[ADS](#) [CAS](#) [PubMed](#) [PubMed Central](#) [Google Scholar](#)

40. 40.

Cannon, J. T. et al. Xenacoelomorpha is the sister group to Nephrozoa. *Nature* **530**, 89–93 (2016).

[ADS](#) [CAS](#) [PubMed](#) [Google Scholar](#)

41. 41.

Bridgham, J. T. et al. Protein evolution by molecular tinkering: diversification of the nuclear receptor superfamily from a ligand-dependent ancestor. *PLoS Biol.* **8**, e1000497 (2010).

[PubMed](#) [PubMed Central](#) [Google Scholar](#)

42. 42.

Lemoine, F. et al. Renewing Felsenstein's phylogenetic bootstrap in the era of big data. *Nature* **556**, 452–456 (2018).

[ADS](#) [CAS](#) [PubMed](#) [PubMed Central](#) [Google Scholar](#)

43. 43.

Yang, Z. PAML 4: phylogenetic analysis by maximum likelihood. *Mol. Biol. Evol.* **24**, 1586–1591 (2007).

[CAS](#) [PubMed](#) [Google Scholar](#)

44. 44.

Cong, X. et al. Determining membrane protein-lipid binding thermodynamics using native mass spectrometry. *J. Am. Chem. Soc.* **138**, 4346–4349 (2016).

[CAS](#) [Google Scholar](#)

45. 45.

Marty, M. T. et al. Bayesian deconvolution of mass and ion mobility spectra: from binary interactions to polydisperse ensembles. *Anal. Chem.* **87**, 4370–4376 (2015).

[CAS](#) [PubMed](#) [PubMed Central](#) [Google Scholar](#)

46. 46.

Mazurenko, S. et al. CalFitter: a web server for analysis of protein thermal denaturation data. *Nucleic Acids Res.* **46** (W1), W344–W349 (2018).

[CAS](#) [PubMed](#) [PubMed Central](#) [Google Scholar](#)

47. 47.

Abraham, M. J. et al. GROMACS: High performance molecular simulations through multi-level parallelism from laptops to supercomputers. *SoftwareX* **1**, 19–25 (2015).

[ADS](#) [Google Scholar](#)

48. 48.

Lindorff-Larsen, K. et al. Improved side-chain torsion potentials for the Amber ff99SB protein force field. *Proteins* **78**, 1950–1958 (2010).

[CAS](#) [PubMed](#) [PubMed Central](#) [Google Scholar](#)

49. 49.

Jorgensen, W. L. et al. Comparison of simple potential functions for simulating liquid water. *J. Chem. Phys.* **79**, 926–935 (1983).

[ADS](#) [CAS](#) [Google Scholar](#)

50. 50.

Wang, J., Wolf, R. M., Caldwell, J. W., Kollman, P. A. & Case, D. A. Development and testing of a general amber force field. *J. Comput. Chem.* **25**, 1157–1174 (2004).

[CAS](#) [PubMed](#) [Google Scholar](#)

51. 51.

Feenstra, K. A. et al. Improving efficiency of large time-scale molecular dynamics simulations of hydrogen-rich systems. *J. Comput. Chem.* **20**, 786–798 (1999).

[CAS](#) [Google Scholar](#)

52. 52.

Larsson, P., Kneisl, R. C. & Marklund, E. G. MkVsites: A tool for creating GROMACS virtual sites parameters to increase performance in all-atom molecular dynamics simulations. *J. Comput. Chem.* **41**, 1564–1569 (2020).

[CAS](#) [PubMed](#) [PubMed Central](#) [Google Scholar](#)

53. 53.

Hess, B. et al. LINCS: a linear constraint solver for molecular simulations. *J. Comput. Chem.* **18**, 1463–1472 (1997).

[CAS](#) [Google Scholar](#)

54. 54.

Miyamoto, S. & Kollman, P. A. Settle: An analytical version of the SHAKE and RATTLE algorithm for rigid water models. *J. Comput. Chem.* **13**, 952–962 (1992).

[CAS](#) [Google Scholar](#)

55. 55.

Berendsen, H. J. C. et al. Molecular dynamics with coupling to an external bath. *J. Chem. Phys.* **81**, 3684–3690 (1984).

[ADS](#) [CAS](#) [Google Scholar](#)

56. 56.

Parrinello, M. & Rahman, A. Polymorphic transitions in single crystals: a new molecular dynamics method. *J. Appl. Phys.* **52**, 7182–7190 (1981).

[ADS](#) [CAS](#) [Google Scholar](#)

57. 57.

Bussi, G., Donadio, D. & Parrinello, M. Canonical sampling through velocity rescaling. *J. Chem. Phys.* **126**, 014101 (2007).

[ADS](#) [PubMed](#) [Google Scholar](#)

58. 58.

Winn, M. D. et al. Overview of the CCP4 suite and current developments. *Acta Crystallogr. D Biol. Crystallogr.* **67**, 235–242 (2011).

[CAS](#) [PubMed](#) [PubMed Central](#) [Google Scholar](#)

59. 59.

Tsai, C. J., Lin, S. L., Wolfson, H. J. & Nussinov, R. Studies of protein-protein interfaces: a statistical analysis of the hydrophobic effect. *Protein Sci.* **6**, 53–64 (1997).

[CAS](#) [PubMed](#) [PubMed Central](#) [Google Scholar](#)

60. 60.

Tien, M. Z., Meyer, A. G., Sydykova, D. K., Spielman, S. J. & Wilke, C. O. Maximum allowed solvent accessibilites of residues in proteins. *PLoS One* **8**, e80635 (2013).

[ADS](#) [PubMed](#) [PubMed Central](#) [Google Scholar](#)

61. 61.

Degiacomi, M. T., Schmidt, C., Baldwin, A. J. & Benesch, J. L. P. Accommodating protein dynamics in the modeling of chemical crosslinks. *Structure* **25**, 1751–1757.e5 (2017).

[CAS](#) [PubMed](#) [Google Scholar](#)

62. 62.

Wang, D. GCevobase: an evolution-based database for GC content in eukaryotic genomes. *Bioinformatics* **34**, 2129–2131 (2018).

[CAS](#) [PubMed](#) [Google Scholar](#)

63. 63.

Zhu, Y. O., Siegal, M. L., Hall, D. W. & Petrov, D. A. Precise estimates of mutation rate and spectrum in yeast. *Proc. Natl Acad. Sci. USA* **111**, E2310–E2318 (2014).

[ADS](#) [CAS](#) [PubMed](#) [Google Scholar](#)

64. 64.

Lee, H., Popodi, E., Tang, H. & Foster, P. L. Rate and molecular spectrum of spontaneous mutations in the bacterium *Escherichia coli* as determined by whole-genome sequencing. *Proc. Natl Acad. Sci. USA* **109**, E2774–E2783 (2012).

[ADS](#) [CAS](#) [PubMed](#) [Google Scholar](#)

65. 65.

Dumont, B. L. Significant strain variation in the mutation spectra of inbred laboratory mice. *Mol. Biol. Evol.* **36**, 865–874 (2019).

[CAS](#) [PubMed](#) [PubMed Central](#) [Google Scholar](#)

66. 66.

Dettman, J. R., Sztepanacz, J. L. & Kassen, R. The properties of spontaneous mutations in the opportunistic pathogen *Pseudomonas aeruginosa*. *BMC Genomics* **17**, 27 (2016).

[PubMed](#) [PubMed Central](#) [Google Scholar](#)

[Download references](#)

# Acknowledgements

We thank J. Bridgman for cell culture training and advice, A. Pillai for assistance with experiments, and members of the Thornton Laboratory for comments. Molecular dynamics computations were performed on resources provided by SNIC through Uppsala Multidisciplinary Center for Advanced Computational Science (UPPMAX) under Projects SNIC 2019/8-36 and SNIC 2019/3-189. Supported by a Chicago Fellowship (G.K.A.H.), NIH R01GM131128 (J.W.T.) and R01GM121931 (J.W.T.).

# Author information

## Affiliations

1. Department of Ecology and Evolution, University of Chicago, Chicago, IL, USA

Georg K. A. Hochberg, Brian P. H. Metzger & Joseph W. Thornton

2. Department of Chemistry, Texas A&M University, College Station, TX, USA

Yang Liu & Arthur Laganowsky

3. Department of Chemistry – BMC, Uppsala University, Uppsala, Sweden

Erik G. Marklund

4. Department of Human Genetics, University of Chicago, Chicago, IL, USA

Joseph W. Thornton

## Authors

1. Georg K. A. Hochberg

[View author publications](#)

You can also search for this author in [PubMed](#) [Google Scholar](#)

2. Yang Liu

[View author publications](#)

You can also search for this author in [PubMed](#) [Google Scholar](#)

3. Erik G. Marklund

[View author publications](#)

You can also search for this author in [PubMed](#) [Google Scholar](#)

4. Brian P. H. Metzger

[View author publications](#)

You can also search for this author in [PubMed](#) [Google Scholar](#)

5. Arthur Laganowsky

[View author publications](#)

You can also search for this author in [PubMed](#) [Google Scholar](#)

6. Joseph W. Thornton

[View author publications](#)

You can also search for this author in [PubMed](#) [Google Scholar](#)

## Contributions

G.K.A.H. and J.W.T. conceived the project and oversaw the manuscript writing. G.K.A.H. performed phylogenetics, ancestral sequence reconstruction, protein purification, cell culture, and biophysical experiments. Y.L. and A.L. performed and interpreted native MS experiments. E.G.M. performed and analysed molecular dynamics simulations. G.K.A.H. and B.P.H.M. designed bioinformatic analyses,

which G.K.A.H. performed. G.K.A.H. and J.W.T. interpreted all data. All authors contributed to manuscript writing.

## Corresponding author

Correspondence to [Joseph W. Thornton](#).

## Ethics declarations

### Competing interests

The authors declare no competing interests.

## Additional information

**Peer review information** *Nature* thanks Douglas Theobald, Claus Wilke and the other, anonymous, reviewer(s) for their contribution to the peer review of this work.

**Publisher's note** Springer Nature remains neutral with regard to jurisdictional claims in published maps and institutional affiliations.

## Extended data figures and tables

### [Extended Data Fig. 1 Phylogeny and alignment of steroid and related receptors.](#)

**a**, Phylogeny of steroid receptors and related nuclear receptor family members. AR, androgen receptors, PR, progesterone receptors, GR, glucocorticoid receptors, MR, mineralocorticoid receptors. Sequence identifiers are in brackets. This topology corresponds to the ‘Chordate tree’ in Extended Data Fig. 2. Scale bar, expected substitutions per site. **b**, Sequence alignment of the human ER and GR LBDs, with the MAP sequences of AncSR1 and AncSR2. Green, C-terminal extension. Most ERs

contain additional sequence on the C terminus that is unalignable, even among ERs.

### **Extended Data Fig. 2 Robustness of ancestral reconstructions.**

**a,b**, Distribution of posterior probabilities (PP) of the maximum a posteriori (MAP) state at each site in reconstructed LBDs (top) and DBDs (bottom) of AncSR1 (**a**) and AncSR2 (**b**). **c**, Stoichiometry of purified alternative LBD reconstructions (AltAll) of AncSR1 (pink) and AncSR2 (green), as measured by SEC-MALS. AncSR1 is a dimer, AncSR2 a monomer. AltAll reconstructions contain the MAP state at unambiguously reconstructed sites and the state with the next highest PP at all ambiguously reconstructed sites. **d**, The ‘chordate’ phylogeny (top) was used for primary ancestral reconstructions; it places the gene duplication yielding ERs and kSRs within the chordates. An alternative less parsimonious tree (‘Bilaterian’ because it places the duplication deep in the Bilateria, bottom), has very slightly higher likelihood but requires two additional gene losses (dashed lines). The Bilaterian topology was used for alternative reconstructions (AltPhy). Node labels, approximate likelihood ratio test statistic and transfer bootstrap value. lnl, log-likelihood. **e**, Distribution of per-site posterior probabilities for reconstructed LBDs on the Bilaterian topology for AncSR1 (top) and AncSR2 (bottom). **f**, Stoichiometry of purified AltPhy versions of AncSR1 (pink) and AncSR2 (green) LBDs, as measured by SEC-MALS. The average molar mass and elution time of AltPhy-AncSR1-LBD are between that of a dimer and a monomer, indicating that it is a fast-exchanging, weaker dimer than other AncSR1-LBD versions.

### **Extended Data Fig. 3 Concentration-dependence of activation and dimerization by AncSR1-LBD and mutants.**

**a**, Activation of AncSR1 from 40 ng ERE response element plasmid as a function of the AncSR1 plasmid concentration. Grey bar, concentration at which assays in Fig. [2f](#) were performed. **b**, Molar fraction in the dimeric form measured by nMS as a function of LBD concentration for AncSR1-LBD (purple) and dimerization-interface mutants SR1-LBD(+3) (black) and SR1-LBD(L184E) (grey). Dissociation constant ( $K_d$ ) estimated by

nonlinear regression is indicated next to each curve. **c**, Dimeric fraction as a function of LBD concentration for AncSR1-LBD (purple) and activation-helix mutant SR1-LBD(L126Q) (grey), which affects activation but not dimerization.

### Extended Data Fig. 4 Entrenchment of the CTE in AncSR2.

**a**, SEC of AncSR2 LBD (top) and mutants that delete the CTE ( $\Delta$ CTE) or contain point mutations that impair CTE-LBD interactions (bottom), when fused to MBP. The mutants elute in the same fraction as AncSR2, demonstrating that they are monomeric and that re-exposing the patch does not re-establish dimerization. **b**, TEV cleavage of AncSR2 mutants in the absence (left) and presence (right) of 2% Triton X-100. The positions of bands corresponding to the uncleaved construct, cleaved MBP, cleaved LBD, and TEV protease are indicated. This experiment was performed twice, with similar results. See Supplementary Fig. 1 for uncropped gels. **c**, Average root mean square deviation (r.m.s.d.) from replicate 2- $\mu$ s molecular dynamics simulations of AncSR2-LBD (WT) and  $\Delta$ CTE mutant. The average C $\alpha$  r.m.s.d. in pairwise comparisons of all simulations is shown as a heatmap. **d**, SEC-MALS trace of AncSR1-LBD fused to the CTE of AncSR2-LBD. The LBD is still dimeric.

### Extended Data Fig. 5 Observed hydrophobicity of interfaces compared to expected hydrophobicity from mutation.

**a**, Difference between the fraction of residues that are hydrophobic in dimer interfaces versus that on solvent-exposed surfaces of the same proteins. The histogram shows the distribution of this difference across every protein in our structural database. **b**, Fraction of hydrophobic residues in dimer interfaces as a function of the number of interface residues. The variation in the fraction is caused mostly by very small interfaces. **c**, Expected equilibrium fraction of hydrophobic amino acids from mutation alone. Black: expectation based on GC content and the genetic code. Red dots and lines: mean and standard deviation of the hydrophobic fraction of residues observed in 200 replicate simulations using mutational spectra from mutation accumulation experiments (Fig. 4b), plotted against GC

content of the organism tested. **d**, GC content of organisms represented by proteins in our database.

## Supplementary information

### Supplementary Data

Supplemental Data: 1 Raw gel images. Uncropped gels for data presented in Extended Data Figure 4b. Boxes are drawn around lanes that were used in for the figure. Supplemental Data: 2 Scaled Q matrices based on mutation accumulation experiments. Row indicates the initial state, column the mutated state. **a**, *M. musculus*. **b**, *S. cerevisiae*. **c**, *E.coli*. **d**, *P aeruginosa*.

### Reporting Summary

## Rights and permissions

### Reprints and Permissions

## About this article



Check for  
updates

## Cite this article

Hochberg, G.K.A., Liu, Y., Marklund, E.G. *et al.* A hydrophobic ratchet entrenches molecular complexes. *Nature* **588**, 503–508 (2020).  
<https://doi.org/10.1038/s41586-020-3021-2>

### Download citation

- Received: 28 November 2019

- Accepted: 20 October 2020
- Published: 09 December 2020
- Issue Date: 17 December 2020
- DOI: <https://doi.org/10.1038/s41586-020-3021-2>

## Comments

By submitting a comment you agree to abide by our [Terms](#) and [Community Guidelines](#). If you find something abusive or that does not comply with our terms or guidelines please flag it as inappropriate.

[Access through your institution](#)

[Change institution](#)

[Buy or subscribe](#)

---

This article was downloaded by **calibre** from <https://www.nature.com/articles/s41586-020-3021-2>

| [Section menu](#) | [Main menu](#) |

- Article
- [Published: 14 September 2020](#)

# Structural basis for the action of the drug trametinib at KSR-bound MEK

- [Zaigham M. Khan](#) ORCID: orcid.org/0000-0002-2471-4054<sup>1,2 na1</sup>,
- [Alexander M. Real](#)<sup>1,2 na1</sup>,
- [William M. Marsiglia](#)<sup>1,2 na1</sup>,
- [Arthur Chow](#)<sup>1,2</sup>,
- [Mary E. Duffy](#)<sup>1,2</sup>,
- [Jayasudhan R. Yerabolu](#)<sup>1,2</sup>,
- [Alex P. Scpton](#)<sup>1,2</sup> &
- [Arvin C. Dar](#) ORCID: orcid.org/0000-0003-0318-4848<sup>1,2</sup>

[Nature](#) volume 588, pages509–514(2020) [Cite this article](#)

- 7889 Accesses
- 55 Altmetric
- [Metrics details](#)

## Subjects

- [Cancer](#)
- [Chemical biology](#)
- [Drug development](#)
- [Kinases](#)
- [X-ray crystallography](#)

# Abstract

The MAPK/ERK kinase MEK is a shared effector of the frequent cancer drivers KRAS and BRAF that has long been pursued as a drug target in oncology<sup>1</sup>, and more recently in immunotherapy<sup>2,3</sup> and ageing<sup>4</sup>. However, many MEK inhibitors are limited owing to on-target toxicities<sup>5,6,7</sup> and drug resistance<sup>8,9,10</sup>. Accordingly, a molecular understanding of the structure and function of MEK within physiological complexes could provide a template for the design of safer and more effective therapies. Here we report X-ray crystal structures of MEK bound to the scaffold KSR (kinase suppressor of RAS) with various MEK inhibitors, including the clinical drug trametinib. The structures reveal an unexpected mode of binding in which trametinib directly engages KSR at the MEK interface. In the bound complex, KSR remodels the prototypical allosteric pocket of the MEK inhibitor, thereby affecting binding and kinetics, including the drug-residence time. Moreover, trametinib binds KSR–MEK but disrupts the related RAF–MEK complex through a mechanism that exploits evolutionarily conserved interface residues that distinguish these sub-complexes. On the basis of these insights, we created trametiglue, which limits adaptive resistance to MEK inhibition by enhancing interfacial binding. Our results reveal the plasticity of an interface pocket within MEK sub-complexes and have implications for the design of next-generation drugs that target the RAS pathway.

[Access through your institution](#)

[Change institution](#)

[Buy or subscribe](#)

## Access options

Subscribe to Journal

Get full journal access for 1 year

185,98 €

only 3,58 € per issue

## Subscribe

All prices are NET prices.  
VAT will be added later in the checkout.

Rent or Buy article

Get time limited or full article access on ReadCube.

from \$8.99

## Rent or Buy

All prices are NET prices.

## **Additional access options:**

- [Log in](#)
- [Access through your institution](#)
- [Learn about institutional subscriptions](#)

**Fig. 1: The trametinib-binding pocket in MEK extends to the KSR interaction interface.**

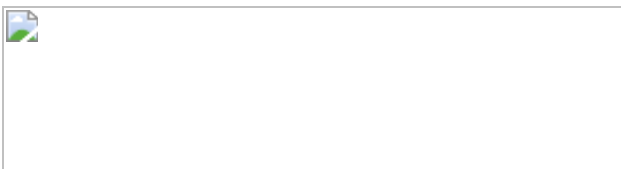


**Fig. 2: Binding of KSR to MEK creates an enlarged allosteric binding pocket for inhibitors.**

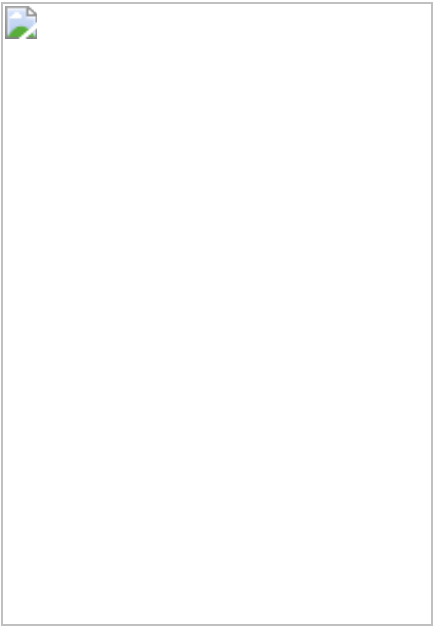


**Fig. 3: The trametinib-binding site distinguishes KSR from RAF.**

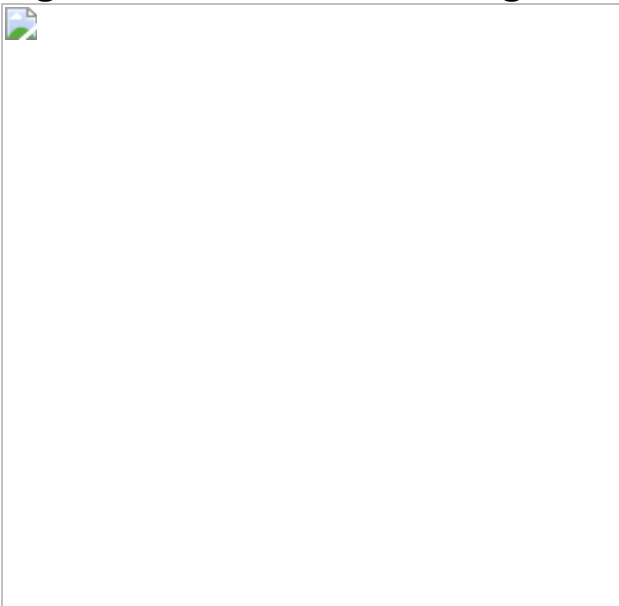
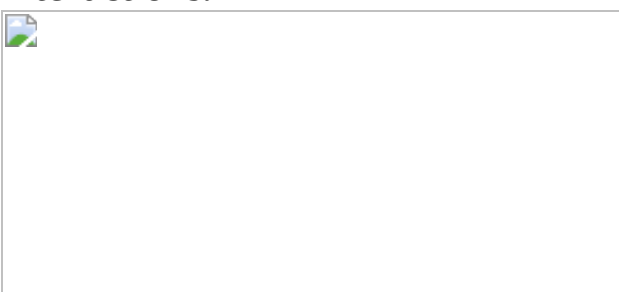


**Fig. 4: Trametiglue targets both KSR–MEK and RAF–MEK with unprecedented potency and selectivity via unique interfacial binding interactions.**



# Data availability

Atomic coordinates and structure factors have been deposited in the Protein Data Bank (PDB) under accession codes [7JUQ](#), [7JUR](#), [7JUS](#), [7JUT](#), [7JUU](#), [7JUV](#), [7JUW](#), [7JUX](#), [7JUY](#), [7JUZ](#), [7JV0](#) and [7JV1](#). [Source data](#) are provided with this paper.

# References

1. 1.

Zhao, Y. & Adjei, A. A. The clinical development of MEK inhibitors. *Nat. Rev. Clin. Oncol.* **11**, 385–400 (2014).

[CAS](#) [PubMed](#) [Google Scholar](#)

2. 2.

Ebert, P. J. R. et al. map kinase inhibition promotes T Cell and anti-tumor activity in combination with PD-L1 checkpoint blockade. *Immunity* **44**, 609–621 (2016).

[CAS](#) [PubMed](#) [Google Scholar](#)

3. 3.

Liu, L. et al. The BRAF and MEK inhibitors dabrafenib and trametinib: effects on immune function and in combination with immunomodulatory antibodies targeting PD-1, PD-L1, and CTLA-4. *Clin. Cancer Res.* **21**, 1639–1651 (2015).

[ADS](#) [CAS](#) [PubMed](#) [Google Scholar](#)

4. 4.

Slack, C. et al. The Ras-Erk-ETS-signaling pathway is a drug target for longevity. *Cell* **162**, 72–83 (2015).

[CAS](#) [PubMed](#) [PubMed Central](#) [Google Scholar](#)

5. 5.

LoRusso, P. M. et al. Phase I pharmacokinetic and pharmacodynamic study of the oral MAPK/ERK kinase inhibitor PD-0325901 in patients with advanced cancers. *Clin. Cancer Res.* **16**, 1924–1937 (2010).

[CAS](#) [PubMed](#) [Google Scholar](#)

6. 6.

Huang, W. et al. PD0325901, a mitogen-activated protein kinase kinase inhibitor, produces ocular toxicity in a rabbit animal model of retinal vein occlusion. *J. Ocul. Pharmacol. Ther.* **25**, 519–530 (2009).

[CAS](#) [PubMed](#) [Google Scholar](#)

7. 7.

Infante, J. R. et al. Safety and efficacy results from the first-in-human study of the oral MEK 1/2 inhibitor GSK1120212. *J. Clin. Orthod.* **28**, 2503–2503 (2010).

[Google Scholar](#)

8. 8.

Emery, C. M. et al. MEK1 mutations confer resistance to MEK and BRAF inhibition. *Proc. Natl Acad. Sci. USA* **106**, 20411–20416 (2009).

[ADS](#) [CAS](#) [PubMed](#) [Google Scholar](#)

9. 9.

Lito, P. et al. Disruption of CRAF-mediated MEK activation is required for effective MEK inhibition in KRAS mutant tumors. *Cancer Cell* **25**, 697–710 (2014).

[CAS](#) [PubMed](#) [PubMed Central](#) [Google Scholar](#)

10. 10.

Gao, Y. et al. V211D mutation in MEK1 causes resistance to MEK Inhibitors in colon cancer. *Cancer Discov.* **9**, 1182–1191 (2019).

[CAS](#) [PubMed](#) [PubMed Central](#) [Google Scholar](#)

11. 11.

Simanshu, D. K., Nissley, D. V. & McCormick, F. RAS proteins and their regulators in human disease. *Cell* **170**, 17–33 (2017).

[CAS](#) [PubMed](#) [PubMed Central](#) [Google Scholar](#)

12. 12.

Moore, A. R., Rosenberg, S. C., McCormick, F. & Malek, S. RAS-targeted therapies: is the undruggable drugged? *Nat. Rev. Drug Discov.* **19**, 533–552 (2020).

[CAS](#) [PubMed](#) [Google Scholar](#)

13. 13.

Long, G. V. et al. Dabrafenib and trametinib versus dabrafenib and placebo for Val600 BRAF-mutant melanoma: a multicentre, double-blind, phase 3 randomised controlled trial. *Lancet* **386**, 444–451 (2015).

[CAS](#) [PubMed](#) [Google Scholar](#)

14. 14.

Kinsey, C. G. et al. Protective autophagy elicited by RAF → MEK → ERK inhibition suggests a treatment strategy for RAS-driven cancers. *Nat. Med.* **25**, 620–627(2019).

[CAS](#) [PubMed](#) [PubMed Central](#) [Google Scholar](#)

15. 15.

Ribas, A. et al. Phase I study combining anti-PD-L1 (MEDI4736) with BRAF (dabrafenib) and/or MEK (trametinib) inhibitors in advanced melanoma. *J. Clin. Orthod.* **33**, 3003–3003 (2015).

[Google Scholar](#)

16. 16.

Canon, J. et al. The clinical KRAS(G12C) inhibitor AMG 510 drives anti-tumour immunity. *Nature* **575**, 217–223 (2019).

[ADS](#) [CAS](#) [PubMed](#) [Google Scholar](#)

17. 17.

Yamaguchi, T. et al. Identification of JTP-70902, a p15(INK4b)-inductive compound, as a novel MEK1/2 inhibitor. *Cancer Sci.* **98**, 1809–1816 (2007).

[CAS](#) [PubMed](#) [Google Scholar](#)

18. 18.

Westbrook, J. D. & Burley, S. K. How structural biologists and the protein data bank contributed to recent FDA new drug approvals. *Structure* **27**, 211–217 (2019).

[CAS](#) [PubMed](#) [Google Scholar](#)

19. 19.

Fischmann, T. O. et al. Crystal structures of MEK1 binary and ternary complexes with nucleotides and inhibitors. *Biochemistry* **48**, 2661–2674 (2009).

[CAS](#) [PubMed](#) [Google Scholar](#)

20. 20.

Ohren, J. F. et al. Structures of human MAP kinase kinase 1 (MEK1) and MEK2 describe novel noncompetitive kinase inhibition. *Nat. Struct. Mol. Biol.* **11**, 1192–1197 (2004).

[CAS](#) [PubMed](#) [Google Scholar](#)

21. 21.

Yoshida, T. et al. Identification and characterization of a novel chemotype MEK inhibitor able to alter the phosphorylation state of MEK1/2. *Oncotarget* **3**, 1533–1545 (2012).

[PubMed](#) [PubMed Central](#) [Google Scholar](#)

22. 22.

Hatzivassiliou, G. et al. Mechanism of MEK inhibition determines efficacy in mutant KRAS- versus BRAF-driven cancers. *Nature* **501**, 232–236 (2013).

[ADS](#) [CAS](#) [PubMed](#) [Google Scholar](#)

23. 23.

Kornfeld, K., Hom, D. B. & Horvitz, H. R. The ksr-1 gene encodes a novel protein kinase involved in Ras-mediated signaling in *C. elegans*. *Cell* **83**, 903–913 (1995).

[CAS](#) [PubMed](#) [Google Scholar](#)

24. 24.

Robers, M. B. et al. Quantitative, real-time measurements of intracellular target engagement using energy transfer. *Methods Mol. Biol.* **1888**, 45–71 (2019).

[CAS](#) [PubMed](#) [Google Scholar](#)

25. 25.

Ishii, N. et al. Enhanced inhibition of ERK signaling by a novel allosteric MEK inhibitor, CH5126766, that suppresses feedback reactivation of RAF activity. *Cancer Res.* **73**, 4050–4060 (2013).

[CAS](#) [PubMed](#) [PubMed Central](#) [Google Scholar](#)

26. 26.

Vauquelin, G. & Charlton, S. J. Long-lasting target binding and rebinding as mechanisms to prolong in vivo drug action. *Br. J. Pharmacol.* **161**, 488–508 (2010).

[CAS](#) [PubMed](#) [PubMed Central](#) [Google Scholar](#)

27. 27.

Lavoie, H. & Therrien, M. Regulation of RAF protein kinases in ERK signalling. *Nat. Rev. Mol. Cell Biol.* **16**, 281–298 (2015).

[CAS](#) [PubMed](#) [Google Scholar](#)

28. 28.

Brennan, D. F. et al. A Raf-induced allosteric transition of KSR stimulates phosphorylation of MEK. *Nature* **472**, 366–369 (2011).

[ADS](#) [CAS](#) [PubMed](#) [Google Scholar](#)

29. 29.

Dhawan, N. S., Scopont, A. P. & Dar, A. C. Small molecule stabilization of the KSR inactive state antagonizes oncogenic Ras signalling. *Nature* **537**, 112–116 (2016).

[ADS](#) [CAS](#) [PubMed](#) [PubMed Central](#) [Google Scholar](#)

30. 30.

Haling, J. R. et al. Structure of the BRAF-MEK complex reveals a kinase activity independent role for BRAF in MAPK signaling. *Cancer Cell* **26**, 402–413 (2014).

[CAS](#) [PubMed](#) [Google Scholar](#)

31. 31.

Liau, N. P. D. et al. Negative regulation of RAF kinase activity by ATP is overcome by 14-3-3-induced dimerization. *Nat. Struct. Mol. Biol.* **27**, 134–141 (2020).

[CAS](#) [PubMed](#) [Google Scholar](#)

32. 32.

Copeland, R. A. The drug-target residence time model: a 10-year retrospective. *Nat. Rev. Drug Discov.* **15**, 87–95 (2016).

[CAS](#) [PubMed](#) [Google Scholar](#)

33. 33.

Gilmartin, A. G. et al. GSK1120212 (JTP-74057) is an inhibitor of MEK activity and activation with favorable pharmacokinetic properties for sustained in vivo pathway inhibition. *Clin. Cancer Res.* **17**, 989–1000 (2011).

[CAS](#) [PubMed](#) [Google Scholar](#)

34. 34.

Yaeger, R. & Corcoran, R. B. Targeting alterations in the RAF-MEK pathway. *Cancer Discov.* **9**, 329–341 (2019).

[CAS](#) [PubMed](#) [PubMed Central](#) [Google Scholar](#)

35. 35.

Sos, M. L. et al. Oncogene mimicry as a mechanism of primary resistance to BRAF inhibitors. *Cell Rep.* **8**, 1037–1048 (2014).

[CAS](#) [PubMed](#) [PubMed Central](#) [Google Scholar](#)

36. 36.

Kung, J. E. & Jura, N. Prospects for pharmacological targeting of pseudokinases. *Nat. Rev. Drug Discov.* **18**, 501–526 (2019).

[CAS](#) [PubMed](#) [Google Scholar](#)

37. 37.

Kabsch, W. XDS. *Acta Crystallogr. D* **66**, 125–132 (2010).

[CAS](#) [PubMed](#) [Google Scholar](#)

38. 38.

McCoy, A. J. et al. Phaser crystallographic software. *J. Appl. Crystallogr.* **40**, 658–674 (2007).

[CAS](#) [PubMed](#) [PubMed Central](#) [Google Scholar](#)

39. 39.

Emsley, P., Lohkamp, B., Scott, W. G. & Cowtan, K. Features and development of Coot. *Acta Crystallogr. D* **66**, 486–501 (2010).

[CAS](#) [PubMed](#) [Google Scholar](#)

40. 40.

Moriarty, N. W., Grosse-Kunstleve, R. W. & Adams, P. D. electronic Ligand Builder and Optimization Workbench (eLBOW): a tool for

ligand coordinate and restraint generation. *Acta Crystallogr. D* **65**, 1074–1080 (2009).

[CAS](#) [PubMed](#) [Google Scholar](#)

41. 41.

Afonine, P. V. et al. Towards automated crystallographic structure refinement with phenix.refine. *Acta Crystallogr. D* **68**, 352–367 (2012).

[CAS](#) [PubMed](#) [Google Scholar](#)

42. 42.

Vasta, J. D. et al. Quantitative, wide-spectrum kinase profiling in live cells for assessing the effect of cellular ATP on target engagement. *Cell Chem. Biol.* **25**, 206–214.e11 (2018).

[CAS](#) [PubMed](#) [PubMed Central](#) [Google Scholar](#)

43. 43.

Viswanatha, R., Li, Z., Hu, Y. & Perrimon, N. Pooled genome-wide CRISPR screening for basal and context-specific fitness gene essentiality in *Drosophila* cells. *eLife* **7**, e36333 (2018).

[PubMed](#) [PubMed Central](#) [Google Scholar](#)

44. 44.

Strub, T. et al. SIRT6 haploinsufficiency induces BRAF<sup>V600E</sup> melanoma cell resistance to MAPK inhibitors via IGF signalling. *Nat. Commun.* **9**, 3440 (2018).

[ADS](#) [PubMed](#) [PubMed Central](#) [Google Scholar](#)

45. 45.

Rajakulendran, T., Sahmi, M., Lefrançois, M., Sicheri, F. & Therrien, M. A dimerization-dependent mechanism drives RAF catalytic activation. *Nature* **461**, 542–545 (2009).

[ADS](#) [CAS](#) [PubMed](#) [Google Scholar](#)

46. 46.

Lavoie, H. et al. MEK drives BRAF activation through allosteric control of KSR proteins. *Nature* **554**, 549–553 (2018).

[ADS](#) [CAS](#) [PubMed](#) [PubMed Central](#) [Google Scholar](#)

[Download references](#)

## Acknowledgements

We thank K. Shokat, R. Parsons, E. Bernstein and laboratories for comments and suggestions on this work and manuscript, and staff at the Advanced Photon Source (LS-CAT sector 21) and the National Synchrotron Light Source II (Beamlines 17-ID-1 AMX and 17-ID-2 FMX) for help with X-ray diffraction experiments. We thank M. Robers and J. Vasta (Promega) for advice on NanoBRET experiments. The Dar laboratory has been supported by innovation awards from the NIH (1DP2CA186570-01) and Damon Runyan Rachleff Foundation, as well as NIH grants 1RO1CA227636 and 5U54OD020353. The authors are also supported by NCI grant P30 CA196521 to the Tisch Cancer Institute. A.M.R. and W.M.M. are recipients of NIH F30 (CA232454) and F99/K00 (CA212474) awards, respectively. A.C. and M.E.D. are recipients of T32 fellowships 5T32CA078207 and 5T32GM062754, respectively. A.C.D. has been supported as a Pew-Stewart Scholar in Cancer Research and a Young Investigator of the Pershing-Square Sohn Cancer Research Alliance.

## Author information

Author notes

1. These authors contributed equally: Zaigham M. Khan, Alexander M. Real, William M. Marsiglia

## Affiliations

1. Department of Oncological Sciences, The Tisch Cancer Institute, Icahn School of Medicine at Mount Sinai, New York, NY, USA

Zaigham M. Khan, Alexander M. Real, William M. Marsiglia, Arthur Chow, Mary E. Duffy, Jayasudhan R. Yerabolu, Alex P. Scpton & Arvin C. Dar

2. Department of Pharmacological Sciences, The Tisch Cancer Institute, Icahn School of Medicine at Mount Sinai, New York, NY, USA

Zaigham M. Khan, Alexander M. Real, William M. Marsiglia, Arthur Chow, Mary E. Duffy, Jayasudhan R. Yerabolu, Alex P. Scpton & Arvin C. Dar

## Authors

1. Zaigham M. Khan

[View author publications](#)

You can also search for this author in [PubMed](#) [Google Scholar](#)

2. Alexander M. Real

[View author publications](#)

You can also search for this author in [PubMed](#) [Google Scholar](#)

3. William M. Marsiglia

[View author publications](#)

You can also search for this author in [PubMed](#) [Google Scholar](#)

4. Arthur Chow

[View author publications](#)

You can also search for this author in [PubMed](#) [Google Scholar](#)

5. Mary E. Duffy

[View author publications](#)

You can also search for this author in [PubMed](#) [Google Scholar](#)

6. Jayasudhan R. Yerabolu

[View author publications](#)

You can also search for this author in [PubMed](#) [Google Scholar](#)

7. Alex P. Scpton

[View author publications](#)

You can also search for this author in [PubMed](#) [Google Scholar](#)

8. Arvin C. Dar

[View author publications](#)

You can also search for this author in [PubMed](#) [Google Scholar](#)

## Contributions

Z.M.K. expressed and purified proteins, conducted bio-layer interferometry binding assays, and solved X-ray crystal structures. W.M.M. conducted NanoBRET studies and synthesized tram-bo. A.M.R. conducted co-immunoprecipitation and signalling assays. A.C. conducted knockdown studies, cell viability and signalling assays. M.E.D. conducted cell viability studies. A.P.S. synthesized trametinib-biotin and trametiglue. J.R.Y. synthesized analogues. All authors analysed data. A.C.D. supervised research and drafted the manuscript with input from all authors.

## Corresponding author

Correspondence to [Arvin C. Dar](#).

# Ethics declarations

## Competing interests

A provisional patent application (no. 63/044,338) has been filed by Mount Sinai.

## Additional information

**Peer review information** *Nature* thanks David Solit and the other, anonymous, reviewer(s) for their contribution to the peer review of this work.

**Publisher's note** Springer Nature remains neutral with regard to jurisdictional claims in published maps and institutional affiliations.

## Extended data figures and tables

### [Extended Data Fig. 1 Summary of ligand-bound complexes of KSR1-MEK1 and KSR2-MEK1.](#)

**a**, Resolution, number of reflections, and ligand omit maps for all described structures. Detailed data collection and refinement statistics are provided in Supplementary Table 1.  $F_o - F_c$  omit electron density maps are all contoured at  $3.0\sigma$ , with a  $2.0 \text{ \AA}$  cut-off value, around the ligands and shown as a blue mesh. **b**, Trametinib bound to KSR2–MEK1–AMP-PNP. **c**, Trametinib contacts include P878 in the pre-helix  $\alpha$ G loop of KSR2. Direct contacts of trametinib with MEK1 also highlighted. **d**, 2D schematic of the trametinib-binding pocket in KSR2–MEK1. **e**, 2D structures, formulas, and molecular masses of MEK inhibitors used in this study.

### [Extended Data Fig. 2 Conformational changes in MEK and KSR after binding to trametinib.](#)

**a**, Close-up view of the trametinib interactions with KSR1 (left) and KSR2 (right). The terminal acetamide group of trametinib stacks between Ile216 in MEK1 and Ala825 in KSR1 or Pro878 in KSR2. Distances with hydrogens included in the models of trametinib and KSR measure 2.4 Å and 3.5 Å between alpha and beta hydrogens of Ala825 in KSR1 and the terminal -CH<sub>3</sub> of trametinib. In comparison, the terminal -CH<sub>3</sub> of trametinib measures 2.2 Å and 3.1 Å from beta and gamma hydrogens of Pro878. Measurements are marked by black arrows. Ser222 at one end of the anti-parallel activation segments between MEK and KSR is highlighted. **b**, The MEK inhibitor allosteric pocket, and activation segment displacement, between the isolated state of MEK1 bound to PD0325901 relative to the KSR1–MEK1 complex bound to trametinib. The displacement in the activation segment was measured based on movement of residue Asn221 in the isolated and KSR1-bound state of MEK1. **c**, Left, distinct activation loop conformers of isolated MEK1 have been observed in complex with PD0325901 (purple; PDB code 3VVH), TAK733 (light brown; 3PP1), selumetinib (light blue; 4U7Z), and cobimetinib (light green; 4LMN). Middle and right, overlay of the KSR1–MEK1 and KSR2–MEK1 structures bound to the indicated MEK inhibitors reveal near identical activation segment conformers, with the exception of the trametinib-bound complex of KSR1–MEK1. **d**, Comparison of activation loop conformations in cobimetinib-bound (left) and trametinib-bound (right) states of the KSR1–MEK1 (top) and KSR2–MEK1 (bottom) complexes.  $F_o - F_c$  omit electron density map, contoured at 2.0 $\sigma$ , with a 3.0 Å cut-off, around the activation loop is shown as a blue mesh. Movement of the MEK activation loop between the two inhibitor-bound states of KSR1–MEK1 is highlighted by a red arrow. Main chain H-bonds between the anti-parallel beta strands in KSR and MEK are shown as dotted lines. **e**, In the trametinib-bound KSR1–MEK1 complex, a four-residue anti-parallel beta strand structure is formed between KSR1 and MEK1. In comparison, the same region forms a three-residue stretch in all other KSR1–MEK1 structures that we determined; the cobimetinib-bound complex is shown as an example for comparison. By contrast, a six-residue long anti-parallel beta strand is formed in the KSR2–MEK1 structures, irrespective of bound MEK inhibitor. The three- and four-residue-long strands in KSR1–MEK1 include residues 769–771/772 for KSR1 and 222/223–225 for MEK1. The six

residue long strands in KSR2–MEK1 include residues 820–825 for KSR2 and 221–226 for MEK1.

### Extended Data Fig. 3 Structural differences between human KSR1 and KSR2.

**a**, Comparison of helices  $\alpha$ G- $\alpha$ G' in the KSR1–MEK1 complex (left) and helix  $\alpha$ G in the KSR2–MEK1 complex. **b**,  $2F_o - F_c$  omit electron density maps contoured at  $1.0\sigma$ , with a  $2.0 \text{ \AA}$  cut-off value, around helices  $\alpha$ G- $\alpha$ G' in KSR1 (left) and  $\alpha$ G in KSR2 (right). **c**,  $2F_o - F_c$  omit electron density maps contoured at  $1.0\sigma$ , with a  $2.0 \text{ \AA}$  cut-off, around strand  $\beta$ 2 in KSR1 (left) and KSR2 (right). **d**,  $2F_o - F_c$  omit electron density maps contoured at  $1.0\sigma$ , with a  $2.0 \text{ \AA}$  cut-off, around the hinge region in KSR1 (left) and KSR2 (right). **e**,  $2F_o - F_c$  omit electron density maps contoured at  $1.0\sigma$ , with a  $2.0 \text{ \AA}$  cut-off, around helix  $\alpha$ D in KSR1 (left) and KSR2 (right). **f**, Positionally equivalent residues His773 in KSR1 and Asn826 in KSR2 form distinct intra- and inter-molecular contacts, respectively. Specifically, His773 in KSR1 forms a hydrogen bond with the backbone carbonyl of Leu821 in the  $\alpha$ F- $\alpha$ G loop of KSR1 (left). Whereas Asn826 in KSR2 forms a hydrogen bond across the interfacial region of the KSR2–MEK1 complex via the backbone carbonyl of M219 in MEK1. **g**, Structure-based sequence alignment of the pseudokinase domains of KSR1 and KSR2 based on structures solved in this study. Boxed regions are highlighted in the top panels **a–f**.

### Extended Data Fig. 4 Intracellular target engagement on MEK and KSR-bound MEK via bioluminescence resonance energy transfer.

**a**, Chemical structure of trametinib-bodipy. We refer to this fluorescent probe compound as ‘tram-bo’. **b**, Legend for schematics used in the bottom panels. **c**, Nano-luciferase tagged fusions of MEK (MEK-luc) and mouse KSR1 (KSR-luc). **d**, BRET emission signal (red arrow) between MEK-luc and tram-bo is expected to occur within multiple distinct states of MEK, including in the KSR-bound and free states of MEK as depicted. **e**, BRET emission (red arrow) between KSR-luc and tram-bo is expected to occur

exclusively in the KSR-bound state of MEK as depicted. **f**, Assay design for steady-state competition experiments. **g**, Assay design for intracellular residence time experiments. **h**, BRET signals between 1  $\mu$ M tram-bo and the indicated luciferase tagged fusion proteins expressed in 293T cells. Increasing concentrations of free trametinib were added to these cells to determine IC<sub>50</sub> values. Dose-dependent competition for free trametinib was observed on MEK-luc and mouse KSR-luc. However, no discernible dose response for trametinib was observed on controls including RET-luc and SRC-luc using either tram-bo or previously established active-site tracers K5 and K4<sup>42</sup>, respectively. **i**, A helix  $\alpha$ G mutant, W781D in mouse KSR1, supports that the BRET signal between wild-type KSR1 and tram-bo depends on intact complex formation between KSR and MEK within cells. In particular, the KSR1(W781D) mutant does not produce any dose dependent BRET signal (using 1  $\mu$ M tram-bo) due to a predicted loss of complexation with MEK1; we previously demonstrated that the W781D mutant (W884D in KSR2 numbering) is a strong loss of function in KSR with respect to ERK pathway activation, and the analogous mutation in BRAF(F667E) prevents direct binding with purified MEK<sup>29</sup>. Trp781 in mouse KSR1 is equivalent to Trp831 in human KSR1, Trp884 in human KSR2, and Phe667 in human BRAF. Structural depiction of the mouse Trp781 residue at the interface of KSR1-MEK1 complex is shown below.

### Extended Data Fig. 5 MEK inhibitor IC<sub>50</sub> measurements and residence time are influenced by protein complex stoichiometry.

**a**, IC<sub>50</sub> values plotted as a function of MEK inhibition for MEK1-luc and KSR1-luc (left). Data are mean and s.e.m. from three independent experiments, each conducted in technical triplicate. CH5126766 was not plotted due to poor fit. MEK1-luc (middle) and KSR1-luc (right) dose-response curves for plotted IC<sub>50</sub> values using 1  $\mu$ M tram-bo. Data are mean and s.e.m. for three independent experiments, each conducted in technical triplicates. **b**, Comparison of MEK inhibitor IC<sub>50</sub> measurements and representative dose-response curves of MEK1-luc, KSR1-luc, MEK1-luc co-expressed with wild-type KSR1, and MEK1-luc co-expressed with KSR1(W781D). Co-expression of wild-type KSR1 with MEK1-luc gives

rise to dose response curves and IC<sub>50</sub> values similar to that of KSR1-luc alone. This effect does not occur for the co-expression of MEK1-luc with KSR1(W781D), indicating that IC<sub>50</sub> differences between MEK1-luc and KSR1-luc depend on the formation of the KSR-MEK complex mediated by helix αG. Data are mean and s.e.m. from three independent experiments, each conducted in technical duplicate. IC<sub>50</sub> values derived from KSR1-luc, MEK1-luc co-expressed with wild-type KSR1 or mutant KSR1(W781D) were compared to those of MEK1-luc for each MEK inhibitor using an ANOVA. \*P < 0.05. For trametinib, data were subjected to a Kruskal–Wallis test and Dunn's multiple comparison post hoc test (MEK1-luc vs KSR1-luc adjusted P > 0.9999, MEK1-luc vs MEK1-luc + KSR1-WT adjusted P > 0.9999, MEK1-luc vs MEK1-luc + KSR1-W781D adjusted P = 0.4298). All other data were subjected to an ordinary one-way ANOVA and Dunnett's multiple comparison post hoc test with a single pooled variance (cobimetinib: MEK1-luc vs KSR1-luc adjusted P = 0.0015, MEK1-luc vs MEK1-luc + KSR1-WT P = 0.0021, MEK1-luc vs MEK1-luc + KSR1-W781D P = 0.9940; PD0325901: MEK1-luc vs KSR1-luc adjusted P = 0.0350, MEK1-luc vs MEK1-luc + KSR1-WT P = 0.1524, MEK1-luc vs MEK1-luc + KSR1-W781D P = 0.9920; selumetinib: MEK1-luc vs KSR1-luc adjusted P = 0.0578, MEK1-luc vs MEK1-luc + KSR1-WT P = 0.0693, MEK1-luc vs MEK1-luc + KSR1-W781D P = 0.9994).

Cobimetinib displayed the largest difference in IC<sub>50</sub> value between MEK1-luc and KSR1-luc or MEK1-luc + KSR1-WT. **c**, Left, schematic for the origin of the BRET signal under co-expression conditions. Right, tram-bo build-up curves for MEK1-luc, KSR1-luc, MEK1-luc co-expressed with wild-type KSR1, and MEK1-luc co-expressed with KSR1(W781D). Co-expression of MEK1-luc and wild-type KSR1 resulted in a lower BRET signal and slower tram-bo build-up compared to MEK1-luc alone. Co-expression of MEK1-luc and KSR(W781D) gave similar curves to MEK1-luc alone, suggesting that complex formation is disfavoured under these conditions.

**Extended Data Fig. 6 KSR and RAF share complementary regulatory roles as MEK scaffolds and activators.**

**a**, KSR and RAF family members appear to have co-evolved. Phylogenetic tree diagrams for the indicated species were generated from reported kinome sequence data that can be found at <http://kinase.com/web/current/kinbase/>. All species that we analysed include at least one RAF and one KSR homologue. **b**, Structures of MEK1 in complex with KSR1 and KSR2 determined here, and previously determined structures of MEK1–BRAF-active conformation (PDB code 4MNE), and MEK1–BRAF-inactive conformation (PDB code 6U2G). **c**, Structural overlay of MEK1-associated complexes highlights variations in the quaternary arrangements of KSR-bound MEK and RAF-bound MEK. Shown are overlays of MEK1–KSR1 with MEK1–KSR2 (left); MEK1–BRAF (PDB code 4MNE) with MEK1–BRAF (PDB code 6U2G) (centre); and MEK1–KSR1 with MEK1–BRAF (PDB code 4MNE). In particular, the N-lobe, including helix  $\alpha$ C, in KSR and RAF proteins are significantly displaced between distinct complexes. However, in contrast, the lower C lobe, including helix  $\alpha$ G, appears relatively fixed in all sets of complexes. **d**, Overlay of all structures, using MEK1 C-lobe as an anchor (centre), demonstrates helix  $\alpha$ G as a common docking site for reciprocal kinase domain interactions between MEK and BRAF or KSR (left inset). Further, the pre-helix  $\alpha$ G loop regions within BRAF and KSR proteins occupy a relatively fixed location relative to MEK (right inset).

### **Extended Data Fig. 7 Variance in the pre-helix $\alpha$ G loops of KSR and RAF proteins determines selectivity for trametinib.**

**a**, The pre-helix  $\alpha$ G loop in BRAF (left; N660-N661-R662) includes an insertion and larger amino acid side chains compared to KSR1 (middle; GAP-A825-A826) and KSR2 (right; GAP-P878-A879), creating a clash with trametinib. **b**, Sequence alignment highlighting conserved variations between RAF kinases and KSR pseudokinases at the trametinib-binding site. Native sequences and mutants in mouse KSR1 and human BRAF used for functional studies in Fig. 3c,d are listed. Mouse KSR1 mutants include K1 (KSR1\_P775N), K2 (KSR1\_A776R), K3 (KSR1\_P775N/A776R), and K4 (KSR1\_insertionN/P775N/A776R). Human BRAF mutants include B1 (BRAF\_N661A), B2 (BRAF\_R662A), B3 (BRAF\_N661A/R662A), and B4 (BRAF\_N660deletion/N661A/R662A). **c, d**, Immunoprecipitation and western blot analysis of endogenous MEK1 from lysates of HCT116 cells

transfected with wild-type KSR1 and mutant K1 (P775N, mouse KSR1 numbering) (left); wild-type BRAF and mutant B2 (R662A) (middle); and untransfected controls (right). Cells were treated with DMSO (D), 200 nM trametinib (T) or 200 nM cobimetinib (C) for 1 h before collecting cells. IgG was used as a control for non-specific binding of proteins during immunoprecipitations. Transfected KSR1 or BRAF were detected using an anti-Flag antibody. All other western blot signals were detected using specific antibodies against endogenous proteins. Blots are representative of three independent experiments. We conducted side-by-side analysis of cobimetinib as a control compound that does not generate direct interfacial contacts like trametinib but displays a similar IC<sub>50</sub> value on the KSR–MEK complex. Note, compare the effects of cobimetinib addition on complex stability to the effects of trametinib in Fig. [3c, d](#). Unlike trametinib, cobimetinib does not affect the KSR1 or BRAF mutants in terms of pulldown through endogenous MEK similar to trametinib. These data support that the ‘bump-and-hole’ model for trametinib selectivity between KSR-bound MEK and RAF-bound MEK. Also note from Fig. [3c, d](#) that all of the tested KSR1 alleles, and also the full swaps of the pre-helix  $\alpha$ G loops between RAF and KSR proteins, resulted in partial or complete loss of pulldown via MEK (Fig. [3c, d](#); lanes 2 vs 10 for mutants K4 and B4), which suggests that the length and composition of interfacial residues within both KSR and RAF proteins are critical and unique determinants of binding towards MEK. **d**, Overlay of four clinical MEK inhibitors highlights the phenyl acetamide group of trametinib as a unique ‘bump’ not found in the other compounds including cobimetinib. **e**, BRET build-up curves with increasing concentrations of tram-bo on the indicated luciferase-tagged versions of human KSR1, KSR2, ARAF, BRAF and CRAF/RAF1. KSR1-luc and KSR2-luc both show higher BRET ratios, and also approximately 10-fold tighter binding, with tram-bo relative to ARAF-luc, BRAF-luc and CRAF-luc. Bottom inset is a y-axis magnification of the top inset. Data points represent the average of two technical replicates; experiments were conducted at least three independent times with similar results.

**Extended Data Fig. 8 In vitro binding of purified MEK, KSR-MEK, and RAF-MEK to trametinib.**

**a**, Representative binding sensograms for 500 nM each of isolated MEK1 or the indicated KSR–MEK and BRAF–MEK complexes on a biosensor immobilized with biotin-conjugated trametinib. Fitting of association and dissociation phases based on one-to-one binding is provided in the Source Data. **b**,  $K_d$  (M),  $K_{on}$  ( $1\text{ M}^{-1}\text{s}^{-1}$ ) and  $K_{dis}$  ( $1\text{ s}^{-1}$ ) values for MEK1 (M), KSR1–MEK1 (K1M1), KSR2–MEK1 (K2M2) and BRAF–MEK1 (BRM1) on biotin-linked trametinib. Individual data points from independent binding experiments ( $n = 29, 14, 22$  and  $9$  for MEK1, KSR1–MEK1, KSR2–MEK1 and BRAF–MEK1, respectively) were used for statistical comparisons. \*\*\*\* $P \leq 0.0001$ . Note, trametinib probably favours dissociation of BRAF from MEK1 for binding. For example, whereas the association and  $K_d$  data between BRAF–MEK1 and isolated MEK1 markedly differ, the off rate and residence time calculations are similar. These data would be consistent with a model in which the equilibrium of BRAF–MEK1 shifts so as to populate the dissociated state under the conditions of the bio-layer interferometry assays. **c**, Residence time values plotted as a function of protein concentration. MEK1 and BRAF–MEK1 display small variations in residence time over the concentrations tested. Whereas KSR2–MEK1 and KSR1–MEK1 demonstrate concentration-dependent changes in residence time. In particular, at low concentrations of KSR–MEK, in which the complexes would be expected to more readily dissociate, the kinetic values of purified KSR1–MEK1 and KSR2–MEK1 approached isolated MEK1 and BRAF–MEK1. **d**, Full binding curve experiment including loading of biotin-conjugated trametinib for 10 min, followed by a wash step, and subsequently treating a low-density streptavidin (SA) sensor with a blocking agent, biocytin for 3 min. The sensors were washed extensively to acquire a zero baseline before binding analysis. Next, sensors were dipped in wells containing 500 nM of each protein for 15 min, followed by a dissociation in running buffer for 15 min. **e**, A biotin-conjugated version of trametinib was immobilized on sensor-heads and binding to MEK1, KSR1–MEK1, KSR2–MEK1 or BRAF–MEK1 was monitored using bio-layer interferometry. Increasing concentrations in twofold increments of proteins from 31.25 nM to 500 nM for MEK1, KSR1–MEK1 and KSR2–MEK1 and 500 nM to 2,000 nM for BRAF–MEK1 were tested. A blank sensor head without immobilized trametinib was used as a control for non-specific binding.  $K_d$  (M),  $K_{on}$

( $1\text{ M}^{-1}\text{ s}^{-1}$ ) and  $K_{\text{dis}}$  ( $1\text{ s}^{-1}$ ) values were derived from fitting each binding curve [Source data](#).

### Extended Data Fig. 9 KSR as a co-receptor for binding to trametinib.

**a**, Literature data on CRISPR depletion screens highlight strong functional interactions between trametinib and KSR. For example, in a *Drosophila* cellular fitness model<sup>43</sup> (left) and a human BRAF(V600E) mutant cell line<sup>44</sup> (right), single-guide RNAs (sgRNAs) towards KSR generated relative outlier sensitivity or resistance to trametinib or a trametinib plus dabrafenib combination, respectively. Raw data from ref. <sup>43</sup> was plotted based on the authors determination of a Z-score for  $\log_2$ -transformed fold change in sgRNA reads for S2 cells treated with trametinib versus a no treatment control (left). Raw data from ref. <sup>44</sup> was plotted based on the authors determination of  $\log_2$ -transformed fold change in sgRNA reads for SKMEL-239 cells treated with a trametinib plus dabrafenib combination relative to a no treatment control (right). sgRNAs towards KSR are highlighted as a red dot; all other sgRNAs analysed in the respective studies are shown as grey dots. KSR emerged as a strong outlier beyond the mean plus standard deviation (black cross hairs) of all genes analysed in each respective study. These screens could be re-investigated based on the model that KSR functions as a direct co-receptor for binding to trametinib and MEK. **b**, Model for the action of trametinib on KSR–MEK and RAF–MEK complexes. In the absence of drug, MEK activation depends on heterodimerization of both RAF and KSR, with phosphorylation on the sites Ser218/Ser222 occurring by active RAF kinases. This model is adapted from structural and biochemical studies previously described<sup>28,29,45,46</sup>. Trametinib could downregulate ERK signalling by impeding direct binding of MEK towards RAF in favour of KSR. In the KSR-bound state of MEK, trametinib would be expected to reside on target for extended periods of time.

### Extended Data Fig. 10 Trametiglue provides durable inhibition of RAS/ERK signalling in models of mutant KRAS and BRAF.

**a**, Left, immunoblot of stable HCT116 (KRAS(G13D)) cancer cells including parental, scramble control shRNA (shSCR), and KSR1 knockdown (shKSR1). Cells were treated with 10 nM trametinib for the indicated time points and collected for analysis on the indicated markers. Right, quantitative PCR was used to confirm specific knockdown of KSR1 in the shKSR1 cells. KSR1 knockdown slows the rebound of activated RAS-MAPK signalling in the presence of trametinib as measured by recovered phosphorylated-ERK1/2 over time (lanes 1–5 and 6–10 versus 11–15). These data support the idea that KSR1 has a positive role in the adaptive resistance of HCT116 cells to trametinib, suggesting that knockdown or trapping of the KSR-bound MEK complex could mitigate this intrinsic drug resistance mechanism. Experiment was conducted twice with similar results. **b**, EC<sub>50</sub> values for cell viability assays for the indicated compounds against a series of human cancer cell lines. Mean and s.d. determined from three independent experiments, each conducted in technical triplicate. **c**, X-ray crystal structure of trametinib bound to the KSR2–MEK1–AMP-PNP complex. MEK1 and KSR2 are coloured pink and green respectively, with several key residues highlighted. Trametinib is shown in stick representation. A  $F_o - F_c$  omit electron density map, contoured at 3.0 $\sigma$  with a 2.0 Å cut-off value around ligand, is shown as a blue mesh. Left panel shows the entire inhibitor-binding pocket; right panel highlights contacts around the phenyl acetamide group of trametinib. **d**, Bar graph plot of mean EC<sub>50</sub> values from **b**. **e**, Clonogenic assay of KRAS-mutant and BRAF-mutant cancer cell lines treated with 10 nM trametinib or 10 nM trametiglue, and 10 nM or 50 nM CH5126766 for 10 days. Experiment was conducted twice with similar results. **f**, Immunoblot analysis of the indicated cell lines treated for 1 h with increasing concentrations of trametiglue and trametinib. These data support the notion that trametiglue, relative to trametinib, is a higher potency inhibitor of RAS-MAPK signalling as measured by phosphorylated ERK1/2 at residues Thr202 and Tyr204 (pERK). Experiment was conducted three times with similar results. **g**, Immunoblot of KRAS-mutant and BRAF-mutant cancer cell lines treated with 10 nM trametinib or trametiglue for various times. Experiment was conducted twice with similar results [Source data](#).

## Supplementary information

## **Supplementary Information**

This file contains Supplementary Notes, including General Chemical Methods, Supplementary Note Figures 1 and 2, Synthetic Procedures and Characterization Data and LC-MS and  $^1\text{H}$  NMR Spectra.

## **Reporting Summary**

### **Supplementary Table 1**

X-ray crystal structure data collection and refinement statistics.

### **Supplementary Figure 1**

Uncropped blots including molecular weight markers.

### **Supplementary Figure 2**

Replicate data for  $\text{IC}_{50}$  determinations and washouts of MEKi via NanoBRET.

### **Supplementary Figure 3**

Hypothetic models for docking of trametinib into isolated MEK.

## **Source data**

### **Source Data Fig. 4**

### **Source Data Extended Data Fig. 8**

### **Source Data Extended Data Fig. 10**

## **Rights and permissions**

## [Reprints and Permissions](#)

## About this article



Check for  
updates

## Cite this article

Khan, Z.M., Real, A.M., Marsiglia, W.M. *et al.* Structural basis for the action of the drug trametinib at KSR-bound MEK. *Nature* **588**, 509–514 (2020). <https://doi.org/10.1038/s41586-020-2760-4>

## [Download citation](#)

- Received: 01 May 2019
- Accepted: 04 September 2020
- Published: 14 September 2020
- Issue Date: 17 December 2020
- DOI: <https://doi.org/10.1038/s41586-020-2760-4>

## Comments

By submitting a comment you agree to abide by our [Terms](#) and [Community Guidelines](#). If you find something abusive or that does not comply with our terms or guidelines please flag it as inappropriate.

[Access through your institution](#)

[Change institution](#)

[Buy or subscribe](#)

This article was downloaded by **calibre** from <https://www.nature.com/articles/s41586-020-2760-4>

| [Section menu](#) | [Main menu](#) |

- Article
- [Published: 02 December 2020](#)

# Structure of the shutdown state of myosin-2

- [Charlotte A. Scarff](#) ORCID: orcid.org/0000-0001-6168-0060<sup>1,2 na1</sup>,
- [Glenn Carrington](#) ORCID: orcid.org/0000-0003-4060-4725<sup>1,2 na1</sup>,
- [David Casas-Mao](#)<sup>1,2 na1</sup>,
- [Joseph M. Chalovich](#) ORCID: orcid.org/0000-0002-1243-4055<sup>3</sup>,
- [Peter J. Knight](#) ORCID: orcid.org/0000-0002-8850-9500<sup>1,2</sup>,
- [Neil A. Ranson](#) ORCID: orcid.org/0000-0002-3640-5275<sup>1,2</sup> &
- [Michelle Peckham](#) ORCID: orcid.org/0000-0002-3754-2028<sup>1,2</sup>

[Nature](#) volume 588, pages515–520(2020)[Cite this article](#)

- 2847 Accesses
- 112 Altmetric
- [Metrics details](#)

## Subjects

- [Contractile proteins](#)
- [Cryoelectron microscopy](#)
- [Myosin](#)

## Abstract

Myosin-2 is essential for processes as diverse as cell division and muscle contraction. Dephosphorylation of its regulatory light chain promotes an

inactive, ‘shutdown’ state with the filament-forming tail folded onto the two heads<sup>1</sup>, which prevents filament formation and inactivates the motors<sup>2</sup>. The mechanism by which this happens is unclear. Here we report a cryo-electron microscopy structure of shutdown smooth muscle myosin with a resolution of 6 Å in the head region. A pseudo-atomic model, obtained by flexible fitting of crystal structures into the density and molecular dynamics simulations, describes interaction interfaces at the atomic level. The N-terminal extension of one regulatory light chain interacts with the tail, and the other with the partner head, revealing how the regulatory light chains stabilize the shutdown state in different ways and how their phosphorylation would allow myosin activation. Additional interactions between the three segments of the coiled coil, the motor domains and the light chains stabilize the shutdown molecule. The structure of the lever in each head is competent to generate force upon activation. This shutdown structure is relevant to all isoforms of myosin-2 and provides a framework for understanding their disease-causing mutations.

[Access through your institution](#)

[Change institution](#)

[Buy or subscribe](#)

## Access options

Subscribe to Journal

Get full journal access for 1 year

185,98 €

only 3,58 € per issue

[Subscribe](#)

All prices are NET prices.

VAT will be added later in the checkout.

Rent or Buy article

Get time limited or full article access on ReadCube.

from \$8.99

[Rent or Buy](#)

All prices are NET prices.

### **Additional access options:**

- [Log in](#)
- [Access through your institution](#)
- [Learn about institutional subscriptions](#)

**Fig. 1: Structure of the heads region of shutdown SmM and contributions of the RLCs to the shutdown state.**

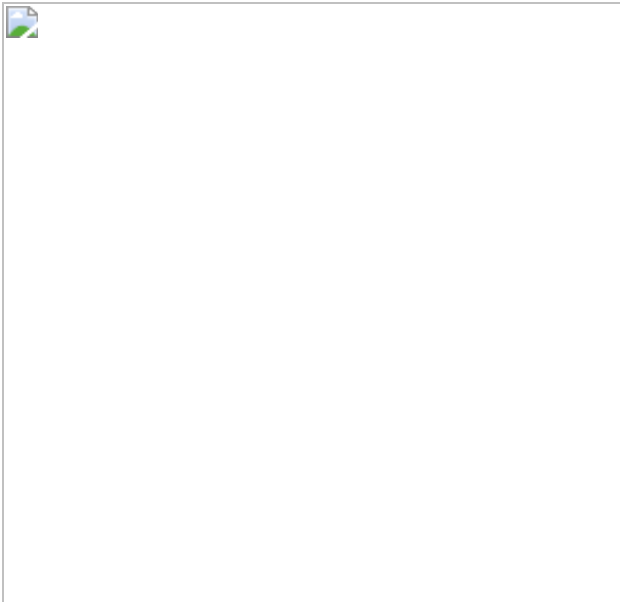


**Fig. 2: Interactions of tail segment 2 with the blocked head.**

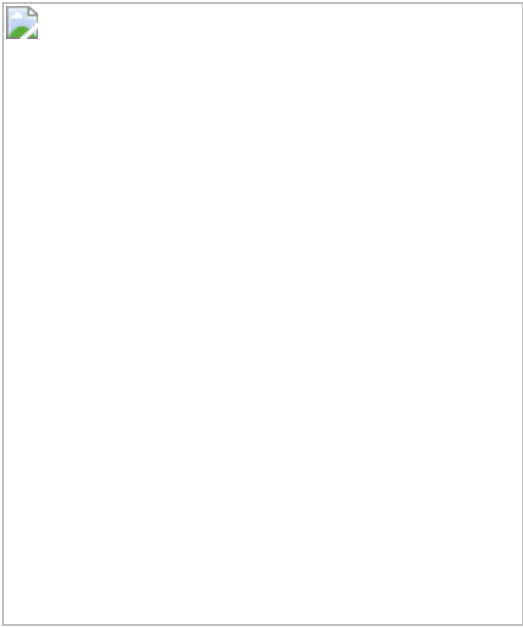


**Fig. 3: The levers of free and blocked heads and the head–tail junction.**

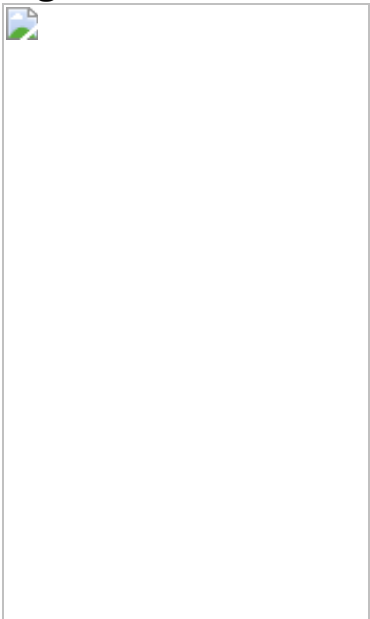


**Fig. 4: Interactions of segments 1 and 3 with blocked- and free-head motors.**

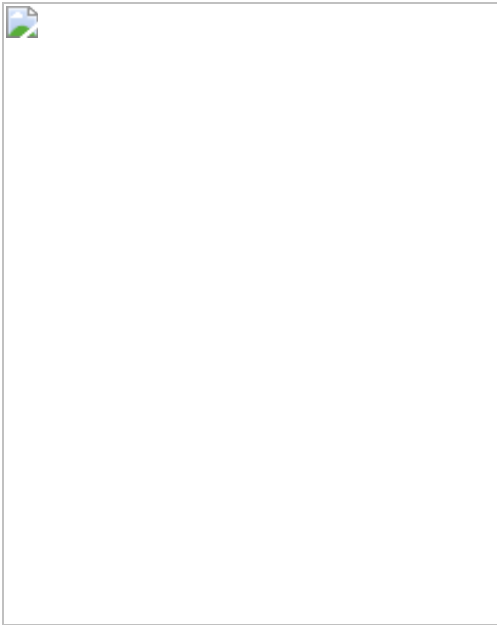


**Fig. 5: Cryo-EM density map and pseudo-atomic model of whole SmM molecule.**



## Data availability

The electron density maps for the SmM shutdown heads region and whole molecule have been deposited into EMDB, with accession codes [EMD-11069](#) and [EMD-11070](#), respectively. The pseudo-atomic model of the SmM shutdown heads region has been deposited in PDB, with accession code [6Z47](#). The following models were used for comparison purposes in our study: PDB 1I84, PDB 3JBH, PDB 5TBY, cardiac IHM model MS01 (<http://spudlab.stanford.edu/homology-models>) and cardiac IHM model SD2<sup>32</sup>.

# References

1. 1.

Lee, K. H. et al. Interacting-heads motif has been conserved as a mechanism of myosin II inhibition since before the origin of animals. *Proc. Natl Acad. Sci. USA* **115**, E1991–E2000 (2018).

[CAS](#) [PubMed](#) [Google Scholar](#)

2. 2.

Cross, R. A., Cross, K. E. & Sobieszek, A. ATP-linked monomer–polymer equilibrium of smooth muscle myosin: the free folded monomer traps ADP.Pi. *EMBO J.* **5**, 2637–2641 (1986).

[CAS](#) [PubMed](#) [PubMed Central](#) [Google Scholar](#)

3. 3.

McLachlan, A. D. & Karn, J. Periodic charge distributions in the myosin rod amino acid sequence match cross-bridge spacings in muscle. *Nature* **299**, 226–231 (1982).

[ADS](#) [CAS](#) [PubMed](#) [Google Scholar](#)

4. 4.

Craig, R., Smith, R. & Kendrick-Jones, J. Light-chain phosphorylation controls the conformation of vertebrate non-muscle and smooth muscle myosin molecules. *Nature* **302**, 436–439 (1983).

[ADS](#) [CAS](#) [PubMed](#) [Google Scholar](#)

5. 5.

Ikebe, M., Hartshorne, D. J. & Elzinga, M. Identification, phosphorylation, and dephosphorylation of a second site for myosin

light chain kinase on the 20,000-dalton light chain of smooth muscle myosin. *J. Biol. Chem.* **261**, 36–39 (1986).

[CAS](#) [PubMed](#) [Google Scholar](#)

6. 6.

Cross, R. A., Jackson, A. P., Citi, S., Kendrick-Jones, J. & Bagshaw, C. R. Active site trapping of nucleotide by smooth and non-muscle myosins. *J. Mol. Biol.* **203**, 173–181 (1988).

[CAS](#) [PubMed](#) [Google Scholar](#)

7. 7.

Wendt, T., Taylor, D., Trybus, K. M. & Taylor, K. Three-dimensional image reconstruction of dephosphorylated smooth muscle heavy meromyosin reveals asymmetry in the interaction between myosin heads and placement of subfragment 2. *Proc. Natl Acad. Sci. USA* **98**, 4361–4366 (2001).

[ADS](#) [CAS](#) [PubMed](#) [Google Scholar](#)

8. 8.

Burgess, S. A. et al. Structures of smooth muscle myosin and heavy meromyosin in the folded, shutdown state. *J. Mol. Biol.* **372**, 1165–1178 (2007).

[CAS](#) [PubMed](#) [Google Scholar](#)

9. 9.

Jung, H. S., Komatsu, S., Ikebe, M. & Craig, R. Head-head and head-tail interaction: a general mechanism for switching off myosin II activity in cells. *Mol. Biol. Cell* **19**, 3234–3242 (2008).

[CAS](#) [PubMed](#) [PubMed Central](#) [Google Scholar](#)

10. 10.

Sellers, J. R. Regulation of cytoplasmic and smooth muscle myosin. *Curr. Opin. Cell Biol.* **3**, 98–104 (1991).

[CAS](#) [PubMed](#) [Google Scholar](#)

11. 11.

Woodhead, J. L. et al. Atomic model of a myosin filament in the relaxed state. *Nature* **436**, 1195–1199 (2005).

[ADS](#) [CAS](#) [PubMed](#) [Google Scholar](#)

12. 12.

Naber, N., Cooke, R. & Pate, E. Slow myosin ATP turnover in the super-relaxed state in tarantula muscle. *J. Mol. Biol.* **411**, 943–950 (2011).

[CAS](#) [PubMed](#) [PubMed Central](#) [Google Scholar](#)

13. 13.

Stewart, M. A., Franks-Skiba, K., Chen, S. & Cooke, R. Myosin ATP turnover rate is a mechanism involved in thermogenesis in resting skeletal muscle fibers. *Proc. Natl Acad. Sci. USA* **107**, 430–435 (2010).

[ADS](#) [CAS](#) [PubMed](#) [Google Scholar](#)

14. 14.

Alamo, L. et al. Effects of myosin variants on interacting-heads motif explain distinct hypertrophic and dilated cardiomyopathy phenotypes. *eLife* **6**, e24634 (2017).

[PubMed](#) [PubMed Central](#) [Google Scholar](#)

15. 15.

Nag, S. et al. The myosin mesa and the basis of hypercontractility caused by hypertrophic cardiomyopathy mutations. *Nat. Struct. Mol. Biol.* **24**, 525–533 (2017).

[CAS](#) [PubMed](#) [PubMed Central](#) [Google Scholar](#)

16. 16.

Liu, J., Wendt, T., Taylor, D. & Taylor, K. Refined model of the 10S conformation of smooth muscle myosin by cryo-electron microscopy 3D image reconstruction. *J. Mol. Biol.* **329**, 963–972 (2003).

[CAS](#) [PubMed](#) [Google Scholar](#)

17. 17.

Jung, H. S. et al. Role of the tail in the regulated state of myosin 2. *J. Mol. Biol.* **408**, 863–878 (2011).

[CAS](#) [PubMed](#) [PubMed Central](#) [Google Scholar](#)

18. 18.

Ikebe, M. et al. Function of the NH<sub>2</sub>-terminal domain of the regulatory light chain on the regulation of smooth muscle myosin. *J. Biol. Chem.* **269**, 28173–28180 (1994).

[CAS](#) [PubMed](#) [Google Scholar](#)

19. 19.

Kast, D., Espinoza-Fonseca, L. M., Yi, C. & Thomas, D. D. Phosphorylation-induced structural changes in smooth muscle myosin regulatory light chain. *Proc. Natl Acad. Sci. USA* **107**, 8207–8212 (2010).

[ADS](#) [CAS](#) [PubMed](#) [Google Scholar](#)

20. 20.

Persechini, A. & Hartshorne, D. J. Phosphorylation of smooth muscle myosin: evidence for cooperativity between the myosin heads. *Science* **213**, 1383–1385 (1981).

[ADS](#) [CAS](#) [PubMed](#) [Google Scholar](#)

21. 21.

Persechini, A. & Hartshorne, D. J. Ordered phosphorylation of the two 20 000 molecular weight light chains of smooth muscle myosin. *Biochemistry* **22**, 470–476 (1983).

[CAS](#) [PubMed](#) [Google Scholar](#)

22. 22.

Ikebe, M., Ogihara, S. & Tonomura, Y. Nonlinear dependence of actin-activated Mg<sup>2+</sup>-ATPase activity on the extent of phosphorylation of gizzard myosin and H-meromyosin. *J. Biochem.* **91**, 1809–1812 (1982).

[CAS](#) [PubMed](#) [Google Scholar](#)

23. 23.

Collins, J. H. Myoinformatics report: myosin regulatory light chain paralogs in the human genome. *J. Muscle Res. Cell Motil.* **27**, 69–74 (2006).

[CAS](#) [PubMed](#) [Google Scholar](#)

24. 24.

Kamm, K. E. & Stull, J. T. Signaling to myosin regulatory light chain in sarcomeres. *J. Biol. Chem.* **286**, 9941–9947 (2011).

[CAS](#) [PubMed](#) [PubMed Central](#) [Google Scholar](#)

25. 25.

Bury, L. et al. Next-generation sequencing for the diagnosis of MYH9-RD: predicting pathogenic variants. *Hum. Mutat.* **41**, 277–290 (2020).

[CAS](#) [PubMed](#) [Google Scholar](#)

26. 26.

Harakalova, M. et al. Incomplete segregation of MYH11 variants with thoracic aortic aneurysms and dissections and patent ductus arteriosus. *Eur. J. Hum. Genet.* **21**, 487–493 (2013).

[CAS](#) [Google Scholar](#)

27. 27.

Kanematsu, T. et al. A case of MYH9 disorders caused by a novel mutation (p.K74E). *Ann. Hematol.* **95**, 161–163 (2016).

[PubMed](#) [Google Scholar](#)

28. 28.

Zaninetti, C. et al. MYH9-related thrombocytopenia: four novel variants affecting the tail domain of the non-muscle myosin heavy chain IIA associated with a mild clinical evolution of the disorder. *Hamostaseologie* **39**, 87–94 (2019).

[PubMed](#) [Google Scholar](#)

29. 29.

Yang, S. et al. The central role of the tail in switching off 10S myosin II activity. *J. Gen. Physiol.* **151**, 1081–1093 (2019).

[CAS](#) [PubMed](#) [PubMed Central](#) [Google Scholar](#)

30. 30.

Yang, Y. et al. Rigor-like structures from muscle myosins reveal key mechanical elements in the transduction pathways of this allosteric motor. *Structure* **15**, 553–564 (2007).

[CAS](#) [PubMed](#) [Google Scholar](#)

31. 31.

Alamo, L. et al. Three-dimensional reconstruction of tarantula myosin filaments suggests how phosphorylation may regulate myosin activity. *J. Mol. Biol.* **384**, 780–797 (2008).

[CAS](#) [PubMed](#) [PubMed Central](#) [Google Scholar](#)

32. 32.

Robert-Paganin, J., Auguin, D. & Houdusse, A. Hypertrophic cardiomyopathy disease results from disparate impairments of cardiac myosin function and auto-inhibition. *Nat. Commun.* **9**, 4019 (2018).

[ADS](#) [PubMed](#) [PubMed Central](#) [Google Scholar](#)

33. 33.

Dominguez, R., Freyzon, Y., Trybus, K. M. & Cohen, C. Crystal structure of a vertebrate smooth muscle myosin motor domain and its complex with the essential light chain: visualization of the pre-power stroke state. *Cell* **94**, 559–571 (1998).

[CAS](#) [PubMed](#) [Google Scholar](#)

34. 34.

Burgess, S. et al. The prepower stroke conformation of myosin V. *J. Cell Biol.* **159**, 983–991 (2002).

[CAS](#) [PubMed](#) [PubMed Central](#) [Google Scholar](#)

35. 35.

Batchelor, M. et al. Myosin tails and single  $\alpha$ -helical domains. *Biochem. Soc. Trans.* **43**, 58–63 (2015).

[CAS](#) [PubMed](#) [Google Scholar](#)

36. 36.

Wolny, M. et al. Stable single  $\alpha$ -helices are constant force springs in proteins. *J. Biol. Chem.* **289**, 27825–27835 (2014).

[CAS](#) [PubMed](#) [PubMed Central](#) [Google Scholar](#)

37. 37.

Blankenfeldt, W., Thomä, N. H., Wray, J. S., Gautel, M. & Schlichting, I. Crystal structures of human cardiac  $\beta$ -myosin II S2- $\Delta$  provide insight into the functional role of the S2 subfragment. *Proc. Natl Acad. Sci. USA* **103**, 17713–17717 (2006).

[ADS](#) [CAS](#) [PubMed](#) [Google Scholar](#)

38. 38.

Behrmann, E. et al. Structure of the rigor actin-tropomyosin-myosin complex. *Cell* **150**, 327–338 (2012).

[CAS](#) [PubMed](#) [PubMed Central](#) [Google Scholar](#)

39. 39.

Woodhead, J. L. & Craig, R. The mesa trail and the interacting heads motif of myosin II. *Arch. Biochem. Biophys.* **680**, 108228 (2020).

[CAS](#) [PubMed](#) [Google Scholar](#)

40. 40.

Alamo, L. et al. Conserved intramolecular interactions maintain myosin interacting-heads motifs explaining tarantula muscle super-

relaxed state structural basis. *J. Mol. Biol.* **428**, 1142–1164 (2016).

[CAS](#) [PubMed](#) [PubMed Central](#) [Google Scholar](#)

41. 41.

Straussman, R., Squire, J. M., Ben-Ya'acov, A. & Ravid, S. Skip residues and charge interactions in myosin II coiled-coils: implications for molecular packing. *J. Mol. Biol.* **353**, 613–628 (2005).

[CAS](#) [PubMed](#) [Google Scholar](#)

42. 42.

Thompson, R. F., Iadanza, M. G., Hesketh, E. L., Rawson, S. & Ranson, N. A. Collection, pre-processing and on-the-fly analysis of data for high-resolution, single-particle cryo-electron microscopy. *Nat. Protoc.* **14**, 100–118 (2019).

[CAS](#) [PubMed](#) [Google Scholar](#)

43. 43.

Fernandez-Leiro, R. & Scheres, S. H. W. A pipeline approach to single-particle processing in RELION. *Acta Crystallogr. D* **73**, 496–502 (2017).

[CAS](#) [Google Scholar](#)

44. 44.

Punjani, A., Rubinstein, J. L., Fleet, D. J. & Brubaker, M. A. cryoSPARC: algorithms for rapid unsupervised cryo-EM structure determination. *Nat. Methods* **14**, 290–296 (2017).

[CAS](#) [PubMed](#) [Google Scholar](#)

45. 45.

Zheng, S. Q. et al. MotionCor2: anisotropic correction of beam-induced motion for improved cryo-electron microscopy. *Nat. Methods* **14**, 331–332 (2017).

[CAS](#) [PubMed](#) [PubMed Central](#) [Google Scholar](#)

46. 46.

Zhang, K. Gctf: real-time CTF determination and correction. *J. Struct. Biol.* **193**, 1–12 (2016).

[ADS](#) [CAS](#) [PubMed](#) [PubMed Central](#) [Google Scholar](#)

47. 47.

Wagner, T. et al. SPHIRE-crYOLO is a fast and accurate fully automated particle picker for cryo-EM. *Commun. Biol.* **2**, 218 (2019).

[Google Scholar](#)

48. 48.

Pettersen, E. F. et al. UCSF Chimera—a visualization system for exploratory research and analysis. *J. Comput. Chem.* **25**, 1605–1612 (2004).

[CAS](#) [Google Scholar](#)

49. 49.

Goddard, T. D. et al. UCSF ChimeraX: meeting modern challenges in visualization and analysis. *Protein Sci.* **27**, 14–25 (2018).

[CAS](#) [Google Scholar](#)

50. 50.

Topf, M. et al. Protein structure fitting and refinement guided by cryo-EM density. *Structure* **16**, 295–307 (2008).

[CAS](#) [PubMed](#) [PubMed Central](#) [Google Scholar](#)

51. 51.

Webb, B. & Sali, A. Comparative protein structure modeling using MODELLER. *Curr. Protoc. Bioinformatics* **54**, 5.6.1–5.6.37 (2016).

[Google Scholar](#)

52. 52.

Offer, G., Hicks, M. R. & Woolfson, D. N. Generalized Crick equations for modeling noncanonical coiled coils. *J. Struct. Biol.* **137**, 41–53 (2002).

[CAS](#) [PubMed](#) [Google Scholar](#)

53. 53.

Emsley, P., Lohkamp, B., Scott, W. G. & Cowtan, K. Features and development of Coot. *Acta Crystallogr. D* **66**, 486–501 (2010).

[CAS](#) [PubMed](#) [Google Scholar](#)

54. 54.

Afonine, P. V. et al. Towards automated crystallographic structure refinement with phenix.refine. *Acta Crystallogr. D* **68**, 352–367 (2012).

[CAS](#) [PubMed](#) [Google Scholar](#)

55. 55.

Chen, V. B. et al. MolProbity: all-atom structure validation for macromolecular crystallography. *Acta Crystallogr. D* **66**, 12–21 (2010).

[CAS](#) [PubMed](#) [Google Scholar](#)

56. 56.

Pintilie, G. D., Zhang, J., Goddard, T. D., Chiu, W. & Gossard, D. C. Quantitative analysis of cryo-EM density map segmentation by watershed and scale-space filtering, and fitting of structures by alignment to regions. *J. Struct. Biol.* **170**, 427–438 (2010).

[CAS](#) [PubMed](#) [PubMed Central](#) [Google Scholar](#)

57. 57.

Maier, J. A. et al. ff14SB: improving the accuracy of protein side chain and backbone parameters from ff99SB. *J. Chem. Theory Comput.* **11**, 3696–3713 (2015).

[CAS](#) [PubMed](#) [PubMed Central](#) [Google Scholar](#)

58. 58.

Case, D. A. et al. *Amber 2020* (Univ. California, 2020).

59. 59.

Ryckaert, J.-P., Ciccotti, G. & Berendsen, H. Numerical integration of the cartesian equations of motion of a system with constraints: Molecular dynamics of n-alkanes. *J. Comput. Phys.* **23**, 327–341 (1977).

[ADS](#) [CAS](#) [Google Scholar](#)

60. 60.

Joosten, R. P., Long, F., Murshudov, G. N. & Perrakis, A. The PDB\_REDQ server for macromolecular structure model optimization. *IUCrJ* **1**, 213–220 (2014).

[CAS](#) [PubMed](#) [PubMed Central](#) [Google Scholar](#)

61. 61.

Olney, J. J., Sellers, J. R. & Cremo, C. R. Structure and function of the 10 S conformation of smooth muscle myosin. *J. Biol. Chem.* **271**, 20375–20384 (1996).

[CAS](#) [PubMed](#) [Google Scholar](#)

62. 62.

Brito, R. et al. A molecular model of phosphorylation-based activation and potentiation of tarantula muscle thick filaments. *J. Mol. Biol.* **414**, 44–61 (2011).

[CAS](#) [PubMed](#) [PubMed Central](#) [Google Scholar](#)

[Download references](#)

## Acknowledgements

We thank staff at the Astbury Biostructure Laboratory for their support, namely R. Thompson for advice regarding cryo-EM grid preparation and D. Maskell for image acquisition; and members of the CryoEM community at Leeds for their help and guidance, particularly M. Byrne for advice on structure validation. This work was supported by the Medical Research Council (grant numbers MR/S023593/1 to M.P. and MR/R009406/1 to M.P. and N.A.R.) and by the Wellcome Trust (WT 094231/Z/10/Z to P.J.K., M.P. and N.A.R.). The FEI Titan Krios microscopes were funded by the University of Leeds (UoL ABSL award) and Wellcome Trust (108466/Z/15/Z).

## Author information

### Author notes

1. These authors contributed equally: Charlotte A. Scarff, Glenn Carrington, David Casas-Mao

## Affiliations

1. The Astbury Centre for Structural and Molecular Biology, Faculty of Biological Sciences, University of Leeds, Leeds, UK

Charlotte A. Scarff, Glenn Carrington, David Casas-Mao, Peter J. Knight, Neil A. Ranson & Michelle Peckham

2. School of Molecular and Cellular Biology, Faculty of Biological Sciences, University of Leeds, Leeds, UK

Charlotte A. Scarff, Glenn Carrington, David Casas-Mao, Peter J. Knight, Neil A. Ranson & Michelle Peckham

3. Department of Biochemistry and Molecular Biology, Brody School of Medicine, East Carolina University, Greenville, NC, USA

Joseph M. Chalovich

## Authors

1. Charlotte A. Scarff

[View author publications](#)

You can also search for this author in [PubMed](#) [Google Scholar](#)

2. Glenn Carrington

[View author publications](#)

You can also search for this author in [PubMed](#) [Google Scholar](#)

3. David Casas-Mao

[View author publications](#)

You can also search for this author in [PubMed](#) [Google Scholar](#)

4. Joseph M. Chalovich

[View author publications](#)

You can also search for this author in [PubMed](#) [Google Scholar](#)

5. Peter J. Knight

[View author publications](#)

You can also search for this author in [PubMed](#) [Google Scholar](#)

6. Neil A. Ranson

[View author publications](#)

You can also search for this author in [PubMed](#) [Google Scholar](#)

7. Michelle Peckham

[View author publications](#)

You can also search for this author in [PubMed](#) [Google Scholar](#)

## Contributions

M.P. and N.A.R. designed the project. J.M.C. purified smooth muscle myosin. C.A.S., D.C.-M. and M.P. performed cryo-EM grid screening and optimization. C.A.S. and D.C.-M. prepared cryo-EM grids for data collection and recorded data. C.A.S., G.C. and D.C.-M. analysed and processed the data. G.C., D.C.-M. and C.A.S. built the model. G.C. performed molecular dynamic simulations. C.A.S., G.C., D.C.-M., M.P. and P.J.K. interpreted the data and the model. M.P. managed the project. M.P., P.J.K. and C.A.S. wrote the manuscript. All authors discussed the results and commented on the manuscript.

## Corresponding author

Correspondence to [Michelle Peckham](#).

## Ethics declarations

## Competing interests

The authors declare no competing interests.

## Additional information

**Peer review information** *Nature* thanks Gregory M. Alushin and Robert Cross for their contribution to the peer review of this work. Peer reviewer reports are available.

**Publisher's note** Springer Nature remains neutral with regard to jurisdictional claims in published maps and institutional affiliations.

## Extended data figures and tables

### [Extended Data Fig. 1 Micrograph, 2-D classification, angular distribution and resolution parameters.](#)

**a**, Representative micrograph of shutdown SmM molecules from 28,817 micrographs. Scale bar 50 nm. **b**, Representative 2D classes (representing approximately 25% of particles that contributed to the final reconstruction). Scale bar 10 nm. **c**, Local resolution of SmM shutdown heads region cryo-EM map. **d**, FSC curve of the heads region reconstruction, illustrating 6.3 Å resolution at 0.143 FSC. **e**, Angular distribution of particles in the heads region 3D reconstruction. **f**, FSC curve of the whole molecule reconstruction. **g**, Angular distribution of particles contributing to the whole molecule 3D reconstruction.

### [Extended data Fig. 2 Interaction of segment 3 with blocked-head RLC and analysis of RLC photo-crosslink.](#)

**a**, Segmented map highlighting latch and mortar regions (boxed), which are shown in more detail in panels **b** and **c** respectively. The position of phosphorylated serine (S20) in the latch (**b**) and in the mortar (**c**) are shown. This illustrates how phosphorylation would disrupt latch-segment 3 and mortar-RLC interactions respectively. **d**, Segmented map showing region of interest for panels **e-g**. **e**, ionic interactions between segment 3 and blocked-head RLC inter-lobe linker and blocked-head heavy chain. **f**, Hydrophobic interface where segment 3 crosses the blocked head RLC. **g**, Same view as **e** and **f** showing photo-crosslinker benzophenone-4-acetamide attached to

C109 of blocked-head RLC and in close proximity to the aliphatic side chain of K1579 of segment 3 chain H. K1579 lies within crosslinked peptide L1554-E1583<sup>61</sup>. **h**, Segmented map (face view) to show the location (boxed) of **i**, which shows an alternative view of photo-crosslinker interaction and the ionic interaction between blocked head RLC E112 and segment 3 R1584. For clarity the non-involved chain of the coiled coil has been omitted in the close-up panels.

**Extended Data Fig. 3 Annotated sequence alignment of heavy chains of human non-muscle myosin 2A (NM2A) and smooth muscle myosin (SmM) with Turkey SmM, showing sites of mutation.**

*HsNM2A: Homo sapiens MYH9; MgSmM: Meleagris gallopavo MYH11; HsSmM: Homo sapiens MYH11.* Boxes delimit structural features. Grey background identifies residues in the *d* position of the coiled coil heptad repeat. Skip residues and bend positions are highlighted. Arrowheads and magenta letters denote known sites of mutation, obtained from the Human Genome Mutation Database (HGMD), Variant of unknown significance: retrieved from the Leiden mutation database.

**Extended data Fig. 4 Comparisons of IHM pseudo-atomic models, free- and blocked-heads and the SAH-domain character of start of segment 1.**

**a-f**, Comparison of pseudo-atomic models of the IHM with LCs omitted to allow comparison of LCD heavy-chain structure. **a**, Pseudo-atomic model of SmM from the present study. **b**, Model (PDB id 1I84) produced from SmM heavy meromyosin IHM 2D crystal 20Å map<sup>7</sup>; tentative assignment of tail omitted. **c**, Model (PDB id 3JBH) produced from IHM of tarantula thick filament 20Å map<sup>40</sup>, fitted with tarantula sequence. **d**, Model (PDB id 5TBY) proposed for human cardiac IHM by homology modelling the cardiac amino acid sequences on the tarantula model<sup>14</sup>. **e**, Model (downloaded from Spudich lab website as MS01.pdb) of human cardiac myosin IHM (produced by use of homology models fitted to tarantula IHM model 3DTP<sup>15</sup>). **f**, Model (downloaded as Supplementary Data 2) for

cardiac IHM produced by use of a cardiac motor domain-ELC crystal structure (5N69) and homology model of RLC fitted into the tarantula thick filament IHM 20 Å map<sup>31</sup>. **g**, Superposition of free- and blocked-head motors (up until pliant region) showing how the LCD regions differ between the heads (without light chains shown), segmented maps and model for motor domains shown. **h**, Blocked-head motor, model in map, **i** morph between blocked-head and free-head model and maps (shown without light chains), **j** Free-head model in map. Map contour level 0.28 (Supplementary Video 3). **k**, SmM heavy-chain sequence at the start of the predicted coiled coil. Coiled-coil seam *a* and *d* residues marked by grey stripes; acidic residues red, basic residues blue. **l**, Heptad net projection of sequence<sup>35</sup> in which the dashed line shows the path of the polypeptide backbone as α-helix, circles and squares indicate the *a* and *d* positions of the heptad repeat and every seventh residue is repeated (in brackets) to allow all ionic interactions to be mapped.

**Extended Data Fig. 5 Interaction between loop 2 (blocked-head motor) and segment 1, the motor-motor interface of the IHM and fit of the SmM IHM structure into filament cryo-EM density maps for tarantula and cardiac myosin filaments.**

**a-b**, EM density map reveals an interaction interface between segment 1 and density attributable to the blocked-head motor loop 2 (dashed line). E913 in segment 1 is highlighted for reference. Map contour level 0.17. **c**, Overall model to show region of interest, the motor-motor interface (boxed). **d**, Ionic interactions across this interface, involving Helix N and HCM loop of the blocked-head motor with 3 successive residues (168-170) close to Helix E in the free-head motor (Supplementary Video 5). **e**, The same region of interest from a recent cardiac IHM pseudo-atomic model<sup>15</sup>. **f**, Superimposition of the motor domains for our structure, and for the cardiac IHM pseudo-atomic model<sup>15</sup> aligned on the free-head (red/pink) with view as in **d**. The blocked head of the cardiac IHM (cyan) is rotated counter-clockwise compared to that for SmM (blue) **g, h**, Fit of the paired heads of the pseudo-atomic model of shutdown SmM into the IHM motifs of reconstructions of thick filaments, using Chimera. The filament axis is vertical and the filament tip is at the top of the page. **g**, The fit to 20 Å map

of tarantula thick filaments (EMD-1950<sup>62</sup>, contour level 28.6). **h**. The fit to 28 Å map of cardiac thick filaments (EMD-2240<sup>14</sup>, contour level 0.14).

### Extended Data Fig. 6 Flexibility of SmM tail ribbon.

**a**, Representative class averages showing flexibility of the tail of myosin molecules (Supplementary Video 7), after alignment of the heads. Numbers at lower left indicate the chord angle of the tail at a position 29.7 nm along the tail from its emergence point from the head (taken to be the fulcrum). The angle is defined in relation to the path of the tail between bend 2 and the fulcrum, see the cartoon at the right. 4895 face view particles were classified into 50 classes of which 5 are shown to represent the range of motion of the tail. **b**, Cumulative frequency plot of tail angles for myosin with fitted Gaussian curve, yielding a variance value of 34°. Scale bar in **a**: 20 nm.

### Extended Data Fig. 7

Diagram to show the dynamic relationship of the shutdown state (10S) to the open ‘active’ state (6S) and filament assembly. The shutdown state and filaments can both compete for 6S.

#### **Extended Data Table 1 Putative residues for stabilizing ionic interactions between regions of the myosin molecule**

[Full size table](#)

#### **Extended Data Table 2 Cryo-EM data collection, refinement and validation statistics**

[Full size table](#)

## Supplementary information

### Reporting Summary

### Video 1

: Shutdown state of SMM (a) Cryo-EM density of SmM (grey) shutdown heads region at an average resolution of 6 Å. Segmented map representation showing heavy chain (blue, red), ELC (purple, orange), and RLC (magenta, green) in complex with segments 2 and 3 (light blue, pink) and fitted pseudo-atomic model. (b) Closeup view of blocked-head RLC latch (lilac) with potential interactions with ring of acidic residues (red spheres) in segment-3 and D132 in its own RLC highlighted. (c) Close up view of the free-head RLC mortar (dark green) with potentially interacting acidic residues (red spheres) in both RLCs.

## Video 2

: Interactions between Segment-2 and the blocked head motor (a) Segmented map density with fitted quasi-atomic model showing ionic interactions between segment-2 (chain G, light blue) and the blocked head motor (blue). (b) Ionic interactions between segment-2 (chain H, pink) and the blocked head ELC (orange). (c) Ionic interactions between segment-2 (chain H, pink) and segment-3 (chain G, light blue) around bend 2.

## Video 3

: Morphing of the free-head motor domain to blocked-head motor domain This shows changes in LCD and converter position (extended fig 4g-j). Motors aligned up until the pliant point (residues 30-787).

## Video 4

: Closeup view of the head-tail junction This shows nearly unbroken  $\alpha$ -helices (red, blue) between the LCD, ending at P849, and the coiled-coil tail.

## Video 5

: Motor-motor domain interactions that stabilise the shutdown state Related to Extended Data Fig. 5.

## Video 6

: Whole Molecule SMM 6 Å map fitted to our 9 Å map, which reveals more of the tail domain. Full length model of SmM fitted to 9Å map, with skip residues (yellow) showing the perturbation to the super-helical twist of the coiled coil.

## Video 7

: Flexing of whole molecule SMM 2D class averages of the whole molecule SmM arranged to show the range of flexing of the tail in plane. Particles in each class shown bottom left. Scale bar 20 nm.

## Peer Review File

## Rights and permissions

### Reprints and Permissions

## About this article



Check for  
updates

## Cite this article

Scarff, C.A., Carrington, G., Casas-Mao, D. *et al.* Structure of the shutdown state of myosin-2. *Nature* **588**, 515–520 (2020).

<https://doi.org/10.1038/s41586-020-2990-5>

### Download citation

- Received: 01 June 2020

- Accepted: 18 September 2020
- Published: 02 December 2020
- Issue Date: 17 December 2020
- DOI: <https://doi.org/10.1038/s41586-020-2990-5>

## Comments

By submitting a comment you agree to abide by our [Terms](#) and [Community Guidelines](#). If you find something abusive or that does not comply with our terms or guidelines please flag it as inappropriate.

[Access through your institution](#)

[Change institution](#)

[Buy or subscribe](#)

---

This article was downloaded by **calibre** from <https://www.nature.com/articles/s41586-020-2990-5>

| [Section menu](#) | [Main menu](#) |

- Article
- [Published: 02 December 2020](#)

# Cryo-EM structure of the inhibited (10S) form of myosin II

- [Shixin Yang ORCID: orcid.org/0000-0002-9794-7537<sup>1</sup> na1 nAff3](#),
- [Prince Tiwari ORCID: orcid.org/0000-0003-4062-1648<sup>1</sup> na1](#),
- [Kyoung Hwan Lee ORCID: orcid.org/0000-0003-1423-8952<sup>1</sup> nAff4](#),
- [Osamu Sato ORCID: orcid.org/0000-0001-9913-1745<sup>2</sup>](#),
- [Mitsuo Ikebe ORCID: orcid.org/0000-0002-8299-6643<sup>2</sup>](#),
- [Raúl Padrón ORCID: orcid.org/0000-0002-1412-2450<sup>1</sup>](#) &
- [Roger Craig ORCID: orcid.org/0000-0002-9707-5409<sup>1</sup>](#)

[Nature](#) volume 588, pages521–525(2020)[Cite this article](#)

- 2502 Accesses
- 15 Altmetric
- [Metrics details](#)

## Subjects

- [Cryoelectron microscopy](#)
- [Motor protein structure](#)
- [Myosin](#)

## Abstract

Myosin II is the motor protein that enables muscle cells to contract and nonmuscle cells to move and change shape<sup>1</sup>. The molecule has two

identical heads attached to an elongated tail, and can exist in two conformations: 10S and 6S, named for their sedimentation coefficients<sup>2,3</sup>. The 6S conformation has an extended tail and assembles into polymeric filaments, which pull on actin filaments to generate force and motion. In 10S myosin, the tail is folded into three segments and the heads bend back and interact with each other and the tail<sup>3,4,5,6,7</sup>, creating a compact conformation in which ATPase activity, actin activation and filament assembly are all highly inhibited<sup>7,8</sup>. This switched-off structure appears to function as a key energy-conserving storage molecule in muscle and nonmuscle cells<sup>9,10,11,12</sup>, which can be activated to form functional filaments as needed<sup>13</sup>—but the mechanism of its inhibition is not understood. Here we have solved the structure of smooth muscle 10S myosin by cryo-electron microscopy with sufficient resolution to enable improved understanding of the function of the head and tail regions of the molecule and of the key intramolecular contacts that cause inhibition. Our results suggest an atomic model for the off state of myosin II, for its activation and unfolding by phosphorylation, and for understanding the clustering of disease-causing mutations near sites of intramolecular interaction.

[Access through your institution](#)

[Change institution](#)

[Buy or subscribe](#)

## Access options

Subscribe to Journal

Get full journal access for 1 year

185,98 €

only 3,58 € per issue

[Subscribe](#)

All prices are NET prices.  
VAT will be added later in the checkout.

Rent or Buy article

Get time limited or full article access on ReadCube.

from \$8.99

[Rent or Buy](#)

All prices are NET prices.

### **Additional access options:**

- [Log in](#)
- [Access through your institution](#)
- [Learn about institutional subscriptions](#)

**Fig. 1: 3D reconstruction of 10S myosin.**

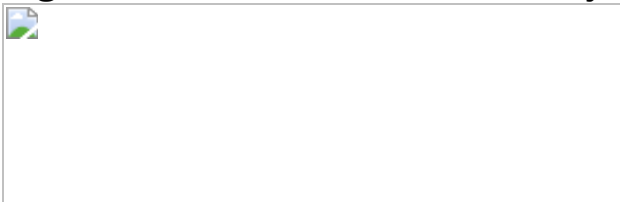


**Fig. 2: Fitting of atomic model to map and locations of mutations.**

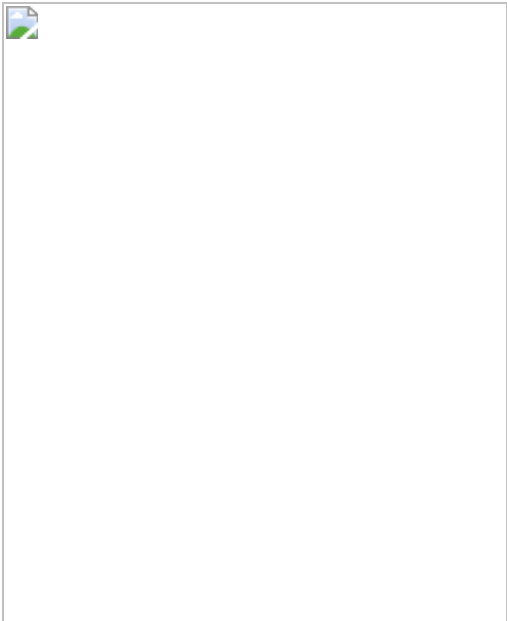
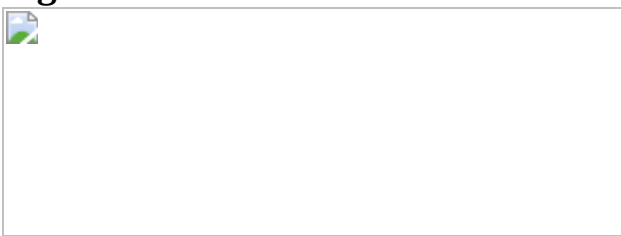


**Fig. 3: Intramolecular interactions in the 10S atomic model.**



## Data availability

Structural data that support the findings of this study on the structure of 10S myosin II have been deposited in the Electron Microscopy Data Bank under accession code [EMD-22145](#) (the electron microscopy density map) and in the Protein Data Bank under accession code [6XE9](#) (the atomic model). PDB data used to build the initial model were PDB [1I84](#) and PDB [2FXM](#).

## References

1. 1.

Geeves, M. A. & Holmes, K. C. Structural mechanism of muscle contraction. *Annu. Rev. Biochem.* **68**, 687–728 (1999).

[CAS](#) [PubMed](#) [Google Scholar](#)

2. 2.

Suzuki, H., Kamata, T., Onishi, H. & Watanabe, S. Adenosine triphosphate-induced reversible change in the conformation of chicken gizzard myosin and heavy meromyosin. *J. Biochem.* **91**, 1699–1705 (1982).

[CAS](#) [PubMed](#) [Google Scholar](#)

3. 3.

Trybus, K. M., Huiatt, T. W. & Lowey, S. A bent monomeric conformation of myosin from smooth muscle. *Proc. Natl Acad. Sci. USA* **79**, 6151–6155 (1982).

[ADS](#) [CAS](#) [PubMed](#) [Google Scholar](#)

4. 4.

Burgess, S. A. et al. Structures of smooth muscle myosin and heavy meromyosin in the folded, shutdown state. *J. Mol. Biol.* **372**, 1165–1178 (2007).

[CAS](#) [PubMed](#) [Google Scholar](#)

5. 5.

Craig, R., Smith, R. & Kendrick-Jones, J. Light-chain phosphorylation controls the conformation of vertebrate non-muscle and smooth muscle myosin molecules. *Nature* **302**, 436–439 (1983).

[ADS](#) [CAS](#) [PubMed](#) [Google Scholar](#)

6. 6.

Wendt, T., Taylor, D., Trybus, K. M. & Taylor, K. Three-dimensional image reconstruction of dephosphorylated smooth muscle heavy meromyosin reveals asymmetry in the interaction between myosin

heads and placement of subfragment 2. *Proc. Natl Acad. Sci. USA* **98**, 4361–4366 (2001).

[ADS](#) [CAS](#) [PubMed](#) [Google Scholar](#)

7. 7.

Yang, S. et al. The central role of the tail in switching off 10S myosin II activity. *J. Gen. Physiol.* **151**, 1081–1093 (2019).

[CAS](#) [PubMed](#) [PubMed Central](#) [Google Scholar](#)

8. 8.

Cross, R. A., Jackson, A. P., Citi, S., Kendrick-Jones, J. & Bagshaw, C. R. Active site trapping of nucleotide by smooth and non-muscle myosins. *J. Mol. Biol.* **203**, 173–181 (1988).

[CAS](#) [PubMed](#) [Google Scholar](#)

9. 9.

Kiboku, T. et al. Nonmuscle myosin II folds into a 10S form via two portions of tail for dynamic subcellular localization. *Genes Cells* **18**, 90–109 (2013).

[CAS](#) [PubMed](#) [Google Scholar](#)

10. 10.

Liu, X. et al. Effect of ATP and regulatory light-chain phosphorylation on the polymerization of mammalian nonmuscle myosin II. *Proc. Natl Acad. Sci. USA* **114**, E6516–E6525 (2017).

[CAS](#) [PubMed](#) [Google Scholar](#)

11. 11.

Breckenridge, M. T., Dulyaninova, N. G. & Egelhoff, T. T. Multiple regulatory steps control mammalian nonmuscle myosin II assembly in live cells. *Mol. Biol. Cell* **20**, 338–347 (2009).

[CAS](#) [PubMed](#) [PubMed Central](#) [Google Scholar](#)

12. 12.

Milton, D. L. et al. Direct evidence for functional smooth muscle myosin II in the 10S self-inhibited monomeric conformation in airway smooth muscle cells. *Proc. Natl Acad. Sci. USA* **108**, 1421–1426 (2011).

[ADS](#) [CAS](#) [PubMed](#) [Google Scholar](#)

13. 13.

Cross, R. A. What is 10S myosin for? *J. Muscle Res. Cell Motil.* **9**, 108–110 (1988).

[CAS](#) [PubMed](#) [Google Scholar](#)

14. 14.

Liu, J., Wendt, T., Taylor, D. & Taylor, K. Refined model of the 10S conformation of smooth muscle myosin by cryo-electron microscopy 3D image reconstruction. *J. Mol. Biol.* **329**, 963–972 (2003).

[CAS](#) [PubMed](#) [Google Scholar](#)

15. 15.

Woodhead, J. L. et al. Atomic model of a myosin filament in the relaxed state. *Nature* **436**, 1195–1199 (2005).

[ADS](#) [CAS](#) [PubMed](#) [Google Scholar](#)

16. 16.

Trybus, K. M. & Lowey, S. Conformational states of smooth muscle myosin. Effects of light chain phosphorylation and ionic strength. *J. Biol. Chem.* **259**, 8564–8571 (1984).

[CAS](#) [PubMed](#) [Google Scholar](#)

17. 17.

Ma, X. & Adelstein, R. S. The role of vertebrate nonmuscle myosin II in development and human disease. *Bioarchitecture* **4**, 88–102 (2014).

[PubMed](#) [PubMed Central](#) [Google Scholar](#)

18. 18.

Lee, K. H. et al. Interacting-heads motif has been conserved as a mechanism of myosin II inhibition since before the origin of animals. *Proc. Natl Acad. Sci. USA* **115**, E1991–E2000 (2018).

[CAS](#) [PubMed](#) [Google Scholar](#)

19. 19.

Blankenfeldt, W., Thomä, N. H., Wray, J. S., Gautel, M. & Schlichting, I. Crystal structures of human cardiac beta-myosin II S2-delta provide insight into the functional role of the S2 subfragment. *Proc. Natl Acad. Sci. USA* **103**, 17713–17717 (2006).

[ADS](#) [CAS](#) [PubMed](#) [Google Scholar](#)

20. 20.

Dominguez, R., Freyzon, Y., Trybus, K. M. & Cohen, C. Crystal structure of a vertebrate smooth muscle myosin motor domain and its complex with the essential light chain: visualization of the pre-power stroke state. *Cell* **94**, 559–571 (1998).

[CAS](#) [PubMed](#) [Google Scholar](#)

21. 21.

Alamo, L. et al. Conserved intramolecular interactions maintain myosin interacting-heads motifs explaining tarantula muscle super-relaxed state structural basis. *J. Mol. Biol.* **428**, 1142–1164 (2016).

[CAS](#) [PubMed](#) [PubMed Central](#) [Google Scholar](#)

22. 22.

Robert-Paganin, J., Auguin, D. & Houdusse, A. Hypertrophic cardiomyopathy disease results from disparate impairments of cardiac myosin function and auto-inhibition. *Nat. Commun.* **9**, 4019 (2018).

[ADS](#) [PubMed](#) [PubMed Central](#) [Google Scholar](#)

23. 23.

Pylypenko, O. & Houdusse, A. M. Essential “ankle” in the myosin lever arm. *Proc. Natl Acad. Sci. USA* **108**, 5–6 (2011).

[ADS](#) [CAS](#) [PubMed](#) [Google Scholar](#)

24. 24.

Anderson, R. L. et al. Deciphering the super relaxed state of human  $\beta$ -cardiac myosin and the mode of action of mavacamten from myosin molecules to muscle fibers. *Proc. Natl Acad. Sci. USA* **115**, E8143–E8152 (2018).

[CAS](#) [PubMed](#) [Google Scholar](#)

25. 25.

Brown, J. H. et al. Visualizing key hinges and a potential major source of compliance in the lever arm of myosin. *Proc. Natl Acad. Sci. USA* **108**, 114–119 (2011).

[ADS](#) [CAS](#) [PubMed](#) [Google Scholar](#)

26. 26.

Rimm, D. L., Sinard, J. H. & Pollard, T. D. Location of the head–tail junction of myosin. *J. Cell Biol.* **108**, 1783–1789 (1989).

[CAS](#) [PubMed](#) [Google Scholar](#)

27. 27.

Tama, F., Feig, M., Liu, J., Brooks, C. L. III & Taylor, K. A. The requirement for mechanical coupling between head and S2 domains in smooth muscle myosin ATPase regulation and its implications for dimeric motor function. *J. Mol. Biol.* **345**, 837–854 (2005).

[CAS](#) [PubMed](#) [Google Scholar](#)

28. 28.

Brown, J. H. et al. An unstable head–rod junction may promote folding into the compact off-state conformation of regulated myosins. *J. Mol. Biol.* **375**, 1434–1443 (2008).

[ADS](#) [CAS](#) [PubMed](#) [Google Scholar](#)

29. 29.

Woolfson, D. N. The design of coiled-coil structures and assemblies. *Adv. Protein Chem.* **70**, 79–112 (2005).

[CAS](#) [PubMed](#) [Google Scholar](#)

30. 30.

Hu, Z., Taylor, D. W., Reedy, M. K., Edwards, R. J. & Taylor, K. A. Structure of myosin filaments from relaxed *Lethocerus* flight muscle by cryo-EM at 6 Å resolution. *Sci. Adv.* **2**, e1600058 (2016).

[ADS](#) [PubMed](#) [PubMed Central](#) [Google Scholar](#)

31. 31.

Taylor, K. C. et al. Skip residues modulate the structural properties of the myosin rod and guide thick filament assembly. *Proc. Natl Acad. Sci. USA* **112**, E3806–E3815 (2015).

[CAS](#) [PubMed](#) [Google Scholar](#)

32. 32.

Olney, J. J., Sellers, J. R. & Cremo, C. R. Structure and function of the 10 S conformation of smooth muscle myosin. *J. Biol. Chem.* **271**, 20375–20384 (1996).

[CAS](#) [PubMed](#) [Google Scholar](#)

33. 33.

Nag, S. et al. The myosin mesa and the basis of hypercontractility caused by hypertrophic cardiomyopathy mutations. *Nat. Struct. Mol. Biol.* **24**, 525–533 (2017).

[CAS](#) [PubMed](#) [PubMed Central](#) [Google Scholar](#)

34. 34.

Woodhead, J. L. & Craig, R. The mesa trail and the interacting heads motif of myosin II. *Arch. Biochem. Biophys.* **680**, 108228 (2020).

[CAS](#) [PubMed](#) [Google Scholar](#)

35. 35.

Zhou, H. X. & Pang, X. Electrostatic interactions in protein structure, folding, binding, and condensation. *Chem. Rev.* **118**, 1691–1741 (2018).

[CAS](#) [PubMed](#) [PubMed Central](#) [Google Scholar](#)

36. 36.

Brito, R. et al. A molecular model of phosphorylation-based activation and potentiation of tarantula muscle thick filaments. *J. Mol. Biol.* **414**, 44–61 (2011).

[CAS](#) [PubMed](#) [PubMed Central](#) [Google Scholar](#)

37. 37.

Li, X. D., Saito, J., Ikebe, R., Mabuchi, K. & Ikebe, M. The interaction between the regulatory light chain domains on two heads is critical for regulation of smooth muscle myosin. *Biochemistry* **39**, 2254–2260 (2000).

[CAS](#) [PubMed](#) [Google Scholar](#)

38. 38.

Abrams, J. et al. Graded effects of unregulated smooth muscle myosin on intestinal architecture, intestinal motility and vascular function in zebrafish. *Dis. Model. Mech.* **9**, 529–540 (2016).

[CAS](#) [PubMed](#) [PubMed Central](#) [Google Scholar](#)

39. 39.

Jung, H. S., Komatsu, S., Ikebe, M. & Craig, R. Head–head and head–tail interaction: a general mechanism for switching off myosin II activity in cells. *Mol. Biol. Cell* **19**, 3234–3242 (2008).

[CAS](#) [PubMed](#) [PubMed Central](#) [Google Scholar](#)

40. 40.

Dulyaninova, N. G. & Bresnick, A. R. The heavy chain has its day: regulation of myosin-II assembly. *Bioarchitecture* **3**, 77–85 (2013).

[PubMed](#) [PubMed Central](#) [Google Scholar](#)

41. 41.

Alamo, L. et al. Effects of myosin variants on interacting-heads motif explain distinct hypertrophic and dilated cardiomyopathy phenotypes. *eLife* **6**, e24634 (2017).

[PubMed](#) [PubMed Central](#) [Google Scholar](#)

42. 42.

Ikebe, M. & Hartshorne, D. J. Effects of  $\text{Ca}^{2+}$  on the conformation and enzymatic activity of smooth muscle myosin. *J. Biol. Chem.* **260**, 13146–13153 (1985).

[CAS](#) [PubMed](#) [Google Scholar](#)

43. 43.

Jung, H. S. et al. Role of the tail in the regulated state of myosin 2. *J. Mol. Biol.* **408**, 863–878 (2011).

[CAS](#) [PubMed](#) [PubMed Central](#) [Google Scholar](#)

44. 44.

Urnavicius, L. et al. The structure of the dynein complex and its interaction with dynein. *Science* **347**, 1441–1446 (2015).

[ADS](#) [CAS](#) [PubMed](#) [PubMed Central](#) [Google Scholar](#)

45. 45.

Takizawa, Y. et al. While the revolution will not be crystallized, biochemistry reigns supreme. *Protein Sci.* **26**, 69–81 (2017).

[CAS](#) [PubMed](#) [Google Scholar](#)

46. 46.

Burgess, S. A., Walker, M. L., Thirumurugan, K., Trinick, J. & Knight, P. J. Use of negative stain and single-particle image processing to explore dynamic properties of flexible macromolecules. *J. Struct. Biol.* **147**, 247–258 (2004).

[CAS](#) [PubMed](#) [Google Scholar](#)

47. 47.

Mastronarde, D. N. Automated electron microscope tomography using robust prediction of specimen movements. *J. Struct. Biol.* **152**, 36–51 (2005).

[PubMed](#) [Google Scholar](#)

48. 48.

Zheng, S. Q. et al. MotionCor2: anisotropic correction of beam-induced motion for improved cryo-electron microscopy. *Nat. Methods* **14**, 331–332 (2017).

[CAS](#) [PubMed](#) [PubMed Central](#) [Google Scholar](#)

49. 49.

Rohou, A. & Grigorieff, N. CTFFIND4: Fast and accurate defocus estimation from electron micrographs. *J. Struct. Biol.* **192**, 216–221 (2015).

[PubMed](#) [PubMed Central](#) [Google Scholar](#)

50. 50.

Zivanov, J. et al. New tools for automated high-resolution cryo-EM structure determination in RELION-3. *eLife* **7**, e42166 (2018).

[PubMed](#) [PubMed Central](#) [Google Scholar](#)

51. 51.

Kucukelbir, A., Sigworth, F. J. & Tagare, H. D. Quantifying the local resolution of cryo-EM density maps. *Nat. Methods* **11**, 63–65 (2014).

[CAS](#) [PubMed](#) [PubMed Central](#) [Google Scholar](#)

52. 52.

Pettersen, E. F. et al. UCSF Chimera—a visualization system for exploratory research and analysis. *J. Comput. Chem.* **25**, 1605–1612 (2004).

[CAS](#) [Google Scholar](#)

53. 53.

Afonine, P. V. et al. Real-space refinement in PHENIX for cryo-EM and crystallography. *Acta Crystallogr. D* **74**, 531–544 (2018).

[CAS](#) [Google Scholar](#)

54. 54.

Emsley, P., Lohkamp, B., Scott, W. G. & Cowtan, K. Features and development of Coot. *Acta Crystallogr. D* **66**, 486–501 (2010).

[CAS](#) [PubMed](#) [Google Scholar](#)

55. 55.

Kim, K. Y., Kovács, M., Kawamoto, S., Sellers, J. R. & Adelstein, R. S. Disease-associated mutations and alternative splicing alter the enzymatic and motile activity of nonmuscle myosins II-B and II-C. *J. Biol. Chem.* **280**, 22769–22775 (2005).

[CAS](#) [PubMed](#) [Google Scholar](#)

56. 56.

Huang, J. et al. Genetic approaches to identify pathological limitations in aortic smooth muscle contraction. *PLoS ONE* **13**, e0193769 (2018).

[PubMed](#) [PubMed Central](#) [Google Scholar](#)

57. 57.

Alhopuro, P. et al. Unregulated smooth-muscle myosin in human intestinal neoplasia. *Proc. Natl Acad. Sci. USA* **105**, 5513–5518 (2008).

[ADS](#) [CAS](#) [PubMed](#) [Google Scholar](#)

58. 58.

Wallace, K. N. et al. Mutation of smooth muscle myosin causes epithelial invasion and cystic expansion of the zebrafish intestine. *Dev. Cell* **8**, 717–726 (2005).

[CAS](#) [PubMed](#) [Google Scholar](#)

59. 59.

Almutawa, W. et al. The R941L mutation in MYH14 disrupts mitochondrial fission and associates with peripheral neuropathy. *EBioMedicine* **45**, 379–392 (2019).

[PubMed](#) [PubMed Central](#) [Google Scholar](#)

60. 60.

Yang, S., Woodhead, J. L., Zhao, F. Q., Sulbarán, G. & Craig, R. An approach to improve the resolution of helical filaments with a large axial rise and flexible subunits. *J. Struct. Biol.* **193**, 45–54 (2016).

[CAS](#) [PubMed](#) [Google Scholar](#)

61. 61.

Espinoza-Fonseca, L. M., Kast, D. & Thomas, D. D. Molecular dynamics simulations reveal a disorder-to-order transition on phosphorylation of smooth muscle myosin. *Biophys. J.* **93**, 2083–2090 (2007).

[CAS](#) [PubMed](#) [PubMed Central](#) [Google Scholar](#)

62. 62.

Sweeney, H. L., Yang, Z., Zhi, G., Stull, J. T. & Trybus, K. M. Charge replacement near the phosphorylatable serine of the myosin regulatory light chain mimics aspects of phosphorylation. *Proc. Natl Acad. Sci. USA* **91**, 1490–1494 (1994).

[ADS](#) [CAS](#) [PubMed](#) [Google Scholar](#)

63. 63.

Gallagher, P. J., Herring, B. P. & Stull, J. T. Myosin light chain kinases. *J. Muscle Res. Cell Motil.* **18**, 1–16 (1997).

[CAS](#) [PubMed](#) [Google Scholar](#)

[Download references](#)

## Acknowledgements

This work was supported by National Institutes of Health grants AR072036, AR067279, and HL139883 (R.C.), HL075030, HL111696 and HL142853 (M.I.), and a University of Texas STARS PLUS Award (M.I.). The content is solely the responsibility of the authors and does not necessarily represent the official views of the National Institutes of Health. We thank K. Subramanian, C. Ouch, W. Royer, C. Xu, C. Gaubitz and N. Stone for advice and discussion on fitting and refinement, K. K. Song and C. Xu for cryo-EM imaging, L. Alamo and A. Pinto for advice on homology modelling, and M. Espinoza-Fonseca for providing the atomic models of the RLC NTEs. Cryo-EM imaging was carried out in the Massachusetts Facility for High-Resolution Electron Cryo-Microscopy at the University of

Massachusetts Medical School. The Titan Krios was purchased with a grant from the Massachusetts Life Sciences Center capital fund. UCSF Chimera, used for molecular graphics and analyses performed in this work, is supported by National Institutes of Health grant GM103311.

## Author information

### Author notes

#### 1. Shixin Yang

Present address: Cryo-EM Shared Resources, Janelia Research Campus, Howard Hughes Medical Institute, Ashburn, VA, USA

#### 2. Kyoung Hwan Lee

Present address: Massachusetts Facility for High-Resolution Electron Cryo-microscopy, University of Massachusetts Medical School, Worcester, MA, USA

#### 3. These authors contributed equally to this work: Shixin Yang, Prince Tiwari

## Affiliations

#### 1. Division of Cell Biology and Imaging, Department of Radiology, University of Massachusetts Medical School, Worcester, MA, USA

Shixin Yang, Prince Tiwari, Kyoung Hwan Lee, Raúl Padrón & Roger Craig

#### 2. Department of Cellular and Molecular Biology, University of Texas Health Science Center at Tyler, Tyler, TX, USA

Osamu Sato & Mitsuo Ikebe

## Authors

1. Shixin Yang

[View author publications](#)

You can also search for this author in [PubMed](#) [Google Scholar](#)

2. Prince Tiwari

[View author publications](#)

You can also search for this author in [PubMed](#) [Google Scholar](#)

3. Kyoung Hwan Lee

[View author publications](#)

You can also search for this author in [PubMed](#) [Google Scholar](#)

4. Osamu Sato

[View author publications](#)

You can also search for this author in [PubMed](#) [Google Scholar](#)

5. Mitsuo Ikebe

[View author publications](#)

You can also search for this author in [PubMed](#) [Google Scholar](#)

6. Raúl Padrón

[View author publications](#)

You can also search for this author in [PubMed](#) [Google Scholar](#)

7. Roger Craig

[View author publications](#)

You can also search for this author in [PubMed](#) [Google Scholar](#)

## Contributions

S.Y. performed data processing and the 3D reconstruction. P.T. carried out specimen optimization, cryo-EM grid preparation, atomic fitting and

refinement, structure analysis, and the density map and PDB depositions. K.H.L. performed preliminary cryo-EM experiments, cryo-EM grid preparation and helped with data collection. O.S. and M.I. prepared the myosin. R.C. and R.P. carried out analysis of the structure and co-wrote the paper. R.C. managed the overall project.

## Corresponding author

Correspondence to [Roger Craig](#).

## Ethics declarations

## Competing interests

The authors declare no competing interests.

## Additional information

**Peer review information** *Nature* thanks Gregory M. Alushin, Robert Cross and the other, anonymous, reviewer(s) for their contribution to the peer review of this work. Peer reviewer reports are available.

**Publisher's note** Springer Nature remains neutral with regard to jurisdictional claims in published maps and institutional affiliations.

## Extended data figures and tables

### [Extended Data Fig. 1 Imaging and processing of 10S myosin II.](#)

**a**, Raw cryo-EM image. Circles indicate individual molecules; red, face view; blue, edge view. This is one of 10,950 micrographs recorded at 300 kV on the Titan Krios, and is representative of those showing the particles most clearly. A preliminary set of 400 micrographs from a different set of grids was first recorded on a Talos Arctica at 200 kV, producing a similar, initial reconstruction, at 9 Å resolution. **b**, Gold-standard Fourier shell

correlation (FSC) curve using half maps; global resolution estimate is 4.3 Å by the FSC 0.143 criterion. **c**, Typical 2D class averages of 10S myosin (25 of a total of 43 good class averages, representing a total of 260,360 particles). Edge views show poor definition of the longer end of the tail (stars), corresponding to mobility in the upper part of the reconstruction (Extended Data Fig. 2). **d**, Enlarged class average showing main features in reconstruction. BH/FH = blocked/free head; Seg = segment number.

### Extended Data Fig. 2 Resolution and atomic fitting of 10S structure.

**a, b**, Front and rear views of density map (contour level 0.0125), showing estimated local resolution according to RESMAP<sup>51</sup>. Resolution of the heads is highest in the MDs (especially the BH), and lower in the RDs (especially the FH), corresponding to local regions of varied mobility. Resolution in the tail is best where it is stabilized by contacts with other domains (seg2 with the BH MD and ELC), especially in the specific  $\alpha$ -helix making the contact. The tail regions at the top are noisy and of low density (Extended Data Fig. 1c). **c, d**, Docking of the refined model to the map shown at high contour cutoff (0.025; cf. Fig. 2a), revealing clear secondary structure and quality of fit (front, rear views respectively). **e–g**, Fitting to show map quality. **e**,  $\beta$ -strand 249–254 of the BH MD, showing side-chain density. **f**,  $\alpha$ -helix 431–443 in the BH MD, showing side-chain density. **g**, Coiled-coil in seg2 contacting the BH MD (1425–1491), showing 5.4 Å  $\alpha$ -helical pitch (cf. d).

### Extended Data Fig. 3 Comparison of free and blocked heads.

**a**, Superposition of BH (red) and FH MDs (green) using Matchmaker in Chimera. There is an almost perfect match, including the converter domains (Cnv), which show no more than ~5 Å movement, suggesting that the two heads are in the same biochemical state. Orientation of heads is that seen in front view of BH. **b, c**, Alignment of MDs of BH and FH, oriented as attached to actin in rigor state. There is a large difference in angle between the BH and FH RDs with respect to their MDs in both longitudinal (**b**) and azimuthal planes (**c**) (defined with respect to plane of filament sliding)<sup>14</sup>. BH and FH were aligned by superposing their MDs on the MD (not shown)

of mammalian actomyosin in the rigor state (PDB 5H53). RLCs and ELCs have been removed for clarity. **d**, Face-view of IHM shows how C termini of the two heads (P849), at bottom of RDs, come within ~28 Å of each other where they meet S2 (not shown). This proximity depends on the differential flexing of the RDs with respect to the MDs in the two heads. If the FH had the BH RD angle, the C termini in the IHM would be too far apart (~ 58 Å) to join to the 20 Å-diameter S2 without its substantial uncoiling. The angle of the FH RD is the major structural difference that brings the C termini of the two heads close enough together to make their simultaneous attachment to S2 possible. Comparison of RD angles was made by superposing the BH and FH MDs. **e**, Comparison of isolated regulatory domain structures in BH and FH (LCs omitted for clarity) after aligning residues K823-P849 (the left half of the molecule). The C-terminal hooks make similar ~90° angles with the RD helix. There is a small difference in angle between the FH and BH helices in the N-terminal half of the RD heavy chain. **f**, Comparison of regulatory domain structures within IHM. The BH RD was superimposed on the FH RD in the N-terminal half. The straighter course of the FH RD brings the FH and BH C termini that attach to S2 closer together by ~7 Å, facilitating attachment to S2 without any substantial unwinding of the coiled coil. This flexibility in the RD, bringing the FH C terminus closer to the BH, thus aids in formation of the IHM, along with the different angles of the RDs with respect to the MDs seen in **b–d**.

#### Extended Data Fig. 4 Structure of head-tail junction.

**a**, Atomic model fitted into the electron density map (contour level 0.021) in the region of the head-tail junction. The map shows tubes of density for the two hooks, which form 90° bends with the  $\alpha$ -helical heavy chain of the RDs. Such tubular density is characteristic of  $\alpha$ -helices in other parts of the structure. P849 is the invariant proline that marks the junction between each head and the tail. View is from front. **b**, IHM front-view showing hooks at C-terminal end of each RD. ELCs and RLCs removed for clarity. **c**, Enlargement of hook region showing ~28 Å distance between invariant prolines at the C terminus of each head heavy chain. **d**, IHM face-view showing  $\alpha$ -helical backbone of BH and FH RDs, hooks, and coiled-coil tail regions. Seg1  $\alpha$ -helices (red, green) continue from BH and FH hooks.

## Extended Data Fig. 5 Variations in the coiled-coil of 10S myosin.

**a**, Oblique view of back of reconstruction. Red arrows indicate relatively regular crossovers of coiled-coil (~60-75 Å apart) as segment 2 wraps around the BH MD, and a long, parallel (untwisted) stretch in segment 3 after leaving hinge 2 (~100 Å; white bar). **b**, Atomic model of tail showing approximate distance between crossovers in coiled coil. Purple residues (numbered) are estimated to be at crossovers as seen in this face view, with distances between them shown. E1535-E1612 is an almost straight, non-coiled region of the tail, especially the green chain. The two heads would connect to the bottom of seg1 at L850. L850-T889 represents the first ~ 5 heptads of S2 (black star), which appear to associate with each other from the start, though with a slightly longer helical pitch in the first few residues. The two  $\alpha$ -helices are shown in different colours for clarity. Their specific connection to the BH or FH is unknown (apart from seg1) due to lack of continuity of density in the top half of the reconstruction. Blue region in seg2 is M1462-K1472 (see text). **c**, Side-view of reconstruction showing the long stretch of untwisted coiled-coil in segment 3, running over the BH. Yellow star here and in **a** shows position of skip residue 1592. **d**, Hinge 2, in face- and end-views, showing continuity of coiling of the two  $\alpha$ -helices about each other through this sharp bend, with local melting of  $\alpha$ -helices likely at the bend. Glu1535 (spheres) is thought to mark the hinge point, although uncertainty in measurement of negative stain images means that the hinge could occur 2-3 amino acids either side of 1535<sup>4</sup>. For this reason, numbering of amino acids in segs 2 and 3 in the atomic model is uncertain to the same degree. Density maps shown at contour level of 0.016.

## Extended Data Fig. 6 Comparison of segment 1 position in filament and 10S molecule.

The different position of seg1 in the IHM of the tarantula filament and the 10S molecule is illustrated by comparing the PDBs of the best fits (tarantula filament, PDB 3JBH; 10S molecule, PDB 6XE9 [this work]). **a**, **b**, Front and rear views of IHM in which the head regions (filament, tan; 10S, blue) have been superposed (using Matchmaker in Chimera). **c**, **d**, Same views as

for **a**, **b**, but with heads removed for clarity. Seg1 is yellow for the filament (bent conformation) and pink for the molecule (straight). The two segments run in different positions, ~ 20 Å apart, centre to centre. Strikingly, the position occupied by seg1 in the filament is taken by seg3 in the 10S molecule (yellow/blue overlap). **e**, **f**, The different seg1 positions are also clear when the filament (red) and 10S (blue) maps are compared. Front and rear views confirm that seg1's in the two reconstructions are laterally displaced from each other. Similar results are obtained for two independent filament maps: EMD-1950 (shown)<sup>36</sup> and EMD-6512<sup>60</sup>.

### Extended Data Fig. 7 Mechanisms of converter domain and actin-binding inhibition in BH and FH.

**a–g**, Converter domain inhibition. **a**, Atomic model of 10S structure. Both heads are in the ADP.Pi state (see text). **b**, 10S model, with a myosin head in ADP state (PDB 3I5F, yellow heavy chain) superimposed on the BH by matching motor domains. The RD in this nucleotide state is straight and the Cnv (pink) is in a very different location from the BH Cnv (purple), clearly clashing with seg2. **c**, **d**, Detail of this clash in front and end views, with other parts of molecule removed. This comparison shows that for the BH to lose its Pi (going to the ADP state), its Cnv will clash with seg2. We conclude that seg2 acts as a physical barrier (reinforced by the mechanical restraint created by the connection of both lever arms to S2), preventing this transition and inhibiting BH ATP turnover. **e**, 10S model, with ADP-state head (PDB 3I5F) superposed on the FH MD. **f**, **g**, Detail of **e**, with LCs removed for clarity. The ADP-state RD and its Cnv (pink) are to the right (red arrow) of the ADP.Pi-state FH. This comparison suggests that for the FH to lose its Pi, the interaction of its Cnv with the BH MD must be broken. We propose that this is inhibited in the 10S structure by the strength of this interaction (BF), reinforced by FH interactions with the tail (TF1, TF2 and TF3). Together these interactions would prevent the ADP.Pi → ADP transition and inhibit FH ATP turnover. **h–k**, Actin-binding inhibition. The BH and FH were attached to actin by superposing their MDs on the MD (not shown) of mammalian actomyosin in the rigor state (PDB 5H53), as described in Extended Data Fig. 3. Segments 2 and 3 were removed for clarity. The modelling shows that attachment via both BH and FH is inhibited due to major steric clashes of other parts of the 10S

structure with actin. **h**, Inhibition of binding via the FH. Front view of IHM shows that S2 clashes (dashed circle) with actin (2 monomers shown). **i**, Rotated 90° around vertical axis with respect to **h**. **j**, Inhibition of binding via the BH. Front view of IHM shows that S2 and the FH both clash with actin (dashed circles). **k**, Rotated 90° around vertical axis with respect to **j**.

### Extended Data Fig. 8 Proposed mechanism of 10S myosin inhibition and activation, based on the atomic model and MD simulations.

Smooth and nonmuscle myosin IIs are activated by phosphorylation of their RLCs on S19, leading to breaking of the 10S intramolecular interactions, unfolding to the extended structure, and assembly into functional filaments. Our atomic model indicates a possible mechanism. Our previous work suggested that the single interaction most critical to the folded conformation is that occurring between seg3 and the BH RD<sup>7</sup>, and we noted how proximity of BH RLC S19 might regulate this interaction. Our atomic model suggests that seg3 in fact contacts the BH RLC at two sites. One is the C-lobe (TB5, Fig. [3a, g, and panel e](#) above). The other involves the 24-residue N-terminal extension of the RLC, the phosphorylation domain (PD<sup>61</sup>), containing S19 (interaction TB6, Fig. [3a](#)). The PD is not observed in structures of the myosin head, but has been modelled by molecular dynamics simulations (**a(i)**, dephosphorylated PD, ribbon and surface charge depictions; red negative, blue positive; upper box, PD sequence, MLCK binding site green; S19, yellow; N-terminal half positively charged)<sup>61</sup>. Our EM map reveals significant density (**b**, red rectangle), extending from F25, that fits this PD (**b** shows best fit of model from **a(i)** to BH PD density) and lies over seg3, below TB5 (red rectangles in **b**, showing fitting; **c**, model based on fit; **e**, zoomed-out model). In the atomic model (**c**), interaction occurs between positively charged residues of the PD N-terminal half and a negatively charged patch (~1560-1572) in seg3<sup>7,43</sup> (**d**, red rectangle; surface charge depiction; red, negatively charged; blue, positively charged; see interaction TB6 in Supplementary Table [1](#)), which could strengthen TB5 (**e**). There is also significant density for a portion of the FH PD (**b**, green rectangle), which fits residues 20-24, while the positively charged N-terminal half (**a**) fits weak density near to negatively

charged residues of BH RLC helix B (**b-e**, green rectangles). This would strengthen interaction BF2 between the RLCs. These interactions involving the RLCs, especially the BH PD with seg3, appear to be the key features creating the off state, supported by the other interactions already described. The structural basis of unfolding upon S19 phosphorylation remains unknown due to the absence of the PD in previous structures. The apparent PD densities we observe suggest the following model (**h**). Phosphorylation appears to occur first on the FH, then the BH<sup>7</sup>. EPR and molecular dynamics simulations suggest that phosphorylation causes straightening and stiffening of the PD<sup>61</sup> (**a**: i. dephosphorylated, ii. phosphorylated, iii. transition, dephosphorylated → phosphorylated). When the unphosphorylated PDs (compact in our map; **e, h**, stage 1 in the activation sequence) are replaced by the phosphorylated (straightened) conformations (grey helices in **f, g**, using PD structures from **a(ii)**), the FH PD interaction with BH RLC helix B is removed (due to straightening and to the reduction in positive charge), which could weaken the RLC-RLC and thus head-head interaction (**f**, FH RLC phosphorylated, purple rectangle)<sup>36</sup>, releasing the FH, while retaining the folded tail structure (**h**, stage 2). When the BH is also phosphorylated, straightening/stiffening of its PD, and reduction in its positive charge, breaks its interaction with seg3 (**g**, red arrow, yellow rectangle; **h**, stage 3). With weakening of these interactions, seg2 could dissociate from the BH MD and ELC, leading to complete unfolding to the 6S structure (**h**, stage 4). In support of this proposal, replacement of charged amino acids near S19 in the RLC PD showed that unfolding upon phosphorylation may be due to net charge reduction of the PDs<sup>62</sup>. This physical model suggests that the two PDs with their phosphorylation sites, and the associated regions of seg3, represent a localized structural confluence in which the key events of activation and deactivation take place (the “phosphorylation zone”, **e-g**). We tested the PD structure suggested by the MD simulations (in the case of the BH) by examining the sharpened map in this region and manually creating a model with the PD sequence to best fit the map using Coot (panel (**i**) above; viewing angle changed slightly from **b** to best show density and model features). The density clearly suggests a short helix followed by a loop and a second helix, with density present for the entire length of the PD. This is the first time that the PD has been directly visualized, as it is disordered in isolated myosin heads. We suggest that it is the binding of the PD to seg3 (occurring only in the 10S

structure) that makes this visualization possible. The atomic model based on this fitting broadly supports the bent, helix–loop–helix conformation suggested by the MD simulations of the unphosphorylated PD (**a(i)**). The model (panel **i**) suggests that basic residues K11, K12, and R13, close to acidic residues D1565 and E1566 in seg3, electrostatically hold seg3 in the folded conformation—the most crucial interaction of the 10S structure—and in close proximity to the regulatory S19. MD simulations suggest that phosphorylation creates a salt bridge between phosphorylated S19 and R16, which causes the PD loop to become  $\alpha$ -helical, straightening and stiffening the PD as a whole<sup>61</sup>. As discussed above, we propose that it is this straightening, and the reduction in positive charge of the PD, that cause the dissociation of seg3 from the PD, leading to unfolding and activation of the 10S structure as a whole (**a, g, h**). From the model it is not clear whether the BH RLC would be fully available for binding by MLCK in the 10S structure. Importantly, even if sufficiently exposed, the interaction of K11–R13 with seg3 could slow binding by MLCK, as these residues are also involved in MLCK substrate recognition<sup>63</sup>. If such hindrance occurs, this would be consistent with the proposal<sup>7</sup> that BH phosphorylation, occurring after FH phosphorylation (**h**), is the final, required step for activation and unfolding.

### **Extended Data Fig. 9 Locations of disease-causing mutations in 10S structure.**

**a**, Overview of 10S molecule showing distribution of mutations, yellow in tail, blue in heads. **b–d**. Enlargements of mutation regions. **b**, Proximity of BH converter (Cnv, purple) and SH3 domain (pink) to seg2 mutations, and of BH SH3 and MD mutations to seg2. **c**, Mutations in segs 1, 2, and 3. V1529 is near hinge 2 and could impact hinge function. R1570 is part of the proposed interaction region of the BH RLC PD on seg3, and could impact RLC function. M860-E866 is a duplication, which could translate seg1, impacting its interactions downstream. **d**, Mutations in seg1 coincident with TT2 interaction. See Fig. [2b](#), Extended Data Table [2](#).

### **Extended Data Table 1 Cryo-EM data collection, refinement and validation statistics**

[Full size table](#)

## **Extended Data Table 2 Locations of disease-causing mutations in smooth and nonmuscle myosin II**

[Full size table](#)

## **Supplementary information**

### **Supplementary Table 1**

10S myosin intramolecular interactions. The Table lists the intramolecular interactions at each site of contact in the 10S structure, with a labelled image of each. The table correlates with Fig. 3 of the text.

### **Reporting Summary**

### **Supplementary Table 2**

Sequence alignment of myosin II heavy chains. The Table shows the alignment of the heavy chain sequences of nonmuscle myosin IIA, B, and C and smooth muscle myosin. This alignment is used in plotting mutations in the different myosins onto the 10S structure (Fig. 2b, c; Extended Data Fig. 9, Extended Data Table 2).

### **Peer Review File**

### **Video 1**

3D map of 10S myosin. The 10S myosin map (EMD-22145) is rotated about Y- and X-axes. BH: heavy chain (HC), red; ELC, dark blue; RLC, orange. FH: HC, green; ELC, pale blue; RLC, yellow. SH3 domains, pink; converter domains, purple. Seg1, forest blue; seg2, cyan; seg3, magenta. See Fig. 1.

### **Video 2**

3D map of 10S myosin fitted with refined atomic model. The translucent map (EMD-22145) fitted with refined model (PDB 6XE9) is rotated about

Y- and X-axes. BH: HC, red; ELC, dark blue; RLC, orange. FH: HC, green; ELC, pale blue; RLC, yellow. SH3 domains, pink; converter domains, purple. Seg1, forest blue; seg2, cyan; seg3, magenta. See Fig. 2a.

### [Video 3](#)

Refined atomic model of 10S myosin (6XE9). The model is rotated about Y- and X-axes. BH: HC, red; ELC, dark blue; RLC, orange. FH: HC, green; ELC, pale blue; RLC, yellow. SH3 domains, pink; converter domains, purple. Seg1, forest blue; seg2, cyan; seg3, magenta.

### [Video 4](#)

Refined atomic model of 10S myosin showing mutation sites. The model (PDB 6XE9) is rotated about Y- and X-axes, showing mutation sites, coloured dark blue in heads and yellow in tail. BH: HC, red; ELC, dark blue; RLC, orange. FH: HC, green; ELC, pale blue; RLC, yellow. SH3 domains, pink; converter domains, purple. Seg1, forest blue; seg2, cyan; seg3, magenta. See Fig. 2b, Extended Data Table 2.

### [Video 5](#)

Refined atomic model of 10S myosin showing putative interaction sites. The model (PDB 6XE9) is rotated about Y- and X-axes, showing intramolecular interaction sites, coloured cyan and yellow to distinguish the interacting partners. BH: HC, red; ELC, dark blue; RLC, orange. FH: HC, green; ELC, pale blue; RLC, yellow. SH3 domains, pink; converter domains, purple. Seg1, forest blue; seg2, cyan; seg3, magenta. See Fig. 3, Supplementary Table 1.

## Rights and permissions

### [Reprints and Permissions](#)

## About this article



Check for  
updates

## Cite this article

Yang, S., Tiwari, P., Lee, K.H. *et al.* Cryo-EM structure of the inhibited (10S) form of myosin II. *Nature* **588**, 521–525 (2020).  
<https://doi.org/10.1038/s41586-020-3007-0>

[Download citation](#)

- Received: 02 July 2020
- Accepted: 01 October 2020
- Published: 02 December 2020
- Issue Date: 17 December 2020
- DOI: <https://doi.org/10.1038/s41586-020-3007-0>

## Comments

By submitting a comment you agree to abide by our [Terms](#) and [Community Guidelines](#). If you find something abusive or that does not comply with our terms or guidelines please flag it as inappropriate.

[Access through your institution](#)

[Change institution](#)

[Buy or subscribe](#)

---

This article was downloaded by **calibre** from <https://www.nature.com/articles/s41586-020-3007-0>

- Matters Arising
- [Published: 16 December 2020](#)

# Beta human papillomaviruses and skin cancer

- [Paul F. Lambert<sup>1</sup>](#),
- [Karl Münger<sup>2</sup>](#),
- [Frank Rösl<sup>3</sup>](#),
- [Daniel Hasche<sup>3</sup>](#) &
- [Massimo Tommasino](#)    [ORCID: orcid.org/0000-0002-0890-8596<sup>4</sup>](#)

[Nature](#) volume 588, pages E20–E21(2020) [Cite this article](#)

- 794 Accesses
- 1 Citations
- 2 Altmetric
- [Metrics details](#)

## Subjects

- [Human papilloma virus](#)
- [Virus–host interactions](#)

[Matters Arising](#) to this article was published on 16 December 2020

The [Original Article](#) was published on 30 October 2019

[Access through your institution](#)  
[Change institution](#)  
[Buy or subscribe](#)

## Access options

Subscribe to Journal

Get full journal access for 1 year

185,98 €

only 3,58 € per issue

[Subscribe](#)

All prices are NET prices.  
VAT will be added later in the checkout.

Rent or Buy article

Get time limited or full article access on ReadCube.

from \$8.99

[Rent or Buy](#)

All prices are NET prices.

### Additional access options:

- [Log in](#)
- [Access through your institution](#)
- [Learn about institutional subscriptions](#)

**Fig. 1: Model for cooperation between some types of β-HPV and UV radiation in promoting cSCCs.**



## References

1. 1.

Rollison, D. E., Viarisio, D., Amorrotu, R. P., Gheit, T. & Tommasino, M. An emerging issue in oncogenic virology: the role of beta human papillomavirus types in the development of cutaneous squamous cell carcinoma. *J. Virol.* **93**, e01003-18 (2019).

[CAS](#) [Article](#) [Google Scholar](#)

2. 2.

Strickley, J. D. et al. Immunity to commensal papillomaviruses protects against skin cancer. *Nature* **575**, 519–522 (2019).

[ADS](#) [CAS](#) [Article](#) [Google Scholar](#)

3. 3.

Zhao, Y. et al. Cutaneous viral infections associated with ultraviolet radiation exposure. *Int. J. Cancer* (2020).

4. 4.

Cladel, N. M. et al. Mouse papillomavirus infections spread to cutaneous sites with progression to malignancy. *J. Gen. Virol.* **98**, 2520–2529 (2017).

[CAS](#) [Article](#) [Google Scholar](#)

5. 5.

Uberoi, A., Yoshida, S., Frazer, I. H., Pitot, H. C. & Lambert, P. F. Role of ultraviolet radiation in papillomavirus-induced disease. *PLoS Pathog.* **12**, e1005664 (2016).

[Article](#) [Google Scholar](#)

6. 6.

Cladel, N. M. et al. Mouse papillomavirus infection persists in mucosal tissues of an immunocompetent mouse strain and progresses to cancer. *Sci. Rep.* **7**, 16932 (2017).

[ADS](#) [Article](#) [Google Scholar](#)

7. 7.

Spurgeon, M. E. et al. A novel *in vivo* infection model to study papillomavirus-mediated disease of the female reproductive tract. *MBio* **10**, e00180-19 (2019).

[CAS](#) [Article](#) [Google Scholar](#)

8. 8.

Hasche, D. et al. The interplay of UV and cutaneous papillomavirus infection in skin cancer development. *PLoS Pathog.* **13**, e1006723 (2017).

[Article](#) [Google Scholar](#)

9. 9.

Viarisio, D. et al. E6 and E7 from beta HPV38 cooperate with ultraviolet light in the development of actinic keratosis-like lesions and squamous cell carcinoma in mice. *PLoS Pathog.* **7**, e1002125 (2011).

[CAS](#) [Article](#) [Google Scholar](#)

10. 10.

Hasche, D., Vinzón, S. E. & Rösl, F. Cutaneous papillomaviruses and non-melanoma skin cancer: causal agents or innocent bystanders? *Front. Microbiol.* **9**, 874 (2018).

[Article](#) [Google Scholar](#)

11. 11.

Venuti, A., Lohse, S., Tommasino, M. & Smola, S. Cross-talk of cutaneous beta human papillomaviruses and the immune system: determinants of disease penetrance. *Phil. Trans. R. Soc. Lond. B* **374**, 20180287 (2019).

[CAS](#) [Article](#) [Google Scholar](#)

12. 12.

Viarisio, D. et al. Beta HPV38 oncoproteins act with a hit-and-run mechanism in ultraviolet radiation-induced skin carcinogenesis in mice. *PLoS Pathog.* **14**, e1006783 (2018).

[Article](#) [Google Scholar](#)

[Download references](#)

## Author information

### Affiliations

1. McArdle Laboratory for Cancer Research, University of Wisconsin, Madison, WI, USA

Paul F. Lambert

2. Developmental, Molecular and Chemical Biology, Tufts University School of Medicine, Boston, MA, USA

Karl Münger

3. Division of Viral Transformation Mechanisms, German Cancer Research Center (DKFZ), Heidelberg, Germany

Frank Rösl & Daniel Hasche

4. Infections and Cancer Biology Group, International Agency for Research on Cancer, World Health Organization, Lyon, France

Massimo Tommasino

## Authors

1. Paul F. Lambert

[View author publications](#)

You can also search for this author in [PubMed](#) [Google Scholar](#)

2. Karl Münger

[View author publications](#)

You can also search for this author in [PubMed](#) [Google Scholar](#)

3. Frank Rösl

[View author publications](#)

You can also search for this author in [PubMed](#) [Google Scholar](#)

4. Daniel Hasche

[View author publications](#)

You can also search for this author in [PubMed](#) [Google Scholar](#)

5. Massimo Tommasino

[View author publications](#)

You can also search for this author in [PubMed](#) [Google Scholar](#)

## Contributions

P.F.L., K.M., F.R., D.H. and M.T. contributed to article preparation and approved the submitted version. Where authors are identified as personnel of the International Agency for Research on Cancer/World Health Organization, the authors alone are responsible for the views expressed in this article and they do not necessarily represent the decisions, policy, or views of the International Agency for Research on Cancer/World Health Organization.

## Corresponding author

Correspondence to [Massimo Tommasino](#).

## Ethics declarations

## Competing interests

The authors declare no competing interests.

## Additional information

**Publisher's note** Springer Nature remains neutral with regard to jurisdictional claims in published maps and institutional affiliations.

## Rights and permissions

[Reprints and Permissions](#)

## About this article



Check for  
updates

## Cite this article

Lambert, P.F., Münger, K., Rösl, F. *et al.* Beta human papillomaviruses and skin cancer. *Nature* **588**, E20–E21 (2020). <https://doi.org/10.1038/s41586-020-3023-0>

[Download citation](#)

- Received: 22 November 2019
- Accepted: 20 October 2020
- Published: 16 December 2020
- Issue Date: 17 December 2020
- DOI: <https://doi.org/10.1038/s41586-020-3023-0>

## Further reading

- [Reply to: Beta human papillomaviruses and skin cancer](#)
  - John D. Strickley
  - , Jonathan L. Messerschmidt
  - , Alfred Bennett Jenson
  - , Joongho Joh
  - & Shadmehr Demehri

*Nature* (2020)

## Comments

By submitting a comment you agree to abide by our [Terms](#) and [Community Guidelines](#). If you find something abusive or that does not comply with our terms or guidelines please flag it as inappropriate.

[Access through your institution](#)

[Change institution](#)

[Buy or subscribe](#)

---

This article was downloaded by **calibre** from <https://www.nature.com/articles/s41586-020-3023-0>

| [Section menu](#) | [Main menu](#) |

- Matters Arising
- [Published: 16 December 2020](#)

# Reply to: Beta human papillomaviruses and skin cancer

- [John D. Strickley<sup>1,2,3,4</sup>](#),
- [Jonathan L. Messerschmidt](#) ORCID: [orcid.org/0000-0002-6132-7256<sup>1,2</sup>](https://orcid.org/0000-0002-6132-7256),
- [Alfred Bennett Jenson<sup>3</sup>](#),
- [Joongho Joh<sup>3,4,5</sup>](#) &
- [Shadmehr Demehri](#) ORCID: [orcid.org/0000-0002-7913-2641<sup>1,2</sup>](https://orcid.org/0000-0002-7913-2641)

*Nature* volume 588, pages E22–E23 (2020) [Cite this article](#)

- 449 Accesses
- 2 Altmetric
- [Metrics details](#)

## Subjects

- [Cancer prevention](#)
- [Immunological surveillance](#)
- [Squamous cell carcinoma](#)
- [Tumour virus infections](#)
- [Virology](#)

The [Original Article](#) was published on 16 December 2020

[Access through your institution](#)  
[Change institution](#)  
[Buy or subscribe](#)

## Access options

Subscribe to Journal

Get full journal access for 1 year

185,98 €

only 3,58 € per issue

[Subscribe](#)

All prices are NET prices.  
VAT will be added later in the checkout.

Rent or Buy article

Get time limited or full article access on ReadCube.

from \$8.99

[Rent or Buy](#)

All prices are NET prices.

### Additional access options:

- [Log in](#)
- [Access through your institution](#)
- [Learn about institutional subscriptions](#)

## References

1. 1.

Lambert, P. F., Münger, K., Rösl, F., Hasche, D. & Tommasino, M. Beta human papillomaviruses and skin cancer. *Nature* <https://doi.org/10.1038/s41586-020-3023-0> (2020).

2. 2.

Strickley, J. D. et al. Immunity to commensal papillomaviruses protects against skin cancer. *Nature* **575**, 519–522 (2019).

[ADS](#) [CAS](#) [Article](#) [Google Scholar](#)

3. 3.

Rollison, D. E., Viarisio, D., Amorrtu, R. P., Gheit, T. & Tommasino, M. An emerging issue in oncogenic virology: the role of beta human papillomavirus types in the development of cutaneous squamous cell carcinoma. *J. Virol.* **93**, e01003-18 (2019).

[CAS](#) [Article](#) [Google Scholar](#)

4. 4.

Wang, J. W. et al. Immunologic control of *Mus musculus* papillomavirus type 1. *PLoS Pathog.* **11**, e1005243 (2015).

[Article](#) [Google Scholar](#)

5. 5.

Joh, J. et al. T cell-mediated antitumor immune response eliminates skin tumors induced by mouse papillomavirus, MmuPV1. *Exp. Mol. Pathol.* **103**, 181–190 (2017).

[CAS](#) [Article](#) [Google Scholar](#)

6. 6.

Meyers, J. M., Uberoi, A., Grace, M., Lambert, P. F. & Munger, K. Cutaneous HPV8 and MmuPV1 E6 proteins target the NOTCH and TGF- $\beta$  tumor suppressors to inhibit differentiation and sustain keratinocyte proliferation. *PLoS Pathog.* **13**, e1006171 (2017).

[Article](#) [Google Scholar](#)

7. 7.

Viarisio, D. et al. Beta HPV38 oncoproteins act with a hit-and-run mechanism in ultraviolet radiation-induced skin carcinogenesis in mice. *PLoS Pathog.* **14**, e1006783 (2018).

[Article](#) [Google Scholar](#)

8. 8.

Cladel, N. M. et al. Mouse papillomavirus infections spread to cutaneous sites with progression to malignancy. *J. Gen. Virol.* **98**, 2520–2529 (2017).

[CAS](#) [Article](#) [Google Scholar](#)

9. 9.

Hasche, D. et al. The interplay of UV and cutaneous papillomavirus infection in skin cancer development. *PLoS Pathog.* **13**, e1006723 (2017).

[Article](#) [Google Scholar](#)

10. 10.

Viarisio, D. et al. E6 and E7 from beta HPV38 cooperate with ultraviolet light in the development of actinic keratosis-like lesions and squamous cell carcinoma in mice. *PLoS Pathog.* **7**, e1002125 (2011).

[CAS](#) [Article](#) [Google Scholar](#)

11. 11.

Uberoi, A., Yoshida, S., Frazer, I. H., Pitot, H. C. & Lambert, P. F. Role of ultraviolet radiation in papillomavirus-induced disease. *PLoS Pathog.* **12**, e1005664 (2016).

[Article](#) [Google Scholar](#)

12. 12.

Inman, G. J. et al. The genomic landscape of cutaneous SCC reveals drivers and a novel azathioprine associated mutational signature. *Nat. Commun.* **9**, 3667 (2018).

[ADS](#) [Article](#) [Google Scholar](#)

13. 13.

Tan, M. J. et al. Cutaneous  $\beta$ -human papillomavirus E6 proteins bind Mastermind-like coactivators and repress Notch signaling. *Proc. Natl Acad. Sci. USA* **109**, E1473–E1480 (2012).

[CAS](#) [Article](#) [Google Scholar](#)

14. 14.

Goh, G. et al. Mutational landscape of MCPyV-positive and MCPyV-negative Merkel cell carcinomas with implications for immunotherapy. *Oncotarget* **7**, 3403–3415 (2016).

[Article](#) [Google Scholar](#)

15. 15.

Arron, S. T., Ruby, J. G., Dybbro, E., Ganem, D. & Derisi, J. L. Transcriptome sequencing demonstrates that human papillomavirus is not active in cutaneous squamous cell carcinoma. *J. Invest. Dermatol.* **131**, 1745–1753 (2011).

[CAS Article](#) [Google Scholar](#)

[Download references](#)

## Author information

### Affiliations

1. Center for Cancer Immunology, Center for Cancer Research,  
Massachusetts General Hospital and Harvard Medical School, Boston,  
MA, USA

John D. Strickley, Jonathan L. Messerschmidt & Shadmehr Demehri

2. Cutaneous Biology Research Center, Department of Dermatology,  
Massachusetts General Hospital and Harvard Medical School, Boston,  
MA, USA

John D. Strickley, Jonathan L. Messerschmidt & Shadmehr Demehri

3. James Graham Brown Cancer Center, University of Louisville,  
Louisville, KY, USA

John D. Strickley, Alfred Bennett Jenson & Joongho Joh

4. Department of Medicine, University of Louisville, Louisville, KY,  
USA

John D. Strickley & Joongho Joh

5. Center for Predictive Medicine, University of Louisville, Louisville,  
KY, USA

Joongho Joh

### Authors

1. John D. Strickley

[View author publications](#)

You can also search for this author in [PubMed](#) [Google Scholar](#)

2. Jonathan L. Messerschmidt

[View author publications](#)

You can also search for this author in [PubMed](#) [Google Scholar](#)

3. Alfred Bennett Jenson

[View author publications](#)

You can also search for this author in [PubMed](#) [Google Scholar](#)

4. Joongho Joh

[View author publications](#)

You can also search for this author in [PubMed](#) [Google Scholar](#)

5. Shadmehr Demehri

[View author publications](#)

You can also search for this author in [PubMed](#) [Google Scholar](#)

## **Contributions**

All authors who wrote the original manuscript and formulated its conclusions (J.D.S., J.L.M., A.B.J., J.J., S.D.) contributed to this response; J.D.S., J.L.M. and S.D. wrote the response; A.B.J. and J.J reviewed and edited the response.

## **Corresponding author**

Correspondence to [Shadmehr Demehri](#).

## **Ethics declarations**

## Competing interests

The authors declare no competing interests.

## Additional information

**Publisher's note** Springer Nature remains neutral with regard to jurisdictional claims in published maps and institutional affiliations.

## Rights and permissions

[Reprints and Permissions](#)

## About this article



Check for  
updates

## Cite this article

Strickley, J.D., Messerschmidt, J.L., Jenson, A.B. *et al.* Reply to: Beta human papillomaviruses and skin cancer. *Nature* **588**, E22–E23 (2020). <https://doi.org/10.1038/s41586-020-3024-z>

[Download citation](#)

- Published: 16 December 2020
- Issue Date: 17 December 2020
- DOI: <https://doi.org/10.1038/s41586-020-3024-z>

## Comments

By submitting a comment you agree to abide by our [Terms](#) and [Community Guidelines](#). If you find something abusive or that does not comply with our terms or guidelines please flag it as inappropriate.

[Access through your institution](#)

[Change institution](#)

[Buy or subscribe](#)

## Associated Content

Collection

### [Cancer at Nature Research](#)

*Nature* | Article

### [Immunity to commensal papillomaviruses protects against skin cancer](#)

- John D. Strickley
- , Jonathan L. Messerschmidt
- , Mary E. Awad
- , Tiancheng Li
- , Tatsuya Hasegawa
- , Dat Thinh Ha
- , Henry W. Nabeta
- , Paul A. Bevins
- , Kenneth H. Ngo
- , Maryam M. Asgari
- , Rosalynn M. Nazarian
- , Victor A. Neel
- , Alfred Bennett Jenson
- , Joongho Joh
- & Shadmehr Demehri

---

This article was downloaded by **calibre** from <https://www.nature.com/articles/s41586-020-3024-z>

| [Section menu](#) | [Main menu](#) |

# Amendments & Corrections

- [\*\*Author Correction: Combinatorial expression of GPCR isoforms affects signalling and drug responses\*\*](#) [25 November 2020]  
Author Correction •
- [\*\*Author Correction: Observed controls on resilience of groundwater to climate variability in sub-Saharan Africa\*\*](#) [03 December 2020]  
Author Correction •

Author Correction: Combinatorial expression of GPCR isoforms affects signalling and drug responses

[Download PDF](#)

- Author Correction
- [Published: 25 November 2020](#)

# Author Correction: Combinatorial expression of GPCR isoforms affects signalling and drug responses

- [Maria Marti-Solano](#) ORCID: [orcid.org/0000-0003-0373-8927](https://orcid.org/0000-0003-0373-8927)<sup>1</sup>,
- [Stephanie E. Crilly](#)<sup>2</sup>,
- [Duccio Malinverni](#)<sup>1,3</sup>,
- [Christian Munk](#)<sup>4</sup>,
- [Matthew Harris](#)<sup>5</sup>,
- [Abigail Pearce](#) ORCID: [orcid.org/0000-0001-9845-0541](https://orcid.org/0000-0001-9845-0541)<sup>5</sup>,
- [Tezz Quon](#)<sup>6</sup>,
- [Amanda E. Mackenzie](#)<sup>6</sup>,
- [Xusheng Wang](#)<sup>7,8</sup>,
- [Junmin Peng](#) ORCID: [orcid.org/0000-0003-0472-7648](https://orcid.org/0000-0003-0472-7648)<sup>7,9</sup>,
- [Andrew B. Tobin](#) ORCID: [orcid.org/0000-0002-1807-3123](https://orcid.org/0000-0002-1807-3123)<sup>6</sup>,
- [Graham Ladds](#) ORCID: [orcid.org/0000-0001-7320-9612](https://orcid.org/0000-0001-7320-9612)<sup>5</sup>,
- [Graeme Milligan](#) ORCID: [orcid.org/0000-0002-6946-3519](https://orcid.org/0000-0002-6946-3519)<sup>6</sup>,
- [David E. Gloriam](#) ORCID: [orcid.org/0000-0002-4299-7561](https://orcid.org/0000-0002-4299-7561)<sup>4</sup>,
- [Manojkumar A. Puthenveedu](#) ORCID: [orcid.org/0000-0002-3177-4231](https://orcid.org/0000-0002-3177-4231)<sup>2,10</sup> &
- [M. Madan Babu](#) ORCID: [orcid.org/0000-0003-0556-6196](https://orcid.org/0000-0003-0556-6196)<sup>1,3</sup>

[Nature](#) volume 588, page E24(2020) [Cite this article](#)

- 1217 Accesses
- 1 Citations
- 4 Altmetric
- [Metrics details](#)

## Subjects

- [Computational biology and bioinformatics](#)
- [Systems biology](#)

The [Original Article](#) was published on 04 November 2020

[Download PDF](#)

Correction to: *Nature* <https://doi.org/10.1038/s41586-020-2888-2> Published online 04 November 2020

In Fig. 4 of this Article, the same graph appeared twice (under both ‘G $\alpha$ 13’ and ‘β-arrestin-2’). The correct figures were present during the review process and this error does not affect the results or conclusions. Note that the numerical values calculated from the curves in Fig. 4 that appear in Extended Data Fig. 6f (pEC<sub>50</sub> and E<sub>max</sub> values for Iodoxamide) were calculated from the correct curves for G $\alpha$ 13 and β-arrestin-2. The ‘β-arrestin-2’ graph of the original Article has been corrected online.

## Author information

### Affiliations

1. MRC Laboratory of Molecular Biology, Cambridge, UK

Maria Marti-Solano, Duccio Malinvern & M. Madan Babu

2. Cellular and Molecular Biology Program, University of Michigan,  
Ann Arbor, MI, USA

Stephanie E. Crilly & Manojkumar A. Puthenveedu

3. Department of Structural Biology and Center for Data Driven  
Discovery, St Jude Children's Research Hospital, Memphis, TN, USA

Duccio Malinvern & M. Madan Babu

4. Department of Drug Design and Pharmacology, University of  
Copenhagen, Copenhagen, Denmark

Christian Munk & David E. Gloriam

5. Department of Pharmacology, University of Cambridge, Cambridge,  
UK

Matthew Harris, Abigail Pearce & Graham Ladds

6. Centre for Translational Pharmacology, Institute of Molecular, Cell  
and Systems Biology, College of Medical, Veterinary and Life  
Sciences, University of Glasgow, Glasgow, UK

Tezz Quon, Amanda E. Mackenzie, Andrew B. Tobin & Graeme  
Milligan

7. Center for Proteomics and Metabolomics, St Jude Children's Research  
Hospital, Memphis, TN, USA

Xusheng Wang & Junmin Peng

8. Department of Biology, University of North Dakota, Grand Forks, ND,  
USA

Xusheng Wang

9. Departments of Structural Biology and Developmental Neurobiology,  
St Jude Children's Research Hospital, Memphis, TN, USA

Junmin Peng

10. Department of Pharmacology, University of Michigan Medical School,  
Ann Arbor, MI, USA

Manojkumar A. Puthenveedu

## Authors

1. Maria Marti-Solano

[View author publications](#)

You can also search for this author in [PubMed](#) [Google Scholar](#)

2. Stephanie E. Crilly

[View author publications](#)

You can also search for this author in [PubMed](#) [Google Scholar](#)

3. Duccio Malinvernì

[View author publications](#)

You can also search for this author in [PubMed](#) [Google Scholar](#)

4. Christian Munk

[View author publications](#)

You can also search for this author in [PubMed](#) [Google Scholar](#)

5. Matthew Harris

[View author publications](#)

You can also search for this author in [PubMed](#) [Google Scholar](#)

6. Abigail Pearce

[View author publications](#)

You can also search for this author in [PubMed](#) [Google Scholar](#)

7. Tezz Quon

[View author publications](#)

You can also search for this author in [PubMed](#) [Google Scholar](#)

8. Amanda E. Mackenzie

[View author publications](#)

You can also search for this author in [PubMed](#) [Google Scholar](#)

9. Xusheng Wang

[View author publications](#)

You can also search for this author in [PubMed](#) [Google Scholar](#)

10. Junmin Peng

[View author publications](#)

You can also search for this author in [PubMed](#) [Google Scholar](#)

11. Andrew B. Tobin

[View author publications](#)

You can also search for this author in [PubMed](#) [Google Scholar](#)

12. Graham Ladds

[View author publications](#)

You can also search for this author in [PubMed](#) [Google Scholar](#)

13. Graeme Milligan

[View author publications](#)

You can also search for this author in [PubMed](#) [Google Scholar](#)

14. David E. Gloriam

[View author publications](#)

You can also search for this author in [PubMed](#) [Google Scholar](#)

15. Manojkumar A. Puthenveedu

[View author publications](#)

You can also search for this author in [PubMed](#) [Google Scholar](#)

16. M. Madan Babu

[View author publications](#)

You can also search for this author in [PubMed](#) [Google Scholar](#)

## Corresponding authors

Correspondence to [Maria Marti-Solano](#) or [M. Madan Babu](#).

## Rights and permissions

[Reprints and Permissions](#)

## About this article



Check for  
updates

## Cite this article

Marti-Solano, M., Crilly, S.E., Malinverni, D. *et al.* Author Correction: Combinatorial expression of GPCR isoforms affects signalling and drug responses. *Nature* **588**, E24 (2020). <https://doi.org/10.1038/s41586-020-2999-9>

[Download citation](#)

- Published: 25 November 2020

- Issue Date: 17 December 2020
- DOI: <https://doi.org/10.1038/s41586-020-2999-9>

## Comments

By submitting a comment you agree to abide by our [Terms](#) and [Community Guidelines](#). If you find something abusive or that does not comply with our terms or guidelines please flag it as inappropriate.

[Download PDF](#)

---

This article was downloaded by **calibre** from <https://www.nature.com/articles/s41586-020-2999-9>

| [Section menu](#) | [Main menu](#) |

Author Correction: Observed controls on resilience of groundwater to climate variability in sub-Saharan Africa

[Download PDF](#)

- Author Correction
- [Published: 03 December 2020](#)

# Author Correction: Observed controls on resilience of groundwater to climate variability in sub-Saharan Africa

- [Mark O. Cuthbert](#) ORCID: [orcid.org/0000-0001-6721-022X<sup>1,2,3,4</sup>](https://orcid.org/0000-0001-6721-022X),
- [Richard G. Taylor<sup>1</sup>](#),
- [Guillaume Favreau<sup>5,30</sup>](#),
- [Martin C. Todd<sup>6</sup>](#),
- [Mohammad Shamsuddoha<sup>1,7</sup>](#),
- [Karen G. Villholth<sup>8</sup>](#),
- [Alan M. MacDonald<sup>9</sup>](#),
- [Bridget R. Scanlon<sup>10</sup>](#),
- [D. O. Valerie Kotchoni<sup>11</sup>](#),
- [Jean-Michel Vouillamoz<sup>12</sup>](#),
- [Fabrice M. A. Lawson<sup>11</sup>](#),
- [Philippe Armand Adjomayi<sup>13</sup>](#),
- [Japhet Kashaigili<sup>14</sup>](#),
- [David Seddon<sup>1</sup>](#),
- [James P. R. Sorensen<sup>15</sup>](#),
- [Girma Yimer Ebrahim<sup>8</sup>](#),
- [Michael Owor<sup>16</sup>](#),
- [Philip M. Nyenje<sup>17</sup>](#),

- [Yahaya Nazoumou<sup>18</sup>](#),
- [Ibrahim Goni<sup>19</sup>](#),
- [Boukari Issoufou Ousmane<sup>18</sup>](#),
- [Tenant Sibanda<sup>20</sup>](#),
- [Matthew J. Ascott<sup>15</sup>](#),
- [David M. J. Macdonald<sup>15</sup>](#),
- [William Agyekum<sup>21</sup>](#),
- [Youssef Koussoubé<sup>22</sup>](#),
- [Heike Wanke<sup>23,24</sup>](#),
- [Hyungjun Kim<sup>25</sup>](#),
- [Yoshihide Wada<sup>26</sup>](#),
- [Min-Hui Lo<sup>27</sup>](#),
- [Taikan Oki<sup>25,28</sup>](#) &
- [Neno Kukuric<sup>29</sup>](#)

[Nature volume 588](#), page E25(2020) [Cite this article](#)

- 644 Accesses
- 2 Altmetric
- [Metrics details](#)

The [Original Article](#) was published on 07 August 2019

[Download PDF](#)

Correction to: *Nature* <https://doi.org/10.1038/s41586-019-1441-7> Published online 07 August 2019

In this Letter, affiliation 12, for Jean-Michel Vouillamoz, should begin “Université Grenoble Alpes, Institut de Recherche pour le Développement”, rather than “Institut de Recherche pour le Développement, Université Grenoble Alpes”. The primary affiliation , for Guillaume Favreau should be affiliation 5, “Université Grenoble Alpes, IRD, CNRS, Grenoble INP,

IGE, Grenoble, France" and his secondary affiliation should be affiliation 30, "Institut de Recherche pour le Développement, Niamey, Niger". These errors have been corrected online.

## Author information

### Affiliations

#### 1. Department of Geography, University College London, London, UK

Mark O. Cuthbert, Richard G. Taylor, Mohammad  
Shamsuddoha & David Seddon

#### 2. School of Earth and Ocean Sciences, Cardiff University, Cardiff, UK

Mark O. Cuthbert

#### 3. Connected Waters Initiative Research Centre, University of New South Wales, Sydney, Australia

Mark O. Cuthbert

#### 4. Water Research Institute, Cardiff University, Cardiff, UK

Mark O. Cuthbert

#### 5. Université Grenoble Alpes, IRD, CNRS, Grenoble INP, IGE, Grenoble, France

Guillaume Favreau

#### 6. Department of Geography, University of Sussex, Falmer, UK

Martin C. Todd

#### 7. Institute for Risk and Disaster Reduction, University College London, London, UK

Mohammad Shamsuddoha

8. International Water Management Institute, Pretoria, South Africa

Karen G. Villholth & Girma Yimer Ebrahim

9. British Geological Survey, Lyell Centre, Edinburgh, UK

Alan M. MacDonald

10. Bureau of Economic Geology, Jackson School of Geosciences,  
University of Texas at Austin, Austin, TX, USA

Bridget R. Scanlon

11. Université d'Abomey-Calavi, Institut Nationale de l'Eau, Chaire  
Internationale de Physique Mathématique et Applications, Institut de  
Recherche pour le Développement, Cotonou, Benin

D. O. Valerie Kotchoni & Fabrice M. A. Lawson

12. Université Grenoble Alpes, Institut de Recherche pour le  
Développement, Centre Nationale de la Recherche Scientifique,  
Institut Polytechnique de Grenoble, Institut des Géosciences de  
l'Environnement, Grenoble, France

Jean-Michel Vouillamoz

13. Direction Générale de l'Eau, Cotonou, Benin

Philippe Armand Adjomayi

14. Department of Forest Resources Assessment and Management,  
Sokoine University of Agriculture, Morogoro, Tanzania

Japhet Kashaigili

15. British Geological Survey, Maclean Building, Wallingford, UK

James P. R. Sorensen, Matthew J. Ascott & David M. J. Macdonald

16. Department of Geology and Petroleum Studies, Makerere University, Kampala, Uganda

Michael Owor

17. Department of Civil and Environmental Engineering, Makerere University, Kampala, Uganda

Philip M. Nyenje

18. Department of Geology, Université Abdou Moumouni, Niamey, Niger

Yahaya Nazoumou & Boukari Issoufou Ousmane

19. Department of Geology, University of Maiduguri, Maiduguri, Nigeria

Ibrahim Goni

20. Cemex, Rugby, UK

Tenant Sibanda

21. Water Research Institute, Accra, Ghana

William Agyekum

22. Département des Sciences de la Terre, Université Ouaga I Pr Joseph Ki-Zerbo, Ouagadougou, Burkina Faso

Youssouf Koussoubé

23. Department of Geology, University of Namibia, Windhoek, Namibia

Heike Wanke

24. Department of Geography and Environmental Management, University of the West of England, Bristol, UK

Heike Wanke

25. Institute of Industrial Science, The University of Tokyo, Tokyo, Japan

Hyungjun Kim & Taikan Oki

26. International Institute for Applied Systems Analysis, Laxenburg,  
Austria

Yoshihide Wada

27. Department of Atmospheric Sciences, National Taiwan University,  
Taipei City, Taiwan

Min-Hui Lo

28. Institute for Future Initiatives, The University of Tokyo, Tokyo, Japan

Taikan Oki

29. International Groundwater Resources Assessment Centre, Delft, The  
Netherlands

Neno Kukuric

30. Institut de Recherche pour le Développement, Niamey, Niger

Guillaume Favreau

## Authors

1. Mark O. Cuthbert

[View author publications](#)

You can also search for this author in [PubMed](#) [Google Scholar](#)

2. Richard G. Taylor

[View author publications](#)

You can also search for this author in [PubMed](#) [Google Scholar](#)

3. Guillaume Favreau

[View author publications](#)

You can also search for this author in [PubMed](#) [Google Scholar](#)

4. Martin C. Todd

[View author publications](#)

You can also search for this author in [PubMed](#) [Google Scholar](#)

5. Mohammad Shamsuddoha

[View author publications](#)

You can also search for this author in [PubMed](#) [Google Scholar](#)

6. Karen G. Villholth

[View author publications](#)

You can also search for this author in [PubMed](#) [Google Scholar](#)

7. Alan M. MacDonald

[View author publications](#)

You can also search for this author in [PubMed](#) [Google Scholar](#)

8. Bridget R. Scanlon

[View author publications](#)

You can also search for this author in [PubMed](#) [Google Scholar](#)

9. D. O. Valerie Kotchoni

[View author publications](#)

You can also search for this author in [PubMed](#) [Google Scholar](#)

10. Jean-Michel Vouillamoz

[View author publications](#)

You can also search for this author in [PubMed](#) [Google Scholar](#)

11. Fabrice M. A. Lawson  
[View author publications](#)

You can also search for this author in [PubMed](#) [Google Scholar](#)

12. Philippe Armand Adjomayi  
[View author publications](#)

You can also search for this author in [PubMed](#) [Google Scholar](#)

13. Japhet Kashaigili  
[View author publications](#)

You can also search for this author in [PubMed](#) [Google Scholar](#)

14. David Seddon  
[View author publications](#)

You can also search for this author in [PubMed](#) [Google Scholar](#)

15. James P. R. Sorensen  
[View author publications](#)

You can also search for this author in [PubMed](#) [Google Scholar](#)

16. Girma Yimer Ebrahim  
[View author publications](#)

You can also search for this author in [PubMed](#) [Google Scholar](#)

17. Michael Owor  
[View author publications](#)

You can also search for this author in [PubMed](#) [Google Scholar](#)

18. Philip M. Nyenje  
[View author publications](#)

You can also search for this author in [PubMed](#) [Google Scholar](#)

19. Yahaya Nazoumou

[View author publications](#)

You can also search for this author in [PubMed](#) [Google Scholar](#)

20. Ibrahim Goni

[View author publications](#)

You can also search for this author in [PubMed](#) [Google Scholar](#)

21. Boukari Issoufou Ousmane

[View author publications](#)

You can also search for this author in [PubMed](#) [Google Scholar](#)

22. Tenant Sibanda

[View author publications](#)

You can also search for this author in [PubMed](#) [Google Scholar](#)

23. Matthew J. Ascott

[View author publications](#)

You can also search for this author in [PubMed](#) [Google Scholar](#)

24. David M. J. Macdonald

[View author publications](#)

You can also search for this author in [PubMed](#) [Google Scholar](#)

25. William Agyekum

[View author publications](#)

You can also search for this author in [PubMed](#) [Google Scholar](#)

26. Youssouf Koussoubé

[View author publications](#)

You can also search for this author in [PubMed](#) [Google Scholar](#)

27. Heike Wanke

[View author publications](#)

You can also search for this author in [PubMed](#) [Google Scholar](#)

28. Hyungjun Kim

[View author publications](#)

You can also search for this author in [PubMed](#) [Google Scholar](#)

29. Yoshihide Wada

[View author publications](#)

You can also search for this author in [PubMed](#) [Google Scholar](#)

30. Min-Hui Lo

[View author publications](#)

You can also search for this author in [PubMed](#) [Google Scholar](#)

31. Taikan Oki

[View author publications](#)

You can also search for this author in [PubMed](#) [Google Scholar](#)

32. Neno Kukuric

[View author publications](#)

You can also search for this author in [PubMed](#) [Google Scholar](#)

## Corresponding author

Correspondence to [Mark O. Cuthbert](#).

## Rights and permissions

## [Reprints and Permissions](#)

## About this article



Check for  
updates

## Cite this article

Cuthbert, M.O., Taylor, R.G., Favreau, G. *et al.* Author Correction: Observed controls on resilience of groundwater to climate variability in sub-Saharan Africa. *Nature* **588**, E25 (2020).  
<https://doi.org/10.1038/s41586-020-2985-2>

## [Download citation](#)

- Published: 03 December 2020
- Issue Date: 17 December 2020
- DOI: <https://doi.org/10.1038/s41586-020-2985-2>

## Comments

By submitting a comment you agree to abide by our [Terms](#) and [Community Guidelines](#). If you find something abusive or that does not comply with our terms or guidelines please flag it as inappropriate.

## [Download PDF](#)

---

This article was downloaded by **calibre** from <https://www.nature.com/articles/s41586-020-2985-2>

# Collections